

Edited by Paul T. Anastas

 **WILEY-VCH**

Green Processes



Volume 8: Green Nanoscience

Volume Editors:
Alvise Perosa
Maurizio Selva



Handbook of Green Chemistry

Volume 8
Green Nanoscience

Edited by
Alvise Perosa and
Maurizio Selva

Related Titles

Jiménez-González, C., Constable, D. J. C.

Green Chemistry and Engineering

A Practical Design Approach

2010

ISBN: 978-0-470-17087-8

Dunn, P., Wells, A., Williams, M. T. (eds.)

Green Chemistry in the Pharmaceutical Industry

2010

ISBN: 978-3-527-32418-7

Loos, K. (ed.)

Biocatalysis in Polymer Chemistry

2010

ISBN: 978-3-527-32618-1

Reichardt, C., Welton, T.

Solvents and Solvent Effects in Organic Chemistry

Fourth, Updated and Enlarged Edition

2010

ISBN: 978-3-527-32473-6

Pignataro, B. (ed.)

Tomorrow's Chemistry Today

**Concepts in Nanoscience, Organic Materials and Environmental Chemistry
Second Edition**

2009

ISBN: 978-3-527-32623-5

Roesky, H. W., Kennepohl, D. (eds.)

Experiments in Green and Sustainable Chemistry

2009

ISBN: 978-3-527-32546-7

Handbook of Green Chemistry

Volume 8
Green Nanoscience

Edited by
Alvise Perosa and Maurizio Selva



WILEY-VCH Verlag GmbH & Co. KGaA

The Editor

Prof. Dr. Paul T. Anastas

Yale University
Center for Green Chemistry & Green Engineering
225 Prospect Street
New Haven, CT 06520
UAS

Volume Editors

Prof. Dr. Alvise Perosa

Universit Ca'Foscari
Dipt. di Scienze Ambientali
Dorsoduro 2137
30123 Venezia
Italy

Prof. Dr. Maurizio Selva

Universit Ca'Foscari
Dipt. di Scienze Ambientali
Calle Larga S. Marta 2137
30123 Venezia
Italy

Handbook of Green Chemistry – Green Processes

Vol. 7: Green Synthesis

ISBN: 978-3-527-32602-0

Vol. 8: Green Nanoscience

ISBN: 978-3-527-32628-0

Vol. 9: Designing Safer Chemicals

ISBN: 978-3-527-32639-6

Set III (3 volumes):

ISBN: 978-3-527-31576-5

Handbook of Green Chemistry

Set (12 volumes):

ISBN: 978-3-527-31404-1

eBook ISBN: 978-3-527-62869-8

The cover picture contains images from Corbis Digital Stock (Dictionary) and PhotoDisc, Inc./Getty Images (Flak containing a blue liquid).

All books published by Wiley-VCH are carefully produced. Nevertheless, authors, editors, and publisher do not warrant the information contained in these books, including this book, to be free of errors. Readers are advised to keep in mind that statements, data, illustrations, procedural details or other items may inadvertently be inaccurate.

Library of Congress Card No.: applied for

British Library Cataloguing-in-Publication Data

A catalogue record for this book is available from the British Library.

Bibliographic information published by the Deutsche Nationalbibliothek

The Deutsche Nationalbibliothek lists this publication in the Deutsche Nationalbibliografie; detailed bibliographic data are available on the Internet at <http://dnb.d-nb.de>.

© 2012 Wiley-VCH Verlag & Co. KGaA,
Boschstr. 12, 69469 Weinheim, Germany

All rights reserved (including those of translation into other languages). No part of this book may be reproduced in any form – by photostriking, microfilm, or any other means – nor transmitted or translated into a machine language without written permission from the publishers. Registered names, trademarks, etc. used in this book, even when not specifically marked as such, are not to be considered unprotected by law.

Composition Thomson Digital, Noida, India

Printing and Binding betz-druck GmbH,
Darmstadt

Cover Design Adam-Design, Weinheim

Printed in the Federal Republic of Germany

Printed on acid-free paper

Print ISBN: 978-3-527-32628-0

Contents

About the Editors XI

List of Contributors XV

1	Formation of Nanoparticles Assisted by Ionic Liquids	1
	<i>Jackson D. Scholten, Martin H.G. Prechtl, and Jairton Dupont</i>	
1.1	Metal Nanoparticles in Ionic Liquids: Synthesis	1
1.1.1	Reduction of Organometallic Precursors	2
1.1.2	Decomposition of Organometallic Precursors	7
1.1.3	Transfer from an Aqueous/Organic Phase to the Ionic Liquid Phase	9
1.1.4	Bombardment of Bulk Materials	10
1.2	Metal Nanoparticles in Ionic Liquids: Stabilization	11
1.3	Metal Nanoparticles in Ionic Liquids: Recyclable Multiphase Catalyst-Systems	13
1.3.1	Hydrogenation of Multiple Bonds with Metal Nanoparticles in Ionic Liquids	14
1.3.2	Carbon–Carbon Cross-Coupling Reactions Catalyzed by Palladium Nanoparticles in Ionic Liquids	17
1.3.3	Functionalization and Defunctionalization Reactions Using Metal Nanoparticles in Ionic Liquids	19
1.3.4	Isotope Exchange Catalyzed by Metal Nanoparticles in Ionic Liquids	22
1.3.5	Application of Metal Nanoparticle Catalysts in Ionic Liquids for Energy- and Environment-Related Systems	24
1.4	General Remarks	26
	References	26
2	CO₂-Expanded Liquids for Nanoparticle Processing	33
	<i>Steven R. Saunders, Christopher B. Roberts, Kendall M. Hurst, Christopher L. Kitchens, Gregory Von White II, and D. Brad Akers</i>	
2.1	Introduction	33
2.1.1	Gas-Expanded Liquids	34
2.2	Controlling Nanoparticle Dispersibility and Precipitation	34

2.3	Size-Selective Fractionation of Nanoparticles	38
2.3.1	Small-Scale Size-Selective Fractionation	40
2.3.2	Large-Scale Size-Selective Fractionation	41
2.4	Tuning the Precipitation Range	45
2.4.1	Effect of Temperature	45
2.4.2	Effect of Solvent	45
2.4.3	Effect of Stabilizing Ligand	47
2.5	Modeling Nanoparticle Dispersibility in CXLs	47
2.6	Thin-Film Deposition	50
2.6.1	Nanoparticle Thin-Film Deposition on MEMS Devices	52
2.7	Formation and Synthesis of Nanoparticles in CXLs	53
2.8	Nanoparticle Phase Transfer Using CXLs	55
2.9	Conclusion	55
	References	56

3 Green Synthesis and Applications of Magnetic Nanoparticles 61

Liane M. Rossi, Alexandre L. Parize, and Joel C. Rubim

3.1	Introduction	61
3.2	Green Synthesis of Magnetic Nanoparticles	62
3.2.1	Background	62
3.2.2	Thermal Decomposition Methods	62
3.2.3	Microemulsion Methods	67
3.2.4	Preparation of Magnetic NPs Using Renewable Resources	68
3.2.5	Synthesis of Magnetic NPs in Ionic Liquids	68
3.2.6	Other Methods	69
3.3	Magnetic Separation as a Green Separation Tool	69
3.3.1	Background	69
3.3.2	Oil Spill Containment and Recovery	71
3.3.3	Heavy Metal Recovery	72
3.3.4	Catalyst Recovery and Recycling	73
3.3.4.1	Metal Complex Catalysts	73
3.3.4.2	Metal Nanoparticle Catalysts	74
3.3.4.3	Organocatalysts	76
3.4	Conclusion	77
	References	78

4 Photocatalysis by Nanostructured TiO₂-based Semiconductors 89

Matteo Cagnello and Paolo Fornasiero

4.1	Introduction	89
4.2	Structure and Photocatalytic Properties	93
4.2.1	Elements Affecting Bandgap and Photocatalytic Activity	93
4.2.2	Influence of the Structure on the Bandgap and the Photocatalytic Activity	97

4.2.3	Nanocomposites for Photocatalytic Applications	99
4.3	Nanostructures, Nanoarchitectures, and Nanocomposites for Pollution Remediation	100
4.3.1	Photocatalytic Applications in Wastewater Treatment	100
4.3.2	Photocatalytic Applications in Gas-Phase Decontamination	104
4.3.3	Photocatalytic Applications to Disinfection	106
4.4	Nanostructures, Nanoarchitectures, and Nanocomposites for Energy Applications	107
4.4.1	Photocatalytic Applications for Hydrogen Production	108
4.4.2	Photoelectrochemical Devices	113
4.4.3	Photocatalytic Applications in Artificial Photosynthesis	115
4.5	Nanostructures, Nanoarchitectures, and Nanocomposites for Green Synthesis	117
4.5.1	Oxidation Reactions	117
4.5.2	Reductions	118
4.5.3	Other Reactions	119
4.6	Materials Stability and Toxicology – Safety Issues	120
4.7	Conclusion	121
	References	122
5	Nanoencapsulation for Process Intensification	137
	<i>Aaron J. Yap, Anthony F. Masters, and Thomas Maschmeyer</i>	
5.1	Introduction and Scope	137
5.2	Cascade Reactions for Process Intensification	138
5.2.1	Background	138
5.2.2	Cascade Reactions with Incompatible Catalysts and Nanoencapsulation	140
5.2.3	Summary of Reactions and Systems	147
5.3	Other Cascade Reactions with Incompatible Catalysts – Polydimethylsiloxane (PDMS) Thimbles for Generic Site Isolation	148
5.4	Potential Methods of Nanoencapsulation	149
5.4.1	Layer-by-Layer (LbL) Methods	149
5.4.2	Sol-Gel-Based Methods	151
5.4.3	Inorganic Methods	153
5.4.3.1	Layered Inorganic Solids	153
5.4.3.2	Inorganic Spheres	154
5.4.4	Polymer-Based Methods	155
5.4.4.1	Micelle/Emulsion Encapsulation	156
5.4.4.2	Vesicle-Based Encapsulation	157
5.4.5	Cage Protein Encapsulation	158
5.4.6	Combinatorial Approaches	158
5.5	Conclusion and Future Directions	159
	References	160

6	Formation of Nanoemulsions by Low-Energy Methods and Their Use as Templates for the Preparation of Polymeric Nanoparticles	165
	<i>Gabriela Calderó and Conxita Solans</i>	
6.1	Introduction	165
6.2	Use of Nano-Emulsions as Templates for the Preparation of Polymeric Nanoparticles	167
	References	170
7	Toxicity of Carbon Nanotubes	175
	<i>Dania Mavia and Silvia Giordani</i>	
7.1	Introduction – Nanotoxicology: Should We Worry?	175
7.2	Toxicity of Carbon Nanotubes	177
7.2.1	Challenges in the Assessment of CNT Toxicity	177
7.2.1.1	Interaction with Dispersing Medium	178
7.2.1.2	Interaction with Cytotoxicity Assays	178
7.2.1.3	Effect of Impurities	180
7.2.1.4	Effect of Dispersion	180
7.3	Dermal Exposure to CNTs	180
7.3.1	Dermal Cytotoxicity	181
7.3.2	<i>In Vivo</i> Dermal Toxicity	182
7.4	Pulmonary Response to CNTs	183
7.4.1	Pulmonary Cytotoxicity	183
7.4.2	<i>In Vivo</i> Pulmonary Toxicity	184
7.5	Toxic Response to CNTs in the Intra-Abdominal Cavity	187
7.5.1	CNT Cytotoxicity in the Intra-Abdominal Cavity	187
7.5.2	<i>In Vivo</i> CNT Toxicity in the Intra-Abdominal Cavity	188
7.6	CNTs and Immunity	189
7.6.1	Recognition of CNTs by Macrophages	189
7.6.2	<i>In Vitro</i> Responses of Macrophages Exposed to CNTs	190
7.6.3	CNTs and Immunity <i>In Vivo</i>	191
7.6.3.1	Local Immune Responses	191
7.6.3.2	Allergic Immune Responses	192
7.6.3.3	Systemic Immune Alterations	192
7.7	CNT Interactions with the Cardiovascular Homeostasis	193
7.7.1	<i>In Vitro</i> Interactions	193
7.7.2	<i>In Vivo</i> CNT Toxicity to Cardiovascular Homeostasis	193
7.8	Genotoxicity and Mutagenicity of CNTs	194
7.8.1	<i>In Vitro</i> Studies	194
7.8.2	<i>In Vivo</i> Studies	194
7.9	Biodistribution and Pharmacokinetics of CNTs	195
7.9.1	Internalization of CNTs into Mammalian Cells	196
7.10	Biodegradation of CNTs	198
7.11	Biocompatibility of CNT-Based Biomaterials	198
7.12	Conclusions – Are CNTs safe?	198
	References	209

8	A Review of Green Synthesis of Nanophase Inorganic Materials for Green Chemistry Applications	217
	<i>Horner Genuino, Hui Huang, Eric Njagi, Lisa Stafford, and Steven L. Suib</i>	
8.1	Introduction	217
8.2	Green Synthesis of Nanophase Inorganic Materials	217
8.2.1	Metal Oxide Nanoparticles	217
8.2.1.1	Hydrothermal Synthesis	218
8.2.1.2	Reflux Synthesis	221
8.2.1.3	Microwave-Assisted Synthesis	222
8.3	Green Synthesis of Metallic Nanoparticles	223
8.4	Green Chemistry Applications of Inorganic Nanomaterials	225
8.4.1	Manganese Oxides	226
8.4.2	Titanium Dioxide	227
8.5	Environmental Applications of Nanomaterials	231
8.5.1	Background	231
8.5.2	Titanium Dioxide Nanomaterials	231
8.5.3	Zinc Oxide Nanomaterials	232
8.5.4	Iron-Based Nanomaterials	232
8.6	Conclusion and Future Perspectives	233
	References	234
9	Use of Extracted Anthocyanin Derivatives in Nanostructures for Solar Energy Conversion	245
	<i>Gabriele Giancane, Vito Sgobba, and Ludovico Valli</i>	
	References	257
10	Nanomaterials from Biobased Amphiphiles: the Functional Role of Unsaturations	261
	<i>Vijai Shankar Balachandran, Swapnil Rohidas Jadhav, and George John</i>	
10.1	Introduction	261
10.1.1	Plant/Crop-Based Resources for Practicing Sustainable Chemistry	263
10.1.2	Self-Assembly and Noncovalent Strategy for the Synthesis of Soft-Materials	264
10.2	Cashew Nut Shell Liquid (CNSL)	265
10.2.1	Extraction of CNSL and Its Components	265
10.2.2	Lipid Nanotubes and Helical Fibers from Cardanyl Glycolipids	266
10.2.3	Self-Assembled Gels from Cardanyl Glycosides	268
10.2.4	Antibacterial Nanocomposite Films for Coatings	273
10.2.5	Stimuli-Responsive Nature of Unsaturations	275
10.3	Conclusion	276
	References	277
Index	281	

About the Editors

Series Editor



Paul T. Anastas joined Yale University as Professor and serves as the Director of the Center for Green Chemistry and Green Engineering there. From 2004–2006, Paul was the Director of the Green Chemistry Institute in Washington, D.C. Until June 2004 he served as Assistant Director for Environment at the White House Office of Science and Technology Policy where his responsibilities included a wide range of environmental science issues including furthering international public-private cooperation in areas of Science for Sustainability such as Green Chemistry. In 1991, he established the industry-government-university partnership Green Chemistry Program, which was expanded to include basic research, and the Presidential Green Chemistry Challenge Awards. He has published and edited several books in the field of Green Chemistry and developed the 12 Principles of Green Chemistry.

Volume Editors

Maurizio Selva earned his Laurea degree (cum Laude) in Industrial Chemistry in 1989, at the Università degli Studi Ca' Foscari Venezia. From 1990 until 1992, Maurizio Selva was first a researcher for the National Council of Research (Italian CNR, research scholarship) and then a grant holder from Tessenderlo Chemie (<http://www.tessenderlo.com>) at the Department of Environmental Sciences of the Università Ca' Foscari Venezia, where he worked as a research associate. In January 1993, he obtained the position of Assistant Professor of organic chemistry at the same University. In 2000, Maurizio Selva was visiting researcher at the NSF Science Technology Center for Environmentally Responsible Solvents and Processes of the University of North Carolina at Chapel Hill (NC, USA), where he studied synthetic organic methodologies based on dense CO₂ as a solvent. In 2002, he was appointed



Maurizio Selva (on the right) and Alvise Perosa (left) lead the Green Chemistry group at the Department of Molecular Sciences and Nanosystems of the University Ca' Foscari Venezia.

Associate Professor of Organic Chemistry at the University of Venice, Italy, where he is currently working. In the period 1999–2003, Maurizio Selva was Director of the Green Chemistry Laboratory of the Interuniversity Consortium Chemistry for the Environment (<http://www.incaweb.org/>), at the Scientific and Technological Park “VEGA” in Marghera, Italy. Since 2009, Maurizio Selva is Deputy-coordinator of the Doctoral School in Chemical Sciences at the Università Ca’ Foscari Venezia, and scientific advisor for the “Coordinamento Interuniversitario Veneto per le Nanotecnologie” (<http://www.civen.org/it/>). Major research interests of Maurizio Selva are focussed on eco-friendly methodologies for organic syntheses. Particularly, based on the use of non-toxic compounds belonging to the class of dialkyl carbonates, of compressed CO₂ as a reagent/solvent under batch and continuous-flow conditions, and of ionic liquids as organocatalysts and mediators for multiphase reaction systems. Maurizio Selva is (has been) active as scientific referent also in projects for research and education joint activities in Green Chemistry, funded by the European Social Fund (ESF) through local Government structures (Regione Veneto).

Alvise Perosa graduated in industrial chemistry in 1992 at the Università Ca’ Foscari of Venice, Italy. In 1996 he obtained his PhD degree in chemistry as a Fulbright fellow at Case Western Reserve University in Cleveland, USA with Tony Pearson. He returned to Venice as a post-doc, where he got deeply involved with green chemistry

as a researcher and through the European Summer School on Green Chemistry, that he coordinated from 1998 to 2006. His research focus was then mainly on the development of new multiphase catalytic systems for synthesis and for detoxification, and on the use of organic carbonates as green alkylating agents. In 2005 Alvise Perosa obtained the position of “ricercatore” of organic chemistry, *i.e.* assistant professor, at the same university. He sits on the scientific board of the Edizioni Ca’ Foscari, on the International Relations Commission of the university, and on the Research Committee of the Department of Molecular Sciences and Nanosystems. Currently Alvise’s research focuses on greener synthesis of tailored ionic liquids and on their applications as organocatalysts including mechanism elucidation. Recent focus is on transformations of platform chemicals from biomass using green reagents, towards renewable chemical building blocks. The Green Organic Synthesis Team (GOST) at the Università Ca’ Foscari of Venice is run jointly with Maurizio Selva. In 2007 Alvise Perosa was visiting scientist at the University of Sydney as an Endeavour Research Fellow of the Australian Government, where he pursued research and collaborations with Thomas Maschmeyer in the fields of new functional catalytic materials for green transformations and for the upgrade of bio-based chemicals. This collaboration is ongoing through a joint PhD program between Venice and Sydney. As scientific consultant of the Green Oil project in 2011 he set up a pilot-plant scale supercritical carbon dioxide extraction/reaction system applied to the valorization of chemicals from biomass.

List of Contributors

D. Brad Akers

Clemson University
Chemical and Biomolecular
Engineering
130 Earle Hall
Clemson, SC 29634
USA

Vijai Shankar Balachandran

City College of New York
Department of Chemistry
160 Convent Avenue
New York, NY 10031
USA
and
City University of New York
Graduate School and University Center
of New York
365 Fifth Avenue
New York, NY 10016
USA

Gabriela Calderó

Institute for Advanced Chemistry of
Catalonia
Consejo Superior de Investigaciones
Científicas (IQAC-CSIC) and
CIBER en Bioingeniería, Biomateriales
y Nanomedicina (CIBER-BBN)
C/ Jordi Girona 18–26
08034 Barcelona
Spain

Matteo Cargnello

University of Trieste
Department of Chemical and
Pharmaceutical Sciences
ICCOM-CNR Trieste Research Unit,
Centre of Excellence for Nanostructured
Materials (CENMAT) and INSTM –
Trieste Research Unit
Via L. Giorgieri 1
34127 Trieste
Italy

Jairton Dupont

Universidade Federal do Rio
Grande do Sul (UFRGS)
Institute of Chemistry
Laboratory of Molecular Catalysis
Av. Bento Gonçalves 9500
91501-970 Porto Alegre, RS
Brazil

Paolo Fornasiero

University of Trieste
Department of Chemical and
Pharmaceutical Sciences
ICCOM-CNR Trieste Research Unit,
Centre of Excellence for Nanostructured
Materials (CENMAT) and
INSTN – Trieste Research Unit
Via L. Giorgieri 1
34127 Trieste
Italy

Homer Genuino

University of Connecticut
Department of Chemistry
55 North Eagleville Road
Unit 3060
Storrs, CT 06269
USA

and

City University of New York
Graduate School and University Center
of New York
365 Fifth Avenue
New York, NY 10016
USA

Gabriele Giancane

Università del Salento
Dipartimento di Ingegneria
dell'Innovazione
Via Monteroni
73100 Lecce
Italy

George John

City College of New York
Department of Chemistry
New York, NY 10031
USA

and

City University of New York
Graduate School and University Center
of New York
365 Fifth Avenue
New York, NY 10016
USA

Silvia Giordani

Trinity College Dublin
School of Chemistry and Centre for
Research on Adaptive Nanostructures
and Nanodevices (CRANN)
College Green
Dublin 2
Ireland

Christopher L. Kitchens

Clemson University
Chemical and Biomolecular
Engineering
130 Earle Hall
Clemson, SC 29634
USA

Hui Huang

University of Connecticut
Department of Chemistry
55 North Eagleville Road
Unit 3060
Storrs, CT 06269
USA

Thomas Maschmeyer

The University of Sydney
School of Chemistry (F11)
Sydney, NSW 2006
Australia

Kendall M. Hurst

Auburn University
Department of Chemical Engineering
212 Ross Hall
Auburn, AL 36849
USA

Anthony F. Masters

The University of Sydney
School of Chemistry (F11)
Sydney, NSW 2006
Australia

Swapnil Rohidas Jadhav

City College of New York
Department of Chemistry
New York, NY 10031
USA

Dania Movic

Trinity College Dublin
 School of Chemistry and Centre for
 Research on Adaptive Nanostructures
 and Nanodevices (CRANN)
 College Green
 Dublin 2
 Ireland

Eric Njagi

University of Connecticut
 Department of Chemistry
 55 North Eagleville Road
 Unit 3060
 Storrs, CT 06269
 USA

Alexandre L. Parize

Universidade de Brasília
 Campus Universitário Darcy Ribeiro
 Instituto de Química
 Asa Norte
 70910970 Brasília, DF
 Brazil

Martin H.G. Prechtli

Universidade Federal do Rio
 Grande do Sul (UFRGS)
 Institute of Chemistry
 Laboratory of Molecular Catalysis
 Av. Bento Gonçalves 9500
 91501-970 Porto Alegre, RS
 Brazil

Christopher B. Roberts

Auburn University
 Department of Chemical Engineering
 212 Ross Hall
 Auburn, AL 36849
 USA

Liane M. Rossi

Universidade de São Paulo
 Instituto de Química
 Departamento de Química
 Fundamental
 Av. Prof. Lineu Prestes 748
 Cidade Universitária
 05508-000 São Paulo, SP
 Brazil

Joel C. Rubim

Universidade de Brasília
 Campus Universitário Darcy Ribeiro
 Instituto de Química
 Asa Norte
 70910970 Brasília, DF
 Brazil

Steven R. Saunders

Auburn University
 Department of Chemical Engineering
 212 Ross Hall
 Auburn, AL 36849
 USA

Jackson D. Scholten

Universidade Federal do Rio
 Grande do Sul (UFRGS)
 Institute of Chemistry
 Laboratory of Molecular Catalysis
 Av. Bento Gonçalves 9500
 91501-970 Porto Alegre, RS
 Brazil

Vito Sgobba

Friedrich-Alexander-Universität
 Erlangen
 Department Chemie und Pharmazie
 Egerlandstrasse 3
 91058 Erlangen
 Germany

Conxita Solans

Institute for Advanced Chemistry of Catalonia
Consejo Superior de Investigaciones Científicas (IQAC-CSIC) and
CIBER en Bioingeniería, Biomateriales y Nanomedicina (CIBER-BBN)
C/ Jordi Girona 18–26
08034 Barcelona
Spain

Lisa Stafford

University of Connecticut
Department of Chemistry
55 North Eagleville Road
Unit 3060
Storrs, CT 06269
USA

Steven L. Suib

University of Connecticut
Department of Chemistry
55 North Eagleville Road
Unit 3060
Storrs, CT 06269
USA
and
University of Connecticut
Department of Chemical Engineering and Institute of Materials Science
191 Auditorium Road
Storrs, CT 06269
USA

Ludovico Valli

Università del Salento
Dipartimento di Ingegneria dell'Innovazione
Via Monteroni
73100 Lecce
Italy

Gregory Von White II

Clemson University
Chemical and Biomolecular Engineering
130 Earle Hall
Clemson, SC 29634
USA

Aaron J. Yap

The University of Sydney
School of Chemistry (F11)
Sydney, NSW 2006
Australia

1

Formation of Nanoparticles Assisted by Ionic Liquids

Jackson D. Scholten, Martin H.G. Prechtl, and Jairton Dupont

Imidazolium ionic liquids (ILs) have proven to be a suitable medium for the generation of a myriad of soluble metal nanoparticles (NPs). In particular, transition-metal NPs with small size and a narrow size distribution have been mainly prepared by reduction of organometallic compounds with molecular hydrogen or by decomposition of complexes in the zerovalent state in ILs. The formation and stabilization of nanoparticles in these fluids occurs with reorganization of the hydrogen bond network and the generation of nanostructures with polar and non-polar regions where the NPs are included. The IL forms a protective layer that is probably composed of imidazolium aggregate anions located immediately adjacent to the NP surface-providing the Columbic repulsion and counteractions that provide the charge balance. These stable transition metal NPs immobilized in the ILs are considered efficient green catalysts for general reactions in multiphase systems. In this chapter, the synthesis, stabilization, and catalytic applications of metal NPs in ILs and the recyclability of these systems are discussed.

1.1

Metal Nanoparticles in Ionic Liquids: Synthesis

Generally, stable and well-dispersed metal NPs have been prepared in ILs by the simple reduction of the M(I–IV) complexes or thermal decomposition of the organometallic precursors in the formal zero oxidation state. Recently, other methods such as the phase transfer of preformed NPs in water or organic solvents to the IL and the bombardment of bulk metal precursors with deposition on the ILs have been reported. However, one of the greatest challenges in the NPs field is to synthesize reproducibly metal NPs with control of the size and shape. Selected studies of the preparation of metal NPs in ILs that, in some cases, provide NPs with different sizes and shapes are considered in this section.

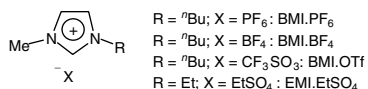
1.1.1

Reduction of Organometallic Precursors

Chemical reduction of the organometallic complexes is to the most often investigated process to produce metal NPs in ILs. This reduction pathway is generally achieved by the use of molecular hydrogen or hydrides as reducing sources. The reduction method was used, for example, to synthesize iridium NPs with irregular shapes and a monomodal size distribution (2.0 nm in diameter) from the reduction of $[\text{Ir}(\text{cod})\text{Cl}]_2$ ($\text{cod} = 1,5\text{-cyclooctadiene}$) by molecular hydrogen (4 atm) in $\text{BMI}.\text{PF}_6$ at 75°C (entry 1, Table 1.1) [1]. Following the same idea, several metal NPs such as rhodium [2], platinum [3], ruthenium [4], and palladium [5] were prepared in different ILs (entries 17, 18, 21 and 34, Table 1.1). These interesting results prompted additional investigations around the synthesis using other metal precursors in non-functionalized or functionalized ILs (Figure 1.1), producing NPs with different sizes and shapes (see Table 1.1).

Noteworthy, it was generally suggested that different factors may influence the control of the size and shape of metal NPs prepared in ILs. Such factors can be related to the type of metal precursor, the nature of the reducing agent, the reaction conditions, and the IL structure. The nature of the reducing agent and the metal complex is important owing to their subsequent generation of by-products that can coordinate to the metal surface and thus act as extra-stabilizers or poisons influencing

Classical non-functionalized ILs



Functionalized ILs

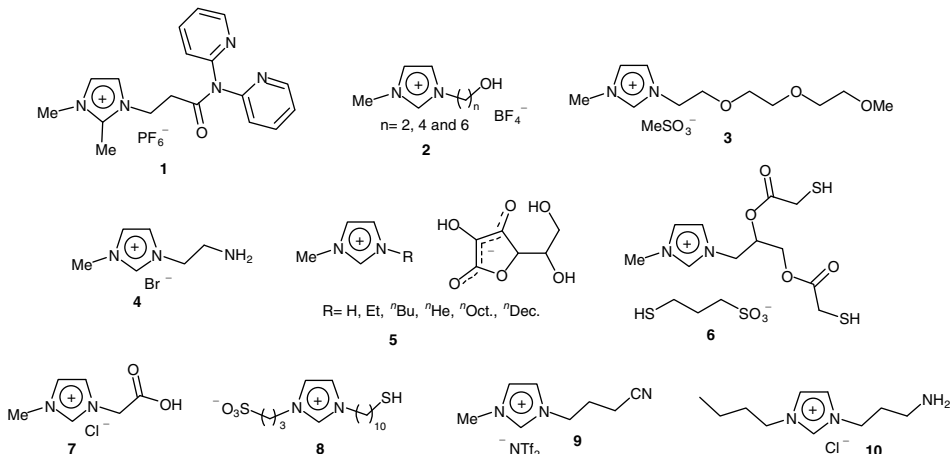


Figure 1.1 Selected examples of imidazolium ILs employed for the synthesis of metal NPs.

Table 1.1 Selected examples of metal NP synthesis in ILs by reduction method (for a complete review, see [25]).

Entry	IL	Metal precursor	Reducing agent	M(0) size (nm ^a)	Ref.
1	BMI.BF ₄ BMI.PF ₆ BMI.CF ₃ SO ₃ EMI.EtSO ₄ BMI.NTF ₂ BMI.BF ₄	[Ir(cod)Cl] ₂	H ₂	2.9 2.0 2.6 1.6 2.1 3.6	[1, 2, 6, 7, 26, 27]
2		[Ir(cod)(MeCN) ₂]BF ₄	H ₂		[28]
3	6	[HAuCl ₄]	NaBH ₄	2.0–3.5	[29]
4	8	[HAuCl ₄ .4H ₂ O]	NaBH ₄	2.4–2.7	[30]
5	3	[HAuCl ₄ .3H ₂ O]	Hydrazine	7.5 ^b	[31]
6	7	[HAuCl ₄]	NaBH ₄	3.5	[20]
7	4	[HAuCl ₄]	Trisodium citrate	23, 42, 98 ^c	[20]
8	10	[HAuCl ₄ .3H ₂ O]	NaBH ₄	33	[32]
9	5	[HAuCl ₄ .3H ₂ O]	Ascorbate	Various shapes and diameters ^d	[21]
10	BMI.PF ₆	[HAuCl ₄ .3H ₂ O]	Imidazolium cation	Prismatic particles ^e	[18]
11	BMI.NTF ₂ BMI.PF ₆ EMI.EtSO ₄	[HAuCl ₄ .4H ₂ O] [HAuCl ₄]	Zn Trisodium citrate NaBH ₄ ^f Ascorbic acid ^g	Dendrites ^h 9.4 3.9	[22] [19]
12				Nanorods Nanosheets ⁱ	
13	BMI.BF ₄	[HAuCl ₄ .3H ₂ O]	Microwaves		[33]
14	6	[Na ₂ Pt(OH) ₆]	NaBH ₄	2.0–3.2	[29]
15	7	[H ₂ PtCl ₆] [Pt(acac) ₂]	NaBH ₄	2.5	[20]
16			1,2-Hexadecanediol	4.5 ^j	[34]

(Continued)

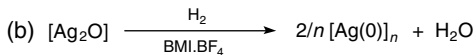
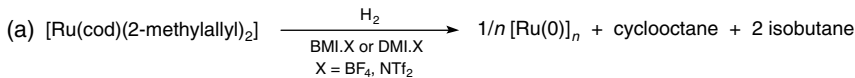
Table 1.1 (Continued)

Entry	IL	Metal precursor	Reducing agent	M(0) size (nm) ^{a)}	Ref.
17	BMI.BF ₄ BMI.PF ₆ BMI.BF ₄ BMI.PF ₆ BMI.CF ₃ SO ₃ BMI.NTF ₂	[PtO ₂] [RuO ₂] [Rui(cod)(2-methylallyl) ₂] BMI.BF ₄ DMI.NTF ₂ DMI.BF ₄	H ₂ H ₂ H ₂ H ₂	3.0 2.3 2.0 2.5 2.5 2.1 2.9 2.1 2.7	[3] [4] [12]
18					
19					
20					
21	BMI.PF ₆	[Ru(cod)(2-methylallyl) ₂] [Pd(acac) ₂] [Pd(cod)Cl ₂] [PdCl ₂] [PdCl ₂] [PdCl ₂] [PdCl ₂] [Pd(OAc) ₂] [Pd(OAc) ₂] [Pd(OAc) ₂]	H ₂ H ₂ H ₂ H ₂ H ₂ H ₂ H ₂ H ₂ H ₂	2.2 4.9 6–8 7 12 ^{b)} 150, 30, and 10 ^{k)} 5–6 1.0 1.3	[13] [5] [8] [8] [9] [35] [10, 11] [36] [37]
22	BMI.PF ₆				
23	BMI.PF ₆				
24	BMI.PF ₆				
25	2				
26	1				
27	BMI.Br or BMI.BF ₄				
28	BMI.PF ₆				
29	BMI.BF ₄ and others	[AgX] (X = BF ₄ , PF ₆ , OTf), or [Ag ₂ O] [AgNO ₃] [AgNO ₃] [AgNO ₃] [AgOTf]	H ₂	2.8–26.1 ^{m)}	[14]
30	2				
31	BMI.MeSO ₄				
32	EMI.OTf				
	BMI.OTf				

33	BML.BF ₄	[AgBF ₄] [RhCl ₃ .3H ₂ O]	e ⁻ H ₂	Dendrites 2.3	[40] [2]
34	BML.PF ₆	[RhCl ₃ .3H ₂ O]	NaBH ₄	2.0 ^{a)}	[41, 42]
35	BML.PF ₆	[RhCl ₃ .nH ₂ O]	H ₂	5.0	[15]
36	BML.BF ₄	[Rh(cod)Cl] ₂	H ₂	15 ^{b)}	[9]
37	BML.PF ₆				

- a) Determined by TEM.
- b) Determined by XRD.
- c) Depends on citrate concentration.
- d) Various particle morphologies can form, such as quasi-spherical, raspberry-like, flakes, or dendritic, depending on the N-alkylimidazolium side chain.
- e) Broad size range of 3–20 µm in diameter and 10–400 nm in thickness in BML.PF₆, whereas uniform, single-crystal nano- and microprisms with a size of about 100 µm in BML.NTf₂.
- f) Dendritic gold nanostructures with a three-order hierarchy resulting from fractal growth.
- g) In the presence of trisodium citrate and cetyltrimethylammonium bromide (CTAB).
- h) In the presence of AgNO₃ and gold spherical nanoseeds
- i) Nanosheets with a size larger than 30 µm in length and thickness of about 50 nm.
- j) In the presence of oleic acid and oleylamine.
- k) Depends on IL.
- l) Pd-biscarbene complex was first formed with a subsequent sonolytic conversion to Pd metal zerovalent species.
- m) Depends on IL, silver precursor, and the presence of a scavenger.
- n) By plasma-electrochemical deposition.
- o) Bipy-THF was used as an extra-stabilizer ligand.

the properties (optical, magnetic, and catalytic) of the metal NPs. This can be applied mainly for precursors containing halides as ligands that generate undesirable coordinative halide anions that coordinate strongly on the metal surface. Hence it is preferable to use precursors containing weak coordinating ligands or hydrocarbons that are reduced and produce only innocuous compounds (Scheme 1.1).



Scheme 1.1 Selected examples of metal precursors containing likely ligands or that produce innocuous compounds after NPs synthesis.

In relation to the reducing agent, hydrogen gas, metal hydrides, and irradiation methods are the most investigated approaches used to produce metal NPs in ILs.

Molecular hydrogen has been widely used as a reducing agent for many reactions owing to its mild reductive character. However, acid is produced as the sole by-product that in some cases must be trapped by the use of Lewis bases (scavengers). In this context, hydrogen was employed as an efficient reducing agent during NP formation in ILs. As an example, soluble and stable Ir(0) NPs (1.6–2.9 nm) were prepared under reductive conditions from the precursor $[\text{Ir}(\text{cod})\text{Cl}]_2$ in different imidazolium ILs (entry 1, Table 1.1) [1, 2, 6, 7].

Several palladium precursors, such as $[\text{Pd}(\text{acac})_2]$ [5], $[\text{Pd}(\text{cod})\text{Cl}_2]$ [8], and $[\text{PdCl}_2]$ [8, 9] dispersed in BMI.PF₆, afford irregular metal NPs with diameters in the range 4.9–12.0 nm (entries 21–24, Table 1.1). In addition, the precursor $[\text{Pd}(\text{OAc})_2]$ dispersed in a functionalized IL (1) was also reduced to Pd(0) NPs (5.0–6.0 nm) in the presence of hydrogen (entry 26, Table 1.1) [10, 11]. This reductive procedure was also extended to the synthesis of Pt(0) [3], Ru(0) [4, 12, 13], Ag(0) [14], and Rh(0) [2, 9, 15] NPs in ILs (see entries 17–20, 29, 34, 36, and 37, Table 1.1).

Metal hydrides have also been extensively studied as reductive agents for the preparation of metal NPs in ILs. Nonetheless, hydride sources are not likely to be used in ILs owing to the easy deprotonation of the imidazolium cation, providing undesirable N-heterocyclic carbenes (NHCs) in the reaction medium [16]. Moreover, these hydrides afford sodium and boron compounds that are difficult to remove from the IL. In most cases, the use of metal hydrides produces irregular spherical metal NPs, probably owing to their strong reducing character, transforming the precursor quickly into the metal NPs (see Table 1.1).

Interestingly, in some cases the IL itself can act as the reductive agent. Spherical metal silver NPs were prepared in a hydroxyl-functionalized IL (2) (entry 30, Table 1.1) [17]. In this case, the hydroxyl moiety of the IL plays a reductive role, being oxidized to the corresponding aldehyde. In a similar manner, for Au(III) precursors, the imidazolium cation itself can act as a reducing agent to yield prismatic particles in BMI.PF₆ with a very broad size range of diameter 3–20 μm and thickness

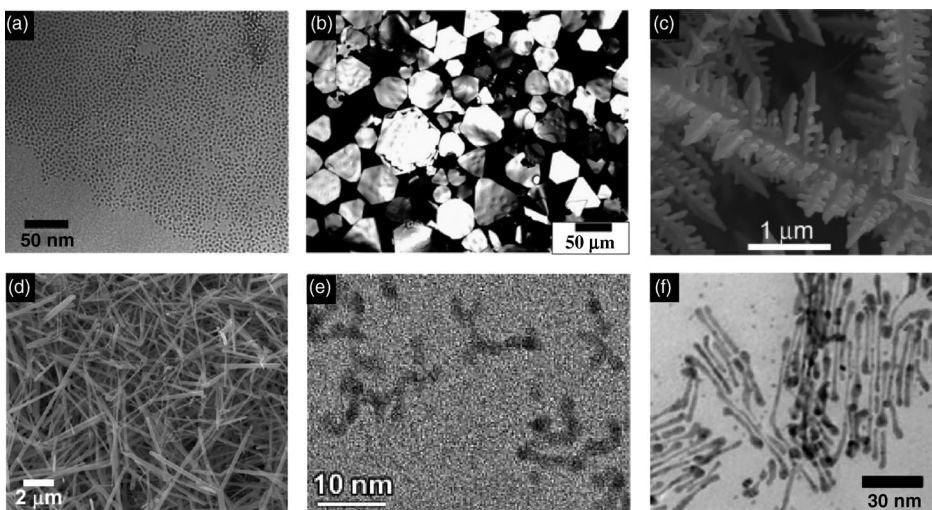


Figure 1.2 Metal NPs prepared in ILs by reduction using different reducing agents: (a) Ru(0) nanospheres [12]; (b) Au(0) prisms [18]; (c) Au(0) dendrites [22]; (d) Ag(0) nanowires [23]; (e) Ir(0) nanoworms [24]; (f) Au(0) nanorods [19]. Reprinted with permission from [25] (© The Royal Society of Chemistry).

10–400 nm (entry 10, Table 1.1) [18]. Moreover, single-crystal nano- and microprisms with larger sizes of diameter \sim 100 μm were prepared using BMI.NTf₂.

In general, the use of soft reducing agents is preferable for obtaining metal NPs with control of the size and shape. This was demonstrated by the formation of variously shaped and sized gold nanostructures in ILs from the reduction of Au(III) with mild reducing agents such as ascorbate and/or citrate (entries 7, 9, and 12, Table 1.1) [19–21]. In fact, the presence of weak reducing agents possibly decelerates the particle's growth and then the stabilization of nanocrystals may be facilitated by the weak coordination ability of imidazolium ILs. Under these reaction conditions, it has been proposed that the size and shape of the NPs is determined by the preferential binding affinity of the imidazolium cations to low-density gold crystal facets [19].

Figure 1.2 shows the different sizes and shapes of metal NPs prepared in ILs using several types of reducing agents.

Noteworthy, irradiation and electrochemical methods have important advantages for the synthesis of metal NPs in ILs. Since they do not generate by-products, these methods are considered the cleanest procedures for obtaining stable metal NPs. Selected examples are summarized in Table 1.1.

1.1.2

Decomposition of Organometallic Precursors

The decomposition of metal precursors in its zerovalent state constitutes a supplementary synthetic method to produce stable and well-dispersed NPs in ILs. As an

example, the decomposition of $[\text{Pt}_2(\text{dba})_3]$ [43] (dba = dibenzylideneacetone) and $[\text{Ru}(\text{cod})(\text{cot})]$ [44] (cot = 1,3,5-cyclooctatriene) dispersed in ILs affords metal NPs with mean diameters of 2.0–2.5 and 2.6 nm, respectively. Particularly for Ru, using a previously reported method developed by Chaudret and co-workers [45, 46], large superstructures 57 nm in diameter were formed and inside these structures Ru(0) NPs (2.6 nm) could be observed.

Interestingly, it was demonstrated that the size of Ru(0) NPs synthesized from the precursor $[\text{Ru}(\text{cod})(\text{cot})]$ dissolved in ILs varies between 0 and 25 °C [47]. In addition, the presence of stirring has a dramatic effect related to the agglomeration of the NPs. Lower temperatures resulted in smaller particles (~1 nm) whereas higher temperatures (25–75 °C) led to slightly larger particles (2–3 nm). Metal NPs prepared at 0 °C under stirring aggregated into large clusters 2–3 nm in size, but no agglomeration was observed for the NPs synthesized without stirring at the same temperature. These observations indicate that at lower temperatures (0 °C), the metal species in IL are better isolated than at high temperatures (25 °C). This effect may be directly related to the type of organization of the ILs [48]. As expected, at low temperatures and without stirring, the organization of supramolecular aggregates in ILs tends to be better maintained, increasing the efficiency of the confinement of the metal species in the IL structure, thus providing smaller particles. On the other hand, the presence of stirring, even at 0 °C, was suggested to perturb this 3D organization and to lead to partial agglomeration of the metal NPs, thereby yielding larger particles. The influence of the IL 3D organization on the size of ruthenium NPs has also been reported [49], where a linear relationship between the NP size and the length of the alkyl chain in IL was observed. In addition, the NP crystal growth could be controlled by the local concentration of the Ru precursor, $[\text{Ru}(\text{cod})(\text{cot})]$, and also be limited to the size of the IL non-polar domain.

This is in agreement with earlier observations on the formation of nickel NPs with a narrow size distribution from the decomposition of $[\text{Ni}(\text{cod})_2]$ in imidazolium ILs [50, 51].

Metal carbonyl compounds are other suitable precursors for the synthesis of NPs by thermal decomposition. The main advantage is the formation of CO that is expelled from the IL phase due to its poor solubility. However, high temperatures are commonly used to decompose such precursors. Metal NPs of Cr(0), Mo(0), and W(0) were prepared by thermal or photolytic decomposition of their respective monometallic carbonyl compounds $[\text{M}(\text{CO})_6]$ dispersed in ILs [52]. Similarly, the precursors $[\text{Fe}_2(\text{CO})_9]$, $[\text{Ru}_3(\text{CO})_{12}]$, and $[\text{Os}_3(\text{CO})_{12}]$ were employed in order to obtain stable metal NPs (1.5–2.5 nm) in BMI.BF₄ [53]. The same procedure was extended to the preparation of Ir(0), Rh(0), and Co(0) NPs in ILs [54].

Independently, irregular Co(0) NPs with diameters of 7.7 and 4.5 nm were generated by thermal decomposition of $[\text{Co}_2(\text{CO})_8]$ dissolved in BMI.NTf₂ and DMI.BF₄, respectively, at 150 °C (Figure 1.3) [55]. Noteworthy, Co(0) nanocubes (79 nm in diameter) were prepared by decomposition of the precursor in DMI.NTf₂ under the same reaction conditions and without additional stabilizers (Figure 1.3) [56]. Together with these shape-controlled NPs, irregular Co(0) NPs (11 nm) were also detected. It was observed that the relative ratio between nanocubes and

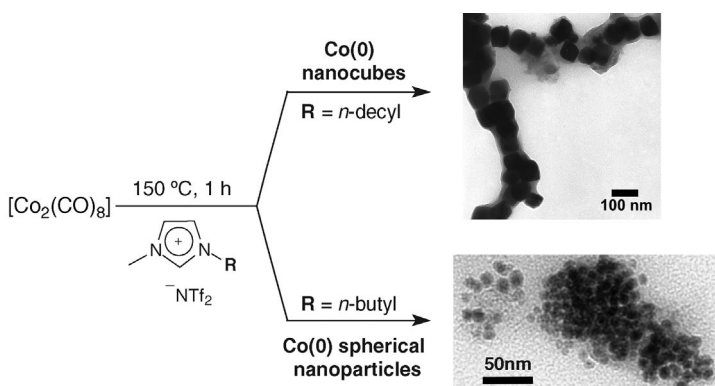


Figure 1.3 Synthesis of $\text{Co}(0)$ NPs exhibiting different sizes and shapes depending on the nature of the IL. Reprinted with permission from [55] and [56] (© Wiley-VCH Verlag GmbH).

irregular $\text{Co}(0)$ NPs depend on the reaction time. In the case of DMI.FAP [FAP = tris (perfluoroethyl)trifluorophosphate], the presence of nanocubes was observable only at the beginning of reaction (5 min) and they were transformed into irregular NPs with a long reaction time. This is interesting because by choosing the type of IL and reaction conditions properly it is possible to modulate the selectivity between shape-controlled and irregular $\text{Co}(0)$ NPs.

1.1.3

Transfer from an Aqueous/Organic Phase to the Ionic Liquid Phase

It is well known that the transfer of metal NPs from an aqueous phase to an organic phase is better achieved in the presence of classical ligands, such as amines and thiols [57]. These compounds, acting as capping ligands on the NP surface, increase the solubility of the NP in the organic phase. In this context, water-soluble $\text{Au}(0)$ NPs prepared in the presence of a thiol-functionalized IL were efficiently transferred to the hydrophobic IL HMI. PF_6^- (HMI = 1-n-hexyl-3-methylimidazolium) [58]. In particular, HPF_6^- was used as phase-transfer agent, inducing NP solubility on the HMI. PF_6^- phase due to the exchange of Cl^- with PF_6^- in the water-soluble thiol-functionalized IL. Hence the NPs could be easily transferred from the aqueous to the IL phase.

In the same context, aqueous gold NPs were prepared by the reduction of $[\text{HAuCl}_4]$ with NaBH_4 in the presence of poly(1-methyl-3-vinylbenzylimidazolium chloride) IL (ILP) [59]. On adding BMI. PF_6^- to the aqueous solution, the $\text{Au}(0)$ NPs were partially transferred from the aqueous phase into the IL phase. Using HPF_6^- in the NP preparation and after addition of BMI. PF_6^- , the NPs were totally transferred to the IL phase without significant aggregation. Thus, the ILP anion exchange from Cl^- to the same anion of the IL employed (in this case PF_6^-) improved the NP transfer to the IL phase. The same result was observed on employing LiNTf_2 during NP synthesis and further addition of BMI. NTf_2 to the

aqueous phase. The same procedure was also extended to the synthesis of Pt(0) and Pd(0) NPs.

The organic phase transfer was observed for surfactant-stabilized Rh(0) NPs previously synthesized in an aqueous solution of *N,N*-dimethyl-*N*-dodecyl-*N*-(2-hydroxyethyl)ammonium chloride (HEA12.Cl) [60]. The addition of LiNTf₂ to the aqueous suspension of Rh-HEA12.Cl transferred the hydrosol NPs to the IL phase (HEA12.NTf₂).

1.1.4

Bombardment of Bulk Materials

Recently, the synthesis of metal NPs in ILs by the bombardment technique has attracted much attention as an alternative method to generate NPs. This clean method consists in the bombardment of large NPs or bulk metals with laser irradiation or gaseous ions that cause the photoejection of electrons, which induces subsequent fragmentations [61], affording smaller particles. This procedure is suitable in some cases for the generation of small NPs from large agglomerated particles. For example, the *in situ* laser irradiation of large Pd(0) (12 nm) and Rh(0) (15 nm) NPs in ILs produces NPs with diameters of 4.2 and 7.2 nm, respectively [9].

In recent years, the sputter deposition technique has proved to be an innovative, simple and clean synthetic method to synthesize metal NPs. In the sputter method, the bombardment of a metal foil surface with energetic gaseous ions causes the physical ejection of surface atoms and/or small metal clusters [62]. These metallic atoms or clusters are dispersed in ILs, resulting in stable NPs without additional stabilizers and reducing agents. The preparation of soluble Au(0) NPs in ILs by simple sputtering of a gold foil has been reported [63, 64]. Moreover, the size of the Au(0) NPs depends on the nature of the IL, achieving 1.9–2.3 nm for a quaternary ammonium IL ($\text{NMe}_3\text{Pr}.\text{NTf}_2$) and 5.5 nm for an imidazolium IL (EMI.BF₄). Noteworthy, the size of the NPs apparently depends on the type of IL but not on the time of sputtering. This technique was also employed for the synthesis of Ag(0) NPs [65, 66] in BMI.PF₆ and Pt(0) [67] NPs in $\text{NMe}_3\text{Pr}.\text{NTf}_2$.

Recently, it was reported that the size and size distribution of gold NPs prepared by sputter deposition in ILs depend particularly on the surface composition of the IL and less so on the surface tension and viscosity [68]. Moreover, under the conditions used, the size of the NPs was independent of the sputtering time. However, the mean diameter of the resultant Au NPs showed a slight tendency to increase with increase in the discharge current (current = 20–110 mA; NP diameter = 3.2–4.6 nm). On applying a higher discharge current, more Au atoms hit the IL surface per unit time, changing the kinetics of particle growth on the surface of the IL. Hence in this case, it was assumed that both nucleation and NP growth occur mainly on the IL surface. Additionally, a considerable change in the NP size was observed on changing the IL surface composition by increasing the concentration of fluorinated moieties (NP size in BMI.X: X = NTf₂ = 3.5 nm; BF₄ = 3.6 nm; PF₆ = 3.7 nm; and FAP = 4.9 nm).

1.2

Metal Nanoparticles in Ionic Liquids: Stabilization

One of the most important aspects related to the synthesis of metal NPs in ILs is a better understanding of how these salts interact with the NPs. However, it is essential to consider the physicochemical properties of the ILs. In particular, imidazolium-based ILs possess unique properties such as high thermal and chemical stability, a large electrochemical window, high ion density, relatively low viscosity, and negligible vapor pressure and are liquids over a wide range of temperatures (down to -80°C) [69]. Noteworthy, imidazolium ILs differ from classical salts in one respect: they display organized supramolecular structures mainly through hydrogen bonds [70–72] that induce structural directionality, in contrast to classical salts where the aggregates present charge-ordered structures. The highly ordered structure of imidazolium salts follows a typical trend where one cation is surrounded by at least three anions and one anion by three cations [73]. Owing to its high organization at the nanomolecular scale, ILs can be used as “entropic drivers” (*IL effect*) to induce ordering of the nanoscale structures. Moreover, recently studies showed that the properties of ILs are based on their formation of aggregates of the type $\{[(\text{DAI})_x(\text{X})_{x-n}]^{n+} \mid (\text{DAI})_x(\text{X})_x]^{n-}\}_m$ (where DAI is the dialkylimidazolium cation and X is the anion) rather than on their isolated ions [74–76]. On the 3D arrangement of the IL, the formation of chains due to the imidazolium cation generates channels in which the anions are accommodated (Figure 1.4).

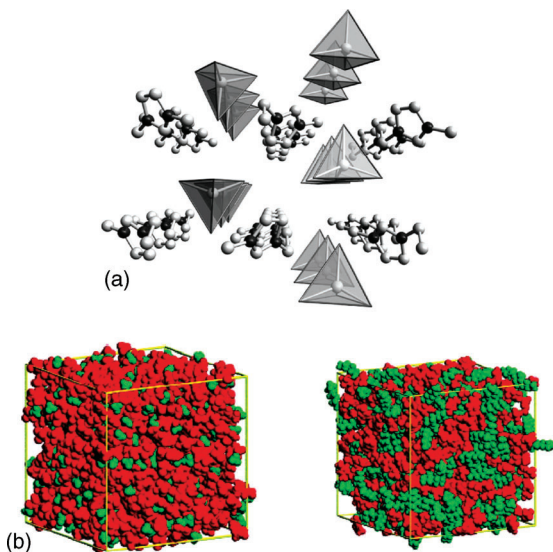


Figure 1.4 (a) Supramolecular 3D organization of imidazolium ILs showing the arrangement of cations (in this case 1-ethyl-3-methylimidazolium) and the tetrahedral anions; (b) simulation studies for the ILs EMI.PF₆ (left) and OMI.PF₆ (right) (700 ions) evidencing the polar (red) and non-polar (green) domains. Reprinted with permission from [77] (© American Chemical Society) and [80] (© Wiley-VCH Verlag GmbH).

Importantly, the presence of polar and non-polar domains in imidazolium ILs [77] affects their solvation and their ability to interact with different species. In fact, polar substrates are preferentially dissolved in polar domains and non-polar compounds in non-polar domains (Figure 1.4) [78, 79]. As a consequence, the final size and shape of NPs can be tuned by the volume of these ILs domains.

Generally, it is most likely that metal NPs are stabilized by the aggregates of the non-functionalized imidazolium ILs rather than by the isolated ions. In addition, the interaction between ILs and the metal NPs have been evidenced by X-ray photo-electron spectroscopy (XPS), small-angle X-ray scattering (SAXS), isotope labeling, and surface-enhanced Raman spectroscopy (SERS) techniques.

XPS of the isolated metal NPs prepared in ILs containing the PF_6^- and BF_4^- anions revealed the IL–metal surface interaction to be M–O (metal–oxide) and M–F contributions in most cases [5, 6, 44, 81]. These results clearly indicate that even relatively weak coordinating anions (PF_6^- and BF_4^-) coordinate with the metal surface. The M–O interaction observed by XPS also indicates that the metal NPs are susceptible to oxidation and the oxide layer is another source for the stabilization of NPs [82]. However, after sputtering of Ar^+ , mainly the M–M component at the 4f region could be detected, indicating that only external atoms on the NP surface were bound to F and O. In particular, XPS of Rh(0) NPs prepared in BMI. PF_6 and in the presence of a bipyridine ligand showed the fluorine signal (residual IL) and nitrogen possibly due to the bipy ligand [41]. *In situ* XPS investigations also demonstrated the chemical interaction between the IL EMI.EtSO₄ and Ir(0) NPs [7]. In the presence of the Ir(0) NPs, the C-2 component of the imidazolium cation shifted 0.3 eV to lower binding energy, indicating that the C-2 is turning into a more pronounced nucleophilic character (probable formation of NHC species) and the IL is interacting with the NP surface.

SAXS measurements of the dispersed metal NPs in ILs indicated the formation of an IL layer surrounding the NPs. Moreover, this IL layer depends on the anion chosen. Remarkably, inconsistent results were attained by the Guinier Approximation law in the small-angle region, indicating that the assumption that the NPs are simply diluted in the ILs cannot be applied in these cases. However, the calculations using Porod's law yielded consistent results. Porod's model assumed the presence of two phases, a crystalline phase (nanocrystal or NPs) and a semi-ordered phase (IL) [71, 83–85]. Hence this model can be used since ILs are not considered as statistical aggregates of anions and cations but instead as a three-dimensional network of anions and cations, forming supramolecular structures of the type $\{[(\text{DAI})_x(\text{X})_{x-n}]^{n+} [(\text{DAI})_{x-n}(\text{X})_x]^{n-}\}_m$. In this context, the two-phase model was adopted to represent the nanocrystals dispersed in the IL [86]. The IL forms a protective layer surrounding the metal NP surface with an extended molecular length of around 2.8–4.0 nm depending on the type of anion, suggesting the presence of semi-organized anionic species composed of supramolecular aggregates of the type $[(\text{DAI})_{x-n}(\text{X})_x]^{n-}$. This protective layer is located immediately adjacent to the NP surface, fairly close to DLVO (Derjaguin–Landau–Verwey–Overbeek)-type stabilization, but this model cannot completely explain the stabilization properties of

imidazolium ILs towards the metal NPs. The DLVO model was not designed to account for counterions with multiple charges, nor was it designed to account for sterically stabilized systems [87, 88].

Isotope labeling experiments have been used as a suitable probe to clarify the interaction mode between metal NPs and ILs. H–D exchange studies during NP formation by reduction of $[\text{Ir}(\text{cod})(\text{MeCN})_2]\text{BF}_4$ dissolved in BMI.NTf₂–acetone in the presence of 1,8-bis(dimethylamino)naphthalene with D₂ at 22 °C showed that ILs with hydrogens mainly in the C-2 position of the imidazolium ring form carbenes (NHCs) on the Ir(0) NP surface [28]. Using the reduction of the precursor $[\text{Ir}(\text{cod})\text{Cl}]_2$ by molecular hydrogen in deuterated ILs during cyclohexene hydrogenation, it was observed that the D/H labeling was preferred at the least acidic positions (C-4/C-5) of the imidazolium cation [89]. These results suggest the formation of transient NHC species and that the IL is likely interacting with the NP surface through the anionic aggregates rather than isolated ions.

Therefore, metal NPs in ILs are probably stabilized by protective layers via the loosely bond anionic moieties of the IL, oxide layer, and/or NHC transient species.

The stabilization of Au(0) NPs promoted by the imidazolium cation of a functionalized IL (**3**) was evidenced using SERS analyses [31]. In fact, a parallel coordination mode of the imidazolium cation on the Au(0) NP surface was revealed by SERS. Moreover, the ether functionality chain of IL is away from the NP surface, thus providing additional steric protection against aggregation. No significant interaction between the IL anion MeSO₃[−] and gold NPs was detected as the Raman signals of the anion were not surface-enhanced in the presence of the NPs. It is reasonable to assume this cation stabilization because zeta potential measurements indicated metal NPs with a negatively charged surface [90]. Analogous results were obtained using Ag(0) NPs in BMI.BF₄ [91]. The presence of small quantities of water caused considerable aggregation of the NPs and precipitation. However, in the absence of water the NPs are well dispersed in the IL, resulting in an observable SERS effect. This effect of water is probably related to the presence of the protective layer of IL. The presence of water prevents the stabilization of NPs by the IL layers causing NP aggregation and further precipitation; without water, these IL layers protect the NP surface against aggregation. In this case, the imidazolium cation interacts with the NPs in a flat mode and the anions form a second layer balancing the charge and do not interact with the NPs.

1.3

Metal Nanoparticles in Ionic Liquids: Recyclable Multiphase Catalyst-Systems

Transition metal NPs dispersed in ILs are recognized as suitable catalyst systems for many reaction types with both typical homogeneous and heterogeneous catalysis (see Sections 1.3.1–1.3.5). The most investigated reactions are the hydrogenation of multiple bonds and arenes [1, 5, 12, 13, 43, 44, 54, 80, 89, 92], carbon–carbon cross-

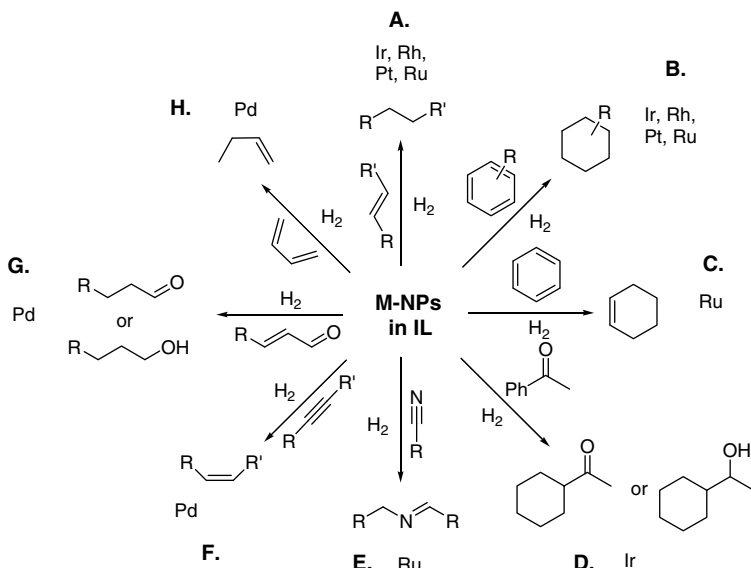
coupling reactions [93–103], bond cleavage reactions (e.g., dehalogenation) [96], carbonylation [104], hydroformylation [15], borylation [105], hydrosilylation [106], isotope labeling [28, 89, 107], and energy-related applications (Fischer–Tropsch synthesis [55, 56, 108], direct methanol fuel cells (DMFCs) [109, 110], and hydrogen storage/generation [111].) Metal NPs can act as a catalyst reservoir for molecular catalyst species, for example in carbon–carbon cross coupling reactions, and the NPs are also accepted as true catalysts for typical heterogeneous reactions with solid-state catalysts [80, 102, 112]. The advantage of immobilizing metal NPs in ILs is that these multiphase systems (NPs/ILs as “stationary phase”) are easily recyclable by simple phase separation of the molecular (organic) “mobile phase,” containing the substrates and product, from the ionic catalytic solution (“stationary phase”) [69]. Nevertheless, there are limitations, such as (i) metal leaching into the organic phase [103, 113], (ii) extraction of organic molecules into the IL layer [114], (iii) mass transfer within the biphasic system due the relatively high viscosity [72], and (iv) when using ILs in the particular case of palladium-catalyzed coupling reactions, the stoichiometrically formed salts as by-products of the coupling reaction are accumulated in the IL layer [115]. At least the last drawback can be overcome by the use of “switchable solvents” [115–117]. In particular amine–alcohol mixtures can be reversibly converted into ILs by conducting the reaction under a carbon dioxide atmosphere (“IL mode”), under nitrogen–argon (“organic solvent mode”), the IL phase is transformed back into the non-ionic form with CO₂ extrusion. In this manner, first the organic product is separated from the polar IL layer (under CO₂), then the by-product salts can be subsequently separated by salt precipitation from solution by converting the IL into a less polar organic solvent.

1.3.1

Hydrogenation of Multiple Bonds with Metal Nanoparticles in Ionic Liquids

Metal NPs immobilized in ILs are highly active and recyclable for hydrogenation reactions in multiphase systems (see Scheme 1.2, Table 1.2, and Figure 1.5).

Several examples with the possibility of recycles in batch reactions show the promising potential for their recyclability without significant loss of catalyst activity (entries 1, 2, 11, 14, 16, and 21, Table 1.2) [4, 44, 118–121]. Nevertheless, in some cases the hydrogenation of arenes and ketones showed aggregation and decreased catalytic activity of the NPs [2, 27]. Noteworthy, the stability of NPs in ILs is superior in comparison with NPs under solventless conditions. As mentioned previously, certain hydrocarbons can be extracted with ILs and vice versa [114]. Therefore, the protective IL layer can be withdrawn from the NP surface, which may induce the particle growth process, leading to bulk metal accompanied by decreasing activity. Moreover, the selectivity can be influenced by the choice of IL and/or type of metal. For example, olefin and arene moieties are preferred for hydrogenation instead of a carbonyl group with Pd(0) and Ir(0) NPs (entries 6 and 22, Table 1.2) [11, 27]. In contrast, a nitro functionality is selectively reduced to an amine with Pt(0) NPs without hydrogenation of the arene moiety (entry 11, Table 1.2) [119]. Selective hydrogenation of 1,3-butadiene to 1-butene is



Scheme 1.2 Selected examples of the hydrogenation of multiple bonds with metal NPs in ILs.

possible with Pd(0) NPs in BMI. BF_4^- owing to the different solubility of the organic molecules in the IL (entry 5, Table 1.2) [5]. An additional example of selective hydrogenation is the conversion of benzene to cyclohexene in the presence of Ru(0) NPs in BMI. PF_6^- at low conversions (entry 17, Table 1.2) [44].

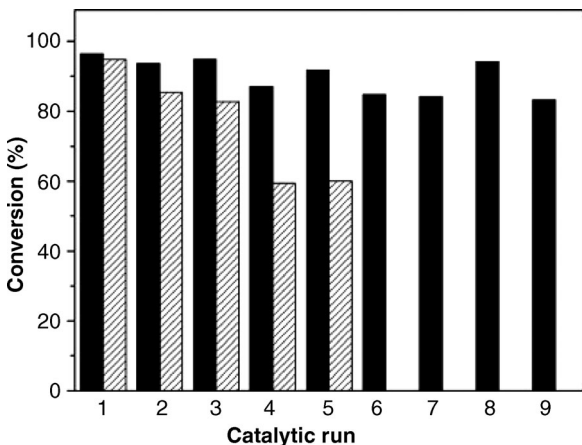


Figure 1.5 Recycling of the Pt(0) NPs in $(\text{C}_2\text{OH})\text{MI} \cdot \text{BF}_4^-$ (black) and Pt(0) NPs in $\text{BMI} \cdot \text{BF}_4^-$ (hatched) systems in the hydrogenation of the nitro group of 2,4-dichloro-3-nitrophenol

(DNP) to the corresponding aniline. Reprinted with permission from [119] (© The Royal Society of Chemistry).

Table 1.2 Examples of double and triple bond hydrogenation with recyclable metal NPs in ILs: alkenes, dienes, arenes, ketones, and aldehydes.

Entry	NP	IL ^{a)}	Substrate/[M] (mol/mol)	Educt	Product	Conversion (%)	Time (h)/T (°C)	Runs	Ref.
1	Pd	BMI.PF ₆	500	Alkene	Alkane	100	5/40	10	[118]
2	Pd	BMI.PF ₆	500	Diene	Alkene	95	2/40	n.d.	[118]
3	Pd	BMI.PF ₆ /TBA.Br	100	Alkene	Alkane	97	20/r.t.	n.d.	[122]
4	Pd	BMI.PF ₆	250	Alkene	Alkane	100	1/40	n.d.	[123]
5	Pd	BML.BF ₄ , BMI.PF ₆	1000	Diene	Alkene	100 ^{b)}	10/40	n.d.	[5]
6	Pd	BM ₂ I.PF ₆	1000	Enone	Ketone	100	3/35	7	[11]
7	Pd	BML.PF ₆	84	Ketone	Alcohol	89	2/40	6	[124]
8	Pt	BML.PF ₆	250	Alkene	Alkane	100	0.4/75	n.d.	[43]
9	Pt	BML.PF ₆	1000	Alkene	Alkane	100	1/40	5	[123]
10	Pt	BML.PF ₆	250	Arene	Cycloalkane	46	10/75	n.d.	[43]
11	Pt	(C ₂ O ₄ H)ML.BF ₄ + polymer	250	Nitroarene	Aniline	100	2/90	9	[119]
12	Rh	BML.PF ₆ ; (BML.BF ₄)	250 (1000)	Alkene	Alkane	100 (95)	2 (2.5)/40 (75)	n.d. (6)	[54, 123]
13	Rh	BML.PF ₆ ; (BML.BF ₄)	250 (4000)	Arene	Cycloalkane	100	22 (16)/75	n.d. (5)	[2, 125]
14	Rh	(C ₂ O ₄ H)ML.BF ₄	4000	Alkene	Alkane	>99	2/40	9	[120]
15	Rh	TBA.Br (CO ₂ induction)	100	Arene	Cycloalkane	100	2/40	5	[126]
16	Ru	BML.BF ₄	500 (67); 1108	Alkene	Alkane	>99; 95	0.6 (1.7)/75; 2-4/90	8 (17); 7	[4, 44, 121]
17	Ru	BML.PF ₆	1500	Arene	Cycloalkene	2 ^{c)}	1.2/75	n.d.	[44]
18	Ru	DML.NTF ₂	200	Arene	Cycloalkane	90	18/75	n.d.	[12]
19	Ru	(BCN)ML.NTf ₂	137	Nitrile	Imine	70	22/90	3	[13]
20	Ir	BML.PF ₆	1200	Alkene	Alkane	100	0.5/75	7	[1, 6, 26]
21	Ir	BML.PF ₆	250	Ketone	Alcohol	100	17.5/75	15	[27]
22	Ir	Solventless	250	Arene	Cycloalkane	97 ^{d)}	n.d./75	n.d.	[27]
23	Ir	Solventless (BML.PF ₆)	250	Arene	Cycloalkane	100	2 (5)/75	7	[2]

a) BMI = 1-*n*-butyl-3-methylimidazolium; (BCN)MI = 1-butyronitrile-3-methylimidazolium; DMI = 1-*n*-decyl-3-methylimidazolium; TBA = tetrabutylammonium; (C₂O₄H)MI = 1-(2-hydroxyethyl)-3-methylimidazolium; n.d. = not determined.

b) 98% in butenes.

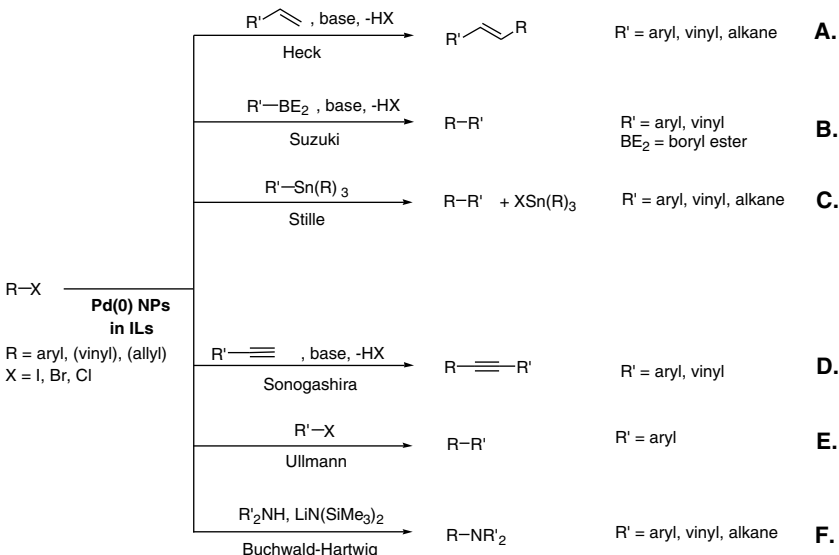
c) 34% in cyclohexene.

1.3.2

Carbon–Carbon Cross-Coupling Reactions Catalyzed by Palladium Nanoparticles in Ionic Liquids

Palladium-catalyzed carbon–carbon cross-coupling reactions are among the best studied reactions in recent decades since their discovery [102, 127–130]. These processes involve molecular Pd complexes, and also palladium salts and ligand-free approaches, where palladium(0) species act as catalytically active species [131–135]. For example, the Heck reaction with aryl iodides or bromides is promoted by a plethora of Pd(II) and Pd(0) sources [128, 130]. At least in the case of ligand-free palladium sources, the involvement of soluble Pd NPs as a reservoir for catalytically active species seems very plausible [136–138]. Noteworthy, it is generally accepted that the true catalyst in the reactions catalyzed by Pd(0) NPs is probably molecular zerovalent species detached from the NP surface that enter the main catalytic cycle and subsequently agglomerate as NPs or even as bulk metal.

This section gives a brief summary of the application of recyclable Pd(0) NP–IL catalyst systems in carbon–carbon cross-coupling reactions (Table 1.3, Scheme 1.3). More in-depth details and mechanistic aspects can be found in reviews of Pd(0) NP-catalyzed coupling reactions in ILs [129, 139, 140].



Scheme 1.3 Pd(0) NP-catalyzed carbon–carbon coupling reactions in ILs: A [36, 94, 102, 103, 113, 134, 146–155]; B [8, 97, 102, 147, 153, 156, 157]; C [97, 98, 153, 158]; D [157, 159]; E [95, 160]; F [161].

For example, the Mizoroki–Heck reaction consists of the reaction of an unsaturated halide with alkenes under basic conditions catalyzed by a Pd source dissolved in

Table 1.3 Examples of Pd(0) NP-catalyzed carbon–carbon bond cross-coupling reactions in ILs.

Entry	Reaction	IL ^{a)}	Ar–X (X =)	Educt/[M] (mol/mol)	Conversion (%)	Runs	Ref.
1	Heck	TBA,Br/TBA,OAc BMI,PF ₆	I, Br, Cl	67 (285) 1000	10–99 (97–99) 100	n.d. (10) n.d.	[146, 148]
2		TBA,Br, BMP,NTf ₂	I	200	6–98	5	[103]
3		(BCN)MI,NTf ₂	I	100	16–99	4	[162]
4		TBA,Br/TBA,OAc	Cl	67	25–98	n.d.	[101]
5	Suzuki	TBA,Br,THEtA,Br	Br, Cl	40	15–99	4	[94]
6		TOA,Br	Br	50	100	n.d.	[97]
7		(BCN)Py,NTf ₂ ,BPy,NTf ₂	I	20	44–65 ^{c)}	9	[147]
8	Stille	THEtA,Br	Br, Cl	40	27–98	5	[158]
9		(BCN)MI,BF ₄	I	20	48–85	4	[97]
10		BMI,PF ₆	I	10	57 ^{c)}	n.d.	[98]
11	Sonegashira	Without IL ^{b)}	I	50	100	4	[157]
12		TBA,OAc	Br	33	81–92	n.d.	[159]
13	Ullmann	TBA,Br/TBA,OAc	I	30	20–80	n.d.	[95]
14	Buchwald–Hartwig					n.d.	[161]

a) BMP = 1-*n*-butyl-1-methylpyrrolidinium; BPy = 1-*n*-butylpyridinium; THEtA = tetraheptylammonium; TOA = tetraoctylammonium; n.d. = not determined.

b) NPs only prepared in the IL 1-methyl-3-(2-mercaptopropoxethyl)imidazolium chloride.

c) Yield of product.

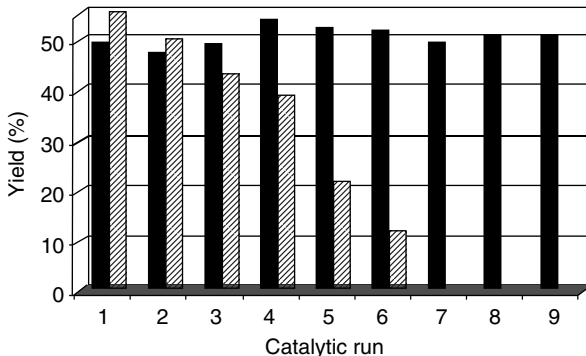


Figure 1.6 Recyclability of the catalyst in $(\text{BCN})\text{Py}.\text{NTf}_2$ (black) and $(\text{PCN})\text{Py}.\text{NTf}_2$ (hatched) in the Stille reaction between phenyltributylstannane and iodobenzene

catalyzed by Pd(0) NPs. $(\text{PCN})\text{Py}$ = 1-pentylnitrilepyridinium. Reprinted with permission from [158] (© American Chemical Society).

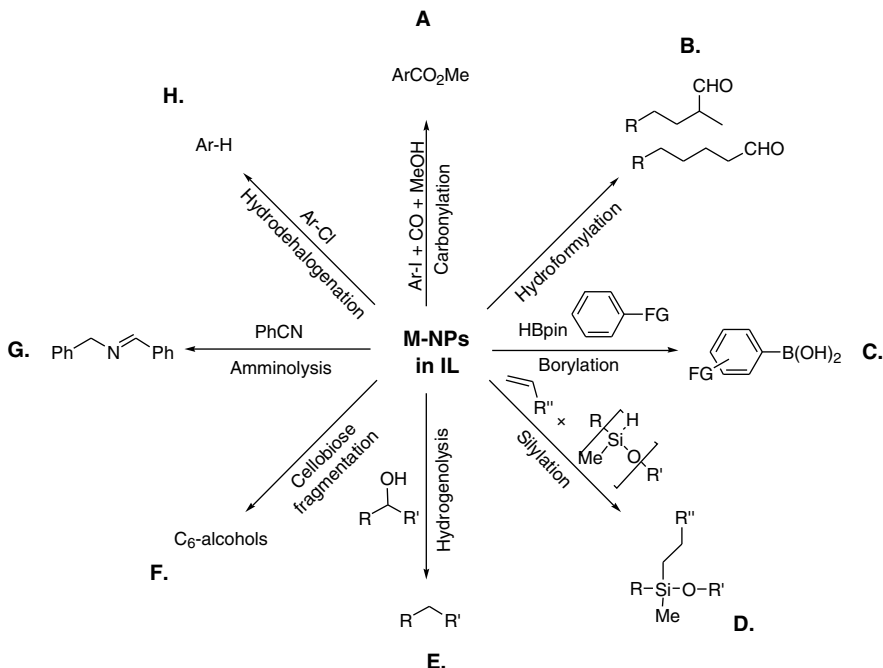
classical organic solvents. However, often the real active species was specified as a molecular Pd species derived from Pd(0) NPs stabilized by the quaternary ammonium salts used in the reaction [136, 141]. These Pd(0) NPs are formed due to the reduction of the Pd(II) specie to Pd(0) in the presence of bases such as excess of phosphines (PPh_3) or sodium acetate. Another aspect is the role of the IL itself; for example, with imidazolium ILs as solvent system, palladium–NHC complexes are key intermediates in the catalytic cycle and for the stabilization of molecular species [142–145].

Convenient recyclable catalyst systems use simple tetraalkylammonium salts as well as imidazolium-based ILs. For example, Pd(0) NPs (1.5–6 nm in size) prepared and stabilized by tetrabutylammonium bromide IL for the Heck reaction of aryl bromides with the 1,1-disubstituted olefins butyl methacrylate and α -methylstyrene in the presence of tetrabutylammonium acetate as base at 120 °C [146]. Aryl chlorides undergo coupling with deactivated olefins under similar conditions (entry 5, Table 1.3) [94]. Interestingly, such Pd(0) NPs in tetraalkylammonium salts or imidazolium ILs are capable of catalyzing a whole range of cross-coupling reactions for several recycles in batch reactions: Heck [36, 94, 102, 103, 113, 134, 146–155], Suzuki [8, 97, 102, 147, 153, 156, 157], Stille (Figure 1.6) [97, 98, 153, 158], Sonogashira [157, 159], Ullmann [95, 160], and Buchwald–Hartwig [161] (Scheme 1.3; Table 1.3).

1.3.3

Functionalization and Defunctionalization Reactions Using Metal Nanoparticles in Ionic Liquids

In recent years, metal NPs synthesized in ILs were recognized as suitable materials to promote the formation of chemical bonds in reactions other than palladium-catalyzed carbon–carbon cross-coupling reactions. For example, aldehydes and esters



Scheme 1.4 Examples of functionalization and defunctionalization reactions in ILs promoted by metal NPs (see references in Table 1.4).

are accessible under hydroformylation [15] and carbonylation [104] conditions, respectively (Scheme 1.4). In both cases the metal NP–IL catalyst-systems show promising potential for recycling in batch experiments (entries A and B, Table 1.4). Moreover, metal NPs catalyzed the direct borylation [105] and silylation [106] of aromatic and olefinic C–H bonds giving an approach to organoboron and organosilicon compounds. Again, the recyclability of the ionic catalyst phase was demonstrated in batch experiments with stable high conversions (entries C and D, Table 1.4; Figure 1.7).

The complete elimination of functional groups is often an undesirable side reaction in organic synthesis, but on the other hand it is a possibility for the recycling of environmentally harmful compounds, for example phenols and haloarenes such as polychlorinated dibenzodioxins (PCDDs or “dioxins”). For example, aryl chlorides can be effectively dechlorinated with Pd(0) NPs in tetrabutylammonium salts with almost quantitative conversions also after 19 runs (entry H, Table 1.4) [96]. On the other hand, a C–O bond cleavage reaction also seems suitable for the fragmentation of sugar-based biomass such as cellulose or cellobiose; in that way, sugar monomers and bioalcohol can be derived from renewable resources (entry F, Table 1.4) [164].

Table 1.4 Examples of functionalization and defunctionalization with metal NPs in ILs: carbonylation, hydroformylation, borylation, hydrosilylation, bond cleavage, hydrogenolysis, aminolysis, and dehalogenation.

Entry	Reaction	NP	Educt/[M] (mol/mol)	IL ^a	Educt	Product	Conversion [%]	Runs	Ref.
A	Methoxycarbonylation	Pd	763	BMI X or BMPy.X (X = PF ₆ , BF ₄ , Cl) Solventless ^b	ArI	Ester	8-83	5	[104]
B	Hydroformylation	Rh	200	THTdP.MS	Alkene	Aldehyde	100	8	[15]
C	Borylation	Ir	167	Pyridinium/ imidazolium ILs	Arene	Ar-B	39-89	6	[105]
D	Hydrosilylation	Pt	Not given	TMGL; Ir ^c	ArSiMe ₂ H	ArSiMe ₂ R	Up to 99	10	[106]
E	Hydrogenolysis	Ru-Cu ^d ;	333 ^e ;		Glycerol; acetophenone	1,2-Propanediol; ethylcyclohexane	100 ^f ; 100 ^g	5;	[2, 163]
F	C–O bond cleavage	Ru	250	Solventless BMI Cl (Water)	Cellulose (Cellobiose)	C ₆ -alcohols	15 (100)	n.d. n.d.	[164]
G	Aminolysis	Ru	137	(BCN)MI.NTF ₂	Nitrile	Imine	70	3	[13]
H	Dehalogenation	Pd	33	TBA.Br/TBA.OAc	Aryl chloride	Arenes	>99	19	[96]

a) BMPy = 1-n-butyl-4-methylpyridinium; THTdP = trihexyltetradecylphosphonium; MS = methylsulfonate; TMGL = 1,1,3,3-tetramethylguanidinium lactate; n.d. = not determined.

b) NPs only prepared in BMI.BF₄.

c) NPs supported in a clay modified with IL.

d) NPs prepared in BMI.PF₆.

e) Molar ratio determined for substrate/Ru.

f) 85% of selectivity in 1,2-propanediol.

g) 42% of selectivity in ethylcyclohexane.

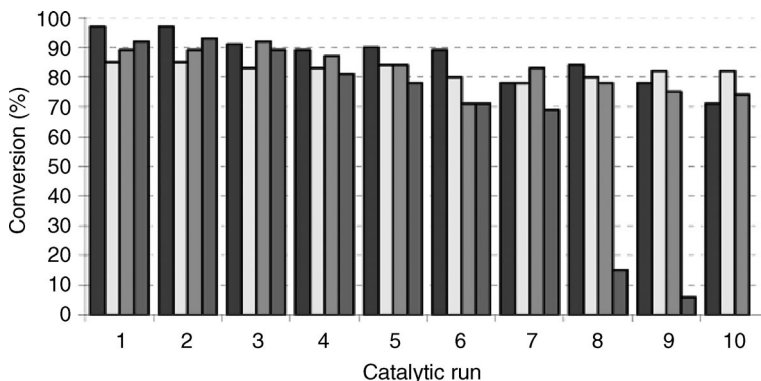


Figure 1.7 Catalyst recycling in the hydrosilylation reaction under inert (N_2) conditions with several platinum precursors, $[K_2PtCl_4]$ (black), $[PtCl_2(C_6H_{10})_2]$ (dark grey), $[PtCl_2(PPh_3)_2]$ (white), and $[Pt(PPh_3)_4]$

(light grey), in BPy.BF₄. The presence of Pt(0) NPs was evidenced during hydrosilylation reactions. Reprinted with permission from [106] (© American Chemical Society).

1.3.4

Isotope Exchange Catalyzed by Metal Nanoparticles in Ionic Liquids

Isotope exchange processes are useful methods for the evaluation of catalysts [165–167]. Moreover, in most cases isotope-enriched compounds are suitable in chemical or pharmaceutical/medicinal research and for the investigation of metabolic processes of pharmaceutical products [168]. Additionally, deuterated polymers have been evaluated for organic light-emitting diodes (OLEDs) and are used in optical communication systems [169]. Another example from clinical research of the use of certain isotopes is boron neutron capture therapy (BNCT), where a ¹⁰B-enriched boron compound is irradiated with low-energy neutrons yielding α -particles and ⁷Li nuclei. BNCT has been focused on, for example, the treatment of cerebral metastases of melanoma, and more recently head, neck, and liver tumors [107]. Therefore, isotope labeling and enrichment of isotopes is of great interest both in academic research and for application in industry and medicine.

It has been demonstrated that metal NPs in ILs are capable of catalyzing isotope exchange in organic molecules and also in inorganic compounds. Investigations on H–D exchange in imidazolium ILs focused on the assumption that NHC carbene species formed from ILs are involved in the stabilization of metal NPs and also play a role in catalytic processes. Most interestingly, there is also a significant isotope exchange in the less acidic positions (4 and 5) of the imidazolium ring (entries 1 and 2, Table 1.5) [28, 89]. This implies the formation of non-classical NHC carbenes derived from the IL, and that these positions also play a role in the catalysis. As discussed earlier, these isotope labeling results indicate that the IL interacts with metal NPs through anionic aggregates of the type $\{[(DAI)_x(X)_{x-n}]^{n+} [(DAI)_{x-n}(X)_x]^{n-}\}_m$ and not as isolated ions [89]. Moreover, they show that metal NPs are probably suitable for deuterium labeling in

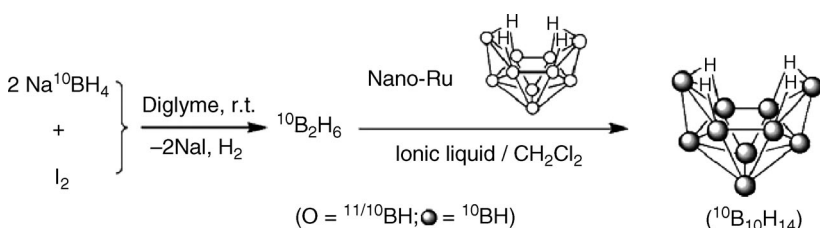
Table 1.5 Examples of isotope exchange reactions with metal NPs in ILs: H-D ($^1\text{H}-^2\text{H}$) and $^{11}\text{B}-^{10}\text{B}$.

Entry	Reaction	NP	Educt/[M] (mol/mol)	[IL ^a]	Educt	Product	Conversion (%)	Runs	Ref.
1	H-D	Ir	Not given	Imidazolium ILs	$[^1\text{H}]$ imidazolium	$[^2\text{H}]$ {2,4,5,8}-Imidazolium	>95 at C-2	n.d.	[28]
2	H-D	Ir	Not given	Imidazolium ILs	$[^2\text{H}]$ imidazolium	$[^1\text{H}]$ {2,4,5}-Imidazolium	10-48	n.d.	[89]
3	$^{11}\text{B}-^{10}\text{B}$	Ru	20	THTdp.DBS	Decaborane	^{10}B -enriched decaborane	90 (^{10}B)	3	[107]

a) THTdp = trihexyltetradecylphosphonium; DBS = dodecylbenzenesulfonate; n.d. = not determined.

heterocycles or more complex molecules; needless to say that heterocycles are key elements in pharmaceutical compounds, and therefore, a cheap deuterium labeling method is very attractive.

The ruthenium-catalyzed isotope exchange of boron atoms in decaborane is remarkable because several bonds are selectively broken and formed with a nanoscale catalyst without altering the structure of the decaborane. Highly enriched [^{10}B] decaborane can be obtained by repeated treatment (six times) of decaborane with $^{10}\text{B}_2\text{H}_6$ in presence of Ru(0) NPs in ILs (entry 3, Table 1.5; Scheme 1.5), where the catalyst was recycled three times in batch experiments without significant activity loss [107].



Scheme 1.5 Catalytic ^{10}B - ^{11}B isotope exchange using Ru(0) NPs in ILs. Reprinted with permission from [107] (© American Chemical Society).

1.3.5

Application of Metal Nanoparticle Catalysts in Ionic Liquids for Energy- and Environment-Related Systems

In the past decades, there has been increasing interest in the development of clean power sources based on hydrogen, water splitting or direct methanol fuel cells (DMFCs) and also for synthetic fuel production in gas-to-liquid (GtL) processes such as Fischer-Tropsch synthesis. For the last process, cobalt and ruthenium NPs protected with ILs have been successfully applied, and recyclability of the catalyst was achieved (entries 1 and 2, Table 1.6) [55, 56, 108]. For both catalysts the product mixture includes alkanes, olefins, and oxygenated compounds in a range from C_5/C_7 to C_{30} . Entry 3 (Table 1.6) is a rare example of a dehydrogenation reaction with metal NPs stabilized in quaternary ammonium salt [111]. Here the model substrate dimethylaminoborane (DMAB) was chosen for the evaluation of recyclable nanocatalysts for a hydrogen generation system based on Rh(0) NPs. Another field of application in the area of energy research involving metal NPs in ILs is their use as oxidation catalysts in fuel cells (entry 5, Table 1.6) [170, 171]. Here, the IL not only take functions as solvent and catalyst stabilizer, but also acts as an electrolyte.

As an example of metal oxide NPs, nanostructured TiO_2 film, often used in photocatalytic reactions, is suitable for the activation of CO_2 as chemical feedstock [172]. It was shown that CO_2 can be converted into low-density polyethylene (LDPE) under electrochemical conditions in the presence of a nanoscale TiO_2 electrode using a mixture of EMI.BF_4^- and water.

Table 1.6 Examples of energy- and environment-related systems with metal NPs in ILs: Fischer–Tropsch synthesis, fuel cells, and hydrogen generation/storage.

Entry	Reaction	NP	IL ^{a)}	Educt	Product	Conversion (%)	Runs	Ref.
1	Fischer–Tropsch	Ru	BMI.BF ₄	H ₂ -CO (2:1)	Not given ^{b)}	75	n.d.	[108]
2	Fischer–Tropsch	Co	BMI.NTF ₂ ; BMI.NTf ₂	H ₂ -CO (2:1)	C ₇ -C ₃₆ ; C ₈ -C ₂₆	35	n.d.	[55, 56]
3	H ₂ generation	Rh	DMA.Hexanoate	DMAB	Aminoborane dimer and H ₂	100	n.d.	[111]
4	Water oxidation	Ag	BMI.BF ₄	Water	O ₂ and H ⁺	n.d.	n.d.	[173]
5	Oxidation (DMFC)	Pt or Pt/Ru	BMI.PF ₆ ; BMI.BF ₄	Methanol	CO ₂	n.d.	n.d.	[170, 171]

a) DMA = dimethylammonium; EMi = 1-ethyl-3-methylimidazolium; DMAB = dimethylaminoborane.

b) Results discussed for the Fischer–Tropsch reaction in water.

1.4

General Remarks

In this chapter, we briefly discussed the synthesis of transition metal NPs with small size and narrow mean diameter by the simple reduction or decomposition of organometallic precursors in the presence of ILs as stabilizing agents. These NPs dispersed in ILs are recyclable catalysts for reactions in multiphase systems. The selectivity of these materials shows that they are capable of catalyzing typical heterogeneous reactions as multisite catalysts (arene hydrogenation, Fischer-Tropsch synthesis) and also homogeneous reactions. Examples of the latter are the Heck reaction and other carbon–carbon coupling reactions. Here, the NPs act as a reservoir for the molecular catalytically active species (single-site). In both cases, the ILs are suitable templates for the formation and stabilization of metal nanoscale catalysts. The metal NP–IL systems often exhibit promising catalytic properties and long-term stability. Especially the use of functionalized ILs shows that the stability and activity can be optimized with coordinating groups.

References

- 1 Dupont, J., Fonseca, G.S., Umpierre, A.P., Fichtner, P.F.P., and Teixeira, S.R. (2002) *Journal of the American Chemical Society*, **124** (16), 4228–4229.
- 2 Fonseca, G.S., Umpierre, A.P., Fichtner, P.F.P., Teixeira, S.R., and Dupont, J. (2003) *Chemistry: A European Journal*, **9** (14), 3263–3269.
- 3 Scheeren, C.W., Domingos, J.B., Machado, G., and Dupont, J. (2008) *Journal of Physical Chemistry C*, **112** (42), 16463–16469.
- 4 Rossi, L.M., Machado, G., Fichtner, P.F.P., Teixeira, S.R., and Dupont, J. (2004) *Catalysis Letters*, **92** (3–4), 149–155.
- 5 Umpierre, A.P., Machado, G., Fecher, G.H., Morais, J., and Dupont, J. (2005) *Advanced Synthesis and Catalysis*, **347** (10), 1404–1412.
- 6 Fonseca, G.S., Machado, G., Teixeira, S.R., Fecher, G.H., Morais, J., Alves, M.C.M., and Dupont, J. (2006) *Journal of Colloid and Interface Science*, **301** (1), 193–204.
- 7 Bernardi, F., Scholten, J.D., Fecher, G.H., Dupont, J., and Morais, J. (2009) *Chemical Physics Letters*, **479**, 113–116.
- 8 Durand, J., Teuma, E., Malbosc, F., Kihn, Y., and Gomez, M. (2008) *Catalysis Communications*, **9** (2), 273–275.
- 9 Gelesky, M.A., Umpierre, A.P., Machado, G., Correia, R.R.B., Magno, W.C., Morais, J., Ebeling, G., and Dupont, J. (2005) *Journal of the American Chemical Society*, **127** (13), 4588–4589.
- 10 Hu, Y., Yu, Y.Y., Hou, Z.S., Li, H., Zhao, X.G., and Feng, B. (2008) *Advanced Synthesis and Catalysis*, **350** (13), 2077–2085.
- 11 Hua, Y., Yang, H., Zhang, Y., Hou, Z., Wang, X., Qiao, Y., Li, H., Feng, B., and Huang, Q. (2009) *Catalysis Communications*, **10** (14), 1903–1907.
- 12 Precht, M.H.G., Scariot, M., Scholten, J.D., Machado, G., Teixeira, S.R., and Dupont, J. (2008) *Inorganic Chemistry*, **47**, 8995–9001.
- 13 Precht, M.H.G., Scholten, J.D., and Dupont, J. (2009) *Journal of Molecular Catalysis A: Chemical*, **313** (1–2), 74–78.
- 14 Redel, E., Thomann, R., and Janiak, C. (2008) *Inorganic Chemistry*, **47** (1), 14–16.
- 15 Bruss, A.J., Gelesky, M.A., Machado, G., and Dupont, J. (2006) *Journal of Molecular Catalysis A: Chemical*, **252** (1–2), 212–218.
- 16 Dupont, J. and Spencer, J. (2004) *Angewandte Chemie International Edition*, **43** (40), 5296–5297.

- 17** Choi, S., Kim, K.S., Yeon, S.H., Cha, J.H., Lee, H., Kim, C.J., and Yoo, I.D. (2007) *Korean Journal of Chemical Engineering*, **24** (5), 856–859.
- 18** Gao, Y., Voigt, A., Zhou, M., and Sundmacher, K. (2008) *European Journal of Inorganic Chemistry*, (24), 3769–3775.
- 19** Ryu, H.J., Sanchez, L., Keul, H.A., Raj, A., and Bockstaller, M.R. (2008) *Angewandte Chemie International Edition*, **47** (40), 7639–7643.
- 20** Zhang, H. and Cui, H. (2009) *Langmuir*, **25** (5), 2604–2612.
- 21** Dinda, E., Si, S., Kotal, A., and Mandal, T.K. (2008) *Chemistry- A European Journal*, **14** (18), 5528–5537.
- 22** Qin, Y., Song, Y., Sun, N.J., Zhao, N., Li, M.X., and Qi, L.M. (2008) *Chemistry of Materials*, **20** (12), 3965–3972.
- 23** Kim, T.Y., Kim, W.J., Hong, S.H., Kim, J.E., and Suh, K.S. (2009) *Angewandte Chemie International Edition*, **48** (21), 3806–3809.
- 24** Migowski, P., Zanchet, D., Machado, G., Gelesky, M.A., Teixeira, S.R. and Dupont, J. (2010) *Physical Chemistry Chemical Physics*, **12** (25), 6826–6833.
- 25** Dupont, J. and Scholten, J.D. (2010) *Chemical Society Reviews*, **39** (5), 1780–1804.
- 26** Fonseca, G.S., Domingos, J.B., Nome, F., and Dupont, J. (2006) *Journal of Molecular Catalysis A: Chemical*, **248** (1–2), 10–16.
- 27** Fonseca, G.S., Scholten, J.D., and Dupont, J. (2004) *Synlett*, (9) 1525–1528.
- 28** Ott, L.S., Cline, M.L., Deetlefs, M., Seddon, K.R., and Finke, R.G. (2005) *Journal of the American Chemical Society*, **127** (16), 5758–5759.
- 29** Kim, K.S., Demberelnyamba, D., and Lee, H. (2004) *Langmuir*, **20** (3), 556–560.
- 30** Tatumi, R. and Fujihara, H. (2005) *Chemical Communications*, (1), 83–85.
- 31** Schrekker, H.S., Gelesky, M.A., Stracke, M.P., Schrekker, C.M.L., Machado, G., Teixeira, S.R., Rubim, J.C., and Dupont, J. (2007) *Journal of Colloid and Interface Science*, **316** (1), 189–195.
- 32** Marcilla, R., Mecerreyres, D., Odriozola, I., Pomposo, J.A., Rodriguez, J., Zalakain, I., and Mondragon, I. (2007) *Nano*, **2** (3), 169–173.
- 33** Li, Z.H., Liu, Z.M., Zhang, J.L., Han, B.X., Du, J.M., Gao, Y.N., and Jiang, T. (2005) *Journal of Physical Chemistry B*, **109** (30), 14445–14448.
- 34** Wang, Y. and Yang, H. (2006) *Chemical Communications*, (24), 2545–2547.
- 35** Dai, C., Zhang, S.M., Li, J., Wu, Z.S., and Zhang, Z.J. (2007) *Chinese Journal of Inorganic Chemistry*, **23**, 1653–1656.
- 36** Deshmukh, R.R., Rajagopal, R., and Srinivasan, K.V. (2001) *Chemical Communications*, (17), 1544–1545.
- 37** Hamill, N.A., Hardacre, C., and McMath, S.E.J. (2002) *Green Chemistry*, **4** (2), 139–142.
- 38** Meiss, S.A., Rohnke, M., Kienle, L., El Abedin, S.Z., Endres, F., and Janek, J. (2007) *ChemPhysChem*, **8** (1), 50–53.
- 39** El Abedin, S.Z., Polleth, M., Meiss, S.A., Janek, J., and Endres, F. (2007) *Green Chemistry*, **9** (6), 549–553.
- 40** Roy, P., Lynch, R., and Schmuki, P. (2009) *Electrochemistry Communications*, **11**, 1567–1570.
- 41** Leger, B., Denicourt-Nowicki, A., Olivier-Bourbigou, H., and Roucoux, A. (2008) *Inorganic Chemistry*, **47** (19), 9090–9096.
- 42** Leger, B., Denicourt-Nowicki, A., Roucoux, A., and Olivier-Bourbigou, H. (2008) *Advanced Synthesis and Catalysis*, **350** (1), 153–159.
- 43** Scheeren, C.W., Machado, G., Dupont, J., Fichtner, P.F.P., and Texeira, S.R. (2003) *Inorganic Chemistry*, **42** (15), 4738–4742.
- 44** Silveira, E.T., Umpierre, A.P., Rossi, L.M., Machado, G., Morais, J., Soares, G.V., Baumvol I.L.R., Teixeira, S.R., Fichtner, P.F.P., and Dupont, J. (2004) *Chemistry- A European Journal*, **10** (15), 3734–3740.
- 45** Vidoni, O., Philippot, K., Amiens, C., Chaudret, B., Balmes, O., Malm, J.O., Bovin, J.O., Senocq, F., and Casanove, M.J. (1999) *Angewandte Chemie International Edition*, **38** (24), 3736–3738.
- 46** Pelzer, K., Vidoni, O., Philippot, K., Chaudret, B., and Colliere, V. (2003) *Advanced Functional Materials*, **13** (2), 118–126.
- 47** Gutel, T., Garcia-Anton, J., Pelzer, K., Philippot, K., Santini, C.C., Chauvin, Y., Chaudret, B., and Basset, J.M. (2007)

- Journal of Materials Chemistry*, **17** (31), 3290–3292.
- 48** Machado, G., Scholten, J.D., de Vargas, T., Teixeira, S.R., Ronchi, L.H., and Dupont, J. (2007) *International Journal of Nanotechnology*, **4** (5), 541–563.
- 49** Gutel, T., Santini, C.C., Philippot, K., Padua, A., Pelzer, K., Chaudret, B., Chauvin, Y., and Basset, J.M. (2009) *Journal of Materials Chemistry*, **19** (22), 3624–3631.
- 50** Migowski, P., Machado, G., Texeira, S.R., Alves, M.C.M., Morais, J., Traverse, A., and Dupont, J. (2007) *Physical Chemistry Chemical Physics*, **9** (34), 4814–4821.
- 51** Migowski, P., Texeira, S.R., Machado, G., Alves, M.C.M., Geshev, J., and Dupont, J. (2007) *Journal of Electron Spectroscopy and Related Phenomena*, **156**, 195–199.
- 52** Redel, E., Thomann, R., and Janiak, C. (2008) *Chemical Communications*, (15), 1789–1791.
- 53** Kramer, J., Redel, E., Thomann, R., and Janiak, C. (2008) *Organometallics*, **27** (9), 1976–1978.
- 54** Redel, E., Kramer, J., Thomann, R., and Janiak, C. (2009) *Journal of Organometallic Chemistry*, **694** (7–8), 1069–1075.
- 55** Silva, D.O., Scholten, J.D., Gelesky, M.A., Teixeira, S.R., Dos Santos, A.C.B., Souza-Aguiar, E.F., and Dupont, J. (2008) *ChemSusChem*, **1** (4), 291–294.
- 56** Scariot, M., Silva, D.O., Scholten, J.D., Machado, G., Teixeira, S.R., Novak, M.A., Ebeling, G., and Dupont, J. (2008) *Angewandte Chemie International Edition*, **47**, 9075–9078.
- 57** Wang, W., Efrima, S., and Regev, O. (1998) *Langmuir*, **14** (3), 602–610.
- 58** Itoh, H., Naka, K., and Chujo, Y. (2004) *Journal of the American Chemical Society*, **126** (10), 3026–3027.
- 59** Zhao, D.B., Fei, Z.F., Ang, W.H., and Dyson, P.J. (2006) *Small*, **2** (7), 879–883.
- 60** Mevellec, V., Leger, B., Mauduit, M., and Roucoux, A. (2005) *Chemical Communications*, (22), 2838–2839.
- 61** Bell, W.C. and Myrick, M.L. (2001) *Journal of Colloid and Interface Science*, **242** (2), 300–305.
- 62** Hofer, W.O. (1991) In: *Sputtering by Particle Bombardment III* (eds Behrisch, R. and Wittmaack, K.), Vol. 64, Springer, Berlin, p. 15.
- 63** Torimoto, T., Okazaki, K., Kiyama, T., Hirahara, K., Tanaka, N., and Kuwabata, S. (2006) *Applied Physics Letters*, **89** (24), 243117.
- 64** Okazaki, K., Kiyama, T., Suzuki, T., Kuwabata, S., and Torimoto, T. (2009) *Chemistry Letters*, **38** (4), 330–331.
- 65** Okazaki, K.I., Kiyama, T., Hirahara, K., Tanaka, N., Kuwabata, S., and Torimoto, T. (2008) *Chemical Communications*, (6), 691–693.
- 66** Suzuki, T., Okazaki, K., Kiyama, T., Kuwabata, S., and Torimoto, T. (2009) *Electrochemistry*, **77** (8), 636–638.
- 67** Tsuda, T., Kurihara, T., Hoshino, Y., Kiyama, T., Okazaki, K.-i., Torimoto, T., and Kuwabata, S. (2009) *Electrochemistry*, **77** (8), 693–695.
- 68** Wender, H., de Oliveira, L.F., Migowski, P., Feil, A.F., Lissner, E., Precht, M.H.G., Texeira, S.R., and Dupont, J. (2010) *Journal of Physical Chemistry C*, **114** (27), 11764–11768.
- 69** Dupont, J., de Souza, R.F., and Suarez, P.A.Z. (2002) *Chemical Reviews*, **102** (10), 3667–3691.
- 70** Tsuzuki, S., Tokuda, H., Hayamizu, K., and Watanabe, M. (2005) *Journal of Physical Chemistry B*, **109** (34), 16474–16481.
- 71** Hardacre, C., Holbrey, J.D., McMath, S.E.J., Bowron, D.T., and Soper, A.K. (2003) *Journal of Chemical Physics*, **118** (1), 273–278.
- 72** Dupont, J., and Suarez, P.A.Z. (2006) *Physical Chemistry Chemical Physics*, **8** (21), 2441–2452.
- 73** Dupont, J. (2004) *Journal of the Brazilian Chemical Society*, **15** (3), 341–350.
- 74** Suarez, P.A.Z., Einloft, S., Dullius, J.E.L., de Souza, R.F., and Dupont, J. (1998) *Journal de Chimie Physique et de Physico-Chimie Biologique*, **95** (7), 1626–1639.
- 75** Gozzo, F.C., Santos, L.S., Augusti, R., Consorti, C.S., Dupont, J., and Eberlin, M.N. (2004) *Chemistry- A European Journal*, **10** (23), 6187–6193.
- 76** Neto, B.A.D., Santos, L.S., Nachtigall, F.M., Eberlin, M.N., and Dupont, J. (2006) *Angewandte Chemie International Edition*, **45** (43), 7251–7254.
- 77** Lopes, J. and Padua, A.A.H. (2006) *Journal of Physical Chemistry B*, **110** (7), 3330–3335.

- 78** Schroder, U., Wadhawan, J.D., Compton, R.G., Marken, F., Suarez, P.A.Z., Consorti, C.S., de Souza, R.F., and Dupont, J. (2000) *New Journal of Chemistry*, **24** (12), 1009–1015.
- 79** Anderson, J.L. and Armstrong, D.W. (2003) *Analytical Chemistry*, **75** (18), 4851–4858.
- 80** Migowski, P. and Dupont, J. (2007) *Chemistry- A European Journal*, **13** (1), 32–39.
- 81** Scheeren, C.W., Machado, G., Teixeira, S.R., Morais, J., Domingos, J.B., and Dupont, J. (2006) *Journal of Physical Chemistry B*, **110**, 13011–13020.
- 82** Ott, L.S. and Finke, R.G. (2006) *Inorganic Chemistry*, **45** (20), 8382–8393.
- 83** Stowell, C.A. and Korgel, B.A. (2005) *Nano Letters*, **5** (7), 1203–1207.
- 84** Korgel, B.A. and Fitzmaurice, D. (1999) *Physical Review B*, **59** (22), 14191–14201.
- 85** Liu, J.C., Han, B.X., Zhang, H.L., Li, G.Z., Zhang, X.G., Wang, J., and Dong, B.Z. (2002) *Chemistry- A European Journal*, **8** (6), 1356–1360.
- 86** Frenkel, A.I., Hills, C.W., and Nuzzo, R.G. (2001) *Journal of Physical Chemistry B*, **105** (51), 12689–12703.
- 87** Ninham, B.W. (1999) *Advances in Colloid and Interface Science*, **83** (1–3), 1–17.
- 88** Bostrom, M., Williams, D.R.M., and Ninham, B.W. (2001) *Physical Review Letters*, **87** (16), 168103.
- 89** Scholten, J.D., Ebeling, G., and Dupont, J. (2007) *Dalton Transactions*, (47) 5554–5560.
- 90** Alvarez-Puebla, R.A., Arceo, E., Goulet, P.J.G., Garrido, J.J., and Aroca, R.F. (2005) *Journal of Physical Chemistry B*, **109** (9), 3787–3792.
- 91** Rubim, J.C., Trindade, F.A., Gelesky, M.A., Aroca, R.F., and Dupont, J. (2008) *Journal of Physical Chemistry C*, **112** (49), 19670–19675.
- 92** Gelesky, M.A., Scheeren, C.W., Foppa, L., Pavan, F.A., Dias, S.L.P., and Dupont, J. (2009) *Biomacromolecules*, **10** (7), 1888–1893.
- 93** Calo, V., Nacci, A., and Monopoli, A. (2006) *European Journal of Organic Chemistry*, (17), 3791–3802.
- 94** Calo, V., Nacci, A., Monopoli, A., and Cotugno, P. (2009) *Angewandte Chemie International Edition*, **48** (33), 6101–6103.
- 95** Calo, V., Nacci, A., Monopoli, A., and Cotugno, P. (2009) *Chemistry- A European Journal*, **15** (5), 1272–1279.
- 96** Calo, V., Nacci, A., Monopoli, A., Damascelli, A., Ieva, E., and Cioffi, N. (2007) *Journal of Organometallic Chemistry*, **692**, 4397–4401.
- 97** Calo, V., Nacci, A., Monopoli, A., and Montingelli, F. (2005) *Journal of Organic Chemistry*, **70** (15), 6040–6044.
- 98** Chiappe, C., Pieraccini, D., Zhao, D.B., Fei, Z.F., and Dyson, P.J. (2006) *Advanced Synthesis and Catalysis*, **348** (1–2), 68–74.
- 99** Cui, Y.G., Biondi, I., Chaubey, M., Yang, X., Fei, Z.F., Scopelliti, R., Hartinger, C.G., Li, Y.D., Chiappe, C., and Dyson, P.J. (2010) *Physical Chemistry Chemical Physics*, **12** (8), 1834–1841.
- 100** Dubbaka, S.R., Zhao, D.B., Fei, Z.F., Volla, C.M.R., Dyson, P.J., and Vogel, P. (2006) *Synlett*, (18) 3155–3157.
- 101** Fei, Z.F., Zhao, D.B., Pieraccini, D., Ang, W.H., Geldbach, T.J., Scopelliti, R., Chiappe, C., and Dyson, P.J. (2007) *Organometallics*, **26** (7), 1588–1598.
- 102** Phan, N.T.S., Van Der Sluys, M., and Jones, C.W. (2006) *Advanced Synthesis and Catalysis*, **348** (6), 609–679.
- 103** Cassol, C.C., Umpierre, A.P., Machado, G., Wolke, S.I., and Dupont, J. (2005) *Journal of the American Chemical Society*, **127** (10), 3298–3299.
- 104** Wojtkow, W., Trzeciak, A.M., Choukroun, R., and Pellegatta, J.L. (2004) *Journal of Molecular Catalysis A: Chemical*, **224** (1–2), 81–86.
- 105** Zhu, Y.H., Chenyan, K., Peng, A.T., Emi, A., Monalisa, W., Louis, L.K.J., Hosmane, N.S., and Maguire, J.A. (2008) *Inorganic Chemistry*, **47** (13), 5756–5761.
- 106** Geldbach, T.J., Zhao, D.B., Castillo, N.C., Laurenczy, G., Weyershausen, B., and Dyson, P.J. (2006) *Journal of the American Chemical Society*, **128** (30), 9773–9780.
- 107** Zhu, Y.H., Widjaja, E., Sia, S.L.P., Zhan, W., Carpenter, K., Maguire, J.A., Hosmane, N.S., and Hawthorne, M.F. (2007) *Journal of the American Chemical Society*, **129** (20), 6507–6512.
- 108** Xiao, C.-x., Cai, Z.-p., Wang, T., Kou, Y., and Yan, N. (2008) *Angewandte Chemie International Edition*, **47**, 746–749.
- 109** He, P., Liu, H., Li, Z., and Li, J. (2005) *Journal of the Electrochemical Society*, **152** (4), E146–E153.

- 110** Miyatake, K., and Watanabe, M. (2005) *Electrochemistry*, **73** (1), 12–19.
- 111** Zahmakiran, M., and Ozkar, S. (2009) *Inorganic Chemistry*, **48** (18), 8955–8964.
- 112** Gu, Y.L. and Li, G.X. (2009) *Advanced Synthesis and Catalysis*, **351** (6), 817–847.
- 113** Consorti, C.S., Flores, F.R., and Dupont, J. (2005) *Journal of the American Chemical Society*, **127** (34), 12054–12065.
- 114** Cassol, C.C., Umpierre, A.P., Ebeling, G., Ferrera, B., Chiaro, S.S.X., and Dupont, J. (2007) *International Journal of Molecular Sciences*, **8**, 593–605.
- 115** Hart, R., Pollet, P., Hahne, D.J., John, E., Llopis-Mestre, V., Blasucci, V., Huttenhower, H., Leitner, W., Eckert, C.A., and Liotta, C.L. (2010) *Tetrahedron*, **66** (5), 1082–1090.
- 116** Jessop, P.G., Heldebrant, D.J., Li, X.W., Eckert, C.A., and Liotta, C.L. (2005) *Nature*, **436** (7054), 1102.
- 117** Liu, Y.X., Jessop, P.G., Cunningham, M., Eckert, C.A., and Liotta, C.L. (2006) *Science*, **313** (5789), 958–960.
- 118** Huang, J., Jiang, T., Han, B.X., Gao, H.X., Chang, Y.H., Zhao, G.Y., and Wu, W.Z. (2003) *Chemical Communications*, (14), 1654–1655.
- 119** Yuan, X., Yan, N., Xiao, C.X., Li, C.N., Fei, Z.F., Cai, Z.P., Kou, Y., and Dyson, P.J. (2010) *Green Chemistry*, **12** (2), 228–233.
- 120** Yang, X., Yan, N., Fei, Z.F., Crespo-Quesada, R.M., Laurenczy, G., Kiwi-Minsker, L., Kou, Y., Li, Y.D., and Dyson, P.J. (2008) *Inorganic Chemistry*, **47** (17), 7444–7446.
- 121** Vollmer, C., Redel, E., Abu-Shandi, K., Thomann, R., Manyar, H., Hardacre, C., and Janiak, C. (2010) *Chemistry- A European Journal*, **16** (12), 3849–3858.
- 122** Le Bras, J., Mukherjee, D.K., Gonzalez, S., Tristany, M., Ganchegui, B., Moreno-Manas, M., Pleixats, R., Henin, F., and Muzart, J. (2004) *New Journal of Chemistry*, **28** (12), 1550–1553.
- 123** Mu, X.D., Evans, D.G., and Kou, Y.A. (2004) *Catalysis Letters*, **97** (3–4), 151–154.
- 124** Jutz, F., Andanson, J.M., and Baiker, A. (2009) *Journal of Catalysis*, **268** (2), 356–366.
- 125** Mu, X.D., Meng, J.Q., Li, Z.C., and Kou, Y. (2005) *Journal of the American Chemical Society*, **127** (27), 9694–9695.
- 126** Cimpeanu, V., Kocevar, M., Parvulescu, V.I., and Leitner, W. (2009) *Angewandte Chemie International Edition*, **48** (6), 1085–1088.
- 127** Moreno-Manas, M. and Pleixats, R. (2003) *Accounts of Chemical Research*, **36** (8), 638–643.
- 128** Beletskaya, I.P. and Cheprakov, A.V. (2000) *Chemical Reviews*, **100** (8), 3009–3066.
- 129** Liu, Y., Wang, S.S., Liu, W., Wan, Q.X., Wu, H.H., and Gao, G.H. (2009) *Current Organic Chemistry*, **13** (13), 1322–1346.
- 130** Yin, L.X. and Liebscher, J. (2007) *Chemical Reviews*, **107** (1), 133–173.
- 131** Bedford, R.B. (2003) *Chemical Communications*, (15), 1787–1796.
- 132** de Vries, A.H.M., Mulders, J., Mommers, J.H.M., Henderickx, H.J.W., and de Vries, J.G. (2003) *Organic Letters*, **5** (18), 3285–3288.
- 133** de Vries, A.H.M., Parlevliet, F.J., Schmieder-van de Vondervoort, L., Mommers, J.H.M., Henderickx, H.J.W., Walet, M.A.M., and de Vries, J.G. (2002) *Advanced Synthesis and Catalysis*, **344** (9), 996–1002.
- 134** Reetz, M.T. and de Vries, J.G. (2004) *Chemical Communications*, (14), 1559–1563.
- 135** Reetz, M.T., Westermann, E., Lohmer, R., and Lohmer, G. (1998) *Tetrahedron Letters*, **39** (46), 8449–8452.
- 136** Reetz, M.T. and Westermann, E. (2000) *Angewandte Chemie International Edition*, **39** (1), 165–168.
- 137** Rocaboy, C. and Gladysz, J.A. (2003) *New Journal of Chemistry*, **27** (1), 39–49.
- 138** Tromp, M., Sietsma, J.R.A., van Bokhoven, J.A., van Strijdonck, G.P.F., van Haaren, R.J., van der Eerden, A.M.J., van Leeuwen, P., and Koningsberger, D.C. (2003) *Chemical Communications*, (1), 128–129.
- 139** Calo, V., Nacci, A., and Monopoli, A. (2004) *Journal of Molecular Catalysis A: Chemical*, **214** (1), 45–56.
- 140** Prechtl, M.H.G., Scholten, J.D., and Dupont, J. (2010) *Molecules*, **15**, 3441–3461.
- 141** Astruc, D. (2007) *Inorganic Chemistry*, **46** (6), 1884–1894.
- 142** Xu, L.J., Chen, W.P., and Xiao, J.L. (2000) *Organometallics*, **19** (6), 1123–1127.
- 143** Lebel, H., Janes, M.K., Charette, A.B., and Nolan, S.P. (2004) *Journal of the American Chemical Society*, **126** (16), 5046–5047.

- 144 Wang, R.H., Zeng, Z., Twamley, B., PiekarSKI, M.M., and Shreeve, J.M. (2007) *European Journal of Organic Chemistry*, (4), 655–661.
- 145 Mathews, C.J., Smith, P.J., Welton, T., White, A.J.P., and Williams, D.J. (2001) *Organometallics*, **20** (18), 3848–3850.
- 146 Calo, V., Nacci, A., Monopoli, A., Detomaso, A., and Iliade, P. (2003) *Organometallics*, **22** (21), 4193–4197.
- 147 Reetz, M.T., Breinbauer, R., and Wanninger, K. (1996) *Tetrahedron Letters*, **37** (26), 4499–4502.
- 148 Calo, V., Nacci, A., Monopoli, A., Fornaro, A., Sabbatini, L., Cioffi, N., and Ditaranto, N. (2004) *Organometallics*, **23** (22), 5154–5158.
- 149 Tao, R.T., Miao, S.D., Liu, Z.M., Xie, Y., Han, B.X., An, G.M., and Ding, K.L. (2009) *Green Chemistry*, **11** (1), 96–101.
- 150 Pryjomska-Ray, I., Gniewek, A., Trzeciak, A.M., Ziolkowski, J.J., and Tylus, W. (2006) *Topics in Catalysis*, **40** (1–4), 173–184.
- 151 Qiao, K., Sugimura, R., Bao, Q.X., Tomida, D., and Yokoyama, C. (2008) *Catalysis Communications*, **9** (15), 2470–2474.
- 152 de Vries, J.G. (2006) *Dalton Transactions*, (3) 421–429.
- 153 Yang, X., Fei, Z.F., Zhao, D.B., Ang, W.H., Li, Y.D., and Dyson, P.J. (2008) *Inorganic Chemistry*, **47** (8), 3292–3297.
- 154 Calo, V., Nacci, A., Monopoli, A., Laera, S., and Cioffi, N. (2003) *Journal of Organic Chemistry*, **68** (7), 2929–2933.
- 155 Karimi, B. and Enders, D. (2006) *Organic Letters*, **8** (6), 1237–1240.
- 156 Fernandez, F., Cordero, B., Durand, J., Muller, G., Malbosc, F., Kihn, Y., Teuma, E., and Gomez, M. (2007) *Dalton Transactions*, (47) 5572–5581.
- 157 Corma, A., Garcia, H., and Leyva, A. (2005) *Tetrahedron*, **61** (41), 9848–9854.
- 158 Zhao, D.B., Fei, Z.F., Geldbach, T.J., Scopelliti, R., and Dyson, P.J. (2004) *Journal of the American Chemical Society*, **126** (48), 15876–15882.
- 159 Gao, S.Y., Zhang, H.J., Wang, X.M., Mai, W.P., Peng, C.Y., and Ge, L.H. (2005) *Nanotechnology*, **16** (8), 1234–1237.
- 160 Pachon, L.D., Elsevier, C.J., and Rothenberg, G. (2006) *Advanced Synthesis and Catalysis*, **348** (12–13), 1705–1710.
- 161 Battistuzzi, G., Bernini, R., Cacchi, S., De Salve, I., and Fabrizi, G. (2007) *Advanced Synthesis and Catalysis*, **349** (3), 297–302.
- 162 Forsyth, S.A., Gunaratne, H.Q.N., Hardacre, C., McKeown, A., Rooney, D.W., and Seddon, K.R. (2005) *Journal of Molecular Catalysis A: Chemical*, **231** (1–2), 61–66.
- 163 Jiang, T., Zhou, Y.X., Liang, S.G., Liu, H.Z., and Han, B.X. (2009) *Green Chemistry*, **11** (7), 1000–1006.
- 164 Yan, N., Zhao, C., Luo, C., Dyson, P.J., Liu, H.C., and Kou, Y. (2006) *Journal of the American Chemical Society*, **128** (27), 8714–8715.
- 165 Yung, C.M., Skaddan, M.B., and Bergman, R.G. (2004) *Journal of the American Chemical Society*, **126** (40), 13033–13043.
- 166 Prechtl, M.H.G., Holscher, M., Ben-David, Y., Theyssen, N., Loschen, R., Milstein, D., and Leitner, W. (2007) *Angewandte Chemie International Edition*, **46** (13), 2269–2272.
- 167 Pery, T., Pelzer, K., Buntkowsky, G., Philippot, K., Limbach, H.H., and Chaudret, B. (2005) *ChemPhysChem*, **6** (4), 605–607.
- 168 Thomas, A.F. (ed.) (1971) *Deuterium Labeling in Organic Chemistry*, Meredith Corporation, New York.
- 169 Yamamoto, M., Yokota, Y., Oshima, K., and Matsubara, S. (2004) *Chemical Communications*, (15), 1714–1715.
- 170 Xue, X., Liu, C., Lu, T., and Xing, W. (2006) *Fuel Cells*, **6** (5), 347–355.
- 171 Xue, X.Z., Lu, T.H., Liu, C.P., Xu, W.L., Su, Y., Lv, Y.Z., and Xing, W. (2005) *Electrochimica Acta*, **50** (16–17), 3470–3478.
- 172 Chu, D., Qin, G.X., Yuan, X.M., Xu, M., Zheng, P., and Lu, J. (2008) *ChemSusChem*, **1** (3), 205–209.
- 173 Zhao, C. and Bond, A.M. (2009) *Journal of the American Chemical Society*, **131** (12), 4279–4287.

2

CO₂-Expanded Liquids for Nanoparticle Processing

*Steven R. Saunders, Christopher B. Roberts, Kendall M. Hurst,
Christopher L. Kitchens, Gregory Von White II, and D. Brad Akers*

2.1

Introduction

Advancements in the field of nanotechnology over the past two decades have demonstrated that nanomaterials have the potential to be as important in the twenty-first century as polymers were in the twentieth. Whereas the vast majority of research dealing with nanotechnology has been synthesis- and application-based, developments in nanoparticle processing have been limited. Of particular interest are nanoparticles with a diameter less than 20 nm, as these materials demonstrate significantly novel and highly size-dependent properties. Large-scale nanoparticle synthesis methods are often solution-based and the products must typically undergo significant post-synthesis processing (e.g., size-selective fractionation to finely tune the size distribution) in order to prepare them for their intended application. Traditional nanoparticle processing is both time and solvent intensive such that relatively large quantities of organic solvents must be disposed of for modest nanoparticle yields. Through the use of tunable solvent systems, specifically CO₂-expanded liquids, it is possible to process nanoparticles in a green, sustainable, and efficient manner that provides complete solvent recycle. The highly adjustable physico-chemical properties of CO₂-expanded liquids provide unique opportunities to control nanoparticle dispersibility and deposition through simple variations in applied CO₂ pressure. As such, nanoparticles can be efficiently removed from the solvent mixture (i.e., precipitated) in a size-selective manner. The residual solvent mixture (consisting of CO₂ and organic solvent components) can be subsequently separated into the individual constituents through further manipulations of temperature and pressure, resulting in opportunities for complete solvent recycle and reuse. This chapter focuses on the use of the tunable properties of CO₂-expanded liquids for the purposes of nanoparticle processing, specifically controlling nanoparticle dispersibility, size-selective fractionation of nanoparticles, creation of self-assembled thin-film monolayers, and the formation and synthesis of nanoparticles.

2.1.1

Gas-Expanded Liquids

Gas-expanded liquids (GXLs) are mixtures of an organic solvent and a compressed gas, where the gas partitions (dissolves) into the liquid phase at applied pressures less than the vapor pressure of the gas. For safety and economic reasons, the most widely utilized GXLs are CO₂-expanded liquids (CXLs), such as hexane–CO₂ mixtures. These CXLs possess highly tunable physico-chemical properties at moderate temperatures and pressures. Through simple adjustments to the applied CO₂ pressure, the properties of the mixed solvent media can be tuned between those of the liquid organic solvent and those of liquid CO₂ (or scCO₂ depending on the temperature) [1]. For example, it is possible to pressurize a polar solvent, such as toluene, with CO₂ to a significant level such that the mass transport properties of the solvent mixture are more similar to those of a gas than to those of the neat polar solvent while maintaining the solubility of the polar solvent [2]. The use of CXLs provides several processing advantages over traditional solvent media, including solvent recovery through simple depressurization, enhanced gas solubility compared with the neat solvent, and lower operating pressures than those required for scCO₂. A more detailed review of GXL properties and applications is available in Jessop and Subramaniam's review [2].

The traditional CXL used for nanoparticle processing has been hexane–CO₂ mixtures since hexane is a good solvent for the aliphatic stabilizing ligands (thiols or carboxylic acids) that are commonly used to passivate the surface of nanoparticles during synthesis as a means of maintaining a stable dispersion in a solvent. The vapor–liquid equilibrium of this hexane–CO₂ mixture, can be predicted using the Peng–Robinson equation of state (PR-EOS) [3–6]. Figure 2.1a demonstrates the volume change of hexane when pressurized with CO₂ such that

$$\frac{\Delta V}{V_0} = \frac{V - V_0}{V_0} \quad (2.1)$$

where V is the total liquid volume at an applied CO₂ pressure and V_0 is the liquid volume of neat hexane at atmospheric conditions. As the applied CO₂ pressure increases, the solubility of CO₂ in the organic solvent (in this case hexane), increases drastically leading to a volume increase and a significant change in the properties of the liquid mixture. Density and molar volume, as demonstrated in Figure 2.1b, can be tuned between those of the organic solvent and those of liquid CO₂. This also implies that other solvent properties, such as solvent strength [7], viscosity [8], and mass diffusion through the solvent [9, 10] can be tuned by simply varying the applied CO₂ pressure.

2.2

Controlling Nanoparticle Dispersibility and Precipitation

The ability to precipitate nanoparticles controllably from a dispersion is required for most post-processing methods, including cleaning [11, 12] and size-selective

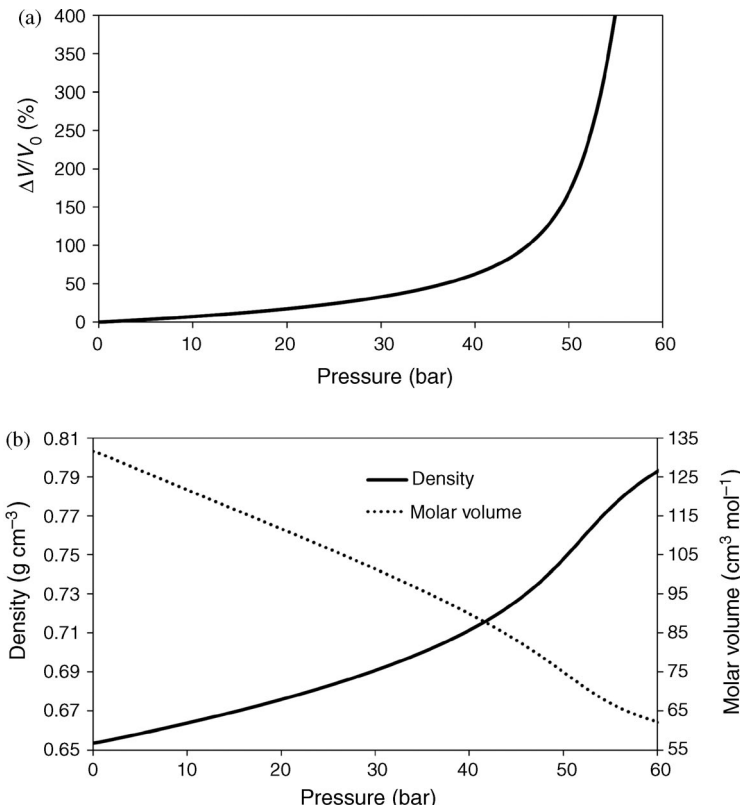


Figure 2.1 Hexane and CO₂ at 25 °C as predicted by the PR-EOS: (a) volume expansion of the liquid phase with pressurization of CO₂ and (b) solvent mixture density and molar volume with pressurization of CO₂.

fractionation [11, 13]. This is typically accomplished through a liquid solvent-antisolvent (LSAS) precipitation [11, 12, 14]. For example, nanoparticles can be stabilized with dodecanethiol (DDT) or any other type of aliphatic ligand (e.g., hexanethiol, octanethiol, dodecyl acid). These nanoparticles can be dispersed in any number of nonpolar solvents, including hexane. LSAS precipitation is typically performed by adding an antisolvent (e.g., ethanol, methanol, acetone) to the primary solvent (e.g., hexane, pentane, toluene, chloroform) where the antisolvent is a poor solvent for the ligand while being miscible with the primary solvent. Any combination of solvents and ligands can be used to perform a LSAS precipitation provided that: (1) the primary solvent is a good solvent for the ligand of choice, (2) the antisolvent is a poor solvent for the ligand of choice, (3) the primary solvent and the antisolvent are miscible, and (4) the poor solvent is strong enough to destabilize the dispersion. If these conditions are met, addition of the antisolvent will destabilize the nanoparticle dispersion, causing reversible flocculation. Using the LSAS method, the solvent mixture is comprised of two components (i.e., liquid solvent and the liquid antisolvent), each with relatively high viscosities and low

nanoparticle diffusivities; as such, precipitation must be induced via centrifugation. The supernatant, containing the mixture of the solvent and the antisolvent, is then disposed of and the precipitated nanoparticles can be redispersed in a neat solvent. In order to clean freshly prepared nanoparticles, this process is repeated several times in order to remove any unreacted reagents which remain solubilized in the supernatant. This process requires large amounts of neat solvents and produces large amounts of solvent waste which must be either disposed of or separated, requiring large amounts of energy. These drawbacks combined with the intensive manual labor involved in these precipitations make this LSAS precipitation method costly, non-sustainable, and environmentally hazardous.

Several problems with the LSAS precipitation can be remedied through the use of CO₂-expanded hexane rather than the hexane–ethanol mixed liquid solvents [15–18]. CO₂ is a non-solvent for the aliphatic capping ligands and is miscible with hexane below the vapor pressure of CO₂, thus satisfying all four requirements for nanoparticle precipitation. Therefore, when a stable dispersion of nanoparticles is pressurized with CO₂, the CO₂ partitions into the liquid phase, reducing the solvent strength of the mixture. At sufficiently high concentrations of CO₂, the solvent strength is reduced to the point of no longer being capable of stabilizing the nanoparticles and the nanoparticles begin to flocculate. LSAS mixtures have relatively high viscosities and low nanoparticle diffusivities due to ethanol being used as the antisolvent, thus precipitation is a slow process which needs to be induced via centrifugation. CO₂-expanded solvents, on the other hand, have been shown to reduce the viscosity by a factor of five [8] and enhance the diffusivity of compounds through the CXL [9, 10] compared with the neat solvent. Due to the decreased viscosities and increased diffusivities of compounds through the CXL, the nanoparticles can be precipitated from a stable dispersion without the need for centrifugation, thereby making the process less energy and time intensive. The final problem with LSAS precipitations is the amount of solvent waste that is produced. The ability to recover the CO₂ and the neat hexane from a CXL precipitation through simple adjustments in pressure and temperature eliminates any waste from the process, significantly improving the sustainability and environmental safety.

The relative amount (number density) of nanoparticles that are dispersed in a liquid can be quantified by tracking the surface plasmon resonance (SPR) band for the nanoparticle material using UV-visible spectroscopy during pressurization with CO₂ [16, 19, 20]. SPR is a delocalized dipole created on the surface of nanometer-sized particulates due to propagating surface electromagnetic waves induced via incident light [21]. The SPR band occurs at the wavelength of light (λ_{SPR}) which is most absorbed by the metallic surface. The SPR band depends on both the material of the nanoparticles and the size of the nanoparticles and a summary of select materials and sizes can be found in Table 2.1. The location of the SPR band depends on the size of the nanoparticle, but as the intensity of the peak is cumulative for all dispersed nanoparticles, tracking the intensity of the maximum absorbed light allows for a qualitative measure of the total number of nanoparticles in a dispersion.

An apparatus for measuring the UV-visible spectrum of a nanoparticle dispersion under pressurized conditions is shown in Figure 2.2 [16, 19, 20]. This apparatus

Table 2.1 Wavelength of maximum absorbance due to surface plasmon resonance for different materials and nanoparticle diameters.

Material	Nanoparticle diameter (nm)	λ_{SPR} (nm)	Ref.
Gold	8.9	517	[22]
	14.8	520	
	21.7	521	
	48.3	533	
Silver	3.66	443	[23]
	4.87	443	
	8.09	472	
	10.64	497	
CdSe/ZnS	5.2	594	[17]
	3.2	563	
	2.4	522	
	1.9	475	

consists of a stainless-steel high-pressure vessel fitted with transparent windows which can be placed in a UV-visible spectrophotometer. A quartz cuvette that contains the liquid nanoparticle dispersion is placed inside the high-pressure vessel in line with the viewing windows. This allows for the measurement of the UV-visible spectrum of the nanoparticle dispersion during pressurization of the vessel with applied CO₂ and concomitant expansion of the liquid mixture within the cuvette. CO₂ can be introduced into the vessel directly from a CO₂ tank under VLE conditions since

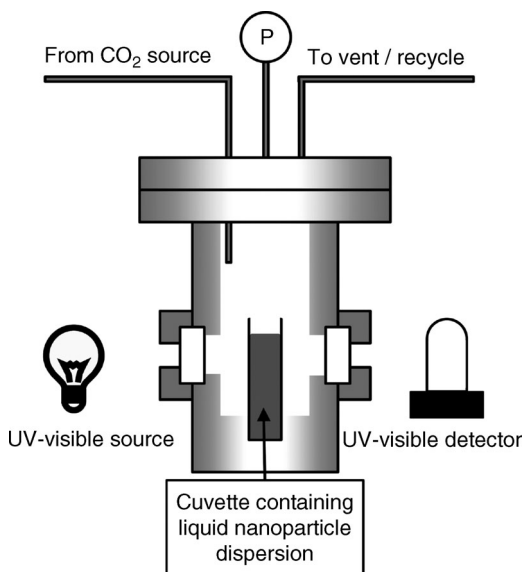


Figure 2.2 Apparatus to quantify nanoparticle precipitation using UV-visible spectroscopy.

the CXL is formed at sub-vapor pressure conditions or, more controllably, from a high-pressure pump. The applied CO₂ pressure is measured using a simple pressure gauge attached to the vessel. After the precipitation studies, CO₂ can be recycled through the vent line and the hexane-nanoparticle dispersion can be recovered.

To precipitate DDT-stabilized nanoparticles from a hexane dispersion, an aliquot of the hexane–nanoparticle dispersion is loaded into the cuvette within the high-pressure vessel and the vessel is then sealed and purged of any nitrogen and oxygen. CO₂ is then used to pressurize the system to a sub-vapor pressure level in order to destabilize and precipitate a portion of the nanoparticles. The UV–visible spectrum is measured once the system has reached equilibrium (determined by the UV–visible spectrum). The pressure is then further increased and the process is repeated. A typical set of UV–visible spectra at varying applied CO₂ pressures is shown in Figure 2.3a. The decrease in absorbance at λ_{SPR} is due to the combination of two effects: (1) precipitation of nanoparticles from the liquid dispersion and (2) a decrease in concentration of nanoparticles in the dispersion due to the volume expansion of the solvent mixture. After correcting for the volume expansion (volumes calculated from PR-EOS and correction term from Beer–Lambert law), a clear trend arises which can be seen in Figure 2.3b. Based on this, the nanoparticles remain completely dispersed up to an applied CO₂ pressure of approximately 35 bar, whereupon a significant decrease in absorbance occurs with further pressurization, signifying precipitation of the nanoparticles. Precipitation of the nanoparticles is a function of the applied CO₂ over a precipitation range; in the case of DDT-stabilized gold nanoparticles, this precipitation range is approximately 35–43 bar. Pressurization of the nanoparticle dispersion to near vapor pressure conditions (approximately 43 bar) of CO₂ would induce complete precipitation of these nanoparticles. This precipitation is completely reversible; depressurization decreases the amount of CO₂ in the solvent mixture, thereby increasing the solvent strength and thus redispersing the nanoparticles.

2.3

Size-Selective Fractionation of Nanoparticles

Traditionally, size-selective fractionation of nanoparticles is performed using stage-wise LSAS precipitations with centrifugation [14]. An amount of antisolvent is added to a stable dispersion of nanoparticles such that only a portion of the nanoparticles are destabilized and precipitated with the assistance of centrifugation. It has been shown that the precipitation of nanoparticles in a poor solvent (as is the case in LSAS precipitation) is due to the inability of the solvent to provide sufficient steric stabilization (repulsive interactions) to overcome the inherent van der Waals attractive forces between nanoparticles in a dispersion [24–26]. The van der Waals potential scales with nanoparticle size [27–29]; as such, the nanoparticles with the largest van der Waals potential (the largest nanoparticles) will precipitate first upon worsening solvent conditions. When a portion of nanoparticles are precipitated from a stable dispersion, these nanoparticles will be the largest fraction of nanoparticles from the original dispersion. In traditional LSAS fractionations, the supernatant

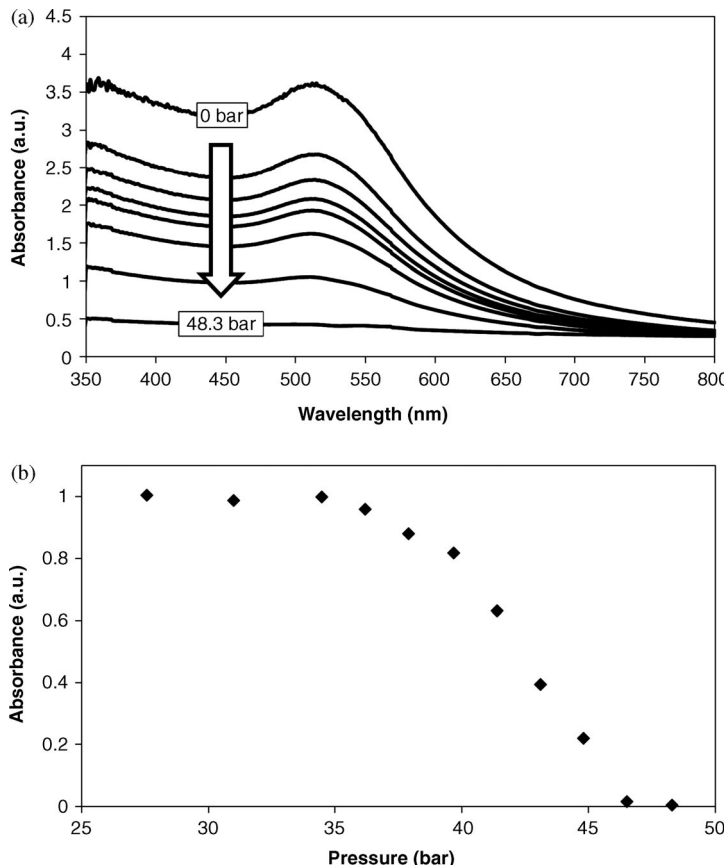


Figure 2.3 (a) UV-visible spectra of the CXL precipitation of dodecanethiol-stabilized Au nanoparticles from hexane at various applied CO₂ pressures (arrow signifies increasing applied CO₂ pressure from 0 to 48.3 bar).

(b) Absorbance at λ_{SPR} after correction for volume expansion and normalization as a function of applied CO₂ pressure. Adapted from [16] © 2005 American Chemical Society.

containing the still dispersed smaller nanoparticles can be recovered for additional fractionations or disposed of and the precipitate can be redispersed in neat solvent. This process needs to be repeated several times in order to produce a monodisperse sample of nanoparticles. However, the repetition produces large quantities of organic solvent waste and occupies large amounts of time due to the centrifugation. This LSAS fractionation process is typically capable of reaching $\leq 30\%$ of the nanoparticles within $\pm 5\%$ of the mean diameter [14].

In an effort to address these limitations, it has been demonstrated that nanoparticles can be controllably, and quickly, precipitated through simple adjustments to the applied CO₂ pressure without producing any organic waste or requiring centrifugation [15–18]. Knowing that the largest particles precipitate first upon worsening

conditions, if some portion of the nanoparticles are precipitated and the remaining dispersion nanoparticles are moved away from the precipitated nanoparticles, an effective size-selective fractionation of nanoparticles should be achieved. To paraphrase, if the location of precipitation is controlled, an effective fractionation is possible. Two types of systems that are capable of utilizing this CXL fractionation technique to prepare monodisperse nanoparticles will be discussed: (1) small-scale benchtop apparatus and (2) large-scale scalable apparatus.

2.3.1

Small-Scale Size-Selective Fractionation

An apparatus to fractionate size-selectively small quantities (sub-milligram quantities of nanoparticle material) is presented in Figure 2.4b [19]. This apparatus consists

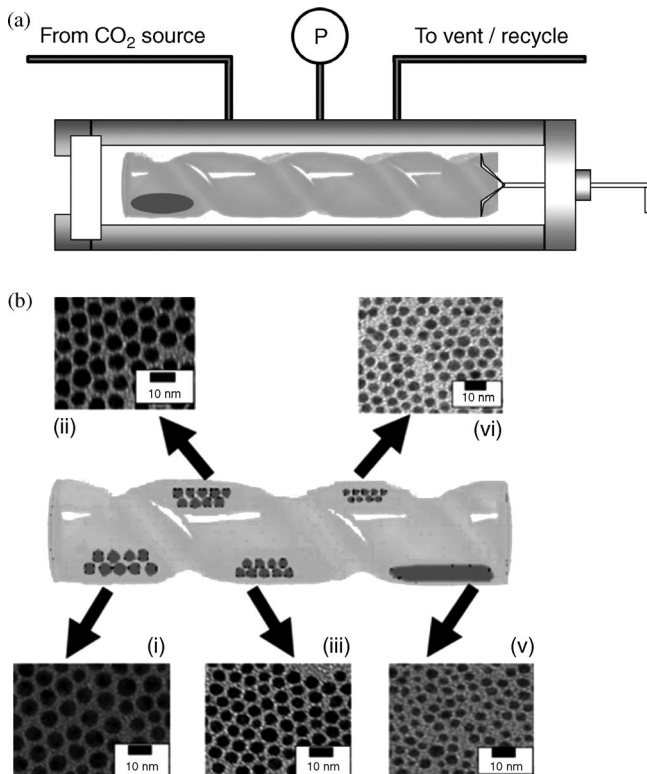


Figure 2.4 (a) Apparatus to size-selectively fractionate small quantities of nanoparticles using CXL fractionation techniques. Adapted from [19] © 2005 American Chemical Society. (b) TEM images of DDT-stabilized silver nanoparticles fractionated from hexane using the CXL fractionation technique in the small-

scale spiral-tube apparatus. The nanoparticle fractions were collected at applied CO₂ pressure of (i) 0–37.9, (ii) 37.9–41.4, (iii) 41.4–43.1, (vi) 43.5–44.8, and (vi) 44.8–48.3 bar. Reproduced from [16] © 2005 American Chemical Society.

of an open-ended glass spiral tube within a stainless-steel high-pressure vessel. CO₂ can be delivered from a CO₂ tank under VLE conditions or from a high-pressure pump which can controllably deliver CO₂. A stainless-steel rod enters the vessel through a Teflon fitting and is connected to the glass tube such that the spiral tube inside the vessel can be rotated about its axis from outside of the vessel. This rotation allows a small drop of a nanoparticle dispersion to be translated along the tube, much like an Archimedes screw.

In order to fractionate nanoparticles with this spiral-tube apparatus, a small volume (< 1 ml) of a nanoparticle dispersion (e.g. DDT-stabilized silver nanoparticles dispersed in hexane) is loaded into the spiral tube, such that the entire drop remains at one end of the tube. The high-pressure vessel is sealed, and all nitrogen and oxygen are purged. The entire vessel is pressurized to some first applied CO₂ pressure that falls within the precipitation range as determined by CXL precipitation UV-visible studies (approximately 35–43 bar for DDT-stabilized silver nanoparticles dispersed in hexane [16]). The hexane dispersion expands, the solvent strength of the mixture decreases, and the largest portion of the nanoparticles precipitates on to the glass tube. The tube is then rotated, forcing the liquid droplet containing the still dispersed smaller nanoparticles to translate along the length of the tube to a new position, leaving the precipitated larger nanoparticles attached to the original location on the glass tube surface. The vessel is then further pressurized to a higher level within the precipitation range and the next largest portion of nanoparticles still dispersed in the droplet precipitates on to the glass tube at the new location. This process can be repeated for as many fractions as needed. Upon completion, the system is depressurized and the glass tube removed. The size-selectively fractionated nanoparticles that reside at different locations along the glass tube can be redispersed by placing a droplet of the neat primary solvent on the specific location to recover the desired fraction. An example of a polydisperse DDT-stabilized silver nanoparticles that have been fractioned into five monodisperse fractions using this CXL fractionation technique is shown in Figure 2.4b to demonstrate the effectiveness of this technique [16].

CXL fractionations can be performed in as little as 20 min for each pressurization stage such that multiple monodisperse fractions can be collected in less than 2 h as opposed to several hours for an LSAS fractionation. The CXL fractionation also produces negligible waste, as all of the solvent and CO₂ can be recovered at the end of the process [16, 19].

2.3.2

Large-Scale Size-Selective Fractionation

The small-scale apparatus was initially designed as a proof-of-concept device to demonstrate that nanoparticle size-selective fractionation was possible using CXLs. The geometry of the device is not amenable to being scaled to handle larger dispersion quantites. An apparatus that is capable of fractionating larger quantites (gram-scale quantities of nanoparticle material) of nanoparticles and that is scalable to even larger quantities is shown schematically in Figure 2.5 [18]. This apparatus maintains the concept of controlling the location of nanoparticle precipitation in

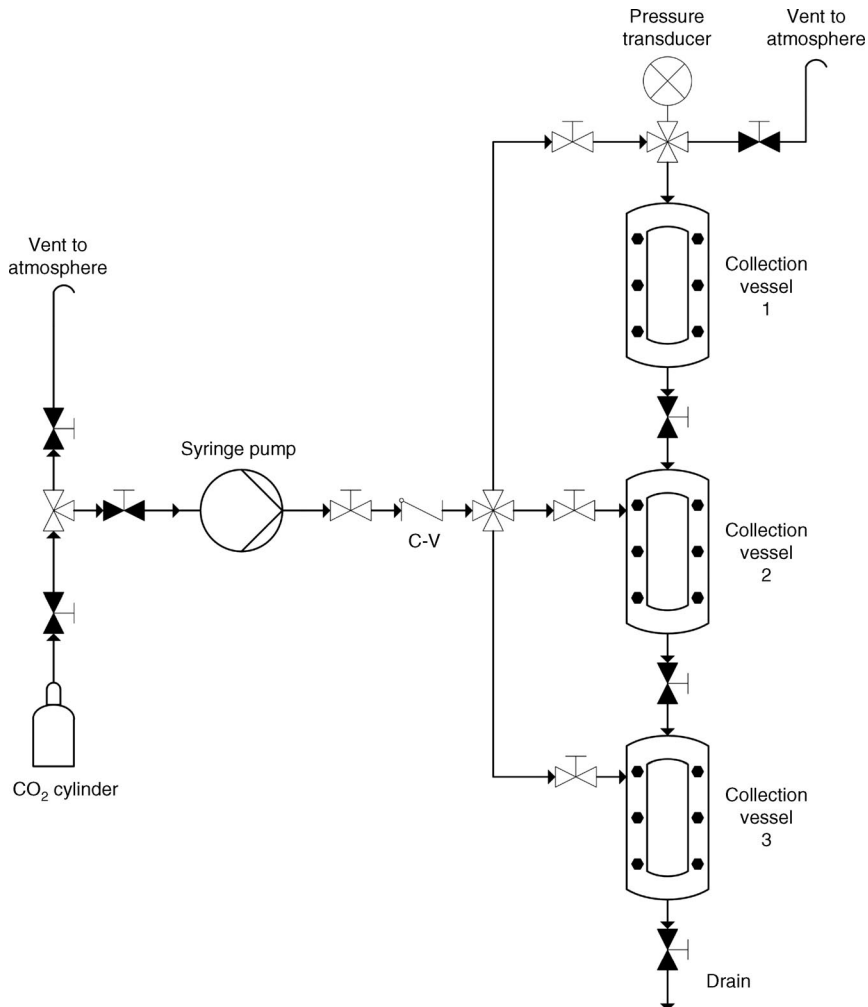


Figure 2.5 Schematic diagram of an apparatus capable of size-selectively fractionating large quantities of nanoparticles. Reproduced from [18] © 2010 IOP Publishing.

order to achieve an effective fractionation. This apparatus consists of vertically mounted high-pressure vessels connected with inline high-pressure valves such that each vessel can be isolated from the others. Within each vessel is a glass liner that prevents nanoparticle contact with the stainless-steel vessel while providing a removable surface upon which precipitation can occur. Each individual vessel can be scaled to handle any volume required. Additional vessels can be added to increase the number of fractions that the original dispersion can be divided into by arranging them into a contiguous series of fractionation stages at increasing levels of applied CO_2 pressure. It is noted that at these scales the rate-determining step for the fractionation process is the diffusion of the CO_2 vapor into the liquid medium [18].

Therefore, the system is infinitely scalable if the time scale for CO₂ diffusion is acceptable or if the mass transport of CO₂ into the liquid phase can be enhanced (e.g., bubbling the CO₂ directly into the liquid).

Fractionations using this apparatus are initiated by introducing the original, polydisperse dispersion of nanoparticles into the first collection vessel and the system is subsequently purged of oxygen and nitrogen. The entire system is then pressurized with CO₂ to a pressure that falls within the known precipitation range, thereby decreasing the solvent strength of the liquid mixture to the point where a portion of the original dispersion is destabilized. As such, these destabilized, larger nanoparticles will precipitate on to the glass liner while the smaller nanoparticles remain dispersed in the solvent mixture. In order to separate the smaller-sized nanoparticles that remain dispersed in the solvent mixture from the larger-sized nanoparticles that have adhered to the glass liner, the isolation valve separating collection vessels 1 and 2 is slowly opened to allow the solvent mixture containing the smaller, still dispersed nanoparticles to drain (via gravity) away from the larger precipitated nanoparticles. The drainage step should be performed slowly and at constant pressure to ensure that the precipitated nanoparticles are not sheared from the liner or inadvertently redispersed due to a change in the solvent strength of the solvent mixture. The entire system is then pressurized to higher pressure (still within the precipitation range) such that the next largest fraction of nanoparticles precipitate and adhere to the liner in collection vessel 2. The still dispersed smallest nanoparticles are then slowly transferred to collection vessel 3 at constant pressure. Once the remaining dispersion has been transferred into the last vessel, the system is depressurized (the CO₂ can be recycled at this point), the liquid remaining in the final vessel which contains the smallest nanoparticle fraction is collected, and the glass liners are removed from the other vessels. The fractions can be recovered from the glass liners through simple washing with neat hexane (assuming aliphatic ligand-stabilized nanoparticles) with the largest fraction of nanoparticles from collection vessel 1, the next largest from collection vessel 2, and so on, and smallest nanoparticles from the liquid recovered from the last vessel. An example of fractionated DDT-stabilized gold nanoparticles precipitated from a 20 ml (~300 mg of gold) hexane dispersion using this CXL fractionation apparatus is shown in Figure 2.6 [18].

This CXL fractionation technique has been effective in size-selectively fractionating silver [16, 19], gold [16, 18], and CdSe/ZnS [17] nanoparticles efficiently and cleanly at different scales. The CXL fractionation technique should be applicable to any material provided that the nanoparticles can be stabilized with an aliphatic ligand tail such as dodecanethiol or tri-*n*-octylphosphine oxide (TOPO). Compared with the LSAS fractionations method, which is capable of reaching $\leq 30\%$ of the nanoparticles within $\pm 5\%$ of the mean diameter after several fractionation stages [14], the CXL precipitation method has been shown to be capable of reaching 40% of the nanoparticles within $\pm 5\%$ of the mean diameter within a single fractionation [20]. It is possible to control the size distributions of the recovered fractions by judiciously selecting the precipitation pressure [18]. Lower pressures correspond to larger mean diameters at a given precipitation stage and vice-versa, while the magnitude of the change in pressure (ΔP) from one stage to the next dictates the broadness of the size

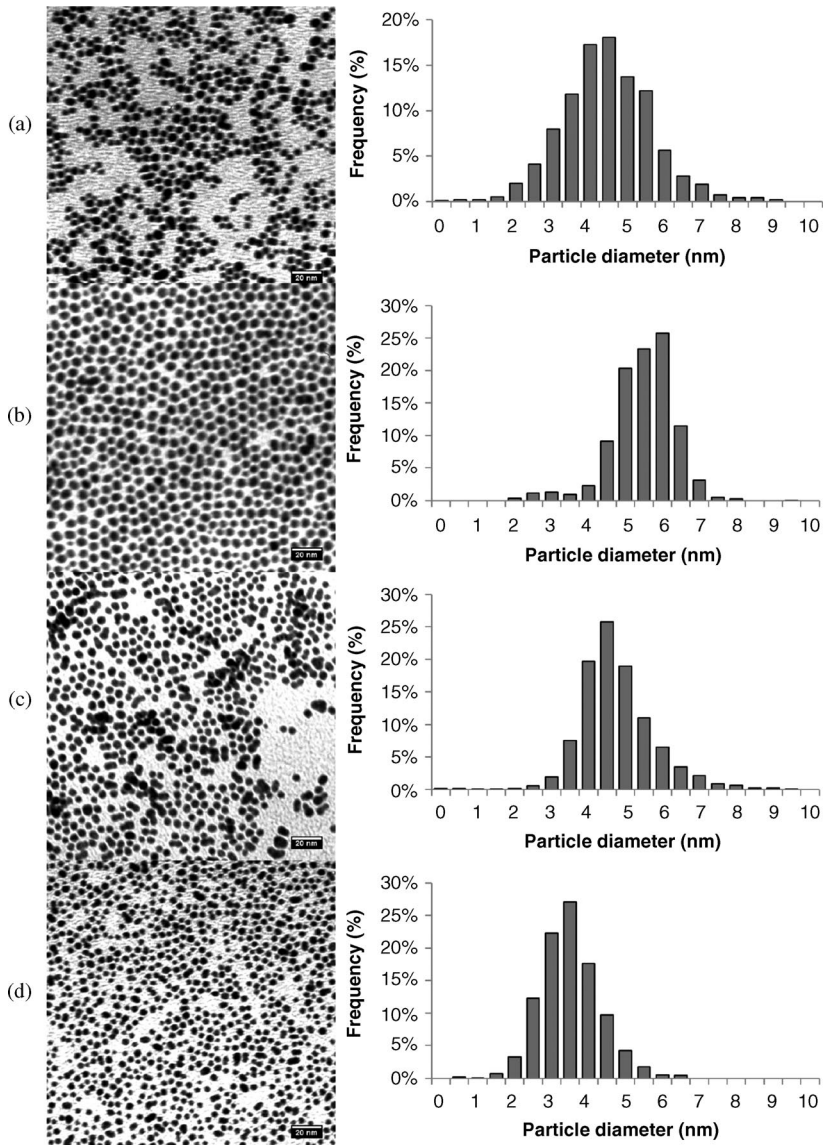


Figure 2.6 TEM images and size distributions of CXL fractionated DDT-stabilized gold nanoparticles using CO₂-expanded hexane. (a) Original sample prior to fractionation; (b) nanoparticles precipitated between 0 and 42.7 bar of applied CO₂ pressure; (c) nanoparticles precipitated between 42.7 and 45.5 bar; and (d) nanoparticles recovered from the last vessel that were not precipitated at 45.5 bar in the previous stage. Scale bars are 20 nm. Reproduced with permission from [18] © 2010 IOP Publishing.

distribution of the nanoparticles collected [16, 18]. The size-selective fractionation via CXL precipitation can provide higher quality nanoparticle fractions than the LSAS precipitation without the need for centrifugation, or the drawback of creating large quantities of waste.

2.4

Tuning the Precipitation Range

Precipitation of DDT-stabilized gold nanoparticles from hexane begins at an applied CO₂ pressure of approximately 35 bar and continues through approximately 48 bar. Although 35 bar may not be considered high pressure, any adjustments to the system that can reduce the onset of precipitation or increase the pressure range over which nanoparticles precipitate will reduce operating costs and increase control over the fractionation process, respectively. Process variables that can be adjusted include, but are not limited to, operating temperature, choice of solvent, and choice of capping ligand [16, 20].

2.4.1

Effect of Temperature

As temperature increases, the density of CO₂ in the vapor phase of a CXL system decreases at a given pressure, causing the amount of CO₂ in the liquid phase to decrease [30]. For example, if an isochoric and isobaric system is heated, CO₂ would need to be released in order maintain volume and pressure, decreasing the density of the vapor phase. The applied CO₂ pressure, at an increased temperature, must be elevated in order to reach the same liquid-phase compositions as at a lower temperature. This implies that lower operating temperatures would be beneficial as lower applied CO₂ pressure would be required. The precipitation curves of DDT-stabilized gold nanoparticles dispersed in hexane precipitated with CO₂ at several operating temperatures are shown in Figure 2.7a. At higher temperatures, higher pressures are needed to induce nanoparticle precipitation [16].

2.4.2

Effect of Solvent

It has been demonstrated that the length of the hydrocarbon solvent molecule can have a significant impact of the stability of sterically stabilized nanoparticles [24, 30]. The solvation of a sterically stabilized nanoparticle depends on the interaction parameter, χ , between the solvent and the ligand [25, 30–33], such that

$$\chi = \frac{\nu}{RT} (\delta_1 - \delta_3)^2 \quad (2.2)$$

where ν is the molar density of the solvent, R is the gas constant, T is the operating temperature and δ_1 and δ_3 are the solubility parameters for the solvent and ligand,

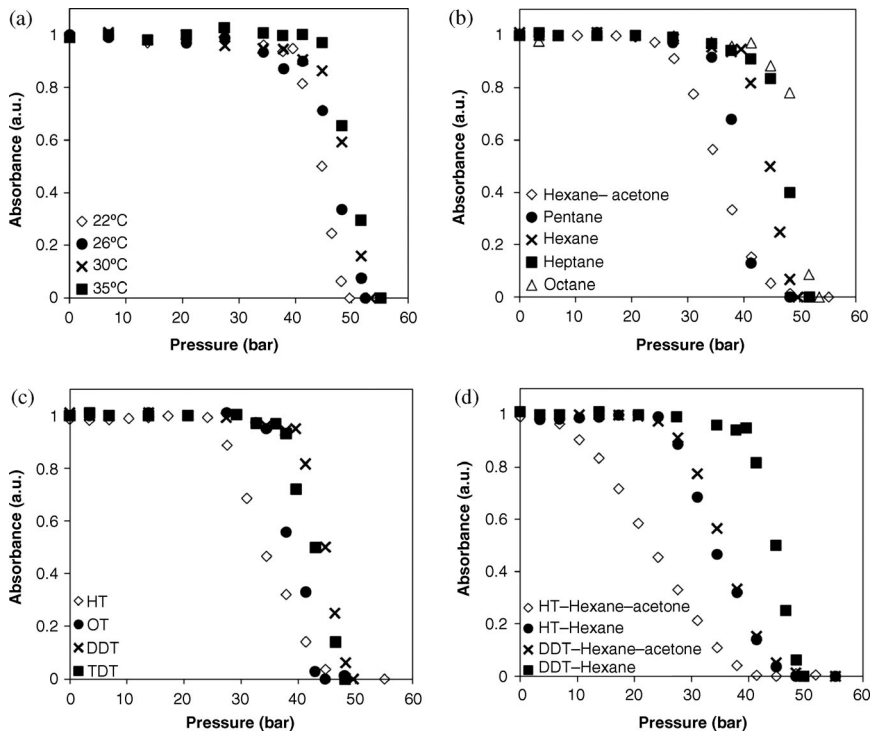


Figure 2.7 Effect of various factors on nanoparticle dispersion (as determined by tracking the absorbance of λ_{SPR}) as a function of applied CO_2 pressure. (a) effect of temperature on DDT-stabilized gold nanoparticles dispersed in hexane; (b) effect of solvent on DDT-stabilized gold nanoparticles at room temperature; (c) effect of ligand on gold

nano particles dispersed in hexane at room temperature; (d) combined effects of solvent and ligand on gold nanoparticles at room temperature. HT, hexanethiol; OT, octanethiol; DDT, dodecanethiol; TDT, *tert*-decane thiol.
Adapted from [16] © 2005 American Chemical Society and [20].

respectively. If a stronger solvent is used to disperse the nanoparticles prior to pressurization with CO_2 , higher applied CO_2 pressures will be required to induce nanoparticle precipitation. Using longer hydrocarbons as the primary solvent will provide stronger stabilization than shorter hydrocarbons but will require higher applied CO_2 pressures to induce precipitation [16]. Figure 2.7b demonstrates the effect of using pentane, hexane, heptane, or octane as the primary solvent when precipitating nanoparticles using the CXL technique.

A second method of adjusting the effect of solvent would involve changing the strength of the primary solvent by adding a secondary liquid antisolvent [20]. This is essentially the goal of LSAS precipitations; however, rather than adding sufficient liquid antisolvent to induce precipitation, the quantity of antisolvent added is only that needed to bring the dispersion to the verge of precipitation while still remaining stabilized. For example, a mixed solvent of hexane and acetone (55 and 45 mol%,

respectively) can maintain and stabilize a dispersion of sub-10 nm DDT-stabilized nanoparticles. As seen in Figure 2.7b, starting with a mixture of hexane and acetone, rather than neat hexane, the applied CO₂ pressure necessary to induce precipitation can be reduced by approximately 15 bar.

2.4.3

Effect of Stabilizing Ligand

Similarly to the effect of hydrocarbon solvent length, increasing the length of the hydrocarbon ligand molecule can increase the stability of nanoparticle dispersions [16]. Shorter ligands have weaker interactions with the solvent compared to longer ligands, as seen in Figure 2.7c. This trend holds true for carbon numbers up to C₁₃ (*tert*-decanethiol) where the pressure needed to induce precipitation is less than that of C₁₂ (dodecanethiol), implying that *tert*-decanethiol does not stabilize the nanoparticles as well as dodecanethiol.

In summary, lower operating temperatures, shorter hydrocarbon solvents, addition of a secondary liquid antisolvent, and shorter hydrocarbon ligands require lower applied CO₂ pressures to induce nanoparticle precipitation. These combined effects can be seen in Figure 2.7d [20]. It should be noted that when precipitation is induced at very low applied CO₂ pressure (e.g., hexanethiol-stabilized nanoparticles dispersed in a mixture of hexane and acetone), the time required for precipitation is drastically increased due to higher liquid viscosities and lower diffusivities. On the other hand, higher operating temperatures, longer hydrocarbon solvents, and longer hydrocarbon ligands require higher applied CO₂ pressures to induce nanoparticle precipitation.

2.5

Modeling Nanoparticle Dispersibility in CXLs

To aid nanoparticle precipitation and fractionation process development further, it is necessary to be able to predict the size of nanoparticles that can be dispersed in a CXL under a given set of conditions. Current methods of predicting nanoparticle dispersibility, including DLVO theory, are not applicable to organic solvent systems [34]. A theoretical model based on the total interaction energy, Φ_{total} , between two interacting nanoparticles of the same size, is capable of predicting the maximum nanoparticle size that can be dispersed in a solvent media under a given set of conditions in conventional liquid solvents [24], compressed liquids [35], supercritical fluids [30, 33], and CXLs [25]. These models followed a “soft-sphere” modeling approach, where the total interaction energy is the sum of the attractive and repulsive potentials which act upon a nanoparticle in a dispersion:

$$\Phi_{\text{total}} = \Phi_{\text{vdW}} + \Phi_{\text{osm}} + \Phi_{\text{elas}} \quad (2.3)$$

where Φ_{vdW} is the van der Waals attractive potential, Φ_{osm} is the osmotic repulsive potential (due to the solvation of the ligands by the solvent), and Φ_{elas} is the elastic

repulsive potential (due to steric interactions between the ligands of one nanoparticle and the core of another). The total interaction energy depends on nanoparticle size, distance between nanoparticles, ligand length, ligand density, and solvent properties. CXL nanoparticle dispersions involve a ternary system where two solvents interact with the stabilizing ligand and should be modeled accordingly.

The van der Waals attractive potential [27] increases with an increase in nanoparticle radius or with a decrease in center-to-center separation distance between nanoparticles:

$$\Phi_{\text{vdw}} = -\frac{A_{131}}{6} \left[\frac{2R^2}{d^2-4R^2} + \frac{2R^2}{d^2} + \ln\left(\frac{d^2-4R^2}{d^2}\right) \right] \quad (2.4)$$

where A_{131} is the Hamaker constant, R is the nanoparticle radius, and d is the center-to-center separation distance. The Hamaker constant is a proportionality factor that accounts for the interaction between two nanoparticles of the same material (component 1) through a solvent medium (component 3). The Hamaker constant for a mixed solvent system such as a CXL can be calculated as

$$A_{131} \approx \left[\sqrt{A_{11}} - \left(\tilde{\phi}_{3'} \sqrt{A_{(33)'}} + \tilde{\phi}_{3''} \sqrt{A_{(33)''}} \right) \right]^2 \quad (2.5)$$

where A_{11} is the Hamaker constant for the nanoparticle material (e.g., $A_{11} = 2.185$ eV for silver), $\tilde{\phi}$ is the solvent volume fraction, and A_{33} is the Hamaker constant for the pure solvent and can be predicted by an equation of state based on Lifshitz theory [29]. Primes ('or '') represent the different solvent components (in this case CO₂ and hexane, respectively) [25].

Two repulsive contributions, osmotic and elastic contributions [31, 32], oppose the van der Waals attractive contribution where the osmotic potential depends on the free energy of the solvent-ligand interactions (due to the solvation of the ligand tails by the solvent) and the elastic potential results from the entropic loss due to the compression of ligand tails between two metal cores. These repulsive contributions depend largely on the ligand length, solvent parameters, nanoparticle radius, and center-to-center distance:

$$\Phi_{\text{osm}} = \begin{cases} \frac{4\pi R k_B T}{\nu_{\text{solv}}/N_A} \phi^2 \chi_{\text{osm}} \left(l - \frac{h}{2} \right)^2 & \text{for } l < h < 2l \\ \frac{4\pi R k_B T}{\nu_{\text{solv}}/N_A} \phi^2 \chi_{\text{osm}} \left\{ l^2 \left[\frac{h}{2l} - \frac{1}{4} - \ln\left(\frac{h}{l}\right) \right] \right\} & \text{for } h < l \end{cases} \quad (2.6)$$

$$\Phi_{\text{elas}} = \frac{2\pi R k_B T l^2 \phi \varrho}{M W_2} \left\{ \frac{h}{l} \ln \left[\frac{h}{l} \left(\frac{3-h/l}{2} \right)^2 \right] - 6 \ln \left(\frac{3-h/l}{2} \right) + 3 \left(1 - \frac{h}{l} \right) \right\} \quad (2.7)$$

where ν_{solv} is the molar volume of the solvent, N_A is Avogadro's number, l is the ligand length available for solvation, h is the nanoparticle surface-to-surface separation distance ($h = d - 2R$), ϱ is the ligand density, and MW_2 is the ligand molecular weight. A mixing rule for χ_{osm} was derived [25] which accounts for the binary solvents of the ternary GXL system:

$$\chi_{\text{osm}} = x_{3'} \left[\frac{1}{2} + \tilde{\phi}_{3''} r_{3'} \chi_{(3'3'')} - r_{3'} \chi_{(3'2)} \right] + x_{3''} \left[\frac{1}{2} - r_{3''} \chi_{(3''2)} \right] \quad (2.8)$$

where $\tilde{\phi}_{3''}$ is the volume fraction of hexane in the solvent mixture excluding the ligand, r is the molecular segment lengths (assumed as $r_{3'} = 1$ and $r_{3''} = \nu_{3''}/\nu_{3'}$), and $x_{3'}$ and $x_{3''}$ are mole fractions of CO_2 and hexane, respectively. Molar compositions and molar volumes for the CO_2 -expanded phase can be calculated from the PR-EOS with the binary interaction parameter set as $k_{12} = 0.125$ [5, 25].

The van der Waals, osmotic, and elastic contributions to the total interaction energy are calculated as a function of the separation distance, h , for CO_2 -expanded hexane at various pressures (below the vapor pressure of CO_2 , 57.2 bar at 20°C) [25]. If the minimum of the total interaction energy curve is greater than or equal to the Boltzmann threshold stabilization energy, $-3/2k_B T$, the nanoparticles have sufficient energy to remain dispersed. However, if the minimum of the total interaction energy curve is less than the Boltzmann threshold stabilization energy, the nanoparticles do not have enough energy to remain dispersed and will precipitate. The size of nanoparticles that can be dispersed under the given set of conditions can be determined by equating the minimum of the potential curve with $-3/2k_B T$ and solving for the corresponding nanoparticle diameter. A detailed explanation of this model for certain CXL systems has been described elsewhere [25, 26], including different phenomenological models to account for the nature of the solvent-ligand interaction.

Determining the physical nature of the solvent-ligand interaction (i.e., what physically occurs when the solvent mixture interacts with the ligand as the solvent strength of the mixture decreases) can be accomplished through small angle neutron scattering (SANS). SANS is a unique technique to monitor the solvent-ligand interaction based on the accessible length scales measurable by SANS. Neutron scattering techniques are sensitive to isotopic substitution, particularly the difference between hydrogen and deuterium [36–38]. Metal nanoparticles stabilized with hydrogenated alkanethiol ligands can be dispersed in a deuterated solvent (e.g., *n*-hexane-*d*-14) in order to provide contrast between the ligand and solvent [39]. Details on measurement and analysis techniques are available in [40]. Using SANS, it is possible to measure the length of the ligand shell as a function of applied CO_2 pressure (or CO_2 solvent composition), as shown in Figure 2.8. SANS studies have shown that the length of the ligand shell gradually decreases with increasing CO_2 antisolvent. At the point of nanoparticle precipitation, dodecanethiol ligands have collapsed to approximately 50% of their original, fully extended length. An additional benefit of SANS is the ability to provide contrast between the nanoparticle ligand and the bulk solvent, allowing measurement of the solvent composition within the ligand shell and also the surface coverage of ligand on the nanoparticle. As the nanoparticle size

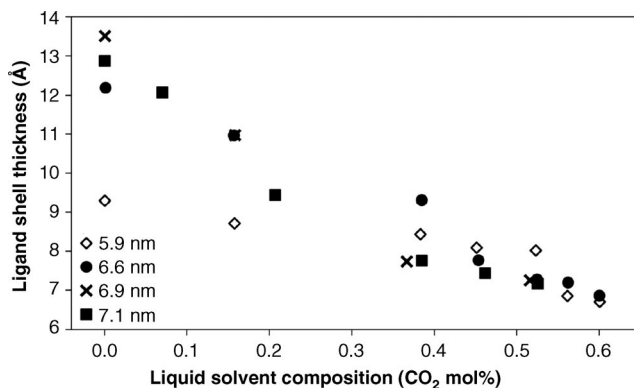


Figure 2.8 SANS measurement of ligand shell thickness as a function of CO₂ composition for differently sized DDT-stabilized silver nanoparticles dispersed in *n*-hexane-*d*₁₄ [40].

increases, the ligand surface coverage decreases [40] to approximately the accepted surface coverage of a flat surface [41]. This implies that precipitation is a function not only of size but also of ligand surface coverage. This is significant for post-synthesis surface modification applications, where monodispersed populations of nanoparticles can be fractionated based on the surface chemistry or the degree of surface modification.

2.6

Thin-Film Deposition

Some of the more interesting nanoparticle applications involve depositing nanoparticles into thin monolayer or multilayer films [42, 43]. Traditionally this has been accomplished through solvent evaporation on the surface (i.e., dropcasting) on which the thin-film should be deposited [43, 44]. The capillary forces created at the liquid/solid interface as the solvent evaporates can help induce self-assembly [41, 45] or to target the location of the thin-film [46]. Although these capillary forces can be useful, they can also cause dewetting effects which can create islands, rings, and highly uneven nanoparticle structures [47–49] and also destroy surface features [50]. Examples of the uneven films that are cast by simple solvent evaporation are shown in Figure 2.9a and c.

One method of overcoming the detrimental solvent dewetting effects is to use liquid CO₂ as the solvent for nanoparticle dispersions [52], since CO₂ does not experience the dewetting instabilities due to its extremely low surface tension [53]. In this case, nanoparticles must be stabilized with fluorinated ligands [30, 33, 54–65] or other CO₂-philic ligands [60, 66–76], such that they will disperse in the CO₂ prior to dropcasting. These fluorinated ligands tend to be toxic and environmentally persistent and, typically, only very small nanoparticles can be dispersed at low concentrations.

CXLs can be used to provide improved solubilities compared with neat CO₂ while still providing the desirable low interfacial properties. The controlled reduction in

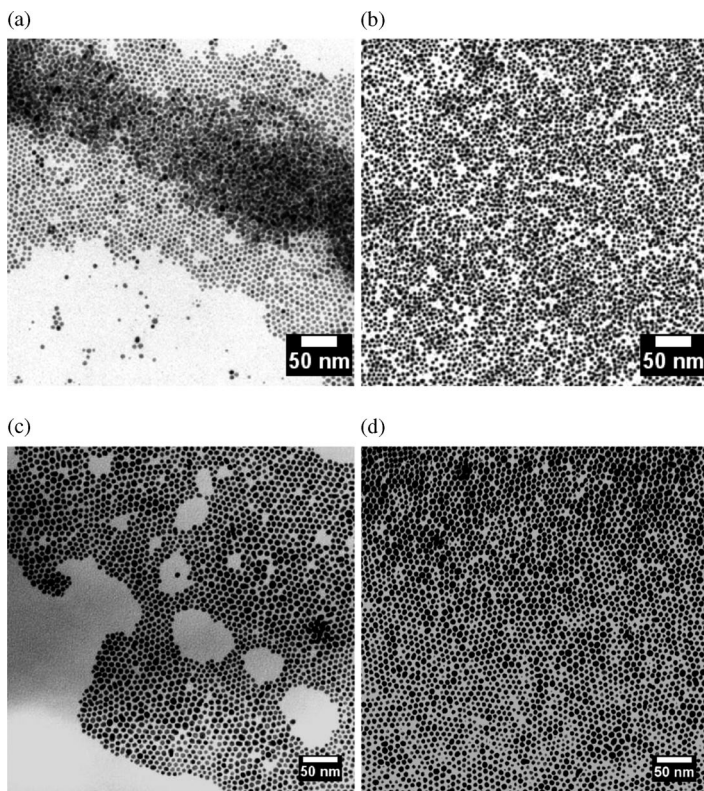


Figure 2.9 DDT-stabilized silver nanoparticle films deposited via (a) hexane evaporation and (b) CXL nanoparticle deposition. Adapted from [15] © 2005 American Chemical Society.

films deposited via (c) hexane evaporation and (d) CXL nanoparticle deposition.
Adapted from [51] © 2006 American Chemical Society.

DDT-stabilized gold nanoparticle

solvent strength of CXLs through pressurization with CO₂ allows nanoparticles to be precipitated controllably from an expanded liquid dispersion and deposited directly on a surface. The next step involves supercritical drying with CO₂ in order to remove the liquid solvent, thereby avoiding the detrimental dewetting and interfacial tensions that exist in conventional solvent-evaporation techniques [15, 51]. Once the nanoparticles have been deposited on the surface, the system is further pressurized to obtain compressed liquid conditions (at approximately 70 bar) and is then slowly flushed with neat liquid CO₂ so as not to disturb the precipitated nanoparticle thin-film while removing the primary organic solvent. Once the primary solvent has been completely removed, the liquid CO₂ system is heated to reach supercritical conditions and then isothermally depressurized to a gaseous state. This process ensures that the nanoparticle thin-film surface never contacts a liquid/vapor interface that can negatively affect the quality of the nanoparticle thin-films and surface features.

Figure 2.9b and d provide examples of silver and gold nanoparticle thin-films deposited using this CXL nanoparticle deposition. It is noted that the CXL deposition process provides uniform, wide-area coverage thin-films compared with solvent-evaporation, dropcast thin-films from the same original nanoparticle dispersions. This CXL deposition is found to create a high-quality conformal map of the substrate surface (i.e., all surfaces exposed to the CXL solvent media are uniformly coated with nanoparticles) [77]. The number of layers (i.e., monolayer versus multilayer) depends on the quantity of nanoparticles in the liquid dispersion used in the CXL deposition [51]. The rate of pressurization from the neat primary solvent to near-vapor pressure conditions (over the nanoparticle precipitation range) can affect the quality of the thin-film. For example, the thin-film of nanoparticles created when the precipitation is performed over the course of 5 h tends to show more order than those created when the precipitation occurs over 0.5 h. The faster precipitation causes nanoparticles to flocculate and deposit on the surface in small groups whereas the slower precipitation allows the nanoparticles to self-assemble on the surface, creating higher quality thin-films [15]. In summary, CXL nanoparticle deposition is a highly effective method of creating high-quality nanoparticle thin-films.

2.6.1

Nanoparticle Thin-Film Deposition on MEMS Devices

The CXL nanoparticle deposition and thin-film formation technique could be employed in a wide range of applications. As an example, one fundamentally new application of CXL-deposited nanoparticle thin-films exists within the microelectromechanical systems (MEMS) industry. MEMS are highly complex microscale devices combining electrical and mechanical components consisting of dimensions as small as a few microns. These devices are typically fabricated using semiconductor processes from silicon-based materials such as silicon dioxide or silicon nitride. Such materials are typically very smooth and very hydrophilic, which can lead to various mechanisms of device failure, namely the capillary collapse of microscale components due to dewetting effects on the hydrophilic surfaces causing irreversible adhesion. The permanent adhesion of microstructures on MEMS is also often caused by attractive interfacial forces between components due to the miniature scale of the devices. A more detailed review of MEMS surface technology is available in [78].

In order to prevent the irreversible adhesion of MEMS microstructures, several studies have been performed to alter the surface of MEMS, either chemically or physically. Chemical alterations have focused on the use of organosilane self-assembled monolayers (SAMs), which prevent the adsorption of ambient moisture and also reduce the inherent attractive forces between the microstructures. Although SAMs are very effective at reducing irreversible adhesion in MEMS, drawbacks include irreproducibility, excess solvent use, and thermal stability. More recent efforts have shifted towards physical alterations in order to increase the surface roughness of MEMS devices.

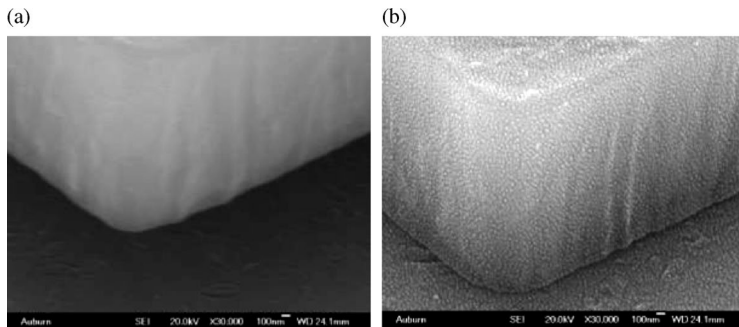


Figure 2.10 SEM images of a cantilever beam tip (a) before and (b) after CXL nanoparticle deposition. Adapted from [77] © IOP Publishing.

One method of increasing MEMS surface roughness is through an *in situ* synthesis of 20–50 nm silicon carbide nanoparticles on the MEMS surface [79]. Although this has been done unintentionally in most cases, increasing surface roughness significantly reduced irreversible adhesion. Typical nanoparticle deposition processes on surfaces via dropcasting or Langmuir–Blodgett films, both of which experience significant dewetting effects, would destroy the microstructure features of a MEMS device. However, using the CXL deposition process described above, it has been shown that the deposition of nanoparticles conformally on all surfaces of a MEMS device can be achieved without any detrimental effects [77]. An example of a MEMS microstructure, a cantilever beam, before and after CXL nanoparticle deposition, is shown in Figure 2.10. Adding a gold nanoparticle thin-film to the surface of a MEMS device reduces the apparent work of adhesion, the amount of work required to separate two adhered microstructure features, by two orders of magnitude. Details on methods of measuring and calculating the apparent work of adhesion can be found in [80].

2.7

Formation and Synthesis of Nanoparticles in CXLs

A variety of methods have been employed to produce micro- and nanoparticles of various polymers, organic and inorganic materials based on technologies that utilize the CO₂ expansion of a solution, including precipitation with a compressed antisolvent (PCA), gas or supercritical antisolvent precipitation (GAS or SAS), depressurization of an expanded liquid organic solution (DELOS), and others. These technologies commonly employ CO₂ as an antisolvent to induce precipitation from saturated organic solvent solutions. A number of extensive reviews are available [81–91] that address these techniques, and as such, will not be addressed in this chapter.

CXLs also have potential as media for inorganic nanoparticle synthesis due to reasonable solubilities of material precursors, capping agents, and reducing agents,

such as hydrogen. For example, CO₂-expanded heptane has been used as a synthesis medium to synthesize silver nanoparticles from a silver isostearate precursor and hydrogen, both of which are soluble in the CXL [92]. It was reported that by using the silver isostearate precursor in CO₂-expanded heptane, nanoparticles with a diameter of 2.64 ± 0.51 nm were effectively synthesized, which were smaller and more narrow in size distribution than analogous nanoparticles synthesized in liquid heptane. This technique takes advantage of the enhanced hydrogen gas solubility in the CXL in order to achieve reduction of the silver ions.

More recently, Kitchens *et al.* [94] have demonstrated the size-controlled, modified Brust arrested precipitation [12] synthesis of silver nanoparticles in CXLs. In short, tetra-*n*-octylammonium bromide was used as a phase-transfer agent to disperse silver ions in a 0.04 M dodecanethiol solution of chloroform. The chloroform solution was then pressurized with CO₂ and a 0.44 M aqueous solution of sodium borohydride was metered into the pressure vessel as a reducing agent. Figure 2.11 presents TEM images and size distributions for nanoparticles synthesized under ambient conditions and at an applied CO₂ pressure of 33.0 bar. Nanoparticles synthesized at an applied CO₂ pressure of 33.0 bar were found to have an average diameter of 5.6 ± 1.7 nm whereas nanoparticles synthesized under ambient conditions had an average diameter of 8.6 ± 2.0 nm. The average nanoparticle size synthesized at the elevated applied CO₂ pressure is smaller than that under ambient conditions, presumably due to the decreased solvent strength. This is the first study to demonstrate the ability to tailor the nanoparticle size using a CXL synthesis by tuning the applied CO₂ pressure and, thus, the bulk solvent strength.

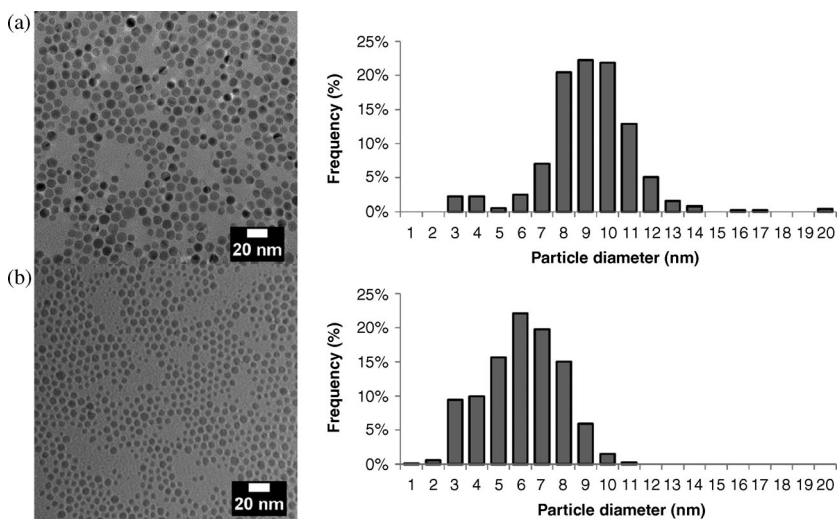


Figure 2.11 TEM images and nanoparticle size distributions of nanoparticles synthesized from a modified Brust arrested precipitation technique (a) under ambient conditions and (b) at an applied CO₂ pressure of 33.0 bar.

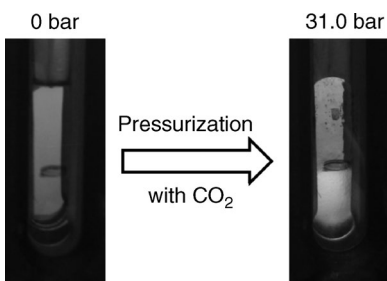


Figure 2.12 OATS phase separation of a THF–water mixture (left) containing dodecanethiol-stabilized gold nanoparticles. Pressurization of the mixture with CO₂ induces a phase separation where the nanoparticles remain in the CO₂-expanded THF (right).

2.8

Nanoparticle Phase Transfer Using CXLs

An additional novel separation operation for CXLs has been termed Organic–Aqueous Tunable Solvents (OATS), which are distinguished by the use of a polar solvent that is completely miscible with water at ambient pressures [10, 94–96]. With the addition of CO₂, which prefers an organic phase, the polarity of the organic phase decreases to the point that a phase separation occurs. Figure 2.12 is an example of DDT-stabilized gold nanoparticles dispersed in a water–THF mixture. With the addition of CO₂ to a pressure of 31.0 bar, the solvent undergoes a phase separation where the nanoparticles remain in the CXL while any salt precursors or water-soluble intermediates can easily be separated from the nanoparticle dispersion through removal of the aqueous phase. This technique may also be beneficial for nanoparticle ligand–exchange reactions where the nanoparticles need to be transferred from an aqueous phase to an organic phase without transitioning a phase boundary.

2.9

Conclusion

This chapter illustrates the utility of CO₂-expanded liquids for a number of nanoparticle operations including improved thin-film formation, precise control over nanoparticle precipitation and fractions, and the manipulation of nanoparticle synthesis methods. The tunable thermo-physical properties of these CXLs afford opportunities to affect nanoparticle dispersibility through reversible changes in solvent strength via simple adjustments to the applied CO₂ pressure. This arrangement makes it possible to utilize non-toxic carbon dioxide as an alternative antisolvent in simple organic nanoparticle dispersion systems that allow for complete recycle and reuse of the organic solvent and the CO₂ antisolvent through simple adjustments to temperature and pressure, thereby reducing organic solvent consumption.

References

- 1 Lazzaroni, M.J., Bush, D., Brown, J.S. and Eckert, C.A. (2005) High-pressure vapor-liquid equilibria of some carbon dioxide plus organic binary systems. *Journal of Chemical and Engineering Data*, **50** (1), 60–65.
- 2 Jessop, P.G. and Subramaniam, B. (2007) Gas-expanded liquids. *Chemical Reviews*, **107** (6), 2666–2694.
- 3 Peng, D. and Robinson, D.B. (1976) New 2-constant equation of state. *Industrial and Engineering Chemistry Research Fundamentals*, **15** (1), 59–64.
- 4 Cassel, E., Matt, M., Rogalski, M. and Solimando, R. (1997) Phase equilibria modelling for binary systems that contain CO₂. *Fluid Phase Equilibria*, **134** (1–2), 63–75.
- 5 Dixon, J. and Johnston, K. (1991) Molecular thermodynamics of solubilities in gas antisolvent crystallization. *AIChE Journal*, **37** (10), 1441–1449.
- 6 Saunders, A.E. and Korgel, B.A. (2004) Second virial coefficient measurements of dilute gold nanocrystal dispersions using small-angle x-ray scattering. *Journal of Physical Chemistry B*, **108** (43), 16732–16738.
- 7 Wyatt, V.T., Bush, D., Lu, J., Hallett, J.P., Liotta, C.L. and Eckert, C.A. (2005) Determination of solvatochromic solvent parameters for the characterization of gas-expanded liquids. *Journal of Supercritical Fluids*, **36** (1), 16–22.
- 8 Kho, Y.W., Conrad, D.C. and Knutson, B.L. (2003) Phase equilibria and thermophysical properties of carbon dioxide-expanded fluorinated solvents. *Fluid Phase Equilibria*, **206** (1–2), 179–193.
- 9 Sassié, P.R., Mourier, P., Caude, M.H. and Rosset, R.H. (1987) Measurement of diffusion coefficients in supercritical carbon dioxide and correlation with the equation of Wilke and Chang. *Analytical Chemistry*, **59** (8), 1164–1170.
- 10 Hallett, J.P., Kitchens, C.L., Hernandez, R., Liotta, C.L. and Eckert, C.A. (2006) Probing the cybotactic region in gas-expanded liquids (GXLs). *Accounts of Chemical Research*, **39** (8), 531–538.
- 11 Murray, C.B., Norris, D.J. and Bawendi, M.G. (1993) Synthesis and characterization of nearly monodisperse CdE (E = sulfur, selenium, tellurium) semiconductor nanocrystallites. *Journal of the American Chemical Society*, **115** (19), 8706–8715.
- 12 Brust, M., Walker, M., Bethell, D., Schiffrin, D.J. and Whyman, R. (1994) Synthesis of thiol-derivatized gold nanoparticles in a 2-phase liquid–liquid system. *Journal of the Chemical Society, Chemical Communications* (7), 801–802.
- 13 Chemseddine, A. and Weller, H. (1993) Highly monodisperse quantum sized CdS particles by size selective precipitation. *Berichte der Bunsen-Gesellschaft für Physikalische Chemie*, **97** (4), 636–638.
- 14 Murray, C.B., Kagan, C.R. and Bawendi, M.G. (2000) Synthesis and characterization of monodisperse nanocrystals and close-packed nanocrystal assemblies. *Annual Review of Materials Science*, **30** (1), 545–610.
- 15 McLeod, M.C., Kitchens, C.L. and Roberts, C.B. (2005) CO₂-expanded liquid deposition of ligand-stabilized nanoparticles as uniform, wide-area nanoparticle films. *Langmuir*, **21** (6), 2414–2418.
- 16 Anand, M., McLeod, M.C., Bell, P.W. and Roberts, C.B. (2005) Tunable solvation effects on the size-selective fractionation of metal nanoparticles in CO₂ gas-expanded solvents. *Journal of Physical Chemistry B*, **109** (48), 22852–22859.
- 17 Anand, M., Odom, L.A. and Roberts, C.B. (2007) Finely controlled size-selective precipitation and separation of CdSe/ZnS semiconductor nanocrystals using CO₂ gas-expanded liquids. *Langmuir*, **23** (13), 7338–7343.
- 18 Saunders, S.R. and Roberts, C.B. (2009) Size-selective fractionation of nanoparticles at an application scale using CO₂ gas-expanded liquids. *Nanotechnology*, **20** (47), 475605.
- 19 McLeod, M.C., Anand, M., Kitchens, C.L. and Roberts, C.B. (2005) Precise and rapid size selection and targeted deposition of nanoparticle populations using CO₂ gas

- expanded liquids. *Nano Letters*, **5** (3), 461–465.
- 20 Saunders, S.R. and Roberts, C.B. (2011) Tuning the precipitation and fractionation of nanoparticles in gas-expanded liquid mixtures. *Journal of Physical Chemistry C*, **115** (2), 9984–9992.
- 21 Schasfoort, R.B.M. and Tudos, A.J. (2008) *Handbook of Surface Plasmon Resonance*, Royal Society of Chemistry., Cambridge.
- 22 Link, S. and El-Sayed, M.A. (1999) Size and temperature dependence of the plasmon absorption of colloidal gold nanoparticles. *Journal of Physical Chemistry B*, **103** (21), 4212–4217.
- 23 Lee, M.H., Dobson, P.J. and Cantor, B. (1992) Optical properties of evaporated small silver particles. *Thin Solid Films*, **219** (1–2), 199–205.
- 24 Kitchens, C.L., McLeod, M.C. and Roberts, C.B. (2003) Solvent effects on the growth and steric stabilization of copper metallic nanoparticles in AOT reverse micelle systems. *Journal of Physical Chemistry B*, **107** (41), 11331–11338.
- 25 Anand, M., You, S.S., Hurst, K.M., Saunders, S.R., Kitchens, C.L., Ashurst, W.R. and Roberts, C.B. (2008) Thermodynamic analysis of nanoparticle size selective fractionation using gas-expanded liquids. *Industrial and Engineering Chemistry Research*, **47** (3), 553–559.
- 26 Saunders, S.R., Anand, M., You, S.S. and Roberts, C.B. (2010) Total interaction energy model to predict nanoparticle dispersibility in CO₂-expanded solvents, in *Computer Aided Chemical Engineering*, vol. 28, Elsevier, Amsterdam, pp. 1651–1656.
- 27 Hamaker, H.C. (1937) The London–van der Waals attraction between spherical particles. *Physica*, **4** (10), 1058–1072.
- 28 Hiemenz, P.C. and Rajagopalan, R. (1997) *Principles of Colloid and Surface Chemistry*, 3rd edn., Marcel Dekker, New York.
- 29 Israelachvili, J.N. (1985) *Intermolecular and Surface Forces: with Applications to Colloidal and Biological Systems*, Academic Press, London.
- 30 Shah, P.S., Holmes, J.D., Johnston, K.P. and Korgel, B.A. (2002) Size-selective dispersion of dodecanethiol-coated nanocrystals in liquid and supercritical ethane by density tuning. *Journal of Physical Chemistry B*, **106** (10), 2545–2551.
- 31 Vincent, B., Luckham, P.F. and Waite, F.A. (1980) The effect of free polymer on the stability of sterically stabilized dispersions. *Journal of Colloid and Interface Science*, **73** (2), 508–521.
- 32 Vincent, B., Edwards, J., Emmett, S. and Jones, A. (1986) Depletion flocculation in dispersions of sterically-stabilised particles (soft spheres). *Colloids Surf*, **18** (2–4), 261–281.
- 33 Shah, P.S., Husain, S., Johnston, K.P. and Korgel, B.A. (2002) Role of steric stabilization on the arrested growth of silver nanocrystals in supercritical carbon dioxide. *Journal of Physical Chemistry B*, **106** (47), 12178–12185.
- 34 Sato, T. (1993) Stability of dispersion. *Journal of Coatings Technology*, **v65** (825), 113.
- 35 Kitchens, C.L. and Roberts, C.B. (2004) Copper nanoparticle synthesis in compressed liquid and supercritical fluid reverse micelle systems. *Industrial and Engineering Chemistry Research*, **43** (19), 6070–6081.
- 36 Melnichenko, Y.B. and Wignall, G.D. (2007) Small-angle neutron scattering in materials science: recent practical applications. *Journal of Applied Physics*, **102** (2), 021101.
- 37 Wignall, G.D. (1999) Neutron scattering studies of polymers in supercritical carbon dioxide. *Journal of Physics: Condensed Matter*, **11** (15), R157–R177.
- 38 Hammouda, B. (2010) SANS from polymers—review of the recent literature. *Polymer Reviews*, **50** (1), 14–39.
- 39 Hammouda, B. (2010) *Probing Nanoscale Structures—the SANS Toolbox*, Technical Report, National Institute of Standards and Technology, Washington, DC.
- 40 Von White, G. and Kitchens, C.L. (2010) Small-angle neutron scattering of silver nanoparticles in gas-expanded hexane. *Journal of Physical Chemistry C*, **114** (39), 16285–16291.
- 41 Korgel, B.A., Fullam, S., Connolly, S. and Fitzmaurice, D. (1998) Assembly and self-organization of silver nanocrystal superlattices: ordered “soft spheres.” *Journal of Physical Chemistry B*, **102** (43), 8379–8388.

- 42** Brust, M. and Kiely, C.J. (2002) Some recent advances in nanostructure preparation from gold and silver particles: a short topical review. *Colloids and Surfaces A: Physicochemical and Engineering Aspects*, **202** (2–3), 175–186.
- 43** Collier, C.P., Vossmeyer, T. and Heath, J.R. (1998) Nanocrystal superlattices. *Annual Review of Physical Chemistry*, **49** (1), 371–404.
- 44** Sigman, M.B., Saunders, A.E. and Korgel, B.A. (2004) Metal nanocrystal superlattice nucleation and growth. *Langmuir*, **20** (3), 978–983.
- 45** Lin, X.M., Jaeger, H.M., Sorensen, C.M. and Klabunde, K.J. (2001) Formation of long-range-ordered nanocrystal superlattices on silicon nitride substrates. *Journal of Physical Chemistry B*, **105** (17), 3353–3357.
- 46** Cui, Y., Björk, M.T., Liddle, J.A., Sönichsen, C., Boussert, B. and Alivisatos, A.P. (2004) Integration of colloidal nanocrystals into lithographically patterned devices. *Nano Letters*, **4** (6), 1093–1098.
- 47** Ohara, P.C., Leff, D.V., Heath, J.R. and Gelbart, W.M. (1995) Crystallization of opals from polydisperse nanoparticles. *Physical Review Letters*, **75** (19), 3466.
- 48** Ohara, P.C. and Gelbart, W.M. (1998) Interplay between hole instability and nanoparticle array formation in ultrathin liquid films. *Langmuir*, **14** (12), 3418–3424.
- 49** Motte, L., Billoudet, F., Lacaze, E., Douin, J. and Pileni, M.P. (1997) Self-organization into 2D and 3D superlattices of nanosized particles differing by their size. *Journal of Physical Chemistry B*, **101** (2), 138–144.
- 50** Blackburn, J.M., Long, D.P., Cabanas, A. and Watkins, J.J. (2001) Deposition of conformal copper and nickel films from supercritical carbon dioxide. *Science*, **294** (5540), 141–145.
- 51** Liu, J.C., Anand, M. and Roberts, C.B. (2006) Synthesis and extraction of beta-D-glucose-stabilized Au nanoparticles processed into low-defect, wide-area thin-films and ordered arrays using CO₂-expanded liquids. *Langmuir*, **22** (9), 3964–3971.
- 52** Shah, P.S., Novick, B.J., Hwang, H.S., Lim, K.T., Carbonell, R.G., Johnston, K.P. and Korgel, B.A. (2003) Kinetics of nonequilibrium nanocrystal monolayer formation: deposition from liquid carbon dioxide. *Nano Letters*, **3** (12), 1671–1675.
- 53** Quinn, E.L. (1927) The surface tension of liquid carbon dioxide. *Journal of the American Chemical Society*, **49** (11), 2704–2711.
- 54** Shah, P.S., Holmes, J.D., Doty, R.C., Johnston, K.P. and Korgel, B.A. (2000) Steric stabilization of nanocrystals in supercritical CO₂ using fluorinated ligands. *Journal of the American Chemical Society*, **122** (17), 4245–4246.
- 55** Esumi, K., Sarashina, S. and Yoshimura, T. (2004) Synthesis of gold nanoparticles from an organometallic compound in supercritical carbon dioxide. *Langmuir*, **20** (13), 5189–5191.
- 56** Saunders, A.E., Shah, P.S., Park, E.J., Lim, K.T., Johnston, K.P. and Korgel, B.A. (2004) Solvent density-dependent steric stabilization of perfluoropolyether-coated nanocrystals in supercritical carbon dioxide. *Journal of Physical Chemistry B*, **108** (41), 15969–15975.
- 57** Ohde, H., Hunt, F. and Wai, C.M. (2001) Synthesis of silver and copper nanoparticles in a water-in-supercritical-carbon dioxide microemulsion. *Chemistry of Materials*, **13** (11), 4130–4135.
- 58** McLeod, M.C., McHenry, R.S., Beckman, E.J. and Roberts, C.B. (2003) Synthesis and stabilization of silver metallic nanoparticles and premetallic intermediates in perfluoropolyether/CO₂ reverse micelle systems. *Journal of Physical Chemistry B*, **107** (12), 2693–2700.
- 59** McLeod, M.C., Gale, W.F. and Roberts, C.B. (2004) Metallic nanoparticle production utilizing a supercritical carbon dioxide flow process. *Langmuir*, **20** (17), 7078–7082.
- 60** Fan, X., McLeod, M.C., Enick, R.M. and Roberts, C.B. (2006) Preparation of silver nanoparticles via reduction of a highly CO₂-soluble hydrocarbon-based metal precursor. *Industrial and Engineering Chemistry Research*, **45** (10), 3343–3347.
- 61** Holmes, J.D., Bhargava, P.A., Korgel, B.A. and Johnston, K.P. (1999) Synthesis of

- cadmium sulfide Q particles in water-in-CO₂ microemulsions. *Langmuir*, **15** (20), 6613–6615.
- 62** Ji, M., Chen, X., Wai, C.M. and Fulton, J.L. (1999) Synthesizing and dispersing silver nanoparticles in a water-in-supercritical carbon dioxide microemulsion. *Journal of the American Chemical Society*, **121** (11), 2631–2632.
- 63** Liu, J., Raveendran, P., Shervani, Z., Ikushima, Y. and Hakuta, Y. (2005) Synthesis of Ag and AgI quantum dots in AOT-stabilized water-in-CO₂ microemulsions. *Chemistry- A European Journal*, **11** (6), 1854–1860.
- 64** Dong, X., Potter, D. and Erkey, C. (2002) Synthesis of CuS nanoparticles in water-in-carbon dioxide microemulsions. *Industrial and Engineering Chemistry Research*, **41** (18), 4489–4493.
- 65** Yu, K.M.K., Steele, A.M., Zhu, J., Fu, Q.J. and Tsang, S.C. (2003) Synthesis of well-dispersed nanoparticles within porous solid structures using surface-tethered surfactants in supercritical CO₂. *Journal of Materials Chemistry*, **13** (1), 130–134.
- 66** Zhang, R., Liu, J., He, J., Han, B., Wu, W., Jiang, T., Liu, Z. and Du, J. (2003) Organicreactions and nanoparticle preparation in CO₂-induced water/P104/p-xylene microemulsions. *Chemistry- A European Journal*, **9** (10), 2167–2172.
- 67** da Rocha, S.R.P., Dickson, J., Cho, D., Rossky, P.J. and Johnston, K.P. (2003) Stubby surfactants for stabilization of water and CO₂ emulsions: trisiloxanes. *Langmuir*, **19** (8), 3114–3120.
- 68** Eastoe, J., Paul, A., Nave, S., Steytler, D.C., Robinson, B.H., Rumsey, E., Thorpe, M. and Heenan, R.K. (2001) Micellization of hydrocarbon surfactants in supercritical carbon dioxide. *Journal of the American Chemical Society*, **123** (5), 988–989.
- 69** Stone, M.T., da Rocha, S.R.P., Rossky, P.J. and Johnston, K.P. (2003) Molecular differences between hydrocarbon and fluorocarbon surfactants at the CO₂/water interface. *Journal of Physical Chemistry B*, **107** (37), 10185–10192.
- 70** Stone, M.T., Smith, P.G., da Rocha, S.R.P., Rossky, P.J. and Johnston, K.P. (2004) Lowinterfacial free volume of stubby surfactants stabilizes water-in-carbon dioxide microemulsions. *Journal of Physical Chemistry B*, **108** (6), 1962–1966.
- 71** Liu, J., Han, B., Li, G., Zhang, X., He, J. and Liu, Z. (2001) Investigation of nonionic surfactant Dynol-604 based reverse microemulsions formed in supercritical carbon dioxide. *Langmuir*, **17** (26), 8040–8043.
- 72** Ryoo, W., Webber, S.E. and Johnston, K.P. (2003) Water-in-carbon dioxide microemulsions with methylated branched hydrocarbon surfactants. *Industrial and Engineering Chemistry Research*, **42** (25), 6348–6358.
- 73** Dickson, J.L., Smith, P.G., Dhanuka, V.V., Srinivasan, V., Stone, M.T., Rossky, P.J., Behles, J.A., Keiper, J.S., Xu, B., Johnson, C., DeSimone, J.M. and Johnston, K.P. (2005) Interfacial properties of fluorocarbon and hydrocarbon phosphate surfactants at the water–CO₂ interface. *Industrial and Engineering Chemistry Research*, **44** (5), 1370–1380.
- 74** Anand, M., Bell, P.W., Fan, X., Enick, R.M. and Roberts, C.B. (2006) Synthesis and steric stabilization of silver nanoparticles in neat carbon dioxide solvent using fluorine-free compounds. *Journal of Physical Chemistry B*, **110** (30), 14693–14701.
- 75** Hollamby, M.J., Trickett, K., Vesperinas, A., Rivett, C., Steytler, D.C., Schnepf, Z., Jones, J., Heenan, R.K., Richardson, R.M., Glatter, O. and Eastoe, J. (2008) Stabilization of CeO₂ nanoparticles in a CO₂ rich solvent. *Chemical Communications* (43), 5628–5630.
- 76** Trickett, K., Xing, D., Eastoe, J., Enick, R., Mohamed, A., Hollamby, M.J., Cummings, S., Rogers, S.E. and Heenan, R.K. (2009) Hydrocarbon metallosurfactants for CO₂. *Langmuir*, **26** (7), 4732–4737.
- 77** Hurst, K.M., Roberts, C. and Ashurst, W. (2009) A gas-expanded liquid nanoparticle deposition technique for reducing the adhesion of silicon microstructures. *Nanotechnology*, **20** (18), 185303.
- 78** Maboudian, R. (1998) Surface processes in MEMS technology. *Surface Science Reports*, **30** (6–8), 207–269.
- 79** DelRio, F.W., Dunn, M.L., Boyce, B.L., Corwin, A.D. and de Boer, M.P. (2006) The

- effect of nanoparticles on rough surface adhesion. *Journal of Applied Physics*, **99** (10), 9.
- 80** Hurst, K., Roberts, C. and Ashurst, W. (2009) A new method to determine adhesion of cantilever beams using beam height experimental data. *Tribol. Lett.*, **35** (1), 9–15.
- 81** Ye, X. and Wai, C.M. (2003) Making nanomaterials in supercritical fluids: a review. *Journal of Chemical Education*, **80** (2), 198.
- 82** Stanton, L.A., Dehghani, F. and Foster, N.R. (2002) Improving drug delivery using polymers. *Australian Journal of Chemistry*, **55** (7), 443–447.
- 83** Tan, H.S. and Borsadia, S. (2001) Particle formation using supercritical fluids: pharmaceutical applications. *Expert Opin. Ther. Pat.*, **11** (5), 861–872.
- 84** Jung, J. and Perrut, M. (2001) Particle design using supercritical fluids: literature and patent survey. *Journal of Supercritical Fluids*, **20** (3), 179–219.
- 85** Cooper, A.I. (2000) Polymer synthesis and processing using supercritical carbon dioxide. *Journal of Materials Chemistry*, **10** (2), 207–234.
- 86** Marr, R. and Gamse, T. (2000) Use of supercritical fluids for different processes including new developments: a review. *Chemical Engineering and Processing*, **39** (1), 19–28.
- 87** Palakodaty, S. and York, P. (1999) Phase behavioral effects on particle formation processes using supercritical fluids. *Pharmacological Research*, **16** (7), 976–985.
- 88** Reverchon, E. (1999) Supercritical antisolvent precipitation of micro- and nano-particles. *Journal of Supercritical Fluids*, **15** (1), 1–21.
- 89** Subramaniam, B., Rajewski, R.A. and Snavely, K. (1997) Pharmaceutical processing with supercritical carbon dioxide. *Journal of Pharmaceutical Sciences*, **86** (8), 885–890.
- 90** Yeo, S.D. and Kiran, E. (2005) Formation of polymer particles with supercritical fluids: a review. *Journal of Supercritical Fluids*, **34** (3), 287–308.
- 91** Tom, J.W. and Debenedetti, P.G. (1991) Particle formation with supercritical fluids: a review. *J. Aerosol Sci.*, **22** (5), 555–584.
- 92** Hsieh, H.T., Chin, W.K. and Tan, C.S. (2010) Facile synthesis of silver nanoparticles in CO₂-expanded liquids from silver isostearate precursor. *Langmuir*, **26** (12), 10031–10035.
- 93** Hart, A.E. and Kitchens, C.L. (2011) Reverse micelle synthesis of monodispersed metallic nanoparticles via a gas expanded liquid system. Presented at the AIChE 2011 Annual Meeting, Minneapolis, Minnesota, United States.
- 94** Blasucci, V.M., Husain, Z.A., Fadhel, A.Z., Donaldson, M.E., Vyhmeister, E., Pollet, P., Liotta, C.L. and Eckert, C.A. (2010) Combining homogeneous catalysis with heterogeneous separation using tunable solvent systems. *Journal of Physical Chemistry A*, **114** (11), 3932–3938.
- 95** Hill, E.M., Broering, J.M., Hallett, J.P., Bommaraju, A.S., Liotta, C.L. and Eckert, C.A. (2007) Coupling chiral homogeneous biocatalytic reactions with benign heterogeneous separation. *Green Chemistry*, **9** (8), 888–893.
- 96** Lu, J., Lazzaroni, J., Hallett, J.P., Bommaraju, A.S., Liotta, C.L. and Eckert, C.A. (2004) Tunable solvents for homogeneous catalyst recycle. *Industrial and Engineering Chemistry Research*, **43** (7), 1586–1590.

3

Green Synthesis and Applications of Magnetic Nanoparticles

Liane M. Rossi, Alexandre L. Parize, and Joel C. Rubim

3.1

Introduction

The synthesis of magnetic nanoparticles (NPs) has been the subject of systematic studies due to the fundamental scientific aspects related to their chemical and physical properties and also to the considerable number of technological applications. Some of these applications have been the subject of reviews, such as in magnetic data storage [1], manipulation of magnetic beads in microfluidic systems and their utilization for biological analysis and chemical catalysis [2], biosensors [3–5], biomedical applications such as targeted drug delivery, contrast agents in magnetic resonance imaging (MRI), tissue repair, immunoassay, detoxification of biological fluids, hyperthermia, cell separation [6–17], and magnetic inks for ink jet printing [18, 19]. It is well known that the size, structure, and shape of the magnetic NPs are strongly related to their applications, and control of the NP size and the size distribution is imperative because the magnetic properties are strongly dependent upon the dimensions of the NPs. Nowadays, public concerns regarding the environment have led researchers in both academia and industry to search for processes for materials synthesis that consider the principles of green chemistry. By green chemistry is understood [20] “the design, development, and implementation of chemical processes and products to reduce or eliminate substances hazardous to human health and the environment.” This idea was further expanded in the well-known 12 Principles of Green Chemistry [21]. In this chapter, we focus on studies that have considered, if not all, at least some principles of green chemistry in the synthesis of magnetic NPs and their applications in the field of separation technologies. Magnetic separation can be considered as a green separation tool and has been applied to the recovery of oil spills, heavy metals, and catalysts, as discussed below.

3.2

Green Synthesis of Magnetic Nanoparticles

3.2.1

Background

The earliest reports on the synthesis of magnetic iron oxide particles forming relatively stable colloids date back to the 1930s [22, 23]. The first stable suspension of magnetic particles was only obtained in 1965 by Papell [24]. Papell's magnetic fluid (MF) was a dispersion of ground magnetite (Fe_3O_4) particles (diameter $<25\text{ }\mu\text{m}$) modified by oleic acid. These particles were dispersed in non-polar solvents (carrier), forming a stable MF that was used to confer magnetic properties to fuels. Subsequently, Rosensweig [25, 26] obtained several kinds of MF based on the dispersion of ground Fe_3O_4 particles in different carriers, such as kerosene, water, fluorocarbons, and esters. In 1982, Massart [27] obtained MFs by a chemical procedure involving the coprecipitation of Fe(II) and Fe(III) hydroxides. Later, Massart's group modified the coprecipitation protocol to obtain ultra-stable and highly concentrated MFs with different magnetic particles based on spinel ferrites such as $(\text{M}_{1-x}^{2+}\text{Fe}_x^{3+})_A(\text{Fe}_{2-x}^{3+}\text{M}_x^{2+})_B\text{O}_4$ ($\text{M} = \text{Mn, Co, Ni, Cu, and Zn}$). The stability of such dispersions is obtained by hydrothermal treatment of the samples with $\text{Fe}(\text{NO}_3)_3$, leading to the formation of an iron-rich protective layer that passivates the NP surface [28]. However, these protocols, in addition to involving several steps, do not allow good control of the size and shape of the NPs. Hence researchers' efforts were focused on a search for synthetic routes in which better control of the shape and size of the magnetic NPs can be achieved. In a comprehensive review, Park *et al.* presented the fundamental concepts involved in the control of the size and shape of semiconductor, metal, and iron oxide NPs in different synthetic routes [29]. Several protocols for the preparation of magnetic NPs with good control of their size and shape can be found in reviews [1, 3, 6–13, 16, 30–38]. However, none of the published protocols meets all green chemistry principles. The synthetic routes mentioned in the following sections were selected as those that meet at least some principles of green chemistry during the synthesis of magnetic NPs composed of iron oxides, mixed metal–iron oxides, metals, metal alloys, and core@ shell magnetic nanostructures.

3.2.2

Thermal Decomposition Methods

The thermal decomposition of iron complexes leading to the formation of different ferrites (MFe_2O_4 , $\text{M} = \text{Fe, Co, Mn, etc.}$) is one of the most commonly used protocols to obtain magnetic NPs with control of size and shape [39]. However, some of them cannot be considered as green processes since the iron precursor, the $\text{Fe}(\text{CO})_5$ complex, is expensive, toxic, and flammable. Therefore, researchers have looked for non-toxic and less expensive iron precursors to be used in the thermal decomposition reactions. The first precursor in substitution of $\text{Fe}(\text{CO})_5$ was the FeCup_3

complex [$\text{Cup} = \text{N-nitrosophenylhydroxylamine, C}_6\text{H}_5\text{N}(\text{NO})\text{O}^-$] as proposed by Rockenberger *et al.* [40]. Using this precursor, $\gamma\text{-Fe}_2\text{O}_3$ NPs of 6 nm size were obtained in a thermal decomposition reaction in the presence of octylamine (OCA) and trioctylamine (TOA) as the solvent [40]. Other metal non-toxic precursors used in the synthesis of magnetic metal oxide NPs include $\text{M}^n(\text{acac})_n$ ($\text{M} = \text{Fe, Co, Mn, Ni, Zn}$, acac = acetylacetone, and $n = 2$ or 3) [41–51], metal-oleates [52–54], $\text{Fe}(\text{Ac})_2$ ($\text{Ac} = \text{acetate}$) [49, 55], and $\text{FeCl}_3 \cdot 6\text{H}_2\text{O}$ [50, 51]. Depending on the composition of the reaction mixture, for instance, the presence of surfactants and reducing agents, magnetic NPs readily dispersible in non-polar solvents or in aqueous solutions were obtained. Oleylamine (OA) is one of the most often used reducing agents [56, 57], but it can also act as a surface modifier leading to magnetic NPs dispersible in organic solvents [41]. Further, triethylene glycol, benzyl alcohol, and 2-pyrrolidone were used as capping and reducing agents for water-dispersible magnetic NPs. The NPs coated with oleic acid or OA lead to magnetic NPs that form stable dispersions only in non-polar solvents, but the NPs can be transferred to water when subjected to a ligand-exchange reaction to modify the chemistry of the NP surface [58]. Table 3.1 displays several synthetic protocols with the reaction conditions and the products obtained.

In the thermal decomposition method, the solvent also plays an important role in controlling the size of the NPs. For instance, Park *et al.* obtained magnetite NPs on an ultra-large scale by adding the iron-oleate complex to an appropriate high-boiling solvent [53]. The size of the NPs was controlled by a suitable choice of solvents with different boiling points. This method of synthesis also involves a reduction step since the precursor is an Fe(III) complex and a mixed-valence iron oxide, $\text{Fe}^{II}\text{OFe}_2\text{O}_3$ (magnetite, Fe_3O_4), is obtained. In Table 3.1, this kind of process is denoted TDR, since during thermal decomposition the reduction of Fe(III) to Fe(II) also occurs. In a simple one-pot reaction process, Pinna *et al.* used $\text{Fe}(\text{acac})_3$ dissolved in benzylamine and obtained two-phase (Fe_3O_4 and $\gamma\text{-Fe}_2\text{O}_3$) NPs [45]. This work represents the first detailed reaction mechanism for the decomposition of the $\text{Fe}(\text{acac})_3$ precursor in which benzylamine acts as a reducing agent leading to the formation of Fe_3O_4 . As proposed by the authors, H_2 is evolved during the reaction and is responsible for the reduction of the Fe(III) to Fe(II).

It is well known that ethanol, in addition to being obtained from renewable resources (e.g., sugar cane), is one of the most commonly used environmentally friendly solvents. Therefore, the use of this solvent in the synthetic protocols for magnetic NPs meets some of the principles of green chemistry. It has recently been reported that Fe_3O_4 NPs can be obtained in a one-pot process using the Fe-urea complex $[\text{Fe}(\text{CON}_2\text{H}_4)_6 \cdot (\text{NO}_3)_3]$ in ethanol [59]. As the precursor is an Fe(III) complex and the product contains Fe(II), this is also a TDR process and urea is probably acting as the reducing agent, and the size of the magnetic NPs was controlled by the reaction time.

As shown in Table 3.1, almost all TDR processes are time consuming. Bilecka *et al.* showed that magnetic NPs can also be obtained via TDR using microwave heating in a very fast process. For instance, highly crystalline metal oxide NPs, including Fe_3O_4 with sizes ranging from 5 to 10 nm, were obtained in good yields in a few minutes or

Table 3.1 Reported methods for the synthesis of magnetic NPs^{a)}.

Magnetic material (mean size, nm)	Precursor/reagents	Surfactant/reducing or precipitating agent	Solvent	Method	T (°C) ^{b)}	Time (h) ^{c)}	Ref.
<i>Metal oxides</i>							
Fe ₃ O ₄ (20.5)	Fe(CON ₂ H ₄) ₆ [NO ₃] ₃	Urea ^{d)}	EtOH	TDR	200	50	[59]
γ-Fe ₂ O ₃ (6–10)	FeCup ₃	OCA/OCA	TOA	TD	225–300	>2	[40]
MFe ₂ O ₄ , M = Fe, Co, Mn	Fe(acac) ₃	AOc/OA	BE, HDD	TDR	265	0.5–1	[41–43]
Fe ₃ O ₄ /γ-Fe ₂ O ₃ (3–10)	M(acac) ₂ , M = Fe, Co, Mn	OAc/OA			>2		
Fe ₃ O ₄ /γ-Fe ₂ O ₃ (15–20)	Fe(acac) ₃	Bam	NMPyr or Pyr	TDR	185	2–9	[44]
Fe ₃ O ₄ (8–12)	Fe(acac) ₃	BA	TDR	200	48		[45, 46]
Fe ₃ O ₄ (8)	Fe(acac) ₃		TDR	175–200	48		
Fe ₃ O ₄ (5–11)	Fe(acac) ₃	TEG	TDR	278	1		[47]
FeO ₄ (5–11)	Fe(acac) ₃	BA	MW/TDR	200	<0.1		[49]
Fe ₃ O ₄ (12)	Fe(acac) ₂	PD	TDR	245	10		[50, 51]
Fe ₃ O ₄ (7–34)	Fe(acac) ₃ or FeCl ₃	HDZ	TDR	80–160	0.5–12		[52]
Fe ₃ O ₄ (12) ^{e)}	Fe(acac) ₃	OAc	TDR	320 ^{e)}	2		[53]
MFe ₂ O ₄ (4–11), M = Fe, Co, Mg, Zn, Mn	Fe(III)-oleate (RCOO) _n M	Linoleic acid	EtOH/W	ISS	90–200	10	[86]
MFe ₂ O ₄ (10–15), M = Fe, Co	FeCl ₃ /FeSO ₄ /MCl ₂	OAc, LAC or RAC	W	COP	96	2	[88]
Fe ₃ O ₄ (11–26)	Fe(OH) ₂		W/EtOH	SC	50	1–4	[102–104]
CoFe ₂ O ₄ (2–5)	Fe(DS) ₂ and Co(DS) ₂	MA	W	ME/COP	Room	2	[70]
MFe ₂ O ₄ (5), M = Fe, Co, Mn	Mso ₄ , M = Fe, Co, Mn	AOT	ISO	ME/COP	Room	2	[71]
MFe ₂ O ₄ (5–10), M = Fe, Mn, Co, Ni, Zn	Fe(NO ₃) ₃ , FeCl ₂ , MnCl ₂ , Co(NO ₃) ₂ , Ni(Ac) ₂ , Zn(NO ₃) ₂	SDBS/HDZ	Xy	ME/CR	90	5	[76]
α-Fe ₂ O ₃ (40)	FeCl ₃	KAc	W/BMI.Cl	HT	150	8	[98]

a-FeOOH	FeCl ₃	Urea	BMI.BF ₄ /W W/NH ₄ OH	HT/MW SC	160 Room	0.5 0.25	[99]
Fe ₃ O ₄ (25, 500)	α-FeOOH		W/BMI.Cl BMI.TF ₂ N BMI.PF ₆	HT/MW TDR	160 150–250	0.5 1.5–3	[100] [57, 101]
ZnFe ₂ O ₄ (~40)	Fe(NO ₃) ₃ , Zn(Ac) ₂	KAc					
MFe ₂ O ₃ , M = Fe, Co, Mn, Ni	Fe(acac) ₃ , M(acac) ₂	OA					
<i>Metals, alloys and core@shell</i>							
Fe (1.5–27)	Fe[N(SiMe ₃) ₂] ₂	HDA/H ₂	MST	TDR	150	0.5–48	[60, 61]
Ni (30–100)	Ni(Ac) ₂	PVP/PVP	EG	MW/TDR	195	0.75	[62]
Co (52–290)	Co(Ac) ₂	PVP/PVP	EG	MW/TDR	180	0.1–0.3	[63]
FePt (3)	Fe(acac) ₂	OAc/OA/HDD	DOE	TDR	286	0.5	[64]
CoNi (3)	Pt(acac) ₂	PVP/PVP	TEG		240	3	[65]
Fe (6)	Co(acac) ₂	SDS/HDZ	W	ME/CR	70	>1	[77]
Co (4–8)	Ni(acac) ₂	NaAO/T ₂ NaBH ₄	W	ME/CR	ni	ni	[78]
Fe (6)	FeCl ₃ ,	PAA/NaBH ₄	W/high pH	CR	Room	Seconds	[109]
Fe (59)	PdCl ₂ seeding agent	CTAB	W/low pH				
CuPt (5)	Co(acac) ₃ , Pt(acac) ₂	H ₂	BMI.TF ₂ N, BMI.BF ₄	TDR	350	2	[97]
Ni (6)	Ni ⁰ (cod) ₂	BMI.CF ₃ SO ₃	ODA	TD	75	0.5	[95, 96]
Au@Co (10@5)	HAuCl ₄ , Co(NO ₃) ₂	ODA	TDR	200	0.3	[67]	
Fe ₃ O ₄ @ZnO (8–13@4.5–5.2)	Fe ^{III} -oleate	OAc	HD	TDR	287	10	[68]
	Zn(Ac) ₂		OD	TDR	317		
Fe@Au (18)	FeSO ₄ , HAuCl ₄	CTAB, BaOH/NaBH ₄	W/Oc	ME/CR			
Fe ₃ O ₄ @SiO ₂ (10@50)	FeCl ₃ , FeCl ₂	OAc/NH ₄ OH	W	COP	80	>10	[79]
	TEOS/NH ₄ OH	Igepal CA520	CH	ME	Room	18	[80]
Fe ₃ O ₄ @SiO ₂ (10@10)	Fe ^{III} -oleate	OAc	OD	TDR	320	19	[81]
	TEOS/NH ₄ OH	T100/heanol	W/CH	ME	Room		
CoFe ₂ O ₄ @SiO ₂ (13@52)	FeDS and CoDS	MA	W	ME/COP	Room	>5 days	[82]

(Continued)

Table 3.1 (Continued)

Magnetic material (mean size, nm)	Precursor/reagents	Surfactant/reducing or precipitating agent	Solvent	Method	T (°C) ^b	Time (h) ^c	Ref.
MnFe ₂ O ₄ @SiO ₂ (12@65)	TEOS/NH ₄ OH FeDS and MnDS	Igepal CO-520 SDBS/NaOH	CH W/toluene	ME ME/COP	350	>5 days	[82]
Co@SiO ₂ (4@2)	TEOS/NH ₄ OH CoCl ₂	Igepal CO-520 DDAB/NaBH ₄ ni	NH ₄ OH/CH W/toluene	ME/CR ME	Room 60	>3 days	[83]
NiFe ₂ O ₄ @SiO ₂ (6@8)	TEOS FeCl ₃ , NiCl ₂	DEG/NaOH/OAc	DEG	COP	230	>3 days	[84]
Fe ₃ O ₄ @SiO ₂ @ZrO ₂ (20–40@8–10)	TEOS/NH ₄ OH FeCl ₃ , FeSO ₄ ZrOCl/NH ₃	Igepal CO-520 NH ₄ OH CTAB	W/CH W EtOH EtOH	ME COP Room	Room >13	[85]	

a) Abbreviations: ni = not informed; MW = microwave; TD = thermal decomposition; R = reduction, ME = microemulsion; CR = chemical reduction; COP = coprecipitation; SC = sonochemical; AC = acetate; acac = acetylacetone; AOT = bis(2-ethylhexyl) sodium sulfosuccinate; BA = benzyl alcohol; BAm = benzylamine; BE = benzyl ether; BMI-Tf₂N = bis(trifluoromethane)sulfonamide of 1-*n*-butyl-3-methylimidazolium; CH = cyclohexane; CTAB = cetyltrimethylammonium bromide; DDAB = didodecyldimethylammonium bromide; DEG = diethylene glycol; DPE = diphenyl ether; DS = dodecyl sulfate; EG = ethylene glycol; EtOH = ethanol; HAD = hexadecylamine; HD = 1-hexadecene; HDD = 1,2-hexadecanediol; HDZ = hydrazine; Igepal CO-520 = polyoxyethylene(5)nonylphenyl ether; ISO = isoctane; LAc = inoleic acid; MA = methylamine; MST = mesitylene; Ni⁰(cod)₂ = bis(η^4 -1,5-cyclooctadiene) Ni(0); NMPyr = N-methylpyrrole; OA = oleylamine; OCA = octylamine; ODA = octadecylamine; PAA = poly(acrylic acid); PD = 2-pyridolidone; Igepal CA-520 = polyoxyethylene(5)isooctylphenyl ether; PVP = polyvinylpyrrolidone; Pyr = pyrrole; RAC = ricinoleic acid; SDBS = sodium dodecyl benzenesulfonate; SDS = sodium dodecyl sulfate; TEOS = triethylsilane; TOA = trioctylamine; T100 = Triton X-100; W = water; XY = xylene.

b) Reaction final temperature.

c) Reaction time.

d) See text for details.

e) Solvent dependent.

even seconds using iron precursors such as $\text{Fe}(\text{acac})_3$, $\text{Fe}(\text{acac})_2$ or $\text{Fe}(\text{Ac})_2$ dissolved in benzyl alcohol [49].

Metallic magnetic NPs of Fe [60, 61], Ni [62], and Co [63], magnetic alloy NPs such as FePt [64] and CoNi [65], and metal(1)@metal(2) core@shell magnetic NPs such as $\text{FeO}@ \text{Fe}_3\text{O}_4$ [66], $\text{Au}@ \text{Co}$ [67], $\text{Fe}_3\text{O}_4@ \text{ZnO}$ [68], and Au–Ni spindly nanostructures [67] can also be obtained by the TDR method. Lacroix and co-workers obtained Fe nanocubes forming superlattices or NPs via TDR of a non-toxic precursor, $\text{Fe}[\text{N}(\text{SiMe}_3)_2]_2$ in mesitylene (1,3,5-trimethylbenzene) at 150 °C under an H_2 atmosphere in the presence of hexadecylamine and oleic acid (OAc) or hexadecylammonium chloride [60, 61]. The microwave-assisted TDR of $\text{Ni}(\text{Ac})_2$ and $\text{Co}(\text{Ac})_2$ in ethylene glycol (EG) in the presence of polyvinylpyrrolidone (PVP) or dodecylamine as capping agent was used to obtain Ni [62] and Co [63] NPs. Monodisperse FePt alloy NPs were obtained by TDR of $\text{Pt}(\text{acac})_2$ and $\text{Fe}(\text{acac})_2$ as precursors, in octyl ether using 1,2-hexadecanediol and OAc as reducing and capping agents, respectively [64]. Similarly, CoNi alloy NPs were obtained in high yields by TDR of $\text{Co}(\text{acac})_2$ and $\text{Ni}(\text{acac})_2$ in an autoclave, using triethylene glycol as solvent and PVP as reducing and capping agent [65]. In a one-pot wet chemical route, Wang *et al.* obtained $\text{Au}@ \text{Co}$ and Au–Ni spindly nanostructures in a TDR process using as precursors HAuCl_4 , $\text{Co}(\text{NO}_3)_2$ and $\text{Ni}(\text{NO}_3)_2$, and octadecylamine (ODA) as both the solvent and the surfactant [67]. The reaction was performed in air and was completed within 10 min. $\text{Fe}_3\text{O}_4@ \text{ZnO}$ NPs were obtained in two steps: (i) the Fe_3O_4 NPs were obtained by TDR of Fe(III)-oleate [69]; (ii) the Fe_3O_4 NPs were added to *n*-octadecene and at a temperature of 317 °C $\text{Zn}(\text{Ac})_2$ was added and thermally decomposed, forming a ZnO shell [68].

3.2.3

Microemulsion Methods

These methods involve the production of magnetic NPs in a nanometer-sized confined environment of a micelle. The micelle behaves like a nanoreactor where a coprecipitation or reduction reaction can take place. Moumen and Pileni *et al.* used micelles of FeDS and CoDS (DS = dodecylsulfate) in water to react with methylamine, leading to the formation of CoFe_2O_4 NPs [70]. MFe_2O_4 ($\text{M} = \text{Fe, Co, Mn}$) NPs were also obtained by coprecipitation of metal sulfates with NH_4OH in reverse micelles of bis(2-ethylhexyl) sodium sulfosuccinate (AOT) in isoctane [71]. In these protocols and others described in the literature [72–75], the coprecipitation reaction is conducted at room temperature and, therefore, does not lead to highly crystalline oxides. Using another approach, Lee *et al.* added a water–ethanol solution of MCl_2 and $\text{Fe}(\text{NO}_3)_3$ to a sonicated mixture of xylene and sodium dodecylbenzenesulfonate in the presence of hydrazine and obtained highly crystalline MFe_2O_4 ($\text{M} = \text{Fe, Co, Mn, Ni, Zn}$) NPs [76]. Other magnetic nanosized materials can be obtained by the microemulsion process, such as Fe [77], Co [78], $\text{Fe}@ \text{Au}$ [79], $\text{Fe}_3\text{O}_4@ \text{SiO}_2$ [80, 81], $\text{MFe}_2\text{O}_4@ \text{SiO}_2$ ($\text{M} = \text{Co, Mn}$) [82], $\text{Co}@ \text{SiO}_2$ [83], $\text{NiFe}_2\text{O}_4@ \text{SiO}_2$ [84], and $\text{Fe}_3\text{O}_4@ \text{mZrO}_2$ [85] (see Table 3.1 for reaction details).

3.2.4

Preparation of Magnetic NPs Using Renewable Resources

One way in which to address the green chemistry principles in the synthesis of magnetic NPs is the use of reagents obtained from renewable resources. For instance, Wang *et al.* [86] reported a liquid–solid–solution (LSS) process for the synthesis of NPs that uses water, ethanol, linoleic acid, and sodium linoleate (both linoleic acid and sodium linoleate can be obtained from soybean oil) and metal salts such as FeCl_3 . Using mixtures of Fe^{3+} and M^{2+} salts in a certain molar ratio, magnetic MFe_2O_4 ($\text{M} = \text{Fe, Co, Mg, Zn or Mn}$) NPs can be effectively prepared through coprecipitation reactions following this LSS phase-transfer and separation method.

The surface modification of magnetic NPs with long-chain fatty acids (LCFAs), such as OAc, is one of the most commonly used processes to obtain magnetic NPs dispersed in non-polar solvents. It has been observed that NPs coated with stearic acid [$\text{CH}_3(\text{CH}_2)_{16}\text{CO}_2\text{H}$], with no double bond in its C_{18} (stearic) tail, does not produce stable ferrofluid suspensions, whereas NPs covered with OAc [$\text{CH}_3(\text{CH}_2)_7\text{CH}=\text{CH}(\text{CH}_2)_7\text{COOH}$] form very stable magnetic fluids. It has been proposed that the presence of a $\text{C}=\text{C}$ double bond in the OAc with a kinked structure is necessary for effective stabilization of the magnetic NPs in non polar solvents [26]. According to Tadmor *et al.* [87], the aggregation observed for stearic acid-coated magnetic NPs is probably due to short-range adhesive interactions arising from the interfacial energy between the organic solvent and the surface of the collapsed stearic surfactant layers. Recently, Jacintho *et al.* [88] used a mixture of fatty acids obtained from raw commercial soybean (oleic and linoleic) and castor oil (ricinoleic) instead of commercial OAc to modify the surface of Fe_3O_4 and CoFe_2O_4 NPs. They observed that dispersions of magnetic NPs covered with mixtures of these fatty acids in cyclohexane are very stable against aggregation in the absence or presence of magnetic fields [88].

3.2.5

Synthesis of Magnetic NPs in Ionic Liquids

Room temperature ionic liquids (ILs), especially those derived from dialkylimidazolium (DAI) compounds, present very interesting properties as solvents for the synthesis of NPs, with excellent thermal and chemical stability and negligible vapor pressure, conferring on them another interesting characteristic, namely that they can be re-used in several reaction cycles [89], which is an important prerequisite for a green chemistry process. It is well known that DAI ILs form supramolecular structures [90] that act as “entropic drivers”, making possible the control of the size and shape of nanostructured materials. Various protocols have been reported that made use of such ILs in the synthesis of magnetic NPs. Some of them, however, involved expensive, toxic, and flammable precursors such as carbonyl complexes [91–94]. Despite the use of $\text{Fe}(\text{CO})_5$ as the iron precursor, Wang *et al.* [92] used the same sample of IL (BMI.Tf₂N) in at least 20 consecutive TDR reaction synthesis of

γ -Fe₂O₃, thus demonstrating the ability of ILs to act as recyclable solvents. Magnetic Ni NPs were obtained in a thermal decomposition reaction in different kinds of IL derived from DAI cation using an organometallic precursor, Ni⁰(cod)₂ (cod=cyclooctadiene), in an H₂ atmosphere [95, 96]. Wang and Yang obtained CoPt NPs and nanorods in the TDR of Co(acac)₃ and Pt(acac)₂ in BMI.Tf₂N using cetyltrimethylammonium bromide (CTAB) as capping and reducing agent [97]. The ability of ILs to help in the control of the size and shape of nanostructured materials was verified in the synthesis of α -Fe₂O₃ as NPs and with other morphologies via an IL-assisted hydrothermal process in BMI.Cl containing water and KAc using FeCl₃ as the precursor [98]. α -FeOOH hollow spheres, β -FeOOH architectures, and Fe₃O₄ hollow spheres (500 nm) were formed in a microwave-assisted hydrothermal reaction in BMI.BF₄ using FeCl₃ as metal precursor [99]. Similarly, ZnFe₂O₄ NPs were obtained in a microwave-assisted hydrothermal process in BMI.BF₄ containing water and urea using Fe(NO₃) and Zn(Ac)₂ as precursors [100]. More recently, it has been demonstrated that MFe₂O₄ (M = Fe, Co, Mn, Ni) NPs can be obtained in a one-pot TDR process in BMI.Tf₂N using Fe(acac)₃ and M(acac)₂ as precursors using OA as reducing and capping agent. The size and shape of the NPs can be controlled by the reaction time and temperature [57, 101]. The same sample of IL was used in at least 20 reaction cycles.

3.2.6

Other Methods

There are some synthetic protocols that use a sonochemical approach to obtain magnetic NPs. Dang and co-workers demonstrated that ultrasonic irradiation of Fe(OH)₂ dissolved in water [102] or water–ethanol [103, 104] can lead to Fe₃O₄ NPs. Recently, it has been reported that Fe₃O₄ [105, 106] or γ -Fe₂O₃ [107] NPs with a controlled size distribution can be obtained by electroprecipitation in aqueous [105, 107] or water–ethanol [106] solutions. In all cases, Fe(III) salts were used as the iron source. Iron NPs can be obtained in the absence or presence of dispersing agents by a chemical reduction process using FeCl₃ in aqueous solution and reducing agents such as hydrazine or NaBH₄ [108, 109]. In order to avoid NP aggregation, dispersing agents such as poly(acrylic acid) (PAA) or PVP can be used. Wu *et al.* obtained monodisperse Ni NPs by the reduction of NiCl₂ with hydrazine in aqueous solution [110].

3.3

Magnetic Separation as a Green Separation Tool

3.3.1

Background

Magnetic separation is the most documented and one of the most useful applications of superparamagnetic NPs. The unique feature of magnetic NPs in the

superparamagnetic regime is their response to a remote magnetic field and the absence of residual magnetization when the field is removed. Magnetic particles below a critical diameter cannot support more than one domain, and are therefore described as “single domain”. This critical diameter (D_c) is approximately $2A^{1/2}/I_s$ (where A is the exchange constant and I_s is the saturation magnetization). For typical materials, D_c values are in the range 10–100 nm, for example, $D_c \approx 12.0$ nm for iron and $D_c \approx 40.0$ nm for magnetite [111]. Much of the behavior of single-domain NPs can be described by assuming that all the atomic moments are rigidly aligned as a single “giant” spin, hence the term superparamagnetism [112]. The energy of a superparamagnetic NP is generally dependent on the magnetization direction, resulting in particular equilibrium directions separated by energy barriers. Therefore, for each particle size there will be a temperature, called the blocking temperature, above which thermal excitations are sufficient to overcome such barriers and rotate the particle magnetization, thus demagnetizing it in such a way that the net magnetic moment is zero. This is characterized by the absence of hysteresis in the M versus H curves. It is important to note that the NPs are still susceptible to an external magnetic field, and in this respect they behave like a paramagnetic material, but removing the applied magnetic field instantaneously reduces the overall net magnetic moment back to zero. Hence the NPs have no “magnetic memory” and any magnetic material or entity attached to a magnetic material in this regime can be separated by applying a remote magnetic field and redispersed immediately after the field has been removed.

Magnetism was first used to separate magnetic from non-magnetic components of a mixture, for example, enrichment of low-grade iron ore, removal of ferromagnetic impurities from large volumes of boiler water in both conventional and nuclear power plants, and removal of weakly magnetic colored impurities from kaolin clay [113]. In the 1970s, the development of new magnetic NPs with improved properties prompted the use of magnetic separation in the biosciences, first to purify cells, cell organelles, and biologically active compounds (nucleic acids, proteins, etc) directly from crude samples. Chemically modified NPs with general specificity ligands (e.g., streptavidin, protein A) and chemically modified NPs with specific recognition groups (e.g., antibodies) are used for the isolation of specific molecules through complementary binding interactions [114]. Several kits are commercially available that work on the principle of magnetic labeling and direct isolation of molecules such as DNA, RNA, and proteins on to streptavidin-coated magnetic beads. Magnetic separation, more recently applied also in other areas of research, has several advantages in comparison with other separation techniques, such as chromatography and extraction, as it avoids the use of solvents and other costly consumables. It permits the target component to be isolated directly from crude samples such as blood, soil, food, or any other complex fluid, which greatly simplifies the separation process as it avoids laborious filtration or centrifugation steps, saving time and energy. High selectivity can be achieved in magnetic separation by means of the functionalization of magnetic NPs with specific ligands to target components of a mixture. The whole separation process can be performed

without removing the sample from the flask or container, which greatly simplifies procedures such as repeated washing steps and especially the isolation of moisture-sensitive components. Scale-up and automation of routine separation and purification steps involving magnetic separation may be possible with no need for elaborate protocols or expensive equipment. The performance of a magnetic separation system depends on two key magnetic components, the magnetic NPs and the magnetic field used to separate them. The field is usually generated by the presence of permanent magnets or electromagnets. Simple magnet blocks typically generate field gradients in the order of $1\text{--}6 \text{ Tm}^{-1}$, and magnet separators with significantly higher field gradients can be designed [115]. In addition, the selection of the magnetic material, shape, size and size distribution of the NP will significantly affect the end separation results.

Considering that magnetic separation, compared with traditional separation methodologies, minimizes the use of solvents, reagents, time and energy, it follows some of the principles of green chemistry and therefore can be considered a green separation technology. In addition to widespread use in the biosciences, this technology has also found use in the field of environmental chemistry in the containment of oil spills and the recovery of heavy metals or catalysts, that are discussed in the following sections.

3.3.2

Oil Spill Containment and Recovery

Containment and clean-up techniques are applied to marine oil spills in order to limit their spreading on water surfaces. It is crucial to contain the spills as quickly as possible in order to mitigate the environmental and health impacts. The most commonly applied containment technique is based on floating barriers used for concentrating oil, making its recovery easier, and also for keeping oil out of sensitive areas or for diverting oil into collection areas. Oil spill containment based on a magnetic separation technique was reported in the 1970s [116]. The use of floating oleophilic magnetic NPs can help to slow the rate of expansion of the surface of the spill and control its spreading by using magnetic belts properly placed in the affected area. Depending on the size of the oil spill, the magnetic material can be dispersed directly into the oil phase or sprayed over the spill by aeroplanes or helicopters. The oil loaded with the magnetic NPs can be magnetically controlled and collected into collecting vessels by using magnets. This represents an environmentally friendly technology since the magnetic material is non-toxic and can be recycled, and represents an alternative to the use of chemical dispersants, which are often very toxic and leave residual oil pollution. Recent developments in this field include the search for high-quality magnetic sorbents based on magnetic NPs coated with long-chain molecules (e.g., OAc), branched polymers or carbon [117–119]. The as-prepared hydrophobic magnetic NPs will disperse in the oil phase and the movement of the oil spill can be remotely controlled by an external magnetic field.

3.3.3

Heavy Metal Recovery

Removal of heavy metal ions from contaminated water is a crucial issue as they can pose severe risks to human health and the environment. Several methods, including chemical precipitation, ion exchange, liquid–liquid extraction, membrane filtration, cementation, and electrodialysis, have been developed for the removal of heavy metal ions from the aqueous phase. Magnetic separation techniques provide a convenient tool for exploring heavy metal recovery by using coated and functionalized magnetic NPs with specific binding characteristics. Magnetic composites have the capability to treat large amounts of wastewater within a short time and can be conveniently separated magnetically; moreover, they could be tailored by using functionalized polymers, molecules, or inorganic coatings to improve surface reactivity and specificity for different metal ions. For example, Wang *et al.* reported the use of magnetic NPs modified with bisphosphonate derivatives to remove 99 and 69% of radioactive metal toxins, as uranyl ions, from water and blood, respectively [120]. Magnetic chitosan nanocomposites have been used for the removal of Pb^{2+} , Cu^{2+} , and Cd^{2+} from water [121]. Thiol-containing polymer-encapsulated magnetic NPs exhibited higher uptake capacities for different heavy metal ions, such as Ag^+ , Pb^{2+} , and Hg^{2+} [122], which is approximately seven times higher than that of chitosan-coated magnetic NPs [123]. Imidazole-functionalized polymer-coated magnetic NPs showed selective binding of divalent metal ions with a binding strength that decreased in the order $\text{Cu}^{2+} >> \text{Ni}^{2+} > \text{Co}^{2+}$ [124]. Removal of mercury using magnetic sorbents has also been reported [125]. The functionalization of magnetic NPs with an EDTA-like chelator allowed the rapid removal of Cd^{2+} , Cu^{2+} , and Pb^{2+} from wastewater [126]. Thiol-functionalized magnetite NPs were used as scavengers for palladium ions from aqueous and organic solutions [127]. However, removal of spent catalysts can be problematic since the metals ions are mostly coordinated to strongly binding ligands. Some of the most useful homogeneous catalysts of Pd, Rh, and Ru (e.g., Grubbs' catalyst, Wilkinson's catalyst, and many other homogeneous catalysts) employ strongly binding, bulky phosphines to prepare the active species, tailor reactivity, and prevent plating out of zero oxidation state metal during the catalytic cycle [128]. In this respect, it should be mentioned that catalytic metal impurities remaining after synthesis can have a detrimental effect on later synthetic steps [129–131], alter the properties of end-use materials [132], and are a health concern if the end product is a pharmaceutical. The concentration limits of, for example, Pd in orally administered drugs should be below 5 ppm, and the parenteral concentration limits should be one-tenth of the limit for the oral doses. Several methods for removing palladium impurities from organic compounds of pharmaceutical interest have been developed, as discussed in a review by Garrett and Prasad [133]. The separation methods include distillation, extraction, precipitation, and solid-phase treatments with solid scavengers comprised of functionalized resins, polymers, silica, and so on [134]. The functionalization of magnetic nanomaterials such as magnetite NPs or other magnetic nanocomposites opens up the possibility of

preparing magnetic scavengers for spent catalysts, although better results are expected in situations where catalytic ions are not coordinated to strongly binding ligands.

3.3.4

Catalyst Recovery and Recycling

The tremendous growth in the application of catalytic routes to the synthesis of complex organic molecules has been driven by academic and industrial discoveries of efficient and selective catalysts for a wide variety of liquid- and multiphase organic reactions. Recent developments have resulted from enormous efforts towards minimization of the costs of manufacture and waste disposal in the economically competitive and ecologically aware market. The practical applications of homogeneous catalysts in industrial processes are hindered by their high costs and also difficulties in removing trace amounts of toxic metals from the organic products. Many different approaches have been suggested to circumvent these problems, such as new separation techniques based on liquid–liquid phase separation, including ionic liquids, fluorous phases, supercritical solvents, and polymeric supports, either as solid phases or as soluble polymeric supports [135]. Each separation method has limitations, such as cost, efficiency, and generation of secondary waste. The heterogenization of homogeneous catalysts on solid supports has attracted great attention [136–140]. Magnetic separation has emerged as a robust, highly efficient and fast separation tool with many advantages compared with catalyst isolation by means of liquid–liquid extraction, chromatography (homogeneous catalysts), or even filtration and centrifugation (heterogeneous catalysts or supported catalysts). Fe, Ni, Co, and iron oxides can be directly collected and recovered by a remote magnetic field. In fact, the first examples of the application of magnetic separation in catalysis were based on the intrinsic magnetic property of such metals [141–146]. Examples of the use of NPs of such materials as magnetically recoverable catalysts can also be found in the recent literature [147, 148]. However, the possibility of using magnetic separation in catalysis was broadened by the introduction of magnetic nanomaterials and nanocomposites as solid supports for the immobilization of catalytically active metals [149], complexes, and even organocatalysts. Although this topic has recently been reviewed [150], we consider it useful to mention selected examples here. We will avoid duplicating information and focus our discussion on examples of metal complexes, metal nanoparticles, and organocatalysts immobilized on magnetic NPs. More examples can be found in the review [150].

3.3.4.1 Metal Complex Catalysts

Catalytically active metal complexes have been anchored on magnetically recoverable supports, mainly magnetic NPs or magnetic NPs coated with inorganic or organic matrixes. One of the first reported examples of a heterogenized magnetically recoverable catalyst was the Rh- complex $\{\text{Rh}(\text{cod})(\eta^6\text{-benzoic acid})\}\text{BF}_4^-$ that was attached to the surface of ferrite NPs through the carboxylic acid functional

groups, a well-known binding group for the surface of ferrite NPs [151]. The supported catalyst showed excellent catalytic activity and regioselectivity in hydroformylation reactions, which is comparable to that of its homogeneous counterpart. Soon afterwards, a chiral Ru complex with phosphonic acid-substituted BINAP $\{\text{Ru}(\text{BINAP-PO}_3\text{H}_2)(\text{DPEN})\text{Cl}_2\}$ [$\text{BINAP-PO}_3\text{H}_2 = (\text{R})\text{-2,2'-bis(diphenylphosphino)-1,1'-binaphthyl-4-phosphonic acid}$ and $\text{DPEN} = (\text{R},\text{R})\text{-1,2-diphenylethylenediamine}$] was immobilized on magnetite NPs via the phosphonate functionality and represents the first reported example of a heterogenized magnetically recoverable asymmetric catalyst [152]. The supported chiral Ru complex catalyzes the asymmetric hydrogenation of aromatic ketones with remarkably high activity and enantioselectivity. Other examples include the heterogenization of $\{\text{Rh}(\text{cod})\text{Cl}\}_2$ into magnetic NP-loaded dendrimers [153] and rhodium–phosphine complexes on magnetite NPs [154]. Gao and co-workers prepared three different catalysts based on palladium complexes with *N*-heterocyclic carbene ligands (NHCPd complexes) immobilized on the surface of magnetic NPs–nanocomposites to generate iron oxide-supported palladium complexes for Suzuki, Heck, and Sonogashira cross-coupling reactions [155–157]. Dipyridylpalladium complexes [158] and palladium(II)–phosphine complexes [38] were also immobilized on the surface of magnetic NPs for the same purpose.

3.3.4.2 Metal Nanoparticle Catalysts

Another class of catalysts that can benefit from magnetic separation is the metal nanoclusters or NPs. The catalytic properties of “soluble” metal NPs have attracted great attention over the past decade as they can be prepared through reproducible syntheses in contrast to traditional colloids that are typically larger, not reproducibly prepared and with irreproducible catalytic activities [159]. However, the use of “soluble” metal NPs in catalysis is limited by the difficulty in the recovery of the catalyst from the reaction products, which are in the same phase [160]. The literature has offered possibilities of recycling such catalysts by means of liquid–liquid biphasic systems (e.g., the catalyst dispersed in the aqueous phase or ILs) [161, 162] or by using solid supports (e.g., the catalyst immobilized on silica, alumina, polymers, etc.) [163–165]. In this context, solid supports endowed with magnetic properties promise to improve the recovery and recycling of metal NP catalysts. A myriad of examples have appeared in the literature in the last decade and this subject has recently been reviewed [150]. Soluble and supported Pd NPs [166] catalyze cross-coupling reactions with improved catalyst stability and handling properties in comparison with homogeneous counterparts. Pd NPs supported on functionalized magnetic NPs with excellent catalytic activity, easy catalyst recovery, and recycling in successive reactions have been reported [62, 167–174], and also highly efficient catalysts under phosphine-free conditions [175]. Pd NPs supported on magnetite NPs [176, 177] and silica coated magnetic NPs [127, 178] are active catalysts for the hydrogenation of alkenes under mild conditions. Pd NPs supported on hydroxyapatite-encapsulated $\gamma\text{-Fe}_2\text{O}_3$ NPs are active catalysts for the dechlorination of various organochlorides using atmospheric molecular hydrogen [179]. Supported Pd NPs of different sizes were prepared on the surface of silica-coated magnetite NPs ($\text{Fe}_3\text{O}_4@\text{SiO}_2$) functionalized with organo-

silanes [178]. Amine and ethylenediamine groups grafted on the surface of the silica support assisted the preparation of magnetically recoverable Pd NPs of ~ 6 and ~ 1 nm, respectively, by H₂ reduction of Pd²⁺ ions previously bound to the modified silica surfaces. The size of the metal NPs was tuned by the functional group grafted on the silica surface, which also resulted in different catalytic activities in hydrogenation reactions. The catalyst comprised of small Pd NPs (~ 1 nm) is less active in the hydrogenation of cyclohexene (turnover frequency 800 h⁻¹, deactivates completely after the fourth recycle of 2500 turnovers each) than the catalyst comprised of ~ 6 nm Pd NPs (turnover frequency 5500 h⁻¹, active up to 20 successive runs of 2500 turnovers each or 50,000 mol mol⁻¹ Pd) under similar reaction conditions (75 °C, 6 atm H₂). Similarly, magnetically recoverable rhodium [80] and platinum [180] NPs were prepared by H₂ reduction of metal ion precursors loaded on the silica-coated magnetic support previously modified with amine groups. The magnetically separable catalytic system, comprised of Rh NPs of $\sim 3\text{--}5$ nm immobilized on Fe₃O₄@-SiO₂, is highly active (turnover frequencies as high as 40 000 and 1100 h⁻¹ were obtained in the hydrogenation of cyclohexene and benzene at 75 °C and 6 atm H₂, respectively) and could be reused up to 20 times for hydrogenation of cyclohexene (180 000 mol mol⁻¹ Rh) and benzene (11 550 mol mol⁻¹ Rh) under mild conditions. This same catalyst has shown very interesting catalytic activities in the liquid hydrogenation of polycyclic aromatic hydrocarbons [181]. The magnetically recoverable Pt(0) NP catalyst presented high catalytic activities for hydrogenation of ketones, alkenes, and arenes in liquid-phase solventless reactions. The substrates were converted to the full hydrogenated forms, but partially hydrogenated products were also isolated by stopping the reaction at the time indicated by the H₂ consumption profile hydrogenation curve (e.g., ethylbenzene was isolated with 98.9% selectivity during hydrogenation of styrene). The advantage of being superparamagnetic promotes easy separation and recycling of the catalyst, which could be reused for up to 14 successive reductions of ketones (15 600 mol mol⁻¹ Pt) without deactivation. The NH₂ groups present on the silica surface guarantee an enhanced metal uptake (65 times higher compared with non-functionalized particles) and most probably contribute to metal retention, which is confirmed by the negligible amount of metal leaching into the liquid products and the high reusability of both Rh and Pt NP catalysts. Using a different approach, Jun *et al.* prepared a core@ shell-type cobalt–platinum magnetic catalyst for the hydrogenation of various unsaturated organic molecules under mild conditions, and also demonstrated their magnetic separation and recycling capabilities [182]. Magnetically recoverable ruthenium NPs [183] were prepared by NaBH₄ reduction of Ru³⁺ loaded into a silica-coated magnetic support previously modified with amine groups. The catalyst was found to be active in both forms, Ru(III) and Ru(0), for selective oxidation of alcohols and hydrogenation of alkenes, respectively. Aryl and alkyl alcohols were converted into aldehydes under mild conditions, with negligible metal leaching. If the metal was properly reduced, Ru(0) NPs were obtained, and the catalyst became active for hydrogenation reactions. An Ru NP catalyst supported on dopamine-modified magnetic NPs and reduced by NaBH₄ was reported [184]. The magnetically recoverable Ru NP catalyst was active for the selective hydrogenation of alkynes to their

respective alkanes at room temperature, and also the transfer hydrogenation of a variety of carbonyl compounds under microwave conditions. Magnetically recoverable ruthenium hydroxide catalysts were also reported [185, 186]. These catalysts are active for the hydration of nitriles with high yield and excellent selectivity, which proceed exclusively in an aqueous medium without using any organic solvents even in the workup stage, and for aerobic oxidations and reductions with 2-propanol [185, 186]. A wide variety of substrates, including aromatic, aliphatic, and heterocyclic, could be converted into the desired products in high to excellent yields without any additives such as bases and electron-transfer mediators. The magnetically recoverable catalysts based on Ru(OH)_x-magnetite NPs could be reused without appreciable loss of the catalytic performance [186]. Magnetically recoverable Au NP catalysts were prepared by reduction of gold ions into a silica-coated magnetic support previously modified with amine groups [187]. The Au NPs were prepared by thermal reduction in air and by hydrogen reduction at mild temperatures of the gold species attached to the magnetic support. Interestingly, the mean particle size of the supported Au NPs was similar, ~5.9 nm, but the polydispersity of the samples and the catalytic performance in oxidation of alcohols were very different [187]. The catalyst reduced by hydrogen exhibited a narrow particle size distribution and was the more active for the oxidation of benzyl alcohol under milder conditions (100% conversion at 3 atm O₂ compared with only 10% conversion of the catalyst prepared by thermal reduction). A mesoporous-silica-protected core–satellite Au nanocomposite catalyst was prepared through a series of simple sol–gel and surface-protected etching processes in order to contain superparamagnetic components for efficient magnetic separation and a mesoporous silica framework for stabilization of the encapsulated catalyst particles [188]. Nickel NPs, in addition to their intrinsic magnetic properties, have also been immobilized into iron oxide-based supports to improve the magnetic separation in catalytic reactions [185]. All the NP-supported catalyst could be isolated and recycled with the assistance of an external magnet, which greatly simplifies the workup procedure and purification of products, minimizing the use of solvents, costly consumables, energy, and time.

3.3.4.3 Organocatalysts

Magnetic separation has also been successfully applied in the field of organocatalysis, the metal-free approach to the synthesis of organic molecules [189], through the functionalization of magnetic NPs or nanocomposites with organic fragments. Catalyst recovery is generally problematic in this field, since filtration has reduced efficiency and extractive isolation of products requires excessive amounts of organic solvents. The immobilization of the organocatalysts on polymers [190] or magnetic solid supports rendered the organocatalysis approach even greener. A magnetic NP-supported acylation organocatalyst was prepared by the immobilization of 4-*N,N*-dimethylaminopyridine (DMAP) into silica-coated magnetic NPs. The DMAP-supported catalyst promoted a range of nucleophilic reactions and can be recovered by exposure to an external magnet and recycled over 30 times without loss of activity [191]. An organocatalyst comprised of glutathione-coated magnetic NPs was explored for Paal–Knorr reactions, the synthesis of pyrrole from

amines [192]. Because of the superparamagnetic nature of the catalyst, within a few seconds after stirring stopped the catalyst was deposited on the magnetic bar; the catalyst was easily removed using an external magnet. This facilitated isolation of crude product by simple decantation instead of tedious extraction processes, thus reducing the use of volatile organic solvents during product workup. This catalyst was also examined for the synthesis of pyrazole and in the aza-Michael reaction. Magnetite NP-supported proline was explored in the CuI-catalyzed Ullmann-type coupling reactions of aryl/heteroaryl bromides with various nitrogen heterocycles. Several *N*-arylations of *N*-heterocycles with aryl and heteroaryl bromides were performed and the catalyst was recovered from the product by exposure to an external magnet [193]. The immobilization of ammonium and phosphonium salts on magnetic NPs by Kawamura and Sato [194] was the first example of a magnetically separable phase-transfer catalyst. Later, the same group prepared magnetically separable crown ethers through the immobilization of crown ethers on magnetite NPs [195]. The supported crown ethers were efficient for phase-transfer reactions, easily recoverable using magnetism, and reusable without loss of catalytic activity. The immobilization of quinuclidine on magnetic NPs was reported to be an efficient, recoverable catalyst for the Morita–Baylis–Hillman (MBH) reaction, one of the most popular C–C bond-forming strategies in modern organic synthesis [196]. The supported catalyst demonstrated activity comparable to that of the classical MBH catalyst DABCO and could be simply recycled with the assistance of an external magnet. Chiral primary amine catalysts were immobilized in magnetic NPs and evaluated as asymmetric bifunctional enamine catalysts in direct aldol reactions [197]. The supported catalyst demonstrated high activity and stereoselectivity smoothly under “on-water” conditions and the catalysts could be easily recycled via magnetic force and reused up to 11 times with essentially no loss of activity and stereoselectivity. The immobilization of ionic liquids on magnetic NPs was first reported by Zheng *et al.* [198]. The supported IL was used as a catalyst in CO₂ cycloaddition reactions at a lower CO₂ pressure. The activity of the supported catalyst is comparable to that of the free IL catalysts for this reaction. The catalysts could be easily recycled using a magnet and reused up to 11 times with essentially no loss of activity [198]. The combination of magnetically and gravimetrically recoverable catalysts such as an NP-bound base and a resin-bound acid, respectively, allow the application of non-complementary catalysts to multi-step, one-pot reaction cascades (e.g., A → B → C). The catalysts are recovered after reaction and reused in subsequent, unrelated reactions [199]. Therefore, magnetic separation was an important tool in organocatalysis facilitating catalyst separation, recycling, and product isolation.

3.4 Conclusion

It has been shown that different kinds of magnetic nanomaterials can be obtained by coprecipitation, hydrothermal and thermal decomposition, and other processes.

From the studies covered in this chapter, it can be concluded that a completely green chemical process in the synthesis of this kind of material is still a challenge. Some protocols, despite using non-toxic precursors, are time- and/or energy-consuming processes or require the use of non-friendly and non-recyclable solvents. Reaction times in microwave-assisted reaction processes have shown to be shorter. On the other hand, the substitution of conventional solvents for chemical and thermally stable ILs allowed the reutilization of the solvent and also provided control of the size and shape of NPs.

The use of magnetically recoverable solid supports that can be easily separated due to the magnetic interaction between the magnetic NPs and an external applied magnetic field represents an alternative separation tool to traditional time-, energy-, and solvent-consuming steps during purification processes. Magnetic separation is clean, fast, and easily scaled up, and it does not make use of other chemical supplies and solvents that represent considerable environmental hazards. Therefore, it can be regarded as a green separation technology with great possibilities for applications in the field of environmental remediation and catalysis.

References

- 1 Sun, S.H. (2006) Recent advances in chemical synthesis, self-assembly, and applications of FePt nanoparticles. *Advanced Materials*, **18** (4), 393–403.
- 2 Gijs, M.A.M., Lacharme, F. and Lehmann, U. (2010) Microfluidic applications of magnetic particles for biological analysis and catalysis. *Chemical Reviews*, **110** (3), 1518–1563.
- 3 Osaka, T., Matsunaga, T., Nakanishi, T., Arakaki, A., Niwa, D. and Iida, H. (2006) Synthesis of magnetic nanoparticles and their application to bioassays. *Analytical and Bioanalytical Chemistry*, **384** (3), 593–600.
- 4 Koh, I. and Josephson, L. (2009) Magnetic nanoparticle sensors. *Sensors*, **9** (10), 8130–8145.
- 5 Haun, J.B., Yoon, T.J., Lee, H. and Weissleder, R. (2010) Magnetic nanoparticle biosensors. *Wiley interdisciplinary reviews. Nanomedicine and nanobiotechnology*, **2** (3), 291–304.
- 6 Jun, Y.W., Seo, J.W. and Cheon, A. (2008) Nanoscaling laws of magnetic nanoparticles and their applicabilities in biomedical sciences. *Accounts of Chemical Research*, **41** (2), 179–189.
- 7 Laurent, S., Forge, D., Port, M., Roch, A., Robic, C., Elst, L.V. and Muller, R.N. (2008) Magnetic iron oxide nanoparticles: synthesis, stabilization, vectorization, physicochemical characterizations, and biological applications. *Chemical Reviews*, **108** (6), 2064–2110.
- 8 Frey, N.A., Peng, S., Cheng, K. and Sun, S.H. (2009) Magnetic nanoparticles: synthesis, functionalization, and applications in bioimaging and magnetic energy storage. *Chemical Society Reviews*, **38** (9), 2532–2542.
- 9 Gao, J.H., Gu, H.W. and Xu, B. (2009) Multifunctional magnetic nanoparticles: design, synthesis, and biomedical applications. *Accounts of Chemical Research*, **42** (8), 1097–1107.
- 10 Laurent, S., Bouthry, S., Mahieu, I., Vander Elst, L. and Muller, R.N. (2009) Iron oxide based MR contrast agents: from chemistry to cell labeling. *Current Medicinal Chemistry*, **16** (35), 4712–4727.
- 11 Nune, S.K., Gundla, P., Thallapally, P.K., Lin, Y.Y., Forrest, M.L. and Berkland, C.J. (2009) Nanoparticles for biomedical imaging. *Expert Opinion on Drug Delivery*, **6** (11), 1175–1194.
- 12 Qiao, R.R., Yang, C.H. and Gao, M.Y. (2009) Superparamagnetic iron oxide

- nano particles: from preparations to *in vivo* MRI applications. *Journal of Materials Chemistry*, **19** (35), 6274–6293.
- 13** Roca, A.G., Costo, R., Rebolledo, A.F., Veintemillas-Verdaguer, S., Tartaj, P., Gonzalez-Carreno, T., Morales, M.P. and Serna, C.J. (2009) Progress in the preparation of magnetic nanoparticles for applications in biomedicine. *Journal of Physics D Applied Physics*, **42** (22), 11.
- 14** Laurent, S., Bridot, J.L., Elst, L.V. and Muller, R.N. (2010) Magnetic iron oxide nanoparticles for biomedical applications. *Future Medicinal Chemistry*, **2** (3), 427–449.
- 15** Lin, M.M., Kim, H.H., Kim, H., Dobson, J. and Kim, D.K. (2010) Surface activation and targeting strategies of superparamagnetic iron oxide nanoparticles in cancer-oriented diagnosis and therapy. *Nanomedicine*, **5** (1), 109–133.
- 16** Veiseh, O., Gunn, J.W. and Zhang, M.Q. (2010) Design and fabrication of magnetic nanoparticles for targeted drug delivery and imaging. *Advanced Drug Delivery Reviews*, **62** (3), 284–304.
- 17** Tartaj, P., Morales, M.P., Verdaguer, S.V., Carreño, T.G. and Serna, C.J. (2006) *Synthesis, Properties and Biomedical Application of Magnetic Nanoparticle: Handbook of Magnetic Materials*, Elsevier, Amsterdam.
- 18** Sambucetti, C.J. (1980) Magnetic ink for jet printing. *IEEE Transactions on Magnetics*, **16** (2), 364–367.
- 19** Kuroda, C.S., Kim, T.Y., Hirano, T., Yoshida, K., Namikawa, T. and Yamazaki, Y. (1999) Preparation of nano-sized Bi–YIG particles for micro optics applications. *Electrochimica Acta*, **44** (21–22), 3921–3925.
- 20** Anastas, P.T. and Warner, J. (1998) *Green Chemistry Theory and Practice*, Oxford University Press, New York.
- 21** Poliakoff, M., Fitzpatrick, J.M., Farren, T.R. and Anastas, P.T. (2002) Green chemistry: science and politics of change. *Science*, **297** (5582), 807–810.
- 22** Bitter, F. (1932) Experiments on the nature of ferromagnetism. *Physical Review*, **41**, 507–515.
- 23** Elmore, W.C. (1938) Ferromagnetic colloid for studying magnetic structures. *Physical Review*, **54**, 309–310.
- 24** Papell, S.S. Low viscosity magnetic fluid obtained by the colloidal suspension of magnetic particles. US Patent (1965) 3,215,572.
- 25** Rosensweig, R.E. Method of substituting one ferrofluid solvent for another. US Patent (1970) 3,917,538.
- 26** Rosensweig, R.E. (1985) *Ferrohydrodynamics*, Cambridge University Press, Cambridge.
- 27** Massart, R. Magnetic fluids and precursors for obtaining them. US Patent (1982) 4,329,241.
- 28** Gomes, J.D., Sousa, M.H., Tourinho, F.A. and Aquino, R. da Silva, G.J., Depeyrot, J., Dubois, E., Perzynski, R. (2008) Synthesis of core–shell ferrite nanoparticles for ferrofluids: chemical and magnetic analysis. *Journal of Physical Chemistry C*, **112** (16), 6220–6227.
- 29** Park, J., Joo, J., Kwon, S.G., Jang, Y. and Hyeon, T. (2007) Synthesis of monodisperse spherical nanocrystals. *Angewandte Chemie International Edition*, **46** (25), 4630–4660.
- 30** LesliePelecky, D.L. and Rieke, R.D. (1996) Magnetic properties of nanostructured materials. *Chemistry of Materials*, **8** (8), 1770–1783.
- 31** Beltran, L.M.C. and Long, J.R. (2005) Directed assembly of metal–cyanide cluster magnets. *Accounts of Chemical Research*, **38** (4), 325–334.
- 32** Niederberger, M., Garnweitner, G., Pinna, N. and Neri, G. (2005) Non-aqueous routes to crystalline metal oxide nanoparticles: formation mechanisms and applications. *Progress in Solid State Chemistry*, **33** (2–4), 59–70.
- 33** Chen, X.M. and Tong, M.L. (2007) Solvothermal *in situ* metal/ligand reactions: a new bridge between coordination chemistry and organic synthetic chemistry. *Accounts of Chemical Research*, **40** (2), 162–170.
- 34** Tavakoli, A., Sohrabi, M. and Kargari, A. (2007) A review of methods for synthesis of nanostructured metals with emphasis on iron compounds. *Chemical Papers*, **61** (3), 151–170.

- 35** Hyeon, T. (2003) Chemical synthesis of magnetic nanoparticles. *Chemical Communications*, (8), 927–934.
- 36** Lu, A.H., Salabas, E.L. and Schuth, F. (2007) Magnetic nanoparticles: synthesis, protection, functionalization, and application. *Angewandte Chemie International Edition*, **46** (8), 1222–1244.
- 37** Jeong, U., Teng, X.W., Wang, Y., Yang, H. and Xia, Y.N. (2007) Superparamagnetic colloids: controlled synthesis and niche applications. *Advanced Materials*, **19** (1), 33–60.
- 38** Shylesh, S., Wang, L. and Thiel, W.R. (2010) Palladium(II)-phosphine complexes supported on magnetic nanoparticles: filtration-free, recyclable catalysts for Suzuki–Miyaura cross-coupling reactions. *Advanced Synthesis and Catalysis*, **352** (2–3), 425–432.
- 39** Hyeon, T., Lee, S.S., Park, J., Chung, Y. and Bin Na, H. (2001) Synthesis of highly crystalline and monodisperse maghemite nanocrystallites without a size-selection process. *Journal of the American Chemical Society*, **123** (51), 12798–12801.
- 40** Rockenberger, J., Scher, E.C. and Alivisatos, A.P. (1999) A new nonhydrolytic single-precursor approach to surfactant-capped nanocrystals of transition metal oxides. *Journal of the American Chemical Society*, **121** (49), 11595–11596.
- 41** Sun, S.H. and Zeng, H. (2002) Size-controlled synthesis of magnetite nanoparticles. *Journal of the American Chemical Society*, **124** (28), 8204–8205.
- 42** Sun, S.H., Zeng, H., Robinson, D.B., Raoux, S., Rice, P.M., Wang, S.X. and Li, G.X. (2004) Monodisperse MFe_2O_4 ($M = Fe, Co, Mn$) nanoparticles. *Journal of the American Chemical Society*, **126** (1), 273–279.
- 43** Zeng, H., Rice, P.M., Wang, S.X. and Sun, S.H. (2004) Shape-controlled synthesis and shape-induced texture of $MnFe_2O_4$ nanoparticles. *Journal of the American Chemical Society*, **126** (37), 11458–11459.
- 44** Tan, Y.W., Zhuang, Z.B., Peng, Q. and Li, Y.D. (2008) Room-temperature soft magnetic iron oxide nanocrystals: synthesis, characterization, and size-dependent magnetic properties. *Chemistry of Materials*, **20** (15), 5029–5034.
- 45** Pinna, N., Garnweinert, G., Antonietti, M. and Niederberger, M. (2005) A general nonaqueous route to binary metal oxide nanocrystals involving a C–C bond cleavage. *Journal of the American Chemical Society*, **127** (15), 5608–5612.
- 46** Pinna, N., Grancharov, S., Beato, P., Bonville, P., Antonietti, M. and Niederberger, M. (2005) Magnetite nanocrystals: nonaqueous synthesis, characterization, and solubility. *Chemistry of Materials*, **17** (11), 3044–3049.
- 47** Wan, J., Cai, W., Meng, X. and Liu, E. (2007) Monodisperse water-soluble magnetite nanoparticles prepared by polyol process for high-performance magnetic resonance imaging. *Chemical Communications*, (47), 5004–5006.
- 48** Cai, W. and Wan, J.Q. (2007) Facile synthesis of superparamagnetic magnetite nanoparticles in liquid polyols. *Journal of Colloid and Interface Science*, **305** (2), 366–370.
- 49** Bilecka, I., Djerdj, I. and Niederberger, M. (2008) One-minute synthesis of crystalline binary and ternary metal oxide nanoparticles. *Chemical Communications*, (7), 886–888.
- 50** Li, Z., Chen, H., Bao, H.B. and Gao, M.Y. (2004) One-pot reaction to synthesize water-soluble magnetite nanocrystals. *Chemistry of Materials*, **16** (8), 1391–1393.
- 51** Li, Z., Sun, Q. and Gao, M.Y. (2005) Preparation of water-soluble magnetite nanocrystals from hydrated ferric salts in 2-pyrrolidone: mechanism leading to Fe_3O_4 . *Angewandte Chemie International Edition*, **44** (1), 123–126.
- 52** Wu, X., Tang, J., Zhang, Y. and Wang, H. (2009) Low temperature synthesis of Fe_3O_4 nanocrystals by hydrothermal decomposition of a metallorganic molecular precursor. *Materials Science and Engineering B*, **157** (1–3), 81–86.
- 53** Park, J., An, K.J., Hwang, Y.S., Park, J.G., Noh, H.J., Kim, J.Y., Park, J.H., Hwang, N.M. and Hyeon, T. (2004) Ultra-large-scale syntheses of monodisperse nanocrystals. *Nature Materials*, **3** (12), 891–895.

- 54 Yu, W.W., Falkner, J.C., Yavuz, C.T. and Colvin, V.L. (2004) Synthesis of monodisperse iron oxide nanocrystals by thermal decomposition of iron carboxylate salts. *Chemical Communications*, (20), 2306–2307.
- 55 Jana, N.R., Chen, Y.F. and Peng, X.G. (2004) Size- and shape-controlled magnetic (Cr, Mn, Fe, Co, Ni) oxide nanocrystals via a simple and general approach. *Chemistry of Materials*, **16** (20), 3931–3935.
- 56 Huo, Z., Tsung, C.-k., Huang, W., Zhang, X. and Yang, P. (2008) Sub-two nanometer single crystal Au nanowires. *Nano Letters*, **8**, 2041–2044.
- 57 Oliveira, F.C.C. The use of ionic liquids in the synthesis of nanostructured magnetic materials (translated from Portuguese), thesis, Universidade de Brasília. (2010).
- 58 Huh, Y.M., Jun, Y.W., Song, H.T., Kim, S., Choi, J.S., Lee, J.H., Yoon, S., Kim, K.S., Shin, J.S., Suh, J.S. and Cheon, J. (2005) *In vivo* magnetic resonance detection of cancer by using multifunctional magnetic nanocrystals. *Journal of the American Chemical Society*, **127** (35), 12387–12391.
- 59 Zhao, S. and Asuha, S. (2010) One-pot synthesis of magnetite nanopowders and their magnetic properties. *Powder Technology*, **197** (3), 295–297.
- 60 Dumestre, F., Chaudret, B., Amiens, C., Renaud, P. and Fejes, P. (2004) Superlattices of iron nanocubes synthesized from $\text{Fe}[\text{N}(\text{SiMe}_3)_2]_2$. *Science*, **303** (5659), 821–823.
- 61 Lacroix, L.M., Lachaize, S., Falqui, A., Respaud, M. and Chaudret, B. (2009) Iron nanoparticle growth in organic superstructures. *Journal of the American Chemical Society*, **131** (2), 549–557.
- 62 Li, D.S. and Komarneni, S. (2006) Microwave-assisted polyol process for synthesis of Ni nanoparticles. *Journal of the American Ceramic Society*, **89** (5), 1510–1517.
- 63 Cheng, W.T. and Cheng, H.W. (2009) Synthesis and characterization of cobalt nano-particles through microwave polyol process. *AICHE Journal*, **55** (6), 1383–1389.
- 64 Liu, C., Wu, X.W., Klemmer, T., Shukla, N., Yang, X.M., Weller, D., Roy, A.G., Tanase, M. and Laughlin, D. (2004) Polyol process synthesis of monodispersed FePt nanoparticles. *Journal of Physical Chemistry B*, **108** (20), 6121–6123.
- 65 Hu, M.J., Lu, Y., Zhang, S., Guo, S.R., Lin, B., Zhang, M. and Yu, S.H. (2008) High yield synthesis of bracelet-like hydrophilic Ni–Co magnetic alloy flux-closure nanorings. *Journal of the American Chemical Society*, **130** (35), 11606–11607.
- 66 Hai, H.T., Yang, H.T., Kura, H., Hasegawa, D., Ogata, Y., Takahashi, M. and Ogawa, T. (2010) Size control and characterization of wustite (core)/spinel (shell) nanocubes obtained by decomposition of iron oleate complex. *Journal of Colloid and Interface Science*, **346** (1), 37–42.
- 67 Wang, D.S. and Li, Y.D. (2010) One-pot protocol for Au-based hybrid magnetic nanostructures via a noble-metal-induced reduction process. *Journal of the American Chemical Society*, **132** (18), 6280–6281.
- 68 Chiu, W., Khiew, P., Cloke, M., Isa, D., Lim, H., Tan, T., Huang, N., Radiman, S., Abd-Shukor, R., Hamid, M.A.A. and Chia, C.H. (2010) Heterogeneous seeded growth: synthesis and characterization of bifunctional $\text{Fe}_3\text{O}_4/\text{ZnO}$ core/shell nanocrystals. *Journal of Physical Chemistry C*, **114** (18), 8212–8218.
- 69 Chiu, W.S., Radiman, S., Abdullah, M.H., Khiew, P.S., Huang, N.M. and Abd-Shukor, R. (2007) One pot synthesis of monodisperse Fe_3O_4 nanocrystals by pyrolysis reaction of organometallic compounds. *Materials Chemistry and Physics*, **106** (2–3), 231–235.
- 70 Moumen, N. and Pileni, M.P. (1996) Control of the size of cobalt ferrite magnetic fluid. *Journal of Physical Chemistry*, **100** (5), 1867–1873.
- 71 Seip, C.T., Carpenter, E.E., O'Connor, C.J., John, V.T. and Li, S.C. (1998) Magnetic properties of a series of ferrite nanoparticles synthesized in reverse micelles. *IEEE Transactions on Magnetics*, **34** (4), 1111–1113.
- 72 Dresco, P.A., Zaitsev, V.S., Gambino, R.J. and Chu, B. (1999) Preparation and properties of magnetite and polymer

- magnetite nanoparticles. *Langmuir*, **15** (6), 1945–1951.
- 73** Liu, C., Zou, B.S., Rondinone, A.J. and Zhang, Z.J. (2000) Reverse micelle synthesis and characterization of superparamagnetic MnFe_2O_4 spinel ferrite nanocrystallites. *Journal of Physical Chemistry B*, **104** (6), 1141–1145.
- 74** Zhou, Z.H., Wang, J., Liu, X. and Chan, H.S.O. (2001) Synthesis of Fe_3O_4 nanoparticles from emulsions. *Journal of Materials Chemistry*, **11** (6), 1704–1709.
- 75** Tartaj, P. and Serna, C.J. (2002) Microemulsion-assisted synthesis of tunable superparamagnetic composites. *Chemistry of Materials*, **14** (10), 4396–4402.
- 76** Lee, Y., Lee, J., Bae, C.J., Park, J.G., Noh, H.J., Park, J.H. and Hyeon, T. (2005) Large-scale synthesis of uniform and crystalline magnetite nanoparticles using reverse micelles as nanoreactors under reflux conditions. *Advanced Functional Materials*, **15** (3), 503–509.
- 77** Yang, C., Xing, J., Guan, Y., Liu, J. and Liu, H. (2004) Synthesis and characterization of superparamagnetic iron nanocomposites by hydrazine reduction. *Journal of Alloys and Compounds*, **385** (1–2), 283–287.
- 78** Lisiecki, I. and Pilani, M.P. (2003) Synthesis of well-defined and low size distribution cobalt nanocrystals: the limited influence of reverse micelles. *Langmuir*, **19** (22), 9486–9489.
- 79** Cho, S.J., Jarrett, B.R., Louie, A.Y. and Kauzlarich, S.M. (2006) Gold-coated iron nanoparticles: a novel magnetic resonance agent for T-1 and T-2 weighted imaging. *Nanotechnology*, **17** (3), 640–644.
- 80** Jacinto, M.J., Kiyohara, P.K., Masunaga, S.H., Jardim, R.F. and Rossi, L.M. (2008) Recoverable rhodium nanoparticles: synthesis, characterization and catalytic performance in hydrogenation reactions. *Applied Catalysis A: General*, **338** (1–2), 52–57.
- 81** Vogt, C., Toprak, M.S., Muhammed, M., Laurent, S., Bridot, J.L. and Muller, R.N. (2010) High quality and tuneable silica shell-magnetic core nanoparticles. *Journal of Nanoparticle Research*, **12** (4), 1137–1147.
- 82** Vestal, C.R. and Zhang, Z.J. (2003) Synthesis and magnetic characterization of Mn and Co spinel ferrite–silica nanoparticles with tunable magnetic core. *Nano Letters*, **3** (12), 1739–1743.
- 83** Haeiwa, T., Segawa, K. and Konishi, K. (2007) Magnetic properties of isolated Co nanoparticles in SiO_2 capsule prepared with reversed micelle. *Journal of Magnetism and Magnetic Materials*, **310** (2), E809–E811.
- 84** Coskun, M., Korkmaz, M., Firat, T., Jaffari, G.H. and Shah, S.I. (2010) Synthesis of SiO_2 coated NiFe_2O_4 nanoparticles and the effect of SiO_2 shell thickness on the magnetic properties. *Journal of Applied Physics*, **107** (9), 3.
- 85** Sarkar, A., Biswas, S.K. and Pramanik, P. (2010) Design of a new nanostructure comprising mesoporous ZrO_2 shell and magnetite core ($\text{Fe}_3\text{O}_4@m\text{ZrO}_2$) and study of its phosphate ion separation efficiency. *Journal of Materials Chemistry*, **20** (21), 4417–4424.
- 86** Wang, X., Zhuang, J., Peng, Q. and Li, Y.D. (2005) A general strategy for nanocrystal synthesis. *Nature*, **437** (7055), 121–124.
- 87** Tadmor, R., Rosensweig, R.E., Frey, J. and Klein, J. (2000) Resolving the puzzle of ferrofluid dispersants. *Langmuir*, **16** (24), 9117–9120.
- 88** Jacintho, G.V.M., Brolo, A.G., Corio, P., Suarez, P.A.Z. and Rubim, J.C. (2009) Structural investigation of MFe_2O_4 ($\text{M} = \text{Fe}, \text{Co}$) magnetic fluids. *Journal of Physical Chemistry C*, **113** (18), 7684–7691.
- 89** Dupont, J., de Souza, R.F. and Suarez, P.A.Z. (2002) Ionic liquid (molten salt) phase organometallic catalysis. *Chemical Reviews*, **102** (10), 3667–3691.
- 90** Dupont, J. (2004) On the solid, liquid and solution structural organization of imidazolium ionic liquids. *Journal of the Brazilian Chemical Society*, **15** (3), 341–350.
- 91** Lee, C.M., Jeong, H.J., Lim, S.T., Sohn, M.H. and Kim, D.W. (2010) Synthesis of iron oxide nanoparticles with control over shape using imidazolium-based ionic liquids. *ACS Applied Materials & Interfaces*, **2** (3), 756–759.
- 92** Wang, Y., Maksimuk, S., Shen, R. and Yang, H. (2007) Synthesis of iron oxide

- nanoparticles using a freshly-made or recycled imidazolium-based ionic liquid. *Green Chemistry*, **9**, 1051.
- 93** Scariot, M., Silva, D.O., Scholten, J.D., Machado, G., Teixeira, S.R., Novak, M.A., Ebeling, G. and Dupont, J. (2008) Cobalt nanocubes in ionic liquids: synthesis and properties. *Angewandte Chemie International Edition*, **47** (47), 9075–9078.
- 94** Kramer, J., Redel, E., Thomann, R. and Janiak, C. (2008) Use of ionic liquids for the synthesis of iron, ruthenium, and osmium nanoparticles from their metal carbonyl precursors. *Organometallics*, **27** (9), 1976–1978.
- 95** Migowski, P., Teixeira, S.R., Machado, G., Alves, M.C.M., Geshev, J. and Dupont, J. (2007) Structural and magnetic characterization of Ni nanoparticles synthesized in ionic liquids. *Journal of Electron Spectroscopy and Related Phenomena*, **156**, 195–199.
- 96** Migowski, P., Machado, G., Texeira, S.R., Alves, M.C.M., Morais, J., Traverse, A. and Dupont, J. (2007) Synthesis and characterization of nickel nanoparticles dispersed in imidazolium ionic liquids. *Physical Chemistry Chemical Physics*, **9** (34), 4814–4821.
- 97** Wang, Y. and Yang, H. (2005) Synthesis of CoPt nanorods in ionic liquids. *Journal of the American Chemical Society*, **127** (15), 5316–5317.
- 98** Lian, J.B., Duan, X.C., Ma, J.M., Peng, P., Kim, T.I. and Zheng, W.J. (2009) Hematite (α - Fe_2O_3) with various morphologies: ionic liquid-assisted synthesis, formation mechanism, and properties. *ACS Nano*, **3** (11), 3749–3761.
- 99** Cao, S.W. and Zhu, Y.J. (2009) Iron oxide hollow spheres: microwave–hydrothermal ionic liquid preparation, formation mechanism, crystal phase and morphology control and properties. *Acta Materialia*, **57** (7), 2154–2165.
- 100** Cao, S.W., Zhu, Y.J., Cheng, G.F. and Huang, Y.H. (2009) ZnFe_2O_4 nanoparticles: microwave–hydrothermal ionic liquid synthesis and photocatalytic property over phenol. *Journal of Hazardous materials*, **171** (1–3), 431–435.
- 101** Oliveira, F.C.C., Rossi, L.M. and Rubim, J.C. (2010) Processo de Obtenção de nanopartículas magnéticas utilizando líquidos iônicos como solventes e sua aplicação na preparação de dispersões estáveis em solventes não polares. BR Patent Prot. INPI: 012100000066, Brasil.
- 102** Dang, F., Kameda, K., Enomoto, N., Hojo, J. and Enpuku, K. (2007) Sonochemical synthesis of the magnetite nanoparticles in aqueous solution. *Journal of the Ceramic Society of Japan*, **115** (1348), 867–872.
- 103** Dang, F., Enomoto, N., Hojo, J. and Enpuku, K. (2008) A novel method to synthesize monodispersed magnetite nanoparticles. *Chemistry Letters*, **37** (5), 530–531.
- 104** Dang, F., Enomoto, N., Hojo, J. and Enpuku, K. (2009) Sonochemical synthesis of monodispersed magnetite nanoparticles by using an ethanol–water mixed solvent. *Ultrasonics Sonochemistry*, **16** (5), 649–654.
- 105** Cabrera, L., Gutierrez, S., Menendez, N., Morales, M.P. and Heffasti, P. (2008) Magnetite nanoparticles: electrochemical synthesis and characterization. *Electrochimica Acta*, **53** (8), 3436–3441.
- 106** Marques, R.F.C., Garcia, C., Lecante, P., Ribeiro, S.J.L., Noe, L., Silva, N.J.O., Amaral, V.S., Millan, A. and Verelst, M. (2008) Electro-precipitation of Fe_3O_4 nanoparticles in ethanol. *Journal of Magnetism and Magnetic Materials*, **320** (19), 2311–2315.
- 107** Park, H., Ayala, P., Deshusses, M.A., Mulchandani, A., Choi, H. and Myung, N.V. (2008) Electrodeposition of maghemite (γ - Fe_2O_3) nanoparticles. *Chemical Engineering Journal*, **139** (1), 208–212.
- 108** Xiaomin, N., Xiaobo, S., Huagui, Z., Dongen, Z., Dandan, Y. and Qingbiao, Z. (2005) Studies on the one-step preparation of iron nanoparticles in solution. *Journal of Crystal Growth*, **275** (3–4), 548–553.
- 109** Huang, K.C. and Ehrman, S.H. (2007) Synthesis of iron nanoparticles via chemical reduction with palladium ion seeds. *Langmuir*, **23** (3), 1419–1426.
- 110** Wu, Z.G., Munoz, M. and Montero, O. (2010) The synthesis of nickel nanoparticles by hydrazine reduction.

- Advanced Powder Technology*, **21** (2), 165–168.
- 111** Frei, E.H., Shtrikman, S. and Treves, D. (1957) Critical size and nucleation field of ideal ferromagnetic particles. *Physical Review*, **106** (3), 446–454.
- 112** Bean, C.P. (1955) Hysteresis loops of mixtures of ferromagnetic micropowders. *Journal of Applied Physics*, **26** (11), 1381–1383.
- 113** Safarik, I. and Safarikova, M. (1997) *Scientific and Clinical Applications of Magnetic Carriers*, in (eds U. Hafeli, W. Schutt, J. Teller and M. Zborowski), Plenum Press, New York, p. 323.
- 114** Safarik I. and Safarikova, M. (1999) Use of magnetic techniques for the isolation of cells. *Journal of Chromatography B*, **722** (1–2), 33–53.
- 115** Hatch, G.P. and Stelter, R.E. (2001) Magnetic design considerations for devices and particles used for biological high-gradient magnetic separation (HGMS) systems. *Journal of Magnetism and Magnetic Materials*, **225** (1–2), 262–276.
- 116** Turbeville, J.E. (1973) Ferromagnetic sorbents for oil spill recovery and control. *Environmental Science and Technology*, **7** (5), 433–438.
- 117** Dao, H.V., Ngeh, L.N., Bigger, S.W. and Orbell, J.D. (2006) Achievement of 100% removal of oil from feathers employing magnetic particle technology. *Journal of Environmental Engineering*, **132** (5), 555–559.
- 118** Machado, L.C.R., Lima, F.W.J., Paniago, R., Ardisson, J.D., Sapag, K. and Lago, R.M. (2006) Polymer coated vermiculite–iron composites: novel floatable magnetic adsorbents for water spilled contaminants. *Applied Clay Science*, **31** (3–4), 207–215.
- 119** Chun, C.L. and Park, J.W. (2001) Oil spill remediation using magnetic separation. *J. Environ. Eng. ASCE*, **127** (5), 443–449.
- 120** Wang, L., Yang, Z.M., Gao, J.H., Xu, K.M., Gu, H.W., Zhang, B., Zhang, X.X. and Xu, B. (2006) A biocompatible method of decorporation: bisphosphonate-modified magnetite nanoparticles to remove uranyl ions from blood. *Journal of the American Chemical Society*, **128** (41), 13358–13359.
- 121** Liu, X.W., Hu, Q.Y., Fang, Z., Zhang, X.J. and Zhang, B.B. (2009) Magnetic chitosan nanocomposites: a useful recyclable tool for heavy metal ion removal. *Langmuir*, **25** (1), 3–8.
- 122** Shin, S. and Jang, J. (2007) Thiol containing polymer encapsulated magnetic nanoparticles as reusable and efficiently separable adsorbent for heavy metal ions. *Chemical Communications*, (41), 4230–4232.
- 123** Navarro, R., Guzman, J., Saucedo, I., Revilla, J. and Guibal, E. (2003) Recovery of metal ions by chitosan: sorption mechanisms and influence of metal speciation. *Macromolecular Bioscience*, **3** (10), 552–561.
- 124** Takafuji, M., Ide, S., Ihara, H. and Xu, Z.H. (2004) Preparation of poly(1-vinylimidazole)-grafted magnetic nanoparticles and their application for removal of metal ions. *Chemistry of Materials*, **16** (10), 1977–1983.
- 125** Dong, J., Xu, Z.H. and Kuznicki, S.M. (2009) Mercury removal from flue gases by novel regenerable magnetic nanocomposite sorbents. *Environmental Science and Technology*, **43** (9), 3266–3271.
- 126** Koehler, F.M., Rossier, M., Waelle, M., Athanassiou, E.K., Limbach, L.K., Grass, R.N., Gunther, D. and Stark, W.J. (2009) Magnetic EDTA: coupling heavy metal chelators to metal nanomagnets for rapid removal of cadmium, lead and copper from contaminated water. *Chemical Communications*, (32), 4862–4864.
- 127** Rossi, L.M., Silva, F.P., Vono, L.L.R., Kiyohara, P.K., Duarte, E.L., Itri, R., Landers, R. and Machado, G. (2007) Superparamagnetic nanoparticle-supported palladium: a highly stable magnetically recoverable and reusable catalyst for hydrogenation reactions. *Green Chemistry*, **9** (4), 379–385.
- 128** Macdonald, J.E. and Veinot, J.G.C. (2008) Removal of residual metal catalysts with iron/iron oxide nanoparticles from coordinating environments. *Langmuir*, **24** (14), 7169–7177.
- 129** Hong, S.H. and Grubbs, R.H. (2007) Efficient removal of ruthenium byproducts from olefin metathesis

- products by simple aqueous extraction. *Organic Letters*, **9** (10), 1955–1957.
- 130** Kettler, P.B. (2003) Platinum group metals in catalysis: fabrication of catalysts and catalyst precursors. *Organic Process Research and Development*, **7** (3), 342–354.
- 131** McEleney, K., Allen, D.P., Holliday, A.E. and Crudden, C.M. (2006) Functionalized mesoporous silicates for the removal of ruthenium from reaction mixtures. *Organic Letters*, **8** (13), 2663–2666.
- 132** Nielsen, K.T., Bechgaard, K. and Krebs, F.C. (2006) Effective removal and quantitative analysis of Pd, Cu, Ni, and Pt catalysts from small-molecule products. *Synth. Stuttgart* (10), 1639–1644.
- 133** Garrett, C.E. and Prasad, K. (2004) The art of meeting palladium specifications in active pharmaceutical ingredients produced by Pd-catalyzed reactions. *Advanced Synthesis and Catalysis*, **346** (8), 889–900.
- 134** Barbas, D., Brozio, J., Johannsen, I. and Allmendinger, T. (2009) Removal of heavy metals from organic reaction mixtures: preparation and application of functionalized resins. *Organic Process Research & Development*, **13** (6), 1068–1079.
- 135** Tzschucke, C.C., Markert, C., Bannwarth, W., Roller, S., Hebel, A. and Haag, R. (2002) Modern separation techniques for the efficient workup in organic synthesis. *Angewandte Chemie International Edition*, **41** (21), 3964–4000.
- 136** Alaerts, L., Wahlen, J., Jacobs, P.A. and De Vos, D.E. (2008) Recent progress in the immobilization of catalysts for selective oxidation in the liquid phase. *Chemical Communications* (15), 1727–1737.
- 137** Corma, A. and Garcia, H. (2006) Silica-bound homogenous catalysts as recoverable and reusable catalysts in organic synthesis. *Advanced Synthesis and Catalysis*, **348** (12–13), 1391–1412.
- 138** De Vos, D.E., Sels, B.F. and Jacobs, P.A. (2002) Immobilization of homogeneous oxidation catalysts. *Advances in Catalysis*, **46**, 1–87.
- 139** De Vos, D.E., Dams, M., Sels, B.F. and Jacobs, P.A. (2002) Ordered mesoporous and microporous molecular sieves functionalized with transition metal complexes as catalysts for selective organic transformations. *Chemical Reviews*, **102** (10), 3615–3640.
- 140** Song, C.E. and Lee, S.G. (2002) Supported chiral catalysts on inorganic materials. *Chemical Reviews*, **102** (10), 3495–3524.
- 141** Yoo, J.S. (1998) Metal recovery and rejuvenation of metal-loaded spent catalysts. *Catalysis Today*, **44** (1–4), 27–46.
- 142** Arnett, R.L. and Buell, B.O. Magnetic separator for removing nickel-on-kieselguhr catalyst from conjugated diene solutions. US Patent (1956) 2,760,638.
- 143** Bremer, J.W.J. Recovery of nickel catalysts from hydrogenated fats. US Patent (1959) 2,875,220.
- 144** Johnston, W.D.J. Separation of magnetic catalysts from polymers such as hydrogenated coumarone-indene resins. US Patent (1941) 2,264,756.
- 145** Reynolds, P.W. and Lamb, S.A. Magnetic separation of metal catalysts. GB Patent (1952) 670,423.
- 146** Reynolds, P.W. and Lamb, S.A. Magnetic separation of metal catalysts. US Patent (1955) 2,723,997.
- 147** Shi, F., Tse, M.K., Pohl, M.M., Bruckner, A., Zhang, S.M. and Beller, M. (2007) Tuning catalytic activity between homogeneous and heterogeneous catalysis: improved activity and selectivity of free nano- Fe_2O_3 in selective oxidations. *Angewandte Chemie International Edition*, **46** (46), 8866–8868.
- 148** Zeng, T.Q., Chen, W.W., Cirtiu, C.M., Moores, A., Song, G.H. and Li, C.J. (2010) Fe_3O_4 nanoparticles: a robust and magnetically recoverable catalyst for three-component coupling of aldehyde, alkyne and amine. *Green Chemistry*, **12** (4), 570–573.
- 149** Tsang, S.C., Caps, V., Paraskevas, I., Chadwick, D. and Thompsett, D. (2004) Magnetically separable, carbon-supported nanocatalysts for the manufacture of fine chemicals. *Angewandte Chemie International Edition*, **43** (42), 5645–5649.
- 150** Shylesh, S., Schünemann, V. and Thiel, W.R. (2010) Magnetically separable nanocatalysts: bridges between homogeneous and heterogeneous

- catalysis. *Angewandte Chemie International Edition*, **49**, 3428–3459.
- 151** Yoon, T.J., Lee, W., Oh, Y.S. and Lee, J.K. (2003) Magnetic nanoparticles as a catalyst vehicle for simple and easy recycling. *New Journal of Chemistry*, **27** (2), 227–229.
- 152** Hu, A.G., Yee, G.T. and Lin, W.B. (2005) Magnetically recoverable chiral catalysts immobilized on magnetite nanoparticles for asymmetric hydrogenation of aromatic ketones. *Journal of the American Chemical Society*, **127** (36), 12486–12487.
- 153** Abu-Reziq, R., Alper, H., Wang, D.S. and Post, M.L. (2006) Metal supported on dendronized magnetic nanoparticles: highly selective hydroformylation catalysts. *Journal of the American Chemical Society*, **128** (15), 5279–5282.
- 154** Laska, U., Frost, C.G., Plucinski, P.K. and Price, G.J. (2008) Rhodium containing magnetic nanoparticles: effective catalysts for hydrogenation and the 1,4-addition of boronic acids. *Catalysis Letters*, **122** (1–2), 68–75.
- 155** Zheng, Y., Stevens, P.D. and Gao, Y. (2006) Magnetic nanoparticles as an orthogonal support of polymer resins: applications to solid-phase Suzuki cross-coupling reactions. *Journal of Organic Chemistry*, **71** (2), 537–542.
- 156** Stevens, P.D., Fan, J.D., Gardimalla, H.M.R., Yen, M. and Gao, Y. (2005) Superparamagnetic nanoparticle-supported catalysis of Suzuki cross-coupling reactions. *Organic Letters*, **7** (11), 2085–2088.
- 157** Stevens, P.D., Li, G.F., Fan, J.D., Yen, M. and Gao, Y. (2005) Recycling of homogeneous Pd catalysts using superparamagnetic nanoparticles as novel soluble supports for Suzuki, Heck, and Sonogashira cross-coupling reactions. *Chemical Communications* (35), 4435–4437.
- 158** Ly, G.H., Mai, W.P., Jin, R. and Gao, L.X. (2008) Immobilization of dipyridyl complex to magnetic nanoparticle via click chemistry as a recyclable catalyst for Suzuki cross-coupling reactions. *Synlett*, (9), 1418–1422.
- 159** Finke, R.G. (2002) Transition-metal n-anoclusters: solution-phase synthesis, then characterization and mechanism of formation of polyoxoanion and tetrabutylammonium stabilized nanoclusters, in *Metal Nanoparticles: Synthesis, Characterization and Applications*, (eds D.L. Feldheim and C.A. Jr.Foss), Marcel Dekker, New York, pp. 17–54.
- 160** Widegren, J.A. and Finke, R.G. (2003) A review of soluble transition-metal nanoclusters as arene hydrogenation catalysts. *Journal of Molecular Catalysis A: Chemical*, **191** (2), 187–207.
- 161** Dupont, J., Fonseca, G.S., Umpierre, A.P., Fichtner, P.F.P. and Teixeira, S.R. (2002) Transition-metal nanoparticles in imidazolium ionic liquids: recyclable catalysts for biphasic hydrogenation reactions. *Journal of the American Chemical Society*, **124** (16), 4228–4229.
- 162** Mevellec, V., Roucoux, A., Ramirez, E., Philippot, K. and Chaudret, B. (2004) Surfactant-stabilized aqueous iridium(0) colloidal suspension: an efficient reusable catalyst for hydrogenation of arenes in biphasic media. *Advanced Synthesis and Catalysis*, **346** (1), 72–76.
- 163** Bönnemann, H. and Brijoux, W. (1996) Catalytically active metal powders and colloids, in *Active Metals: Preparation, Characterization, Applications* (ed A. Fürstner,), VCH Verlag GmbH, Weinheim, pp. 339–379.
- 164** Niederer, J.P.M., Arnold, A.B.J., Holderich, W.F., Spliethof, B., Tesche, B., Reetz, M. and Bonnemann, H. (2002) Noble metal nanoparticles incorporated in mesoporous hosts. *Topics in Catalysis*, **18** (3–4), 265–269.
- 165** Zheng, N.F. and Stucky, G.D. (2006) A general synthetic strategy for oxide-supported metal nanoparticle catalysts. *Journal of the American Chemical Society*, **128** (44), 14278–14280.
- 166** Astruc, D. (2007) Palladium nanoparticles as efficient green homogeneous and heterogeneous carbon–carbon coupling precatalysts: a unifying view. *Inorganic Chemistry*, **46** (6), 1884–1894.
- 167** Amali, A.J. and Rana, R.K. (2009) Stabilisation of Pd(0) on surface functionalised Fe₃O₄ nanoparticles:

- magnetically recoverable and stable recyclable catalyst for hydrogenation and Suzuki–Miyaura reactions. *Green Chemistry*, **11** (11), 1781–1786.
- 168** Baruwati, B., Guin, D. and Manorama, S.V. (2007) Pd on surface-modified NiFe_2O_4 nanoparticles: a magnetically recoverable catalyst for Suzuki and Heck reactions. *Organic Letters*, **9** (26), 5377–5380.
- 169** Kim, J., Lee, J.E., Lee, J., Jang, Y., Kim, S.W., An, K., Yu, H.H. and Hyeon, T. (2006) Generalized fabrication of multifunctional nanoparticle assemblies on silica spheres. *Angewandte Chemie International Edition*, **45** (29), 4789–4793.
- 170** Laska, U., Frost, C.G., Price, G.J. and Plucinski, P.K. (2009) Easy-separable magnetic nanoparticle-supported Pd catalysts: kinetics, stability and catalyst reuse. *Journal of Catalysis*, **268** (2), 318–328.
- 171** Wang, Z.F., Shen, B., Zou, A.H. and He, N.Y. (2005) Synthesis of Pd/ Fe_3O_4 nanoparticle-based catalyst for the cross-coupling of acrylic acid with iodobenzene. *Chemical Engineering Journal*, **113** (1), 27–34.
- 172** Wang, Z.F., Xiao, P.F., Shen, B. and He, N.Y. (2006) Synthesis of palladium-coated magnetic nanoparticle and its application in Heck reaction. *Colloids and Surfaces A: Physicochemical and Engineering Aspects*, **276** (1–3), 116–121.
- 173** Yoon, H., Ko, S. and Jang, J. (2007) Nitrogen-doped magnetic carbon nanoparticles as catalyst supports for efficient recovery and recycling. *Chemical Communications* (14), 1468–1470.
- 174** Yinghuai, Z., Peng, S.C., Emi, A., Zhenshun, S., Monalisa and Kemp, R.A. (2007) Supported ultra small palladium on magnetic nanoparticles used as catalysts for Suzuki cross-coupling and Heck reactions. *Advanced Synthesis and Catalysis*, **349**, 1917–1922.
- 175** Liu, J.M., Peng, X.G., Sun, W., Zhao, Y.W. and Xia, C.G. (2008) Magnetically separable Pd catalyst for carbonylative Sonogashira coupling reactions for the synthesis of alpha,beta-alkynyl ketones. *Organic Letters*, **10** (18), 3933–3936.
- 176** Rossi, L.M., Vono, L.L.R., Silva, F.P., Kiyohara, P.K., Duarte, E.L. and Matos, J.R. (2007) Magnetically recoverable scavenger for palladium based on thiol-modified magnetite nanoparticles. *Applied Catalysis A: General*, **330**, 139–144.
- 177** Guin, D., Baruwati, B. and Manorama, S.V. (2007) Pd on amine-terminated ferrite nanoparticles: a complete magnetically recoverable facile catalyst for hydrogenation reactions. *Organic Letters*, **9** (7), 1419–1421.
- 178** Rossi, L.M., Nangoi, I.M. and Costa, N.J.S. (2009) Ligand-assisted preparation of palladium supported nanoparticles: a step toward size control. *Inorganic Chemistry*, **48** (11), 4640–4642.
- 179** Hara, T., Kaneta, T., Mori, K., Mitsudome, T., Mizugaki, T., Ebitani, K. and Kaneda, K. (2007) Magnetically recoverable heterogeneous catalyst: palladium nanocluster supported on hydroxyapatite-encapsulated gamma- Fe_2O_3 nanocrystallites for highly efficient dehalogenation with molecular hydrogen. *Green Chemistry*, **9**, 1246–1251.
- 180** Jacinto, M.J., Landers, R. and Rossi, L.M. (2009) Preparation of supported Pt(0) nanoparticles as efficient recyclable catalysts for hydrogenation of alkenes and ketones. *Catalysis Communications*, **10** (15), 1971–1974.
- 181** Jacinto, M.J., Santos, O., Landers, R., Kiyohara, P.K. and Rossi, L.M. (2009) On the catalytic hydrogenation of polycyclic aromatic hydrocarbons into less toxic compounds by a facile recoverable catalyst. *Applied Catalysis B: Environmental*, **90** (3–4), 688–692.
- 182** Jun, C.H., Park, Y.J., Yeon, Y.R., Choi, J.R., Lee, W.R., Ko, S.J. and Cheon, J. (2006) Demonstration of a magnetic and catalytic Co@Pt nanoparticle as a dual-function nanoplateform. *Chemical Communications* (15), 1619–1621.
- 183** Jacinto, M.J., Santos, O., Jardim, R.F., Landers, R. and Rossi, L.M. (2009) Preparation of recoverable Ru catalysts for liquid-phase oxidation and hydrogenation reactions. *Applied Catalysis A: General*, **360** (2), 177–182.
- 184** Baruwati, B., Polshettiwar, V. and Varma, R.S. (2009) Magnetically recoverable supported ruthenium catalyst for hydrogenation of alkynes and transfer

- hydrogenation of carbonyl compounds. *Tetrahedron Letters*, **50** (11), 1215–1218.
- 185** Polshettiwar, V., Baruwati, B. and Varma, R.S. (2009) Nanoparticle-supported and magnetically recoverable nickel catalyst: a robust and economic hydrogenation and transfer hydrogenation protocol. *Green Chemistry*, **11** (1), 127–131.
- 186** Kotani, M., Koike, T., Yamaguchi, K. and Mizuno, N. (2006) Ruthenium hydroxide on magnetite as a magnetically separable heterogeneous catalyst for liquid-phase oxidation and reduction. *Green Chemistry*, **8** (8), 735–741.
- 187** Oliveira, R.L., Kiyohara, P.K. and Rossi, L.M. (2010) High performance magnetic separation of gold nanoparticles for catalytic oxidation of alcohols. *Green Chemistry*, **12** (1), 144–149.
- 188** Ge, J.P., Zhang, Q., Zhang, T.R. and Yin, Y.D. (2008) Core–satellite nanocomposite catalysts protected by a porous silica shell: controllable reactivity, high stability, and magnetic recyclability. *Angewandte Chemie International Edition*, **47** (46), 8924–8928.
- 189** MacMillan, D.W.C. (2008) The advent and development of organocatalysis. *Nature*, **455** (7211), 304–308.
- 190** Benaglia, M., Puglisi, A. and Cozzi, F. (2003) Polymer-supported organic catalysts. *Chemical Reviews*, **103** (9), 3401–3429.
- 191** O'Dalaigh, C., Corr, S.A., Gun'ko, Y. and Connon, S.J. (2007) A magnetic-nanoparticle-supported 4-*N*, *N*-dialkylaminopyridine catalyst: excellent reactivity combined with facile catalyst recovery and recyclability. *Angewandte Chemie International Edition*, **46** (23), 4329–4332.
- 192** Polshettiwar, V., Baruwati, B. and Varma, R.S. (2009) Magnetic nanoparticle-supported glutathione: a conceptually sustainable organocatalyst. *Chemical Communications* (14), 1837–1839.
- 193** Gruttadaria, M., Giacalone, F. and Noto, R. (2008) Supported proline and proline-derivatives as recyclable organocatalysts. *Chemical Society Reviews*, **37** (8), 1666–1688.
- 194** Kawamura, M. and Sato, K. (2006) Magnetically separable phase-transfer catalysts. *Chemical Communications* (45), 4718–4719.
- 195** Kawamura, M. and Sato, K. (2007) Magnetic nanoparticle-supported crown ethers. *Chemical Communications* (32), 3404–3405.
- 196** Luo, S.Z., Zheng, X.X., Xu, H., Mi, X.L., Zhang, L. and Cheng, J.P. (2007) Magnetic nanoparticle-supported Morita–Baylis–Hillman catalysts. *Advanced Synthesis and Catalysis*, **349** (16), 2431–2434.
- 197** Luo, S.Z., Zheng, X.X. and Cheng, J.P. (2008) Asymmetric bifunctional primary aminocatalysis on magnetic nanoparticles. *Chemical Communications* (44), 5719–5721.
- 198** Zheng, X.X., Luo, S.Z., Zhang, L. and Cheng, J.P. (2009) Magnetic nanoparticle supported ionic liquid catalysts for CO₂ cycloaddition reactions. *Green Chemistry*, **11** (4), 455–458.
- 199** Phan, N.T.S., Gill, C.S., Nguyen, J.V., Zhang, Z.J. and Jones, C.W. (2006) Expanding the utility of one-pot multistep reaction networks through compartmentation and recovery of the catalyst. *Angewandte Chemie International Edition*, **45** (14), 2209–2212.

4

Photocatalysis by Nanostructured TiO₂-based Semiconductors

Matteo Cagnello and Paolo Fornasiero

4.1

Introduction

Catalysis, as soon as it was born, dealt with dimensions in the range of nanometers. However, only from the 1970s did the systematic study of properties in the nanometer regime stimulate tremendous enhancements in the preparation of new and improved materials. The manipulation of materials down to the molecular level allowed novel and unexpected properties to be revealed. This resulted in the cheap production of transportation fuels, novel polymers and plastics, more effective drugs, and many thousands of other products which are now present in our everyday life.

Nanotechnology has provided significant new tools and applications in photocatalysis. Despite photocatalysis being a well-established concept, the reduced dimensions of nanoscale materials conferred different and often improved performances to photocatalysts. This also allowed the systematic study of the properties that have a large influence on catalytic activity. Therefore, the tools offered by nanotechnology can be readily employed in photocatalysis to improve the results in terms of efficiency and productivity.

Photocatalysis essentially consists in the catalysis exerted by materials (semiconductors) under irradiation of light at an appropriate wavelength. It is therefore an essential part of the sustainable chemistry strategy. Since many good literature reviews are available that explain recent results in understanding the processes involved in photocatalysis [1–5], only the fundamental concepts will be considered here.

The difference between the valence and conduction bands (VB and CB, respectively) of a semiconductor, called the energy gap (E_g) or bandgap, determines which wavelength must be used since the incident photons must have an energy equal to or higher than that of the bandgap. If this condition is reached, a photon is absorbed by the material and an electron is excited from the VB to the CB, leaving a positive charge in the VB and giving rise to the formation of a electron–hole pair ($e^- - h^+$). The destiny

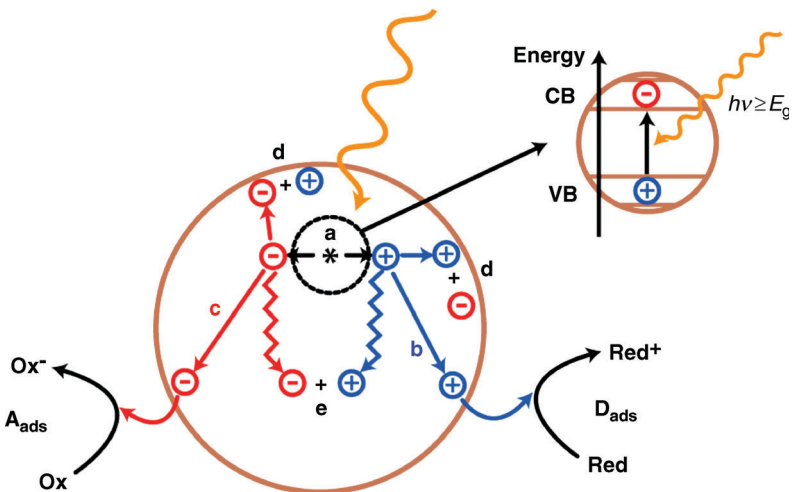


Figure 4.1 Schematic representation of the processes involved after absorption by a semiconductor particle of a photon of wavelength of energy equal to or higher than E_g : (a) electron–hole pair formation; (b)

of the adsorbed donor D; (c) reduction of the adsorbed acceptor A; (d) and (e) charge recombination at the surface or in the bulk, respectively. Adapted from [5]. © (1995) American Chemical Society.

of the electron–hole pair that is formed is very often their recombination in either the bulk or surface; however, they can also act as reductive and oxidative agents, respectively, for compounds adsorbed on the surface of the photocatalysts (Figure 4.1).

For many semiconductors, the bandgap is in the order of about 3 eV and therefore the incident radiation must have a wavelength in the UV or near-visible region. Since semiconductors, unlike metals, lack a continuum of interband states, the electron–hole recombination is not immediate and the lifetime can be sufficiently long to ensure the diffusion of these species on the surface of the material, leading to the initiation of redox processes. These reactions may include the transformation of adsorbed organic species or, more usually, reaction with water with the generation of hydroxyl radicals (OH^\bullet), which are powerful and indiscriminate oxidizing agents.

A first distinction should be made on the basis of the semiconductor used in photocatalysis. Titanium dioxide (titania, TiO_2) is the most commonly used semiconductor since it is stable under irradiation, corrosion resistant, nontoxic, abundant, and cheap. However, its large bandgap (E_g is ~ 3.2 eV for anatase and ~ 3.0 eV for rutile, the two photocatalytically active polymorphs) does not allow the use of visible light for its applications, taking into account that only a small part of sunlight is composed of UV radiation (less than 5% of the total). For this reason, other metal oxides, metal sulfides, oxysulfides, oxynitrides, and composites have been studied for photocatalytic applications [6, 7]. Many studies have also been directed to the extension of the absorption in the visible region of titania by doping or by formation of nanocomposites. The properties of titania have been excellently reviewed [3] and

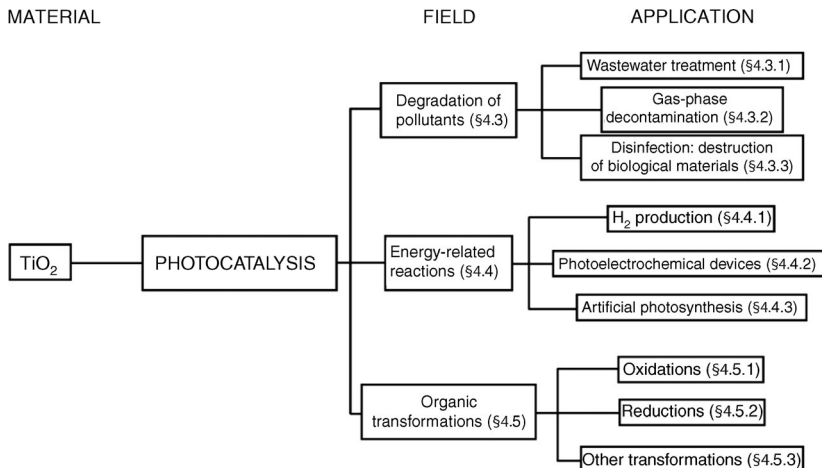


Figure 4.2 Schematic representation of the main areas of application of TiO_2 -based photocatalysis and the organization of the present chapter.

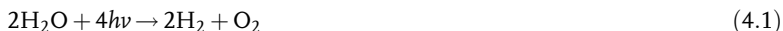
therefore will not be discussed here. Only a few elements, when appropriate, will be reported in this chapter.

Photocatalysis has a number of uses: abatement of organic pollutants [8], water purification [9], hydrogen production [10, 11], transformation of organic compounds and selective organic synthesis [12, 13], and conversion of solar into electric energy [14]. In more detail, the first three fields are among the greatest successes achieved by photocatalysis. Figure 4.2 shows a schematic representation of the main fields of application of photocatalysis and the organization of Sections 4.3–4.5 of this chapter.

One of the most important fields of application of photocatalysis is the photodegradation of organic compounds. These processes are used in particular for environmental decontamination, especially for wastewater treatment and air purification, because of the ability of semiconductors to totally degrade organics to CO_2 , H_2O , and inorganic anions under UV or visible light. This behavior is attributed to the photoinduced formation of radicals, such as OH^\bullet , or to the adsorption and direct degradation of the pollutants.

Photocatalysis can also be applied in the sustainable production of fuels, which is one of the greatest challenges that the world must face [15]. The increasing demand for energy and the expanding needs of the world population are posing key problems. Reserves of fossil fuels are limited and, sooner or later, will be exhausted. Therefore, there is an extreme need to find new options to obtain energy and resources in a sustainable way. The extensive use of fossil fuels (oil in particular), the well-established related infrastructures and the still low production costs made our economies strongly dependent on this energy source. Therefore, the development of a new and sustainable energy strategy is a very complex but urgent task. Only an integrated strategy, which involves different approaches, can successfully contribute

to the long-term replacement of the enormous amounts of fossil fuels that are currently used. In this context, photolysis of water to produce H_2 is one of the most fascinating options, although much research work is still needed to obtain an H_2 -based economy. The use of H_2 in combination with a fuel cell can produce electricity with a superior efficiency with respect to conventional combustion engines. These devices emit only water and heat, thus contributing to the reduction of CO_2 emissions in the atmosphere. Moreover, H_2 is an important building block in the preparation of synthetic fuels. The option of using artificial photosynthesis to produce solar fuels is, of course, another challenging goal in chemistry. The most important chemical step in this field is certainly, the splitting of water into hydrogen and oxygen under visible light:



However, a sensitizer is needed since water does not absorb visible light. This approach received a tremendous push in the 1970s after Fujishima and Honda published their pioneering work on photolysis of water on titania electrodes [16] at the time of the first oil crises.

Photoinduced organic transformations are studied since they allow specific products to be obtained in high yields and with high selectivity using inexpensive reactions. Moreover, the increasing stringent environmental rules for chemical processes require alternative and benign synthetic processes to be found, and heterogeneous photocatalysis is aimed in this direction, as indicated by the large number of publications in this field, highlighted in recent comprehensive reviews [12, 13, 17]. In addition, there is also a need to find alternatives in the production of the building blocks currently used in the chemical industry for the preparation of large commodities. Even in this case, photocatalysis can play an important role in the synthesis of bulk and fine chemicals in a more sustainable way.

All the applications of photocatalysis have one common point: they can help in obtaining processes that obey the requirements of green chemistry. In fact, many of the principles of sustainable chemistry are applied to photoinduced transformations in all areas of application [18]. The major achievement of photocatalysis is the use of catalysis and light, which are two of the pillars of sustainable chemistry.

This chapter is organized as outlined in Figure 4.2. Section 4.2 describes the influence of the structure on the photocatalytic properties, and in particular on the bandgap of the materials. Sections 4.3–4.5 are dedicated to the applications of photocatalysts for the abatement of organic compounds (Section 4.3), energy applications (Section 4.4), and green organic synthesis (Section 4.5). Finally, Section 4.6 is devoted to highlighting some safety issues of nanostructured TiO_2 -based photocatalysts, including toxicology. This chapter is not intended to be an exhaustive analysis of the applications of TiO_2 -based materials in photocatalysis, but rather the application of sustainable chemistry principles in the preparation and use of nanoscale photocatalytic materials with some selected examples from the recent literature highlighting these points. Moreover, the chapter focuses on photocatalysts based on inorganic materials.

4.2

Structure and Photocatalytic Properties

Despite the large amount of work produced, a complete understanding of the processes involved in heterogeneous photocatalysis is not yet available. However, it is well recognized that the photocatalytic activity of a sample depends strongly on its structure and composition. The central point in photocatalysis is the presence of a semiconductor material, as already noted in the Introduction. The possibility of tuning particle morphology, dimensions, and surface properties of the semiconductors is therefore fundamental to improving the efficacy of photoinduced processes, because in this way the electronic properties (e.g., position of the bands) can be tailored by adequately modifying the position of either the VB or CB, either by formation of nanocomposites or by introducing dopants that can increase the lifetime of the electron–hole pair, or by increasing the number of active sites (e.g., OH groups on the surface of metal oxides such as TiO₂).

It is often impossible to distinguish how a single element contributes to the final photocatalytic activity because, in most situations, a combination of different factors is involved. In general, the material properties that mostly influence photocatalysis are the particle size and morphology, the crystalline phase and composition, and the textural properties (surface area and number of active sites for radical formation). All these characteristics are sensitive to the preparation conditions, post-synthetic treatments, heating processes and the history of each sample. These elements will be discussed in the light of some examples in the next section. In this section, variations in the bandgap associated to structure and composition of the semiconductors are discussed. Subsection 4.2.2 is specially dedicated to manipulation of TiO₂-based materials for the extension of the absorption in the visible region with the final aim of obtaining more sustainable photocatalysts.

4.2.1

Elements Affecting Bandgap and Photocatalytic Activity

The key point when discussing nanostructured materials is that quantum size effects are present. The chemistry of nanomaterials is strongly dependent on their critical size [19]. Furthermore, even the shape of the particles and their morphology are particularly important for the reactivity, as the interaction of light with the surface is significantly dependent on these material properties. For example, the dependence of the optical properties of nanowires on the shapes of the nanocrystals is well recognized [20, 21]. Furthermore, the bandgap of semiconductor nanocrystals is strongly dependent on the particle size [22, 23], and it is well accepted that the smaller the particle size, the larger is the bandgap [24]. This is due to the fact that, when decreasing the particle size, the energy levels become discrete, and thus the spacing between HOMO and LUMO becomes larger (Figure 4.3).

However, when the particle size is decreased, the surface area of the material is increased, as is the number of active sites where molecules can adsorb and react to form radicals. The surface properties of the semiconductors are important in

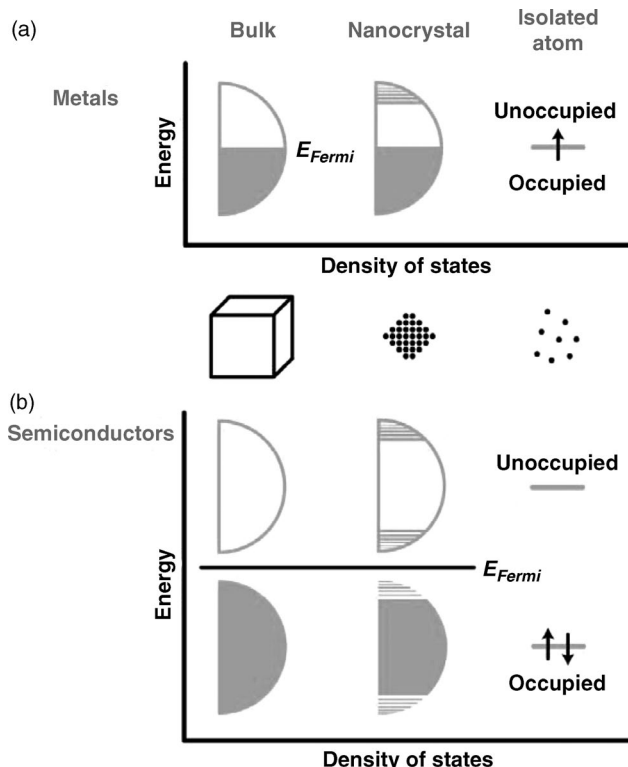


Figure 4.3 Density of states for (a) metal and (b) semiconductor nanocrystals. The HOMO–LUMO gap increases in semiconductor nanocrystals of smaller sizes. Adapted from [19], reproduced with permission from Wiley-VCH Verlag GmbH.

guaranteeing high activity. In the case of group 2–6 and 3–5 semiconductors, many experimental and theoretical studies evidenced how the bandgap is very sensitive to particle size [22]. Also in the case of titania, the bandgap was found to be dependent on particle size, with strong implications for its use in photocatalytic reactions [12, 25]. Regarding the shape and morphology of the particles, recent intriguing examples provided by Alivisatos and his group evidenced the possibility of tuning the shapes of different semiconductor colloidal particles such as CdSe with spherical and rod morphologies [26], magnetic cobalt nanorods and spherical nanocrystals with interesting two- and three-dimensional superstructures [27], high aspect ratio CdSe nanorods [28], and assemblies of nanocrystals with linear and branched topologies with the formation of colloidal quantum dots and rods connected at branched and linear junctions within single nanocrystals [29], to cite some examples. In most cases, the change in size and shape of semiconductor nanocrystals was demonstrated to involve a dramatic change in many of their properties, such as optical, electronic, thermochemical, and other fundamental characteristics [30]. The composition of mixed semiconductors (especially for group 2–6 and 3–5 semicon-

ductors) and alloying effects are other factors that can be used to tune the bandgap [31].

In the case of TiO_2 , few studies have addressed the sole particle size dependence of the photocatalytic activity. An unusual red shift in the UV/Vis absorption spectrum as a consequence of the decrease in particle size was observed for functionalized TiO_2 nanoparticles dispersed in organic solvents, but no photocatalytic applications were reported [32]. Phenol degradation was found to occur better in samples with a particle size of 8 nm than in those having smaller sizes (3 nm) due to the better crystallinity of the former and to the blue shift in the absorption of the sample with smaller particle size (bandgap increases) [33]. The special particle morphology of titania nanowires and nanoparticles obtained by treatment of titanates gave rise to materials with increased photocatalytic activity than the starting precursors, but many reasons (e.g., higher crystallinity and surface area, increased number of active sites) justified the observed activity [34].

The crystalline phase and quality of TiO_2 are also of extreme importance for its catalytic activity. Titania exists in Nature as three polymorphs, namely *anatase*, *rutile*, and *brookite*. Rutile is the thermodynamically stable form, and brookite does not usually show appreciable photocatalytic activity [3]. The different polymorphs possess different reactivity towards organic molecules, as predicted also by density functional theory (DFT) calculations [35]. Anatase is often indicated as the most active phase. However, the commercially available most active titania sample, Degussa P25, is a mixture of anatase and rutile, with anatase accounting for 60–80% of the total. Moreover, some reactions can be sensitive to various parameters, altering the order of reactivity between the TiO_2 polymorphs. It was reported that large prismatic rutile crystals (width 50–100 nm, length 250–500 nm; Figure 4.4) showed the best photocatalytic activity in phenol degradation due to the large rutile particle size, high aspect

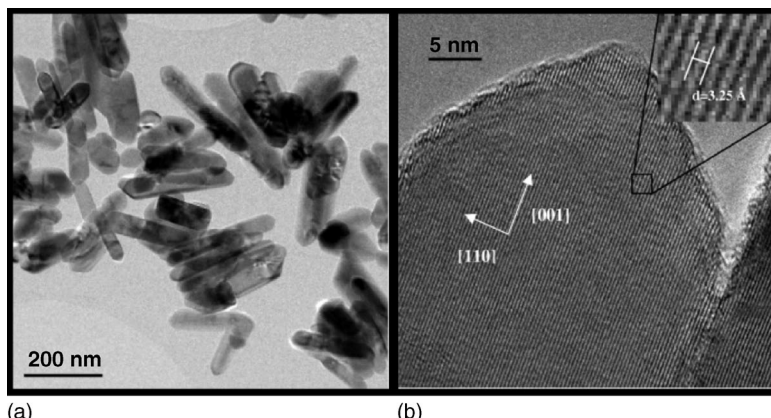


Figure 4.4 High aspect ratio (high length to width ratio), pure rutile TiO_2 crystals [(a) TEM and (b) HRTEM images] exhibited high photocatalytic activity (higher than Degussa

P25) in phenol degradation, thus evidencing the structure sensitivity of different reactions.
Reprinted in part from [36] © (2007) American Chemical Society.

ratio (high length to width ratio) of rutile crystals, and the consequent high concentration of surface acidic sites [36].

Some other studies showed that the combination of the three polymorphs with reduced crystallite size and high surface area can lead to the best photocatalysts for 4-chlorophenol degradation [37], or that particles in the dimension range 25–40 nm give the best performances [38]. Therefore, many elements contribute to the final photocatalytic activity and sometimes the increased contribution of one parameter can compensate for the decrease of another one. For example, better photocatalytic activity can be obtained even if the surface area decreases, with a concomitant increase in the crystallinity of the sample, which finally results in a higher number of electron–hole pairs formed on the surface by UV illumination and in their increased lifetime (slower recombination) [39]. Better crystallinity can be obtained with the use of ionic liquids during the synthesis [39], with a consequent increase of activity.

A pivotal example of the control of the nanostructure was recently reported by Yang *et al.* [40]. Generally, H- or O-terminating anatase TiO_2 surfaces are dominated by the thermodynamically stable (101) facet. (001) facets are much more reactive but they have a very high surface energy, so that typically they do not form under the usual experimental conditions. By using theoretical calculations, the authors found that F-terminated TiO_2 surfaces can lead to the production of a high percentage of (001) facets with high stability. Therefore, by using TiF_4 as starting precursor and HF as directing agent, they were able to synthesize TiO_2 single crystals showing (001) reactive facets in proportions as high as 47%. Furthermore, a thermal treatment at 600 °C allowed clean TiO_2 surfaces to be obtained while keeping the reactive facets intact.

Two main consecutive processes guide a photocatalytic reaction: electron–hole pair formation and adsorption of molecules on the catalyst surface to produce radicals. Whereas particle size and crystalline quality affect the initial electron–hole pair formation and their diffusion, the surface area affects the second step of the process. A correlation between anatase content and phenol degradation was found in mesoporous titania samples prepared by the sol–gel approach, but surface area and grain size were also shown to play a role in the observed activity. A direct correlation between rate constant and anatase content divided by surface area was in fact clearly found [41]. Methylene blue removal was demonstrated to be morphology dependent for TiO_2 nanotubes obtained by the hydrothermal procedure. The main factor accounting for this activity is the high surface area of the tubes [42]. Sipos and co-workers carried out a detailed study to explain the photocatalytic activity of flame-made titania for phenol decomposition. They observed that, despite the similar textural and crystalline structures of the samples, they displayed very different catalytic activities, and they attributed this difference to particle shape. Samples having only polyhedral particles (observed by TEM) showed the best activities in comparison with those containing a mixture of spherical and polyhedral particles [43]. However, when the complete mineralization of a given compound is required, it was observed that hydrophilicity and surface area were the main parameters for obtaining active catalysts [44].

The influence of different factors on photocatalytic performance is well documented also for systems not based on titania. For instance, ZnO hollow spheres show

good photocatalytic activity for Rhodamine B degradation as a result of optimization of the surface area, porous structure, and crystallite sizes [45].

4.2.2

Influence of the Structure on the Bandgap and the Photocatalytic Activity

In this section, we report some examples to show how the bandgap and the photocatalytic activity can be modified by chemical manipulation. The production of materials that absorb visible light is an extremely important achievement in the field of photocatalysis. In fact, as visible light contains only about 5% of UV radiation, obtaining photocatalysts that absorb visible light is essential step for sustainable applications of these materials. In the case of titania, extension of its absorption spectrum to the visible range can be achieved with different methods: (i) chemical doping with elements that are able to alter the electronic structure of titania; (ii) sensitization with inorganic or organic compounds through noncovalent interactions and charge-transfer processes; and (iii) coupling of the electronic properties of metal nanoparticles and those of titania. Very informative reports in this field are already available in the literature [4], so here attention is directed towards examples where the nanostructure is important for the final properties of the materials.

One of the first reports on the chemical doping of titania for visible light absorption showed that N could be very useful in narrowing the bandgap [46]. In fact, N-doped TiO_2 was found to be very efficient in methylene blue and acetaldehyde degradation under visible light illumination whereas the undoped TiO_2 sample was not. Theoretical calculations evidenced that the major contribution to the visible light absorption is due to the fact that the p states of N can mix with O 2p states, leading to a narrowing of the bandgap. Some more recent results indicated that N-doped TiO_2 nanobelts extend the absorption region of undoped TiO_2 . At the same time, the photocatalytic activity under UV light is reduced and the visible light response is due only to N 2p levels near the TiO_2 valence band [47]. Another recent study on N-doped TiO_2 materials demonstrated that N doping can also provide oxygen vacancies which are beneficial for degrading dyes [29, 48]. Many studies have addressed the question of the importance of oxygen vacancies for the photocatalytic properties of the materials [49–51]. A low-temperature hydrothermal route involving the use of hydrogen peroxide was reported to lead to high-content N– TiO_2 materials (up to 5 at.% of N incorporated), with very good activities for degradation of methylene blue [52].

Another important element that recently attracted attention as a dopant for titania-based materials is carbon [53]. It was found that a C– TiO_2 sample was not only five times more active than N-doped material for the photomineralization of 4-chlorophenol under visible light, but also showed photocatalytic activity for a variety of reactions such as degradation of dyes in air and the gas-phase degradation of acetaldehyde, benzene, and CO in air [54]. Samples of C-doped titania prepared by oxidative annealing of TiC powders demonstrated good activity in methylene blue degradation under light in the visible range [55].

Fluoride is also used as an anionic dopant. An early study demonstrated that F substitutes surface OH species leading to an increase in the degradation of phenol at least three times faster than an undoped sample [56]. Other anions are also effective as dopants in reducing the TiO_2 bandgap. Chloride, for example, was shown to give active photocatalysts in the visible range thanks to the red shift in the absorption spectra ($E_g = 3$ eV) but also increased surface acidity [57].

Boron can also be introduced as a dopant to produce visible light active photocatalysts. Bandgaps as small as 2.9 eV can be obtained by incorporating B in the TiO_2 lattice by using $NaBH_4$ as boron source [58]. Phosphorus was also used to dope TiO_2 , and although it does not lead to a substantial decrease in the bandgap (from 3.2 eV in the undoped TiO_2 to 3.15 eV in P– TiO_2), it was found to be an effective photocatalyst for methylene blue and 4-chlorophenol decomposition under visible light [59].

In addition to nonmetals, metals can be used to dope titania and to reduce its bandgap. Doping with Ce, N, and both elements can lead to narrowing of the bandgap down to 2.5 eV [60], with the 4f orbitals of Ce that can accept electron from both the Ce_2O_3 ground state and the TiO_2 VB, thus accounting for the red-shifted absorption wavelength. Theoretical calculations showed that doping TiO_2 with W [61] or co-doping with N and W would lead to a decrease of the bandgap [62]. Whereas doping with W can produce active materials, other studies indicated that the doping with V, Mo, or Nb has a minor effect on the photocatalytic activity under visible light [63].

The unique combination of the one-dimensional structure of TiO_2 nanorods and doping with Fe was reported to give good photocatalysts for oxidation reactions under visible light [64]. This was caused by both the structure, which enhanced the transfer and transport of charge carriers, and the narrowing of the bandgap induced by Fe doping. The introduction of Nd(III) by chemical vapor deposition allowed the TiO_2 bandgap to be lowered by 0.55 eV with the formation of a new LUMO at lower energy, with the possibility of tailoring the bandgap by varying the amount of Nd(III) in the TiO_2 lattice [65].

Multiple doping has also been examined. Contemporary doping with C, N, and S extends the absorption to the visible region [66], but a report indicated that the use of thiourea for contemporary N and S doping led to only N being obtained as dopant, while retaining good photoactivity under visible light [67]. By co-doping titania with B and N, a further increase in the photocatalytic degradation of dyes was observed. The incorporation of N did not appreciably change the textural properties of titania, whereas B inhibited crystallite growth and induced an increase in the surface area. A remarkable improvement in the activity was found only when B was added in a molar ratio in excess with respect to N, and this was attributed to the capacity of B to create reactive Ti(III) species, which, in turn, might induce the formation of reactive superoxide species [68].

Sometimes there is a significant difference in bulk and surface doping, as reported in the case of B and V co-doping, where improvement in the degradation of methylene blue was observed only when V was present at the surface of the photocatalyst [69].

Ionic liquids can be covalently bound to the surface of TiO_2 in order to obtain a modification of VB and CB of titania and finally enhance the absorption of visible

light by the materials [70]. A charge-transfer mechanism was observed to be the key factor for visible light absorption in fullerol-modified TiO₂ [71]. Visible photons are absorbed by the organic molecule and then electrons are injected in TiO₂ with good yields in dye degradation and H₂ production.

The concept of plasmonic photocatalysts recently emerged as a very promising route to active photocatalysts. This approach consists in the absorption of light by surface plasmons of metal nanoparticles, such as Ag, followed by transfer of the energy to the surrounding TiO₂ support in core–shell Ag@TiO₂ composites. The first example of this type of photocatalyst was developed by Awazu *et al.* and demonstrated to be an active species in the decomposition of methylene blue; an enhancement by a factor of seven with respect to TiO₂ itself was reported [72]. A more recent similar example involved the preparation of Ag@C composites with the same working principle and with good activity for decomposition of dyes under visible light [73]. In a similar way, Au–TiO₂ photocatalysts with a very low noble metal loading (0.3 wt.%) were recently reported to give high productivity of H₂ under artificial solar light illumination [74]. This process is feasible due to the absorption of Au nanoparticles at their localized surface plasmon resonance (between 500 and 600 nm) followed by transfer of energy to the titania support. Moreover, such an effect of energy transfer, as recently reported for Ag–Au systems [75], can be used to tailor the absorption properties of mixed metal particles deposited on semiconductors. The highest light-harvesting power and substrate activation can be obtained in this way by careful choice of the metals.

4.2.3

Nanocomposites for Photocatalytic Applications

One of the main problems associated with photocatalysis is the fast recombination of the electron–hole pairs formed following light absorption. It is possible to diminish the extent of this undesirable process by using efficient surface traps. These traps can be positioned on the surface of photocatalysts to increase their performance. The most common approach is the use of metal or nonmetal ions and their impregnation on the surface of the photocatalysts, with the consequent transfer of photogenerated electrons to the surface states. Another approach is the use of a second semiconductor for an efficient charge transfer between coupled states of the two semiconductors, thus preparing nanocomposites. If the choice of the two (or more) materials is adequate, charge carrier recombination is strongly reduced.

The formation of nanocomposites can be done using different arrangements, for example, the dispersion of a semiconductor in a continuous matrix, the formation of stacked layers, core–shell geometries, or simply physically contacted, with consequences for the energy transfer between the phases (Figure 4.5) [76].

Nanocomposites of WO_x–TiO₂ showed good activity for the degradation of dyes under visible light, and in this case it was suggested that absorption of photons by WO_x species (due to its reduced bandgap) created holes in its VB, which were then transferred to the VB of TiO₂ [77] thanks to the energy level alignment between them [78]. A similar mechanism was recently reported for Bi₂WO₆–TiO₂ hierarchical nanocomposites for the degradation of methylene blue under visible light, with a

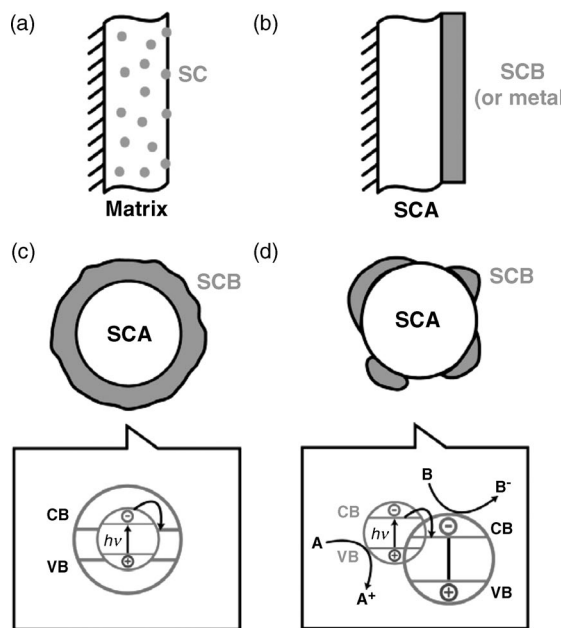


Figure 4.5 Schematic representation of four different possibilities to form semiconductor nanocomposites from a semiconductor A (SCA) and a semiconductor B (SCB), namely semiconductor–matrix (a), layered

configuration (b), core–shell geometry (c), and coupled semiconductors (d). The bottom panels are a pictorial scheme of the energy diagrams of configurations (c) and (d). Adapted from [76] © (2001) American Chemical Society.

heterojunction between the two oxides that can promote charge separation resulting in the formation of holes on TiO_2 having higher oxidation power [79]. La_2O_3 deposition on F-doped TiO_2 was found to improve the visible light response of the titania and to reduce the recombination phenomena thanks to the presence of a lanthana phase [80].

4.3

Nanostructures, Nanoarchitectures, and Nanocomposites for Pollution Remediation

4.3.1

Photocatalytic Applications in Wastewater Treatment

The problem of wastewater treatment is one of the issues where photocatalysis plays a major role. Some model molecules are used to mimic the most common water pollutants, and among these, dyes and phenols are the most commonly used.

Supercritical (sc) CO_2 can be used as solvent to prepare N-doped and N,Zr-doped TiO_2 materials [81] and the doping with N influences the crystallinity of the final

materials, giving rise to smaller crystallites but also to an increased number of defects. Nevertheless, both TiO_2 and Zr– TiO_2 samples doped with N showed high photocatalytic degradation of methylene blue. The synthesis of high surface area TiO_2 materials using scCO₂ can also be achieved with the so-called nanoscale permeation process, with the production of materials that are effective in methylene blue degradation [82]. The enhanced activity was attributed to the high surface area and thus to the presence of a high concentration of surface hydroxyl groups, which could act as active centers for the formation of reactive OH radicals.

Different examples of the use of ionic liquids in the preparation of photocatalysts for wastewater treatment have been reported. TiO_2 -based materials were obtained by a method consisting in the destabilization of an ionic liquid-like solution to give Zr- and Si-doped materials which were active for methyl orange degradation [83]. Other transition metal (Cr, Mn, Fe, Co, Ni, Cu, and Zn)-doped TiO_2 materials were obtained using a sol–gel procedure modified with the use of an ionic liquid and were active in the photodegradation of dyes [84].

N-doped titania demonstrated promising activity under visible light for the degradation of Rhodamine B in aqueous solutions [85]. In thin-films of N-doped TiO_2 , the formation of nitride phases enhanced the catalytic properties of the film [86].

Mixed Ti–W oxides, after deposition of Pt, are active in the mineralization of toluene with sunlight excitation due to the low bandgap (2.7 eV) caused by the presence of both W and Pt in the anatase structure [87]. Vanadium was also used to prepare visible light active photocatalysts in dye degradation [88].

Cr- and N-doped titania showed improved activity under visible light in the degradation of methylene blue and isopropyl alcohol [89]. I-doped TiO_2 showed better activity than Degussa P25 for methylene blue degradation. The sample composed of anatase and rutile showed better activity than that with only anatase [90] for phenol degradation [91].

The synergy between Fe(III) and Au co-dopants on titania produced active photocatalysts for 2,4-chlorophenol degradation under visible light because Fe(III) played a role in extending light absorption towards lower frequency, and Au nanoparticles acted as traps for visible light-induced electrons, resulting in a reduction in the recombination rate [92]. Nevertheless, some contribution arising from homogeneous Fe(III)-promoted Fenton-like reactions cannot be fully excluded. This approach can be extended to Ag@Fe– TiO_2 core–shell photocatalysts, with a synergic effect of the two metals in promoting the degradation of organic dyes [93]. Pt can also be used in combination with TiO_2 for dye degradation either under UV light, where Pt acts as a charge scavenger reducing the recombination of charges, and visible light, where it absorbs photons to promote the photocatalytic process [94].

Bi_2O_3 -impregnated titania was also an effective material in dye degradation under visible light thanks to its direct bandgap of 2.8 eV [95]. Bi(III) doping can also lead to visible light absorption [96]. Formation of heterostructures of Bi_2WO_6 – TiO_2 were recently reported for the preparation of visible light-active catalysts for dye degradation thanks to energy transfers from Rhodamine B, titania, and finally to Bi_2WO_6 [97].

Nanocrystalline TiO_2 has proved to be active in metal photodeposition, an important process for removal of toxic inorganic species, such as As, from wastewater [98].

The fast electron–hole recombination is a main problem even when photocatalysts other than TiO_2 are used. This problem can be reduced by forming nanocomposites, such as in the case of Bi_2O_3 and $BiVO_4$. The formation of an optimum concentration of the two components led to a maximum in the photocatalytic degradation of Rhodamine B [99]. Nanocomposites of anatase titania and polyoxotungstates were effective visible light-active photocatalysts for the degradation of 10 different dyes in water [100].

Zinc ferrite-doped titania composites [$TiO_2(ZnFe_2O_4)$] have been employed as active catalysts under visible light irradiation for methyl orange degradation. The surface properties were found to be the most important parameter for controlling the catalytic response [101]. Similar nanocomposites with TiO_2 dispersed on the surface of $CoFe_2O_4$ cores were obtained recently, with the advantage of the easy separation of the photocatalysts after reaction by taking advantage of the magnetic properties of $CoFe_2O_4$ (Figure 4.6). These materials were less active than undoped TiO_2 in the photodegradation of Rhodamine B, where the amount of TiO_2 is the essential parameter. However, they showed a better performance in atrazine degradation due to the surface charge of the nanocomposites formed after photoinduced processes that enhanced dye adsorption on the surface of the photocatalyst [102].

A similar strategy was used to prepare $BaFe_{12}O_{19}$ – TiO_2 core–shell materials, with the core of $BaFe_{12}O_{19}$ used to magnetically recover the catalyst and the shell of TiO_2 that promoted degradation of dyes. The activity was dependent on the shell thick-

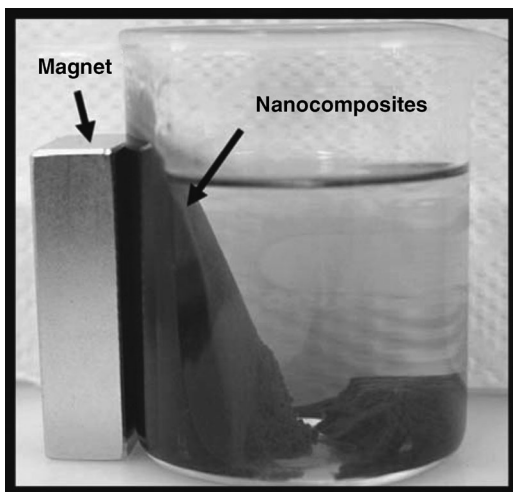


Figure 4.6 Example of the recovery of TiO_2 – $CoFe_2O_4$ nanocomposite from an aqueous suspension after its use as a photocatalyst in the degradation of atrazine. The separation takes

advantage of the magnetic nature of the material. Reprinted from [102] © (2010) with permission from Elsevier.

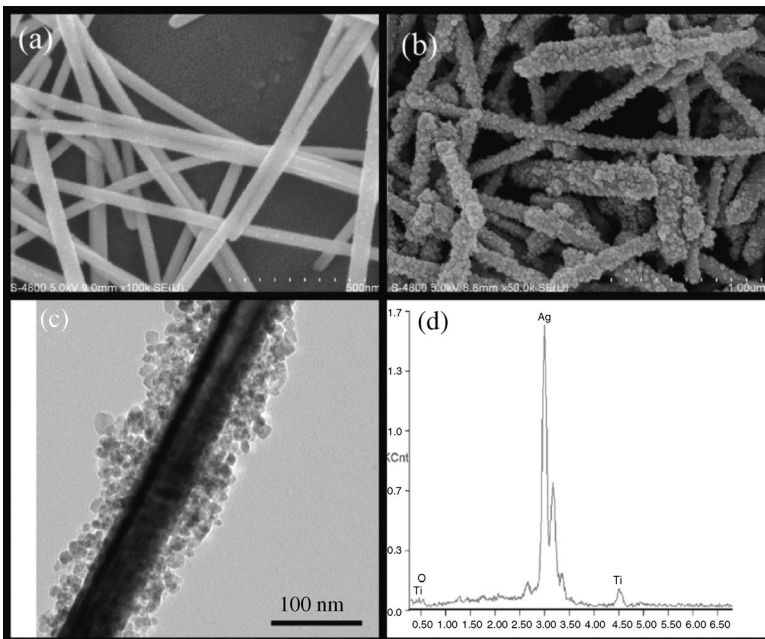


Figure 4.7 SEM images of pristine Ag nanowires (a) and SEM (b), TEM (c), and EDS (d) of Ag@TiO₂ nanocomposite nanowires. Reprinted from [106] © (2010) with permission from Elsevier.

ness [103]. Similarly, Ag–TiO₂–SiO₂–Fe₃O₄ nanocomposites were studied for the degradation of dyes [104]. A micro arc oxidation process was used to prepare WO₃–TiO₂ nanocomposites with absorption in the visible range due to the shift in the bandgap energy to 2.9 eV caused by the incorporation of W both in the surface of the composites and in the lattice of TiO₂ [105]. Ag@TiO₂ nanocomposite nanowires fabricated by a vapor thermal method showed higher catalytic activity than Degussa P25 for degradation of dyes due to the hierarchical structure that was easily accessible to light and reactants (Figure 4.7). These nanocomposites have fairly good stability as no sign of deactivation after five recycles was observed [106].

Mesoporous C–TiO₂ composites with controllable textural properties were recently reported to exhibit good performance for Rhodamine B degradation [107]. Nanocomposites of Degussa P25 and graphene were prepared using a one-step hydrothermal reaction and were used as efficient photocatalysts in the degradation of methylene blue, with good properties of adsorptivity of dyes, extended light absorption range and efficient charge separation [108].

Even though TiO₂-based materials have been far more investigated than any other photocatalyst and this chapter is dedicated to these systems, it is important at least to mention here some of the promising alternative materials studied for wastewater treatment. CdS hollow nanospheres were prepared in a single-step hydrothermal route by Li *et al.* [109] using the ionic liquid 1-butyl-3-methylimidazolium

hexafluorophosphate as template, which was necessary to obtain hollow structures with good activity in the decolorization of methylene blue. β -FeOOH nanorods were functionalized with ionic liquids to enhance their dispersion in water and the generation of Fe(II) species through the photo-Fenton reaction, and therefore its photocatalytic activity for water treatment [110]. $ZnFe_2O_4$ nanoparticles were prepared using a microwave–hydrothermal ionic liquid synthesis and the choice of appropriate conditions allowed the preparation of active photocatalysts for the degradation of phenol [111]. ZnS or $Zn_{1-x}Cd_xS$ nanoparticles were prepared in ionic liquids using a room-temperature approach [112, 113] and investigated for the decolorization of methylene blue.

ZnO is an interesting photocatalyst for dye degradation as it absorbs a large fraction of the solar spectrum [114]. Nanostructure is very important and reaction rates are strongly dependent on crystallographic orientations [115]. Hexagonal plate-like ZnO nanocrystals were found to display a methylene blue degradation rate at least five times higher than rod-shaped crystals, which clearly suggested that the polar (001) and (00-1) facets are more active surfaces than the nonpolar surfaces perpendicular to them [116]. ZnO photocorrosion remains a major issue with this material [7].

Intriguing heterogeneous lollipop-like V_2O_5 – ZnO nanostructures were recently reported to be synthesized by using combined hydrothermal and magnetron sputtering methods, with a resultant final material where core–shell ensembles were present (Figure 4.8). These interesting structures were active in the photocatalytic degradation of 2,6-dichlorophenol under visible light [117].

CeO_2 was found to be a good photocatalysts working under visible light for degradation of dyes through the production of reactive O_2^- species [118].

Recently, nanocomposites of calcium and bismuth mixed oxides obtained by flame synthesis were used for the degradation of organic dyes under visible light, with good activity due to the formation of relatively high surface area materials and oxygen vacancy formation in the flame process [119].

Bi_2O_3 showed interesting properties for the photocatalytic degradation of dyes and phenol after being irradiated with UV light due to the formation of the nanocomposite Bi_2O_3 – Bi_2O_{4-x} . The amount of oxidized species formed over the surface of the pristine oxide could be controlled by changing the exposure time and it was found to affect the final activity [120].

4.3.2

Photocatalytic Applications in Gas-Phase Decontamination

Photocatalytic oxidation can be an effective way of removing pollutants in the gas phase, such as NO_x , SO_x , and volatile organic compounds (VOCs).

NO_x can be effectively photo-oxidized by TiO_2 . Mesostructured C-doped TiO_2 was demonstrated to be a good material for its removal under visible light [121]. The bandgap, its mesostructure, and surface properties are important elements for its activity. N-doped materials can be prepared by a precipitation route (in addition to S doping), with visible light response and activity in NO oxidative destruction [122]. N-doped $SrTiO_3$ materials prepared by mechanical activation were active for NO

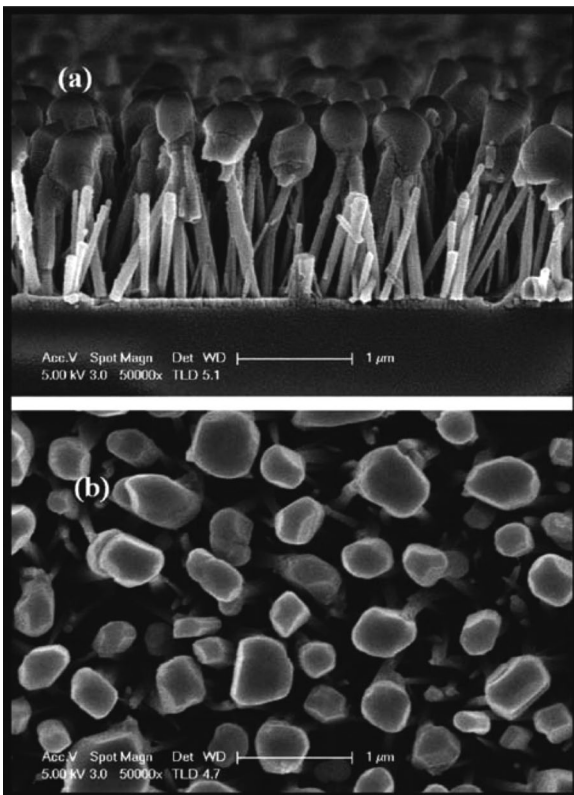


Figure 4.8 SEM cross-section (a) and top surface (b) images of lollipop-like V₂O₅–ZnO core–shell structures. The top heads are V₂O₅ crystal balls and the stems are ZnO nanorods. Reprinted from [117] © (2010) American Chemical Society.

removal under visible light excitation [123]. N-doped TiO₂ demonstrated activity under visible light also in the case of acetaldehyde and trichloroethylene decomposition, but no correlation between N doping and photoactivity was found [124]. Trichloroethylene decomposition was found to be dependent on the size and shape of the titania particles [125]. The photocatalytic oxidation of methylcyclohexane vapor in an oxygen flow was tested over Ti_{1-x}Sn_xO materials. The addition of Sn contributes to an increase in activity, even though the material transforms from anatase to rutile during calcination [126].

TiO₂ hollow spheres have recently been shown to contribute to the degradation of acetone in air as a model of a VOC, with activities higher than Degussa P25 and related not only to surface factors and crystallization but also to the presence of F⁻ ions (used in the preparation of spheres) [127]. TiO₂–SiO₂ composites with high surface area, despite a dramatic blue shift in the bandgap to 3.55 eV due to the formation of Ti–O–Si bonds, showed a high absorption capability and very good activity in the photo-oxidation of benzene in the gas phase [128]. Good activity in the same reaction

was also demonstrated by Ln(III)- and Nd(III)-doped TiO_2 materials [129]. In the case of TiO_2 particles encapsulated in hollow silica shells, an interesting effect due to the particular core–shell structure was found. These structures were not active in the gas-phase decomposition of acetone owing to the difficulty for the substrate to reach the titania core, especially with increasing silica shell thickness. However, when gaseous 2-propanol was used, very good activity was found. This was explained by the fact that acetone, which is the first decomposition product, was not able to escape from the titania core and therefore was subjected to further degradation [130].

The doping of TiO_2 with N and Ni provided a good catalyst for the degradation of formaldehyde under visible light. The presence of Ni suppressed the recombination of photo-induced electron–hole pairs, and raised the photo quantum efficiency, leading to the enhancement of photocatalytic performance [131]. S-doped TiO_2 materials also showed very good photocatalytic activity under blue and yellow visible light for the degradation of gaseous trichloroethylene and dimethyl sulfide [132].

C-doped TiO_2 was employed for the photocatalytic removal of NO_x . The presence of carbon, in the form of coke-like species, was responsible for visible light absorption and thus for the good activity of the photocatalyst under green light irradiation [133].

The removal of H_2S in the gas phase was found to proceed with good results when composites of TiO_2 and $SiMgO_x$ materials were employed, owing to the synergic effect of the photocatalytic activity of the former material and the adsorptive properties of the latter for SO_2 [134].

4.3.3

Photocatalytic Applications to Disinfection

Water is becoming a very important resource nowadays as its supply is steadily decreasing. Around 1 billion people have serious problems in accessing drinking water resources, especially in developing countries. Health risks may arise from consumption of water contaminated with infectious agents or toxic chemicals, and improvements in access to safe drinking water are a target of primary importance. Furthermore, generally the regions that have problems associated with drinking water are those where sunlight is abundant. Therefore, the possibility of using photocatalysis for water remediation and disinfection is an attractive way to help solve the problems related to drinking water [135].

Different mechanisms to explain the disinfection ability of photocatalysts have been proposed [136]. One of the first studies of *Escherichia coli* inactivation by photocatalytic TiO_2 action suggested the lipid peroxidation reaction as the mechanism of bacterial death [137]. A recent study indicated that both degradation of formaldehyde and inactivation of *E. coli* depended on the amount of reactive oxygen species formed under irradiation [138]. The action with which viruses and bacteria are inactivated by TiO_2 photocatalysts seems to involve various species, namely free hydroxyl radicals in the bulk solution for the former and free and surface-bound hydroxyl radicals and other oxygen reactive species for the latter [139]. Different factors were taken into account in a study of *E. coli* inactivation in addition to the presence of the photocatalyst: treatment with H_2O_2 , which enhanced the inactivation

rate; addition of inorganic ions, with rates positively affected by both cations and anions; and the presence of organic compounds, which negatively affected the inactivation process [140]. Another detailed study indicated that not all UV regions (e.g., UVA, UVB and UVC) are active for bacterial remediation, and parameters such as amount of TiO_2 , intensity of light, and bacterial concentration were studied [141].

Pure TiO_2 was recently reported to be active in the disinfection of water contaminated by spores of the type *Fusarium solani* [142], *Bacillus anthracis* [143], or *Cryptosporidium parvum* oocysts [144], or when supported as nanocomposites on zeolite H β for *E. coli* deactivation [145], and it found applications in water treatment as a replacement for chlorine. Ag– TiO_2 immobilized systems were used for inactivation of bacteria, coupling the visible light response of the system and the strong bactericidal effect of Ag [146]. Silver was deposited on hydroxyapatite to form nanocomposites with a high capacity for bacterial adsorption and inactivation [147], or used for airborne bacterial remediation in indoor air [148].

Even in this field, the achievement of visible light-active materials is essential and well documented in the literature. AgBr–Ag– Bi_2WO_6 nanojunction systems were used to inactivate *E. coli* K-12 under visible light. The system shows high efficiency due to the formation of hydroxyl radicals, which were found to be responsible for the observed activity [149]. Visible light was also used for the inactivation of both Gram-negative and Gram-positive bacteria using nanocomposites of palladium oxide and nitrogen-doped titania, with drastic effects on cell walls and cell membranes [150]. The combination of palladium and nitrogen-doped titania was also demonstrated to possess a “memory” catalytic disinfection capability after visible light illumination was turned off for extended periods of up to 8 h caused by the coupling of the charge separation ability of the composites and the reduction of PdO to Pd metal [151]. Carbon-sensitized nitrogen-doped titania materials were more active than N– TiO_2 itself for *E. coli* inactivation due to the narrowing of the bandgap ($E_g = 2.85$ eV) and the consequent stronger absorption of visible light [152]. The addition of a salt of Fe(III) to a TiO_2 slurry enhanced the rate of inactivation of bacteria under simulated sunlight [153]. Very good results were obtained for the inactivation of *Micrococcus lyliae* Gram-positive bacteria under visible light using an S-doped TiO_2 photocatalyst, resulting in almost complete inactivation of the bacteria in 1 hour (Figure 4.9), with the high activity being attributed to the high formation rate of hydroxyl radicals [154].

4.4

Nanostructures, Nanoarchitectures, and Nanocomposites for Energy Applications

As indicated in the Introduction, hydrogen production by photocatalysis employing solar light can be a viable solution for the sustainable production of energy and for solving urgent environmental issues associated with the use of fossil fuels. The application of TiO_2 and TiO_2 -based nanostructured materials for photocatalytic water splitting [11], photoelectrochemical devices, and dye-sensitized cells [14, 155] are relevant. However, some barriers pose serious problems for the commercialization of these devices, as the efficiency is still too low. In this section, we focus on the

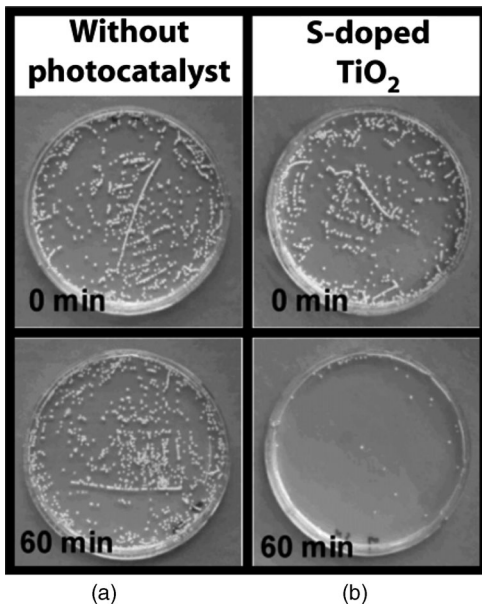


Figure 4.9 Images of *Micrococcus lylae* colonies before and after irradiation with visible light for a blank sample (a) and for the S-doped TiO_2 material (b), showing the high activity for

bacteria inactivation of the photocatalyst.
Reprinted from [154] © (2005) American Chemical Society.

photocatalytic production of hydrogen and some examples of photoelectrochemical applications, with particular attention to the relationships between the nanostructure and the improved observed reactivity. Owing to the complexity of the area of dye-sensitized cells, which would require extensive discussion on the nature, role, and stability of the sensitizers, we decided to avoid such a discussion, directing readers to recent excellent reviews [156, 157].

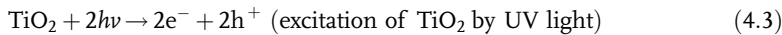
4.4.1

Photocatalytic Applications for Hydrogen Production

Fujishima and Honda [16, 158] reported the photodecomposition of water using semiconductor photoelectrolysis cells (Figure 4.10). When the surface of the TiO_2 electrode was irradiated with UV light, oxygen evolution was observed at the TiO_2 electrode surface and hydrogen at the Pt black electrode. The overall water photodecomposition reaction:



can be separated into the following steps:



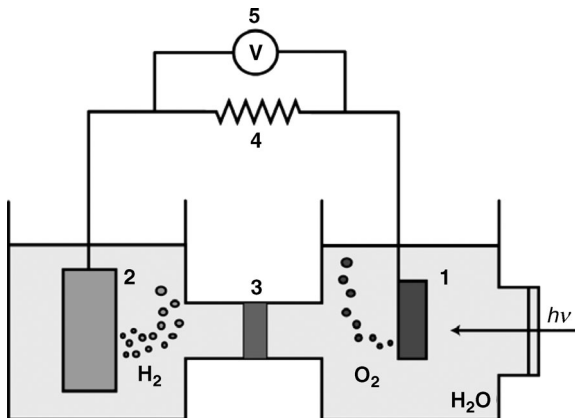
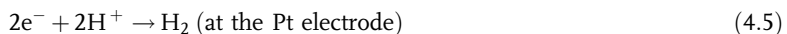


Figure 4.10 Schematic representation of photocatalytic water splitting using TiO_2 electrode connected to a Pt electrode. (1) titania electrode; (2) Pt electrode; (3) sintered-glass diaphragm; (4) the outer load; (5) voltmeter. Adapted from [158] with permission from The Chemical Society of Japan.



Platinum-loaded TiO_2 systems can be considered as a “short-circuited” photoelectrochemical cell where the TiO_2 semiconductor electrode and metal Pt counter-electrode are brought into contact [159]. Light irradiation can induce electron–hole ($e^- - h^+$) pair formation and surface oxidation and also reduction reactions on each Pt/ TiO_2 particle (Figure 4.11). These powder-based systems lack the advantage of

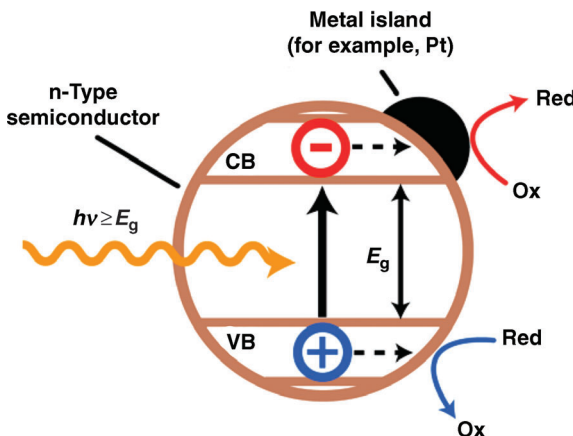


Figure 4.11 Schematic representation of a photocatalytic reaction occurring on a titania particle on which Pt nanoparticles have been deposited. Adapted from [160] with permission from Springer Science and Business Media.

having a large separation in the space between the oxidation and reduction sites present in electrochemical cells. However, the distance between such sites on particles can still be considered large compared with those found in photochemical redox reactions in solutions. Unfortunately, fast H_2 and O_2 recombination occurs in the presence of noble metals such as Pt, drastically reducing the efficiency of the system. At the present stage, however, over such a semiconductor particle photocatalyst, the quantum yield (q_e) for overall water splitting is still very low ($q_e < 1\%$), while a high q_e (10%) can often be obtained by the addition of a so-called “sacrificial agent” [160].

Sacrificial agents are substances that are more easily oxidized than water and they range from inorganic ions and compounds to organic species such as alcohols. These sacrificial agents can interact with the photogenerated holes, reducing the extent of electron–hole recombination. At the same time, as they are involved in the oxidation process, it is also possible to avoid oxygen evolution and therefore there is no problem of a back-recombination of H_2 and O_2 . In the case of alcohols, such as methanol, ethanol, and glycerol, or carbohydrates, such as glucose, their full oxidation leads to CO_2 in a so-called photoreforming process. Simultaneous evolution of H_2 and O_2 under UV irradiation was observed using an $IO_3^- - I^-$ redox mediator [161]. In the latter case, water was reduced to H_2 and I^- was oxidized to IO_3^- over Pt-loaded TiO_2 -anatase. At the same time, water was oxidized to O_2 and IO_3^- was reduced to I^- over TiO_2 -rutile (Figure 4.12). However, these photocatalytic systems did not operate under visible light, and recovering the powder photocatalyst was difficult.

Thin film-photocatalysts represent a very promising system as hydrogen and oxygen can be generated separately (Figure 4.13) [160].

Simultaneous doping by both B and N is a particularly attractive way to prepare visible light-active photocatalysts. One of the main advantages is that generally the TiO_2 particle size decreases upon B doping, and B can also act as shallow trap for electrons, thus increasing the life of photoinduced electrons and holes. Recently, platinized $B,N-TiO_2$ was reported to be a good photocatalyst for H_2 production under visible light [162]. Composite catalysts consisting of Pt-, N- and W-doped titania are

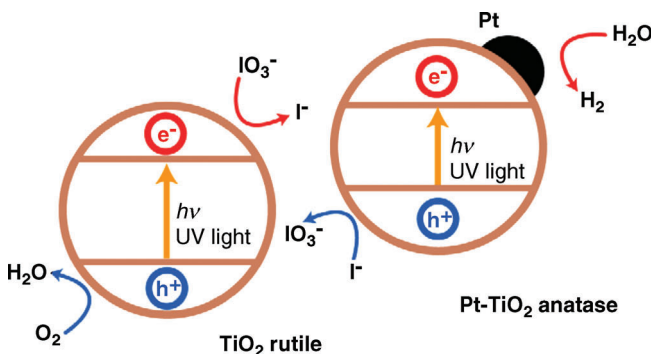


Figure 4.12 Schematic representation of the proposed reaction mechanism for overall photocatalytic water splitting using $IO_3^- - I^-$ redox mediator and a mixture of $Pt-TiO_2$ -anatase and TiO_2 -rutile photocatalysts. Adapted from [161] © (2001) with permission from Elsevier.

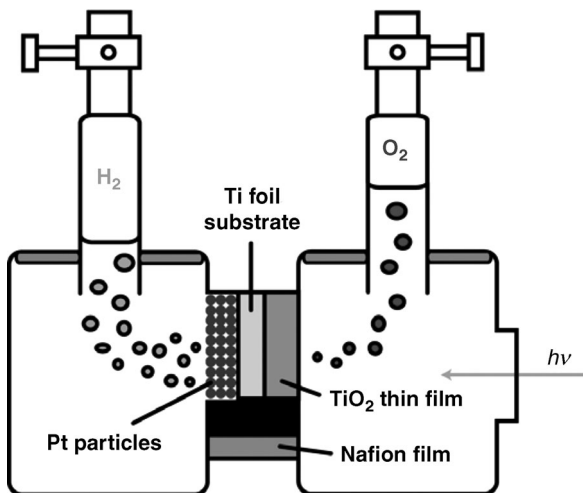


Figure 4.13 Schematic representation of a device for separate evolution of H_2 and O_2 using a TiO_2 thin-film photocatalyst. The electrolytes are 1.0 M aqueous NaOH (right side) and 0.5 M

aqueous H_2SO_4 (left side). Adapted from [160] with permission from Springer Science and Business Media.

also effective materials for hydrogen production from $\text{Na}_2\text{S}-\text{Na}_2\text{SO}_3$ solutions under visible light [163]. Ce, N co-doping [60] and In, N co-doping on Pd– TiO_2 systems [164] were used to extend TiO_2 absorption to the visible range. The doping of titania nanoparticles with both Sn and Eu resulted in the preparation of visible light-active photocatalysts for H_2 production from water-methanol mixtures [165], with improved activity due to the higher reducing power of the system and the formation of oxygen vacancies. Platinized Be-doped titania samples were found to give a double result: when the beryllium ion was present in the bulk, the production of H_2 was inhibited, due to the high hole–electron recombination probability, whereas when it was on the surface, an increase in the reaction rate was observed due to the creation of oxygen vacancies that diminished the recombination probability [166].

Deposition of metal nanoparticles is another method to enhance photocatalytic production due to the absorption of visible light radiation induced by the particles combined with their action as electron reservoirs. Pt is one of the most commonly used metals due to its high efficiency. Au is less efficient under similar conditions [167]. The good activity of Pt was demonstrated even when complex molecules such as glycerol are used [168], with the advantage that glycerol, being a by-product of biodiesel production, is a promising substrate for sustainable production of H_2 [169]. Glucose is another biomass-derived product and the deposition of various noble metals on TiO_2 allowed its photoreforming with good results [170]. It has been proposed that the conversion of glucose occurs via a complex reaction pathway which implies the formation of various radicals, aldehydes, and carboxylic acids (Figure 4.14) [170]. Some of these intermediates are relatively stable and contribute to catalyst surface coverage/poisoning. Indeed, reactions carried out using glycerol or

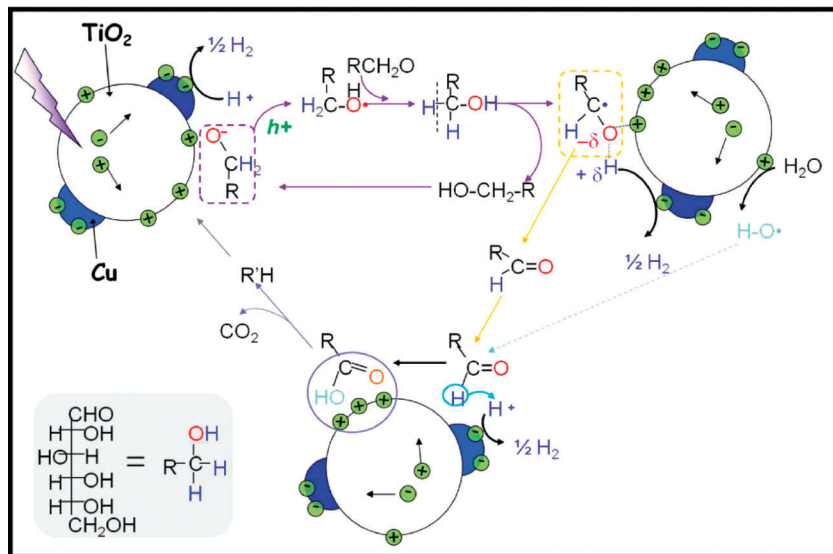


Figure 4.14 Schematic representation of the proposed mechanism of the photocatalytic reforming of glucose on Pt–TiO₂ involving the formation of various radicals, aldehydes, and carboxylic acids. Adapted from [170] © (2008) with permission from Elsevier.

glucose show a maximum in hydrogen production followed by a relatively rapid decline.

The production of H₂ can be coupled with the advantageous degradation of organic pollutants using Pt-sensitized titania [171, 172]. Pt–TiO₂ thin films showed an impressive efficiency in H₂ production from water–ethanol solutions [173]. Platinized Ta₂O₅–TiO₂ mesoporous composites were also investigated for H₂ production under visible light in water–methanol mixtures [174], and even N- and Zr,N-doped Ta₂O₅ materials performed well in this reaction [175].

Cu–CuO_x nanoparticles (with a content of about 10 wt.%) on titania are effective for the production of hydrogen under sacrificial conditions [176–178]. A fairly low concentration of Cu (2.5 wt.%) was sufficient to allow promising H₂ production from ethanol–water and glycerol–water mixtures in the case of CuO_x nanoparticles encapsulated into porous titania [179]. A key limitation of this system is photocorrosion under oxidizing conditions (oxygen and carboxylic acids as by-products of partial oxidation of the sacrificial agent). However, in the presence of UV irradiation, Cu photodeposition can occur, preventing loss of Cu [179].

Bare CuO_x-supported nanostructures showed some activity in H₂ production from methanol–water mixture under UV–visible irradiation [180]. Ni is also used as a dopant, and small amounts (1 wt.%) of this element in mesoporous titania guarantee good activity in water–methanol mixtures under UV–visible light [181]. Indium-tantalum oxide Ni-doped materials also provided photocatalysts with promising efficiencies for direct water splitting [182]. TiO₂ nanotubes doped with Ir and Co nanoparticles were effective for visible light water splitting even in the absence of

sacrificial agents, owing to the lowering of the bandgap from about 3.0 eV to 2.5 and 2.6 eV, respectively. The small dimensions of the particles were essential to obtain the observed activity [183]. Fe- and Cr-doped TiO₂ thin films were used for water splitting under visible light [184], and SnO-TiO₂ mixed oxides showed good activity in methanol–water mixtures due to the presence of defect levels in the bandgap of TiO₂ [185].

Nanocomposites of CdS–TiO₂ nanotubes showed good activity for H₂ production under visible light by means of the dispersed CdS phase and its synergistic effect in combination with TiO₂ nanotubes [186]. CdS-supported TiO₂ particle systems also showed very good activity in hydrogen production from aqueous H₂S solutions [187]. Pt deposited on WS₂-TiO₂ mesoporous composites was used for visible-light production of H₂ in the presence of Na₂S as radical scavenger [188]. Pt-loaded mesoporous zirconium–titanium phosphates also displayed good photoactivity in hydrogen production from carbonate solution [189].

4.4.2

Photoelectrochemical Devices

The successful strategy to achieve real sustainable development is based on the design of new processes in terms of efficiency, selectivity, and economic–environmental impact that are able to produce simultaneous energy, hydrogen, and chemicals of industrial interest starting from renewable resources [186, 190, 191]. In this scenario, direct alcohol fuel cells (DAFCs) give the opportunity to produce clean energy because they do not involve combustion processes of fossil fuels, thus reducing pollutant emissions [192, 193].

The large-scale spread of DAFCs is closely related to the development of efficient anodic and cathodic materials, characterized by very fast electrochemical kinetics, stability at the high current densities in alkaline environments and modest cost. This objective requires cathodes without noble metals and anodes with very low amounts of noble metals. In order to improve the cheapness and sustainability of the processes described above, the most accepted opinion is the possibility of using solar light by means of the introduction of TiO₂, pure or doped, into the electrode material formulation. Figure 4.15 shows a typical laboratory-scale photoelectrocatalytic reactor.

Chu *et al.* observed an enhancement in the ethanol oxidation activity when the TiO₂-based anode of a DAFC cell, working in an acidic environment, was under solar light illumination [195]. The anode was composed of Pt, Ni, and Ru nanoparticles supported on a TiO₂ film. The good performance of this fuel cell was correlated with the photoreforming activity of TiO₂, even if some possible photoinduced electronic modifications in the metal phase in contact with TiO₂ cannot be excluded. TiO₂ nanoparticles dispersed on carbon fiber paper were also employed as the anode of an electrolytic cell in which the photoactivity of TiO₂ drives the whole process. Under UV irradiation, complete oxidation of alcohol to CO₂ takes place at the anode, whereas at the cathode H₂ is produced with no need for external applied bias [196]. This was accomplished by the particular design of the photoelectrochemical device (Figure 4.16).

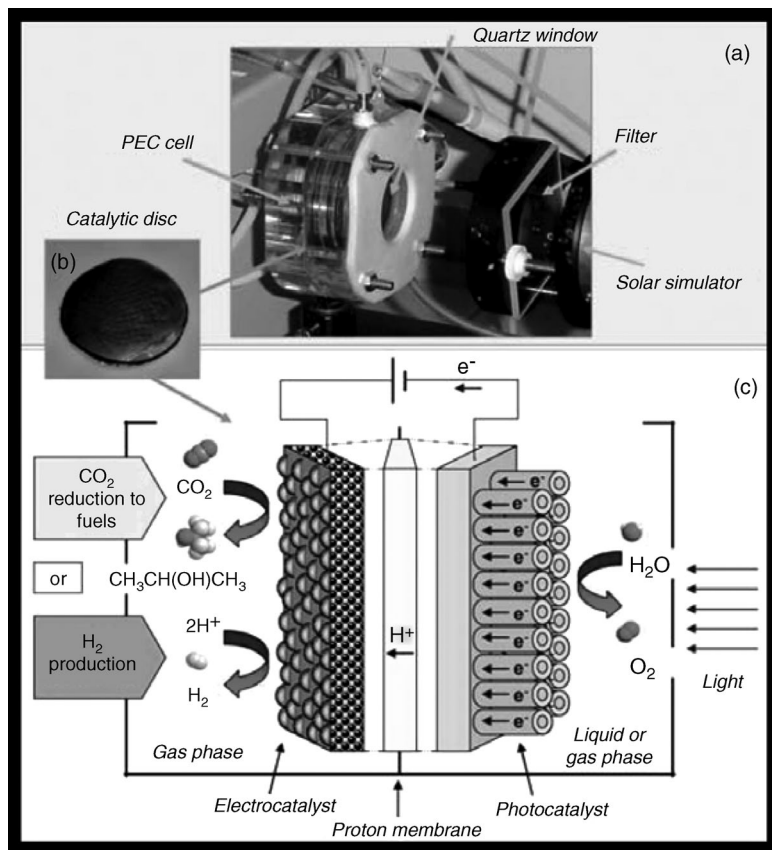


Figure 4.15 (a) Photograph of a laboratory-scale photoelectrochemical device; (b) image of the photo/electrocatalytic disc; (c) schematic representation of the photoelectrochemical

device for CO_2 reduction to fuels and H_2 production. Reprinted from [194]. Reproduced by permission of The Royal Society of Chemistry.

The same group, in a previous work, reported on the realization of a hybrid anode electrode [197]. An appreciable improvement in methanol oxidation activity was observed at the anode in direct methanol fuel cells containing Pt–Ru and TiO_2 particles. Such an improvement was ascribed to a synergic effect of the two components (photocatalyst and metal catalyst). A similar behavior was also reported for a Pt– TiO_2 -based electrode [198]. Another recent study involved the electrolysis of aqueous solutions of alcohols performed on a TiO_2 nanotube-based anode under solar irradiation [199].

The advantages of the presence of TiO_2 in fuel cells or electrolyzers have been the subject of growing interest and studies have indicated that the semiconductor significantly influences both the alcohol oxidation [200–203] and the oxygen reduction [204–207] processes.

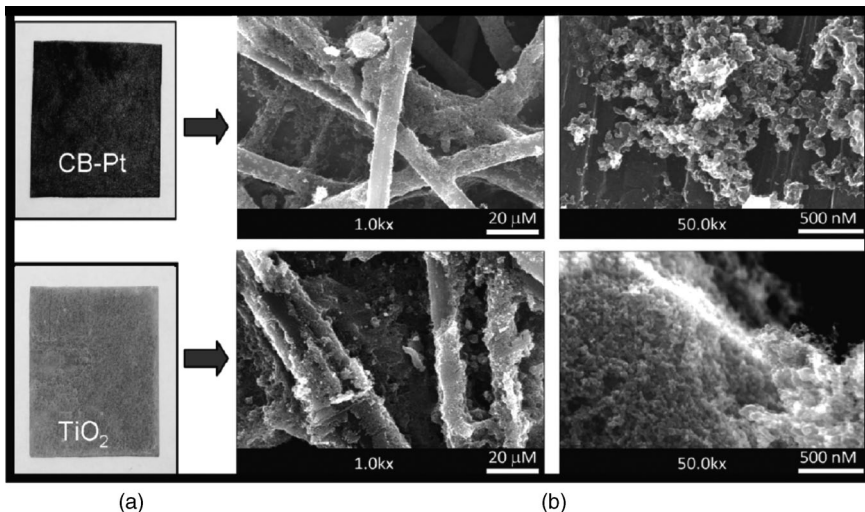


Figure 4.16 (a) Photographs of paper sheets coated with carbon black-supported Pt (CB-Pt), acting as cathode, and with TiO₂, acting as photoanode, assembled on the opposite sides of a Nafion membrane [(b) SEM images of the

assemblies] to construct a photoelectrochemical device for H₂ production with no applied bias. Reprinted from [196] © (2009) American Chemical Society.

4.4.3

Photocatalytic Applications in Artificial Photosynthesis

The conversion of solar into chemical energy is one of the most promising routes for the replacement of fossil fuels and for the sustainable development of our future energetic strategy. In photosynthesis, solar energy is converted to chemical energy by reaction of CO₂ and H₂O to give compounds such as sugars (e.g., glucose) and O₂. One of the key elements in this process is photoinduced electron transfer. Following light excitement, a charge-separated state is manipulated in order to prepare the various molecules needed by plants [208]. The complexity of the artificial photosynthesis that could be based on the same elements that compose the naturally occurring photosynthetic process appears immediately clear: (1) an antenna system for light harvesting; (2) a reaction center for charge separation; (3) a charge transport system to deliver the oxidizing and reducing equivalents to catalytic sites; and (4) a membrane to provide physical separation of the products (Figure 4.17).

Readers are directed to specific reviews on the general topic of artificial photosynthesis [156, 210–212] and we highlight here some aspects related to the role of the TiO₂ component.

It has been reported that titania-based catalysts induce artificial photosynthesis, yielding single-carbon molecules in photocatalytic CO₂ reduction, such as CO, CH₄, CH₃OH, formaldehyde, and formic acid. Aqueous suspensions of titania-based catalysts were first used in photoelectrocatalytic CO₂ reduction [213]. Copper–TiO₂ aqueous suspensions were found active in the photocatalytic CO₂ reduction to

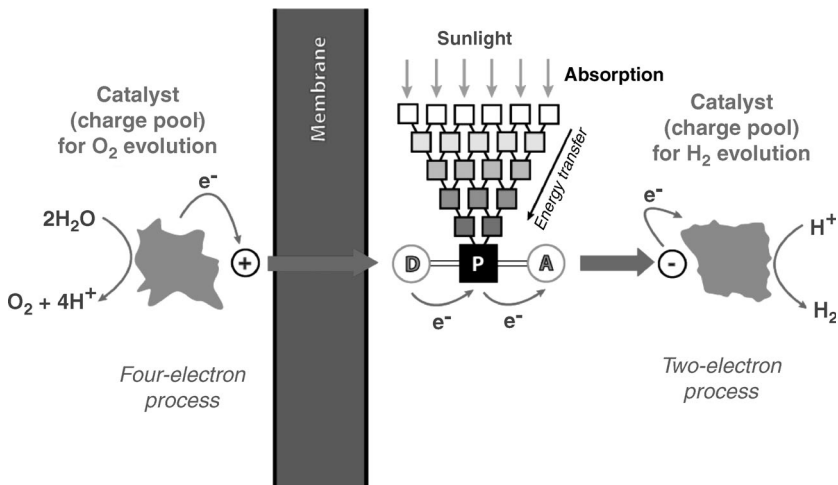


Figure 4.17 Schematic representation of an ideal system for artificial photosynthesis. The fundamental elements are present: a light harvesting system, a triad for charge separation (D–P–A, Donor–Primary acceptor–Acceptor), a

catalyst for hydrogen evolution, a catalyst for oxygen evolution, and a membrane that keeps the two environments separated. Adapted from [209] © (1997) with permission from Elsevier.

CH_3OH and $HCHO$ [214, 215]. Generally, methane and/or methanol are the products reported to be formed [216]. Based on EPR data, Anpo *et al.* indicated the existence of isolated excited $(Ti^{3+}-O^-)^{3\times}$ sites [156, 217], over which simultaneous reduction of CO_2 and decomposition of H_2O are proposed to lead to CO and C radicals, and H and OH radicals, respectively. Subsequently, these photoinduced C, H, and OH radicals recombine to final products, such as CH_4 and CH_3OH . Lin and Frei observed for mesoporous materials that carbon residues can be involved in the production of primary products in the photocatalytic reduction of CO_2 [218]. Recently, Yang *et al.* [219] showed that, even for crystalline TiO_2 materials, water-induced gasification of carbon residues might affect the product quantities and distribution of artificial photosynthesis. This contribution can be particularly significant if alkoxides are used as precursors or if carbon-supported TiO_2 is used.

Zhou *et al.* obtained nitrogen-doped titanium dioxide replicas via a two-step infiltration process with natural leaves as templates [220]. The replicas inherited the hierarchical structures of the natural leaf at the macro-, micro-, and nanoscales. These materials showed enhanced light-harvesting and photocatalytic hydrogen evolution activities. The photocatalytic water splitting activity of the artificial leaf structures was eight times higher than that of titanium dioxide synthesized without templates.

The extension of this approach to artificial leaves based on titanates, niobates, tantalates, metal nitrides and phosphides, metal sulfides, and other transition metal oxides appears possible and useful in order to enhance the photocatalytic efficiency. In addition, the construction of multicomponent systems such as TiO_2-CdS or MoS_2-CdSe for overall water splitting could also lead to further improvements. This

concept is a step forward for the development of efficient artificial photosynthesis devices.

4.5

Nanostructures, Nanoarchitectures, and Nanocomposites for Green Synthesis

Photocatalysis can be profitably used to direct appropriate synthetic transformations in organic compounds [12, 13, 221]. In this case, selectivity is essential, while for conventional applications in environmental catalysis the ability to fully oxidize a large number of compounds is a prerequisite. The wide applicability of TiO₂-based materials for pollution abatement, in both the liquid and gas phases, resides in their ability to fully oxidize a large variety of pollutants, dyes, drugs, and various other compounds to CO₂ and H₂O and other inorganic species. The apparent contradiction between material specification in photocatalytic applications in green organic synthesis and in environmental applications can be solved by careful tuning the properties by material nanostructuring. In fact, as stated previously, nanostructured or “space-confined” photocatalysts can display photocatalytic activities different from those of the bulk materials [222–224]. Despite generally considered unselective transformations, especially in water, recently selective photocatalytic reactions have emerged and, although not reporting real preparative-scale conditions, they represent a promising potential of the application of heterogeneous photocatalysis to organic synthesis. We limit the discussion here to the use of TiO₂-based materials. These materials can be employed alone or in combination with metals, introduced generally by impregnation. As a general problem, yields of the desired products are often low since once generated, the desired compounds might undergo photocatalytic decomposition.

4.5.1

Oxidation Reactions

Oxidation reactions are the most studied processes owing to the well-known ability of illuminated TiO₂ in water to produce reactive oxygen species. In this context, heterogeneous photocatalysis could contribute to the replacement of hazardous compounds such as KMnO₄ and K₂Cr₂O₇ [13].

TiO₂-based materials have proved to be potentially very useful in the hydroxylation of aromatics. The transformation of benzene to phenol and hydroquinone represents an industrially important example. The yields of these reactions are generally not higher than 10–15%, but better yields were obtained with TiO₂ particles dispersed in the zeolite HSM-5 owing to the lower affinity of phenol for the catalytic surface and therefore to its lower degradation after being produced [225]. The same effect was observed more recently by using mesoporous TiO₂. In this way, yields in phenol production of 34% and selectivity up to 81% were obtained [226]. Other studies demonstrated that by tailoring surface properties it was possible to tune the photo-reactivity, thus leading to the possibility of transformation of a general hydrophobic compound into a hydrophilic compound [227]. Photo-oxidation of monosubstituted

benzene derivatives and the influence of the substituent were studied [228]. Recently, the oxidation of 4-chlorophenol over TiO_2 nanoparticles supported on activated carbon showed a dependence on the acidity of the support [229].

The transformation of alkanes to oxygenated compounds (e.g., alcohols, ketones, acids) is another industrially important reaction in which photocatalytic oxidation can play a key role. Important transformations are those when CO_2 or ring-opening products are not observed in photocatalyzed reactions, thus evidencing their selectivity [230]. The further selective oxidation of alcohols to aldehydes is of practical importance in the synthesis of fine chemicals, fragrances, and pharmaceuticals. Nanostructured TiO_2 showed selective oxidation of 4-methoxybenzyl alcohol to the corresponding aldehyde in higher yield (42%) than commercial Degussa P25 [231]. In gas-phase reactions, primary and secondary alcohols were photo-oxidized on immobilized TiO_2 with moderate yields but with very high selectivity (>95%) to the corresponding carbonyl compounds [232].

Alkene epoxidation is generally conducted under stoichiometric conditions with peracids with the formation of 1 mol of acid as by-product. Therefore, the study of more efficient conditions would give a great improvement to this field. The use of bulk TiO_2 gave poor results, whereas dispersed TiO_2 nanoparticles deposited on silica by the sol–gel process showed good selectivity (62%) in the epoxidation of styrene [233]. Remarkably, “single-site” $Ti-SiO_2$ photocatalysts were reported to catalyze the epoxidation of various alkenes using molecular oxygen with extremely good selectivity (even >99%) just by adding acetonitrile [234].

Oxidations of polycyclic aromatic hydrocarbons over TiO_2 have been studied, for example, naphthalene oxidation to various oxygenated species [235] and phenanthrene to obtain coumarin derivatives as important compounds in the production of pharmaceuticals and dyes [236].

4.5.2

Reductions

Reduction reactions are generally less often used than photocatalytically assisted oxidations, mainly because the reduction power of a valence band electron is lower than the oxidation ability of a valence band hole. However, even in this case they can contribute to replacing dangerous reductants such as CO or hydrides with safer procedures.

One of the most studied reactions is the reduction of nitroaromatic compounds. In this reaction, the addition of alcohols and the removal of O_2 generally improve the yields due to the effect of hole scavenging in reducing side reactions [237]. Therefore, good results were obtained in the reduction of different nitro compounds [238] and when cyclohexene was added, a mixture of products was observed [239]. Recently, N-doped TiO_2 and KI were used for the photoreduction of nitroaromatics to the corresponding anilines with very short reaction times (<20 min), high yields (>90%), and wide functional group tolerance [240]. The best activity was obtained with UV irradiation and some promising results were also reported with the use of visible light.

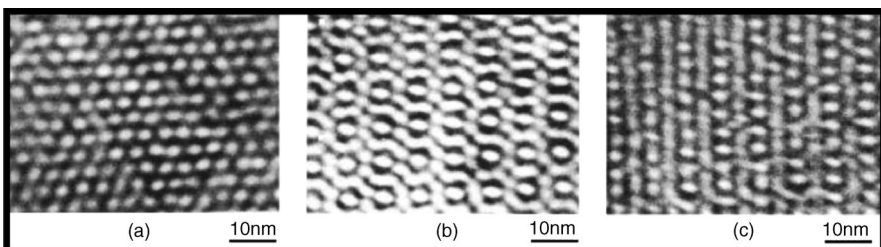


Figure 4.18 TEM images showing the mesostructures of TiO₂ species dispersed in SiO₂ transparent thin films with (a) a hexagonal ordered pore arrangement and (b, c) cubic symmetry. Reproduced from [247] © (2003) with permission from Elsevier.

CO₂ reduction is another important reaction due to environmental issues associated with its release into the atmosphere and, moreover, with the fact that this process is ideally integrated in a wider scenario where the production of valuable chemicals and energy in a single device could be a very attractive solution for many environmental concerns (see also Section 4.4.3) [194]. CO₂ can be reduced with water to a mixture of methane, methanol, and CO on anchored titanium catalysts or to methane on fine TiO₂ powders [217]. In the presence of hole scavengers such as alcohols [241], Cu-doped TiO₂ was shown to be able to convert CO₂ photocatalytically to methanol [242]. In Cu–TiO₂ photocatalysts, different parameters such as copper precursor, post-treatment procedures, and wavelength of incoming radiation were found to influence the activity [243, 244]. Selective reduction of CO₂ to methanol and CH₄ was observed to proceed in good yield on TiO₂–SiO₂ catalysts [245]. Improvements were gained by immobilizing TiO₂ species on self-standing SiO₂ transparent thin films obtained in two different mesostructures by controlling the sol–gel preparation conditions (Figure 4.18). [246, 247].

4.5.3

Other Reactions

The presence of two types of catalytic centers (e.g., oxidative and reductive) in the same material can give rise to the possibility of multi-step photocatalysis in a one-pot procedure. C–C coupling, for example, is a field of great interest and a recent very good review was published [221]. C–N coupling reactions are also of interest.

A catalyst prepared by supporting TiO₂ (2%) on zeolite H β promoted the formation of dihydropyrazine from ethylenediamine and propylene glycol with good yields (20%), whereas pure TiO₂ showed no activity [248]. One-pot cyclizations are very interesting reactions since they allow complex compounds to be obtained in a single step. For example, it was demonstrated that cyclization of lysine occurred with high selectivity (77%) using a Pt–TiO₂ photocatalyst with 15 nm anatase crystallites [249]. Addition–cyclization reactions were reported to be efficiently photoinduced by TiO₂, as in the case of *N,N*-dimethylamine and menthyloxyfuranone [250]. These selected examples highlight once again the potential of photocatalysis as a green synthetic route in organic chemistry.

4.6

Materials Stability and Toxicology – Safety Issues

With the growing impact of nanotechnology, as already evidenced in the Introduction, the presence of nanoparticles in commercially available products is becoming more common. However, owing to the relatively short period of investigation of this novel class of materials, studies addressing their stability and related to their safety are not yet numerous, and their toxicological profiles are often unknown. Two relevant cases brought these topics to the attention of scientists: the Magic-Nano case in Germany, where aerosol products used to coat glass and ceramics with a protective, dirt-repellent film, caused 100 consumers to be hospitalized [251], and the case of titania nanoparticles in solar sunscreens that were reported to be toxic in mice [252]. Therefore, the need for appropriate tests of the toxicity of nanomaterials continues to grow. The effects on health of such materials are being investigated with regulatory concerns moving from the traditional PM10 (particulate matter with aerodynamic diameter less than 10 μm) to PM5, PM2.5, and below, as the increased toxicity of smaller particles has been identified. Most of the studies were focused on the effects of ultrafine particles, especially on respiratory system [253]. Comparatively few studies have addressed ecological systems [254, 255], and research on human health has been mainly focused on oxidative stress [256] and inflammatory and fibrotic reactions [257]. Nanomaterials can be divided into three main classes, and their toxicology has been excellently reviewed: carbon materials (nanotubes, fullerenes, graphite) [258–261]; metal-containing materials (metal nanoparticles, metal oxides) [262–264]; and semiconductor nanoparticles [264, 265]. A more recent review highlighted studies addressing all these materials [266].

Among these nanomaterials, the toxicity of titania is a widely explored topic because of its extensive use in manufacturing, wastewater treatments, and also in consumer products (toothpastes, sunscreens, cosmetics and food products) [267, 268]. Studies have already assessed the pulmonary toxicological effects of ultrafine TiO_2 particles after chronic exposure with the resulting formation of tumors and other effects. A detailed study evidenced that rats, mice, and hamsters exposed to doses of ultrafine TiO_2 particles showed different responses that could be explained in terms of particle dosimetry differences among the rodent species [269]. Titania particles with different coatings (Al_2O_3 alone or in combination with amorphous SiO_2) were found to cause only mild adverse pulmonary effects in rats, with the particles bearing both alumina and silica coatings being the most toxic, thus showing how the surface treatment can induce toxicity of titania particles [270]. A more recent study on the exposure of mice to 2–5 nm titania particles showed significant but moderate inflammatory responses in lungs only in subacute conditions, and this was resolved in the third week after exposure [271]. Even the size of the particles is important, as it was demonstrated that ultrafine or nanoparticles caused increased lung toxicity compared with larger particles at equivalent mass concentration [272].

The presence of titania particles in sunscreens was the main reason for the investigation of its dermal penetration properties, and a study suggested that fine particles (10–50 nm) can penetrate the skin, although the sample size was too small to

be statistically relevant [273]. In a careful study, it was reported that the probable sites of particle penetration were hair follicles or pores, since higher amounts of particles penetrated in hairy samples of skin [274], as also demonstrated by the penetration of fluorescent spheres in the micrometer range [275].

Another specific and important aspect to consider is the possibility that an environmentally heterogeneous photocatalyst can lead to the undesirable formation of reaction intermediates which are more toxic than the starting reagents. For instance, the TiO₂-based photodegradation of ethanol, a relatively innocuous air pollutant, occurs through its transformation into the more toxic acetaldehyde. Condensation reactions can also lead to the formation of traces of methyl formate, ethyl formate, or methyl acetate. Catalyst design is therefore important to increase the overall oxidation rate to ensure complete mineralization (formation of CO₂ and H₂O).

In addition, problems related to leaching of photocatalysts into the environment must be considered as metals are generally toxic, especially when present as reduced micro- or nanoparticles.

4.7 Conclusion

Environmental concerns and energy issues are posing great challenges to the scientists of our era. The discovery of innovative sustainable procedures that allow both the production of energy and large quantities of commodities and the reduction of environmental hazards and concerns are major objectives. In this context, photocatalysis can play a prominent role since both light and photocatalysis are two of the pillars of the sustainable chemistry concept. A progressive understanding of nanoeffects in photocatalysis has allowed outstanding applications and promising results to be obtained in many different fields such as environmental remediation, organic synthesis, hydrogen production, and solar energy conversion. TiO₂ and related materials are among the most investigated materials due to their remarkable stability and activity. They have found increasing applications in wastewater and gas after-treatment, even though there is still tremendous ongoing research to increase their activity, especially under visible light. Although much more basic and applied research need to be carried out to solve many open questions in this area, this chapter has highlighted some key applications of TiO₂-based photocatalysts and how their nanostructure is important for their reactivity and stability.

Acknowledgments

Professor Mauro Graziani is gratefully acknowledged for helpful suggestions and for reading the manuscript. Dr. Valentina Gombac, Dr. Tiziano Montini and Dr. Barbara Lorenzut are acknowledged for helpful discussions. The University of Trieste, ICCOM-CNR, PRIN2007 “Sustainable processes of 2nd generation for H₂ production from renewable sources,” Fondo Trieste, Regione Friuli Venezia Giulia, and Fondazione CRTrieste are acknowledged for financial support.

References

- 1 Fox, M.A. and Dulay, M.T. (1993) Heterogeneous photocatalysis. *Chemical Reviews*, **93** (1), 341–357.
- 2 Mills, A. and Le Hunte, S. (1997) An overview of semiconductor photocatalysis. *Journal of Photochemistry and Photobiology A: Chemistry*, **108** (1), 1–35.
- 3 Carp, O., Huisman, C.L., and Reller, A. (2004) Photoinduced reactivity of titanium dioxide. *Progress in Solid State Chemistry*, **32** (1–2), 33–177.
- 4 Chen, X. and Mao, S.S. (2007) Titanium dioxide nanomaterials: synthesis, properties, modifications and applications. *Chemical Reviews*, **107** (7), 2891–2959.
- 5 Hoffmann, M.R., Martin, S.T., Choi, W., and Bahnemann, D.W. (1995) Environmental applications of semiconductor photocatalysis. *Chemical Reviews*, **95** (1), 69–96.
- 6 Zhu, J. and Zäch, M. (2009) Nanostructured materials for photocatalytic hydrogen production. *Current Opinion in Colloid and Interface Science*, **14** (4), 260–269.
- 7 Hernandez-Alonso, M.D., Fresno, F., Suarez, S., and Coronado, J.M. (2009) Development of alternative photocatalysts to TiO_2 : challenges and opportunities. *Energy & Environmental Science*, **2** (12), 1231–1257.
- 8 Herrmann, J.M. (1999) Heterogeneous photocatalysis: fundamentals and applications to the removal of various types of aqueous pollutants. *Catalysis Today*, **53** (1), 115–129.
- 9 Mills, A., Davies, R.H. and Worsley, D. (1993) Water purification by semiconductor photocatalysis. *Chemical Society Reviews*, **22** (6), 417–425.
- 10 Esswein, A.J. and Nocera, D.G. (2007) Hydrogen production by molecular photocatalysis. *Chemical Reviews*, **107** (10), 4022–4047.
- 11 Ni, M., Leung, M.K.H., Leung, D.Y.C., and Sumathy, K. (2007) A review and recent developments in photocatalytic water-splitting using TiO_2 for hydrogen production. *Renewable & Sustainable Energy Reviews*, **11** (3), 401–425.
- 12 Shiraishi, Y. and Hirai, T. (2008) Selective organic transformations on titanium oxide-based photocatalysts. *Journal of Photochemistry and Photobiology C: Photochemistry Reviews*, **9** (4), 157–170.
- 13 Palmisano, G., Augugliaro, V., Pagliaro, M., and Palmisano, L. (2007) Photocatalysis: a promising route for 21st century organic chemistry. *Chemical Communications* (33), 3425–3437.
- 14 Grätzel, M. (2001) Photoelectrochemical cells. *Nature*, **414** (6861), 338–344.
- 15 Armaroli, N. and Balzani, V. (2007) The future of energy supply: challenges and opportunities. *Angewandte Chemie International Edition*, **46** (1–2), 52–66.
- 16 Fujishima, A. and Honda, K. (1972) Electrochemical photolysis of water at a Semiconductor electrode. *Nature*, **238** (5358), 37–38.
- 17 Protti, S. and Fagnoni, M. (2009) The sunny side of chemistry: green synthesis by solar light. *Photochemical & Photobiological Sciences*, **8** (11), 1499–1516.
- 18 Anastas, P.T. and Warner, J.C. (1998) *Green Chemistry: Theory and Practice*, Oxford University Press, New York.
- 19 Rao, C.N.R., Kulkarni, G.U., Thomas, P.J., and Edwards, P.P. (2002) Size-dependent chemistry: properties of nanocrystals. *Chemistry- A European Journal*, **8** (1), 28–35.
- 20 Burda, C., Chen, X., Narayanan, R. and El-Sayed, M.A. (2005) Chemistry and properties of nanocrystals of different shapes. *Chemical Reviews*, **105** (4), 1025–1102.
- 21 Xia, Y., Xiong, Y., Lim, B., and Skrabalak, S.E. (2009) Shape-controlled synthesis of metal nanocrystals: simple chemistry meets complex physics? *Angewandte Chemie International Edition*, **48** (1), 60–103.
- 22 Li, M. and Li, J.C. (2006) Size effects on the band-gap of semiconductor compounds. *Materials Letters*, **60** (20), 2526–2529.
- 23 Kasuya, A., Milczarek, G., Dmitruk, I., Barnakov, Y., Czajka, R., Perales, O., Liu,

- X., Tohji, K., Jeyadevan, B., Shinoda, K., Ogawa, T., Arai, T., Hihara, T., and Sumiyama, K. (2002) Size- and shape-controls and electronic functions of nanometer-scale semiconductors and oxides. *Colloids and Surfaces A: Physicochemical and Engineering Aspects*, **202** (2–3), 291–296.
- 24** Brus, L. (1986) Electronic wave functions in semiconductor clusters: experiment and theory. *Journal of Physical Chemistry*, **90** (12), 2555–2560.
- 25** Lin, H., Huang, C.P., Li, W., Ni, C., Shah, S.I., and Tseng, Y.H. (2006) Size dependency of nanocrystalline TiO₂ on its optical property and photocatalytic reactivity exemplified by 2-chlorophenol. *Applied Catalysis B: Environmental*, **68** (1–2), 1–11.
- 26** Peng, X., Manna, L., Yang, W., Wickham, J., Scher, E., Kadavanich, A., and Alivisatos, A.P. (2000) Shape control of CdSe nanocrystals. *Nature*, **404** (6773), 59–61.
- 27** Puntés, V.F., Krishnan, K.M., and Alivisatos, A.P. (2001) Colloidal nanocrystal shape and size control: the case of cobalt. *Science*, **291** (5511), 2115–2117.
- 28** Manna, L., Scher, E.C., and Alivisatos, A.P. (2000) Synthesis of soluble and processable rod-, arrow-, teardrop-, and tetrapod-shaped CdSe nanocrystals. *Journal of the American Chemical Society*, **122** (51), 12700–12706.
- 29** Milliron, D., Hughes, S.M., Cui, Y., Manna, L., Li, J., Wang, L.W., and Alivisatos, A.P. (2004) Colloidal nanocrystal heterostructures with linear and branched topology. *Nature*, **430** (6996), 190–195.
- 30** Alivisatos, A.P. (1996) Perspectives on the physical chemistry of semiconductor nanocrystals. *Journal of Physical Chemistry*, **100** (31), 13226–13239.
- 31** Wang, Y., Ouyang, G., Wang, L.L., Tang, L.M., Tang, D.S., and Sun, C.Q. (2008) Size- and composition-induced band-gap change of nanostructured compound of II–VI semiconductors. *Chemical Physics Letters*, **463** (4–6), 383–386.
- 32** Niederberger, M., Garnweinertner, G., Krumeich, F., Nesper, R., Cölfen, H. and Antonietti, M. (2004) Tailoring the surface and solubility properties of nanocrystalline titania by a nonaqueous *in situ* functionalization process. *Chemistry of Materials*, **16** (7), 1202–1208.
- 33** Calza, P., Pelizzetti, E., Mogyorósi, K., Kun, R., and Dékány, I. (2007) Size dependent photocatalytic activity of hydrothermally crystallized titania nanoparticles on poorly adsorbing phenol in absence and presence of fluoride ion. *Applied Catalysis B: Environmental*, **72** (3–4), 314–321.
- 34** Mao, Y. and Wong, S.S. (2006) Size-andshape-dependent transformation of nanosized titanate into analogous anatase titania nanostructures. *Journal of the American Chemical Society*, **128** (25), 8217–8226.
- 35** Li, W.K., Gong, X.Q., Lu, G., and Selloni, A. (2008) Different reactivities of TiO₂ polymorphs: comparative DFT calculations of water and formic acid adsorption at anatase and brookite TiO₂ surfaces. *Journal of Physical Chemistry C*, **112** (17), 6594–6596.
- 36** Testino, A., Bellobono, I.R., Buscaglia, V., Canevali, C., D'Arienzo, M., Polizzi, S., Scotti, R., and Morazzoni, F. (2007) Optimizing the photocatalytic properties of hydrothermal TiO₂ by the control of phase composition and particle morphology. A systematic approach. *Journal of the American Chemical Society*, **129** (12), 3564–3575.
- 37** Bakardjieva, S., Stengl, V., Szatmary, L., Subrt, J., Lukac, J., Murafa, N., Niznansky, D., Cizek, K., Jirkovsky, J., and Petrova, N. (2006) Transformation of brookite-type TiO₂ nanocrystals to rutile: correlation between microstructure and photoactivity. *Journal of Materials Chemistry*, **16** (18), 1709–1716.
- 38** Almquist, C.B. and Biswas, P. (2002) Role of synthesis method and particle size of nanostructured TiO₂ on its photoactivity. *Journal of Catalysis*, **212** (2), 145–156.
- 39** Boujday, S., Wünsch, F., Portes, P., Bocquet, J.F., and Colbeau-Justin, C. (2004) Photocatalytic and electronic properties of TiO₂ powders elaborated by sol-gel route and supercritical drying. *Solar Energy Materials & Solar Cells*, **83** (4), 421–433.
- 40** Yang, H.G., Sun, C.H., Qiao, S.Z., Zou, J., Liu, G., Smith, S.C., Cheng, H.M., and

- Lu, G.Q. (2008) Anatase TiO_2 single crystals with a large percentage of reactive facets. *Nature*, **453** (7195), 638–641.
- 41 Alapi, T., Sipos, P., Ilisz, I., Wittmann, G., Ambrus, Z., Kircsi, I., Mogyorósi, K., and Dombi, A. (2006) Synthesis and characterization of titania photocatalysts: the influence of pretreatment on the activity. *Applied Catalysis A: General*, **303** (1), 1–8.
- 42 Baiju, K.V., Shukla, S., Biju, S., Reddy, M.L.P., and Warrier, K.G.K. (2009) Morphology-dependent dye-removal mechanism as observed for anatase-titania photocatalyst. *Catalysis Letters*, **131** (3–4), 663–671.
- 43 Balázs, N., Mogyorósi, K., Sránkó, D.F., Pallagi, A., Alapi, T., Oszkó, A., Dombi, A., and Sipos, P. (2008) The effect of particle shape on the activity of nanocrystalline TiO_2 photocatalysts in phenol decomposition. *Applied Catalysis B: Environmental*, **84** (3–4), 356–362.
- 44 Mogyorósi, K., Balázs, N., Sránkó, D.F., Tombácz, E., Dékány, I., Oszkó, A., Sipos, P., and Dombi, A. (2010) The effect of particle shape on the activity of nanocrystalline TiO_2 photocatalysts in phenol decomposition. Part 3: the importance of surface quality. *Applied Catalysis B: Environmental*, **96** (3–4), 577–585.
- 45 Yu, J. and Yu, X. (2008) Hydrothermal synthesis and photocatalytic activity of zinc oxide hollow spheres. *Environmental Science and Technology*, **42** (13), 4902–4907.
- 46 Asahi, R., Morikawa, T., Ohwaki, T., Aoki, K., and Taga, Y. (2001) Visible-light photocatalysis in nitrogen-doped titanium oxides. *Science*, **293** (5528), 269–271.
- 47 Wang, J., Tafen, D.N., Lewis, J.P., Hong, Z., Manivannan, A., Zhi, M., Li, M., and Wu, N. (2009) Origin of photocatalytic activity of nitrogen-doped TiO_2 nanobelts. *Journal of the American Chemical Society*, **131** (34), 12290–12297.
- 48 Yang, G., Jiang, Z., Shi, H., Xiao, T., and Yan, Z. (2010) Preparation of highly visible-light active N-doped TiO_2 photocatalyst. *Journal of Materials Chemistry*, **20** (25), 5301–5309.
- 49 Papageorgiou, A.C., Beglitis, N.S., Pang, C.L., Teobaldi, G., Cabailh, G., Chen, Q., Fisher, A.J., Hofer, W.A., and Thornton, G. (2010) Electron traps and their effect on the surface chemistry of TiO_2 (110). *Proceedings of the National Academy of Sciences of the U.S.A.*, **107** (6), 2391–2396.
- 50 Thompson, T.L. and Yates, J. (2005) TiO_2 -based photocatalysis: surface defects, oxygen and charge transfer. *Topics in Catalysis*, **35** (3–4), 197–210.
- 51 Wahlström, E., Vestergaard, E.K., Schaub, R., Rønnau, A., Vestergaard, M., Lægsgaard, E., Stensgaard, I., and Besenbacher, F. (2004) Electron transfer-induced dynamics of oxygen molecules on the TiO_2 (110) surface. *Science*, **303** (5657), 511–513.
- 52 Jagadale, T.C., Takale, S.P., Sonawane, R.S., Joshi, H.M., Patil, S.I., Kale, B.B., and Ogale, S.B. (2008) N-doped TiO_2 nanoparticle based visible light photocatalyst by modified peroxide sol-gel method. *Journal of Physical Chemistry C*, **112** (37), 14595–14602.
- 53 Di Valentin, C., Pacchioni, G., and Selloni, A. (2005) Theory of carbon doping of titanium dioxide. *Chemistry of Materials*, **17** (26), 6656–6665.
- 54 Sakthivel, S. and Kisch, H. (2003) Daylight photocatalysis by carbon-modified titanium dioxide. *Angewandte Chemie International Edition*, **42** (40), 4908–4911.
- 55 Choi, Y., Umebayashi, T., and Yoshikawa, M. (2004) Fabrication and characterization of C-doped anatase TiO_2 photocatalysts. *Journal of Materials Science*, **39** (5), 1837–1839.
- 56 Minero, C., Mariella, G., Maurino, V., and Pelizzetti, E. (2000) Photocatalytic transformation of organic compounds in the presence of inorganic anions. 1. Hydroxyl-mediated and direct electron-transfer reactions of phenol on a titanium dioxide–fluoride system. *Langmuir*, **16** (6), 2632–2641.
- 57 Xu, H., Zheng, Z., Zhang, L., Zhang, H., and Deng, F. (2008) Hierarchical chlorine-doped rutile TiO_2 spherical clusters of nanorods: large-scale synthesis and high photocatalytic activity. *Journal of Solid State Chemistry*, **181** (9), 2516–2522.
- 58 Xu, J., Ao, Y., Chen, M., and Fu, D. (2009) Low-temperature preparation of boron-

- doped titania by hydrothermal method and its photocatalytic activity. *Journal of Alloys and Compounds*, **484** (1–2), 73–79.
- 59 Lin, L., Lin, W., Xie, J.L., Zhu, Y.X., Zhao, B.Y., and Xie, Y.C. (2007) Photocatalytic properties of phosphor-doped titania nanoparticles. *Applied Catalysis B: Environmental*, **75** (1–2), 52–58.
- 60 Sun, X., Liu, H., Dong, J., Wei, J., and Zhang, Y. (2010) Preparation and characterization of Ce/N-codoped TiO₂ particles for production of H₂ by photocatalytic splitting water under visible light. *Catalysis Letters*, **135** (3–4), 219–225.
- 61 Lorret, O., Francová, D., Waldner, G., and Stelzer, N. (2009) W-doped titania nanoparticles for UV and visible-light photocatalytic reactions. *Applied Catalysis B: Environmental*, **91** (1–2), 39–46.
- 62 Long, R. and English, N.J. (2010) Synergistic effects on band gap-narrowing in titania by codoping from first-principles calculations. *Chemistry of Materials*, **22** (5), 1616–1623.
- 63 Kubacka, A., Colón, G., and Fernández-García, M. (2009) Cationic (V,Mo, Nb, W) doping of TiO₂-anatase: areal alternative for visible light-driven photocatalysts. *Catalysis Today*, **143** (3–4), 286–292.
- 64 Yu, J., Xiang, Q., and Zhou, M. (2009) Preparation, characterization and visible-light-driven photocatalytic activity of Fe-doped titania nanorods and first-principles study for electronic structures. *Applied Catalysis B: Environmental*, **90** (3–4), 595–602.
- 65 Li, W., Wang, Y., Lin, H., Shah, S.I., Huang, C.P., Doren, D.J., Rykov, S.A., Chen, J.G., and Barteau, M.A. (2003) Band gap tailoring of Nd³⁺-doped TiO₂ nanoparticles. *Applied Physics Letters*, **83** (20), 4143–4145.
- 66 Ao, Y., Xu, J., Fu, D., and Yuan, C. (2009) Synthesis of C,N, S-tridoped mesoporous titania with enhanced visible light-induced photocatalytic activity. *Microporous and Mesoporous Materials*, **122** (1–3), 1–6.
- 67 Sakthivel, S., Janczarek, M., and Kisch, H. (2004) Visible light activity and photoelectrochemical properties of nitrogen-doped TiO₂. *Journal of Physical Chemistry B*, **108** (50), 19384–19387.
- 68 Gombac, V., De Rogatis, L., Gasparotto, A., Vicario, G., Montini, T., Barreca, D., Balducci, G., Fornasiero, P., Tondello, E., and Graziani, M. (2007) TiO₂nanopowders doped with boron and nitrogen for photocatalytic applications. *Chemical Physics*, **339** (1–3), 111–123.
- 69 Bettinelli, M., Dallacasa, V., Falcomer, D., Fornasiero, P., Gombac, V., Montini, T., Romanò, L., and Speghini, A. (2007) Photocatalytic activity of TiO₂ doped with boron and vanadium. *Journal of Hazardous materials*, **146** (3), 529–534.
- 70 Hu, S., Wang, A., Li, X., Wang, Y., and Löwe, H. (2010) Hydrothermal synthesis of ionic liquid [Bmim]OH-modified TiO₂ nanoparticles with enhanced photocatalytic activity under visible light. *Chemistry - An Asian Journal*, **5** (5), 1171–1177.
- 71 Park, Y., Singh, N.J., Kim, K.S., Tachikawa, T., Majima, T., and Choi, W. (2009) Fullerol-titania charge-transfer-mediated photocatalysis working under visible light. *Chemistry- A European Journal*, **15** (41), 10843–10850.
- 72 Awazu, K., Fujimaki, M., Rockstuhl, C., Tominaga, J., Murakami, H., Ohki, Y., Yoshida, N., and Watanabe, T. (2008) A plasmonic photocatalyst consisting of silver nanoparticles embedded in titanium dioxide. *Journal of the American Chemical Society*, **130** (5), 1676–1680.
- 73 Sun, S., Wang, W., Zhang, L., Shang, M., and Wang, L. (2009) Ag@C core/shell nanocomposite as a highly efficient plasmonic photocatalyst. *Catalysis Communications*, **11** (4), 290–293.
- 74 Rosselet, O., Shankar, M.V., Du, M.K.-L., Schmidlin, L., Keller, N., and Keller, V. (2010) Solar light photocatalytic hydrogen production from water over Pt and Au/TiO₂ (anatase/rutile) photocatalysts: influence of noble metal and porogen promotion. *Journal of Catalysis*, **269** (1), 179–190.
- 75 Chen, C.W., Wang, C.H., Wei, C.M., Hsieh, C.Y., Chen, Y.T., Chen, Y.F., Lai, C.W., Liu, C.L., Hsieh, C.C., and Chou, P.T. (2009) Highly sensitive emission sensor based on surface plasmon enhanced energy transfer between goldnanoclusters and silver nanoparticles. *Journal of Physical Chemistry C*, **114** (2), 799–802.

- 76** Rajeshwar, K., de Tacconi, N.R., and Chenthamarakshan, C.R. (2001) Semiconductor-based composite materials: preparation, properties, and performance. *Chemistry of Materials*, **13** (9), 2765–2782.
- 77** Sajjad, A.K.L., Shamaila, S., Tian, B., Chen, F., and Zhang, J. (2010) Comparative studies of operational parameters of degradation of azo dyes invisible light by highly efficient WO_x/TiO_2 photocatalyst. *Journal of Hazardous materials*, **177** (1–3), 781–791.
- 78** Wang, S.J., Cheng, G., Jiang, X.H., Li, Y.C., Huang, Y.B., and Du, Z.L. (2006) Direct observation of photoinduced charge redistribution of WO_3-TiO_2 double layer nanocomposite films by photoassisted Kelvin force microscopy. *Applied Physics Letters*, **88** (21), 212108.
- 79** Zhou, Y., Krumeich, F., Heel, A., and Patzke, G.R. (2010) One-step hydrothermal coating approach to photocatalytically active oxide composites. *Dalton Transactions*, **39** (26), 6043–6048.
- 80** Cao, G., Li, Y., Zhang, Q., and Wang, H. (2010) Synthesis and characterization of $La_2O_3/TiO_{2-x}F_x$ and the visible light photocatalytic oxidation of 4-chlorophenol. *Journal of Hazardous materials*, **178** (1–3), 440–449.
- 81** Lucky, R.A. and Charpentier, P.A. (2010) N-doped ZrO_2/TiO_2 bimetallic materials synthesized in supercritical CO_2 : morphology and photocatalytic activity. *Applied Catalysis B: Environmental*, **96** (3–4), 516–523.
- 82** Li, Y., Ma, M., Wang, X., and Chen, G. (2009) Photocatalytic activity of porous titania nanocrystals prepared by nanoscale permeation process in supercritical CO_2 : effects of supercritical conditions. *Catalysis Communications*, **10** (15), 1985–1989.
- 83** Estruga, M., Domingo, C., Domènech, X., and Ayllón, J.A. (2010) Zirconium-doped and silicon-doped TiO_2 photocatalysts synthesis from ionic-liquid-like precursors. *Journal of Colloid and Interface Science*, **344** (2), 327–333.
- 84** Ghasemi, S., Rahimnejad, S., Setayesh, S.R., Rohani, S., and Gholami, M.R. (2009) Transition metal ions effect on the properties and photocatalytic activity of nanocrystalline TiO_2 prepared in an ionic liquid. *Journal of Hazardous materials*, **172** (2–3), 1573–1578.
- 85** Cong, Y., Zhang, J., Chen, F., and Anpo, M. (2007) Synthesis and characterization of nitrogen-doped TiO_2 nanophotocatalyst with high visible light activity. *Journal of Physical Chemistry C*, **111** (19), 6976–6982.
- 86** Martinez-Ferrero, E., Sakatani, Y., Boissire, C., Grossi, D., Fuertes, A., Fraxedas, J., and Sanchez, C. (2007) Nanostructured titanium oxynitride porous thin films as efficient visible-active photocatalysts. *Advanced Functional Materials*, **17** (16), 3348–3354.
- 87** Fernandez-Garcia, M., Fuerte, A., Hernandez-Alonso, M.D., Soria, J., and Martinez-Arias, A. (2007) Platinization of sunlight active Ti–W mixed oxide photocatalysts. *Journal of Catalysis*, **245** (1), 84–90.
- 88** Wu, J.C.S and Chen, C.H. (2004) A visible-light response vanadium-doped titania nanocatalyst by sol–gel method. *Journal of Photochemistry and Photobiology A: Chemistry*, **163** (3), 509–515.
- 89** Pan, C.C. and Wu, J.C.S. (2006) Visible-light response Cr-doped $TiO_{2-x}N_x$ photocatalysts. *Materials Chemistry and Physics*, **100** (1), 102–107.
- 90** Liu, G., Chen, Z., Dong, C., Zhao, Y., Li, F., Lu, G.Q., and Cheng, H.M. (2006) Visible light photocatalyst: iodine-doped mesoporous titania with a bicrystalline framework. *Journal of Physical Chemistry B*, **110** (42), 20823–20828.
- 91** Hong, X., Wang, Z., Cai, W., Lu, F., Zhang, J., Yang, Y., Ma, N., and Liu, Y. (2005) Visible-light-activated nanoparticle photocatalyst of iodine-doped titanium dioxide. *Chemistry of Materials*, **17** (6), 1548–1552.
- 92** Wu, Y., Zhang, J., Xiao, L., and Chen, F. (2009) Preparation and characterization of TiO_2 photocatalysts by Fe^{3+} doping together with Au deposition for the degradation of organic pollutants. *Applied Catalysis B: Environmental*, **88** (3–4), 525–532.
- 93** Wang, W., Zhang, J., Chen, F., He, D., and Anpo, M. (2008) Preparation and photocatalytic properties of Fe^{3+} -doped

- Ag@TiO₂ core–shell nanoparticles. *Journal of Colloid and Interface Science*, **323** (1), 182–186.
- 94** Kowalska, E., Remita, H., Colbeau-Justin, C., Hupka, J., and Belloni, J. (2008) Modification of titanium dioxide with platinum ions and clusters: application in photocatalysis. *Journal of Physical Chemistry C*, **112** (4), 1124–1131.
- 95** Shamaila, S., Sajjad, A.K.L., Chen, F., and Zhang, J. (2010) Study on highly visible light active Bi₂O₃ loaded ordered mesoporous titania. *Applied Catalysis B: Environmental*, **94** (3–4), 272–280.
- 96** Ji, T., Yang, F., Lv, Y., Zhou, J., and Sun, J. (2009) Synthesis and visible-light photocatalytic activity of Bi-doped TiO₂ nanobelts. *Materials Letters*, **63** (23), 2044–2046.
- 97** Colon, G., Lopez, S.M., Hidalgo, M.C., and Navio, J.A. (2010) Sunlight highly photoactive Bi₂WO₆–TiO₂ heterostructures for Rhodamine B degradation. *Chemical Communications*, **46** (26), 4809–4811.
- 98** Pena, M.E., Korfiatis, G.P., Patel, M., Lippincott, L., and Meng, X. (2005) Adsorption of As(V) and As(III) by nanocrystalline titanium dioxide. *Water Research*, **39** (11), 2327–2337.
- 99** Li, L. and Yan, B. (2009) BiVO₄/Bi₂O₃ submicrometer sphere composite: microstructure and photocatalytic activity under visible-light irradiation. *Journal of Alloys and Compounds*, **476** (1–2), 624–628.
- 100** Yang, Y., Wu, Q., Guo, Y., Hu, C., and Wang, E. (2005) Efficient degradation of dye pollutants on nanoporous polyoxotungstate–anatase composite under visible-light irradiation. *Journal of Molecular Catalysis A: Chemical*, **225** (2), 203–212.
- 101** Cheng, P., Li, W., Zhou, T., Jin, Y., and Gu, M. (2004) Physical and photocatalytic properties of zinc ferrite doped titania under visible light irradiation. *Journal of Photochemistry and Photobiology A: Chemistry*, **168** (1–2), 97–101.
- 102** Mourão, H.A.J.L., Malagutti, A.R., and Ribeiro, C. (2010) Synthesis of TiO₂-coated CoFe₂O₄ photocatalysts applied to the photodegradation of atrazine and Rhodamine B in water. *Appl. Catal. A: Gen.*, **382** (2), 284–292.
- 103** Fu, W., Yang, H., Li, M., Chang, L., Yu, Q., Xu, J., and Zou, G. (2006) Preparation and photocatalytic characteristics of core–shell structure TiO₂/BaFe₁₂O₁₉ nanoparticles. *Materials Letters*, **60** (21–22), 2723–2727.
- 104** Xu, M.W., Bao, S.J., and Zhang, X.G. (2005) Enhanced photocatalytic activity of magnetic TiO₂ photocatalyst by silver deposition. *Materials Letters*, **59** (17), 2194–2198.
- 105** Bayati, M.R., Golestani-Fard, F., and Moshfegh, A.Z. (2010) Visible photodecomposition of methylene blue over micro arc oxidized WO₃-loaded TiO₂ nano-porous layers. *Applied Catalysis A: General*, **382** (2), 322–331.
- 106** Cheng, B., Le, Y., and Yu, J. (2010) Preparation and enhanced photocatalytic activity of Ag@TiO₂ core–shell nanocomposite nanowires. *Journal of Hazardous materials*, **177** (1–3), 971–977.
- 107** Liu, R., Ren, Y., Shi, Y., Zhang, F., Zhang, L., Tu, B., and Zhao, D. (2007) Controlled synthesis of ordered mesoporous C–TiO₂ nanocomposites with crystalline titania frameworks from organic–inorganic–amphiphilic coassembly. *Chemistry of Materials*, **20** (3), 1140–1146.
- 108** Zhang, H., Lv, X., Li, Y., Wang, Y., and Li, J. (2009) P25–graphene composite as a high performance photocatalyst. *ACS Nano*, **4** (1), 380–386.
- 109** Li, X., Gao, Y., Yu, L., and Zheng, L. (2010) Template-free synthesis of CdS hollow nanospheres based on an ionic liquid assisted hydrothermal process and their application in photocatalysis. *Journal of Solid State Chemistry*, **183** (6), 1423–1432.
- 110** Park, H., Lee, Y.C., Choi, B.G., Choi, Y.S., Yang, J.W., and Hong, W.H. (2010) Energy transfer in ionic-liquid-functionalized inorganic nanorods for highly efficient photocatalytic applications. *Small*, **6** (2), 290–295.
- 111** Cao, S.W., Zhu, Y.J., Cheng, G.F., and Huang, Y.H. (2009) ZnFe₂O₄ nanoparticles: microwave–hydrothermal ionic liquid synthesis and photocatalytic property over phenol.

- Journal of Hazardous materials*, **171** (1–3), 431–435.
- 112** Taghvaei, V., Habibi-Yangjeh, A., and Behboudnia, M. (2010) Hydrothermal and template-free preparation and characterization of nanocrystalline ZnS in presence of a low-cost ionic liquid and photocatalytic activity. *Physica E*, **42** (7), 1973–1978.
- 113** Esmaili, M. and Habibi-Yangjeh, A. (2010) Microwave-assisted preparation and characterization of $Zn_{1-x}Cd_xS$ nanoparticles in presence of an ionic liquid and their photocatalytic activities. *Journal of Alloys and Compounds*, **496** (1–2), 650–655.
- 114** Sakthivel, S., Neppolian, B., Shankar, M.V., Arabindoo, B., Palanichamy, M. and Murugesan, V. (2003) Solar photocatalytic degradation of azo dye: comparison of photocatalytic efficiency of ZnO and TiO_2 . *Solar Energy Mater. Solar Cells*, **77** (1), 65–82.
- 115** Kislov, N., Lahiri, J., Verma, H., Goswami, D.Y., Stefanakos, E., and Batzill, M. (2009) Photocatalytic degradation of methyl orange over single crystalline ZnO : orientation dependence of photoactivity and photostability of ZnO . *Langmuir*, **25** (5), 3310–3315.
- 116** McLaren, A., Valdes-Solis, T., Li, G., and Tsang, S.C. (2009) Shape and size effects of ZnO nanocrystals on photocatalytic activity. *Journal of the American Chemical Society*, **131** (35), 12540–12541.
- 117** Zou, C.W., Rao, Y.F., Alyamani, A., Chu, W., Chen, M.J., Patterson, D.A., Emanuelsson, E.A.C., and Gao, W. (2010) Heterogeneous lollipop-like V_2O_5/ZnO array: a promising composite nanostructure for visible light photocatalysis. *Langmuir*, **26** (14), 11615–20.
- 118** Ji, P., Zhang, J., Chen, F., and Anpo, M. (2009) Study of adsorption and degradation of Acid Orange 7 on the surface of CeO_2 under visible light irradiation. *Applied Catalysis B: Environmental*, **85** (3–4), 148–154.
- 119** Solarska, R., Heel, A., Ropka, J., Braun, A., Holzer, L., Ye, J., and Graule, T. (2010) Nanoscale calcium bismuth mixed oxide with enhanced photocatalytic performance under visible light. *Applied Catalysis A: General*, **382** (2), 190–196.
- 120** Hameed, A., Montini, T., Gombac, V., and Fornasiero, P. (2008) Surface phases and photocatalytic activity correlation of Bi_2O_3/Bi_2O_{4-x} nanocomposite. *Journal of the American Chemical Society*, **130** (30), 9658–9659.
- 121** Huang, Y., Ho, W., Lee, S., Zhang, L., Li, G., and Yu, J.C. (2008) Effect of carbon doping on the mesoporous structure of nanocrystalline titanium dioxide and its solar-light-driven photocatalytic degradation of NO_x . *Langmuir*, **24** (7), 3510–3516.
- 122** Yin, S., Ihara, K., Aita, Y., Komatsu, M., and Sato, T. (2006) Visible-light induced photocatalytic activity of $TiO_{2-x}A_y$ ($A = N, S$) prepared by precipitation route. *Journal of Photochemistry and Photobiology A: Chemistry*, **179** (1–2), 105–114.
- 123** Wang, J., Yin, S., Komatsu, M., Zhang, Q., Saito, F., and Sato, T. (2004) Photo-oxidation properties of nitrogen doped $SrTiO_3$ made by mechanical activation. *Applied Catalysis B: Environmental*, **52** (1), 11–21.
- 124** Li, D., Haneda, H., Hishita, S., and Ohashi, N. (2005) Visible-light-driven nitrogen-doped TiO_2 photocatalysts: effect of nitrogen precursors on their photocatalysis for decomposition of gas-phase organic pollutants. *Materials Science and Engineering B*, **117** (1), 67–75.
- 125** Maira, A.J., Yeung, K.L., Lee, C.Y., Yue, P.L., and Chan, C.K. (2000) Size effects in gas-phase photo-oxidation of trichloroethylene using nanometer-sized TiO_2 catalysts. *Journal of Catalysis*, **192** (1), 185–196.
- 126** Fresno, F., Coronado, J.M., Tudela, D., and Soria, J. (2005) Influence of the structural characteristics of $Ti_{1-x}Sn_xO_2$ nanoparticles on their photocatalytic activity for the elimination of methylcyclohexane vapors. *Applied Catalysis B: Environmental*, **55** (3), 159–167.
- 127** Yu, J. and Zhang, J. (2010) A simple template-free approach to TiO_2 hollow spheres with enhanced photocatalytic activity. *Dalton Transactions*, **39** (25), 5860–5867.
- 128** Li, Y. and Kim, S.J. (2005) Synthesis and characterization of nano titania particles

- embedded in mesoporous silica with both high photocatalytic activity and adsorption capability. *Journal of Physical Chemistry B*, **109** (25), 12309–12315.
- 129** Li, F.B., Li, X.Z., Ao, C.H., Lee, S.C., and Hou, M.F. (2005) Enhanced photocatalytic degradation of VOCs using $\text{Ln}^{3+}-\text{TiO}_2$ catalysts for indoor air purification. *Chemosphere*, **59** (6), 787–800.
- 130** Ikeda, S., Kobayashi, H., Ikoma, Y., Harada, T., Yamazaki, S., and Matsumura, M. (2009) Structural effects of titanium(IV) oxide encapsulated in a hollow silica shell on photocatalytic activity for gas-phase decomposition of organics. *Applied Catalysis A: General*, **369** (1–2), 113–118.
- 131** Zhang, X. and Liu, Q. (2008) Visible-light-induced degradation of formaldehyde over titania photocatalyst co-doped with nitrogen and nickel. *Applied Surface Science*, **254** (15), 4780–4785.
- 132** Demeestere, K., Dewulf, J., Ohno, T., Salgado, P.H., and Van Langenhove, H. (2005) Visible light mediated photocatalytic degradation of gaseous trichloroethylene and dimethyl sulfide on modified titanium dioxide. *Applied Catalysis B: Environmental*, **61** (1–2), 140–149.
- 133** Kuo, C.S., Tseng, Y.H., Huang, C.H., and Li, Y.Y. (2007) Carbon-containing nano-titania prepared by chemical vapor deposition and its visible-light-responsive photocatalytic activity. *Journal of Molecular Catalysis A: Chemical*, **270** (1–2), 93–100.
- 134** Portela, R., Suárez, S., Rasmussen, S.B., Arconada, N., Castro, Y., Durán, A., Ávila, P., Coronado, J.M., and Sánchez, B. (2010) Photocatalytic-based strategies for H_2S elimination. *Catalysis Today*, **151** (1–2), 64–70.
- 135** Fernández, P., Blanco, J., Sichel, C., and Malato, S. (2005) Water disinfection by solar photocatalysis using compound parabolic collectors. *Catalysis Today*, **101** (3–4), 345–352.
- 136** Dalrymple, O.K., Stefanakos, E., Trotz, M.A., and Goswami, D.Y. (2010) A review of the mechanisms and modeling of photocatalytic disinfection. *Appl. Catal. B: Environ.*, **98** (1–2), 27–38.
- 137** Maness, P.C., Smolinski, S., Blake, D.M., Huang, Z., Wolfrum, E.J., and Jacoby, W.A. (1999) Bactericidal activity of photocatalytic TiO_2 reaction: toward an understanding of its killing mechanism. *Applied and Environment Microbiology*, **65** (9), 4094–4098.
- 138** Chen, F., Yang, X., Xu, F., Wu, Q., and Zhang, Y. (2009) Correlation of photocatalytic bactericidal effect and organic matter degradation of TiO_2 . Part I: observation of phenomena. *Environmental Science and Technology*, **43** (4), 1180–1184.
- 139** Cho, M., Chung, H., Choi, W., and Yoon, J. (2005) Different inactivation behaviors of MS-2 phage and *Escherichia coli* in TiO_2 photocatalytic disinfection. *Applied and Environment Microbiology*, **71** (1), 270–275.
- 140** Rincón, A.G., and Pulgarín, C. (2004) Effect of pH, inorganic ions, organic matter and H_2O_2 on *E. coli* K12 photocatalytic inactivation by TiO_2 : implications in solar water disinfection. *Applied Catalysis B: Environmental*, **51** (4), 283–302.
- 141** Benabbou, A.K., Derriche, Z., Felix, C., Lejeune, P., and Guillard, C. (2007) Photocatalytic inactivation of *Escherichia coli*: effect of concentration of TiO_2 and microorganism, nature, and intensity of UV irradiation. *Appl. Catal. B: Environ.*, **76** (3–4), 257–263.
- 142** Fernández-Ibáñez, P., Sichel, C., Polo-López, M.I., de Cara-García, M., and Tello, J.C. (2009) Photocatalytic disinfection of natural well water contaminated by *Fusarium solani* using TiO_2 slurry in solar CPC photo-reactors. *Catalysis Today*, **144** (1–2), 62–68.
- 143** Prasad, G.K., Agarwal, G.S., Singh, B., Rai, G.P., and Vijayaraghavan, R. (2009) Photocatalytic inactivation of *Bacillus anthracis* by titania nanomaterials. *Journal of Hazardous materials*, **165** (1–3), 506–510.
- 144** Ryu, H., Gerrity, D., Crittenden, J.C., and Abbaszadegan, M. (2008) Photocatalytic inactivation of *Cryptosporidium parvum* with TiO_2 and low-pressure ultraviolet irradiation. *Water Research*, **42** (6–7), 1523–1530.
- 145** Pratap Reddy, M., Phil, H.H., and Subrahmanyam, M. (2008) Photocatalytic

- disinfection of *Escherichia coli* over titanium(IV) oxide supported on H β zeolite. *Catalysis Letters*, **123** (1–2), 56–64.
- 146** van Grieken, R., Marugán, J., Sordo, C., Martínez, P., and Pablos, C. (2009) Photocatalytic inactivation of bacteria in water using suspended and immobilized silver-TiO₂. *Applied Catalysis B: Environmental*, **93** (1–2), 112–118.
- 147** Pratap Reddy, M., Venugopal, A., and Subrahmanyam, M. (2007) Hydroxyapatite-supported Ag-TiO₂ as *Escherichia coli* disinfection photocatalyst. *Water Research*, **41** (2), 379–386.
- 148** Vohra, A., Goswami, D.Y., Deshpande, D.A., and Block, S.S. (2006) Enhanced photocatalytic disinfection of indoor air. *Applied Catalysis B: Environmental*, **64** (1–2), 57–65.
- 149** Zhang, L.S., Wong, K.H., Yip, H.Y., Hu, C., Yu, J.C., Chan, C.Y., and Wong, P.K. (2010) Effective photocatalytic disinfection of *E. coli* K-12 using AgBr-A-Bi₂WO₆ nanojunction system irradiated by visible light: the role of diffusing hydroxyl radicals. *Environmental Science and Technology*, **44** (4), 1392–1398.
- 150** Wu, P., Xie, R., Imlay, J.A., and Shang, J.K. (2009) Visible-light-induced photocatalytic inactivation of bacteria by composite photocatalysts of palladium oxide and nitrogen-doped titanium oxide. *Applied Catalysis B: Environmental*, **88** (3–4), 576–581.
- 151** Li, Q., Li, Y.W., Wu, P., Xie, R., and Shang, J.K. (2008) Palladium oxide nanoparticles on nitrogen-doped titanium oxide: accelerated photocatalytic disinfection and post-illumination catalytic “memory”. *Advanced Materials*, **20** (19), 3717–3723.
- 152** Li, Q., Xie, R., Li, Y.W., Mintz, E.A., and Shang, J.K. (2007) Enhanced visible-light-induced photocatalytic disinfection of *E. coli* by carbon-sensitized nitrogen-doped titanium oxide. *Environmental Science and Technology*, **41** (14), 5050–5056.
- 153** Rincón, A.G., and Pulgarín, C. (2006) Comparative evaluation of Fe³⁺ and TiO₂ photoassisted processes in solar photocatalytic disinfection of water. *Applied Catalysis B: Environmental*, **63** (3–4), 222–231.
- 154** Yu, J.C., Ho, W., Yu, J., Yip, H., Wong, P.K., and Zhao, J. (2005) Efficient visible-light-induced photocatalytic disinfection on sulfur-doped nanocrystalline titania. *Environmental Science and Technology*, **39** (4), 1175–1179.
- 155** O'Regan, B., and Grätzel, M. (1991) A low-cost, high-efficiency solar cell based on dye-sensitized colloidal TiO₂ films. *Nature*, **353** (6346), 737–740.
- 156** Grätzel, M. (2005) Solar energy conversion by dye-sensitized photovoltaic cells. *Inorganic Chemistry*, **44** (20), 6841–6851.
- 157** Li, B., Wang, L., Kang, B., Wang, P., and Qiu, Y. (2006) Review of recent progress in solid-state dye-sensitized solar cells. *Solar Energy Materials & Solar Cells*, **90** (5), 549–573.
- 158** Fujishima, A. and Honda, K. (1971) Electrochemical evidence for the mechanism of the primary stage of photosynthesis. *Bulletin of the Chemical Society of Japan*, **44** (4), 1148–1150.
- 159** Sato, S. and White, J.M. (1980) Photodecomposition of water over Pt/TiO₂ catalysts. *Chemical Physics Letters*, **72** (1), 83–86.
- 160** Kitano, M., Tsujimaru, K., and Anpo, M. (2008) Hydrogen production using highly active titanium oxide-based photocatalysts. *Topics in Catalysis*, **49** (1–2), 4–17.
- 161** Abe, R., Sayama, K., Domen, K., and Arakawa, H. (2001) A new type of water splitting system composed of two different TiO₂ photocatalysts (anatase, rutile) and a IO₃⁻/I⁻ shuttle redox mediator. *Chemical Physics Letters*, **344** (3–4), 339–344.
- 162** Li, Y., Ma, G., Peng, S., Lu, G., and Li, S. (2008) Boron and nitrogen co-doped titania with enhanced visible-light photocatalytic activity for hydrogen evolution. *Applied Surface Science*, **254** (21), 6831–6836.
- 163** Yang, H., Guo, L., Yan, W., and Liu, H. (2006) A novel composite photocatalyst for water splitting hydrogen production. *Journal of Power Sources*, **159** (2), 1305–1309.
- 164** Sasikala, R., Shirole, A.R., Sudarsan, V., Jagannath Sudakar, C., Naik, R., Rao, R., and Bharadwaj, S.R. (2010) Enhanced photocatalytic activity of indium and nitrogen co-doped TiO₂-Pd

- nano composites for hydrogen generation. *Applied Catalysis A: General*, **377** (1–2), 47–54.
- 165** Sasikala, R., Sudarsan, V., Sudakar, C., Naik, R., Sakuntala, T., and Bharadwaj, S.R. (2008) Enhanced photocatalytic hydrogen evolution over nanometer sized Sn and Eu doped titanium oxide. *International Journal of Hydrogen Energy*, **33** (19), 4966–4973.
- 166** Peng, S., Li, Y., Jiang, F., Lu, G., and Li, S. (2004) Effect of Be^{2+} doping TiO_2 on its photocatalytic activity. *Chemical Physics Letters*, **398** (1–3), 235–239.
- 167** Bamwenda, G.R., Tsubota, S., Nakamura, T., and Haruta, M. (1995) Photoassisted hydrogen production from a water–ethanol solution: a comparison of activities of $\text{Au}-\text{TiO}_2$ and $\text{Pt}-\text{TiO}_2$. *Journal of Photochemistry and Photobiology A: Chemistry*, **89** (2), 177–189.
- 168** Daskalaki, V.M. and Kondarides, D.I. (2009) Efficient production of hydrogen by photo-induced reforming of glycerol at ambient conditions. *Catalysis Today*, **144** (1–2), 75–80.
- 169** Sivasamy, A., Cheah, K.Y., Fornasiero, P., Kemausuor, F., Zinoviev, S., and Miertus, S. (2009) Catalytic applications in the production of biodiesel from vegetable oils. *ChemSusChem*, **2** (4), 278–300.
- 170** Fu, X., Long, J., Wang, X., Leung, D.Y.C., Ding, Z., Wu, L., Zhang, Z., Li, Z., and Fu, X. (2008) Photocatalytic reforming of biomass: a systematic study of hydrogen evolution from glucose solution. *International Journal of Hydrogen Energy*, **33** (22), 6484–6491.
- 171** Patsoura, A., Kondarides, D.I., and Verykios, X.E. (2007) Photocatalytic degradation of organic pollutants with simultaneous production of hydrogen. *Catalysis Today*, **124** (3–4), 94–102.
- 172** Patsoura, A., Kondarides, D.I., and Verykios, X.E. (2006) Enhancement of photoinduced hydrogen production from irradiated Pt/TiO_2 suspensions with simultaneous degradation of azo-dyes. *Applied Catalysis B: Environmental*, **64** (3–4), 171–179.
- 173** Strataki, N., Bekiari, V., Kondarides, D.I., and Lianos, P. (2007) Hydrogen production by photocatalytic alcohol reforming employing highly efficient nanocrystalline titania films. *Applied Catalysis B: Environmental*, **77** (1–2), 184–189.
- 174** Stodolny, M. and Laniecki, M. (2009) Synthesis and characterization of mesoporous $\text{Ta}_2\text{O}_5-\text{TiO}_2$ photocatalysts for water splitting. *Catalysis Today*, **142** (3–4), 314–319.
- 175** Maeda, K., Terashima, H., Kase, K., and Domen, K. (2009) Nanoparticulate precursor route to fine particles of TaON and ZrO_2-TaON solid solution and their photocatalytic activity for hydrogen evolution under visible light. *Applied Catalysis A: General*, **357** (2), 206–212.
- 176** Xu, S. and Sun, D.D. (2009) Significant improvement of photocatalytic hydrogen generation rate over TiO_2 with deposited CuO . *International Journal of Hydrogen Energy*, **34** (15), 6096–6104.
- 177** Yoong, L.S., Chong, F.K., and Dutta, B.K. (2009) Development of copper-doped TiO_2 photocatalyst for hydrogen production under visible light. *Energy*, **34** (10), 1652–1661.
- 178** Bandara, J., Udawatta, C.P.K., and Rajapakse, C.S.K. (2005) Highly stable CuO incorporated TiO_2 catalyst for photocatalytic hydrogen production from H_2O . *Photochemical & Photobiological Sciences*, **4** (11), 857–861.
- 179** Gombac, V., Sordelli, L., Montini, T., Delgado, J.J., Adamski, A., Adami, G., Cargnello, M., Bernal, S., and Fornasiero, P. (2010) $\text{CuO}_x-\text{TiO}_2$ photocatalysts for H_2 production from ethanol and glycerol solutions. *Journal of Physical Chemistry A*, **114** (11), 3916–3925.
- 180** Barreca, D., Fornasiero, P., Gasparotto, A., Gombac, V., Maccato, C., Montini, T., and Tondello, E. (2009) The potential of supported Cu_2O and CuO nanosystems in photocatalytic H_2 production. *ChemSusChem*, **2** (3), 230–233.
- 181** Jing, D., Zhang, Y., and Guo, L. (2005) Study on the synthesis of Ni doped mesoporous TiO_2 and its photocatalytic activity for hydrogen evolution in aqueous methanol solution. *Chemical Physics Letters*, **415** (1–3), 74–78.
- 182** Zou, Z., Ye, J., Sayama, K., and Arakawa, H. (2001) Direct splitting of water under visible light irradiation with an oxide

- semiconductor photocatalyst. *Nature*, **414** (6864), 625–627.
- 183** Khan, M.A. and Yang, O.B. (2009) Photocatalytic water splitting for hydrogen production under visible light on Ir and Co ionized titania nanotube. *Catalysis Today*, **146** (1–2), 177–182.
- 184** Dholam, R., Patel, N., Adami, M., and Miotello, A. (2009) Hydrogen production by photocatalytic water-splitting using Cr- or Fe-doped TiO_2 composite thin films photocatalyst. *International Journal of Hydrogen Energy*, **34** (13), 5337–5346.
- 185** Sasikala, R., Shirole, A., Sudarsan, V., Sakuntala, T., Sudakar, C., Naik, R., and Bharadwaj, S.R. (2009) Highly dispersed phase of SnO_2 on TiO_2 nanoparticles synthesized by polyol-mediated route: photocatalytic activity for hydrogen generation. *International Journal of Hydrogen Energy*, **34** (9), 3621–3630.
- 186** Li, C., Yuan, J., Han, B., Jiang, L., and Shangguan, W. (2010) TiO_2 nanotubes incorporated with CdS for photocatalytic hydrogen production from splitting water under visible light irradiation. *International Journal of Hydrogen Energy*, **35** (13), 7073–7079.
- 187** Jang, J.S., Li, W., Oh, S.H., and Lee, J.S. (2006) Fabrication of CdS/ TiO_2 nano-bulk composite photocatalysts for hydrogen production from aqueous H_2S solution under visible light. *Chemical Physics Letters*, **425** (4–6), 278–282.
- 188** Jing, D. and Guo, L. (2007) WS_2 sensitized mesoporous TiO_2 for efficient photocatalytic hydrogen production from water under visible light irradiation. *Catalysis Communications*, **8** (5), 795–799.
- 189** Kapoor, M.P., Inagaki, S., and Yoshida, H. (2005) Novel zirconium–titanium phosphates mesoporous materials for hydrogen production by photoinduced water splitting. *Journal of Physical Chemistry B*, **109** (19), 9231–9238.
- 190** Centi, G. and van Santen, R.A. (2007) *Catalysis for Renewables: from Feedstock to Energy Production*, Wiley-VCH Verlag GmbH, Weinheim.
- 191** Bambagioni, V., Bevilacqua, M., Bianchini, C., Filippi, J., Lavacchi, A., Marchionni, A., Vizza, F., and Shen, P.K. (2010) Self-sustainable production of hydrogen, chemicals, and energy from renewable alcohols by electrocatalysis. *ChemSusChem*, **3** (7), 851–855.
- 192** Bianchini, C. and Shen, P.K. (2009) Palladium-based electrocatalysts for alcohol oxidation in half cells and in direct alcohol fuel cells. *Chemical Reviews*, **109** (9), 4183–4206.
- 193** Lamy, C., Coutanceau, C., and Leger, J.-M. (2009) The direct ethanol fuel cell: a challenge to convert bioethanol cleanly into electric energy, in *Catalysis for Sustainable Energy Production*, (eds P. Barbaro and C. Bianchini), Wiley-VCH Verlag GmbH, Weinheim, pp. 3–46.
- 194** Ampelli, C., Centi, G., Passalacqua, R., and Perathoner, S. (2010) Synthesis of solar fuels by a novel photoelectrocatalytic approach. *Energy & Environmental Science*, **3** (3), 292–301.
- 195** Chu, D., Wang, S., Zheng, P., Wang, J., Zha, L., Hou, Y., He, J., Xiao, Y., Lin, H., and Tian, Z. (2009) Anode catalysts for direct ethanol fuel cells utilizing directly solar light illumination. *ChemSusChem*, **2** (2), 171–176.
- 196** Seger, B. and Kamat, P.V. (2009) Fuel cell geared in reverse: photocatalytic hydrogen production using a TiO_2 /Nafion/Pt membrane assembly with no applied bias. *Journal of Physical Chemistry*, **113** (43), 18946–18952.
- 197** Drew, K., Girishkumar, G., Vinodgopal, K., and Kamat, P.V. (2005) Boosting fuel cell performance with a semiconductor photocatalyst: TiO_2 /Pt–Ru hybrid catalyst for methanol oxidation. *Journal of Physical Chemistry B*, **109** (24), 11851–11857.
- 198** Park, K.W., Han, S.B., and Lee, J.M. (2007) Photo(UV)-enhanced performance of Pt– TiO_2 nanostructure electrode for methanol oxidation. *Electrochemistry Communications*, **9** (7), 1578–1581.
- 199** Mohapatra, S.K., Raja, K.S., Mahajan, V.K., and Misra, M. (2008) Efficient photoelectrolysis of water using TiO_2 nanotube arrays by minimizing recombination losses with organic additives. *Journal of Physical Chemistry C*, **112** (29), 11007–11012.
- 200** Wang, M., Guo, D.J., and Li, H.L. (2005) High activity of novel Pd/ TiO_2 nanotube

- catalysts for methanol electro-oxidation. *Journal of Solid State Chemistry*, **178** (6), 1996–2000.
- 201** Song, H., Qiu, X., Guo, D., and Li, F. (2008) Role of structural H₂O in TiO₂ nanotubes in enhancing Pt/C direct ethanol fuel cell anode electro-catalysts. *Journal of Power Sources*, **178** (1), 97–102.
- 202** Muhamad, E.N., Takeguchi, T., Wang, G., Anzai, Y., and Ueda, W. (2009) Electrochemical characteristics of Pd anode catalyst modified with TiO₂ nanoparticles in polymer electrolyte fuel cell. *Journal of the Electrochemical Society*, **156** (1), B32–B37.
- 203** Fu, Y., Wei, Z.D., Chen, S.G., Li, L., Feng, Y.C., Wang, Y.Q., Ma, X.L., Liao, M.J., Shen, P.K., and Jiang, S.P. (2009) Synthesis of Pd/TiO₂ nanotubes/Ti for oxygen reduction reaction in acidic solution. *Journal of Power Sources*, **189** (2), 982–987.
- 204** Selvarani, G., Maheswari, S., Sridhar, P., Pitchumani, S., and Shukla, A.K. (2009) Carbon-supported Pt-TiO₂ as a methanol-tolerant oxygen-reduction catalyst for DMFCs. *Journal of the Electrochemical Society*, **156** (11), B1354–B1360.
- 205** Liu, X., Chen, J., Liu, G., Zhang, L., Zhang, H., and Yi, B. (2010) Enhanced long-term durability of proton exchange membrane fuel cell cathode by employing Pt/TiO₂/C catalysts. *Journal of Power Sources*, **195** (13), 4098–4103.
- 206** Shim, J., Lee, C.R., Lee, H.K., Lee, J.S., and Cairns, E.J. (2001) Electrochemical characteristics of Pt-WO₃/C and Pt-TiO₂/C electrocatalysts in a polymer electrolyte fuel cell. *Journal of Power Sources*, **102** (1–2), 172–177.
- 207** Xiong, L. and Manthiram, A. (2004) Synthesis and characterization of methanol tolerant Pt/TiO_x/C nanocomposites for oxygen reduction in direct methanol fuel Cells. *Electrochimica Acta*, **49** (24), 4163–4170.
- 208** Balzani, V., Credi, A., and Venturi, M. (2008) Photochemical conversion of solarenergy. *ChemSusChem*, **1** (1–2), 26–58.
- 209** Balzani, V., Credi, A., and Venturi, M. (1997) Photoprocesses. *Current Opinion in Chemical Biology*, **1** (4), 506–513.
- 210** Gust, D., Moore, T.A., and Moore, A.L. (2001) Mimicking photosynthetic solar energy transduction. *Accounts of Chemical Research*, **34** (1), 40–48.
- 211** Bard, A.J. and Fox, M.A. (1995) Artificial photosynthesis: solar splitting of water to hydrogen and oxygen. *Accounts of Chemical Research*, **28** (3), 141–145.
- 212** Imahori, H., Mori, Y., and Matano, Y. (2003) Nanostructured artificial photosynthesis. *Journal of Photochemistry and Photobiology C: Photochemistry Reviews*, **4** (1), 51–83.
- 213** Inoue, T., Fujishima, A., Konishi, S., and Honda, K. (1979) Photoelectrocatalytic reduction of carbon dioxide in aqueous suspensions of semiconductor powers. *Nature*, **277** (5698), 637–638.
- 214** Hirano, K., Inoue, K., and Yatsu, T. (1992) Photocatalysed reduction of CO₂ in aqueous TiO₂ suspension mixed with copper powder. *Journal of Photochemistry and Photobiology A: Chemistry*, **64** (2), 255–258.
- 215** Adachi, K., Ohta, K., and Mizuno, T. (1994) Photocatalytic reduction of carbon dioxide to hydrocarbon using copper-loaded titanium dioxide. *Solar Energy*, **53** (2), 187–190.
- 216** Kocí, K., Obalová, L., and Lacný, Z. (2008) Photocatalytic reduction of CO₂ over TiO₂ based catalysts. *Chemical Papers*, **62** (6), 1–9.
- 217** Anpo, M., Yamashita, H., Ichihashi, Y., and Ehara, S. (1995) Photocatalytic reduction of CO₂ with H₂O on various titanium oxide catalysts. *Journal of Electroanalytical Chemistry*, **396** (1–2), 21–26.
- 218** Lin, W. and Frei, H. (2005) Photochemical CO₂ splitting by metal-to-metal charge-transfer excitation in mesoporous ZrCu (I)-MCM-41 silicate sieve. *Journal of the American Chemical Society*, **127** (6), 1610–1611.
- 219** Yang, C.C., Yu, Y.H., van der Linden, B., Wu, J.C.S., and Mul, G. (2010) Artificial photosynthesis over crystalline TiO₂-based catalysts: fact or fiction? *Journal of the American Chemical Society*, **132** (24), 8398–8406.
- 220** Zhou, H., Li, X., Fan, T., Osterloh, F.E., Ding, J., Sabio, E.M., Zhang, D., and Guo, Q. (2010) Artificial inorganic leafs for efficient photochemical hydrogen production inspired by natural

- photosynthesis. *Advanced Materials*, **22** (9), 951–956.
- 221** Fagnoni, M., Dondi, D., Ravelli, D., and Albini, A. (2007) Photocatalysis for the formation of the C–C bond. *Chemical Reviews*, **107** (6), 2725–2756.
- 222** Corma, A. and Garcia, H. (2004) Zeolite-based photocatalysts. *Chemical Communications* (13), 1443–1459.
- 223** Anpo, M. and Thomas, J.M. (2006) Single-site photocatalytic solids for the decomposition of undesirable molecules. *Chemical Communications*, (31), 3273–3278.
- 224** Shchukin, D.G. and Sviridov, D.V. (2006) Photocatalytic processes in spatially confined micro- and nanoreactors. *Journal of Photochemistry and Photobiology C: Photochemistry Reviews*, **7** (1), 23–39.
- 225** Chen, J., Eberlein, L., and Langford, C.H. (2002) Pathways of phenol and benzene photooxidation using TiO_2 supported on a zeolite. *Journal of Photochemistry and Photobiology A: Chemistry*, **148** (1–3), 183–189.
- 226** Shiraishi, Y., Saito, N., and Hirai, T. (2005) Adsorption-driven photocatalytic activity of mesoporous titanium dioxide. *Journal of the American Chemical Society*, **127** (37), 12820–12822.
- 227** Shiraishi, Y., Sugano, Y., Inoue, D., and Hirai, T. (2009) Effect of substrate polarity on photocatalytic activity of titanium dioxide particles embedded in mesoporous silica. *Journal of Catalysis*, **264** (2), 175–182.
- 228** Palmisano, G., Addamo, M., Augugliaro, V., Caronna, T., García-López, E., Loddo, V., and Palmisano, L. (2006) Influence of the substituent on selective photocatalytic oxidation of aromatic compounds in aqueous TiO_2 suspensions. *Chemical Communications* (9), 1012–1014.
- 229** Matos, J., Garcia, A., Cordero, T., Chovelon, J.M., and Ferronato, C. (2009) Eco-friendly TiO_2 -AC photocatalyst for the selective photooxidation of 4-chlorophenol. *Catalysis Letters*, **130** (3–4), 568–574.
- 230** Gonzalez, M.A., Howell, S.G., and Sikdar, S.K. (1999) Photocatalytic selective oxidation of hydrocarbons in the aqueous phase. *Journal of Catalysis*, **183** (1), 159–162.
- 231** Palmisano, G., Yurdakal, S., Augugliaro, V., Loddo, V., and Palmisano, L. (2007) Photocatalytic selective oxidation of 4-methoxybenzyl alcohol to aldehyde in aqueous suspension of home-prepared titanium dioxide catalyst. *Advanced Synthesis and Catalysis*, **349** (6), 964–970.
- 232** Pillai, U.R. and Sahle-Demessie, E. (2002) Selective oxidation of alcohols in gas phase using light-activated titanium dioxide. *Journal of Catalysis*, **211** (2), 434–444.
- 233** Li, X. and Kotal, C. (2002) Photocatalytic selective epoxidation of styrene by molecular oxygen over highly dispersed titanium dioxide species on silica. *Journal of Materials Science Letters*, **21** (19), 1525–1527.
- 234** Shiraishi, Y., Morishita, M., and Hirai, T. (2005) Acetonitrile-assisted highly selective photocatalytic epoxidation of olefins on Ti-containing silica with molecular oxygen. *Chemical Communications* (48), 5977–5979.
- 235** Soana, F., Sturini, M., Cermenati, L., and Albini, A. (2000) Titanium dioxide photocatalyzed oxygenation of naphthalene and some of its derivatives. *Journal of the Chemical Society, Perkin Transactions 2*, **2** (4), 699–704.
- 236** Higashida, S., Harada, A., Kawakatsu, R., Fujiwara, N., and Matsumura, M. (2006) Synthesis of a coumarin compound from phenanthrene by a TiO_2 -photocatalyzed reaction. *Chemical Communications*, (26), 2804–2806.
- 237** Brezová, V., Blazková, A., Surina, I., and Havlínová, B. (1997) Solvent effect on the photocatalytic reduction of 4-nitrophenol in titanium dioxide suspensions. *Journal of Photochemistry and Photobiology A: Chemistry*, **107** (1–3), 233–237.
- 238** Ferry, J.L. and Glaze, W.H. (1998) Photocatalytic reduction of nitro organics over illuminated titanium dioxide: role of the TiO_2 surface. *Langmuir*, **14** (13), 3551–3555.
- 239** Maldotti, A., Andreotti, L., Molinari, A., Tollari, S., Penoni, A., and Cenini, S. (2000) Photochemical and photocatalytic reduction of nitrobenzene in the presence of cyclohexene. *Journal of Photochemistry and Photobiology A: Chemistry*, **133** (1–2), 129–133.
- 240** Wang, H., Yan, J., Chang, W., and Zhang, Z. (2009) Practical synthesis of aromatic amines by photocatalytic reduction of aromatic nitro compounds on nanoparticles N-doped TiO_2 . *Catalysis Communications*, **10** (6), 989–994.

- 241 Kaneko, S., Shimizu, Y., Ohta, K., and Mizuno, T. (1998) Photocatalytic reduction of high pressure carbon dioxide using TiO₂ powders with a positive hole scavenger. *Journal of Photochemistry and Photobiology A: Chemistry*, **115** (3), 223–226.
- 242 Yahaya, A.H., Gondal, M.A., and Hameed,A.A. (2004) Selective laser enhanced photocatalytic conversion of CO₂ into methanol. *Chemical Physics Letters*, **400** (1–3), 206–212.
- 243 Tseng, I.H., Chang, W.C., and Wu, J.C.S. (2002) Photoreduction of CO₂ using sol-gel derived titania and titania-supported copper catalysts. *Applied Catalysis B: Environmental*, **37** (1), 37–48.
- 244 Tseng, I.H., Wu, J.C.S., and Chou, H.Y. (2004) Effects of sol-gel procedures on the photocatalysis of Cu/TiO₂ in CO₂ photoreduction. *Journal of Catalysis*, **221** (2), 432–440.
- 245 Ikeue, K., Yamashita, H., and Anpo, M. (1999) Photocatalytic reduction of CO₂ with H₂O on titanium oxides prepared within the FSM-16 mesoporous zeolite. *Chemistry Letters*, **28** (11), 1135–1136.
- 246 Ikeue, K., Nozaki, S., Ogawa, M., and Anpo, M. (2002) Characterization of self-standing Ti-containing porous silica thin films and their reactivity for the photocatalytic reduction of CO₂ with H₂O. *Catalysis Today*, **74** (3–4), 241–248.
- 247 Shioya, Y., Ikeue, K., Ogawa, M., and Anpo, M. (2003) Synthesis of transparent Ti-containing mesoporous silica thin film materials and their unique photocatalytic activity for the reduction of CO₂ with H₂O. *Applied Catalysis A: General*, **254** (2), 251–259.
- 248 Rao, K.V.S., Srinivas, B., Subrahmanyam, M., and Prasad, A.R. (2000) A novel one step photocatalytic synthesis of dihydropyrazine from ethylenediamine and propylene glycol. *Chemical Communications* (16), 1533–1534.
- 249 Ohtani, B., Iwai, K., Kominami, H., Matsuura, T., Kera, Y., and Nishimoto, S. (1995) Titanium(IV) oxide photocatalyst of ultra-high activity for selective N-cyclization of an amino acid in aqueous suspensions. *Chemical Physics Letters*, **242** (3), 315–319.
- 250 Marinkovic, S. and Hoffmann, N. (2004) Diastereoselective radical tandem addition–cyclization reactions of aromatic tertiary amines by semiconductor-sensitized photochemical electron transfer. *European Journal of Organic Chemistry* (14), 3102–3107.
- 251 Wolinsky, H. (2006) Nanoregulation: a recent scare involving nanotech products reveals that the technology is not yet properly regulated. *EMBO Rep.*, **7** (9), 858–861.
- 252 Long, T.C., Saleh, N., Tilton, R.D., Lowry, G.V., and Veronesi, B. (2006) Titanium dioxide (P25) produces reactiveoxygen species in immortalizedbrain microglia (BV2): implications for nanoparticle neurotoxicity. *Environmental Science and Technology*, **40** (14), 4346–4352.
- 253 Oberdörster, G., Oberdörster, E., and Oberdörster, J. (2007) Concepts of nanoparticle dose metric and response metric. *Environmental Health Perspectives*, **115** (6), A290.
- 254 Klaine, S.J., Alvarez, P.J.J., Batley, G.E., Fernandes, T.F., Handy, R.D., Lyon, D.Y., Mahendra, S., McLaughlin, M.J., and Lead, J.R. (2008) Nanomaterials in the environment: behavior, fate, bioavailability, and effects. *Environmental Toxicology and Chemistry*, **27** (9), 1825–1851.
- 255 Handy, R.D., Henry, T.B., Scown, T.M., Johnston, B.D., and Tyler, C.R. (2008) Manufactured nanoparticles: their uptake and effects on fish – a mechanistic analysis. *Ecotoxicology*, **17** (5), 396–409.
- 256 Pulskamp, K., Diabaté, S., and Krug, H.F. (2007) Carbon nanotubes show no sign of acute toxicity but induce intracellular reactive oxygen species in dependence on contaminants. *Toxicology Letters*, **168** (1), 58–74.
- 257 Müller, K., Skepper, J.N., Posfai, M., Trivedi, R., Howarth, S., Corot, C., Lancelot, E., Thompson, P.W., Brown, A.P., and Gillard, J.H. (2007) Effect of ultrasmall superparamagnetic iron oxide nanoparticles (Ferumoxtran-10) on human monocyte-macrophages *invitro*. *Biomaterials*, **28** (9), 1629–1642.
- 258 Helland, A., Wick, P., Koehler, A., Schmid, K., and Som, C. (2007) Reviewing the environmental and human health knowledge base of carbon nanotubes. *Environmental Health Perspectives*, **115** (8), 1125–1131.

- 259** Hurt, R.H., Monthioux, M., and Kane, A. (2006) Toxicology of carbon nanomaterials: status, trends, and perspectives on the special issue. *Carbon*, **44** (6), 1028–1033.
- 260** Murr, L.E., Garza, K.M., Soto, K.F., Carrasco, A., Powell, T.G., Ramirez, D.A., Guerrero, P.A., Lopez, D.A., and VenzorIII, J. (2005) Cytotoxicity assessment of some carbon nanotubes and related carbon nanoparticle aggregates and the implications for anthropogenic carbon nanotube aggregates in the environment. *International Journal of Environmental Research and Public Health*, **2** (1), 31–42.
- 261** Shvedova, A.A., Castranova, V., Kisin, E.R., Schwegler-Berry, D., Murray, A.R., Gandelsman, V.Z., Maynard, A., and Baron, P. (2003) Exposure to carbon nanotube material: assessment of nanotube cytotoxicity using human keratinocyte cells. *Journal of Toxicology and Environmental Health, Part A: Current Issues*, **66** (20), 1909–1926.
- 262** Donaldson, K., Tran, L., Jimenez, L.A., Duffin, R., Newby, D.E., Mills, N., MacNee, W., and Stone, V. (2005) Combustion-derived nanoparticles: a review of their toxicology following inhalation exposure. *Particle and Fibre Toxicology* (2), 10.
- 263** Connor, E.E., Mwamuka, J., Gole, A., Murphy, C.J., and Wyatt, M.D. (2005) Gold nanoparticles are taken up by human cells but do not cause acute cytotoxicity. *Small*, **1** (3), 325–327.
- 264** Lewinski, N., Colvin, V., and Drezek, R. (2008) Cytotoxicity of nanoparticles. *Small*, **4** (1), 26–49.
- 265** Hardman, R. (2006) A toxicologic review of quantum dots: toxicity depends on physicochemical and environmental factors. *Environmental Health Perspectives*, **114** (2), 165–172.
- 266** Landsiedel, R., Ma-Hock, L., Kroll, A., Hahn, D., Schnkenburger, J., Wiench, K., and Wohleben, W. (2010) Testing metal-oxide nanomaterials for human safety. *Advanced Materials*, **22** (24), 2601–2627.
- 267** Lanone, S., Rogerieux, F., Geys, J., Dupont, A., Maillet-Marechal, E., Boczkowski, J., Lacroix, G., and Hoet, P. (2009) Comparative toxicity of 24 manufactured nanoparticles in human alveolar epithelial and macrophage cell lines. *Part. Fibre Toxicol* (6), 14.
- 268** Limbach, L.K., Wick, P., Manser, P., Grass, R.N., Bruinink, A., and Stark, W.J. (2007) Exposure of engineered nanoparticles to human lung epithelial cells: influence of chemical composition and catalytic activity on oxidative stress. *Environmental Science and Technology*, **41** (11), 4158–63.
- 269** Bermudez, E., Mangum, J.B., Wong, B.A., Asgharian, B., Hext, P.M., Warheit, D.B., and Everitt, J.I. (2004) Pulmonary responses of mice, rats, and hamsters to subchronic inhalation of ultrafine titanium dioxide particles. *Toxicological Sciences*, **77** (2), 347–357.
- 270** Warheit, D.B., Brock, W.J., Lee, K.P., Webb, T.R., and Reed, K.L. (2005) Comparative pulmonary toxicity inhalation and instillation studies with different TiO_2 particle formulations: impact of surface treatments on particle toxicity. *Toxicological Sciences*, **88** (2), 514–524.
- 271** Grassian, V.H., O'Shaughnessy, P.T., damcakova-Dodd, A., Pettibone, J.M., and Thorne, P.S. (2007) Inhalation exposure study of titanium dioxide nanoparticles with a primary particle size of 2 to 5 nm. *Environmental Health Perspectives*, **115** (3), 397–402.
- 272** Oberdörster, G., Oberdörster, E., and Oberdörster, J. (2005) Nanotoxicology: an emerging discipline evolving from studies of ultrafine particles. *Environmental Health Perspectives*, **113** (7), 823–839.
- 273** Tan, M.H., Commens, C.A., Burnett, L., and Snitch, P.J. (1996) A pilot study on the percutaneous absorption of microfine titanium dioxide from sunscreens. *Australasian Journal of Dermatology*, **37** (4), 185–187.
- 274** Bennat, C. and Müller-Goymann, C.C. (2000) Skin penetration and stabilization of formulations containing microfine titanium dioxide as physical UV filter. *International Journal of Cosmetic Science*, **22** (4), 271–283.
- 275** Toll, R., Jacobi, U., Richter, H., Lademann, J., Schaefer, H., and Blume-Peytavi, U. (2004) Penetration profile of microspheres in follicular targeting of terminal hair follicles. *Journal of Investigative Dermatology*, **123** (1), 168–176.

5

Nanoencapsulation for Process Intensification

Aaron J. Yap, Anthony F. Masters, and Thomas Maschmeyer

What could we do with layered structures with just the right layers? What would the properties of materials be if we could really arrange the atoms the way we want them? They would be very interesting to investigate.

There's Plenty of Room at the Bottom

Richard P. Feynman

29 December 1959 [1]

5.1

Introduction and Scope

Catalyst nanoencapsulation is an excellent fit to the concepts of green chemistry [2] in the area of process intensification – enabling incompatible catalysts to function in the same reactor, thereby achieving what otherwise simply cannot be done.

By eliminating at least one separation in a multistep reaction, this application of catalysis reduces solvent and energy demands, eliminates the isolation of intermediate derivatives and, with fewer unit operations, can often provide an inherently safer operating procedure. Process intensification by catalyst nanoencapsulation thus embraces five of the 12 Principles of Green Chemistry [3]. The combination of otherwise incompatible catalysts to perform multiple reactions in a single reactor is a sub-set of so-called cascade, serial, tandem [4], domino [5], or multicomponent [6–8] reactions. These replace multistep syntheses that involve multiple separations and work-ups. Such strategies become particularly important in the production of specialty chemicals and pharmaceuticals, since it has been estimated that the pharmaceutical industry, although producing only 0.1% of the chemicals that the petrochemical industry does, generates the same amount of waste [9–12].

Although the scope of this chapter is limited to catalyst nanoencapsulation for the purpose of process intensification, we take a broad view of the definition of nanoencapsulation. The capsule or catalyst, or both, may be on the nanoscale. Additionally, the various methods of nanoencapsulation may be of the order of up to a few microns.

5.2

Cascade Reactions for Process Intensification

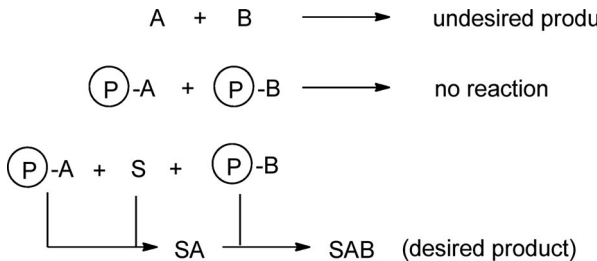
5.2.1

Background

The literature on cascade reactions is vast. Most examples, however, involve the use of a single catalyst to promote successive reactions [13, 14], the use of multiple catalysts to effect the required transformations in a single medium under the same reaction conditions [15], or require different reaction conditions for different steps [16]. What is less common is a synthetic cascade involving two or more incompatible catalysts operating in the same reactor, but able to function in concert. An example of the potential complexity and degree of difficulty of this problem is provided by a recent classification of different bond-forming steps involved in cascade reactions – cationic, anionic, radical, pericyclic, photochemical, transition metal-catalyzed, oxidative or reductive, and enzymatic reactions [5]. Clearly, several reactions within this admittedly simple classification are incompatible. This incompatibility becomes even more marked when recognizing that even within the same category, different catalysts may function optimally only under different reaction conditions of, for example, solvent or pH range. To some extent this represents an inherent drawback of combining “unit operations” and cannot be avoided – the price of process intensification is often reduced flexibility in the system and careful analysis of overall benefits needs to be performed to judge the suitability of any individual strategy. Two general approaches can be envisaged to address this difficulty. In the longer term, new catalysts or catalyst combinations, capable of individually conducting sequential reactions and/or of operating together in the same medium, need to be discovered. In the shorter term, however, the individual incompatible catalysts can be combined by creating individual nanoscale compartments for the specific catalysts and the media in which they operate, such that the compartment is permeable to the reactants and substrates, but not to the catalysts, or the media in which they operate (if these are different).

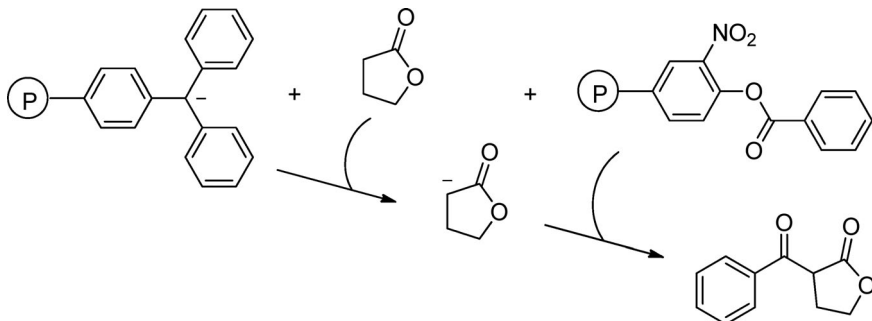
A stoichiometric forerunner of this approach was the “wolf and lamb” reaction, reported by Patchornik and co-workers in 1981 [17]. Two reagents that in solution react with each other quickly to give an undesired product (hence “wolf and lamb”) were immobilized on solid polymeric supports (two insoluble and mutually immiscible polymers, Scheme 5.1), rendering them unreactive towards each other. This allowed the formation of the desired product through the use of a “messenger” reagent.

In a specific example in the same paper [17], one polymer contained triphenylmethane fragments and the other *o*-nitrophenol moieties (A and B, respectively, in Scheme 5.1). The triphenylmethane residues were reacted with an alkylolithium and converted to surface-confined trityllithium species. This derivatized polymer was then mixed with an excess of the second polymer and the combination was used in the stoichiometric benzoylation of γ -butyrolactone (Scheme 5.2) or of phenylacetetonitrile (Scheme 5.3). The procedure was also demonstrated successfully using solid sodium hydride instead of the lithiated polymer.

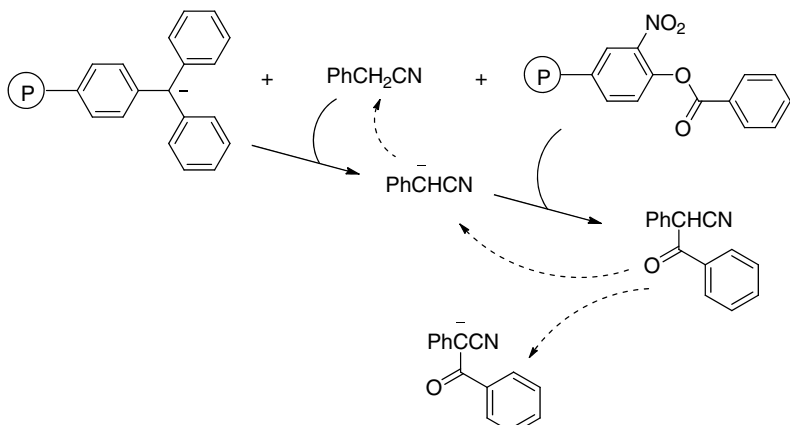


Scheme 5.1 Principle of “wolf and lamb” reaction. When reagents A and B are allowed to interact in solution, they react to give an undesired product. This problem is overcome

by immobilizing them on different polymeric supports. A soluble “messenger” molecule, S, is then used to conduct the reaction giving the desired product [17].



Scheme 5.2 “Wolf and lamb” stoichiometric benzoylation of γ -butyrolactone using two polymer-confined reagents [17].



Scheme 5.3 “Wolf and lamb” stoichiometric benzoylation of phenylacetonitrile using two polymer-confined reagents [17].

When the reaction is performed with soluble analogs of the polymer-bound fragments, multiple side reactions occur. These included the exchange of protons between the product and unreacted acylating agent, or, if the concentration of the base A was increased to avoid this situation, the formation of undesired ketones [17, 18]. The use of polymeric supports allowed the deprotonated soluble messenger molecule S to react upon formation with the polymer-supported reactant B to give the product in a single step, a situation also superior to that of the two-step reaction with soluble reactants. Ultimately, the reaction proceeded with high yields and selectivity and also with increased ease of separation of the polymeric reagents from the product.

In this stoichiometric forerunner, the use of a polymeric support demonstrated the concept of using an immobilization method to prevent reagents from reacting with each other in an undesired manner, permitting a reaction to occur that is not normally possible. By analogy, there are possibilities where various immobilization methods (in this case, we are interested in nanoencapsulation methods) are used to enable two incompatible catalysts to work concomitantly in an otherwise impossible reaction.

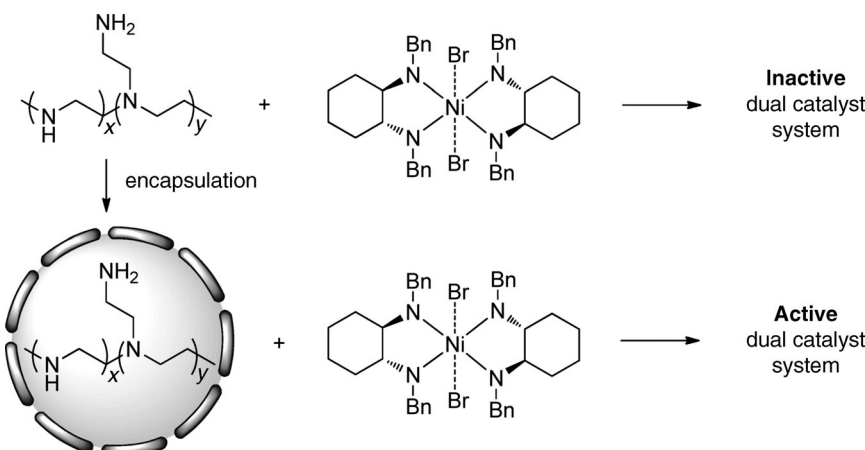
With this understanding of cascade reactions for the purpose of process intensification, we now turn our attention to the relatively few literature examples that exhibit these features.

5.2.2

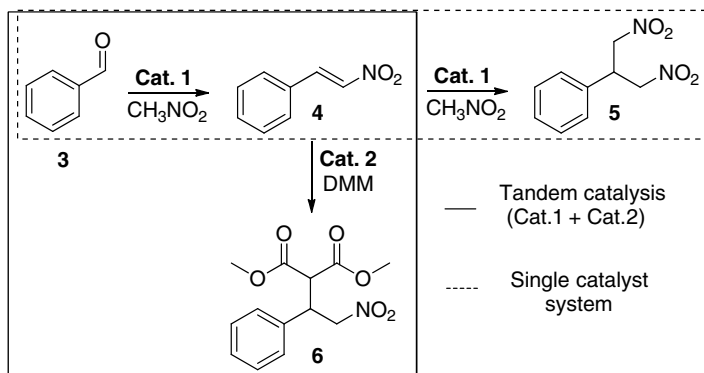
Cascade Reactions with Incompatible Catalysts and Nanoencapsulation

In 2006, Poe *et al.* reported a cascade reaction employing two incompatible catalysts, one of which was microencapsulated [19]. In this case, an organic amine was encapsulated and used in conjunction with a nickel-based Lewis acid catalyst (Scheme 5.4).

Without microencapsulation, precipitation of both catalysts rendered them inactive (Scheme 5.5). Moreover, the addition of the second nickel-based catalyst (Cat. 2)



Scheme 5.4 Encapsulation of the amine by cross-linking allows the use of two incompatible catalysts [19].



Scheme 5.5 The dual catalyst system gives access to intermediate 4, which gives the otherwise inaccessible Michael adduct 6 after addition of dimethyl malonate (DMM) instead of the dinitro product 5 [19].

allowed the formation of an otherwise inaccessible product (6); if only the amine (Cat. 1) was used, a two-step reaction with product 5 was catalyzed by the amine, but if both catalysts were used, the product of the first of these amine-catalyzed reactions (4) was intercepted by the transition metal catalyst and a different product (6) was obtained.

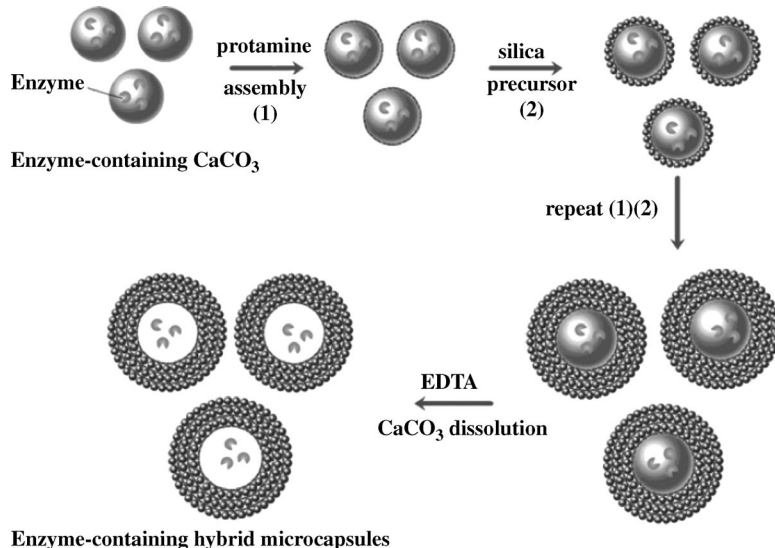
Extending these ideas to enzymatic catalysis, Jiang *et al.* reported the use of protamine–silica hybrid microcapsules in combination with a host gel-like bead structure to encapsulate several enzymes individually in the enzymatic conversion of CO_2 to methanol [20]. They used a layer-by-layer (LbL) method where alternately charged layers were deposited on an enzyme-containing CaCO_3 core. The layers, however, were not polyelectrolytes, but protamine and silica (Scheme 5.6).

The resulting enzyme-containing microcapsules (which can contain different enzymes in different capsules, as was the case here) were then embedded within a Ca-alginate bead, designated a capsules-in-bead structured microreactor (Scheme 5.7).

The three different enzymes used in combination in this system were FateDH, FalddH, and ADH. FateDH catalyzes the initial reduction of CO_2 to formate, FalddH the reduction of formate to formaldehyde, and ADH the reduction of formaldehyde to methanol. Interestingly, the enzymes when immobilized were more active than a combination of the free enzymes, which is claimed to be due to a reduction of spatial interference among the different enzymes. Moreover, due to the immobilization of enzymes within the microreactor, the intermediate species have significantly reduced distances to travel between active sites [21, 22].

The use of an enzyme in a cascade using nanoencapsulation has also been demonstrated [23]. In this case, the dynamic kinetic resolution (DKR) of secondary alcohols was achieved with an acidic zeolite and an incompatible enzyme, *Candida antarctica* lipase B (CALB) (Scheme 5.8).

The encapsulation process used was the LbL method, employing alternately charged polymers, namely PDA [poly(diallyldimethylammonium chloride)] and PSS

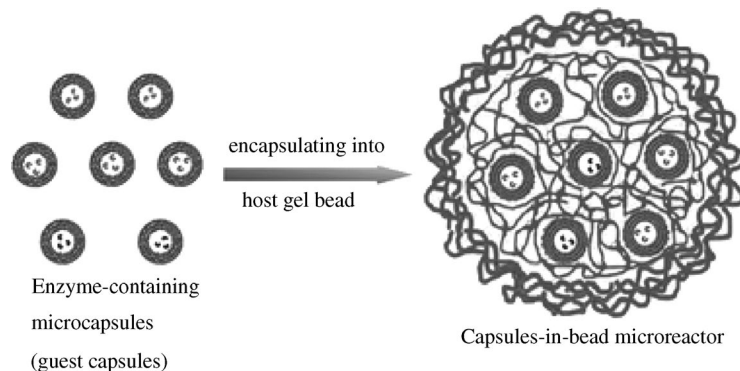


Scheme 5.6 Assembly of hybrid microcapsules. Oppositely charged layers of protamine and silica precursor are alternately deposited on an enzyme-containing CaCO_3 bead, producing a core–shell microcapsule

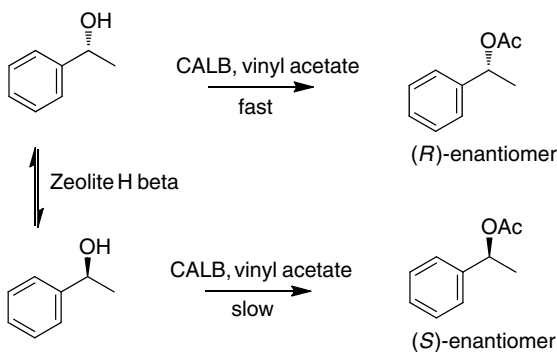
(steps 1 and 2), from which the CaCO_3 in the core is removed by dissolution with EDTA. Reproduced from [20] by permission of The Royal Society of Chemistry.

[poly(sodium 4-styrenesulfonate)] deposited on the zeolite with the object of protecting the enzyme from the surface acidity of the zeolite. A yield of 70% and an enantiomeric excess (*ee*) of 86 (cf. 41% yield and *ee* of 11 without the use of nanoencapsulation) could be achieved.

DKR with lipase TL (from *Pseudomonas stutzeri*) was part of the reaction scheme in work reported by Hoyos *et al.* [24]. Here the lipase is immobilized using a number of

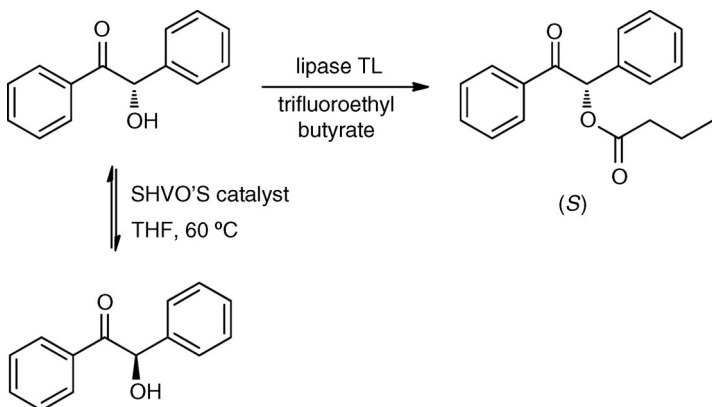


Scheme 5.7 Encapsulation of enzyme microcapsules into a gel-like structure (host gel bead) resulting in a “capsules-in-bead” microreactor. Reproduced from [20] by permission of The Royal Society of Chemistry.



Scheme 5.8 DKR of a secondary alcohol using an acidic zeolite racemization catalyst in conjunction with CALB. The zeolite was encapsulated using an LbL method in order to overcome the incompatibility of the two catalysts.

methods, including a sol–gel matrix derived from isobutyltrimethoxysilane and tetramethoxysilane, static emulsion–silicone spheres, and silicone elastomer spheres. The best results were achieved with silicone elastomer spheres. The DKR involved Shvo's isomerization catalyst and is illustrated in Scheme 5.9.

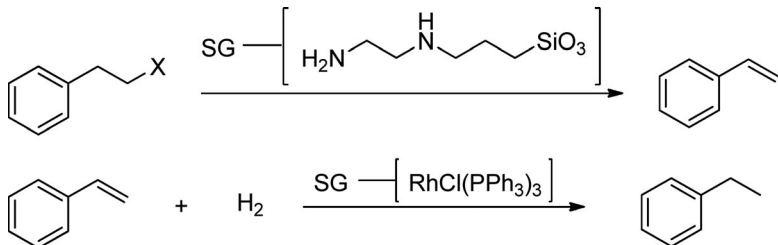


Scheme 5.9 DKR using Shvo's catalyst as racemization catalyst and immobilized lipase TL to yield the desired ester. The lipase was immobilized with silicone elastomer spheres [24].

Unlike in the previous example, here the catalysts are not reported specifically to deactivate one another. Rather, the immobilization of the lipase in these silica elastomer spheres allows access to reaction conditions that are otherwise unavailable, namely higher temperatures, as the lipase is no longer deactivated and is able to undergo multiple reaction cycles, resulting in a much higher enzyme productivity, in terms of mass of product per unit mass of protein. The activity of the lipase is also observed to have increased, possibly not only from its ability to access higher temperatures when immobilized, but also due to the increased stability of the active

conformation of the enzyme inside the spheres due to spatial constraints resulting in reduced degrees of freedom.

In a similar vein, Gelman *et al.* [25] demonstrated encapsulation by the use of two SiO₂ sol–gel matrices [26, 27] to immobilize two catalysts: Wilkinson’s catalyst and an amine that acts as a base catalyst. The reaction is illustrated in Scheme 5.10.



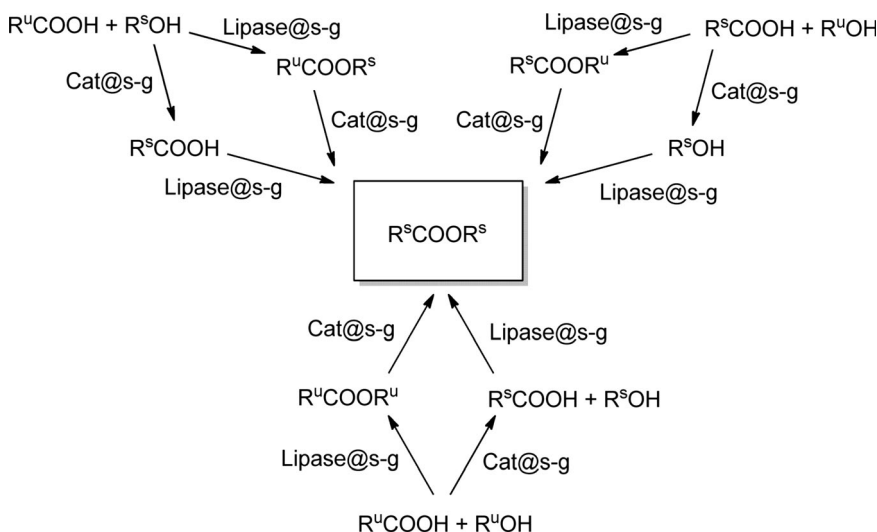
Scheme 5.10 The use of two otherwise incompatible catalysts enabled by their immobilization in a sol–gel matrix (SG) to perform a two-step cascade [25].

They observed the complete deactivation of the rhodium catalyst whether immobilized or not in the presence of free amines. When no amine was present, styrene formation was not observed. After 17 h of a reaction in which both catalysts were immobilized, the yield of the product, ethylbenzene, was 52%, again demonstrating the principle of enabling two otherwise incompatible catalysts to work concomitantly in order to achieve process intensification.

The same immobilization techniques have been applied by Gelman’s group for other cascade reactions. A homogeneous rhodium catalyst {RhCl[P(C₆H₅)₃]₃ or Rh₂Co₂(CO)₁₂} and a lipase (*Mucor miehei*, coated on SIRAN beads, i.e., glass beads, referred to as @s-g) were used in one-pot sequences where the hydrogenation of a double bond catalyzed by the rhodium complex was followed by esterification catalyzed by the lipase [28]. The system is summarized in Scheme 5.11.

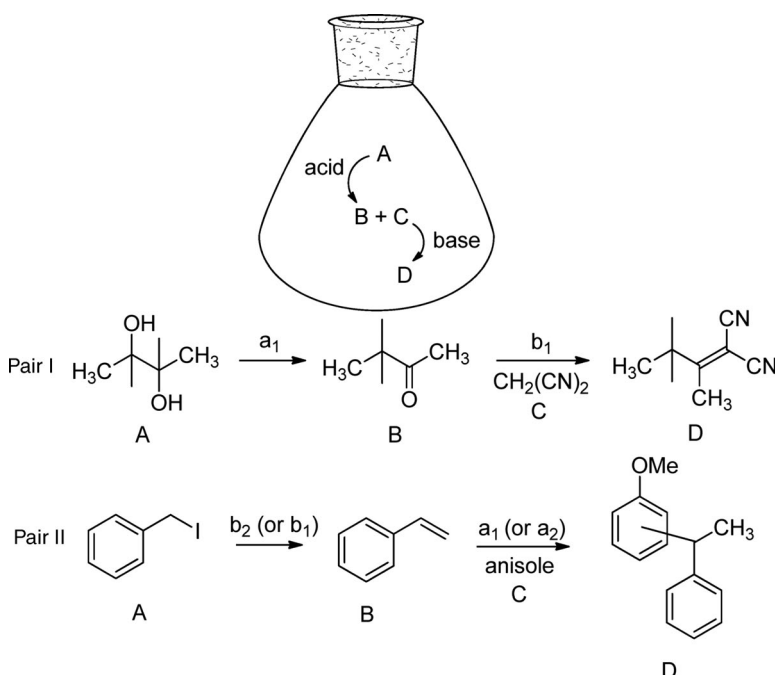
When only the enzyme was entrapped in the sol–gel, the rhodium complexes poisoned the enzyme, resulting in low yields, whereas when both enzyme and complex were trapped in separate sol–gel mixtures, good yields were achieved. In one particular case, this procedure resulted in an increase in yield of 1-pentyl undecanoate from 1-undecenoic acid and 1-pentanol by a factor of 6.5, indicating successful site isolation of the mutually interfering catalysts.

Furthermore, the same sol–gel matrices have been used in a system where acid and base catalysis occur in the same pot without quenching either catalyst [29]. In this case, the acids were either entrapped Nafion (perfluorinated resin sulfonic super acid, a₁) or entrapped molybdic acid (MO₃–SiO₂, a₂), while the bases were two ORMSILs (organically modified silica sol–gel materials), one with H₂N(CH₂)₂NH(CH₂)₃ groups (b₁) and the other guanidine base residues (b₂) (Scheme 5.12).



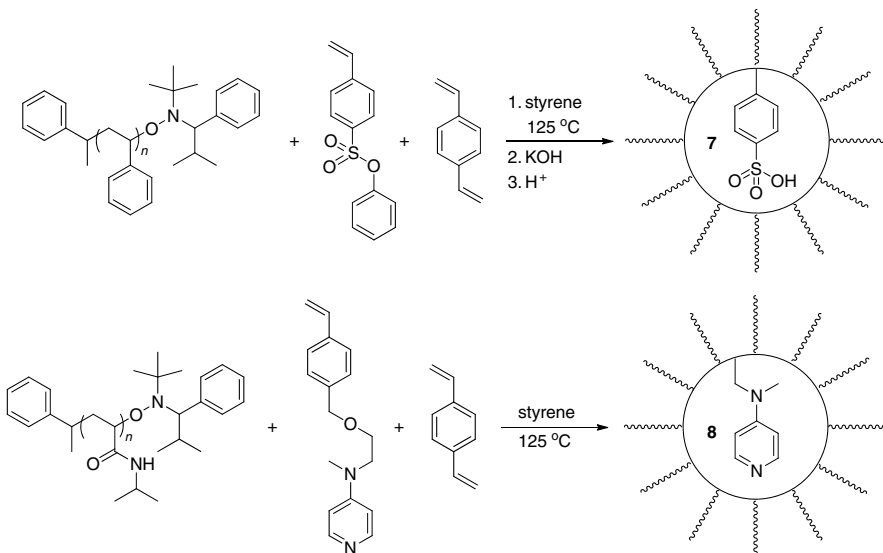
Scheme 5.11 Reaction routes for various saturated and unsaturated carboxylic acids and alcohols using a rhodium catalyst and a lipase. @s-g indicates sol–gel encapsulation of the catalyst; superscript u and s indicate unsaturated and saturated compounds,

respectively [28]. R^u (acid): $\text{CH}_2=\text{CH}(\text{CH}_2)_8$. R^s (acid): $\text{CH}_3(\text{CH}_2)_9$, $\text{CH}_3(\text{CH}_2)_7$, $\text{CH}_3(\text{CH}_2)_{10}$. R^u (alcohol): $\text{CH}=\text{CHCH}_2$, $\text{CH}=\text{CHCH}(\text{CH}_3)\text{CH}_2$. R^s (alcohol): $\text{CH}_3(\text{CH}_2)_2$, $\text{CH}_3(\text{CH}_2)_4$, (S)-(-)- $\text{CH}_3\text{CH}_2\text{CH}(\text{CH}_3)\text{CH}_2$.



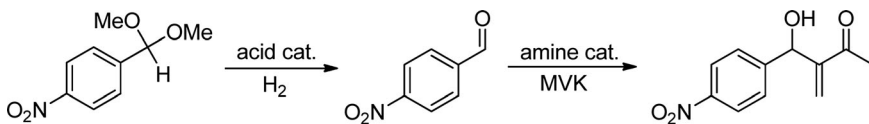
Scheme 5.12 Cascade reactions with acid- and base-catalyzed steps in the same pot [29]. The acids and bases are defined in the text.

The same concept of using mutually interfering acid and base catalysts was achieved by Fréchet's group through the use of star polymer systems [30]. The synthesis of the catalysts is outlined in Scheme 5.13. The "arms" of the star polymers prevent the catalysts from interfering with each other and allow the cascade reaction to proceed unhindered.



Scheme 5.13 Synthesis of star polymers to isolate *p*-toluenesulfonic acid (PSTA, **7**) or 4-(dialkylamino)pyridines (**8**) [30].

In this particular system, 4-nitrobenzaldehyde dimethyl acetal is deprotected by the acid catalyst, followed by the addition of methyl vinyl ketone (MVK) in an amine-catalyzed Baylis–Hillman reaction to give the product (Scheme 5.14). A yield of 65% for the final product was observed when the catalysts described in Scheme 5.13 were used, compared with no observed yield for the reaction with their soluble analogs.



Scheme 5.14 One-pot cascade involving acid-catalyzed acetal hydrolysis followed by the addition of methyl vinyl ketone (MVK) in an amine-catalyzed Baylis–Hillman reaction. The acid and base used were synthesized as in Scheme 5.13 [30].

The same system was used by Fréchet's group to achieve a multicomponent one-pot cascade reaction with mutually interfering acid and proline-derived pyrrolidine catalysts [31]. The concept is illustrated in Figure 5.1. The protonation of imidazolidone (**3**) by the immobilized PSTA (**5**) gives the desired iminium catalyst (**6**), while

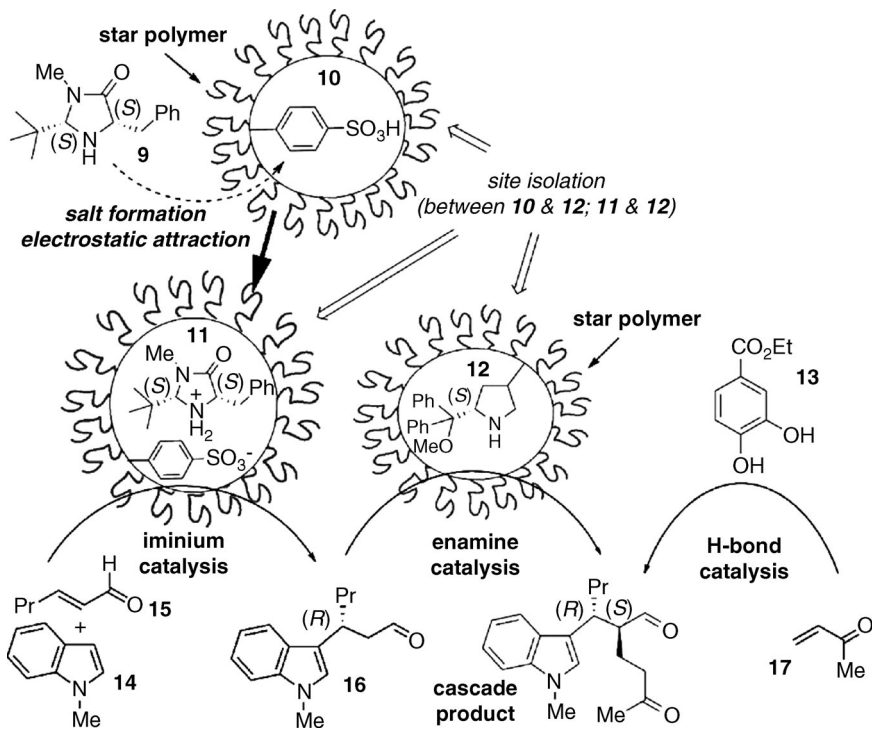


Figure 5.1 The use of multiple catalysts encapsulated in star polymers to enable a one-pot cascade reaction containing interfering catalysts. Catalyst 11 is formed via the protonation of imidazolidinone (9) by immobilized PSTA (10), and is responsible for the nucleophilic addition of *N*-methylindole (14)

to 2-hexenal (15). The product (16) is then involved in a Michael addition to MVK (17), catalyzed by 11 to give the cascade product. MVK requires activation by 13 for the reaction to proceed. Reproduced with permission from [31].

the immobilized pyrrolidone catalyses the Michael addition of MVK to the product of the iminium catalysis, giving the final cascade product. Furthermore a hydrogen-bond donor catalyst (8) is used to activate MVK. When soluble analogs of the catalysts were used, yields were 4% or lower, *cf.* up to 89% with *ee* > 99 when the star polymer catalysts were employed.

5.2.3

Summary of Reactions and Systems

The reactions and systems are summarized in Table 5.1.

To the best of the authors' knowledge, these examples comprise most of the literature that fits the criteria of cascade reactions with incompatible catalysts achieved with nanoencapsulation. However, there are many more examples where cascade reactions have been achieved with incompatible catalysts, but without the use

Table 5.1 Reactions, catalysts, and encapsulation methods.

Ref.	Reaction and catalysts	Encapsulation method
[19]	Addition of nitromethane to benzaldehyde catalyzed by amine followed by Michael addition of DMM catalyzed by Ni complex	Cross-linking of amine itself
[20]	Multiple-enzyme conversion of CO ₂ to formate, then formaldehyde, then methanol by FadDH, FaldDH, and ADH	Enzymes loaded in CaCO ₃ followed by LbL deposition and dissolution of core, then encapsulation into a gel bead
[23]	DKR of secondary alcohols with acidic zeolite (for racemization) and enzyme (CALB) (for esterification)	LbL deposition onto zeolite itself
[24]	DKR of α -hydroxy ketones with Shvo's catalyst (racemization) and lipase TL (esterification)	Lipase encapsulated by silicone elastomer spheres
[25]	Amine catalyzed conversion of β -iodoethylbenzene to styrene, followed by hydrogenation to ethylbenzene catalyzed by Wilkinson's catalyst	Sol-gel immobilization of both catalysts
[28]	Ester formation catalyzed by lipase (<i>Mucor miehei</i>) in conjunction with hydrogenation catalyzed by a rhodium complex	Sol-gel immobilization of both catalysts
[29]	Acid (Nafion or molybdic acid)- and base (diamine-based or guanidine residues)-catalyzed reactions in the same pot	Sol-gel immobilization of both catalysts
[30]	Acid (PSTA)-catalyzed acetal hydrolysis followed by base-catalyzed [4-(dialkylamino) pyridine] Baylis–Hillman addition of MVK	Catalysts are part of the monomers used to make the resulting star polymer-encapsulated catalysts
[31]	Iminium-catalyzed nucleophilic addition of N-methylindole to 2-hexenal, followed by enamine-catalyzed formation of product	Star polymer encapsulation

of nanoencapsulation. These are of interest because of their potential as nanoencapsulation targets.

5.3

Other Cascade Reactions with Incompatible Catalysts – Polydimethylsiloxane (PDMS) Thimbles for Generic Site Isolation

Although on a millimeter rather than a nanometer scale, the use of PDMS thimbles is a lucid example of performing cascade reactions with otherwise incompatible catalysts. One of the key properties of PDMS that is exploited in these cascades is its ability to occlude large molecules, which more often than not are organometallic or enzymatic catalysts. PDMS is also hydrophobic and does not allow high flux rates of very polar molecules, including water, while having the capability of allowing most small organic molecules to pass through [32, 33].

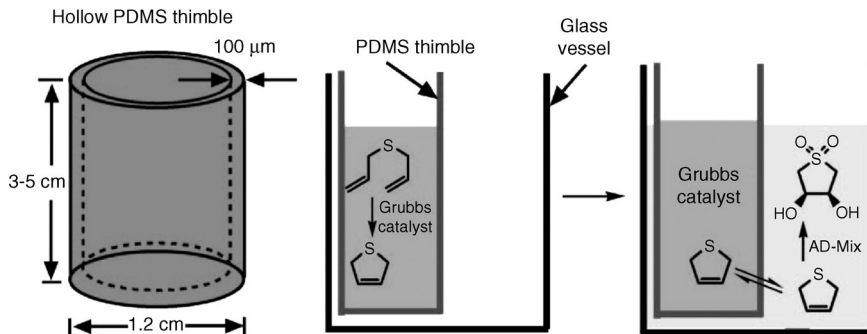


Figure 5.2 The use of hollow PDMS thimbles to achieve site separation of Grubbs catalyst and an osmium dihydroxylation catalyst [34]. The solution of the Grubbs catalyst was placed on the interior of the PDMS thimble in which a metathesis reaction was then performed. After

completion, the commercially available AD-mix (containing the Sharpless dihydroxylation catalyst) was then added to the outside of the thimble to perform the dihydroxylation. Reproduced with permission from [34].

Bowden and co-workers demonstrated the utility of such a system in multiple cascade reactions, including the use of an otherwise incompatible combination of a Grubbs catalyst and an osmium dihydroxylation catalyst (Figure 5.2) [34].

Moreover, in this example, the solvent systems used are also incompatible. The Grubbs catalyst is used in a relatively dry, nonpolar solvent to dissolve the substrates, whereas the AD-mix is placed in various alcohol–water mixtures.

The same approach has also been used in a reaction cascade involving 4-dimethylaminopyridine (DMAP) and an acid catalyst [35]. These two catalysts are mutually incompatible as the acid quenches the DMAP, but site isolation using a PDMS thimble enables the cascade to proceed successfully (Figure 5.3).

One of the drawbacks with such a macroscopic system is the increased time for the diffusion of molecules relative to that in nanoscale systems. Molecules will clearly take longer to pass through thick barriers and to diffuse great distances than in the nanoscale regime. Therefore, the nanoencapsulation of such systems is desirable as it potentially reduces these limitations very significantly. Our attention now proceeds to various potential methods for nanoencapsulation.

5.4

Potential Methods of Nanoencapsulation

5.4.1

Layer-by-Layer (LbL) Methods

As mentioned in Section 5.2.2, the LbL method generally involves the addition of alternately charged layers, often onto a sacrificial solid that has a charged surface (Figure 5.4).

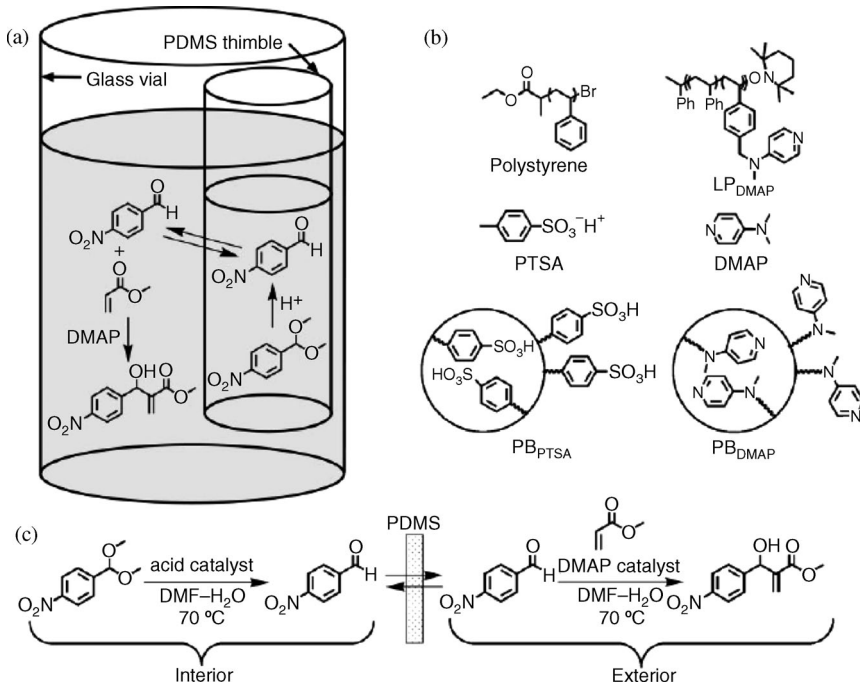


Figure 5.3 (a) The experimental set-up with a PDMS thimble contained in glass vial. The substrate, an acetal, is within the PDMS thimble and undergoes an acid-catalyzed transformation into an aldehyde. The aldehyde then diffuses to the exterior and undergoes the Baylis–Hillman reaction catalyzed by DMAP to give the product. (b) Various acid and base

catalysts used: LP_{DMAP} [linear polymer containing styrene–DMAP (51:49)], $\text{p-toluenesulfonic acid}$ (PTSA), and polymer beads with DMAP or PTSA bonded to their interiors and exteriors (PB_{DMAP} and PB_{PTSA} , respectively). (c) Reactions that occur in the interior and exterior of thimbles. Reproduced with permission from [35].

The solid, which can be derived from inorganic solids [37–39] or polymers [36, 40–43], is then dissolved by an agent that is permeable to the resulting polyelectrolyte membrane. It is also possible to envisage loading the solid with a catalyst, often an enzyme [39, 44]. The method of nanoencapsulation can vary; polyelectrolytes can be deposited on crystals of an enzyme itself [45], leading to a site-isolated enzyme [46], or an enzyme can be loaded on to a silica particle, which is then the template to be encapsulated [39]. In such cases, the silica can be removed by an $\text{HF-NH}_4\text{F}$ buffer without denaturation of the protein. Several reviews are available on LbL templating [47–50]. The layers themselves, although often organic and polymeric in nature [51], can also be inorganic [52, 53]. They can even be lipid based and therefore mimic cell walls [54]. The properties of these polyelectrolyte capsules can vary with composition and provide some interesting possibilities combined with their site-isolation effects. For example, pH changes can affect the permeability of these capsules [55]. Biocompatible capsules can be obtained by using natural polyelectrolytes, such as amino acids [56]. There are also possibilities whereby a catalyst, an enzyme [57], or a metal [58]

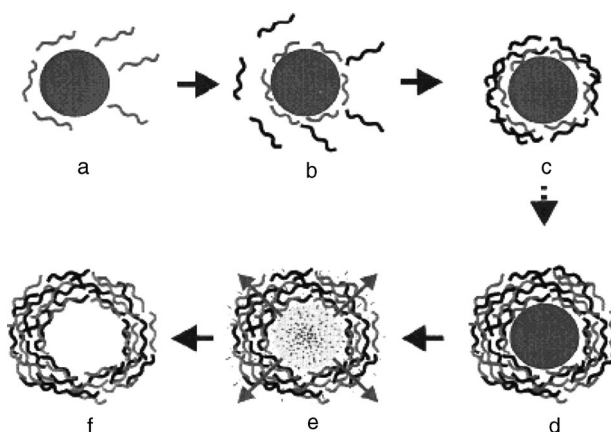


Figure 5.4 LbL assembly of polyelectrolyte capsule. Alternately charged molecules are added to the template several times, giving species (d). This is followed by dissolution of the template (e) leaving the polyelectrolyte capsule. Reproduced with permission from [36].

can be entrapped within, rather than be encapsulated by, the polyelectrolyte layers, providing yet another avenue for nanoencapsulation (Figure 5.5).

5.4.2

Sol–Gel-Based Methods

Sol–gel-entrapped catalysts provide a generic method for the encapsulation of a wide variety of catalysts. Comprehensive reviews are available [59–61]. The essence of the concept is captured in Figure 5.6.

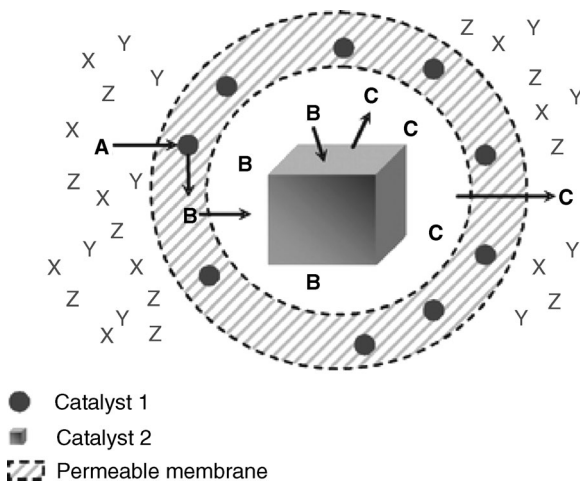


Figure 5.5 Synthesis of an encapsulated metal catalyst by the LbL method with a different metal catalyst in the membrane walls. Reproduced by permission of the PCCP Owner Societies [58].

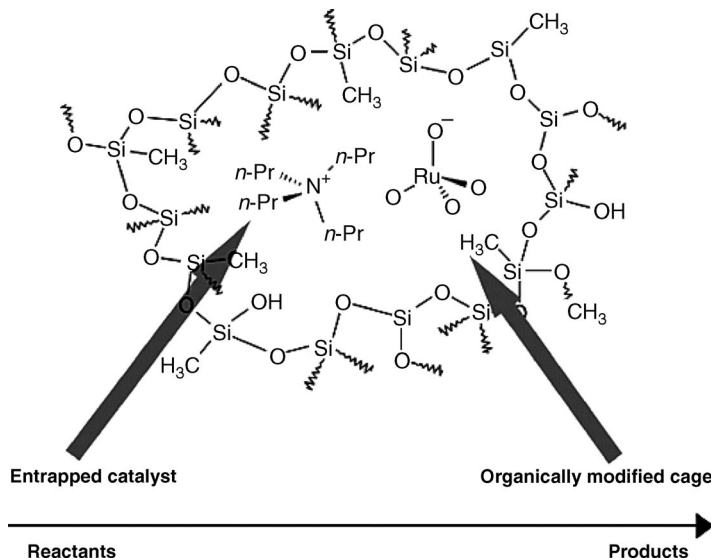


Figure 5.6 Sol-gel nanocomposites are composed of an entrapped catalyst and an organically modified SiO_2 based matrix. Reproduced with permission from [60].

The exact procedure for entrapment will depend on the nature of the catalyst and the required sol-gel, but for enzyme entrapment it generally involves the hydrolysis or partial hydrolysis of an alkoxysilane precursor, giving a precursor sol-gel solution, followed by addition of more solvent and of the catalyst. Figure 5.7 provides a simple representation of this process.

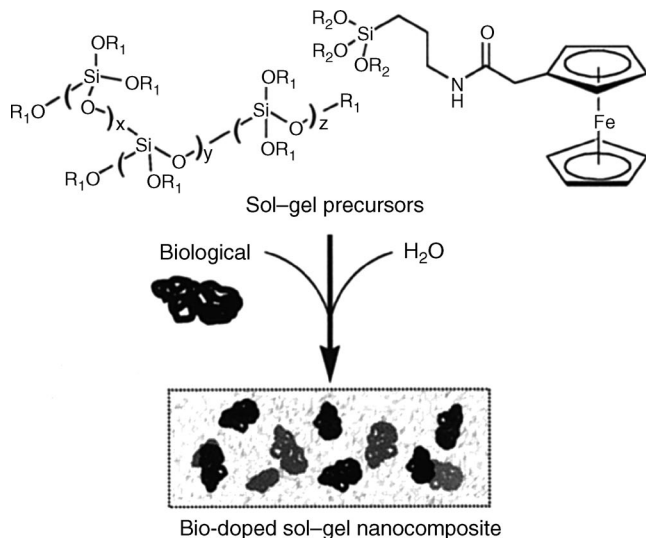
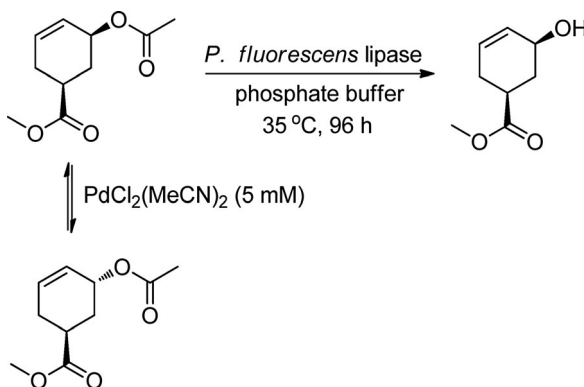


Figure 5.7 General schematic for the formation of a bio-doped sol-gel nanocomposite. Reproduced with permission from [59].

Precursors are generally ORMOSILs, that is, organically modified silicates. The procedure for metal catalysts is similar to that for lipases, apart from the use of an argon atmosphere. More details of these procedures can be found in the literature [26].

Another example of the use of an SiO_2 sol–gel matrix mentioned in Section 5.2.2 is in a DKR with immobilized *P. fluorescens* in combination with a $[\text{PdCl}_2(\text{MeCN})_2]$ complex [62]. The lipase performs the hydrolysis to the desired (−)-alcohol product while the Pd complex racemizes the starting acetate without altering the product (Scheme 5.15).



Scheme 5.15 DKR of cyclohexenyl acetate to give a (−)-cyclohexenol with *P. fluorescens* lipase immobilized in an SiO_2 sol–gel matrix [62].

Although the catalysts do not interfere with each other, the immobilization process resulted in higher yields and *e*es than with the raw enzyme; the initial activity was over five times greater. Additionally, the biocomposite with enzyme was able to be recycled and maintained its activity, which demonstrates the utility of such an immobilization system for potential cascades with mutually interfering catalysts.

5.4.3

Inorganic Methods

5.4.3.1 Layered Inorganic Solids

Layered inorganic solids have been used for site isolation, for example, nickel phosphine complexes confined within the interlayer spaces of sepiolite have been used as olefin hydrogenation catalysts [63], and similarly there has been the encapsulation of metal complexes into zirconium phosphates [64]. The principal idea is illustrated in Figure 5.8. The metal complex can be encapsulated by covalent means (a) or by non-covalent interactions (b).

Similar methods of encapsulation are also observed in pillared clays, which were also introduced as catalysts as long ago as the early 1980s. The field has been thoroughly reviewed up to 2000 [65]. Layered double hydroxide structures have also been used for the entrapment of metal coordination compounds [66].

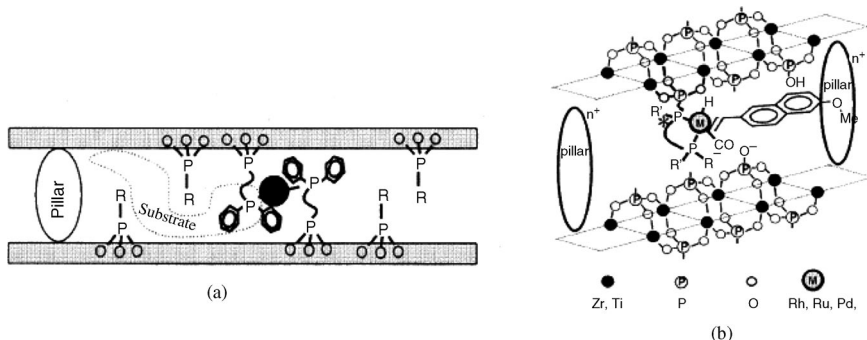


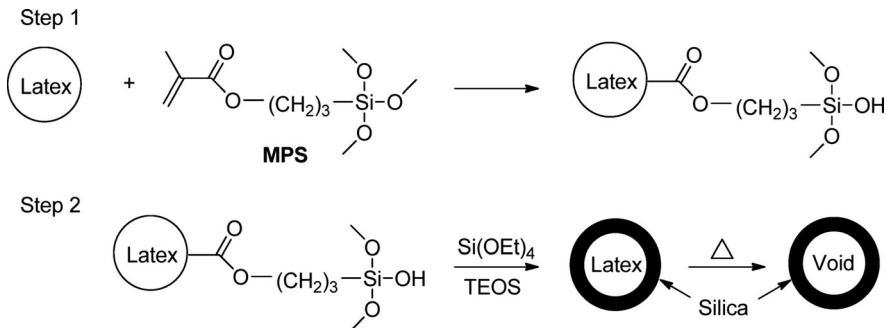
Figure 5.8 Entrapment of metal complexes into layered zirconium phosphates. (a) Covalent attachment of the complex; (b) the complex held in place by non-covalent interactions. Reproduced with permission from [64].

5.4.3.2 Inorganic Spheres

Common to all encapsulation methods is the provision for the passage of reagents and products through or past the walls of the compartment. In zeolites and mesoporous materials, this is enabled by their open porous structure. It is not surprising, then, that porous silica has been used as a material for encapsulation processes, which has already been seen in LbL methods [43]. Moreover, “ship-in-a-bottle” approaches have been well documented, whereby the encapsulation of individual molecules, molecular clusters, and small metal particles is achieved within zeolites [67]. There is a wealth of literature on the immobilization of catalysts on silica or other inorganic materials [68–72], but this is beyond the scope of this chapter. However, these methods potentially provide another method to avoid a situation where one catalyst interferes with another, or to allow the use of a catalyst in a system limited by the reaction conditions. For example, the increased stability of a catalyst may allow a reaction to run at a desired higher temperature, or allow for the use of an otherwise insoluble catalyst [73].

Of greater interest for our purposes is the synthesis of silica or other inorganic nanospheres for the encapsulation of catalysts. This has been achieved for zirconium oxide nanospheres outside of LbL methods [74] by a process in which the desired catalyst is embedded within a sacrificial material, ideally made to be spherical and monodisperse (Figure 5.9). The resulting nanospheres are then coated with the required encapsulation material, followed by removal of the sacrificial material, akin to the LbL method. The ZrO₂ shell in this case allows the Au catalyst to be used at higher temperatures without sintering and the corresponding reduction in catalytic activity.

Similar structures using a ‘silica-in-carbon’ core–shell structure have also been synthesized [76], which afford new possibilities for nanoencapsulation. Carbon can be removed by calcination, leaving silica, and (if the positions of silica and carbon are reversed) a carbon shell can be created using NH₄OH solution to dissolve the silica. The formation of silica microparticles using silanol-functionalized polystyrene latexes proceeds along similar lines (Scheme 5.16) [77].



Scheme 5.16 Preparation of silica nanoparticles via the formation of silanol-functionalized polystyrene microparticles (step 1), followed by cross-linking with tetraethyl

orthosilicate (TEOS) (step 2), giving a silica-coated polystyrene latex. Calcination was then performed to remove the polystyrene core [77].

5.4.4

Polymer-Based Methods

Having already examined the use of the LbL method to make various nanocapsules, including polymer nanocapsules, and having already encountered the use of star polymers for catalyst encapsulation, we turn our attention to other methods for the formation of polymeric nanocapsules. Useful reviews of the formation of these capsules using various methods are available [78–84].

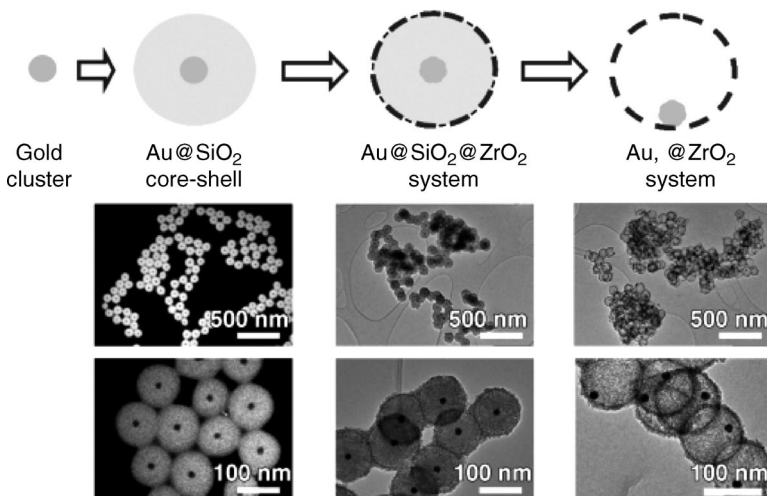


Figure 5.9 Synthesis of gold nanoparticles within ZrO_2 . A gold colloid is first prepared then coated with silica using a modified Stöber process [75]. The silica is removed using NaOH . Reproduced with permission from [74].

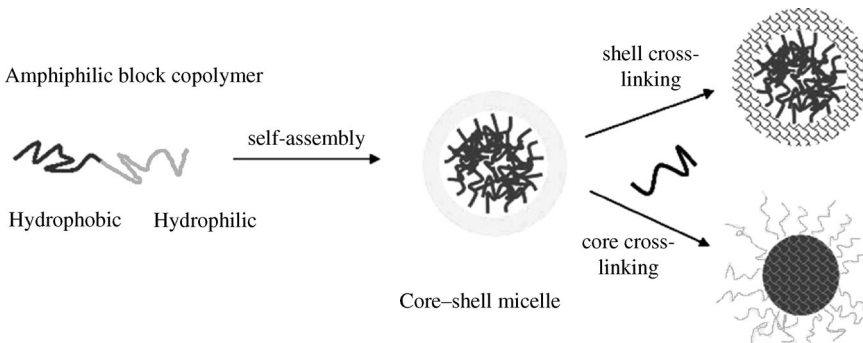


Figure 5.10 Synthesis of a polymeric shell (top route) or a stabilized polymer core (bottom route). Reproduced with permission from [85].

5.4.4.1 Micelle/Emulsion Encapsulation

The formation of polymeric capsules can also be achieved by the cross-linking of self-assembled amphiphilic block copolymers [85]. The hydrophobic section of the polymer in an aqueous solution will tend to aggregate on the interior of the micelle, whereas the hydrophilic ends will form the outer “shell” of the micelle. If the hydrophilic end is appropriately functionalized, it can be cross-linked, giving a polymeric shell. The overarching concept is shown in Figure 5.10.

The utility of this method resides in the ability to change easily the type of functionalization of the resulting capsule (including the core), which is most important for the purposes of this review. This concept is illustrated in Figure 5.11.

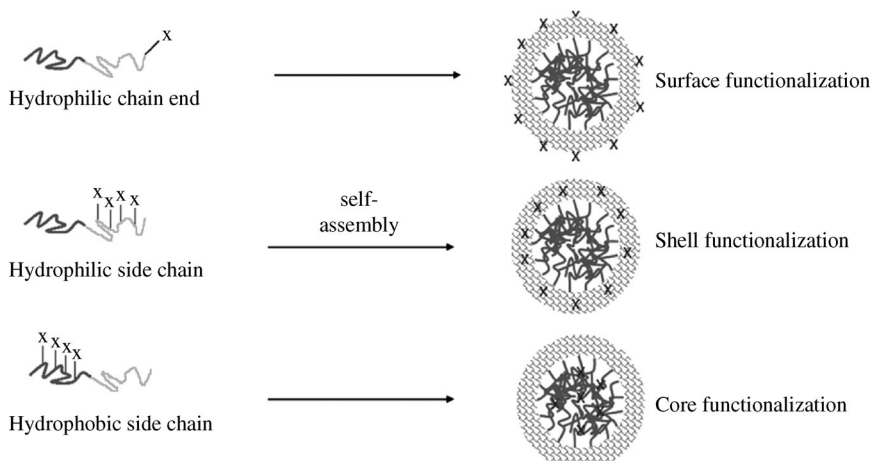


Figure 5.11 Different functionalizations based on the location of the desired functional group on the building block copolymer. This can be extended to the formation of a catalyst-in-nanoreactor system, for example, in [79]. Reproduced with permission from [85].

Polymer capsules can also be formed through the use of emulsion polymerization [86]. An emulsion with the desired initiator and monomer is stabilized with surfactants to avoid Ostwald ripening and to provide a liquid core, as the polymer is carefully chosen to be more hydrophilic than the stabilizer. The polymerization is then conducted, resulting in hollow polymer spheres. This method is comparable to the emulsion of an aqueous enzyme solution in an organic solvent, followed by the addition of the desired membrane material to give encapsulated enzymes [87]. The enzymes are then transferred to a suitable aqueous medium by centrifugation. There also is the combination of emulsion polymerization with phase-inversion techniques to make porous microcapsules [88, 89], including for catalysis [90]. A polymer solution is dropped into a heated aqueous coagulation bath containing a surfactant, which gives rise to microcapsule membranes.

5.4.4.2 Vesicle-Based Encapsulation

The use of self-assembly in these micellar/emulsion techniques is also demonstrated in the use of vesicles and other phases as routes for the encapsulation of catalysts. For example, polymer nanocapsules with semipermeable walls were produced by the polymerization of *tert*-butylstyrene and divinylbenzene on the interior of liposomal bilayers formed from dimyristoylphosphatidylcholine (DMPC) [91]. The system did not leach dye molecules that were added to the precursor solution after polymerization, indicating successful encapsulation of the dye molecules. Interestingly the dye molecules were able to undergo simple reactions, such as their protonation or deprotonation at the same rate as for unencapsulated dye, and this was attributed to the high reagent flux through the membrane. This is counter to the weakness of many other encapsulation systems, which usually result in longer reaction times due to the requirement of diffusion of molecules through the membrane.

Phospholipid vesicles have also been used as a starting point for the formation of nanocapsules [92]. Vesicles were formed using a polymerizable phospholipid, 1,2-dipalmitoyl-*sn*-glycero-3-phospho-*N*-(2-hydroxymethyl)-3,5-divinylbenzamide (DPPE-DVBA). DPPE-DVBA was coated on to a tube wall as a lipid film, then hydrated by a buffer solution containing an enzyme and heated with occasional vortex mixing. The cross-linking of the phospholipid building blocks subsequently stabilized the resulting enzyme-containing phospholipid capsule. The capsules were then used in a hydrolysis reaction to demonstrate the activity of the encapsulated enzyme (Figure 5.12). Similar concepts have also been used to make synthetic cells from amphiphilic molecules [93].

The vesicles made from lipid bilayers are analogous to polymersomes, which are vesicles formed from high molecular weight amphiphilic block copolymers [94–96]. Unlike the micelles discussed earlier from the similar copolymer components, the presence of bilayer walls formed from the aggregation of hydrophobic domains provides new properties. They can be designed to respond, for example, by opening or by disassembly, to external stimuli such as pH, heat, light, and redox processes [97]. This makes them usable as scaffolds for cascade reactions, even those with combinations of enzymes [98, 99].

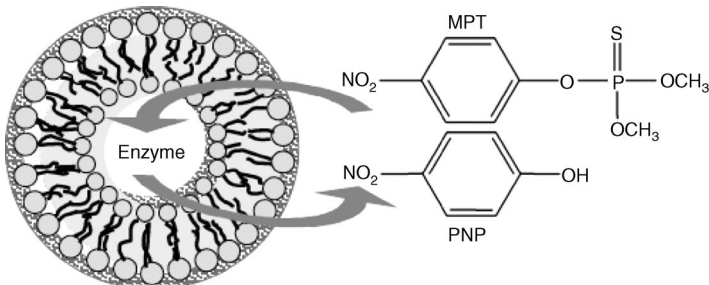


Figure 5.12 Hydrolysis of methylparathion to *p*-nitrophenol. The cross-linked phospholipid-based nanocapsules are permeable to reactant and product, while allowing for the retention of enzyme activity. Reproduced with permission from [92].

5.4.5

Cage Protein Encapsulation

Many of the prior encapsulation techniques have been applied to the site isolation of enzymatic catalysts. However, a protein itself can be used as the encapsulation vessel. Recently, Watanabe and co-workers encapsulated nanometal clusters or multiple organometallic fragments within the spherical protein apo-ferritin [100–102]. The clusters can be monometallic, bimetallic alloys, or core–shell nanomaterials, and the clusters and organometallic fragments are able to catalyze reactions such as hydrogenations and polymerizations in aqueous solution [103–105]. Substrates are presumably admitted to the interior of the ferritin via narrow hydrophilic channels through the ferritin shell [106]. The size and polarity of the substrates in catalytic reactions can be controlled and selected on the basis of their ability to pass through these channels, the width and polarity of which may, in principle, be altered by site-specific mutagenesis.

Although the systems described here have not been used for nanoencapsulated cascade reactions, or of course, for mutually incompatible catalysts, they offer an attractive possibility for the extension of this field, especially given the availability of a wide range of protein-based nanometer-sized cages, such as chaperonins, DNA binding proteins, and the extensive class of viruses [107].

5.4.6

Combinatorial Approaches

It is possible for these nanoencapsulation methods to be combined to provide new strategies for process intensification. The idea itself is not new; in the printing industry, dye-impregnated microscapules that were intercalated into paper had long been used as inks [108]. Examples of hybrid capsules can be found [109–111], including the combination of the LbL method with enzyme-loaded liposomes [112], or with block copolymers on a sacrificial gold core [113]. These approaches are

additional glimpses into the concept of process intensification; by combining encapsulation technologies, chemists should be able to overcome the problems of incompatible catalysts.

5.5

Conclusion and Future Directions

The use of multiple otherwise incompatible catalysts allows multistep reactions to proceed in one reaction vessel, providing many potential benefits. In this chapter, literature examples of nanoencapsulation for the purpose of process intensification have been discussed comprehensively. Current efforts in the literature are mostly concentrated in the areas of LbL template-based nanoencapsulation and sol-gel immobilization. Other cascade reactions (without the use of nanoencapsulation) that allow the use of incompatible catalysts were also examined and showcased as potential targets for nanoencapsulation approaches. Finally, different methods for nanoencapsulation were investigated, thereby suggesting potential ways forward for cascade reactions that use incompatible catalysts, solvent systems, or simply incompatible reaction conditions.

Many challenges remain to be addressed in this field. The use of immobilized catalysts can often reduce the activity of a catalyst. Reduced reaction rates due to diffusion limitations through a permeable membrane capsule and the ease or practicality of the synthesis of these catalyst scaffolds are issues that may pose problems. In some cases, these issues have been resolved, but this is often at the expense of other properties of the capsule. For example, the use of thin walls to reduce mass transfer limitations can be at the expense of nanocapsule strength and stability.

Nonetheless, a wide variety of potential methods are available to achieve the goal of nanoencapsulation for the purpose of facilitating the use of two or more incompatible catalysts in cascade reactions. The many multistep reactions that are of importance in the fine chemicals industry are prime targets for the application of the principles of nanoencapsulation and, therefore, of green chemistry.

Abbreviations

DKR	dynamic kinetic resolution
DMAP	dimethylaminopyridine
DMM	dimethyl malonate
DMPC	dimyristoylphosphatidylcholine
DPPE-DVBA	<i>sn</i> -glycero-3-phospho- <i>N</i> -(2-hydroxymethyl)-3,5-divinylbenzamide
EDTA	ethylenediaminetetraacetic acid
LbL	layer-by-layer
MVK	methyl vinyl ketone
ORMOSIL	organically modified silica

PDA	poly(diallyldimethylammonium) chloride
PDMS	polydimethylsiloxane
PSS	poly(sodium 4-styrenesulfonate)
PSTA	p-toluenesulfonic acid
TEOS	tetraethyl orthosilicate

Acknowledgments

The authors thank the Australian Research Council for funding and the Australian Government for the award of an Australian Postgraduate Award (A.J.Y.).

References

- 1 Feynman, R.P. (1960) There's plenty of room at the bottom. *Caltech Engineering & Science*, **23** (5), 22–36, <http://www.zyvex.com/nanotech/feynman.html>. (last accessed 10 June 2010).
- 2 American Chemical Society Principles of Green Chemistry and Green Engineering http://portal.acs.org/portal.acs/corg/content?_nfpb=true&_pageLabel=PP_SUPERARTICLE&node_id=1415&use_sec=false&sec_url_var=region1&__uuid=05c95de5-a389-403e-b043-db9ce2792b49 (last accessed 10 June 2010).
- 3 Anastas, P.T. and Warner, J.C. (1998) *Green Chemistry: Theory and Practice*, Oxford University Press, New York.
- 4 Wasilke, J.-C., Obrey, S.J., Baker, R.T. and Bazan, G.C. (2005) *Chemical Reviews*, **105**, 1001–1020.
- 5 Tietze, L.F., Brasche, G. and Gericke, K.M. (2006) *Domino Reactions in Organic Synthesis*, Wiley-VCH Verlag GmbH, Weinheim.
- 6 Zhu J. and Bienaymé H. (eds.) (2005) *Multicomponent Reactions*, Wiley-VCH Verlag GmbH, Weinheim.
- 7 Elders, N., van der Born, D., Hendrickx, Loes J.D., Timmer, Brian J.J., Krause, A., Janssen, E., de Kanter, Frans J.J., Ruijter, E. and Orru, Romano V.A. (2009) *Angewandte Chemie International Edition*, **48**, 5856–5859.
- 8 Brauch, S., Gabriel, L. and Westermann, B. (2010) *Chemical Communications*, **46**, 3387–3389.
- 9 Proctor, L., Dunn, P.J., Hawkins, J.M., Wells, A.S. and Williams, M.T. (2010) (eds P.J. Dunn, A. Wells and M.T. Williams), *Green Chemistry in the Pharmaceutical Industry*, Chapter 11, Wiley-VCH Verlag GmbH, Weinheim, pp. 221–242.
- 10 Sheldon R.A., (2000) *Pure and Applied Chemistry*, **72**, 1233–1246.
- 11 Jimenez-Gonzalez, C., Curzons, A.D., Constable, D.J.C. and Cunningham, V.L. (2004) *Int. J. Life Cycle Assess.*, **9**, 114–121.
- 12 Sheldon, R.A., (2010) (eds P.J. Dunn, A. Wells and M.T. Williams), *Green Chemistry in the Pharmaceutical Industry*, Chapter 1, Wiley-VCH Verlag GmbH, Weinheim, pp. 1–20.
- 13 Glueck S.M., Mayer, S.F., Kroutil, W. and Faber, K. (2002) *Pure and Applied Chemistry*, **74**, 2253–2257.
- 14 Grondal, C., Jeanty, M. and Enders, D. (2010) *Nature Chemistry*, **2**, 167–178.
- 15 Wang, Y., Yu, D.-F., Liu, Y.-Z., Wei, H., Luo, Y.-C., Dixon, D.J. and Xu, P.-F. (2010) *Chemistry- A European Journal*, **16**, 3922–3925.
- 16 Nicolaou, K.C., Edmonds, D.J. and Bulger, P.G. (2006) *Angewandte Chemie International Edition*, **45**, 7134–7186.
- 17 Cohen, B.J., Kraus, M.J. and Patchornik, A. (1981) *Journal of the American Chemical Society*, **103**, 7620–7629.
- 18 Kraus, M.A. and Patchornik, A. (1971) *Journal of the American Chemical Society*, **93**, 7325–7327.

- 19** Poe, S.L., Kobaslija, M. and McQuade, D.T. (2006) *Journal of the American Chemical Society*, **128**, 15586–15587.
- 20** Jiang, Y.J., Sun, Q.Y., Zhang, L. and Jiang, Z.Y. (2009) *Journal of Materials Chemistry*, **19**, 9068–9074.
- 21** Leduc, P.R., Wong, M.S., Ferreira, P.M., Groff, R.E., Haslinger, K., Koonce, M.P., Lee, W.Y., Love, J.C., McCammon, J.A., Monteiro-Riviere, N.A., Rotello, V.M., Rubloff, G.W., Westervelt, R. and Yoda, M. (2007) *Nature Nanotechnology*, **23**–7.
- 22** El-Zahab, B., Donnelly, D. and Wang, P. (2008) *Biotechnology and Bioengineering*, **99**, 508–514.
- 23** Fois, A.F., Yap, A., Masters, A.F. and Maschmeyer, T. (2008) *Topics in Catalysis*, **48**, 153–157.
- 24** Hoyos, P., Buthe, A., Ansorge-Schumacher, M.B., Sinisterra, J.V. and Alcántara, A.R. (2008) *Journal of Molecular Catalysis B: Enzymatic*, **52**–53, 133–139.
- 25** Gelman, F., Blum, J. and Avnir, D. (2000) *Journal of the American Chemical Society*, **122**, 11999–12000.
- 26** Sertchook, H., Avnir, D., Blum, J., Joo, F., Katho, A., Schumann, H., Weimann, R. and Wernik, S. (1996) *Journal of Molecular Catalysis A: Chemical*, **108**, 153–160.
- 27** Gill, I. and Ballesteros, A. (1998) *Journal of the American Chemical Society*, **120**, 8587–8598.
- 28** Gelman, F., Blum, J. and Avnir, D. (2002) *Journal of the American Chemical Society*, **124**, 14460–14463.
- 29** Gelman, F., Blum, J. and Avnir, D. (2001) *Angewandte Chemie International Edition*, **40**, 3647–3649.
- 30** Helms, B., Guillaudeu, S.J., Xie, Y., McMurdo, M., Hawker, C.J. and Fréchet, J.M.J. (2005) *Angewandte Chemie International Edition*, **44**, 6384–6387.
- 31** Chi, Y., Scroggins, S.T. and Fréchet, J.M.J. (2008) *Journal of the American Chemical Society*, **130**, 6322–6323.
- 32** Schafer, T., Di Paolo, R.E., Franco, R. and Crespo, J.G. (2005) *Chemical Communications*, 2594–2596.
- 33** Shah, M.R., Noble, R.D. and Clough, D.E. (2007) *Journal of Membrane Science*, **287**, 111–118.
- 34** Mwangi, M.T., Schulz, M.D. and Bowden, N.B. (2009) *Organic Letters*, **11**, 33–36.
- 35** Miller, A.L. and Bowden, N.B. (2008) *Advanced Materials*, **20**, 4195–4199.
- 36** Donath, E., Sukhorukov, G.B., Caruso, F., Davis, S.A. and Möhwald, H. (1998) *Angewandte Chemie International Edition*, **37**, 2201–2205.
- 37** Liang, Z.J., Susha, A. and Caruso, F. (2003) *Chemistry of Materials*, **15**, 3176–3183.
- 38** Srivastava, S. and Kotov, N.A. (2008) *Accounts of Chemical Research*, **41**, 1831–1841.
- 39** Yu, A.M., Wang, Y.J., Barlow, E. and Caruso, F. (2005) *Advanced Materials*, **17**, 1737–1741.
- 40** Donath, E., Walther, D., Shilov, V.N., Knippel, E., Budde, A., Lowack, K., Helm, C.A. and Möhwald, H. (1997) *Langmuir*, **13**, 5294–5305.
- 41** Caruso, F., Kurth, D.G., Volkmer, D., Koop, M.J. and Müller, A. (1998) *Langmuir*, **14**, 3462–3465.
- 42** Sukhorukov, G.B., Donath, E., Lichtenfeld, H., Knippel, E., Knippel, M., Budde, A. and Möhwald, H. (1998) *Colloids Surf. A*, **137**, 253–266.
- 43** Caruso, F., Caruso, R.A. and Möhwald, H. (1998) *Science*, **282**, 1111–1114.
- 44** Sukhorukov, G.B., Volodkin, D.V., Gunther, A.M., Petrov, A.I., Shenoy, D.B. and Mohwald, H. (2004) *Journal of Materials Chemistry*, **14**, 2073–2081.
- 45** Caruso, F., Trau, D., Möhwald, H. and Renneberg, R. (2000) *Langmuir*, **16**, 1485–1488.
- 46** Jin, W., Shi, X. and Caruso, F. (2001) *Journal of the American Chemical Society*, **123**, 8121–8122.
- 47** Wang, Y., Angelatos, A.S. and Caruso, F. (2008) *Chemistry of Materials*, **20**, 848–858.
- 48** Sukhorukov, G.B. (2002) (eds R. Arshady, and A. Guyot), *Microspheres, Microcapsules and Liposomes*, Vol. 5: *Dendrimers, Assemblies and Nanocomposites*, Citus Books, London, Author: are the amended details correct?
- 49** Boudou T., Crouzier, T., Ren, K.F., Blin, G. and Picart, C. (2010) *Advanced Materials*, **22**, 441–467.
- 50** Schlenoff, J.B. (2009) *Langmuir*, **25**, 14007–14010.
- 51** del Mercato, L.L., Rivera-Gil, P., Abbasi, A.Z., Ochs, M., Ganas, C., Zins, I., Sonnichsen, C. and Parak, W.J. (2010) *Nanoscale*, **2**, 458–467.

- 52** Caruso, F. (2003) *Colloid Chem.*, **227**, 145–168.
- 53** Caruso, F., Shi, X.Y., Caruso, R.A. and Susha, A. (2001) *Advanced Materials*, **13**, 740–744.
- 54** He, Q., Duan, L., Qi, W., Wang, K., Cui, Y., Yan, X. and Li, J. (2008) *Advanced Materials*, **20**, 2933–2937.
- 55** Shchukin, D.G. and Sukhorukov, G.B. (2004) *Advanced Materials*, **16**, 671–682.
- 56** Cui, H.G., Webber, M.J. and Stupp, S.I. (2010) *Biopolymers*, **94**, 1–18.
- 57** Caruso, F. and Schüller, C. (2000) *Langmuir*, **16**, 9595–9603.
- 58** Turkenburg, D.H., Antipov, A.A., Thathagar, M.B., Rothenberg, G., Sukhorukov, G.B. and Eiser, E. (2005) *Physical Chemistry Chemical Physics*, **7**, 2237–2240.
- 59** Gill, I. (2001) *Chemistry of Materials*, **13**, 3404–3421.
- 60** Ciriminna, R. and Pagliaro, M. (2006) *Organic Process Research and Development*, **10**, 320–326.
- 61** Reetz, M.T. (1997) *Advanced Materials*, **9**, 943–&.
- 62** Gill, I., Pastor, E. and Ballesteros, A. (1999) *Journal of the American Chemical Society*, **121**, 9487–9496.
- 63** Allum, K.G., Metcalfe, C.J.L. and Thomasson, D.J. (1969) Germany Patent DE 1815631.
- 64** Lücke, B., Köckritz, A., Vorlop, K.-D., Bischoff, S. and Kant, M. (2004) *Topics in Catalysis*, **29**, 111–118.
- 65** Gil, A., Gandiacutea, L.M. and Vicente, M.A. (2000) *Catal. Rev.*, **42**, 145–212.
- 66** Rives, V. and Ulibarri, M.A. (1999) *Coordination Chemistry Reviews*, **181**, 61–120.
- 67** Herron, N. (1986) *Inorganic Chemistry*, **25**, 4714–4717.
- 68** Giraldo, L.F., López, B.L., Pérez, L., Urrego, S., Sierra, L. and Mesa, M. (2007) *Macromolecular Symposium*, **258**, 129–141.
- 69** Severn, J.R., Chadwick, J.C., Duchateau, R. and Friederichs, N. (2005) *Chemical Reviews*, **105**, 4073–4147.
- 70** Corma, A. and Garcia, H. (2006) *Advanced Synthesis and Catalysis*, **348**, 1391–1412.
- 71** Simons, C., Hanefeld, U., Arends, I.W.C.E., Sheldon, R.A. and Maschmeyer, T. (2004) *Chemistry- A European Journal*, **10**, 5829–5835.
- 72** Veum, L., Kanerva, L.T., Halling, P.J., Maschmeyer, T. and Hanefeld, U. (2005) *Advanced Synthesis and Catalysis*, **347**, 1015–1021.
- 73** Sakai, T., Wang, K. and Ema, T. (2008) *Tetrahedron*, **64**, 2178–2183.
- 74** Arnal, P.M., Comotti, M. and Schüth, F. (2006) *Angewandte Chemie International Edition*, **45**, 8224–8227.
- 75** Stöber, W., Fink, A. and Bohn, E. (1968) *Journal of Colloid and Interface Science*, **26**, 62–69.
- 76** Wan, Y., Min, Y.-L. and Yu, S.-H. (2008) *Langmuir*, **24**, 5024–5028.
- 77** Tissot, I., Reymond, J.P., Lefebvre, F. and Bourgeat-Lami, E. (2002) *Chemistry of Materials*, **14**, 1325–1331.
- 78** Meier, W. (2000) *Chemical Society Reviews*, **29**, 295–303.
- 79** Vriezema, D.M., Aragones, M.C., Elemans, J., Cornelissen, J., Rowan, A.E. and Nolte, R.J.M. (2005) *Chemical Reviews*, **105**, 1445–1489.
- 80** Yow, H.N. and Routh, A.F. (2006) *Soft Matter*, **2**, 940–949.
- 81** Peyratout, C.S. and Dähne, L. (2004) *Angewandte Chemie International Edition*, **43**, 3762–3783.
- 82** Arshady, R. (1989) *Journal of Microencapsulation*, **6**, 13–28.
- 83** Arshady, R. (1989) *Journal of Microencapsulation*, **6**, 1–12.
- 84** Atkin, R., Davies, P., Hardy, J. and Vincent, B. (2004) *Macromolecules*, **37**, 7979–7985.
- 85** O'Reilly, R.K. (2007) *Philosophical Transactions of the Royal Society A*, **365**, 2863–2878.
- 86** Romio, A.P., Bernardy, N., Semma, E.L., Araújo, P.H.H. and Sayer, C. (2009) *Materials Science and Engineering C: Materials for Biological Applications*, **29**, 514–518.
- 87** Chang, T.M.S. (1964) *Science*, **146**, 524–525.
- 88** Wang, G.J., Chu, L.Y., Chen, W.M. and Zhou, M.Y. (2005) *Journal of Membrane Science*, **252**, 279–284.
- 89** Wang, G.J., Chu, L.Y., Zhou, M.Y. and Chen, W.M. (2006) *Journal of Membrane Science*, **284**, 301–312.
- 90** Buonomenna, M.G., Figoli, A., Spezzano, I., Davoli, M. and Drioli, E. (2008) *Applied Catalysis B: Environmental*, **80**, 185–194.
- 91** Dergunov, S.A., Miksa, B., Ganus, B., Lindner, E. and Pinkhassik, E. (2010) *Chemical Communications*, 1485–1487.

- 92** Lawson, G.E., Lee, Y., Raushel, F.M. and Singh, A. (2005) *Advanced Functional Materials*, **15**, 267–272.
- 93** Roodbeen, R. and van Hest, J.C.M. (2009) *BioEssays*, **31**, 1299–1308.
- 94** Discher, B.M., Won, Y.-Y., Ege, D.S., Lee, J.C.-M., Bates, F.S., Discher, D.E. and Hammer, D.A. (1999) *Science*, **284**, 1143–1146.
- 95** LoPresti, C., Lomas, H., Massignani, M., Smart, T. and Battaglia, G. (2009) *Journal of Materials Chemistry*, **19**, 3576–3590.
- 96** Lensen, D., Vriezema, D.M. and van Hest, J.C.M. (2008) *Macromolecular Bioscience*, **8**, 991–1005.
- 97** Du, J. and O'Reilly, R.K. (2009) *Soft Matter*, **5**, 3544–3561.
- 98** Vriezema, D.M., Garcia, P.M.L., Oltra, N.S., Natzakis, N.S., Kuiper, S.M., Nolte, R.J.M., Rowan, A.E. and van Hest, J.C.M. (2007) *Angewandte Chemie International Edition*, **46**, 7378–7382.
- 99** Kuiper, S.M., Nallani, M., Vriezema, D.M., Cornelissen, J.J.L.M., van Hest, J.C.M., Nolte, R.J.M. and Rowan, A.E. (2008) *Organic & Biomolecular Chemistry*, **6**, 4315–4318.
- 100** Abe, S., Niemeyer, J., Abe, M., Takezawa, Y., Ueno, T., Hikage, T., Erker, G. and Watanabe, Y. (2008) *Journal of the American Chemical Society*, **130**, 10512–10514.
- 101** Ueno, T., Abe, M., Hirata, K., Abe, S., Suzuki, M., Shimizu, N., Yamamoto, M., Takata, M. and Watanabe, Y. (2009) *Journal of the American Chemical Society*, **131**, 5094–5100.
- 102** Abe, S., Hikage, T., Watanabe, Y., Kitagawa, S. and Ueno, T. (2010) *Inorganic Chemistry*, **49**, 6967–6973.
- 103** Ueno, T., Suzuki, M., Goto, T., Matsumoto, T., Nagayama, K. and Watanabe, Y. (2004) *Angewandte Chemie International Edition*, **43**, 2527–2530.
- 104** Abe, S., Hirata, K., Ueno, T., Morino, K., Shimizu, N., Yamamoto, M., Takata, M., Yashima, E. and Watanabe, Y. (2009) *Journal of the American Chemical Society*, **131**, 6958–6960.
- 105** Suzuki, M., Abe, M., Ueno, T., Abe, S., Goto, T., Toda, Y., Akita, T., Yamadae, Y. and Watanabe, Y. (2009) *Chemical Communications*, 4871–4873.
- 106** Lawson, D.M., Artymiuk, P.J., Yewdall, S.J., Smith, J.M.A., Livingstone, J.C., Treffry, A., Luzzago, A., Levi, S., Arosio, P., Cesareni, G., Thomas, C.D., Shaw, W.V. and Harrison, P.M. (1991) *Nature*, **349**, 541–544.
- 107** Uchida, M., Kang, S., Reichhardt, C., Harlen, K. and Douglas, T. (2010) *Biochimica et Biophysica Acta*, **1800**, 834–845.
- 108** Schleicher, L. and Green, B.K. (1956) US Patent 2,730,456.
- 109** van Dongen, S.F.M., de Hoog, H.-P.M., Peters, R.J.R.W., Nallani M., Nolte R.J.M. and van Hest, J.C.M. (2009) *Chemical Reviews*, **109**, 6212–6274.
- 110** Ni K.Bourgeat-Lami, E., Sheibat-Othman, N., Shan, G., Fevotte G. (2008) *Macromolecular Symposium* **271**, 120–128.
- 111** Zou, H., Wu, S. and Shen, J. (2008) *Chemical Reviews*, **108**, 3893–3957.
- 112** Chandrawati, R., Hosta-Rigau, L., Vanderstraeten, D., Lokuliana, S.S., Städler, B., Albericio, F. and Caruso, F. (2010) *ACS Nano*, **4**, 1351–1361.
- 113** Boyer, C., Whittaker, M.R., Nouvel, C. and Davis, T.P. (2010) *Macromolecules*, **43**, 1792–1799.

6

Formation of Nanoemulsions by Low-Energy Methods and Their Use as Templates for the Preparation of Polymeric Nanoparticles

Gabriela Calderó and Conxita Solans

6.1

Introduction

Emulsions with extremely small droplet sizes, typically in the range 20–200 nm, have been denoted nanoemulsions [1, 2], miniemulsions [3–5], submicrometer-sized emulsions [6], finely dispersed emulsions [7], ultrafine emulsions [8], and so on. The term nanoemulsion [1, 2] is preferred by the present authors because in addition to giving an idea about the nanoscale size range of the droplets, it is concise and it avoids confusion with the term microemulsion. There is a fundamental difference between microemulsions and nanoemulsions: microemulsions are equilibrium systems (i.e., thermodynamically stable), whereas nanoemulsions are nonequilibrium systems, which means that they tend to separate into the constituent phases. Nevertheless, properly formulated nanoemulsions may possess high kinetic stability (e.g., for several years) [1, 2]. The characteristic size of nanoemulsions confers stability against sedimentation or creaming and gives a visually transparent or translucent aspect (resembling microemulsions).

Nanoemulsions, being nonequilibrium systems, require energy input for their formation, either from mechanical devices (high-energy methods) or from the chemical potential of the components (low-energy methods). The latter are of special interest from basic, applied, and energy-savings viewpoints. Among the different low-energy emulsification methods, those based on phase inversions will be the subject of this chapter. An interesting advantage of these methods is that they allow the preparation of very small and uniform droplets. In phase-inversion methods, the spontaneous curvature of the surfactant changes during emulsification. The phase transitions that occur during the emulsification process release chemical energy, used to form the nanoemulsion droplets. For ethoxylated nonionic surfactants, a change in temperature causes a change in curvature due to a change in the hydration of the poly(oxyethylene) chains of the surfactant. The emulsification method based on a change in temperature is known as the phase-inversion temperature (PIT) method and was introduced by Shinoda and Saito in 1968 [9]. The relation between nanoemulsion formation by the PIT method and

phase behavior has been systematically studied [10–12]. The emulsification method based on the phase transitions that take place on changing the composition at constant temperature during emulsification is the so-called phase-inversion composition (PIC) method [13, 14]. Low interfacial tension values and the presence of lamellar liquid crystalline or bicontinuous microemulsion phases (i.e., surfactant aggregates with zero or almost zero curvature) are among the factors that have been shown to be important for the formation of nanoemulsions with either the PIT or PIC method [10–15]. However, other types of structures, such as micellar cubic liquid crystalline phases, and also the kinetics of the emulsification process may also play a key role in the properties of the resulting nanoemulsions [16, 17].

From the point of view of green chemistry and processes, nanoemulsions offer interesting advantages considering both safety and cleanliness. This can be achieved through the selection of the appropriate composition of the nanoemulsions and also their preparation by low-energy methods. Concerning their composition, it should be mentioned that compared with microemulsions, which are dispersed systems with droplets in a similar size range, nanoemulsions can be obtained at lower surfactant concentrations. Whereas microemulsions may need surfactant concentrations as high as 30%, nanoemulsions can be prepared at surfactant concentrations below 10% [18]. Concerning their preparation, the possibility of obtaining nanoemulsions by low-energy emulsification constitutes not only an environmentally friendly but also an economically beneficial approach. The advantageous features of nanoemulsions, such as small droplet size, colloidal stability, and high surface area are attracting interest in a growing range of fields, including pharmaceutical [14, 19–24], cosmetic [25–28], agrochemical [29–31], food [32–34], textile [35, 36], and bitumen [37, 38] formulations, to mention only a few examples. The key applications of nanoemulsions, however, can be summarized mainly in two groups, regardless of the intended purpose of use: on the one hand their application as carrier and/or delivery systems of active molecules and on the other their use as nano-reactors generally for the preparation of nanoparticles. In this chapter, attention is focused on the latter aspect.

Nanoparticles are solid materials with sizes in the nanometer range, generally below 500 nm. There are a wide variety of methods for the preparation of nanoparticles, determined principally by their composition (lipids [39, 40], metal oxides [41], polymers [42–48], etc.). The nanoemulsion approach [2, 49] is used extensively for the preparation of nanoparticles of polymeric nature. These can be obtained either by polymerization reactions taking place at the interface or in the dispersed droplets of the nanoemulsion [46–48, 50, 51] or by starting from preformed polymers incorporated in the dispersed phase of the nanoemulsion [42–45, 52–54]. The use of the latter method is advantageous because it avoids employing reactive substances, thus improving the safety of the system, and reducing the number of purification steps needed to remove excess of reactants (residual monomers, initiator, catalysts, etc.) or by-products. Among the preformed polymers, cellulose derivatives are an interesting group, as cellulose is a renewable and very abundant polymer in Nature. Although cellulose itself is poorly soluble in most solvents, this

drawback has been overcome by its functionalization, mainly as esters and ethers. It is worth mentioning that the insolubility of cellulose in water has been attributed to the formation of intra- and intermolecular hydrogen bonds by the three hydroxyl groups present at each anhydroglucoside unit of the polymer [55]. Therefore, the substitution of the hydroxyl groups by appropriate substituents can give rise to water-soluble (methylcellulose, hydroxyethylcellulose, carboxymethylcellulose, etc.) and oil-soluble (cellulose acetate, nitrocellulose, ethylcellulose, etc.) derivatives. In this context, ethylcellulose is an attractive semisynthetic cellulose derivative which is listed as GRAS (“Generally Recognized As Safe”) by the US Food and Drug Administration (FDA), and is employed in many applications such as inks, paper, food, cosmetics, and pharmaceutical products [55–58]. This material has been used for many years for the preparation of micro- and nanoparticles by different methods [44, 59–71]. However, most methods fail to meet the requirements of safety and cleanliness implied in green chemistry. On the one hand, most of the methods described are based on the use of volatile solvents that are not acceptable owing to their toxicity to human health (e.g., methylene chloride [72], benzene [73, 74], toluene [75], and tetrahydrofuran [64]) and some of them are in addition included in the SIN List Database (that is, “Substitute it Now!” list) of the European Community Regulation on chemicals and their safe use, known as REACH. Therefore, there is a need for further research on the use of greener solvents for the preparation of nanoparticles. On the other hand, there is a lack of sustainable processes focusing on the reduction of energy consumption. In recent years, the preparation of ethylcellulose nanoparticles by low-energy emulsification methods and subsequent solvent evaporation has been reported [54, 75, 76]. Some effort has also been devoted to designing processes that proceed at room temperature, avoiding heating steps [54, 75, 77]. A challenging issue is to fulfill both safety and environmentally friendly requirements.

6.2

Use of Nano-emulsions as Templates for the Preparation of Polymeric Nanoparticles

The formation of ethylcellulose nanoemulsions by a low-energy method for nanoparticle preparation was reported recently. The nanoemulsions were obtained in a water–polyoxyethylene 4 sorbitan monolaurate–ethylcellulose solution system by the PIC method at 25 °C [54]. The solvent chosen for the preparation of the ethylcellulose solution was ethyl acetate, which is classed as a solvent with low toxic potential (Class 3) by ICH Guidelines [78]. Oil/water (O/W) nanoemulsions were formed at oil/surfactant (O/S) ratios between 30 : 70 and 70 : 30 and water contents above 40 wt% (Figure 6.1). Compared with other nanoemulsions prepared by the same method, the O/S ratios at which they are formed are high, that is, the amount of surfactant needed for nanoemulsion preparation is rather low [14]. For further studies, compositions with volatile organic compound (VOC) contents below 7 wt% and surfactant concentrations between 3 and 5 wt% were chosen, that is, nanoemulsions with a constant water content of 90% and O/S ratios from 50:50 to 70:30.

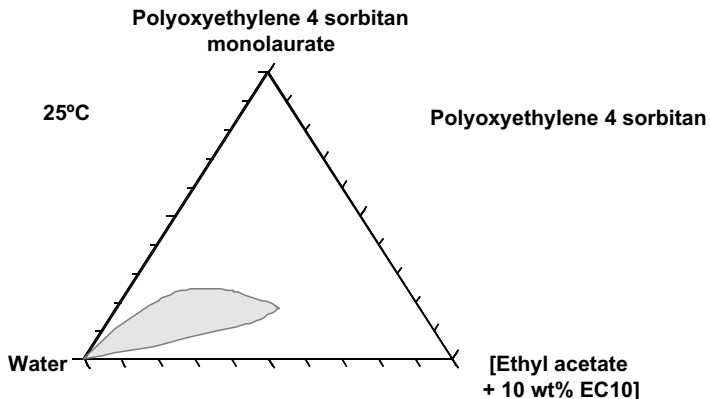


Figure 6.1 O/W nanoemulsion region in the water/polyoxyethylene 4 sorbitan monolaurate/[10% ethylcellulose (EC10) in ethyl acetate] system at 25 °C. Reproduced with permission from [54].

Phase inversion along the dilution path (by addition of water to the oil/surfactant mixture) followed for nanoemulsion preparation was confirmed by conductivity measurements, and was found to be essential for obtaining finely dispersed systems, as transparent dispersions were not obtained if the order of addition of the components was changed following an experimental path with no phase inversion (Figure 6.2).

The droplet sizes of the nanoemulsions characterized by dynamic light scattering at O/S ratios between 50:0 and 70:30 and a constant water content of 90 wt% were between 200 and 220 nm, displaying a slight increase with increasing O/S ratio. Figure 6.3 shows a typical cryo-transmission electron microscope (TEM) image of an

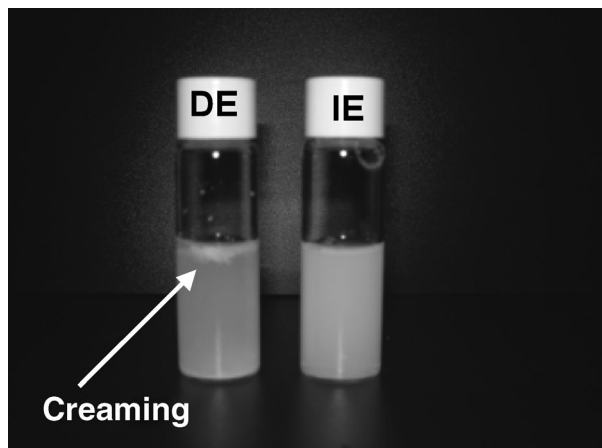


Figure 6.2 Visual appearances of the composition with an O/S of 70:30 and 90 wt% water content when prepared by direct emulsification (DE) and by inversion emulsification (IE).

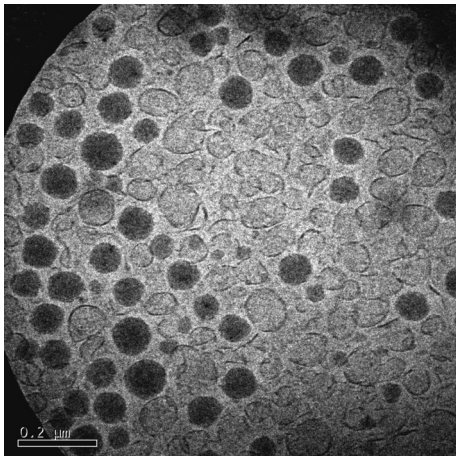


Figure 6.3 Cryo-TEM image of the nanoemulsions of the water/polyoxyethylene 4 sorbitan monolaurate/[10% EC10 in ethyl acetate] system with an O/S ratio of 70:30 and a water content of 90 wt%.

ethylcellulose nanoemulsion in which a high density of dispersed droplets of globular shape can be observed.

The nanoemulsion mean droplet sizes were much smaller than those obtained in other systems using polar oil mixtures (above 500 nm) [18]. The findings verify that the low-energy emulsification methods are valid not only for aliphatic [9, 10, 13, 75, 76, 79–81] and semipolar oils [82–84], as reported in most studies devoted to low-energy emulsification, but also for polar solvent–preformed polymer mixtures. These nanoemulsions show good kinetic stability at 25 °C over a period of at least 24 h,

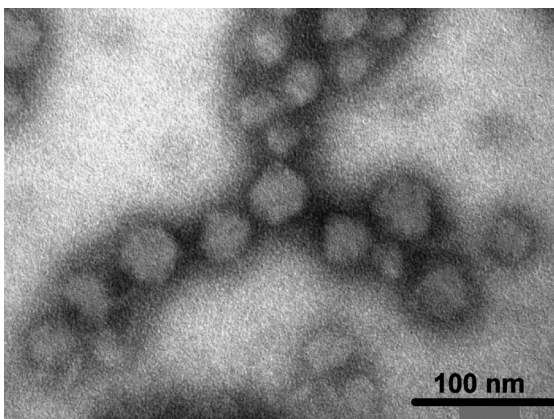


Figure 6.4 TEM image of the dispersion of nanoparticles obtained after evaporation of the solvent of a nanoemulsion with an O/S of 70:30 and a water content of 90 wt% and negative staining with a phosphotungstic acid solution. Reproduced with permission from [54].

considerably longer than the time needed to complete nanoparticle preparation by solvent evaporation. It was shown that composition variables such as O/S ratio and also the emulsification path involving phase inversion play a key role in the formation of stable, nanometer-sized emulsions. Nanoparticles prepared from these nanoemulsions displayed a round shape (Figure 6.4).

The particle size was below 50 nm (as determined by TEM image analysis), considerably smaller than that of the starting nanoemulsion, and showed a slight mean particle size increase and a broader size distribution with increasing O/S ratio, supporting the template effect of the nanoemulsion. The authors showed that these nanoparticles are interesting not only from a basic viewpoint but also for applications where safety and environmental concerns are important issues.

References

- 1 Solans, C., Esquena, J., Forgiarini, A.M., Usón, N., Morales, D., Izquierdo, P., Azemar, N. and Garcia-Celma, M.J. (2003) Nano-emulsions: formation, properties and applications. *Surf. Sci. Ser.*, **109**, 525–554.
- 2 Solans, C., Izquierdo, P., Nolla, J., Azemar, N. and Garcia-Celma, M.J. (2005) Nano-emulsions. *Current Opinion in Colloid and Interface Science*, **10** (3–4), 102–110.
- 3 Ugelstadt, J., El-Aasser, M.S. and Vanderhoff, J.W. (1973) Emulsion polymerization: initiation of polymerization in monomer droplets. *Journal of Polymer Science: Polymer Chemistry Edition*, **11**, 503–513.
- 4 El-Aasser, M.S., Lack, C.D., Choi, Y.T., Min, T.L. and Vanderhoff, J.W. (1984) Interfacial aspects of miniemulsions and miniemulsion polymers. *Colloids Surf.*, **12**, 79–97.
- 5 Miñana-Pérez, M., Gutron, C., Zundel, C., Andrérez, J.M. and Salager, J.L. (1999) Miniemulsion formation by transitional inversion. *Journal of Dispersion Science and Technology*, **20**, 893–905.
- 6 Zeevi, A., Klang, S., Alard, V., Brossard, F. and Benita, S. (1994) The design and characterization of a positively charged submicron emulsion containing a sunscreen agent. *International Journal of Pharmaceutics*, **108** (1), 57–58.
- 7 Sagitani, H. (1981) Making homogeneous and fine droplet o/w emulsions using nonionic surfactants. *Journal of the American Oil Chemists Society*, **58**, 738.
- 8 Nakajima, H. (1997) Microemulsions in Cosmetics. (eds C. Solans and H. Kunieda) *Industrial Applications of Microemulsions*, V 66. Marcel Dekker, New York, pp. 175–197.
- 9 Shinoda, K. and Saito, H. (1969) The stability of O/W type emulsions as functions of temperature and the HLB of emulsifiers: the emulsification by PIT-method. *Journal of Colloid and Interface Science*, **30**, 258–263.
- 10 Izquierdo, P., Esquena, J., Tadros, T.F., Dederen, C., Garcia, M.J., Azemar, N. and Solans, C. (2002) Formation and stability of nano-emulsions prepared using the phase inversion temperature method. *Langmuir*, **18** (1), 26–30.
- 11 Morales, D., Gutiérrez, J.M., García-Celma, M.J. and Solans, C. (2003) A study of the relation between bicontinuous microemulsions and oil/water nanoemulsion formation. *Langmuir*, **19**, 7196–7200.
- 12 Izquierdo, P., Feng, J., Esquena, J., Tadros, T.F., Dederen, J.C., Garcia, M.J., Azemar, N. and Solans, C. (2005) The influence of surfactant mixing ratio on nano-emulsion formation by the PIT method. *Journal of Colloid and Interface Science*, **285** (1), 388–394.
- 13 Forgiarini, A., Esquena, J., Gonzalez, C. and Solans, C. (2001) Formation of nano-emulsions by low-energy emulsification methods at constant temperature. *Langmuir*, **17** (7), 2076–2083.

- 14** Sadurní, N., Solans, C., Azemar, N. and García-Celma, M.J. (2005) Studies on the formation of O/W nano-emulsions, by low-energy emulsification methods, suitable for pharmaceutical applications. *Emulsion polymerization: initiation of polymerization in monomer droplets.*, **26**, 438–445.
- 15** Fernández, P., André, V., Rieger, J. and Kühnle, A. (2004) Nano-emulsion formation by emulsion phase inversion. *Colloids and Surfaces A: Physicochemical and Engineering Aspects*, **251**, 53–58.
- 16** Solé, I., Maestro, A., González, C., Solans, C. and Gutiérrez, J.M. (2006) Optimization of nano-emulsion preparation by low-energy methods in an ionic surfactant system. *Langmuir*, **22** (20), 8326–8332.
- 17** Gutiérrez, J.M., González, C., Maestro, A., Solé, I., Pey, C.M. and Nolla, J. (2008) Nano-emulsions: new applications and optimization of their preparation. *Current Opinion in Colloid and Interface Science*, **13**, 245–251.
- 18** Bouchemal, K., Briançon, S., Perrier, E. and Fessi, H. (2004) Nano-emulsion formulation using spontaneous emulsification: solvent, oil and surfactant optimisation. *International Journal of Pharmaceutics*, **280**, 241–251.
- 19** Lee, V.A., Karthikeyan, R., Rawls, H.R. and Amaechi, B.T. (2010) Anti-cariogenic effect of a cetylpyridinium chloride-containing nanoemulsion. *J. Dent.*, **38**, 742–749.
- 20** Izquierdo, P., Wiechers, J.W., Escribano, E., García-Celma, M.J., Tadros, T.F., Esquena, J., Federen, J.C. and Solans, C. (2007) A study on the influence of emulsion droplet size on the skin penetration of tetracaine. *Skin Pharmacology and Physiology*, **20**, 263–270.
- 21** Hwang, T.-L., Fang, C.-L., Chen, C.-H. and Fang, J.-Y. (2009) Permeation enhancer-containing water-in-oil nanoemulsions as carriers for intravesical cisplatin delivery. *Pharmacological Research*, **26** (10), 2314–2323.
- 22** Klang, V., Matsko, N., Zimmermann, A.M., Vojnikovic, E. and Valenta, C. (2010) Enhancement of stability and skin permeation by sucrose stearate and cyclodextrins in progesterone nanoemulsions. *International Journal of Pharmaceutics*, **393**, 152–160.
- 23** Younenang Piemi, M.P., Korner, D., Benita, S. and Marty, J.P. (1999) Positively and negatively charged submicron emulsions for enhanced topical delivery of antifungal drugs. *Journal of Controlled Release*, **58**, 177–187.
- 24** Ganta, S. and Amiji, M. (2009) Coadministration of paclitaxel and curcumin in nanoemulsion formulations to overcome multidrug resistance in tumor cells. *Molecular Pharmacology*, **6** (3), 928–939.
- 25** Sonneville-Aubrun, O., Simonnet, J.-T. and L'Alloret, F. (2004) Nanoemulsions: a new vehicle for skincare products. *Advances in Colloid and Interface Science*, **108–109**, 145–149.
- 26** Maruno, M. and da Rocha-Filho, P.A. (2010) O/W nanoemulsion after 15 years of preparation: a suitable vehicle for pharmaceutical and cosmetic applications. *Journal of Dispersion Science and Technology*, **31**, 17–22.
- 27** Calderó, G., Pi Subirana, R., Llosas Bigorra, J. and Torres Fernandez, M. (2001) Use of alkyl(ether) phosphates (I). European Patent EP 1264633.
- 28** Sonneville-Aubrun, O. and Simonnet, J.-Th. (2001) Nanoemulsion based on anionic polymers, and uses thereof especially in the cosmetic, dermatological, pharmaceutical and/or ophthalmic fields. European Patent EP 1160005.
- 29** Lee, G.W.J. and Tadros, Th.F. (1982) Formation and stability of emulsions produced by dilution of emulsifiable concentrates. Part I. An investigation of the dispersion on dilution of emulsifiable concentrates containing cationic and non-ionic surfactants. *Colloids Surf.*, **5**, 105–115.
- 30** Jon, D.I., Prettypaul, D.I., Benning, M.J., Narayanan, K.S. and Ianniello, R.M. (1998) (eds J.D. Nalewaja, G.R. Goss, and R.S. Tann.) *Pesticide Formulations and Application Systems*, Vol. 18 ASTM STP1347, American Society for Testing and Materials West Conshohocken, PA, pp. 228–241.
- 31** Wang L, Li, X., Zhang, G., Dong, J. and Eastoe, J. (2007) Oil-in-water nanoemulsions for pesticide formulations. *Journal of Colloid and Interface Science*, **314**, 230–235.
- 32** Henry, J.V.L., Fryer, P.J., Frith, W.J. and Norton, I.T. (2010) The influence of phospholipids and food proteins on the

- size and stability of model sub-micron emulsions. *Food Hydrocolloids*, **24**, 66–71.
- 33** Qian, C. and McClements, D.J. (2011) Formation of nanoemulsions stabilized by model food-grade emulsifiers using high-pressure homogenization: factors affecting particle size. *Food Hydrocolloids*, **25** (5), 1000–1008.
- 34** Lee, S.J. and McClements, D.J. (2010) Fabrication of protein-stabilized nanoemulsions using a combined homogenization and amphiphilic solvent dissolution/evaporation approach. *Food Hydrocolloids*, **24**, 560–569.
- 35** Chattopadhyay, D.P. and Vyas, D.D. (2010) Effect of silicone nano-emulsion softener on physical properties of cotton fabric. *Indian Journal of Fibre and Textile Research*, **35** (1), 68–71.
- 36** Parvinzadeh, M. and Hajiraiissi, R. (2008) Effect of nano and micro emulsion silicone softeners on properties of polyester fibers. *Tenside Surfactants Detergents*, **45** (5), 254–257.
- 37** Lesueur, D., Herrero, L., Uguet, N., Hurtado, J., Peña, J.L., Potti, J.J., Walter, J. and Lancaster, I. (2008) Bitumen nano-emulsions and their interest for cold recycling of bituminous mix. *Carreteras*, **4** (158), 48–53.
- 38** Lesueur, D., Uguet Canal, N., Hurtado Aznar, J. and Herrero, L. (2009) Bitumen nanoemulsions. *Carreteras*, **4** (163), 33–46.
- 39** Mehner, W. and Mäder, K. (2001) Solid lipid nanoparticles. Production, characterization and applications. *Advanced Drug Delivery Reviews*, **47**, 165.
- 40** Perrier, T., Saulnier, P., Fouchet, F., Lautram, N. and Benoit, J.P. (2010) Post-insertion into Lipid NanoCapsules (LNCs): from experimental aspects to mechanisms. *International Journal of Pharmaceutics*, **396**, 204–209.
- 41** Willert, M., Rothe, R., Landfester, K. and Antonietti, M. (2001) Synthesis of inorganic and metallic nanoparticles by miniemulsification of molten salts and metals. *Chemistry of Materials*, **13**, 4681–4685.
- 42** Pinto Reis, C., Neufeld, R.J., Ribeiro, A.J., Veiga, F. and Nanoencapsulation., I. (2006) Methods for preparation of drug loaded polymeric nanoparticles. *Nanomedicine: Nanotechnology, Biology, and Medicine*, **2**, 8–21.
- 43** Vauthier, Ch. and Bouchemal, K. (2009) Methods for the preparation and manufacture of polymeric nanoparticles. *Pharmacological Research*, **26**, 1025–1058.
- 44** Desgouilles, S., Vauthier, C., Bazile, D., Vacus, J., Grossiord, J.L., Veillard, M. and Couvreur, P. (2003) The design of nanoparticles obtained by solvent evaporation. A comprehensive study. *Langmuir*, **19**, 9504–9510.
- 45** Song, X., Zhao, Y., Hou, S., Xu, F., Zhao, R., He, J., Cai, Z., Li, Y. and Chen, Q. (2008) Dual agents loaded PLGA nanoparticles: systematic study of particle size and drug entrapment efficiency. *European Journal of Pharmaceutics and Biopharmaceutics*, **69**, 445–453.
- 46** Asua, J.M. (2002) Miniemulsion polymerization. *Progress in Polymer Science*, **27**, 1283–1346.
- 47** Tiarks, F., Landfester, K. and Antonietti, M. (2001) Preparation of polymeric nanocapsules by miniemulsion polymerization. *Langmuir*, **17**, 908–918.
- 48** Landfester, K. (2001) The generation of nanoparticles in miniemulsions. *Advanced Materials*, **13**, 765–768.
- 49** Anton, N., Benoit, J.P. and Saulnier, P. (2008) Design and production of nanoparticles formulated from nanoemulsion templates – a review. *Journal of Controlled Release*, **128**, 185–199.
- 50** Steinhilber, D., Seiffert, S., Heyman, J.A., Paulus, F., Weitz, D.A. and Haag, R. (2011) Hyperbranched polyglycerols on the nanometer and micrometer scale. *Biomaterials*, **32**, 1311–1316.
- 51** Galindo-Alvarez, J., Boyd, D., Marchal, Ph., Tribet, Ch., Perrin, P., Bégué, E.M., Durand, A. and Sadler, V. (2011) Miniemulsion polymerization templates: a systematic comparison between low energy emulsification (Near-PIT) and ultrasound emulsification methods. *Colloids and Surfaces A: Physicochemical and Engineering Aspects*, **374** (1–3), 134–141.
- 52** Venier-Julienne, M.C. and Benoit, J.P. (1996) Preparation, purification and morphology of polymeric nanoparticles as drug carriers. *Pharmaceutica Acta Helveticae*, **71**, 121–128.
- 53** Moinard-Chécot, D., Chevalier, Y., Briançon, S., Beney, L. and Fessi, H.

- (2008) Mechanism of nanocapsules formation by the emulsion-diffusion process. *Journal of Colloid and Interface Science*, **317**, 458–468.
- 54** Calderó, G., García-Celma, M.J. and Solans, C. (2011) Formation of polymeric nano-emulsions by a low-energy method and their use for nanoparticle preparation. *Journal of Colloid and Interface Science*, **353**, 406–411.
- 55** Doenges, R. (1990) Non-ionic cellulose ethers. *British Polymer Journal*, **23** (4), 315–326.
- 56** Rekhi, G.S. and Jambhekar, S.S. (1995) Ethylcellulose – a polymer review. *Drug Development and Industrial Pharmacy* **21** 61–77.
- 57** Rowe, R.C., Sheskey, P.J., and Owen, S.C. (2006) Ethylcellulose. *Handbook of Pharmaceutical Excipients*, 5th edn., Pharmaceutical Press, London, p. 278.
- 58** Kamitakahara, H., Funakoshi, T., Nakai, S., Takano, T. and Nakatubo, F. (2010) Synthesis and structure/property relationships of regioselective 2-O-, 3-O- and 6-O-ethyl celluloses. *Macromolecular Bioscience*, **10**, 638–647.
- 59** Ubrich, N., Bouillot, Ph., Pellerin, Ch., Hoffman, M. and Maincent Ph. (2004) Preparation of propranolol hydrochloride nanoparticles: a comparative study. *Journal of Controlled Release*, **97** 291–300.
- 60** Jelvehgari, M., Siah-Shadbad, M.R., Azarmi, S., Martin, G.P. and Nokhodchi, A. (2006) The microsponge delivery system of benzoyl peroxide: preparation, characterization and release studies. *International Journal of Pharmaceutics*, **308**, 124–132.
- 61** Lavasanifar, A., Ghalandari, R., Ataei, Z., Zolfaghari, M.E. and Mortazavi, S.A. (1997) Microencapsulation of theophylline using ethylcellulose: *in vitro* drug release and kinetic modelling. *Journal of Microencapsulation*, **14**, 91–100.
- 62** Chen, H., Wu, J.-C. and Chen, H.-Y. (1995) Preparation of ethylcellulose microcapsules containing theophylline by using emulsion non-solvent addition method. *Journal of Microencapsulation*, **12**, 137–147.
- 63** Perugini, P., Simeoni, S., Scalia, S., Genta, I., Modena, T., Conti, B. and Pavanetto, F. (2002) Effect of nanoparticle encapsulation on the photostability of the sunscreen agent, 2-ethylhexyl-*p*-methoxycinnamate. *International Journal of Pharmaceutics*, **246**, 37–45.
- 64** Allémann, E., Gurny, R. and Doelker, E. (1992) Preparation of aqueous polymeric nanodispersions by a reversible salting-out process: influence of process parameters on particle size. *International Journal of Pharmaceutics*, **87**, 247–253.
- 65** Jalsenjak, I., Nicolaïdou, C.F. and Nixon, J.R. (1976) The *in vitro* dissolution of phenobarbitone sodium from ethylcellulose microcapsules. *Journal of Pharmacy and Pharmacology*, **28**, 912–914.
- 66** Özyazici, M., Sevgi, F. and Ertan, G. (1996) Micromeritic studies on nicardipine hydrochloride microcapsules. *International Journal of Pharmaceutics*, **138**, 25–35.
- 67** Benita, S. and Donbrow, M. (1982) Dissolution rate control of the release kinetics of water-soluble compounds from ethylcellulose film-type microcapsules. *International Journal of Pharmaceutics*, **12**, 251–264.
- 68** Tirkkonen, S. and Paronen, P. (1992) Enhancement of drug release from ethylcellulose microcapsules using solid sodium chloride in the wall. *International Journal of Pharmaceutics*, **88**, 39–51.
- 69** Zang, Z.-Y., Ping, Q.-N. and Xiao, B. (2000) Microencapsulation and characterization of tramadol–resin complexes. *Journal of Controlled Release*, **66**, 107–113.
- 70** Grattard, N., Pernin, M., Marty, B., Roudaut, G., Champion, D. and Le Meste, M. (2002) Study of release kinetics of small and high molecular weight substances dispersed into spray-dried ethylcellulose microspheres. *Journal of Controlled Release*, **84**, 125–135.
- 71** Chen, L., Li, B., Zhang, Y., Wu, Y., Hua, Z., Liu, Z. and Lu, W. (2003) Particle formation of ethyl cellulose using supercritical CO₂ as antisolvent. *Energy and the Environment – Proceedings of the International Conference on Energy and the Environment*, Shanghai Vol. 2, pp. 1460–1465.
- 72** André-Abrant, A., Taverdet, J.-L. and Jay, J. (2001) Microencapsulation par évaporation de solvant. *European Polymer Journal*, **37**, 955–963.

- 73** Morales, M.E., Ruiz, M.A., Oliva, I., Oliva, M. and Gallardo, V. (2007) Chemical characterization with XPS of the surface of polymer microparticles loaded with morphine. *International Journal of Pharmaceutics*, **333**, 162–166.
- 74** Arias, J.L., López-Viota, M., López-Viota, J. and Delgado, A.V. (2010) Iron/ethylcellulose (core/shell) nanoplatform loaded with 5-fluorouracil for cancer targeting. *Colloids and Surfaces B: Biointerfaces*, **77**, 111–116.
- 75** Spernath, L. and Magdassi, S. (2007) Preparation of ethylcellulose nanoparticles from nano-emulsion obtained by inversion at constant temperature. *Micro & Nano Letters*, **2**, 90–95.
- 76** Generalova, A.N., Sizova, S.V., Oleinikov, V.A., Zubov, V.P., Artemyev, M.V., Spernath, L., Kamyshny, A. and Magdassi Sh. (2009) Highly fluorescent ethyl cellulose nanoparticles containing embedded semiconductor nanocrystals. *Colloids and Surfaces A: Physicochemical and Engineering Aspects*, **342** 59–64.
- 77** Arias, J.L., López-Viota, M., Ruiz, M.A., López-Viota, J. and Delgado, A.V. (2007) Development of carbonyl iron/ethylcellulose core/shell nanoparticles for biomedical applications. *International Journal of Pharmaceutics*, **339**, 237–245.
- 78** ICH (2005) *International Conference on Harmonisation of Technical Requirements for Registration of Pharmaceuticals for Human Use. Impurities: Guideline for Residual Solvents*. ICH Harmonised Tripartite Guideline.
- 79** Wang, L., Mutch, K.J., Eastoe, J., Heenan, R.K. and Dong, J. (2008) Nanoemulsions prepared by a two-step low-energy process. *Langmuir*, **24**, 6092–6099.
- 80** Wang, L., Tabor, R., Eastoe, J., Li, X., Heenan, R.K. and Dong, J. (2009) Formation and stability of nanoemulsions with mixed ionic–nonionic surfactants. *Physical Chemistry Chemical Physics*, **11**, 9772–9778.
- 81** Morales, D., Solans, C., Gutiérrez, J.M., García-Celma, M.J. and Olsson, U. (2006) Oil/water droplet formation by temperature change in the water/C16E6/mineral oil system. *Langmuir*, **22**, 3014–3020.
- 82** Wadle, A., Förster, Th. and von Rybinski, W. (1993) Influence of the microemulsion phase structure on the phase inversion temperature emulsification of polar oils. *Colloids and Surfaces A: Physicochemical and Engineering Aspects*, **76**, 51–57.
- 83** Yang, H.J., Cho, W.G. and Park, S.N. (2009) Stability of oil-in-water nanoemulsions prepared using the phase inversion composition method. *Journal of Industrial and Engineering Chemistry*, **15**, 331–335.
- 84** Förster, Th., von Rybinski, W. and Wadle, A. (1995) Influence of microemulsion phases on the preparation of fine-disperse emulsions. *Advances in Colloid and Interface Science*, **58**, 119–149.

7

Toxicity of Carbon Nanotubes

Dania Movia and Silvia Giordani

7.1

Introduction – Nanotoxicology: Should We Worry?

The rapid rate of development and commercialization of engineered nanomaterials (ENMs) in the last decade, and the increasing research interest in the new and unusual properties of nanotechnology-related pharmaceutical and medical devices, have highlighted the need for assessing potential health risks posed by nanoscale materials. A recent study on the public perception of ENMs showed that 50% of the general public have at least some familiarity with nanotechnology, and those who perceive greater benefits outnumber those who perceive greater risks [1]. As consumers continually increase their expectations about the safety of products [2], a healthy debate among toxicologists, regulators, and the public is taking place; what emerges is a paucity of metrological and toxicological data, with only a few specific ENMs investigated in a limited number of test systems [3].

The main concerns voiced by toxicology experts about the potential toxicity of ENMs are fueled by consideration of the different properties of ENMs compared with bulk states. First, in comparison with bulk materials, ENMs possess a higher surface area, thus enhancing the contact area with their surroundings. This could expose catalytic or reactive sites on the ENM surface, inducing in some cases the formation of reactive oxygen species [4]. Increased surface area may also promote dissolution of the ENM and thus lead to the release of potentially toxic ions, such as heavy metals [5]. Second, owing to their small size, ENMs may enter in many cells and organs to a greater extent than do bulk materials. Long-term toxic effects due to prolonged accumulation and retention in the organism therefore need to be considered. Third, the shape of ENMs may play a crucial role in determining toxic responses. Geometric effects have been shown, for example, in the case of carbon nanotubes (CNTs), which caused “frustrated phagocytosis” effects in macrophage models [6]. Additionally, differences in synthetic methods, impurities, coatings, and surface functionalization can lead to thousands of possible ENM variants. Consequently, nanotoxicology challenges include (1) the large number of substances that need to be tested and (2) how to offer increased efficiency in tests design and costs.

Over the past 5 years, there has been an on-going debate on the most appropriate test strategies to use for evaluating the potential hazards of ENMs. Clearly, not all can be evaluated in *in vivo* studies [2], as a single *in vivo* study can cost US\$50 000 [7]: traditional *in vivo* studies conducted on even those ENMs currently in commerce could total a billion dollars and it could take 30–50 years to be completed. International efforts have geared towards establishing characterization schemes and consistent approaches for various ENMs [4, 8–10]. Currently, nanotechnology policies and regulation are encouraging the development of new test models, the implementation of *in vitro* high-throughput screening tools [2, 7, 11], and the assessment of the physicochemical properties of the tested nanomaterial within existing experimental test systems [12–14]. The toxicological outputs of a specific ENM may be different depending on, for example, the specific protein content of the environment, concentrations of impurities, and methods used to “dissolve” the ENMs [14, 15]. Agglomeration and aggregation are also recognized as a major issue in the evaluation of the effects of ENMs. For the same reason, what constitutes “dose” for a nanomaterial may not always be “mass” (ppm, mg kg⁻¹, mol l⁻¹) and the dose metric of concern may be related to some aspect of the ENM physical structure [8]. This is well known in particle and fiber toxicology, where the dose metric may be expressed as the surface area of the particle or the number of fibers of a given length [13]. Any changes to the physical structure (such as particle size through agglomeration) within the experimental test system may therefore affect the “dose” of the ENMs.

In 2005, the US Environmental Protection Agency (EPA), with support from the US National Toxicology Program (NTP), funded a project at the National Research Council (NRC) for developing a long-range vision for toxicity testing and a strategic plan for implementing that vision [16]. In summary, NRC proposed a largely *in vitro* approach for the evaluation of toxicity of substances of public health concern. In recent years, there have been many attempts to apply this approach to the study of ENMs, and a number of paradigms have emerged in nanotoxicology: the bio–nano interface/protein corona paradigm [17], the oxidative stress paradigm [10], and the pathogenic fiber paradigm [18], to name just a few. Such theoretical paradigms are helpful as platforms from which to interpret a large number of *in vitro* data. However, although this approach may have merit in accelerating the rate of gathering toxicological data on ENMs by predicting their hazard potential, it does not state the *in vivo* disease outcome, which depends on a number of variables that cannot be included in *in vitro* studies. The serious limitations of *in vitro* models, including the number of co-cultured cell types and the methods of exposing cells, do not reproduce the physiological relevance of coordinated responses among various cell types in tissues and organs, and the delivery of ENMs in a single dose does not reflect *in vivo* realistic conditions, where ENMs are likely to accumulate gradually. An important question in nanotoxicology therefore relates to the selection of doses. High doses may, for example, never be reached under realistic exposure conditions in secondary organs. Likewise, the relevance of *in vivo* bolus-type instillation studies comes into question when researchers use doses that far exceed those achieved in a realistic human exposure scenario. Verification of such studies will be necessary by investigating the biokinetics of ENMs.

7.2

Toxicity of Carbon Nanotubes

Among ENMs, the toxicity of CNTs is one of the better researched nanotoxicity areas. CNTs represent a relatively newly discovered allotrope of carbon that is seen to have a wide range of potential applications within nanotechnology [19]. Individual nanotubes, formed by a single wall (SWNTs) or multiple concentric walls (MWNTs) of graphite sheets, have diameters as small as 0.7 nm and lengths exceeding 1 μm . At present, CNTs can be produced by different techniques, such as electric arc discharge, catalytic decomposition, chemical vapor deposition (CVD), and the high-pressure CO disproportionation process (HiPCO) [20]. Due to the synthetic mechanism, high concentrations of undesirable defects and carbonaceous and metal catalyst impurities are generally present in the as-produced CNT materials.

Concern over the potential toxic impact of CNTs on environmental and human health is recent. Up to 2006, there were fewer than 10 published research studies focusing on CNT toxicity [21]. From that year onwards, the number of reports investigating *in vitro* and *in vivo* toxicity of CNTs has increased exponentially. Both test models reveal concerns regarding CNT toxicity, providing at times contradictory results, and raising more questions. Because of these divergent reports, specific pathways and mechanisms through which CNTs may exert their toxic effects *in vivo* remain unknown. The main mechanisms proposed are: (1) oxidative stress due to redox features in the presence of physiologically relevant redox agents [22, 23]; (2) inflammatory and fibrogenic responses in lungs, accompanied by a pulmonary function decline and enhanced susceptibility to infections [24]; (3) toxic effect of transition metals or other environmental contaminants present in as-produced CNTs [25, 26]; and (4) ineffective recognition of CNTs by macrophages [27]. The clinical implications of CNT toxicity are still uncertain, since human exposure data and specific applications of CNTs are not yet clearly defined.

CNTs can enter the human body through dermal contact, inhalation, intentional injection, or ingestion [21]. Additionally, CNTs could translocate to distant organs and tissues, such as the intraperitoneal cavity. The interaction of carbon nanotubes with the immune system, particularly macrophages, may play a significant role in such translocation processes [22]. The purpose of this chapter is to provide a review of the main *in vitro* and *in vivo* data reported in the literature to date regarding the toxicity of CNTs, when encountering the body through various portals of entry. We also focus on the identification of the major challenges associated with the assessment of CNT toxicity in *in vitro* systems, and we briefly review the biodistribution and biodegradation pathways of CNTs.

7.2.1

Challenges in the Assessment of CNT Toxicity

Several factors are associated with the difficulty in assessing CNT toxicity. Among them, CNT interactions with components of the dispersing medium, the cytotoxicity assay employed, impurities, CNT surface chemistry, and dispersion state are the

main parameters. Such factors may also be sources of discrepancies in the CNT toxicity data available in the literature.

7.2.1.1 Interaction with Dispersing Medium

Toxicological testing of CNTs typically involves their dispersion within a biological medium, followed by their addition to a cell line of interest or by administration to animal models. However, the degree of interaction between CNTs and the medium employed, and the influence of such interactions on cellular responses are not completely exploited. Considerable interaction between carbon nanotubes and components of the cell culture medium, such as Phenol Red, riboflavin, and fetal bovine serum, have been evidenced as a result of physisorption through van der Waals forces [28]. Such a spontaneous accumulation of bio-compounds at the solid–liquid interface (and the subsequent formation of bio-coatings on the ENM surface) is a process commonly denoted as formation of biomolecule “corona.” If a nanomaterial enters the cell, modification of the components absorbed on its surface is expected, with variations depending on the cell compartment of interest [15]. *In vivo* this may be translated into slow exchange of the protein corona depending on the organ involved or in different bioavailability thresholds in the various areas of the body. These interactions may potentially play a role in the toxicity of CNTs [29] by reducing the availability of proteins and nutrients to the cells [28], modifying the conformational state of the components and their functionality [14], influencing the cell recognition [14, 30], or adsorbing cell-signaling immunomodulating agents (cytokines) on the CNT surface [31].

7.2.1.2 Interaction with Cytotoxicity Assays

A number of *in vitro* toxicity assays have been developed to determine cell viability and/or cytotoxicity in cultured cells. These assays often use colorimetric or fluorescent dyes as markers assessing membrane integrity or cellular metabolism. Whereas these assays have shown to provide accurate data for various molecular families, they have been shown to provide less reliable results when assessing ENM cytotoxicity. CNTs interact with various commonly used cytotoxicity assays, resulting in interference with the absorption/fluorescence properties of the dye employed. The results may under- or overestimate the toxic response, providing confusing results, false-positive results, and conflicting reports. For this reason, Wörle-Knirsch *et al.* [32], followed by Casey *et al.* [33] and Monteiro-Riviere *et al.* [34], advised caution when performing even established toxicity assays in the presence of significant quantities of carbon nanostructures, and encouraged the use of at least two or more independent test assays to validate *in vitro* results on ENMs. Table 7.1 summarizes potential interactions reported in the literature between CNTs and various cytotoxic assays.

The knowledge gathered so far consists of data based on a nonstandardized CNT material; thus, all the studies reviewed in Table 7.1 have to be considered as isolated and not directly comparable experiments. In particular, from the divergent interpretation of the WST-1 assay output in two different studies, it is clear that a standardized CNT reference material used by all toxicologists is needed. It is also important to keep in mind that the employment of viability tests based on the

Table 7.1 Summary of cytotoxicity assays used in *in vitro* toxicity studies on CNTs.

Assay	Stain/dye	Target	Data reliability	Ref.
Calcein AM (CAM)	Live cells: green stained	Cell membrane	Yes ^{a)}	[34]
Coomassie Brilliant Blue G250 dye	Binds specifically to tyrosine side chains of proteins	Cell membrane	No	[33]
CytoTox One Homogeneous Membrane Integrity (CTO)	LDH released by cells with damaged membrane results in the conversion of resazurin into a fluorescent resorufin product	Cell membrane	No	[34]
Lactate dehydrogenase (LDH)	LDH released by cells with damaged membrane results in the conversion of a tetrazolium compound into a water-soluble fluorescent formazan dye	Cell membrane	Yes ^{a)}	[34]
Trypan Blue exclusion (TB)	Dead cells: blue stained	Cell metabolism	No	[33, 34]
Alamar Blue (AB)	Live cells: resazurin reduction to red fluorescent dye resorufin	Cell metabolism	Yes	[34]
Celtitier 96 Aqueous One (96 AQ)	Live cells: tetrazolium conversion to soluble purple formazan salt	Cell metabolism	Yes	[34]
CellTiter-Blue (CTB)	Kit form of AB	Cell metabolism	Yes	[32]
Mitochondrial Membrane Potential (MMP)	Detection of metalloproteinase activity	Cell metabolism	Yes	[34]
MTT	Live cells: tetrazolium conversion to insoluble purple formazan salt	Cell metabolism	No	[32–34]
WST-1	Live cells: tetrazolium conversion to water-soluble purple formazan salt	Cell metabolism	Yes	[32]
Live/Dead (LD)	Dead cells: red stained. Live cells: green stained	Dead cells: nucleic acid. Live cells: cell membrane	No Yes ^{a)}	[33] [34]
Neutral Red (NR)	Live cells: red lysosomes	Lysosomal membrane	No	[33, 34]

a) Difficult interpretation due to deposition of CNTs on the cell monolayer.

evaluation of cellular metabolic activity may give false-positive results, as many different conditions can increase or decrease the metabolic activity of treated cells while the number of viable cells remains constant.

7.2.1.3 Effect of Impurities

Variation of the content of impurities in the different CNT preparations [21] offers additional challenges in the accurate and consistent assessment of CNT toxicity. As-produced CNTs generally contain high amounts of catalytic metal particles, such as iron and nickel, used as precursors in their synthesis. The cytotoxicity of high concentrations of these metals is well known [35, 36], mainly due to oxidative stress and induction of inflammatory processes generated by catalytic reactions at the metal particle surface [37]. Another very important contaminant is amorphous carbon, which exhibits comparable biological effects to carbon black or relevant ambient air particles.

7.2.1.4 Effect of Dispersion

The poor dispersibility of CNTs in biological media can affect both the cytotoxicity [38] and the *in vivo* toxicity [39] of such nanomaterials.

In vitro, cell responses seem to depend strongly on the dispersing agent employed. Decreased oxidative stress was shown in primary bronchial epithelial (NHBE) cells and in alveolar epithelial carcinoma (A549) cells when incubated with SWNTs dispersed in cell culture medium with fetal calf serum (FCS) supplement; whereas addition of dipalmitoylphosphatidylcholine (DPPC), the major constituent of lung surfactant, resulted in increasing oxidative stress [40]. Alpatova *et al.* [38] demonstrated that noncovalent functionalized SWNTs by a range of natural (gum arabic, amylase, Suwanee River natural organic matter) and synthetic (polyvinylpyrrolidone, Triton X-100) surfactants did not cause any cell viability loss in cultured *Escherichia coli* and rat liver epithelial (WB-F344) cells, when the dispersing agent itself was noncytotoxic. Similar results were reported previously by Dong *et al.* [41], showing that the cytotoxicity of SWNTs incubated with human astrocytoma cells depends on the toxicity of the surfactant employed.

In vivo, SWNTs individually dispersed by Pluronic F108NF were demonstrated to be nontoxic after intratracheal administration to mice, whereas aggregated SWNTs caused granuloma-like structures with mild fibrosis in the lungs of the treated animals [39].

7.3

Dermal Exposure to CNTs

Dermal contact is one of the main routes of both occupational and environmental exposure to CNTs.

Skin toxicity is determined by the penetration and transport of the compound being tested through the lipid matrix in the outer skin layers (the stratum corneum)

and by subsequent interaction with a variety of cell types in the subsurface layers [29]. The physicochemical properties of CNTs and their nonhomogeneous composition may affect their ability to penetrate the skin by affecting, for example, their rate of absorption, or their uptake in skin cells. These properties are therefore key parameters in the dermal toxicological responses to CNTs [29].

7.3.1

Dermal Cytotoxicity

MWNTs were found to be cytotoxic in human skin fibroblasts (HSF42) and human epidermal keratinocytes (HEK) [42–44], whereas SWNTs were toxic in human keratinocyte (HaCaT) cultures [25, 26, 45]. Reduced cell proliferation and oxidative stress were reported also in epithelial (HeLa) cells [45] and murine epidermal cells (JB6 P+) [46] upon incubation with SWNTs.

Briefly, HSF42 cells exposed to high concentrations (0.6 mg ml^{-1}) of MWNTs underwent apoptosis/necrosis with a concomitant reduction in proliferation, indicative of an inflammation response [42]. The phenotypic observations were also correlated with changes in the mRNA levels in the cells exposed to MWNT samples. The genes up/down-regulated were associated with metabolism, apoptosis, cell cycle, stress response, cellular transport, and inflammatory response. In the same way, Witzmann and Monteiro-Riviere [44] showed that after 24 h the expression of 36 proteins was altered in HEK cells exposed to MWNTs, whereas at 48 h the level of 106 proteins was significantly changed. Such proteins were associated with metabolism, cell signaling, stress, and also cytoskeleton elements and vesicular tracking components. Similarly, Zollanvari *et al.* [47] showed that HEK cells treated with SWNTs were characterized by different expression of genes involved in a number of cellular processes, including regulation of transcription and translation, protein localization, transport, cell cycle progression, cell migration, cytoskeleton reorganization, and signal transduction. The majority of these genes show significant changes in expression at both the low (0.001 mg ml^{-1}) and high (1 mg ml^{-1}) doses. Notably, the gene expression of SWNT-treated cells became closer to the gene expression of the control cultures over time.

Exposure of HaCaT cell cultures to SWNTs resulted in accelerated oxidative stress (i.e., increased free radical and peroxide generation, and depletion of total antioxidant reserves), loss in cell viability, reduced cell proliferation, and morphological alterations to cellular structure [25, 45]. The dermal cytotoxicity of SWNTs was found to be dose dependent and material dependent in HaCaT cells, with higher cytotoxicity in the case of HiPCO SWNTs than SWNT samples produced by arc discharge techniques [26]. According to several studies [25, 26, 46], the different cytotoxicity thresholds were determined by the presence of iron in the HiPCO SWNTs and by differences in the metal–carbon residue ratio between the two SWNT samples. Controversially, Monteiro-Riviere *et al.* [43] gave divergent dermal toxicity warnings, showing that MWNTs purified from residual metal impurities caused an inflammatory response in HEK cells. Purified MWNTs were localized within the cytoplasmic vacuoles of cells; they induced the release of

pro-inflammatory cytokines [interleukin-8 (IL-8)], and cell viability decreased in a time- and dose-dependent manner. The lack of catalyst particles in the MWNT sample led the authors to conclude that CNTs themselves were a potential dermatological hazard.

Notably, the cytotoxic response of cultured dermal cells exposed to CNTs seems to depend on the functionalization grade of the CNTs tested [31, 48]. Sayes *et al.* [48] showed that SWNTs purified and functionalized with phenyl-SO₃H, phenyl-SO₃Na or phenyl-(COOH)₂ were less toxic than nonfunctionalized nanotubes solubilized by a surfactant coating (1% Pluronic F108) in human dermal fibroblasts (HDF). The metabolic activity of HDF cells was found to be unchanged after exposure to functionalized SWNTs, and the cell death was decreased by increasing the degree of covalent functionalization. Even though functionalized SWNTs did not cause significant cell death, optical and atomic force microscopy suggested a relatively significant interaction of SWNTs with the cell membrane. This interaction might be useful in the development of nanotube-based drug delivery systems, but it could also lead to inflammatory and cytotoxic effects. Similarly, SWNTs purified and functionalized with 6-aminohexanoic acid (AHA-SWNTs) were noncytotoxic in HEK cells at 0.05 µg ml⁻¹ concentration after 24 h of exposure [31]. However, the increase in IL-6 and IL-8 secretion indicated that AHA-SWNTs could initiate an early inflammatory response. The authors showed that the cytotoxic responses could be further decreased by surfactant coating of the functionalized tubes (1% Pluronic F127). This may be correlated either with a higher debundling of the nanotubes, or with AHA-SWNT surface properties being altered by the surfactant coating, shielding some of the cell membrane receptors and therefore decreasing the cytokine release. *In vitro* cytotoxic assays in human epithelial carcinoma (KB) cells revealed in fact that the surface properties of MWNTs strongly influenced the cellular response [49]. In particular, neutral or negatively charged MWNTs were noncytotoxic to KB cells up to 100 µg ml⁻¹, whereas MWNTs with positive charges on their surface demonstrated cytotoxicity (decreased cell viability) at 50 µg ml⁻¹.

7.3.2

In Vivo Dermal Toxicity

Only a few *in vivo* dermal toxicity studies have been reported so far. Huczko and Lange [50] evaluated the potential of raw CNTs to induce skin irritation by conducting two routine dermatological tests (patch test on 40 volunteers with allergy susceptibilities and Draize rabbit eye test on four albino rabbits). Koyama *et al.* [51] showed the biological responses to four different types of carbon nanotubes (SWNTs, two types of MWNTs with different diameters, and cup-stacked carbon nanotubes) after their subcutaneous implantation in mice. Both tests [50, 51] showed no or poor irritation effects. However, the *in vitro* studies in epidermal cell lines exposed to CNTs, and also a more recent report on the toxic outcomes of topical exposure of mice to SWNTs [46], have raised concerns over these assessments. Clearly, this is an area requiring further scientific evaluation.

7.4

Pulmonary Response to CNTs

In contrast to conventional materials of larger mean diameter, CNTs may potentially be more toxic to the lungs and affect the normal tissue function by escaping from the phagocytic defenses, redistributing from their site of deposition, and thus activating inflammatory and immunological responses [52]. The current knowledge about the lung toxicity of CNTs is fragmentary, and sometimes contradictory. This is partly because the studies that have explored CNT lung toxicity have used different types of CNTs (SWNTs or MWNTs, raw or purified CNTs, doped or undoped CNTs), produced by different methods (electric arc discharge, HiPCO, catalytic decomposition), in varying *in vitro* and *in vivo* models.

7.4.1

Pulmonary Cytotoxicity

It is generally accepted that the main parameters determining the *in vitro* pulmonary toxicity of CNTs are (1) the CNTs dose [26, 42, 45] and (2) the catalyst content in the CNTs samples [26, 53]. Dose-dependent cytotoxic responses (i.e., cells cycle arrest and increased apoptosis/necrosis) were reported after exposure to SWNTs in A549 cells [26, 45, 53], human lung carcinoma cells (H2199), and cultured human embryonic lung fibroblasts (IMR-90) [42]. In parallel, in a more recent study SWNTs showed very low acute toxicity when incubated in A549 cells [54]. However, the levels of adenylate kinase (AK) and IL-8 released by cells and quantified in this study indicated a loss of the cell membrane integrity and an inflammation response; this could trigger cytotoxic effects in the long term. Herzog *et al.* [26] showed that the cytotoxicity of SWNTs may vary when different techniques are used for producing SWNT samples. In particular, higher pulmonary cytotoxicity was found in cells exposed to HiPCO SWNTs than in cells exposed to arc discharge SWNTs. This difference was explained by the different contents of catalytic impurities in the two samples (10 wt% Fe in HiPCO SWNTs, <1 wt% Ni and Y in SWNTs produced by the arc discharge process). Others investigators, however, do not agree with this theory. Simon-Deckers *et al.* [55], for example, showed that neither the presence of metal catalyst impurities nor the tube length influenced the cytotoxicity of MWNTs in A549 cell cultures.

Notably, Herzog *et al.* [56] reported a suppression of immunological response in A549 cells and primary normal human bronchial (NHBE) cells following exposure to SWNTs. This may have negative consequences as it renders the pulmonary immune system less reactive towards infections. Stimulation with TNF- α was used to mimic a diseased epithelium, showing that under these experimental conditions NHBE cells were more sensitive to SWNT exposure. Finally, dispersion of SWNTs in DPPC, the main component of lung fluid, triggered an increase in SWNT cytotoxicity.

Even if *in vitro* models can mimic only partially the complex responses *in vivo*, the behavior of lung epithelial cells in *in vitro* experiments resembles in some respects the pathological observations of *in vivo* experiments. First, the formation of

granulomas shown *in vivo* [57, 58], indicating a cellular attraction by CNTs, was observed in a similar fashion *in vitro* when human A549 cells were exposed to SWNTs over a period of more than 12 h [32]. Second, anuclear macrophages and other mitotic changes were observed in lung sections of mice exposed to inhaled SWNTs, suggesting that SWNTs were interfering with the mitotic spindle [59]. This speculation finds corroboration in recent *in vitro* work that showed how cultured primary and immortalized human lung epithelial cells exposed to SWNTs presented fragmented centrosomes, multiple mitotic spindle poles, and aneuploid chromosome number after 24 h of exposure [60]. This interference during the cell division could be due to the similarity between the shape of SWNTs bundles and the microtubules that form the mitotic spindle in cells, and it might be associated with a greater risk of developing cancer. Third, *in vivo* studies have demonstrated that the grade of dispersion of CNTs is a key factor in determining adverse pulmonary effects [39, 61]. This translates *in vitro* with different cellular responses in bronchial epithelial (BEAS-2B) cells treated with MWNTs at different dispersion grades [62].

7.4.2

In Vivo Pulmonary Toxicity

The first study on the potential lung toxicity of CNTs was carried out in 2001 on guinea pigs [63]. No evidence of changes in the pulmonary function (i.e., tidal volume, frequency of breath, and lung resistance) or lung inflammatory reaction was found after 4 weeks. The authors concluded that “working with soot containing carbon nanotubes is unlikely to be associated with any health risk” [63]. However, the physicochemical characteristics of the CNT material tested were not specified, the number of animals tested was limited, and the exposure time was relatively short. This may have influenced the results reported, since the pulmonary persistence (biopersistence) of an inhaled particle often determines its toxicity [64].

Little progress was made after these preliminary findings until 2004, when Lam *et al.* investigated the pulmonary toxicity of three types of SWNTs (raw HiPCO SWNTs, purified HiPCO SWNTs, and Ni-catalyzed arc discharge SWNTs) instilled in mice [58]. It was found that all three SWNT samples induced dose-dependent lung lesions and interstitial inflammation after 7 days. These lesions persisted and worsened after 90 days.

Controversial results were reported by Warheit *et al.* in two studies [57, 65] in which rats were exposed to raw SWNTs. Cell proliferation and cytotoxicity indices indicated that exposure to SWNTs produced only transient inflammation. Histological examination of exposed animals, however, identified the development of granulomas, which were non-dose dependent, nonuniform in distribution and not progressive after 1 month. The presence of granulomas was considered inconsistent with the lack of severe lung inflammation. These two reports highlighted the need for more research on the potential pulmonary toxicity of CNTs, shifting the scientific focus towards this aim.

Following their preliminary study in 2001 [63], Huczko *et al.* published a follow-up study in 2005 [66]. In this investigation, five different samples of MWNTs

(unrefined MWNTs produced by CVD and arc discharge, and commercially available CNTs from Nanolab, Pyrograf, and Showa Denko) were intratracheally instilled into guinea pigs. Unlike in the preliminary study [63], significant evidence of pulmonary toxicity was observed after 90 days. Lung histology reported multiple lesions in all CNT-exposed animals and alveolar macrophage infiltration was found in all animals except for those instilled with Pyrograf CNTs. In conjunction with their previous work, the authors concluded that the exposure time was a critical parameter in the induction of lung pathology. The pathogenic effects (in the form of *Bronchiolitis obliterans* organizing pneumonia) of intratracheal exposure to MWNTs was confirmed in a similar report published the following year by the same group [67].

Chronic lung effects using rodent models were also reported by Muller *et al.* (purified MWNTs) [68] and Warheit (SWNTs) [65]. Both studies revealed dose-dependent inflammation and granuloma formation in the rat lungs. Biopersistence tests revealed that the clearance rate was slow, with MWNT material remaining in the lungs after 60 days [68].

In accordance with international guidelines, Muller *et al.* [69] recently examined in detail how the physicochemical properties of CNTs may modulate the lung toxicity of the tubes. MWNT samples were prepared by three different protocols: (1) grinding the CNTs to introduce structural defects, and subsequently heating in vacuum at 600 °C to reduce oxygenated carbon functionalities and metallic oxides; (2) grinding and subsequently heating in an inert atmosphere at 2400 °C to eliminate metals and anneal the defects; and (3) heating at 2400 °C in an inert atmosphere and subsequently grinding, to introduce defects in metal-deprived carbon frameworks. Detailed characterization of defects, metals, and oxygenated functionalities present on the MWNT surface was carried out for each sample by a comprehensive set of spectroscopic techniques [70]. The CNTs were administered intratracheally to rats to evaluate both the short-term response (3 days) in bronchoalveolar lavage fluid and the long-term (60 days) lung response [69]. *In vitro* experiments were also performed on rat lung epithelial (RLEs) cells to assess the genotoxic potential of the MWNT samples. The results showed that the acute pulmonary toxicity and the genotoxicity of CNTs were reduced upon heating but restored upon grinding, indicating that the intrinsic toxicity of CNTs was mainly mediated by the presence of defective sites on their surface. Long-term lung response was not influenced by any treatment; the authors concluded that this may reflect a progressive passivation of the CNT surface (e.g., through the deposition of endogenous proteins) that gradually reduced the differences between the various samples tested.

In summary, intratracheal instillation of CNTs has shown that their potential in eliciting adverse pulmonary effects is influenced by exposure time, CNT dose, CNT biopersistence, surface defects, and metal contamination [71, 72]. Despite the use of surfactants, all studies showed that intratracheal instillation caused major difficulties due to the agglomerative nature of CNTs in a biological environment. More realistic exposure methods, namely inhalation rather than intratracheal administration, are therefore needed for determining the pulmonary toxicity [59, 65, 73]. Several investigations have been performed by using administration different from intra-

tracheal instillation [24, 59, 74–78]. Among them, pharyngeal aspiration of CNTs was shown to generate pulmonary inflammation in animal models [24, 77]. Pharyngeal aspiration is a technique in which a drop of CNTs suspended in aqueous solution is placed on the back of the animal tongue; the animal is then held until the drop has been aerosolized. Shvedova *et al.* [24] found that pharyngeal aspiration of SWNTs induced a robust acute inflammatory reaction (1–3 days post-exposure), followed by granuloma formation, progressive interstitial fibrosis, and alveolar wall thickening up to 60 days post-exposure. Although the formation of granulomas was mainly associated with deposition of dense micrometer-scale SWNT aggregates, a unique fibrogenic response was also apparent in areas distant from their deposition sites. The authors associated the two different toxic outcomes with distinct CNT morphologies generated by the aspiration technique adopted. The first morphology observed was compact SWNT aggregates (>500 nm in diameter); these aggregates were associated with acute inflammation and granuloma formation at the particle deposition sites. The second morphology, dispersed SWNTs (aggregates <50 nm in diameter), was instead associated with diffuse interstitial fibrosis and alveolar wall thickening in areas distant from the deposition sites [24, 71]. Mercer *et al.* [76] showed that dispersed SWNTs administered by pharyngeal aspiration were rapidly incorporated into the alveolar interstitium as compared with aggregated SWNTs, causing increased collagen deposition. However, pharyngeal aspiration is an inhalation technique that still does not mimic physiological respiration, bypassing the nose and delivering CNTs as a bolus dose.

In order to avoid potential artifacts (due to SWNT agglomeration) in the evaluation of CNT pulmonary toxicity, an aerosolization technique [79] was tested in mice by Shvedova *et al.* [59], thus allowing exposures to stable and uniform SWNT dispersions. The experimental data suggested that the pathological outcomes were very similar to those seen after pharyngeal exposure, leading to pulmonary toxicity through the same chain of pathological pathways (i.e., early inflammatory response and oxidative stress culminating in the development of multifocal granulomatous pneumonia and interstitial fibrosis). Aerosol administration resulted, however, in more adverse effects than pharyngeal aspiration. The authors concluded that this toxic outcome was due to exposure to smaller SWNT structures generated by aerosol. However, this hypothesis is not commonly accepted in the nanotoxicology field, and recent reports validated the hypothesis that a better dispersed CNTs suspension leads to less pulmonary adverse effects *in vivo* [39, 61, 75]. Li *et al.* [75] showed that MWNTs induced lung damage and inflammation after a single intratracheal instillation, but not after aerosol exposure. They concluded that the different results observed between these two administration methods were probably due to different sizes of the MWNT agglomerates, which were smaller when CNTs were aerosolized. Elgrabli *et al.* [61] studied the pulmonary toxicity of a well-dispersed MWNT suspension in bovine serum albumin (BSA) for up to 6 months after a single intratracheal instillation in rats at doses that, according to previous studies [80], were 10 or 100 times higher than the potential exposure of workers in industry. The results evidenced apoptosis of alveolar macrophages, but no other sign of pulmonary cytotoxicity was detected. Notably, Mutlu *et al.* [39] showed that SWNTs individually

dispersed by Pluronic F108NF were cleared over time, and examination of lung sections revealed that CNTs were taken up by macrophages.

Finally, the toxic pulmonary effects of nasally administered MWNTs and N-doped MWNTs (CNx) were compared with those of MWNTs and CNx administered through different routes [74]: oral, intratracheal, and intraperitoneal. Interestingly, administration of MWNTs or CNx nanotubes to mice did not induce distress or local tissue responses except when the samples were instilled intratracheally. MWNTs injected into the mouse's trachea induced, in fact, severe granulomatous inflammatory responses. In mice challenged orally, aggregates of nanotubes were identified in the feces after 24 h; these mice did not show signs of intestinal occlusion or diarrhea and the intestines were free of nanotube aggregates or inflammatory lesions. Mice challenged by the intraperitoneal route revealed aggregates of nanotubes dispersed between the intestinal loops without evidence of inflammation or tissue damage, and internal organs (such as liver, lungs, spleen, kidney, and heart) appeared normal. Finally, neither mortality nor clinical signs of distress were observed when nanotubes were administered by nasal instillation. At all times and with all doses, histological examination of lung tissue sections failed to reveal deposition of nanotubes and no inflammatory changes were noticed. The authors speculated on the ability of the nasal mucosa to trap and expel the nanotube material.

These findings [24, 74], correlated with the significant energy and agitation needed for releasing CNTs into the air [80], give support to the hypothesis that, owing to their tendency to agglomerate into bundles, the possibility of being exposed to respirable-sized, harmful CNTs is low. Cumulative effects, especially if increased quantities are handled, justify however the introduction of safety measures and the call for more studies that accurately establish the pulmonary toxicology of CNTs [68]. Further, the potential CNT lung insult could trigger the development of systemic toxicities by release of inflammatory proteins, activation of circulating blood cells, and altered pulmonary microbial clearance. It has been demonstrated, for example, that SWNT-induced pulmonary toxicity elicited cardiovascular dysfunction [81] and/or increased sensitivity to microbial infections [82–84].

7.5

Toxic Response to CNTs in the Intra-Abdominal Cavity

Recently, the toxicological responses of CNTs in the intra-abdominal cavity have attracted significant attention. Studies have been carried out mainly *in vivo*, and only three *in vitro* models have been tested. The significance of these studies is unknown, however, since no evidence indicating that CNTs can reach the pleural space is currently available.

7.5.1

CNT Cytotoxicity in the Intra-Abdominal Cavity

Cultured human mesothelial cells were sensitive to CNT exposure. Both SWNTs with a high content of nickel [85] and MWNTs characterized by low metal contamina-

tion [86] caused DNA damage and acute inflammation. The degree of agglomeration was found to be an important factor in the cytotoxicity of CNTs in the intra-abdominal cavity [87]. SWNTs dispersed by noncytotoxic polyoxyethylene sorbitan monooleate demonstrated, in fact, low toxicity to human mesothelioma (MSTO-211H) cell line, as compared with agglomerated SWNTs.

7.5.2

In Vivo CNT Toxicity in the Intra-Abdominal Cavity

Five recent studies investigated the potential toxic risk if CNTs reach the pleural cavity after inhalation exposure [6, 88–91]. Three of these *in vivo* studies revealed that if CNTs are delivered to the abdominal cavity of mice or rats, they could induce a serious potential carcinogenic risk resembling that associated with exposure to certain asbestos fibers [6, 88, 89]. The other two studies described nontoxic responses [90, 91].

In the first study [88], the authors used an animal model susceptible to develop mesothelioma rapidly (p53 heterozygous mice). MWNTs were dispersed at high dosage in a surfactant (Tween 80) solution and administered intraperitoneally. Animal morbidity and histological examination of the mesothelium after 25 weeks showed a carcinogenic effect. In addition, the death rate for the MWNT-exposed group was significantly greater than that for the positive control (asbestos-exposed) group. It should be noted, however, that this study has been criticized for the use of an extraordinarily high exposure dose (3 mg per mouse) [6, 91]. In the second study [6], Poland *et al.* documented an acute toxic response to a significantly lower dose (50 µg per mouse) of MWNTs of various lengths, dispersed in saline using bovine serum albumin. The accumulation of MWNTs in the diaphragmatic mesothelium and the subsequent degree of granuloma lesion formation were significantly higher after injection of rigid, long (20 µm) MWNTs than with low aspect ratio, tangled nanotube aggregates. This suggests an increased risk associated with exposure to long and rigid CNTs, presumably because macrophages cannot completely engulf long fibers. Although this study did not assess whether the granuloma lesions progressed to tumor formation, the symptoms arising from exposure to long MWNTs resembled those of animals exposed to asbestos (positive control). The third study [89] reported the induction of peritoneal mesothelioma in rats after intrascrotal injection of MWNTs. The rats were analyzed immediately after death, when becoming moribund, or at the end of the maximum observation period scheduled (52 weeks). After 37–40 weeks, histological examination revealed that MWNTs caused carcinogenicity and induced peritoneal mesothelioma. Only one rat survived for 52 weeks.

Nontoxic responses were reported by Chiaretti *et al.* [90], who investigated the pathological effects of MWNTs on the parenchymal tissues after intraperitoneal administration. Only high doses of MWNTs (20 and 40 mg kg⁻¹) caused death of animals in the first day (20 and 33%, respectively), whereas doses of 5 and 10 mg kg⁻¹ had no effect after 7 days. In addition, repeated administration of 5 mg kg⁻¹ doses did not cause any lesion in the abdominal cavity or in the pleural and pericardial cavities. Only a small irritation was observed at the injection point. It should be emphasized that this study did not address the carcinogenicity risk associated with CNT exposure,

the study of which requires an investigation of the chronic effects following administration. Notably, Muller *et al.* [91] did not find a carcinogenic response 2 years after exposing rats to intraperitoneally administered MWNTs.

The studies described above are important proof-of-principle investigations pointing to a debate about the carcinogenic hazard of MWNTs in the abdominal cavity. There are a number of open questions that need to be resolved before a final assessment can be made. In this respect, Oberdöster recently summarized such a challenge with three key questions: “do they (MWNTs) translocate from the deposition site in the lung to the pleura? If so, what is the efficiency of such translocation in terms of the dose retained in pleural tissues? What are the dimensions (in particular length) of the translocated MWNTs?” [92].

7.6

CNTs and Immunity

It is well known that ultrafine particles (mainly carbon nanoparticles) may promote immune responses to allergens, and they are associated with the development and aggravation of asthma and respiratory allergy [93]. CNTs may be effective in enhancing the antibody responses to coadministered allergens when inhaled. However, the fibrous morphology of CNTs differs strongly from that of ultrafine particles; this, along with other specific CNT characteristics, may influence their adjuvant effect on allergic responses. The studies presented here demonstrate an allergy-promoting capacity of CNTs and call for further work evaluating the hazards of CNTs in relation to the development of allergic immune responses.

7.6.1

Recognition of CNTs by Macrophages

Macrophage function as “sensors” is essential for the elimination of pathogens, and also for the regulation of the adaptive immune response and of the inflammatory response [94].

Macrophages may be considered the primary responders to ENMs. Interaction of ENMs with macrophages commonly results in the production and release of reactive oxygen species (ROS) and nitric oxide (NO) [95], which are required for effective phagocytosis and digestion of pathogens by macrophages. Enhanced uncontrolled production of ROS and NO is usually associated with apoptotic death of macrophages [96]. Additionally, the interaction of ROS with NO can result in the formation of peroxynitrite (ONOO^-), a potent oxidizing agent associated with oxidative/nitrosative stress and tissue damage [97]. The ROS production levels induced by exposure to CNTs are, therefore, a key parameter in defining their toxicity, and the presence of catalytically active transition metals (Fe, Co, Ni) in as-produced CNTs is critical to the fate of ROS produced by inflammatory cells (macrophages) [71]. Recent studies showed that SWNTs with high iron contents displayed high redox activity in an *in vitro* cell-free model system, resulting in ascorbate oxidation, and generating

high levels of ascorbate radicals detectable by electron paramagnetic resonance (EPR) [98]. The conformation of CNTs is a key parameter in determining the ROS production [99]. Rothen-Rutishauser *et al.* [99] examined the oxidative potential of straight (50 and 10 mm long) and tangled CNTs. Briefly, in a cell-free model, the tangled nanotubes showed higher oxidative potential than straight CNTs. High ROS levels were detected in cultured macrophages exposed to tangled tubes after 30 min, whereas straight tubes increased ROS production after 4 h. Interestingly, straight fibers generated a slower but more prolonged effect in animals.

The redox effects of SWNTs and their transition metal content can be realized locally during the immediate contact of CNTs with cells, or systemically through ROS and other reactive intermediates generated [71]. As the lifetime of free radical intermediates is short, it is likely that systemic outcomes are less effective than local effects. It is therefore important to assess the extent to which CNTs are recognized and engulfed by macrophages. It has been established that functionalized SWNTs are readily ingested by macrophages [100]. By contrast, nonfunctionalized SWNTs are poorly recognized by macrophages and do not effectively induce typical macrophage activation responses [98]. CNTs uptake appears to be due to macromolecules and/or proteins coating the nanotube surface rather than to macrophage recognition of the CNTs themselves [101].

7.6.2

In Vitro Responses of Macrophages Exposed to CNTs

In vitro evaluation of the inflammatory potential of CNTs in macrophages was first reported in 2005, when Jia *et al.* [102] showed that both SWNTs and MWNTs decreased dose dependently the cell viability and the phagocytic function of alveolar macrophages. SWNT and MWNT samples were found to have a greater negative impact on cell viability than the positive control (quartz); this may be due to the well-known interaction of the MTT assay employed in this study with various carbon-based nanomaterials [32–34]. Concerns regarding this work were also raised by later studies [72, 98, 103], which found that CNTs did not induce any cytotoxic effect in cultured macrophage models. Dutta *et al.* [103] showed, for example, that SWNTs failed to stimulate cyclooxygenase-2 in RAW 264.7 cells; similarly, SWNTs or MWNTs failed to activate NO, TNF- α , or IL-8 in rat alveolar macrophages (NR8383) [104].

As mentioned before, the presence of iron in SWNT samples is important in determining redox-dependent responses of macrophages. In particular, low levels of metal impurities might be responsible for the reduced production of inflammatory mediator (NO) and for the subsequent reduced toxicity of SWNTs. Kagan *et al.* [98] studied the effects of iron-rich (nonpurified) SWNTs (26 wt% of iron) and purified SWNTs (0.23 wt% of iron) in RAW 264.7 macrophages. Fiorito *et al.* [72] compared the ability of highly purified SWNTs to elicit inflammatory responses in murine (J774) cells and human monocyte-derived (MDMs) macrophages. Both reports showed minimal cell activation and phagocytic activity when macrophages were incubated with purified SWNTs, and no intracellular production of ROS and NO was

registered. Likewise, acid-treated (purified) SWNTs were less cytotoxic than unpurified SWNTs in human monocyte-derived (HMMs) macrophages [105], and SWNTs also failed to generate intracellular ROS in NR8383 cells after removal of contaminating iron [104].

It should be mentioned, however, that some investigators do identify CNTs as the principle cause of cytotoxicity in macrophages, rather than the catalysts. Cheng *et al.* [106] reported, in fact, comparable toxicities of unpurified and purified MWNTs in human monocyte-derived macrophages (HMMs). The authors suggested that the cytotoxicity was not elicited by the residual iron, but by the compromised cell membrane integrity and oxidative stress generated by incomplete phagocytosis or “impalation” of MWNTs.

Two studies [68, 107] illustrated that the CNTs length might be a key parameter in modulating the immune response to CNTs exposure. First, Muller *et al.* [68] postulated that grinding purified MWNTs in an oscillatory ball-mill, and thus decreasing the tube length and agglomeration, leads to increased cytotoxic and proinflammatory responses in cultured peritoneal macrophages (taken from Sprague–Dawley rats). Later, Sato *et al.* [107] investigated the activation of the human acute monocytic leukemia (THP-1) cell line after exposure to CNTs of different lengths (220 and 825 nm long CNT samples) *in vitro* and after subcutaneous implantation *in vivo*. Whereas *in vitro* both the 220 and 825 nm CNTs induced THP-1 activation with no influence of variation in the CNT length, the degree of inflammatory response to 220 nm CNTs in subcutaneous tissue in rats was lower than that of 825 nm CNTs. This result was associated with the capability of macrophages to envelop 220 nm CNTs more readily than 825 nm CNTs.

7.6.3

CNTs and Immunity *In Vivo*

Local immune responses [51, 108], allergic immune responses [109, 110], and systemic immune suppression [82, 83] have been reported *in vivo* after exposure to CNTs.

7.6.3.1 Local Immune Responses

Koyama *et al.* [51] studied the biological responses to SWNTs and MWNTs subcutaneously implanted for up to 3 months in mice. After 2 weeks, all CNT samples activated major antigen–antibody responses, resulting in higher CD4⁺/CD8⁺ T-cell (i.e., lymphocytes that play a central role in cell-mediated immunity) levels in the blood, but no severe inflammatory aspects surrounding the implantation sites. According to Park *et al.* [108], local pulmonary immune responses can be triggered by pulmonary exposure to CNTs in mice. Dose-dependent increases in the content of several pro-inflammatory cytokines (such as, IL-1 β , TNF- α , IL-6, IL-4, IL-5, IL-10, IL-12 and IFN- γ) were documented in bronchoalveolar lavage (BAL) fluid and blood of exposed animals. Increased concentrations of IgE were found in blood of mice exposed to CNTs. The total numbers of immune cells in BAL fluid

were significantly increased in treated groups and the distribution of neutrophils was elevated 1 day post-instillation. Based on these observations, the authors suggested that pulmonary exposure to CNTs caused activation of alveolar macrophages and recruitment of immune cells into the lung, and facilitated differentiation of CD4⁺ T cells into Th1 and Th2 cells. Overall, these responses might trigger allergic pulmonary outcomes or sensitivity to microbial infections as a response to CNT exposure. It was shown that pre-exposure to SWNTs significantly decreased the pulmonary clearance, and sequential exposure to SWNTs/*Listeria monocytogenes* (LM) amplified lung inflammation (i.e., increased levels of BAL neutrophils, alveolar macrophages, lymphocytes, and lactate dehydrogenase), and collagen formation [84]. The decreased bacterial clearance in SWNTs-pre-exposed mice was associated with decreased phagocytosis of bacteria by macrophages and a decrease in NO production by these cells. Pre-incubation of alveolar macrophages with SWNTs *in vitro* also resulted in suppressed phagocytizing activity towards LM. Failure of clearing bacteria may lead to increased susceptibility to lung infection in populations exposed to CNTs.

7.6.3.2 Allergic Immune Responses

Assessment of acute effects of CNTs on the innate immune system revealed that SWNTs and MWNTs administered along with allergen ovalbumin (OVA) promoted allergic responses in mice [109, 110]. Briefly, exposure to CNTs increased the serum levels of OVA-specific IgE, the eosinophil counts in BAL, and the secretion of Th2 cytokines from mediastinal lymph nodes [109]. Analogously, Ryman-Rasmussen *et al.* [110] demonstrated that pulmonary fibrosis and allergic asthma was developed in mice after combined OVA sensitization and MWNT inhalation. Significant airway fibrosis was found at 14 days post-exposure in mice that received a combination of OVA and MWNTs, but not in mice that received OVA or MWNTs only. The combination of OVA and MWNTs increased synergistically the IL-5 mRNA levels, thus causing airway fibrosis, and MWNTs were found in macrophages. The authors concluded that inhaled MWNTs require pre-existing inflammation to cause airway fibrosis. Thus, populations with pre-existing allergic inflammation may be susceptible to pathologies elicited by respirable MWNTs. This opinion was shared by other workers, who reported that the capability of MWNTs to induce fibrosis in rats was enhanced by exposing the animals to bacterial lipopolysaccharide (LPS), an environmental agent that causes lung inflammation [111].

7.6.3.3 Systemic Immune Alterations

Recently, it has been shown that inhalation of MWNTs caused suppression of the systemic immunity without resulting in significant lung inflammation or tissue damage [82, 83]. Inhaled MWNTs in fact modified the functionality of spleen cells in exposed mice [82]. Notably, the activity of cyclooxygenase (COX) enzymes in spleen was affected as a response to a cytokine (TGF β) released from the lungs. This cytokine activated the COX pathway in the spleen, triggering T-cell dysfunction and systemic immunosuppression [83].

7.7

CNT Interactions with the Cardiovascular Homeostasis

Concerning applications where CNTs are injected into the human body, few investigators have explored the outcome of CNTs in contact with the intravascular environment and components of circulating blood (particularly platelets) [112–114].

7.7.1

In Vitro Interactions

There is some *in vitro* evidence that CNTs can affect vascular hemostasis and aggravate thrombosis by activating platelets [112, 113]. Incubation of human platelets with various carbon nanostructures (SWNTs, MWNTs, C₆₀ fullerenes, mixed carbon nanoparticles) resulted in a concentration-dependent increase in platelet aggregation [113]. CNTs were demonstrated to activate platelets by inducing extracellular Ca²⁺ influx [112]. Higher aggregation was found for SWNTs than MWNTs, with little or no granular release in both cases [113]. Radomski *et al.* [113] demonstrated that platelet aggregation also occurred *in vivo*, and identified the nanotube shape and surface as the main factors determining the potential of such nanomaterial in activating platelets. It is possible that CNTs mimic bridge-like structures generally involved in platelet–platelet interactions, stimulating the agglomeration. In parallel, surface charge may play a role in the interactions with the receptor that was found to be involved in the CNT-mediated platelet activation (GPIIb/IIIa).

In parallel, Tamura *et al.* [114] conducted a brief investigation into the cytotoxic effect of purified CNTs in cultured neutrophils isolated from human blood. Purified CNTs significantly increased superoxide anion and TNF- α production after 1 h, and caused cell death. Unfortunately, no details of the CNT structure, synthesis, or handling methods were provided.

7.7.2

In Vivo CNT Toxicity to Cardiovascular Homeostasis

Adverse dose-dependent cardiovascular oxidative effects, including distressed aortic mitochondrial homeostasis (a sensitive marker of oxidative insult) and acceleration of atherogenesis, have been reported following pharyngeal instillation of SWNTs in mice [81]. Likewise, an acute systemic prothrombotic response was detected following MWNT-induced lung inflammation [115]. SWNTs might therefore mediate cardiovascular effects through platelet activation in the exposed lungs. It has been suggested that such systemic responses were determined by many inflammatory mediators expressed in the lungs and then released in the circulating blood flow [116]. If persistent, these molecules (coding for inflammation, oxidative stress, remodeling, and thrombosis) can cause endothelial dysfunction and acceleration of atherosclerosis progression [117]. SWNTs were shown also to alter the cardiac activity by affecting the arterial baroreflex function (BRF) of sinus mode in rats exposed by intratracheal instillation [118].

Radomski *et al.* [113] demonstrated that the CNTs were efficient in causing platelet aggregation both *in vitro* and *in vivo*, accelerating significantly the rate of development of carotid artery thrombosis in rats. Platelet aggregation was likely to result from MMP-dependent activation of GPIIb/IIa receptor.

These findings suggest that CNT exposure should be evaluated as a potential cardiovascular risk factor. It should be noted, however, that no thrombosis or other adverse effects on the cardiovascular homeostasis were reported after intravenous injection in healthy animals, when this administration route was used for investigating the biokinetics of CNTs [119–126].

7.8

Genotoxicity and Mutagenicity of CNTs

Inflammation and pulmonary fibrosis have been associated with an increased risk for lung cancer, thus justifying assessments of genotoxic events possibly accompanying CNT exposure. However, the results obtained to date are not consistent.

7.8.1

In Vitro Studies

Kisin *et al.* [127] examined the genotoxic effects of purified SWNTs, showing a dose-dependent increase in the frequency of DNA damage in lung fibroblast (V79) cells after exposure to SWNTs. However, SWNTs also decreased the viability of the cells; this might have interfered with the accurate evaluation of the genotoxic response to SWNTs in fibroblasts [101]. Zhu *et al.* [128] demonstrated the DNA damage and increased mutation frequency in mouse embryonic stem cells in response to MWNT exposure. Furthermore, Karlsson *et al.* [129] reported a significant increase in DNA damage caused by MWNTs in A549 cells, but no oxidative DNA lesions. However, no increased mutation frequencies in either YG1024 or YG1029 strains of *Salmonella typhimurium* were detected after incubation with SWNT samples.

7.8.2

In Vivo Studies

Shvedova *et al.* [59] demonstrated that inhalation of SWNTs resulted in mutations of the *k-ras* gene locus in the lung of mice. Among the mutated genes implicated in pulmonary tumorigenesis, the *k-ras* oncogene is relevant in lung tumors of mice exposed to chemicals.

A pilot study performed by Szendi and Varga [130] showed that single oral exposure to SWNTs (90% purity) or MWNTs (95–98% purity) did not increase urinary mutagenicity in rats. Additionally, no significant genotoxic effects were found in human lymphocytes after a single exposure to MWNTs. Folkmann *et al.* [131] showed that intragastric administration of SWNTs was associated with elevated levels of oxidative damage to DNA in the liver and lung of rats. The authors concluded that this was likely caused by a direct genotoxic ability rather than an inhibition of the DNA repair system.

7.9

Biodistribution and Pharmacokinetics of CNTs

The translocation and biodistribution of CNTs are key factors in defining the toxicity of CNTs, and they rely largely on their physicochemical characteristics [10, 122, 125, 132].

Several studies concerning the biodistribution and clearance of CNTs have been reported [119–126]; most of them investigated the biokinetics of covalently functionalized CNTs, whereas only a few evaluated the distribution of noncovalently modified CNTs in the body.

Wang *et al.* [125] first radiotraced the distribution of ^{125}I -labeled hydroxylated SWNTs ($[^{125}\text{I}]SWNT\text{-OH}$) in mice after intraperitoneal administration. $[^{125}\text{I}]SWNT\text{-OH}$ distributed quickly throughout the whole body. The preferred organs for accumulation were the stomach, kidneys, and bone. Most importantly from the safety point of view, no tissue damage or distress was reported: 94% of the CNTs were excreted into the urine and 6% in the feces.

More recently [121], the biodistribution and blood circulation half-life of ammonium-functionalized SWNTs, partially covalently modified with the chelating molecule diethylenetriaminepentaacetate (DTPA) and radiolabeled with ^{111}In ($[^{111}\text{In}]DTPA\text{-SWNTs}$), were studied. The biodistribution profiles showed that $[^{111}\text{In}]DTPA\text{-SWNTs}$ were distributed in the kidneys, muscle, skin, and bone 30 min after their intravenous administration (60 μg) in mice. DTPA-SWNTs and DTPA-MWNTs functionalized with the same procedure were rapidly cleared from all tissues after intravenous administration (400 μg), and a maximum blood circulation half-life of 3 h was determined [121]. A blood circulation half-life of 1 h was shown instead for raw SWNTs suspended in an aqueous solution of Pluronic F108 and injected intravenously in rabbits [119]. DTPA-MWNTs did not accumulate in the lungs and liver, whereas purified intact MWNTs were found in these organs in the form of large clusters [120]. The authors suggested that the accumulation grade of MWNTs in the different organs could be modulated by varying the functionalization on to the MWNTs surface [123]. In particular, the higher the functionalization grade, the less the MWNTs accumulated in the tissues, whereas, the functional groups did not play a major role in defining the biokinetics of MWNTs.

$[^{111}\text{In}]DTPA\text{-CNTs}$ were excreted intact through the renal route into the bladder and urine [121], indicating that no biodegradation of CNTs occurred *in vivo*. Significant residual deposits of DTPA-MWNTs in the kidney were not evidenced [120]. It was clarified that DTPA-MWNTs began to permeate through the renal glomerular filtration system within 5 min post-intravenous administration to rats [120], and terminated in a few hours. The authors stated that the mechanism of CNT filtration “involves the acquisition of a spatial conformation in which the longitudinal CNT dimension is perpendicular to the endothelial fenestrations, since only the traverse dimension of CNT (cross section is between 20 and 30 nm) is small enough to allow permeation” [122]. According to this study, the CNT length would not be a key parameter in determining renal clearance of these nanostructures. Aggregates or bundles would not be able though to cross the glomerular membrane [133] and may accumulate in the liver, spleen, or lungs. Similar conclusions were reported recently on the mechanisms of elimination of SWNTs by Ruggiero *et al.* [124]. The

renal clearance of SWNTs covalently functionalized with various ligands, SWNT-[⁶⁴C](DOTA)(AF488)(AF680)], was monitored in mice by means of three different imaging techniques (dynamic positron emission tomography, near-infrared fluorescence imaging, and microscopy). According to the experimental data, SWNTs were rapidly cleared by glomerular filtration in the kidneys with only partial tubular readorption. No active secretion was involved in the process. This means that the elimination of a major fraction (85% of the injected dose) of the SWNTs tested (average length, 200–300 nm; molecular weight, ~350–500 kDa) followed rapid, “first-pass” pharmacokinetics, similarly to the clearance of small molecules (molecular weight, ~30–50 kDa). According to the theoretical explanations offered in this study, SWNTs have a great tendency to align with the blood flow and they are therefore rapidly excreted through the renal filter.

[¹⁴C]taurine-labeled MWNTs were administered to mice by three different exposure routes (intravenous injection, gavage, and intratracheal instillation) and their biodistribution was monitored [134]. After intravenous injection, [¹⁴C]taurine-labeled MWNTs accumulated in the liver, heart, and lung; after gavage administration, [¹⁴C]taurine-labeled MWNTs was only detectable in the stomach, intestine, and feces. No [¹⁴C]taurine-labeled MWNTs were detected in the blood. Finally, [¹⁴C]taurine-labeled MWNTs were partly cleared from the lungs after intratracheal instillation. Since various cell and tissue types have demonstrated a high affinity for uptake of taurine, it should be noted that the label used in this investigation may have influenced the biodistribution of the MWNTs tested [101].

The biodistribution of noncovalently modified CNTs was also investigated following intravenous administration in mice [126]. Raman spectroscopy was used to detect the blood concentration of SWNTs coated with poly(ethylene glycol) (PEG) (PEG-SWNTs) and the accumulation of SWNTs in various organs over a period of several months. The results indicated that PEG coatings increased the blood half-life by up to 1 day, while near-complete clearance of PEG-SWNTs was achieved after 2 months with no changes in the health conditions of the animals exposed. PEGylation of CNTs is known to decrease significantly their cytotoxicity [135]. Since PEG-SWNTs were seen to accumulate in the intestines, feces, kidneys, and bladder of mice, the authors concluded that the main excretion route of PEG-SWNTs was *via* biliary and renal pathways.

The findings summarized here have implications in the understanding of the ability of CNTs to translocate biological barriers; this has an important impact in both the design and the determination of the health risks of biomedical applications of CNTs. ⁶⁴Cu-labeled MWNTs accumulated, for example, in the testes after intravenous injection in mice, without affecting the fertility of the treated animals and causing temporary tissue damage that was repaired after 60 days [136]. Experimental work is still needed to assess the capacity of CNTs to migrate to and accumulate in tissues prone to malignancy, such as the mesothelium.

7.9.1

Internalization of CNTs into Mammalian Cells

The translocation properties of CNTs through cellular membranes may be a key factor in determining the biodistribution and cytotoxicity of CNTs.

It is commonly accepted that the cellular uptake of CNTs depends on their length, surface chemistry, and aggregation. Becker *et al.* [137] demonstrated a length-selective cellular uptake of DNA-wrapped SWNTs in cultured human fibroblast (IMR90) cells, with an approximate uptake threshold of 189 ± 17 nm, whereas Jin *et al.* reported an uptake threshold from 130 to 660 nm in fibroblast (NIH-3T3) cells [138]. CNTs functionalized by a covalent or noncovalent approach can penetrate the mammalian cells membrane [119, 139, 140]. For example, water-soluble functionalized CNTs were able to translocate into cell cytoplasm [141], and CNTs condensed with plasmid DNA were able to deliver it intracellularly, thus enhancing marker gene expression [142]. Dumortier *et al.* showed that only well-dispersed SWNTs were internalized by lymphocytes and macrophages. Covalently functionalized MWNTs were found inside various cell types and were able to traffic through various cellular membranes [139].

Determination of the exact mechanism leading to cellular internalization of CNTs is of great importance [143], but discrepancies in the reported mechanisms are evident in the literature. Some researchers proposed an energy-dependent endocytosis mechanism [127, 144–148], whereas other studies demonstrated that functionalized CNTs are able to penetrate cells in a passive way [139, 141, 149]. Indeed, both mechanisms may occur. Kostarelos *et al.* [139] studied extensively the uptake of a range of functionalized CNTs (SWNTs, MWNTs) in a variety of cells, such as adherent mammalian cell monolayers (A549, HeLa, and MOD-K cells), mammalian cells suspensions (Jurkat), fungal cells (*Cryptococcus neoformans*), yeast (*Saccharomyces cerevisiae*), and bacteria (*Escherichia coli*). Cellular internalization was reported for all CNT samples, in all cell types, even in those cells lacking the capability for endocytosis. The nature of the functionalization group did not influence the internalization; in particular, even negatively charged or neutral CNTs were taken up by cells. CNT internalization was also seen after inhibition of endocytosis, thus suggesting that it did not depend only on endocytosis. Kam *et al.* [144] observed, however, a considerable reduction in the cellular uptake of CNTs labeled with a fluorescent macromolecule under endocytosis-inhibiting conditions. According to the literature, such discrepancies could be attributed to the differences between the CNTs studied [143]. Finally, Mu *et al.* [150] designed a model describing the cellular uptake of covalently functionalized MWNTs. According to this model, MWNTs aggregates are taken up by endocytosis, whereas single MWNTs penetrate the cellular membranes. All CNTs are then recruited into lysosomes for excretion.

Another important question is whether exocytosis occurs after CNT internalization. Evidence of exocytosis of DNA-coated SWNTs in fibroblast (NIH-3T3) cells was recently presented [148]. The exocytosis rate was close to that of endocytosis after a minor temporary offset, thus keeping the accumulation of SWNTs inside the cell below the cytotoxic levels.

Finally, the subcellular localization of CNTs is still controversial. Some reports showed that CNTs enter the cell without reaching the nucleus [140], whereas others demonstrated that CNTs can enter the nucleus [105, 141, 150]. Recently, Zhou *et al.* [151] demonstrated the possibility of manipulating the intracellular localization of noncovalently modified SWNTs by varying the conjugated molecule.

7.10

Biodegradation of CNTs

Degradability is an important factor in the assessment of the toxicity of nanomaterials [71]. Nondegradable nanomaterials may in fact accumulate in organs and/or intracellularly, where they would exert toxic effects.

The enzymatic degradation of carboxylated SWNTs has been proven in a cell-free system with a plant-derived enzyme [horseradish peroxidase (HRP)] and small amounts of H₂O₂ [152]. This result indicated a promising possibility for CNTs to be degraded by HRP in environmentally relevant settings. More recently, the biodegradation of carboxylated CNTs by human myeloperoxidase (hMPO) has been reported in cell-free models, and also in physiologically relevant environments (*in vitro* cell culture of neutrophils and macrophages) [153]. Importantly, SWNTs fully biodegraded by myeloperoxidase were inefficient in inducing the typical inflammatory and oxidative stress responses evidenced when CNTs are pharyngeally administered to mice.

7.11

Biocompatibility of CNT-Based Biomaterials

Despite the evidence for the cytotoxicity of CNTs, there are an increasing number of published studies that support the potential development of CNT-based biomaterials for tissue regeneration (e.g., neuronal substrates [143] and orthopedic materials [154–156]), cancer treatment [157], and drug/vaccine delivery systems [158, 159]. Most of these applications will involve the implantation and/or administration of such materials into patients; as for any therapeutic or diagnostic agent used, the toxic potential of the CNTs must be evaluated in relation to their potential benefits [160]. For this reason, detailed investigations of the interactions between CNTs/CNT-based implants and various cell types have been carried out [154, 155, 161]. A comprehensive description of such results, however, is beyond the scope of this chapter. Extensive reviews on the biocompatibility of implantable CNT composite materials [21, 143, 162] and of CNT drug-delivery systems [162] are available.

7.12

Conclusions – Are CNTs safe?

To summarize information on CNT toxicity, in Tables 7.2 and 7.3 are compiled *in vitro* and *in vivo* toxicity outcomes, respectively, after exposure to CNTs.

At first glance, the *in vitro* studies on CNT toxicity appear to be confusing, inconclusive, or contradictory. However, if one considers interference with dye-based viability assays, agglomeration issues, and oxidative stress due to catalyst contamination, the data available to date seem to favor the conclusion that well-dispersed, purified, and/or functionalized CNTs exhibit relatively low toxicity.

Table 7.2 Summary of *in vitro* toxicity outcomes after exposure to CNTs. The term “CNTs” indicates that the material was not identified as single- (SWNTs) or multi-walled (MWNTs) carbon nanotubes. Percentage of catalytically active transition metals in the CNTs is reported when indicated by the authors.

CNTs tested	Production method and impurities content	Cellular model	Cytotoxic effect	Ref.
<i>Dermal cytotoxicity</i>				
SWNTs	Arc discharge	A549	Catalysts worsen cytotoxicity	[53]
SWNTs	Arc discharge (<1 wt% Ni and Y)	HaCaT	Reduced cell proliferation	[26]
MWNTs	CVD	HEK	Dose-dependent inflammation	[43]
MWNTs			Time-dependent inflammation	
SWNTs	CVD	HSF4/2	Dose-dependent cytotoxicity	[42]
SWNTs	HiPCO	HaCaT	Time-dependent cytotoxicity	[25]
SWNTs	HiPCO	HaCaT	Oxidative stress (ROS production, NF-κB activation)	[45]
SWNTs		HeLa	Cell proliferation inhibited	
SWNTs	HiPCO (30 wt% Fe vs. 0.23 wt% Fe)	JB6 P + EpiDerm FTF engineered skin	Unpurified SWNTs: free radical generation, oxidative stress, inflammation	[46]
SWNTs	HiPCO (10 wt% Fe)	HaCaT	Reduced cell proliferation	[26]
6-Aminohexanoic acid	HiPCO	HEK	Dose-dependent cytotoxicity	[31]
SWNTs			Time-dependent cytotoxicity Aggregation-dependent cytotoxicity	
Phenyl-functionalized SWNTs	HiPCO (<1 wt% Fe)	HDF	Cytotoxicity as a function of chemical derivatization	[48]
SWNTs	Not specified	HEK	Changes in gene expression in SWNTs-treated cells become closer to control cells over time	[47]
<i>Pulmonary cytotoxicity</i>				
SWNTs	Arc-discharge (<1 wt% of Ni and Y)	A549	Reduced cell proliferation	[26]
		BEAS-2B		(Continued)

Table 7.2 (Continued)

CNTs tested	Production method and impurities content	Cellular model	Cytotoxic effect	Ref.
MWNTs MWNTs	CVD CVD (4.24 and 0.08 wt% Fe)	IMR-90 A549	Dose-dependent cytotoxicity Cytotoxicity not influenced by either catalyst content or length	[42] [55]
SWNTs	HiPCO	A549 H1299	MWNT internalization Cell proliferation inhibited	[45]
SWNTs	HiPCO (10 wt% Fe)	A549 NHBF	Suppression of inflammatory mediators	[56]
SWNTs	HiPCO (10 wt% Fe)	A549 BEAS-2B	Reduced cell proliferation	[26]
SWNTs	HiPCO (10 w.% iron)	A549	Very low acute toxicity Increase in lamellar bodies	[54]
<i>In vitro inflammatory response</i>		Guinea pigs alveolar macrophages	Dose-dependent inflammation	[102]
Purified SWNTs	Arc discharge	Guinea pigs alveolar macrophages	Dose-dependent inflammation	[102]
Purified MWNTs	CVD	J774 MDMs	None	[72]
SWNTs	CVD (0 wt% Co and Ni)	HMM	Decreased cell viability	[106]
MWNTs	CVD (6.2 wt% Fe and 0.0005 wt% Fe)	RAW 264.7	No intracellular production of superoxide radicals or NO	[98]
SWNTs	HiPCO (0.3 wt% Fe)		Enhancement of lipid peroxidation and GSH depletion proportional to the iron content	

CNTs (800 and 200 nm length)	Not specified	THP-1	[107]
<i>Vascular system</i>			
MWNTs	Not specified (minimum purity: >90 wt%)	Human platelets	[112]
SWNTs	Not specified (minimum purity: >90 wt%)	Human platelets	[112]
SWNTs	Not specified (minimum purity: >90 wt%)	Human platelets	[113]
MWNTs	Not specified	Human platelets	[113]
CNTs	Not specified	Human neutrophils	[114]
<i>Additional cell models</i>			
MWNTs (50%) + SWNTs (30%)	Arc-discharge	Jurkat cells	[163]
SWNTs	(0 wt% catalyst) Arc discharge	MSTO-211H	[87]
SWNTs	CVD	Jurkat cells	[163]
MWNTs	(1 wt% Co and Mo)	Jurkat cells	[163]
MWNTs	CVD (<0.1 wt% Fe)	HUVEC	[164]
SWNTs	(10–20 wt% Co, Mo, or W) Not specified	HEK293	[165]
MWNTs	Not specified (Sigma-Aldrich)	Caco-2	[90]
MWNTs	Not specified (Sigma-Aldrich)	MCF-7	[90]
		hSMCs	
Inflammatory response			
		Platelet activation and aggregation by inducing Ca^{2+} influx	
		Platelet activation and aggregation by inducing Ca^{2+} influx	
		Platelet aggregation ($25 \mu\text{g ml}^{-1}$)	
		Platelet aggregation ($25 \mu\text{g ml}^{-1}$)	
		Decreased cell viability	
		Inflammatory response	
		Aggregation-dependent cytotoxicity	
		Contaminant-dependent cytotoxicity	
		Aggregation-dependent cytotoxicity	
		Aggregation-dependent cytotoxicity	
		Contaminant-dependent cytotoxicity	
		Aggregation-dependent cytotoxicity	
		Contaminant-dependent cytotoxicity	
		None	
		Reduced cell proliferation	
		Reduced cell adhesion	
		Dose-dependent cytotoxicity	
		Time-dependent cytotoxicity	
		None	
		Dose-dependent inhibition of cell proliferation	
		No inflammation	

Table 7.3 Summary of *in vivo* toxicity outcomes after administration of CNTs. The term “CNTs” indicates that the material was not identified as single- (SWNTs) or multi-walled (MWNTs) carbon nanotubes.

CNTs tested	Production method and impurities content	Model	Administration	Time ^{a)}	Toxic outcome	Ref.
<i>Dermal toxicity</i>						
CNTs	Arc discharge	Human	Patch test	96 h	None	[50]
CNTs	Arc discharge	Rabbit	Eyes instillation	72 h	None	[50]
MWNTs	CVD (3–5 wt% Fe)	Mice	Subcutaneous implantation	90 d	Low	[51]
SWNTs	CVD (1–1.5 wt% Fe)	Mice	Subcutaneous implantation	90 d	Low	[51]
SWNTs	HPCO (30 wt% Fe)	Mice	Topical exposure	5 d	Oxidative stress Skin thickening Inflammation	[46]
<i>Pulmonary toxicity</i>						
CNTs	Arc discharge	Guinea pigs	Intratracheal instillation	28 d	None	[63]
MWNTs	Arc discharge	Guinea pigs	Intratracheal instillation	90 d	Time-dependent	[66]
SWNTs	HPCO (unpurified; 26.9 wt% Fe, 0.78 wt% Ni; purified: 2.14 wt% Fe)	Mice	Intratracheal instillation	90 d	Dose-dependent	[58]
Purified MWNTs	Catalytic decomposition (<2.2 wt.% catalyst)	Rats	Intratracheal instillation	60 d	Toxic	[68]
MWNTs	Catalytic decomposition	Rats	Intratracheal instillation	60 d	Defect-dependent acute toxic reactions	[69]
MWNTs	CVD (2–2.5 wt% Fe)	Guinea pigs	Intratracheal instillation	90 d	Time-dependent	[66]
MWNTs	CVD (2–2.5 wt% Fe)	Mice	Nasal administration	30 d	None	[74]

MWNTs	CVD (2–2.5 wt% Fe)	Mice	Intratracheal instillation	30 d	Dose-dependent granulomatous responses	[74]
MWNTs	CVD	Rats	Intratracheal instillation	180 d	Agglomeration-dependent toxicity	[61]
SWNTs	HPCO (0.23 wt% Fe)	Mice	Pharyngeal aspiration	60 d	Acute inflammation	[24]
SWNTs	HPCO (17.7 wt% Fe)	Mice	Inhalation vs. pharyngeal aspiration	28 d	Similar chain of pathological events Higher toxicity by inhalation	[59]
SWNTs	HPCO	Mice	Pharyngeal aspiration	30 d	Higher SWNT dispersion causes higher toxic outcomes	[76]
SWNTs	(<2 wt% Fe) Laser ablation (5 wt% Ni and Co)	Rats	Intratracheal instillation	90 d	Controversial	[57, 65]
MWNTs	Not specified (Nanolab)	Guinea pigs	Intratracheal instillation	90 d	Time-dependent Pneumonitis reactions observed	[66]
MWNTs	Not specified (Pyrograf PR1)	Guinea pigs	Intratracheal instillation	90 d	Time-dependent Pneumonitis reactions observed	[67]
MWNTs	Not specified (Showa Denko)	Guinea pigs	Intratracheal instillation	90 d	Time-dependent Pneumonitis reactions observed	[66]
					(Continued)	

Table 7.3 (Continued)

CNTs tested	Production method and impurities content	Model	Administration	Time ^{a)}	Toxic outcome	Ref.
SWNTs	Not specified (Sigma-Aldrich)	Mice	Pharyngeal aspiration	24 h	Pulmonary inflammatory responses	[77]
MWNTs	Not specified (Shenzhen Nanotech Port; <0.2 wt% Ni)	Mice	Intratracheal instillation Inhalation	24 d	Pulmonary toxicity induced only by intratracheal instillation	[75]
<i>In vivo immune responses</i>						
Purified MWNTs	Catalytic decomposition	Rat	Intratracheal instillation	60 d	Peritoneal macrophages; dose-dependent, agglomeration-dependent inflammation (TNF- α up-regulation)	[68]
MWNTs, SWNTs	CVD (5 wt% catalysts)	Mice	Subcutaneous injection/intranasal administration	26 d	Allergic responses	[109]
MWNTs	CVD (0.34 wt% Ni, 0.03 wt% La)	Mice	Aerosol	14 d	Lung fibrosis	[110]
MWNTs	CVD (0.5 wt% Ni, 0.5 wt% Fe)	Mice	Aerosol	14 d	No pulmonary toxicity Suppression of systemic immunity	[82, 83]

MWNTs	Not specified (<10 wt% catalysts)	Mice	Intratracheal instillation	14 d	Alveolar macrophages; activation; production pro-inflammatory cytokines Blood: high-levels pro-inflammatory cytokines; differentiation of CD4 ⁺ T cell to Th1 and Th2 cells Length-dependent inflammation	[108]
CNTs	Not specified (800 and 200 nm-length)	Rat	Subcutaneous implantation			
MWNTs	CVD (2–2.5 wt% Fe) HiPCO	Mice	Oral administration	30 d	Nontoxic Elimination after 24 h	[74]
Pluronic F108-SWNTs		Rabbit	Intravenous administration	24 h	Non toxic Blood half-life = 1 h Accumulation in the liver	[119]
SWNTs-[⁶⁷ GA(DOTA) (AF488)(AF680)]	HiPCO	Mice	Intravenous administration	7 d	Nontoxic Renal clearance No active secretion	[124]
PEG-SWNTs	HiPCO	Mice	Intravenous administration	90 d	Nontoxic Blood half-life = 1 d Complete clearance after 2 months	[126]

(Continued)

Table 7.3 (Continued)

CNTs tested	Production method and impurities content	Model	Administration	Time ^{a)}	Toxic outcome	Ref.
[¹¹¹ In]DTPA-CNTs	MWNTs; SWNTs; method not specified	Mice	Intravenous administration	3 h	Nontoxic	[121]
MWNTs	Not specified	Rabbit	Intravenous administration		Blood half-life = 3 h Renal clearance	
[¹¹¹ In]DTPA-MWNTs	Not specified	Rats	Intravenous administration	24 h	Carotid artery thrombosis	[113]
NH ₃ ⁺ -MWNTs	Not specified	Mice	Intravenous administration	30 min	Non toxic	[120]
NH ₃ ⁺ -MWNTs	Not specified	Mice	Intravenous administration	24 h	Renal clearance No accumulation in liver and lungs	[122]
Abdominal cavity MWNTs	Catalytic decomposition (0.37 wt% Al, <0.01 wt% Fe, <0.01 wt% Co)	Rats	Intraperitoneal administration	104 wk	Non toxic Functionalization grade influences accumulation in organs	[91]
					No mesothelioma formation	

MWNTs	Catalytic decomposition (1.97 wt% Al, 0.49 wt% Fe, 0.48 wt% Co) CVD	Rats	Intraperitoneal administration	104 wk	No mesothelioma formation	[91]
MWNTs	Not specified (Mitsui)	Mice	Intraperitoneal administration	30 d	Nontoxic	[74]
MWNTs	Not specified (Mitsui)	p53 (+/-) mice	Intraperitoneal administration	175 d	Carcinogenic effect	[88]
MWNTs	Not specified (Mitsui)	Rats	Intracrotal injection	52 wk	Carcinogenic effect	[89]
MWNTs	Not specified (Mitsui; NanoLab, University of Manchester)	Mice	Intraperitoneal administration	7 d	Length-dependent pathogenicity	[6]
[¹²⁵ I]SWNT-OH	Not specified	Mice	Intraperitoneal administration		Nontoxic	[125]
MWNTs	Not specified (Sigma- Aldrich)	Mice	Intraperitoneal administration	7 d	Renal clearance Partial death only at high concentrations (20/40 mg kg ⁻¹)	[90]

a) The maximum time of treatment: in between time points where possibly tested; d = days, wk = weeks.

However, *in vivo* studies illustrated in this chapter confirm that the toxicity and/or biocompatibility of CNTs are not fully established. Perhaps most importantly, it is clear that the use of a more coordinated global approach is imperative to define and describe the toxicological responses triggered by CNTs. Since CNT samples vary greatly in terms of composition depending on production and purification methods, the impact of such variability on CNT toxicity needs to be addressed in a controlled manner. Briefly, current studies into lung toxicity need to be intensified with investigations into the respirability of CNTs. Additionally, accurate information on the ease with which CNTs can be absorbed through the skin is vital for addressing their potential dermal toxicity. Finally, more studies on the efficacy and speed with which CNTs can be distributed and accumulated *in vivo* are also required. Assessing this is important, not only for estimating the impact of environmental exposure to CNTs on human health, but also for determining the potential of CNTs as drug-delivery systems and components of biomedical implants. Current data indicate that functionalized CNTs exhibit lower toxicity than unmodified or unrefined nanotubes. Further research needs to be conducted to confirm that this is the case. Keeping in mind the recent discovery of the biodegradability of CNTs, it is imperative to establish the long-term stability of these conjugates *in vivo*. Furthermore, it may be prudent to recognize that some of the unwanted (toxic) responses of CNTs may lead to desirable outcomes depending on the specific context. For instance, the controlled induction of CNT-dependent cellular toxicity could serve as a novel and effective approach for combating cancer.

The success of CNT technology is dependent upon the continuation of research into the toxicology of CNTs and CNT-related materials.

Abbreviations

BAL	bronchoalveolar lavage
BSA	bovine serum albumin
CNT	carbon nanotube
COX	cyclooxygenase
CVD	chemical vapor deposition
DPPC	dipalmitoylphosphatidylcholine
ENMs	engineered nanomaterials
EPR	electron paramagnetic resonance
HiPCO	high-pressure carbon monoxide
hMPO	human myeloperoxidase
HRP	horseradish peroxidase
LPS	bacterial lipopolysaccharide
MWNT	multi-walled carbon nanotube
NF-κB	nuclear factor-kappa B
NO	nitric oxide
OVA	ovalbumin
PBS	phosphate-buffered saline
SWNT	single-walled carbon nanotube

References

- 1 Satterfield, T. *et al.* (2009) Anticipating the perceived risk of nanotechnologies. *Nature Nanotechnology*, **4** (11), 752–758.
- 2 Hartung, T. (2009) Toxicology for the twenty-first century. *Nature*, **460** (7252), 208–212.
- 3 Faunce, T.A. (2008) Toxicological and public good considerations for the regulation of nanomaterial-containing medical products. *Expert Opinion on Drug Safety*, **7** (2), 103–106.
- 4 Meng, H. *et al.* (2009) A predictive toxicological paradigm for the safety assessment of nanomaterials. *ACS Nano*, **3** (7), 1620–1627.
- 5 George, S. *et al.* (2010) Use of a rapid cytotoxicity screening approach to engineer a safer zinc oxide nanoparticle through iron doping. *ACS Nano*, **4** (1), 15–29.
- 6 Poland, C.A. *et al.* (2008) Carbon nanotubes introduced into the abdominal cavity of mice show asbestos-like pathogenicity in a pilot study. *Nature Nanotechnology*, **3** (7), 423–428.
- 7 Service, R.F. (2008) Nanotechnology – can high-speed tests sort out which nanomaterials are safe? *Science*, **321** (5892), 1036–1037.
- 8 Stone, V., Johnston, H. and Schins, R.P.F. (2009) Development of *in vitro* systems for nanotoxicology: methodological considerations. *Critical Reviews in Toxicology*, **39** (7), 613–626.
- 9 Jones, C.F. and Grainger, D.W. (2009) *In vitro* assessments of nanomaterial toxicity. *Advanced Drug Delivery Reviews*, **61** (6), 438–456.
- 10 Nel, A. *et al.* (2006) Toxic potential of materials at the nanolevel. *Science*, **311** (5761), 622–627.
- 11 Walker, N.J. and Bucher, J.R. (2009) A 21st century paradigm for evaluating the health hazards of nanoscale materials? *Toxicological Sciences*, **110** (2), 251–254.
- 12 Rivera Gil, P. *et al.* (2010) Correlating physico-chemical with toxicological properties of nanoparticles: the present and the future. *ACS Nano*, **4** (10), 5527–5531.
- 13 Oberdorster, G. *et al.* (2005) Principles for characterizing the potential human health effects from exposure to nanomaterials: elements of a screening strategy. *Particle and Fibre Toxicology*, **2** (1), 8.
- 14 Nel, A.E. *et al.* (2009) Understanding biophysicochemical interactions at the nano–bio interface. *Nature Materials*, **8** (7), 543–557.
- 15 Walczyk, D. *et al.* (2010) What the cell “sees” in bionanoscience. *Journal of the American Chemical Society*, **132** (16), 5761–5768.
- 16 Collins, F.S., Gray, G.M. and Bucher, J.R. (2008) Toxicology – transforming environmental health protection. *Science*, **319** (5865), 906–907.
- 17 Lynch, I. *et al.* (2007) The nanoparticle–protein complex as a biological entity; a complex fluids and surface science challenge for the 21st century. *Advances in Colloid and Interface Science*, **134**–135, 167–174.
- 18 Donaldson, K. *et al.* (2010) Asbestos, carbon nanotubes and the pleural mesothelium: a review of the hypothesis regarding the role of long fibre retention in the parietal pleura, inflammation and mesothelioma. *Particle and Fibre Toxicology*, **7**, 5.
- 19 Hirsch, A. (2010) The era of carbon allotropes. *Nat. Mater.*, **9** (11), 868–871.
- 20 Tasis, D. *et al.* (2006) Chemistry of carbon nanotubes. *Chemical Reviews*, **106** (3), 1105–36.
- 21 Smart, S.K. *et al.* (2006) The biocompatibility of carbon nanotubes. *Carbon*, **44** (6), 1034–1047.
- 22 Zheng, M. and Diner, B.A. (2004) Solution redox chemistry of carbon nanotubes. *Journal of the American Chemical Society*, **126** (47), 15490–4.
- 23 Donaldson, K., Beswick, P.H. and Gilmour, P.S. (1996) Free radical activity associated with the surface of particles: a unifying factor in determining biological activity? *Toxicology Letters*, **88** (1–3), 293–8.
- 24 Shvedova, A.A. *et al.* (2005) Unusual inflammatory and fibrogenic pulmonary responses to single-walled carbon

- nanotubes in mice. *American Journal of Physiology - Lung Cellular and Molecular Physiology*, **289** (5), L698–L708.
- 25 Shvedova, A.A. *et al.* (2003) Exposure to carbon nanotube material: assessment of nanotube cytotoxicity using human keratinocyte cells. *Journal of toxicology and environmental health. Part A*, **66** (20), 1909–1926.
- 26 Herzog, E. *et al.* (2007) A new approach to the toxicity testing of carbon-based nanomaterials – the clonogenic assay. *Toxicology Letters*, **174** (1–3), 49–60.
- 27 Kagan, V.E., Bayir, H. and Shvedova, A.A. (2005) Nanomedicine and nanotoxicology: two sides of the same coin. *Nanomedicine*, **1** (4), 313–6.
- 28 Casey, A. *et al.* (2007) Probing the interaction of single walled carbon nanotubes within cell culture medium as a precursor to toxicity testing. *Carbon*, **45** (1), 34–40.
- 29 Monteiro-Riviere, N.A. and Inman, A.O. (2006) Challenges for assessing carbon nanomaterial toxicity to the skin. *Carbon*, **44** (6), 1070–1078.
- 30 Feliu, N. and Fadeel, B. (2010) Nanotoxicology: no small matter. *Nanoscale*, **2** (12), 2514–20.
- 31 Zhang, L.W. *et al.* (2007) Biological interactions of functionalized single-wall carbon nanotubes in human epidermal keratinocytes. *International Journal of Toxicology*, **26** (2), 103–113.
- 32 Worle-Knirsch, J.M., Pulskamp, K. and Krug, H.F. (2006) Oops they did it again! Carbon nanotubes hoax scientists in viability assays. *Nano Letters*, **6** (6), 1261–1268.
- 33 Casey, A. *et al.* (2007) Spectroscopic analysis confirms the interactions between single walled carbon nanotubes and various dyes commonly used to assess cytotoxicity. *Carbon*, **45** (7), 1425–1432.
- 34 Monteiro-Riviere, N.A., Inman, A.O. and Zhang, L.W. (2009) Limitations and relative utility of screening assays to assess engineered nanoparticle toxicity in a human cell line. *Toxicology and Applied Pharmacology*, **234** (2), 222–235.
- 35 Donaldson, K. *et al.* (1997) Free radical activity of PM10: iron-mediated generation of hydroxyl radicals. *Environmental Health Perspectives*, **105**, 1285–1289.
- 36 Gilmour, P.S. *et al.* (1997) Free radical activity of industrial fibers: role of iron in oxidative stress and activation of transcription factors. *Environmental Health Perspectives*, **105**, 1313–1317.
- 37 Voinov, M.A. *et al.* (2011) Surface-mediated production of hydroxyl radicals as a mechanism of iron oxide nanoparticle biotoxicity. *Journal of the American Chemical Society*, **133** (1), 35–41.
- 38 Alpatova, A.L. *et al.* (2010) Single-walled carbon nanotubes dispersed in aqueous media via noncovalent functionalization: effect of dispersant on the stability, cytotoxicity, and epigenetic toxicity of nanotube suspensions. *Water Research*, **44** (2), 505–520.
- 39 Mutlu, G.M. *et al.* (2010) Biocompatible nanoscale dispersion of single-walled carbon nanotubes minimizes *in vivo* pulmonary toxicity. *Nano Letters*, **10** (5), 1664–1670.
- 40 Herzog, E. *et al.* (2009) Dispersion medium modulates oxidative stress response of human lung epithelial cells upon exposure to carbon nanomaterial samples. *Toxicology and Applied Pharmacology*, **236** (3), 276–281.
- 41 Dong, L.F. *et al.* (2009) Cytotoxicity effects of different surfactant molecules conjugated to carbon nanotubes on human astrocytoma cells. *Nanoscale Research Letters*, **4** (12), 1517–1523.
- 42 Ding, L. *et al.* (2005) Molecular characterization of the cytotoxic mechanism of multiwall carbon nanotubes and nano-onions on human skin fibroblast. *Nano Letters*, **5** (12), 2448–64.
- 43 Monteiro-Riviere, N.A. *et al.* (2005) Multi-walled carbon nanotube interactions with human epidermal keratinocytes. *Toxicology Letters*, **155** (3), 377–384.
- 44 Witzmann, A.F. and Monteiro-Riviere, N.A. (2006) Multi-walled carbon nanotube exposure alters protein expression in human keratinocytes. *Nanomedicine*, **2** (3), 158–168.
- 45 Manna, S.K. *et al.* (2005) Single-walled carbon nanotube induces oxidative stress

- and activates nuclear transcription factor-kappa B in human keratinocytes. *Nano Letters*, **5** (9), 1676–1684.
- 46 Murray, A.R. *et al.* (2009) Oxidative stress and inflammatory response in dermal toxicity of single-walled carbon nanotubes. *Toxicology*, **257** (3), 161–171.
- 47 Zollanvari, A. *et al.* (2009) Analysis and modeling of time-course gene-expression profiles from nanomaterial-exposed primary human epidermal keratinocytes. *BMC Bioinformatics*, **10**, (Suppl. 11) S10.
- 48 Sayes, C.M. *et al.* (2006) Functionalization density dependence of single-walled carbon nanotubes cytotoxicity *in vitro*. *Toxicology Letters*, **161** (2), 135–142.
- 49 Shen, M.W. *et al.* (2009) Polyethyleneimine-mediated functionalization of multiwalled carbon nanotubes: synthesis, characterization, and *in vitro* toxicity assay. *Journal of Physical Chemistry C*, **113** (8), 3150–3156.
- 50 Huczko, A. and Lange, H. (2001) Carbon nanotubes: experimental evidence for a null risk of skin irritation and allergy. *Fullerene Science and Technology*, **9** (2), 247–250.
- 51 Koyama, S. *et al.* (2006) Role of systemic T-cells and histopathological aspects after subcutaneous implantation of various carbon nanotubes in mice. *Carbon*, **44** (6), 1079–1092.
- 52 Donaldson, K. *et al.* (2004) Nanotoxicology. *Journal of Occupational and Environmental Medicine*, **61** (9), 727–728.
- 53 Bruinink, A., Manser, P. and Hasler, S. (2009) *In vitro* effects of SWCNT: role of treatment duration. *Physical Status Solidi B*, **246** (11–12), 2423–2427.
- 54 Davoren, M. *et al.* (2007) *In vitro* toxicity evaluation of single walled carbon nanotubes on human A549 lung cells. *Toxicology in Vitro*, **21** (3), 438–448.
- 55 Simon-Deckers, A. *et al.* (2008) *In vitro* investigation of oxide nanoparticle and carbon nanotube toxicity and intracellular accumulation in A549 human pneumocytes. *Toxicology*, **253** (1–3), 137–146.
- 56 Herzog, E. *et al.* (2009) SWCNT suppress inflammatory mediator responses in human lung epithelium *in vitro*. *Toxicology and Applied Pharmacology*, **234** (3), 378–390.
- 57 Warheit, D.B. *et al.* (2004) Comparative pulmonary toxicity assessment of single-wall carbon nanotubes in rats. *Toxicological Sciences*, **77** (1), 117–125.
- 58 Lam, C.W. *et al.* (2004) Pulmonary toxicity of single-wall carbon nanotubes in mice 7 and 90 days after intratracheal instillation. *Toxicological Sciences*, **77** (1), 126–134.
- 59 Shvedova, A.A. *et al.* (2008) Inhalation vs. aspiration of single-walled carbon nanotubes in C57BL/6 mice: inflammation, fibrosis, oxidative stress, and mutagenesis. *American Journal of Physiology - Lung Cellular and Molecular Physiology*, **295** (4), L552–L565.
- 60 Sargent, L.M. *et al.* (2009) Induction of aneuploidy by single-walled carbon nanotubes. *Environmental and Molecular Mutagenesis*, **50** (8), 708–717.
- 61 Elgrably, D. *et al.* (2008) Induction of apoptosis and absence of inflammation in rat lung after intratracheal instillation of multiwalled carbon nanotubes. *Toxicology*, **253** (1–3), 131–136.
- 62 Wang, X. *et al.* (2010) Quantitative techniques for assessing and controlling the dispersion and biological effects of multiwalled carbon nanotubes in mammalian tissue culture cells. *ACS Nano*, **4** (12), 7241–7252.
- 63 Huczko, A. *et al.* (2001) Physiological testing of carbon nanotubes: are they asbestos-like? *Fullerene Science and Technology*, **9** (2), 251–254.
- 64 Oberdörster, G. (2002) Toxicokinetics and effects of fibrous and nonfibrous particles. *Inhalation Toxicology*, **14** (1), 29–56.
- 65 Warheit, D.B. (2006) What is currently known about the health risks related to carbon nanotube exposures? *Carbon*, **44** (6), 1064–1069.
- 66 Huczko, A. *et al.* (2005) Pulmonary toxicity of 1-D nanocarbon materials. *Fullerenes, Nanotubes, and Carbon Nanostructures*, **13** (2), 141–145.
- 67 Grubek-Jaworska, H. *et al.* (2006) Preliminary results on the pathogenic effects of intratracheal exposure to one-dimensional nanocarbons. *Carbon*, **44** (6), 1057–1063.

- 68** Muller, J. *et al.* (2005) Respiratory toxicity of multi-wall carbon nanotubes. *Toxicology and Applied Pharmacology*, **207** (3), 221–231.
- 69** Muller, J. *et al.* (2008) Structural defects play a major role in the acute lung toxicity of multiwall carbon nanotubes: toxicological aspects. *Chemical Research in Toxicology*, **21** (9), 1698–1705.
- 70** Fenoglio, I. *et al.* (2008) Structural defects play a major role in the acute lung toxicity of multiwall carbon nanotubes: physicochemical aspects. *Chemical Research in Toxicology*, **21** (9), 1690–1697.
- 71** Shvedova, A.A. and Kagan, V.E. (2010) The role of nanotoxicology in realizing the ‘helping without harm’ paradigm of nanomedicine: lessons from studies of pulmonary effects of single-walled carbon nanotubes. *Journal of Internal Medicine*, **267** (1), 106–118.
- 72** Fiorito, S. *et al.* (2006) Effects of fullerenes and single-wall carbon nanotubes on murine and human macrophages. *Carbon*, **44** (6), 1100–1105.
- 73** Muller, J., Huaux, F. and Lison, D. (2006) Respiratory toxicity of carbon nanotubes: how worried should we be? *Carbon*, **44** (6), 1048–1056.
- 74** Carrero-Sanchez, J.C. *et al.* (2006) Biocompatibility and toxicological studies of carbon nanotubes doped with nitrogen. *Nano Letters*, **6** (8), 1609–1616.
- 75** Li, J.G. *et al.* (2007) Comparative study of pathological lesions induced by multiwalled carbon nanotubes in lungs of mice by intratracheal instillation and inhalation. *Environmental Toxicology*, **22** (4), 415–421.
- 76** Mercer, R.R. *et al.* (2008) Alteration of deposition pattern and pulmonary response as a result of improved dispersion of aspirated single-walled carbon nanotubes in a mouse model. *American Journal of Physiology - Lung Cellular and Molecular Physiology*, **294** (1), L87–L97.
- 77** Tong, H. *et al.* (2009) Influence of acid functionalization on the cardiopulmonary toxicity of carbon nanotubes and carbon black particles in mice. *Toxicology and Applied Pharmacology*, **239** (3), 224–232.
- 78** Ma-Hock, L. *et al.* (2009) Inhalation toxicity of multiwall carbon nanotubes in rats exposed for 3 months. *Toxicological Sciences*, **112** (2), 468–481.
- 79** Baron, P.A. *et al.* (2008) Aerosolization of single-walled carbon nanotubes for an inhalation study. *Inhalation Toxicology*, **20** (8), 751–760.
- 80** Maynard, A.D. *et al.* (2004) Exposure to carbon nanotube material: aerosol release during the handling of unrefined single-walled carbon nanotube material. *Journal of toxicology and environmental health. Part A*, **67** (1), 87–107.
- 81** Li, Z. *et al.* (2007) Cardiovascular effects of pulmonary exposure to single-wall carbon nanotubes. *Environmental Health Perspectives*, **115** (3), 377–382.
- 82** Mitchell, L.A. *et al.* (2007) Pulmonary and systemic immune response to inhaled multiwalled carbon nanotubes. *Toxicological Sciences*, **100** (1), 203–214.
- 83** Mitchell, L.A. *et al.* (2009) Mechanisms for how inhaled multiwalled carbon nanotubes suppress systemic immune function in mice. *Nature Nanotechnology*, **4** (7), 451–456.
- 84** Shvedova, A.A. *et al.* (2007) Vitamin E deficiency enhances pulmonary inflammatory response and oxidative stress induced by single-walled carbon nanotubes in C57BL/6 mice. *Toxicology and Applied Pharmacology*, **221** (3), 339–348.
- 85** Pacurari, M. *et al.* (2008) Raw single-wall carbon nanotubes induce oxidative stress and activate MAPKs, AP-1, NF-kappa B, and Akt in normal and malignant human mesothelial cells. *Environmental Health Perspectives*, **116** (9), 1211–1217.
- 86** Pacurari, M. *et al.* (2008) Oxidative and molecular interactions of multi-wall carbon nanotubes (MWCNT) in normal and malignant human mesothelial cells. *Nanotoxicology*, **2** (3), 155–170.
- 87** Wick, P. *et al.* (2007) The degree and kind of agglomeration affect carbon nanotubecytotoxicity. *Toxicology Letters*, **168** (2), 121–131.
- 88** Takagi, A. *et al.* (2008) Induction of mesothelioma in p53 +/− mouse by intraperitoneal application of multi-wall

- carbon nanotube. *Journal of Toxicological Sciences*, **33** (1), 105–116.
- 89 Sakamoto, Y. *et al.* (2009) Induction of mesothelioma by a single intrascrotal administration of multi-wall carbon nanotube in intact male Fischer 344 rats. *Journal of Toxicological Sciences*, **34** (1), 65–76.
- 90 Chiaretti, M. *et al.* (2008) Carbon nanotubes toxicology and effects on metabolism and immunological modification *in vitro* and *in vivo*. *Journal of Physics: Condensed Matter*, **20** (47).
- 91 Muller, J. *et al.* (2009) Absence of carcinogenic response to multiwall carbon nanotubes in a 2-year bioassay in the peritoneal cavity of the rat. *Toxicological Sciences*, **110** (2), 442–448.
- 92 Oberdörster, G. (2010) Safety assessment for nanotechnology and nanomedicine: concepts of nanotoxicology. *Journal of Internal Medicine*, **267** (1), 89–105.
- 93 Granum, B. and Lovik, M. (2002) The effect of particles on allergic immune responses. *Toxicological Sciences*, **65** (1), 7–17.
- 94 Plowden, J. *et al.* (2004) Innate immunity in aging: impact on macrophage function. *Aging Cell*, **3** (4), 161–167.
- 95 Bayir, H. *et al.* (2005) Enhanced oxidative stress in iNOS-deficient mice after traumatic brain injury: support for a neuroprotective role of iNOS. *Journal of Cerebral Blood Flow & Metabolism*, **25** (6), 673–684.
- 96 DeLeo, F.R. (2004) Modulation of phagocyte apoptosis by bacterial pathogens. *Apoptosis*, **9** (4), 399–413.
- 97 Ricciardolo, F.L.M. *et al.* (2006) Reactive nitrogen species in the respiratory tract. *European Journal of Pharmacology*, **533** (1–3), 240–252.
- 98 Kagan, V.E. *et al.* (2006) Direct and indirect effects of single walled carbon nanotubes on RAW 264.7 macrophages: role of iron. *Toxicology Letters*, **165** (1), 88–100.
- 99 Rothen-Rutishauser, B. *et al.* (2010) Relating the physicochemical characteristics and dispersion of multiwalled carbon nanotubes in different suspension media to their oxidative reactivity *in vitro* and inflammation *in vivo*. *Nanotoxicology*, **4** (3), 331–342.
- 100 Dumortier, H. *et al.* (2006) Functionalized carbon nanotubes are non-cytotoxic and preserve the functionality of primary immune cells. *Nano Letters*, **6** (7), 1522–1528.
- 101 Shvedova, A.A. *et al.* (2009) Mechanisms of pulmonary toxicity and medical applications of carbon nanotubes: two faces of Janus? *Pharmacology & Therapeutics*, **121** (2), 192–204.
- 102 Jia, G. *et al.* (2005) Cytotoxicity of carbon nanomaterials: single-wall nanotube, multi-wall nanotube, and fullerene. *Environmental Science and Technology*, **39** (5), 1378–1383.
- 103 Dutta, D. *et al.* (2007) Adsorbed proteins influence the biological activity and molecular targeting of nanomaterials. *Toxicological Sciences*, **100** (1), 303–315.
- 104 Pulskamp, K., Diabate, S. and Krug, H.F. (2007) Carbon nanotubes show no sign of acute toxicity but induce intracellular reactive oxygen species in dependence on contaminants. *Toxicology Letters*, **168** (1), 58–74.
- 105 Porter, A.E. *et al.* (2009) Uptake of noncytotoxic acid-treated single-walled carbon nanotubes into the cytoplasm of human macrophage cells. *ACS Nano*, **3** (6), 1485–1492.
- 106 Cheng, C. *et al.* (2009) Toxicity and imaging of multi-walled carbon nanotubes in human macrophage cells. *Biomaterials*, **30** (25), 4152–4160.
- 107 Sato, Y. *et al.* (2005) Influence of length on cytotoxicity of multi-walled carbon nanotubes against human acute monocytic leukemia cell line THP-1 *in vitro* and subcutaneous tissue of rats *in vivo*. *Molecular BioSystems*, **1** (2), 176–182.
- 108 Park, E.J. *et al.* (2009) Pro-inflammatory and potential allergic responses resulting from B cell activation in mice treated with multi-walled carbon nanotubes by intratracheal instillation. *Toxicology*, **259** (3), 113–121.
- 109 Nygaard, U.C. *et al.* (2009) Single-walled and multi-walled carbon nanotubes promote allergic immune responses in

- mice. *Toxicological Sciences*, **109** (1), 113–123.
- 110** Ryman-Rasmussen, J.P. *et al.* (2009) Inhaled multiwalled carbon nanotubes potentiate airway fibrosis in murine allergic asthma. *American Journal of Respiratory Cell and Molecular Biology*, **40** (3), 349–358.
- 111** Cesta, M.F. *et al.* (2010) Bacterial lipopolysaccharide enhances PDGF signaling and pulmonary fibrosis in rats exposed to carbon nanotubes. *American Journal of Respiratory Cell and Molecular Biology*, **43** (2), 142–151.
- 112** Semerová, J. *et al.* (2009) Carbon nanotubes activate blood platelets by inducing extracellular Ca^{2+} influx sensitive to calcium entry inhibitors. *Nano Letters*, **9** (9), 3312–3317.
- 113** Radomski, A. *et al.* (2005) Nanoparticle-induced platelet aggregation and vascular thrombosis. *British Journal of Pharmacology*, **146** (6), 882–893.
- 114** Tamura, K. *et al.* (2004) Effects of micro/nano particle size on cell function and morphology. *Bioceramics* 16 (eds Barbosa, M.A., *et al.*), Trans Tech Publications, Uetikon-Zurich, pp. 919–922.
- 115** Nemmar, A. *et al.* (2007) Enhanced peripheral thrombogenicity after lung inflammation is mediated by platelet-leukocyte activation: role of P-selectin. *Journal of Thrombosis and Haemostasis*, **5** (6), 1217–1226.
- 116** Erdely, A. *et al.* (2009) Cross-talk between lung and systemic circulation during carbon nanotube respiratory exposure. Potential biomarkers. *Nano Letters*, **9** (1), 36–43.
- 117** Simeonova, P.P. and Erdely, A. (2009) Engineered nanoparticle respiratory exposure and potential risks for cardiovascular toxicity: predictive tests and biomarkers. *Inhalation Toxicology*, **21** (s1), 68–73.
- 118** Legramante, J.M. *et al.* (2009) Cardiac autonomic regulation after lung exposure to carbon nanotubes. *Human & Experimental Toxicology*, **28** (6–7), 369–375.
- 119** Cherukuri, P. *et al.* (2006) Mammalian pharmacokinetics of carbon nanotubes using intrinsic near-infrared fluorescence. *Proceedings of the National Academy of Sciences of the U.S.A.*, **103** (50), 18882–18886.
- 120** Lacerda, L. *et al.* (2008) Dynamic imaging of functionalized multi-walled carbon nanotube systemic circulation and urinary excretion. *Advanced Materials*, **20** (2), 225–230.
- 121** Singh, R. *et al.* (2006) Tissue biodistribution and blood clearance rates of intravenously administered carbon nanotube radiotracers. *Proceedings of the National Academy of Sciences of the U.S.A.*, **103** (9), 3357–3362.
- 122** Lacerda, L. *et al.* (2008) Carbon-nanotube shape and individualization critical for renal excretion. *Small*, **4** (8), 1130–1132.
- 123** Lacerda, L. *et al.* (2008) Tissue histology and physiology following intravenous administration of different types of functionalized multiwalled carbon nanotubes. *Nanomedicine*, **3** (2), 149–161.
- 124** Ruggiero, A. *et al.* (2010) Paradoxical glomerular filtration of carbon nanotubes. *Proceedings of the National Academy of Sciences of the U.S.A.*, **107** (27), 12369–12374.
- 125** Wang, H.F. *et al.* (2004) Biodistribution of carbon single-wall carbon nanotubes in mice. *Journal of Nanoscience and Nanotechnology*, **4** (8), 1019–1024.
- 126** Liu, Z. *et al.* (2008) Circulation and long-term fate of functionalized, biocompatible single-walled carbon nanotubes in mice probed by Raman spectroscopy. *Proceedings of the National Academy of Sciences of the U.S.A.*, **105** (5), 1410–1415.
- 127** Kisin, E.R. *et al.* (2007) Single-walled carbon nanotubes: geno- and cytotoxic effects in lung fibroblast V79 cells. *Journal of toxicology and environmental health. Part A: Current*, **70** (24), 2071–2079.
- 128** Zhu, L. *et al.* (2007) DNA damage induced by multiwalled carbon nanotubes in mouse embryonic stem cells. *Nano Letters Issues*, **7** (12), 3592–3597.
- 129** Karlsson, H.L. *et al.* (2008) Copper oxide nanoparticles are highly toxic: a comparison between metal oxide nanoparticles and carbon nanotubes. *Chemical Research in Toxicology*, **21** (9), 1726–1732.

- 130 Szendi, K. and Varga, C. (2008) Lack of genotoxicity of carbon nanotubes in a pilot study. *Anticancer Research*, **28** (1A), 349–352.
- 131 Folkmann, J.K. *et al.* (2009) Oxidatively damaged DNA in rats exposed by oral gavage to C-60 fullerenes and single-walled carbon nanotubes. *Environmental Health Perspectives*, **117** (5), 703–708.
- 132 Kostarelos, K. (2003) Rational design and engineering of delivery systems for therapeutics: biomedical exercises in colloid and surface science. *Advances in Colloid and Interface Science*, **106**, 147–168.
- 133 Kostarelos, K. (2010) Carbon nanotubes: fibrillar pharmacology. *Nature Materials*, **9** (10), 793–795.
- 134 Deng, X. *et al.* (2007) Translocation and fate of multi-walled carbon nanotubes *in vivo*. *Carbon*, **45** (7), 1419–1424.
- 135 Heister, E. *et al.* (2010) Higher dispersion efficacy of functionalized carbon nanotubes in chemical and biological environments. *ACS Nano*, **4** (5), 2615–2626.
- 136 Bai, Y.H. *et al.* (2010) Repeated administrations of carbon nanotubes in male mice cause reversible testis damage without affecting fertility. *Nature Nanotechnology*, **5** (9), 683–689.
- 137 Becker, M.L. *et al.* (2007) Length-dependent uptake of DNA-wrapped single-walled carbon nanotubes. *Advanced Materials*, **19** (7), 939–945.
- 138 Jin, H. *et al.* (2009) Size-dependent cellular uptake and expulsion of single-walled carbon nanotubes: single particle tracking and a generic uptake model for nanoparticles. *ACS Nano*, **3** (1), 149–158.
- 139 Kostarelos, K. *et al.* (2007) Cellular uptake of functionalized carbon nanotubes is independent of functional group and cell type. *Nature Nanotechnology*, **2** (2), 108–113.
- 140 Lacerda, L. *et al.* (2007) Intracellular trafficking of carbon nanotubes by confocal laser scanning microscopy. *Advanced Materials*, **19** (11), 1480–1484.
- 141 Pantarotto, D. *et al.* (2004) Translocation of bioactive peptides across cell membranes by carbon nanotubes. *Chemical Communications*, 16–17.
- 142 Pantarotto, D. *et al.* (2004) Functionalized carbon nanotubes for plasmid DNA gene delivery. *Angewandte Chemie International Edition*, **43** (39), 5242–5246.
- 143 Cui, H.F. *et al.* (2010) Interfacing carbon nanotubes with living mammalian cells and cytotoxicity issues. *Chemical Research in Toxicology*, **23** (7), 1131–1147.
- 144 Kam, N.W.S. and Dai, H.J. (2005) Carbon nanotubes as intracellular protein transporters: generality and biological functionality. *Journal of the American Chemical Society*, **127** (16), 6021–6026.
- 145 Heller, D.A. *et al.* (2005) Single-walled carbon nanotube spectroscopy in live cells: towards long-term labels and optical sensors. *Advanced Materials*, **17** (23), 2793–2799.
- 146 Kam, N.W.S. *et al.* (2005) Carbon nanotubes as multifunctional biological transporters and near-infrared agents for selective cancer cell destruction. *Proceedings of the National Academy of Sciences of the U.S.A.*, **102** (33), 11600–11605.
- 147 Feazell, R.P. *et al.* (2007) Soluble single-walled carbon nanotubes as longboat delivery systems for platinum(IV) anticancer drug design. *Journal of the American Chemical Society*, **129** (27), 8438–8439.
- 148 Jin, H., Heller, D.A. and Strano, M.S. (2008) Single-particle tracking of endocytosis and exocytosis of single-walled carbon nanotubes in NIH-3T3 cells. *Nano Letters*, **8** (6), 1577–1585.
- 149 Van den Bossche, J. *et al.* (2010) Efficient receptor-independent intracellular translocation of aptamers mediated by conjugation to carbon nanotubes. *Chemical Communications*, 7379–7381.
- 150 Mu, Q.X., Broughton, D.L. and Yan, B. (2009) Endosomal leakage and nuclear translocation of multiwalled carbon nanotubes: developing a model for celluptake. *Nano Letters*, **9** (12), 4370–4375.
- 151 Zhou, F.F. *et al.* (2010) New insights of transmembranal mechanism and subcellular localization of noncovalently

- modified single-walled carbon nanotubes. *Nano Letters*, **10** (5), 1677–1681.
- 152** Allen, B.L. *et al.* (2009) Mechanistic investigations of horseradish peroxidase-catalyzed degradation of single-walled carbon nanotubes. *Journal of the American Chemical Society*, **131** (47), 17194–17205.
- 153** Kagan, V.E. *et al.* (2010) Carbon nanotubes degraded by neutrophil myeloperoxidase induce less pulmonary inflammation. *Nature Nanotechnology*, **5** (5), 354–359.
- 154** Chlopek, J. *et al.* (2006) *In vitro* studies of carbon nanotubes biocompatibility. *Carbon*, **44** (6), 1106–1111.
- 155** Nayak, T.R. *et al.* (2010) Thin films of functionalized multiwalled carbon nanotubes as suitable scaffold materials for stem cells proliferation and bone formation. *ACS Nano*, **4** (12), 7717–7725.
- 156** Tutak, W. *et al.* (2009) Toxicity induced enhanced extracellular matrix production in osteoblastic cells cultured on single-walled carbon nanotube networks. *Nanotechnology*, **20** (25), 255101.
- 157** Burke, A. *et al.* (2009) Long-term survival following a single treatment of kidney tumors with multiwalled carbon nanotubes and near-infrared radiation. *Proceedings of the National Academy of Sciences of the U.S.A.*, **106** (31), 12897–12902.
- 158** Moghimi, S.M. and Kissel, T. (2006) Particulate nanomedicines. *Advanced Drug Delivery Reviews*, **58** (14), 1451–1455.
- 159** Crinelli, R. *et al.* (2010) Oxidized ultrashort nanotubes as carbon scaffolds for the construction of cell-penetrating NF- κ B decoy molecules. *ACS Nano*, **4** (5), 2791–2803.
- 160** Kostarelos, K. (2008) The long and short of carbon nanotube toxicity. *Nature Biotechnology*, **26** (7), 774–776.
- 161** Pantarotto, D. *et al.* (2003) Immunization with peptide-functionalized carbon nanotubes enhances virus-specific neutralizing antibody responses. *Chem. Biol.*, **10**, 961–966.
- 162** Lacerda, L. *et al.* (2006) Carbon nanotubes as nanomedicines: from toxicology to pharmacology. *Advanced Drug Delivery Reviews*, **58** (14), 1460–1470.
- 163** De Nicola, M. *et al.* (2008) Carbon nanotubes on Jurkat cells: effects on cell viability and plasma membrane potential. *Journal of Physics: Condensed Matter*, **20** (47), 474204.
- 164** Flahaut, E. *et al.* (2006) Investigation of the cytotoxicity of CCVD carbon nanotubes towards human umbilical vein endothelial cells. *Carbon*, **44** (6), 1093–1099.
- 165** Cui, D.X. *et al.* (2005) Effect of single wall carbon nanotubes on human HEK293 cells. *Toxicology Letters*, **155** (1), 73–85.

8

A Review of Green Synthesis of Nanophase Inorganic Materials for Green Chemistry Applications

Homer Genuino, Hui Huang, Eric Njagi, Lisa Stafford, and Steven L. Suib

8.1

Introduction

This chapter presents a summary of environmentally friendly ways to synthesize inorganic nanomaterials that are used in green chemical applications such as environmental remediation, decomposition of hazardous wastes, dye degradation, and other areas. Environmental and energy needs of modern society have catalyzed the advancement of nanoscience and nanotechnology. This research area requires synthetic techniques to be more environmentally benign and energy saving [1]. In this review, we summarize green syntheses of nanophase inorganic materials and applications of such materials in heterogeneous catalysis, environmental catalysis, and remediation technologies in the past 5 years. The use of chemicals, heating sources, and various procedures in the syntheses are discussed. A significant current focus is in the advancement of single-step low-temperature syntheses of nanophase metal oxide and metallic nanoparticles without using surfactants or templates. Novel physical and chemical properties of such materials are discussed. How these materials can be applied and engineered to meet current environmental requirements is also described. Four major areas are covered: green synthesis of nanophase inorganic materials; green synthesis of metallic nanoparticles; green chemistry applications of inorganic nanomaterials; and environmental applications of nanomaterials.

8.2

Green Synthesis of Nanophase Inorganic Materials

8.2.1

Metal Oxide Nanoparticles

Various methods have been used to synthesize metal oxide nanoparticles. The methods discussed here include hydrothermal alteration, reflux, and microwave-assisted methods.

8.2.1.1 Hydrothermal Synthesis

Hydrothermal synthesis is a powerful method used for the fabrication of nanophase materials due to the relatively low temperature during synthesis, facile separation of nanoparticles in the product, and ready availability of apparatus for such syntheses. Versatile physical and chemical properties of nanomaterials can be obtained with the use of this method that involves various techniques (e.g., control of reaction time, temperature and choice of oxidant and its concentration). Several extensive reviews are available that discuss the fundamental properties and applications of this method [2, 3]. These reviews cover the synthesis of nanomaterials with different pore textures, different types of composition [2, 4–6], and different dimensionalities in terms of morphology [6–8].

A significant number of publications that deal with the use of various hydrothermal techniques to synthesize nanomaterials are available. This part of the chapter mainly concerns bottom-up synthetic approaches to fabricate metal oxide nanoparticles, specifically manganese oxide nanomaterials. In a typical hydrothermal synthetic route, an oxidant and a reducing agent were introduced in an aqueous solution with a suitable pH buffer. These reagents were reacted at a certain temperature and reaction time under high pressure. By varying the temperature and reaction time, different manganese dioxide materials with different morphologies or crystal structures were easily attained.

Yuan *et al.* [9] used $\text{K}_2\text{Cr}_2\text{O}_7$ to oxidize Mn^{2+} in an acidic aqueous solution, resulting in a cryptomelane-type manganese oxide material (K-OMS-2) with a well-defined three-dimensional dendrite nanostructure. The field emission scanning electron microscopy (FE-SEM) images of K-OMS-2 are shown in Figure 8.1a–c. The same group [10] further studied the redox reaction of $\text{Na}_2\text{Cr}_2\text{O}_7$ and Mn^{2+} under similar conditions, resulting in a γ -phase MnO_2 (Figure 8.1d and e). Under the same reaction conditions, they extended their work by exploring the redox reaction between RbCrO_4 and Mn^{2+} [11]. A rubidium-type OMS-2 material was formed (Figure 8.1f and g) with a similar nanostructure morphology to K-OMS-2.

With the same concept, a series of oxidants were used to oxidize Mn^{2+} under various conditions, resulting in a variety of MnO_2 materials with different crystalline phases and nanostructures. As an example, sodium chlorate, perchlorate, and bromate have been extensively used in hydrothermal reactions. Ding *et al.* [12] synthesized hierarchical nanoarchitected ε -phase MnO_2 materials by using NaClO_4 as an oxidant and MnCl_2 as a reducing reagent under neutral conditions at different reaction temperatures. The reaction time was proven to be crucial in the crystal growing process. Pyramid-shaped nuclei MnO_2 were formed after reaction for 2 h as observed using FE-SEM, and more comprehensive nanostructures with three-, four-, or five-branched architectures were formed when the reaction time was doubled. These branched nanostructures eventually tended to stabilize at a six-branched structure after the reaction time reached 12 h. Jia *et al.* [13] performed the redox reaction between NaClO_3 and MnSO_4 in a surfactant-free process. Multipod-like ω - MnOOH nanostructured materials were hydrothermally synthesized when the reaction time was in the range 4–6 h, whereas pyrolusite phase MnO_2 was formed when the reaction time was prolonged to 12–24 h. Wu *et al.* [14] carried out the redox

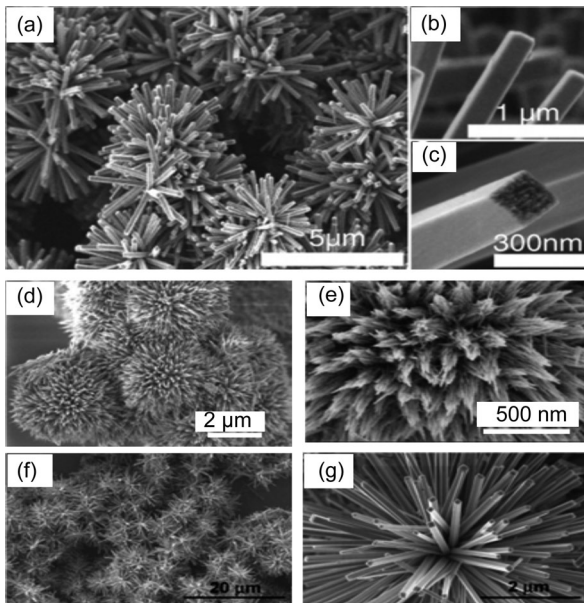


Figure 8.1 FE-SEM images of K-OMS-2 [(a)–(c)], γ -MnO₂ [(d) and (e)], and Rb-OMS-2 [(f) and (g)] nanomaterials synthesized using the hydrothermal method. Reprinted with permission from [9–11] © (2011) American Chemical Society and Wiley-VCH GmbH & Co. KGaA.

reaction of NaBrO₃ and MnSO₄ under neutral conditions, resulting in a γ -phase hexagon-based MnO₂ with a “layer-cake-like” and “intertexture-like” nanostructure. The γ -MnO₂ state consisted of akhtenskite (ϵ -MnO₂), pyrolusite (β -MnO₂), and ramsdellite, forming a heterogeneous phase.

A series of oxidants containing group VIB elements was also used to oxidize Mn²⁺ in a hydrothermal reaction to pursue novel morphologies of MnO₂ materials. Galindo *et al.* [15] carried out the reaction between oxone and Mn²⁺ at 120 °C for 20 h, leading to the formation of uniformly hollow microstructures of cryptomelane-type OMS-2 materials. The same group also performed the reaction between KMnO₄ and Mn(OAc)₂ resulting in K-OMS-2 nanorods. Potassium persulfate was used by Yuan *et al.* [16] to oxidize MnSO₄ under neutral conditions at a relatively high temperature (250 °C). Ultra-long K-OMS-2 nanowires were obtained, which were further converted to inorganic paper-like materials. In another study, Tang *et al.* [17] used H₂O₂ to oxidize Mn(NO₃)₂ under neutral conditions. Dandelion-like β -phase MnO₂ materials with a microstructure composed of nanofibers were obtained.

The alternation of temperature in a hydrothermal reaction was demonstrated to be crucial in changing the crystal phases or morphologies of nanomaterials. In the case of K₂Cr₂O₇, when the reaction temperature was increased to 180 °C, K-OMS-2 microspheres consisting of nanoneedles were synthesized in contrast to the nanocluster arrays composed of tetragonal prism nanorods synthesized at 120 °C (Figure 8.1a–c). In the case of Na₂Cr₂O₇, when the reaction temperature was 100 °C, Na-OMS-2 phase was formed. However, when the reaction temperature was

Table 8.1 Standard half-cell potentials of some oxidant species in aqueous solution at 25 °C.

Oxidant species	Half redox equation (acidic condition)	E°_{red} (V)
$\text{Cr}_2\text{O}_7^{2-}$	$\text{Cr}_2\text{O}_7^{2-} + 14\text{H}^+ + 6\text{e}^- = 2\text{Cr}^{3+} + 7\text{H}_2\text{O}$	+1.33
ClO_4^-	$2\text{ClO}_4^- + 16\text{H}^+ + 14\text{e}^- = \text{Cl}_2 + 8\text{H}_2\text{O}$	+1.39
ClO_3^-	$2\text{ClO}_3^- + 12\text{H}^+ + 10\text{e}^- = \text{Cl}_2 + 3\text{H}_2\text{O}$	+1.47
BrO_3^-	$2\text{BrO}_3^- + 12\text{H}^+ + 10\text{e}^- = \text{Br}_2 + 6\text{H}_2\text{O}$	+1.52
$\text{S}_2\text{O}_8^{2-}$	$\text{S}_2\text{O}_8^{2-} + 2\text{e}^- = 2\text{SO}_4^{2-}$	+2.01
H_2O_2	$\text{H}_2\text{O}_2 + 2\text{H}^+ + 2\text{e}^- = 2\text{H}_2\text{O}$	+1.78

increased to 120 and 180 °C, ϵ -phase and pyrolusite-phase MnO_2 were formed, respectively. The morphologies of these products are mainly flower-like but composed of nanofibers with different sizes. Such reaction temperature effects were also observed in the case of RbCrO_4 . Rb-containing OMS-2 nanomaterials were formed at 120 °C, whereas pyrolusite-phase MnO_2 nanomaterials were synthesized at 180 °C. By increasing the reaction temperature from 160 to 180 °C, the morphology of $\epsilon\text{-MnO}_2$ changes from a six-branched star-like shape to a hexagonal dipyramidal morphology.

The redox potential of the reacting couple was suggested to play a key role in forming different nanoarchitected materials. Table 8.1 presents a list of oxidant species and their corresponding standard reduction potentials, E°_{red} , in acidic aqueous solution at 25 °C. Precise control over nucleation and growth processes can lead to the formation of uniform and monodisperse nanostructures. In the case of $\text{K}_2\text{Cr}_2\text{O}_7$, the closeness of the standard potentials of the $\text{Cr}_2\text{O}_7^{2-}/\text{Cr}^{3+}$ (1.33 V) and $\text{Mn}^{4+}/\text{Mn}^{2+}$ (1.23 V) couples is critical in the formation of well-organized K-OMS-2 materials with complex morphologies.

This tuning redox potential concept has now been extended to fabricate other metals, metal oxides, and mixed metal oxide materials. A recent study used ammonia persulfate to oxidize Co^{2+} and Ce^{3+} in a neutral aqueous solution [18]. Figure 8.2a and b show the powder X-ray diffraction (XRD) patterns of CoOOH and CeO_2 materials, respectively. Both of these materials have hollow-sphere morphologies. More recently, NaBiO_3 was used to oxidize CeCl_3 in order to obtain a series of mixed metal oxide materials [19]. Figure 8.2c shows the transmission electron microscopy (TEM) image of as-synthesized nanocrystals with the compositional formula $\text{Ce}_{0.84}\text{Bi}_{0.16}\text{O}_{1.92}$.

The control of the pore size of OMS-2 materials is also of great interest to many researchers. Recently, Huang *et al.* [20] developed a single-step hydrothermal process to synthesize OMS materials with relative large pore sizes, as shown in Figure 8.3. In this reaction, metallic permanganate salts were directly decomposed in water within a hydrothermal reaction vessel. When $\text{Mg}(\text{MnO}_4)_2$ was used, todorokite-type OMS materials with a 3×3 tunnel pore texture was formed (Figure 8.3a), whereas NaMnO_4 led to the formation of a manganese oxide material with a 2×4 tunnel structure (Figure 8.3b). The advantages of using hydrothermal synthesis include minimization of the use of chemicals and wastes and reduction of the reaction time,

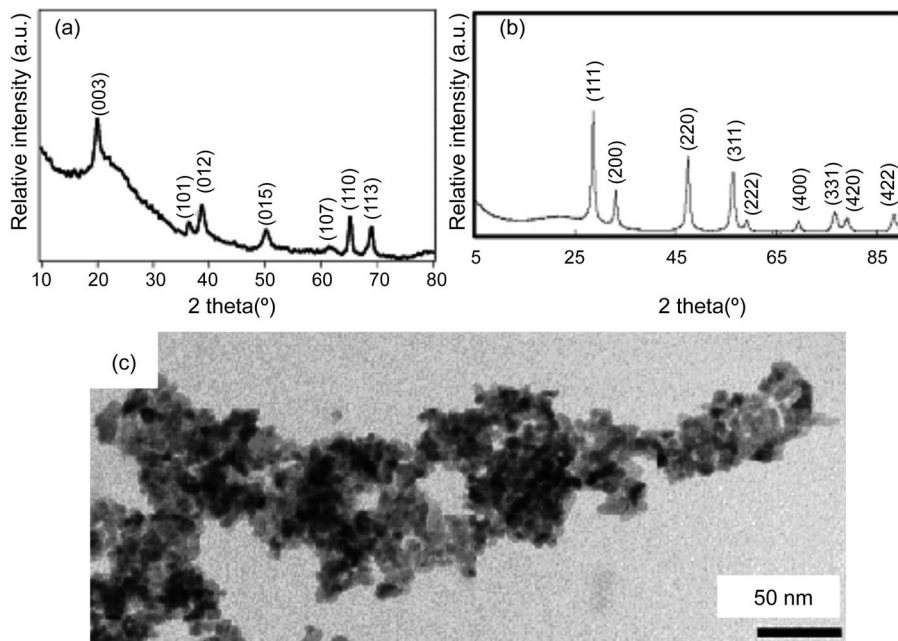


Figure 8.2 XRD patterns of (a) CoOOH and (b) CeO₂. (c) TEM image of Ce_{0.84}Bi_{0.16}O_{1.92} nanocrystals. Reprinted with permission from [18, 19] © (2011) American Chemical Society and Wiley-VCH GmbH & Co. KGaA.

as compared with conventional reaction routes under similar reaction conditions. The OMS materials formed are semiconducting and have attracted tremendous interest in green chemistry research, including environmental catalysis, heterogeneous catalysis, and power source applications.

8.2.1.2 Reflux Synthesis

Reflux synthesis methods in wet chemistry include techniques that normally involve relatively lower reaction temperatures compared with hydrothermal synthesis, a very

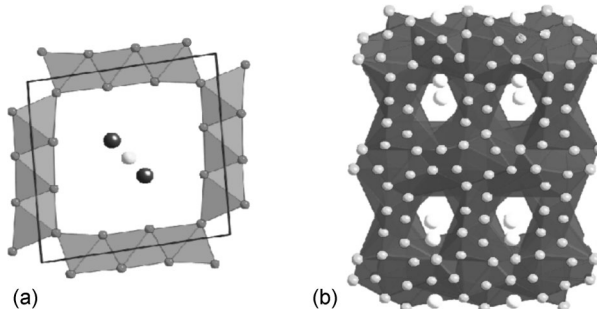


Figure 8.3 Crystal structures OMS materials of (a) 3 × 3 and (b) 2 × 4 tunnel types.

positive aspect in the fabrication of metal oxide nanomaterials. Chen *et al.* [21] and Bharathi *et al.* [22] separately used a reflux method to prepare akaganeite nanostructured materials which were further converted to highly mesoporous hematite nanorods and spindle-like nanostructures upon heating at 300 °C. Iwasaki *et al.* [23] prepared WO₃ nanocrystals ranging from 5 to 20 nm in diameter. Some of the as-synthesized samples showed photocatalytic activities in the visible light spectral range. Khagram *et al.* [24] synthesized NiO nanocrystals with a particle size of about 2.7 nm using methanol as the reflux solvent. Matos *et al.* [25] compared a hydrothermal method with a reflux method for the synthesis of ZrO₂ nanomaterials. The presence of H₂O₂ in synthesis systems reduced the particle size of such materials. This phenomenon was also observed in the synthesis of K-OMS-2 nanomaterials [26]. Direct preparation of Cu₂O hollow nanospheres was reported by Yang *et al.* [27] with the use of 2-propanol under refluxing conditions. Other metal oxides, such as LiMn₂O₄ [28] and BaMoO₄, [29], nanomaterials, were also synthesized using reflux methods.

In our laboratory, Xu *et al.* [30] prepared urchin-like CuO nanocrystals using urea as a precipitating reagent under refluxing conditions. The materials showed efficient performance in a catalytic olefin epoxidation test. A reflux method was also used to prepare doped OMS materials at low temperature. Calvert *et al.* [31] successfully doped tungsten into the OMS-2 framework using a reflux method. More recently, Jin *et al.* [32] used this method to prepare Ti-containing ε-MnO₂ materials which showed high capacity in an Li air battery test and good performance for liquid-phase toluene oxidation under aerated conditions.

8.2.1.3 Microwave-Assisted Synthesis

The search for new heating methods to process reactions has led to the use of microwave radiation as an alternative power source to carry out chemical reactions. Microwave-assisted methods include techniques that were first adopted to conduct organic reactions in 1986 by Gedye *et al.* [33]. Since then, microwave technology has been used to fabricate polymeric materials and synthesize inorganic materials. Microwave-assisted synthesis methods provide a much faster way not only to prepare materials but also to create smaller particulate materials, thus contributing to energy savings and satisfying the demands for more environmentally benign materials and procedures. In recent years, reviews have appeared on preparing electrode materials [34], porous materials [35, 36], and zeolite membranes [37]. Many papers have been published on the microwave-assisted synthesis of inorganic nanomaterials since 2005. Here, we review the recent advances in microwave-assisted hydrothermal (MW-HT) and reflux (MW-R) techniques in the generation of oxide nanocrystals.

MW-HT techniques can shorten the reaction time. For example, Ivanov *et al.* [38] synthesized ZnO nanocrystals in 10 min with the assistance of microwave hydrothermal methods. Huang *et al.* [39] also demonstrated the use of microwave radiation in the hydrothermal synthesis of ZnO complex nanostructures. These nanocrystals showed high photocatalytic activity in a model reaction of Methyl Orange photo-degradation. Li *et al.* [40] synthesized WO₃ nanorods in 20 min and showed high

performance in sensing ethanol. Pure anatase-phase TiO_2 materials were synthesized by Baldassari *et al.* [41] in an acidic medium in 30 min. Room temperature superparamagnetic $\gamma\text{-Fe}_2\text{O}_3$ nanoparticles were prepared by Sreeja and Joy [42]. Co_3O_4 nanocrystals were prepared by Ma *et al.* [43] at 200 °C in 1 h. Temperature control was critical in the formation of Co_3O_4 phase. Cao *et al.* [44] prepared hollow-sphere CeO_2 nanocrystals. An Ostwald ripening mechanism coupled with a self-templated, self-assembly process was proposed as the mechanism for the formation of the hollow structures. Huang *et al.* [45] used this technique to synthesize well-crystallized OMS-2 nanomaterials in less than 1 min. Time- and temperature-dependent studies were conducted to illustrate the mechanism of the formation of nanowires. The temperature was proven to be the key factor in forming these nanowires. Xu *et al.* [46] also used this technique to synthesize nickel hydroxide nanomaterials with three-dimensional flower-like morphologies. In a comparative study, MW-HT techniques were found to be superior to conventional hydrothermal method in terms of energy consumption and reaction time. Enhanced crystallinity, generation of homogeneous morphologies, and production of uniform particle sizes of the nanomaterials were observed using the MW-HT synthesis method. In addition to the single metal oxide system, MW-HT techniques have also been used to prepare mixed metal oxide systems [47–57].

Microwave-assisted reflux synthesis is an attractive method for synthesizing high surface area and large quantities of nanomaterials. For example, Ding *et al.* [58] prepared cobalt hydroxide-like compounds with a surface area of $176 \text{ m}^2 \text{ g}^{-1}$ which could be transformed into the spinel structure of Co_3O_4 with a surface area of $61 \text{ m}^2 \text{ g}^{-1}$. The structures of these materials were self-assemblies of nanosheets with a uniform small thickness of $\sim 5 \text{ nm}$. Nyutu *et al.* [59] synthesized multi-gram scale quantities of K-OMS-2 nanomaterials in the size range 4–20 nm in a single batch with very high surface areas up to $227 \text{ m}^2 \text{ g}^{-1}$. This technique was also applied to fabricate metal oxide solutions [60, 61] and hybrid materials [62].

8.3

Green Synthesis of Metallic Nanoparticles

Metallic nanoparticles exhibit novel dimension-dependent properties leading to attractive applications in catalysis [63], optoelectronics [64], and environmental remediation [65–70]. Metallic nanoparticles of specific sizes and morphologies can be readily synthesized using various chemical and physical methods [71–75]. However, most of these methods use aggressive reducing agents, toxic solvents, and nonbiodegradable stabilizing agents, or have high energy consumption, and as such pose potential environmental and biological risks [76].

Biological methods using plant extracts and microorganisms have been proposed as alternative environmentally friendly methods in the synthesis of metallic nanoparticles. Biomolecules can function as both reducing and capping agents, eliminating the use and generation of substances hazardous to human health and the environment. Moreover, biological methods can afford completely green synthetic

protocols if environmentally benign solvents are employed in the extraction process. Thus, metallic nanoparticles synthesized using biological methods may find widespread technological and medicinal applications.

Noble metals such as gold, silver, and platinum are extensively used for jewelry and in various biomedical applications, including drug delivery, imaging, photothermal therapy, and immunochromatography [77]. Consequently, there is a growing need to synthesize noble metal nanoparticles using methods that do not involve toxic chemicals. Gold and silver nanoparticles have been synthesized using various plant extracts, including hibiscus (*Hibiscus rosa sinensis*) leaf extract [77], black tea leaf extract [78], Indian gooseberry (*Emblica officinalis*) fruit extract [79], sundried camphor (*Cinnamomum camphora*) leaves [80], coffee and green tea extracts [81], and *Aloe vera* plant extract [82]. Metallic silver nanoparticles have been synthesized using various plant extracts, including magnolia (*Magnolia kobus*) leaf broth [83], coffee and tea extracts [81], *Cassia fistula* leaf broth [84], and *Eclipta* leaf extract [85].

Gold nanoparticles of various sizes and morphologies (spherical, triangular, and hexagonal) were prepared using extracts of lemongrass (*Cymbopogon flexuosus*) [86]. The size of the nanoparticles was controlled by varying the concentration of the lemongrass extract in the reaction medium. The average size of triangular and hexagonal particles decreased with increasing concentration of the lemongrass extract. Additionally, the ratio of the number of spherical nanoparticles to triangular/hexagonal particles in the reaction medium increased with increasing concentration of the lemongrass extract.

Gold nanotriangles were also synthesized using tamarind (*Tamarindus indica*) leaf extract [87]. Chloroaurate ions were rapidly reduced by the tamarind leaf extract leading to the formation of flat, crystalline gold nanotriangles with a thickness of 20–40 nm. Stable monodispersed gold nanoparticles were synthesized using glucose and starch as reducing and protecting agent, respectively [88]. The sizes of the synthesized gold nanoparticles decreased with increasing starch concentration. Higher concentrations of starch also led to the formation of larger amounts of gold nanoparticles.

Gold nanostructures of various sizes and morphologies were synthesized at room temperature using naturally occurring biodegradable plant surfactants [76]. The sizes and shapes (spherical, prisms, and hexagonal) of the synthesized nanoparticles were dependent on the concentration of the gold ions and the type of plant surfactant used for preparation.

Gold and platinum nanostructures were synthesized at room temperature using vitamin B₂ (riboflavin) as both the reducing and capping agent [89]. The morphology (spheres, nanowires and nanorods) of the synthesized nanoparticles was found to be dependent on the density of the solvent used in the preparation. High-density solvents led to the formation of nanospheres whereas nanorods and nanowires resulted in low-density solvents. The size of the nanoparticles decreased with increase in density of the solvent. Cao *et al.* [90] reported that the reduction of Au³⁺ ions by halloysites resulted in the formation of gold–halloysite nanocomposites. The shapes and sizes of the synthesized gold nanoparticles were dependent on the type of halloysite used in the synthesis.

Metallic iron nanoparticles of various sizes and morphologies were synthesized using tea extracts [91, 92]. The size and crystallinity (hexagonal metallic iron, amorphous iron, and $\alpha\text{-Fe}_2\text{O}_3$) of the synthesized iron nanoparticles were dependent on the concentration of the tea extract in the reaction mixture [92]. Iron and silver nanorods of uniform sizes and shapes were synthesized in poly(ethylene glycol) solutions using microwave irradiation [93]. Microwave irradiation provided rapid and homogeneous heating, leading to the formation of uniform nanomaterials with small sizes. The formation of nanorods depended on the concentration of poly(ethylene glycol); nanoparticle formation was favored at higher concentrations whereas at low concentrations, nanorod nucleation with nanoparticles was the major route. Palladium nanoparticles were synthesized using *Cinnamomum zeylanicum* bark extract [94]. Palladium nanoparticles with an average size of 15–20 nm were synthesized using the bark extract. The concentration of the extract, pH, and temperature did not have any significant effect on the size and shape of the nanoparticles formed. Palladium nanoparticles were also synthesized at room temperature using coffee and tea extracts [81]. Spherical Pd nanoparticles with sizes ranging from 5 to 100 nm were formed depending on the source of the coffee or tea extract.

Metallic nanoparticles have been synthesized *in vivo* using plants. Intracellular synthesis of gold nanoparticles was demonstrated using the sweet desert willow (*Chilopsis linearis*) plant [95]. The average size of Au nanoparticles formed in various tissues was dependent on the concentration of Au in the respective tissues. Haverkamp *et al.* [96] synthesized a gold–silver–copper alloy *in vivo* using the *Brassica juncea* plant.

Metallic nanoparticles have also been synthesized using microorganisms. Gold nanoparticles of various morphologies were synthesized using the bacterium *Rhodopseudomonas capsulata* [97]. The morphology of the synthesized nanoparticles was dependent on the pH of the solution. Spherical gold nanoparticles were produced at pH 7 whereas gold nanoplates were synthesized at pH 4. Rapid extracellular biosynthesis of stable silver nanoparticles was demonstrated using the filamentous fungus *Aspergillus fumigatus* and the fungus *Trichoderma asperellum* [98, 99], and crystalline silver nanoparticles with sizes in the range 5–25 and 13–18 nm were formed, respectively.

8.4

Green Chemistry Applications of Inorganic Nanomaterials

Green chemistry has been around for decades but was subsequently defined by Anastas and Warner as “benign by design” [100]. The principles of green chemistry include taking into consideration factors such as waste prevention, atom economy, less hazardous chemical syntheses, designing safer chemicals, safer solvents, and reaction media, designing for energy efficiency, renewable feedstocks, reduction of derivatives, catalytic versus stoichiometric reactions, considering degradation products, and real-time monitoring [101]. Essentially, green chemistry strives to utilize safer solvents, minimal solvent, or even no solvent in reactions that consume little

energy and do not generate any hazardous by-products or end-products in either the short or long term. As the focus here is on catalytic rather than stoichiometric reactions, the present content is already limited, in at least one category, to green chemistry principles.

Nanomaterials have been around for hundreds of years and are typically defined as particles of size ranging from 1 to 100 nm in at least one dimension. The inorganic nanomaterial catalysts discussed here are manganese oxides and titanium dioxide. Outside the scope of this chapter are polymers, pillared clays, coordination compounds, and inorganic–organic hybrid materials such as metal–organic frameworks.

8.4.1

Manganese Oxides

Manganese oxide octahedral molecular sieves (OMSs) are benign materials. In Nature, OMSs are found as manganese nodules on the ocean floor. OMS materials are excellent catalysts due to the mixed valency of the manganese: Mn^{4+} , Mn^{3+} , and sometimes Mn^{2+} are present. Further, these catalysts are both porous and semiconducting and their activities can be regenerated with air or oxygen. Of all the OMS materials synthesized, K-OMS-2 is the most useful. This is partly due to the high selectivity of most K-OMS-2-catalyzed reactions. Thus, OMS materials are green owing to their benign nature, ability to be regenerated, and high and distinct catalytic selectivity. High selectivity means that there are few to no by-products and energy and chemicals need not be wasted on separation techniques. Finally, manganese is widely available and inexpensive. Other OMS materials include OMS-1; the numbering refers to the order in which these structures were discovered and not the tunnel structure – for example, OMS-1 has a 3×3 tunnel structure [102].

Nanomaterials can also be tuned for specific purposes through doping. Specifically, the effect of the presence of manganese oxides on photocatalysis involving primarily titanium dioxide will be considered in this section. Titanium dioxide is a well-known photocatalyst and will be considered separately. K-OMS-2, which has a cryptomelane structure, is illustrated in Figure 8.4. Not all the literature discussed in this section, however, involves OMS tunnel structure materials. For example, amorphous manganese oxide (AMO) is also discussed as a photocatalyst. Manganite (MnOOH) is also included in battery applications.

Green OMS reactions can be grouped into the following categories: selective transformations, environmental applications, fuel cell applications, battery applications, and photocatalysis. Some relevant publications for each category are summarized in Table 8.2. Environmental applications such as the removal of organic dyes are relevant as this technology can be applied to wastewater treatment. Fuel cells use renewable feedstocks such as waste gas from landfills or wastewater treatment facilities, and strive for energy efficiency. Battery research has focused on energy efficiency, and photocatalysis uses a renewable feedstock and is energy efficient.

OMS materials are also “green” in that they are heterogeneous catalysts. Heterogeneous catalysts do not leach into the system and are therefore completely recoverable. In addition, doping of OMS materials with iron allows separation of

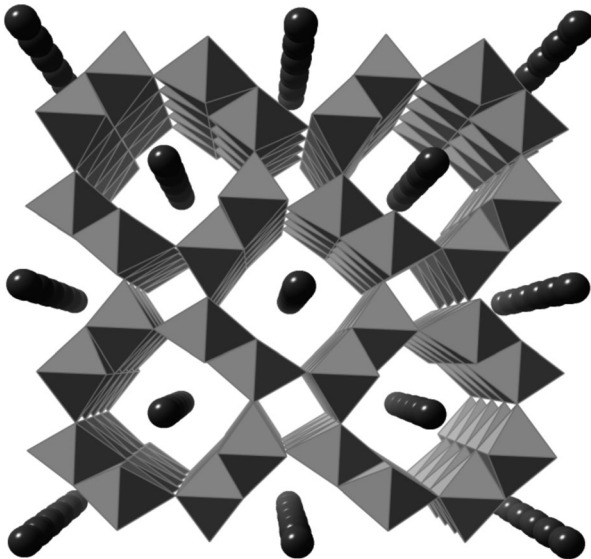


Figure 8.4 K-OMS-2 has the formula $\text{KMn}_8\text{O}_{16}\cdot n\text{H}_2\text{O}$ and has a 2×2 tunnel structure. The manganese octahedra are light gray and the potassium ions are dark gray

spheres and sit in the tunnel sites. Image generated using CrystalMaker (CrystalMaker Software, Oxford, UK; www.crystalmaker.com).

the catalyst via magnetism, further ensuring recoverability and reuse of the catalyst [131].

8.4.2

Titanium Dioxide

Research on titanium dioxide started with A. Fujishima in the late 1960s while he was a graduate student at the University of Tokyo. The work began with the study of oxide semiconductors, specifically zinc oxide. Fujishima discovered that the rutile form of titanium dioxide, when part of a complete electrochemical circuit with platinum black as the other electrode, decomposed water into oxygen and hydrogen using light in the ultraviolet (UV)-visible region of the spectrum. No external voltage was required to generate hydrogen gas, making this a major discovery. Titanium dioxide is an extremely effective photocatalyst owing to its high stability, low cost, and strong oxidant properties. Holes generated on the surface of titanium dioxide have a redox potential of + 2.53 V versus the standard hydrogen electrode. This allows TiO_2 to oxidize water to produce hydroxyl radicals [132].

There are three crystal structures of titanium dioxide: rutile, anatase, and brookite. The most active phase is rutile, which has a tetragonal structure [133], as shown in Figure 8.5 [134].

At present, titanium dioxide meets green chemistry principles, including energy efficiency and renewable feedstocks through a wide variety of heterogeneous photo-

Table 8.2 Selected green OMS publications by category.

Green chemistry category	Publications or patents
Selective transformations	Selective styrene ring opening [103] One-pot domino process for regioselective synthesis of α -carbonyl furans [104] Tandem process for synthesis of quinoxalines [105] Atmospheric oxidation of toluene [106] Cyclohexane oxidation [107] Synthesis of imines from alcohols [108] Synthesis of 2-aminodiphenylamine [109] $9H$ -Fluorene oxidation [110] Dehydrogenation of ethane in the presence of CO ₂ [111] Decomposition of methane [112] Carbon monoxide oxidation [113]
Environmental applications	Oxidation of volatile organic compounds (VOCs) [114] Decomposition of organic dyes [115] Removal of aqueous phenol [116] Superwetting nanowire membranes for selective absorption [117]
Fuel cell applications	Manganese dioxide as a new cathode catalyst in microbial fuel cells [118] OMS-2 catalysts in proton exchange membrane fuel cell applications [119] An improved cathode for alkaline fuel cells [120] Nanostructured manganese oxide as a cathodic catalyst for enhanced oxygen reduction in a microbial fuel cell [121] Carbon-supported tetragonal MnOOH catalysts for oxygen reduction reaction in alkaline media [122]
Battery applications	Titanium containing γ -MnO ₂ (TM) hollow spheres: synthesis and catalytic activities in Li-air batteries [123] Orthorhombic LiMnO ₂ nanorods for lithium ion battery application [124] Electrochemical characterization of MnOOH–carbon nanocomposite cathodes for metal–air batteries [125] Electrocatalytic activity of nanosized manganite [126]
Photocatalysis	Photocatalysts in 2-propanol oxidation [127] Photodegradation of N-nitrosodimethylamine in water [128] MnO ₂ -doped anatase TiO ₂ for photocatalytic degradation of organic contaminants in aqueous solution [129] Photocatalytic degradation of phenol with TiO ₂ and ZnO in the presence of manganese dioxides [130]

catalytic applications. Environmental applications include degradation of organic dyes in wastewater [135, 136]. Titanium dioxide is widely used in building materials, including glass, tiles, and cement [137] for pollution degradation. Pollutants are oxidized to smaller species at the TiO₂ surface which are then washed away by rainwater, which shows enhanced activity due to the superhydrophilicity of this material.

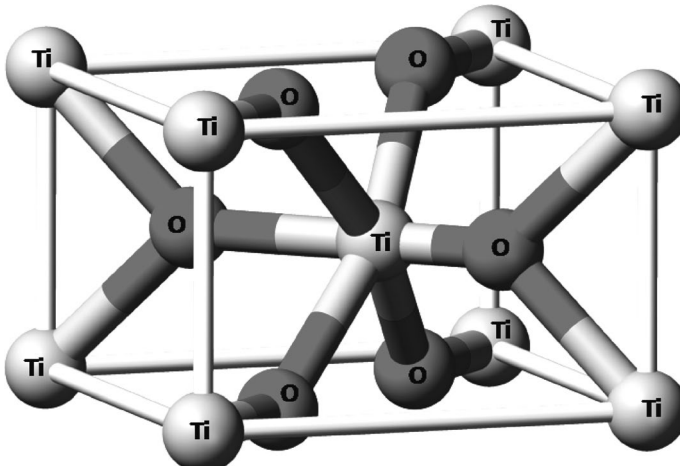


Figure 8.5 Ball-and-stick model of the unit cell of rutile structure.

Sol-gel coatings with both TiO_2 and SiO_2 were used by Kesmez *et al.* in 2009 [138] and Prado *et al.* in 2010 [139] for improvements in glass transmittance and self-cleaning ability. In general, SiO_2 is added to increase the transmittance of the glass (or decrease anti-reflectance), which is decreased by doping the glass with TiO_2 . Kesmez *et al.* [138] used Rhodamine B to measure photocatalytic ability. SiO_2 thickness as the bottom layer was kept constant at 89 nm while the TiO_2 top layer was varied. SiO_2 increased the transmittance by 6% compared with uncoated glass. The optimum film thickness of TiO_2 was found to be 42.9 nm when using butyl glycol as the solvent, based on decomposition of the dye. There was an overall increase in transmittance over bare glass of 0.8%. Prado *et al.* [139] studied the photodegradation of methylene blue as a function of the TiO_2 pore size and found that mesoporous TiO_2 layers showed increased photodegradation over denser layers. They also measured an overall increase in transmittance in the layered $\text{SiO}_2/\text{TiO}_2$ glass. Photodegradation was enhanced by 25–30% over the more commonly used compact TiO_2 . The only drawback of titanium dioxide is that its wide band gap ($E_g = 3.2 \text{ eV}$) limits its use to the UV region. Thus, Burunkaya *et al.* [140] doped titanium dioxide with Sn^{4+} and Ce^3 , broadening the absorbance, and found enhanced photoactivity at a concentration of both ions of 1%, with Sn^{4+} being more active. There was, however, an overall decrease in transmittance of the glass with both dopants.

Another area of active titanium dioxide research involves its use in textiles. Self-cleaning textiles save water and detergent in some instances preventing the release of phosphates into the environment. Kiwi and Pulgarin combined nanocrystalline anatase TiO_2 with silver to create a fabric that was both self-cleaning and resistant to bacteria and fungi [141]. Veronovski *et al.* [142] evaluated both the photocatalytic and antimicrobial properties of TiO_2 together with the effect of modifying the fabric on its end use, for example, drape and softness of the material. In addition to dirt and

pollutants, the TiO_2 might oxidize the cellulose present in the fabric itself. Two self-cleaning coatings were therefore developed, one with just titanium dioxide and the other with a composite of $\text{TiO}_2\text{--SiO}_2$ since SiO_2 reduces the effect of the TiO_2 . The composite coating has little effect on the handle of the fabric and also displays enhanced photodegradation as compared with the fabric treated with only TiO_2 and the untreated fabric.

Moafi *et al.* [143] studied the ability of titania *versus* zirconia to photocatalyze methylene blue and eosin yellow on polyacrylonitrile fibers. TiO_2 particles ranging from 10–20 nm in size and ZrO_2 particles ranging from 20–40 nm in size were dispersed on the fiber surface. Photocatalytic activity of TiO_2 was greater.

Mihailović *et al.* [144] pretreated polyester fabrics with both oxygen and argon plasmas, and the treated fabrics were then loaded with TiO_2 nanoparticles. Plasma pretreatment was employed to enhance the bonding of the nanoparticles to the polyester fibers. Plasma treatment with oxygen was more favorable than with argon, most likely due to increased wetting of the polyester fabric that allowed for increased deposition of nanoparticles on the fabric surface. The oxygen-treated TiO_2 fabric also displayed greater antibacterial ability against the Gram-negative bacterium *Escherichia coli*. Finally, self-cleaning of blueberry stains was also greatest on the oxygen-treated TiO_2 fabric as compared with the argon-treated TiO_2 fabric and the untreated polyester fabric.

Bedford and Steckl [145] utilized coaxial electrospinning to bind TiO_2 nanoparticles to hydroxyl groups on cellulose acetate fibers “in flight.” Following deacylation, a fiber with a higher surface area-to-volume ratio than surface-loaded fibers was prepared. These fibers showed enhanced degradation of blue dye stains over surface-loaded fibers: Surface-coated fibers degraded stains to 20% of the initial concentration whereas coaxially electrospun fibers fully degraded stains in 7–8 h.

Another area of titanium dioxide photocatalytic research is in the coating of TiO_2 on plastics such as polycarbonate and polystyrene surfaces. This is valuable for the automobile and construction industries. Yaghoubi *et al.* [146] reported a sol-gel route for the deposition of 30 nm anatase TiO_2 particles on polycarbonate. A self-cleaning layer was formed and mechanical properties such as hardness and scratch resistance were improved. Lam *et al.* [147] also deposited titania on polycarbonate. However, they used UVC treatment and NaOH etching of the polycarbonate prior to application of the TiO_2 . The NaOH-etched polycarbonate exhibited increased wetting and antifogging properties as compared with the UVC-treated material. Further, NaOH-etched polycarbonate degraded Methylene Blue better than non-etched materials.

The above-mentioned applications are a result of two distinct characteristics of titanium dioxide: the photocatalytic activity and the photoinduced superhydrophilic nature of this material. These properties work in tandem. The photocatalytic phenomenon is a result of holes generated at the surface having high redox potential and therefore oxidizing ability. These holes break bonds between the titanium and oxygen atoms. In the presence of water, hydroxyl groups are formed, creating a layer of hydrogen atoms protruding from the surface. These atoms can hydrogen bond with water in the environment and thus lead to superhydrophilicity [148].

8.5

Environmental Applications of Nanomaterials

The use of nanomaterials is important in environmental science and technology in terms of their applications in green chemistry, pollution prevention, remediation of contaminated soils and water, and sensing and detection of pollutants. These applications are directed towards environmental improvement and pollution control.

8.5.1

Background

One of the major breakthroughs in nanotechnology is the use of nanomaterials as catalysts for environmental applications [149]. Nanomaterials have been developed to improve the properties of catalysts, enhance reactivity towards pollutants, and improve their mobility in various environmental media [150]. Nanomaterials offer applications to pollution prevention through improved catalytic processes that reduce the use of toxic chemicals and eliminate wastes. Nanomaterials also offer applications in environmental remediation and, in the near future, opportunities to create better sensors for process controls.

This section covers environmental applications of nanomaterials insofar as they are directly applied to the pollutant of interest. The photocatalytic degradation of organic pollutants and remediation of polluted soils and water are discussed here. The high surface areas and photocatalytic activities of semiconductor nanomaterials have attracted many researchers. Semiconductor nanomaterials are commercially available, stable, and relatively nontoxic and cheap. Prominent examples that are discussed are metal oxides such as TiO_2 and ZnO and a variety of Fe-based nanomaterials.

Bimetallic nanomaterials such as Pd/Fe, Ni/Fe, and Pd/Au are also active catalysts for the degradation of organic contaminants, including halogenated pesticides, nitroaromatics, polychlorinated biphenyls, and halogenated aliphatics (ethenes and methanes) [151].

8.5.2

Titanium Dioxide Nanomaterials

Nanoscale TiO_2 photocatalysts are widely used for environmental applications [152]. Through advanced oxidation process, TiO_2 nanomaterials have the ability to mineralize toxic and nonbiodegradable organic pollutants completely into CO_2 and H_2O , and inorganic constituents [153]. Photodegradation of organic pollutants such as hexahydro-1,3,5-trinitro-1,3,5-triazine [154], organophosphorus pesticides such as monocrotophos, parathion, dichorovos, and methamidophos [155], nitrobenzene [156], and various dyes [157] were recently investigated.

Metal ions or their oxides were combined with TiO_2 nanomaterials in order to improve the catalytic activity and selectivity of the TiO_2 photocatalysts. Ag-doped TiO_2 was used to degrade gaseous sulfur compounds [158]. Ag nanoparticle-doped TiO_2

was also utilized for the efficient degradation of diazo dyes [159]. Doping nanoscale TiO₂ with transition metals such as Cr³⁺, Fe³⁺, and Ni²⁺ was carried out to improve the gas-phase degradation of benzene [160]. Cerium-doped nano TiO₂ and composite nanoparticles were used for phenol degradation [161]. Phenol was also degraded using TiO₂/SrO composite nanomaterials [162]. TiO₂/MoO₃ nanocomposite photocatalysts [163] and vanadium-doped TiO₂ nanoparticles [164] were used for the degradation of Methyl Orange dye. Composite materials such as FeZn/TiO₂ [165] and TiO₂/SiC [166] were used for the degradation of 2-propanol. SiO₂ and TiO₂ nanospheres were combined to degrade benzene [167] and Rhodamine B [168] in aqueous solution. Cr and TiO₂ were also combined to degrade gaseous formaldehyde [169]. *p*-Chlorophenol was degraded using Zr⁴⁺-doped TiO₂ [170] and Cu-doped TiO₂ [171] nanopowders. Noble metal/titanium dioxide nanocomposites (Pt/TiO₂, Pd/TiO₂, and bimetallic Pt-Pd/TiO₂) were prepared and tested for the photocatalytic oxidation of Methyl Orange dye in an aqueous phase [172].

8.5.3

Zinc Oxide Nanomaterials

The photocatalytic activity of ZnO nanomaterials for the degradation of some organic pollutants in water [173] (e.g., dyes [174]) was explored by several groups to achieve environmental benefits. Recent studies have indicated that ZnO can be used under acidic or alkaline conditions with the proper treatment [175, 176]. ZnO nanomaterials were used as photocatalysts for the degradation of phenol [177] and chlorinated phenols such as 2,4,6-trichlorophenol [178]. ZnO nanomaterials were also used for the degradation of Methylene Blue [179], direct dyes [180], Acid Red [181], and Ethyl Violet [182].

ZnO photocatalyst can also be coupled with other materials in order to improve its chemical and physical properties [183] and photocatalytic activity [184]. Nanosized ZnO was immobilized on aluminum foil for the degradation of phenol [185]. Lanthanum and ZnO were combined to degrade 2,4,6-trichlorophenol [186]. Compared with TiO₂ nanomaterial, ZnO nanomaterial generally absorbs a significant amount of the solar spectrum in the visible range; therefore, ZnO nanomaterials were combined with TiO₂ nanomaterials used as a photocatalyst [187].

8.5.4

Iron-Based Nanomaterials

Iron-based nanomaterials generally include iron sulfide nanoparticles, bimetallic iron nanoparticles, nanoscale iron oxide, and nanoscale zerovalent iron (NZVI) [188]. Iron-based nanomaterials rapidly and effectively transform various environmental contaminants into benign products. NZVI is a promising *in situ* remediation agent [189]. For example, NZVI particles rapidly dechlorinate chlorinated organic pollutants or immobilize heavy metals found in contaminated groundwater [190]. This is due to the high oxidizing capacities of NZVI particles [191], reducing the concentration of the contaminant to near zero. Other notable advantages of NZVI-

based site remediation include reduction of the overall cost and time of clean-up and elimination of the need for treatment and disposal of contaminated samples. Other pollutants degraded by iron-based nanoparticles include carbon tetrachloride, trichloroethylene, tetrachloroethylene, pentachloroethylene, and organochlorine pesticides [191]. Benzoic acid [192, 193] and polychlorinated biphenyls [194] are also effectively degraded. Further, iron-based nanoparticles can effectively adsorb heavy metals such as Ni^{2+} and Hg^{2+} and toxic anions such as $\text{Cr}_2\text{O}_7^{2-}$ and NO_3^- [195, 196] in water. Lindane and atrazine are also destroyed by stabilized iron-based nanoparticles [197].

The use of nanoscale materials in the clean-up of hazardous waste sites is termed nanoremediation. Remediation of soil contaminated with pentachlorophenol using NZVI was studied [198]. In a separate study, soils contaminated with polychlorinated biphenyls was treated using iron nanoparticles [194]. NZVI and iron oxide have been suggested to be used as a colloidal reactive barrier for *in situ* groundwater remediation due to its strong and specific interactions with Pb and As compounds [199].

Remediation of contaminated groundwater using NZVI technology has also been investigated [200]. For instance, Bromothymol Blue dyes were shown to be degraded using NZVI prepared from tea polyphenols [201]. Iron oxide nanomaterials also showed excellent abilities to remove organic pollutants and heavy metals from contaminated water [202]. Magnetic nanoparticles can be incorporated with the iron-based nanoparticles in order to tune their properties and improve their catalytic performance [203].

8.6

Conclusion and Future Perspectives

Studies on the use of hydrothermal, microwave-assisted, and reflux synthesis methods for the development and application of nanomaterials have been reviewed. An important aspect of the green synthesis of metallic nanoparticles involves techniques that make use of biological materials such as plant extracts and micro-organisms. The design of nanomaterials and control of their desired properties have been reviewed. The unique properties of manufactured nanomaterials offer many potential benefits.

The applications of nanomaterials in the field of environmental science are broad. The widespread use of nanomaterials in photocatalysis, organic pollutant degradation, process emission treatments, and pollution monitoring allows faster reactions, benign end-products, and zero pollution (green chemistry) [100]. The tunable physical and chemical properties of inorganic nanomaterials inspire innovative solutions to persistent environmental challenges. In the near future, the use of nanotechnologies and materials will play a vital role in efforts to develop better methods for the detection and decontamination of harmful biological agents. However, appropriate characterization of the nanomaterials is essential for understanding the potential implications of their applications.

Acknowledgment

We gratefully acknowledge the support of this research by the US Department of Energy, Office of Basic Energy Sciences, Division of Chemical, Geochemical, and Biological Sciences.

References

- 1 Horvath, I.T. and Anastas, P.T. (2007) Innovations and green chemistry. *Chemical Reviews*, **107**, 2169–2173.
- 2 Sheets, W.C., Mugnier, E., Barnabe, A., Marks, T.J. and Poeppelmeier, K.R. (2006) Hydrothermal synthesis of delafossite-type oxides. *Chemistry of Materials*, **18**, 7–20.
- 3 Byrappa, K. and Adschari, T. (2007) Hydrothermal technology for nanotechnology. *Progress in Crystal Growth and Characterization of Materials*, **53**, 117–166.
- 4 Liu, Z., Zhou, X. and Qian, Y. (2010) Synthetic methodologies for carbon nanomaterials. *Advanced Materials*, **22**, 1963–1966.
- 5 Tosheva, L. and Valtchev, V.P. (2005) Nanozeolites: synthesis, crystallization mechanism, and applications. *Chemistry of Materials*, **17**, 2494–2513.
- 6 Chen, A. and Holt-Hindle, P. (2010) Platinum-based nanostructured materials: synthesis, properties, and applications. *Chemical Reviews*, **110**, 3767–3804.
- 7 Djurisic, A.B., Xi, Y.Y., Hsu, Y.F. and Chan, W.K. (2007) Hydrothermal synthesis of nanostructures. *Recent Patents on Nanotechnology*, **1**, 121–128.
- 8 Yao, W. and Yu, S. (2007) Recent advances in hydrothermal syntheses of low dimensional nanoarchitectures. *International Journal of Nanotechnology*, **4**, 129–162.
- 9 Yuan, J., Li, W., Gomez, S. and Suib, S.L. (2005) Shape-controlled synthesis of manganese oxide octahedral molecular sieve three-dimensional nanostructures. *Journal of the American Chemical Society*, **127**, 14184–14185.
- 10 Li, W., Yuan, J., Shen, X., Gomez-Mower, S., Xu, L., Sithambaram, S., Aindow, M. and Suib, S.L. (2006) Hydrothermal synthesis of structure- and shape-controlled manganese oxide octahedral molecular sieve nanomaterials. *Advanced Functional Materials*, **16**, 1247–1253.
- 11 Li, W., Yuan, J., Gomez-Mower, S., Sithambaram, S. and Suib, S.L. (2006) Synthesis of single crystal manganese oxide octahedral molecular sieve (OMS) nanostructures with tunable tunnels and shapes. *Journal of Physical Chemistry B*, **110**, 3066–3070.
- 12 Ding, Y., Shen, X., Gomez, S., Luo, H., Aindow, M. and Suib, S.L. (2006) Hydrothermal growth of manganese dioxide into three-dimensional hierarchical nanoarchitectures. *Advanced Functional Materials*, **16**, 549–555.
- 13 Jia, Y., Xu, J., Zhou, L., Liu, H. and Hu, Y. (2008) A simple one step approach to preparation of γ -MnOOH multipods and β -MnO₂ nanorods. *Materials Letters*, **62**, 1336–1338.
- 14 Wu, C., Xie, W., Zhang, M., Bai, L., Yang, J. and Xie, Y. (2009) Environmentally friendly γ -MnO₂ hexagon-based nanoarchitectures: structural understanding and their energy-saving applications. *Chemistry-A European Journal*, **15**, 492–500.
- 15 Galindo, H.M., Carvajal, Y., Njagi, E., Ristau, R.A. and Suib, S.L. (2010) Facile one-step template-free synthesis of uniform hollow microstructures of cryptomelane-type manganese oxide K-OMS-2. *Langmuir*, **26**, 13677–13683.
- 16 Yuan, J., Laubernds, K., Villegas, J., Gomez, S. and Suib, S.L. (2004) Spontaneous formation of inorganic paper-like materials. *Advanced Materials*, **16**, 1729–1732.
- 17 Tang, B., Wang, G., Zhuo, L. and Ge, J. (2006) Novel dandelion-like beta-manganese dioxide microstructures and

- their magnetic properties. *Nanotechnology*, **17**, 947–951.
- 18** Chen, C., Firliet, B.T., Abbas, S.F., Sithambaram, S., Garces, H.F. and Suib, S.L. (2009) Controlled synthesis of self-assembled metal oxide hollow spheres via tuning redox potentials: versatile nanostructured cobalt and cobalt manganese oxides. *Advanced Materials*, **20**, 1205–1209.
- 19** Sardar, K., Playford, H.Y., Darton, R.J., Barney, E.R., Hannon, A.C., Tompsett, D., Fisher, J., Kashtiban, R.J., Sloan, J., Ramos, S., Cibin, G. and Walton, R.I. (2010) Nanocrystalline cerium–bismuth oxides: synthesis, structural characterization, and redox properties. *Chemistry of Materials*, **22** 6191–6201.
- 20** Huang, H., Chen, C., Xu, L., Genuino, H., Garcia-Martinez, J., Garces, H.F., Jin, L., King’ondu Kithongo, C. and Suib, S.L. (2010) Single-step synthesis of manganese oxide octahedral molecular sieves with large pore sizes. *Chemical Communications*, 5945–5947.
- 21** Chen, M., Jiang, J., Zhou, X. and Diao, G. (2008) Preparation of akaganeite nanorods and their transformation to sphere shape hematite. *Journal for Nanoscience and Nanotechnology*, **8**, 3942–3948.
- 22** Bharathi, S., Nataraj, D., Mangalaraj, D., Masuda, Y., Senthil, K. and Yong, K. (2010) Highly mesoporous α -Fe₂O₃ nanostructures: preparation, characterization and improved photocatalytic performance towards Rhodamine B (RhB). *Journal of Physics D: Applied Physics*, **43**, 015501.
- 23** Iwasaki, M. and Park, W. (2008) Synthesis of nanometer-sized WO₃ particles by facile wet process and their photocatalytic properties. *Journal of Nanomaterials*, 169536.
- 24** Khagram, P., Tomson, F., Brydson, R.M.D. and Crook, R. (2010) Synthesis of high quality monodisperse nickel oxide nanocrystals. *Journal of Physics: Conference Series*, **245**, 012063.
- 25** Matos, J.M.E., Anjos, F.M.J., Cavalcante, L.S., Santos, V., Leal, S.H., Santos, L.S. Jr., Santos, M.R.M.C. and Longo, E. (2009) Reflux synthesis and hydrothermal processing of ZrO₂ nanopowders at low temperature. *Materials Chemistry and Physics*, **117**, 455–459.
- 26** Villegas, J.C., Garces, L.J., Gomez, S., Durand, J.P. and Suib, S.L. (2005) Particle size control of cryptomelane nanomaterials by use of H₂O₂ in acidic conditions. *Chemistry of Materials*, **17**, 1910–1918.
- 27** Yang, M., Zhang, Y., Pang, G. and Feng, S. (2007) Preparation of Cu₂O hollow nanospheres under reflux conditions. *European Journal of Inorganic Chemistry*, 3841–3844.
- 28** Zhou, F., Zhao, X., Zheng, H., Shen, T. and Tang, C. (2005) Low-temperature refluxing synthesis of nanosized LiMn₂O₄ cathode materials. *Chemistry Letters*, **34**, 1270–1271.
- 29** Luo, Z., Li, H., Shu, H., Wang, K., Xia, J. and Yan, Y. (2008) Self-assembly of BaMoO₄ single-crystalline nanosheets into microspheres. *Materials Chemistry and Physics*, **110**, 17–20.
- 30** Xu, L., Sithambaram, S., Zhang, Y., Chen, C., Jin, L., Joesten, R. and Suib, S.L. (2009) Novel urchin-like CuO synthesized by a facile reflux method with efficient olefin epoxidation catalytic performance. *Chemistry of Materials*, **21**, 1253–1259.
- 31** Calvert, C., Joesten, R., Ngala, K., Villegas, J., Morey, A., Shen, X. and Suib, S.L. (2008) Synthesis, characterization, and Rietveld refinement of tungsten-framework-doped porous manganese oxide (K-OMS-2) material. *Chemistry of Materials*, **20**, 6382–6388.
- 32** Jin, L., Chen, C., Crisostomo, V.M.B., Xu, L., Son, Y. and Suib, S.L. (2009) γ -MnO₂ octahedral molecular sieve: preparation, characterization, and catalytic activity in the atmospheric oxidation of toluene. *Applied Catalysis A: General*, **355**, 169–175.
- 33** Gedye, R., Smith, F., Westaway, K., Ali, H., Baldisera, L., Laberge, L. and Rousell, J. (1986) The use of microwave ovens for rapid organic synthesis. *Tetrahedron Letters*, **27**, 279–282.
- 34** Balaji, S., Mutharasu, D., Sankara Subramanian, N. and Ramanathan, K. (2009) A review on microwave synthesis of electrode materials for lithium-ion batteries. *Ionics*, **15**, 765–777.
- 35** Cao, Y., Wei, H. and Xia, Z. (2009) Advances in microwave assisted synthesis

- of ordered mesoporous materials. *Transactions of Nonferrous Metals Society of China*, **19**, 656–664.
- 36** Tompsett, G.A., Conner, W.C. and Yngvesson, K.S. (2006) Microwave synthesis of nanoporous materials. *ChemPhysChem*, **7**, 296–319.
- 37** Li, Y. and Yang, W. (2008) Microwave synthesis of zeolite membranes: a review. *Journal of Membrane Science*, **316**, 3–17.
- 38** Ivanov, V.K., Shaporev, A.S., Sharikov, F.Y. and Baranchikov, A.Y. (2007) Hydrothermal and microwave-assisted synthesis of nanocrystalline ZnO photocatalysts. *Superlattices and Microstructures*, **42**, 421–424.
- 39** Huang, J., Xia, C., Cao, L. and Zeng, X. (2008) Facile microwave hydrothermal synthesis of zinc oxide one-dimensional nanostructure with three-dimensional morphology. *Materials Science and Engineering: B*, **150**, 187–193.
- 40** Li, Y., Su, X., Jian, J. and Wang, J. (2010) Ethanol sensing properties of tungsten oxide nanorods prepared by microwave hydrothermal method. *Ceramics International*, **36**, 1917–1920.
- 41** Baldassari, S., Komarneni, S., Mariani, E. and Villa, C. (2005) Rapid microwave–hydrothermal synthesis of anatase form of titanium dioxide. *Journal of the American Ceramic Society*, **88**, 3238–3240.
- 42** Sreeja, V. and Joy, P.A. (2007) Microwave–hydrothermal synthesis of α -Fe₂O₃ nanoparticles and their magnetic properties. *Materials Research Bulletin*, **42**, 1570–1576.
- 43** Ma, G., Zhou, S. and Huang, S. (2005) Microwave hydrothermal synthesis and characterization of Co₃O₄ nanocrystals. *International Journal of Modern Physics B*, **19**, 2841–2846.
- 44** Cao, C., Cui, Z., Chen, C., Song, W. and Cai, W. (2010) Ceria hollow nanospheres produced by a template-free microwave-assisted hydrothermal method for heavymetal ion removal and catalysis. *Journal of Physical Chemistry C*, **114**, 9865–9870.
- 45** Huang, H., Sithambaram, S., Chen, C., King'ondu Kithongo, C., Xu, L., Iyer, A., Garces, H.F. and Suib, S.L. (2010) Microwave-assisted hydrothermal synthesis of cryptomelane-type octahedral molecular sieves (OMS-2) and their catalytic studies. *Chemistry of Materials*, **22**, 3664–3669.
- 46** Xu, L., Ding, Y., Chen, C., Zhao, L., Rimkus, C., Joesten, R. and Suib, S.L. (2008) 3D flowerlike α -nickel hydroxide with enhanced electrochemical activity synthesized by microwave-assisted hydrothermal method. *Chemistry of Materials*, **20**, 308–316.
- 47** Dai, S., Liu, Y. and Lu, Y. (2010) Preparation of Eu³⁺ doped (Y,Gd)₂O₃ flowers from (Y,Gd)₂(CO₃)₃·nH₂O flowerlike precursors: microwave hydrothermal synthesis, growth mechanism and luminescence property. *Journal of Colloid and Interface Science*, **349**, 34–40.
- 48** Ifrah, S., Kaddouri, A., Gelin, P. and Leonard, D. (2007) Conventional hydrothermal process versus microwave-assisted hydrothermal synthesis of La_{1-x}Ag_xMnO_{3+δ} (x = 0, 0.2) perovskites used in methane combustion. *Comptes Rendus Chimie*, **10**, 1216–1226.
- 49** Krishnaveni, T., Komarneni, S. and Murthy, S. (2006) Microwave hydrothermal synthesis and characterization of nanosize NiCuZn ferrites. *Synth. React. Inorg. Met.-Org. Nano-Met. Chem.*, **36**, 143–148.
- 50** Lu, C. and Shen, B. (2010) Electrochemical characteristics of LiNi_{1/3}Co_{1/3}Mn_{1/3}O₂ powders prepared from microwave–hydrothermally derived precursors. *Synthesis and Reactivity in Inorganic and Metal-Organic Chemistry*, **497**, 159–165.
- 51** Moreira, M.L., Andres, J., Varela, J.A. and Longo, E. (2009) Synthesis of fine micro-sized BaZrO₃ powders based on a decaoctahedron shape by the microwave-assisted hydrothermal method. *Crystal Growth and Design*, **9**, 833–839.
- 52** Sadhana, K., Praveena, K., Bharadwaj, S. and Murthy, S.R. (2009) Microwave–hydrothermal synthesis of BaTiO₃ + NiCuZnFe₂O₄ nanocomposites. *Journal of Alloys and Compounds*, **472**, 484–488.
- 53** Raju, V.S.R., Murthy, S.R., Gao, F., Lu, Q. and Komarneni, S. (2006) Microwave hydrothermal synthesis of nanosize PbO added Mg–Cu–Zn ferrites. *Journal of Materials Science*, **41**, 1475–1479.

- 54 Shen, B., Ma, J., Wu, H. and Lu, C. (2008) Microwave-mediated hydrothermal synthesis and electrochemical properties of $\text{LiNi}_{1/3}\text{Co}_{1/3}\text{Mn}_{1/3}\text{O}_2$ powders. *Materials Letters*, **62**, 4075–4077.
- 55 Xie, H., Shen, D., Wang, X. and Shen, G. (2008) Microwave hydrothermal synthesis and visible-light photocatalytic activity of $\gamma\text{-Bi}_2\text{MoO}_6$ nanoplates. *Materials Chemistry and Physics*, **110**, 332–336.
- 56 Xie, Y., Yin, S., Hashimoto, T., Kimura, H. and Sato, T. (2009) Microwave–hydrothermal synthesis of nano-sized Sn^{2+} -doped BaTiO_3 powders and dielectric properties of corresponding ceramics obtained by spark plasma sintering method. *Journal of Materials Science*, **44**, 4834–4839.
- 57 Sun, W., Li, C., Li, J. and Liu, W. (2006) Microwave–hydrothermal synthesis of tetragonal BaTiO_3 under various conditions. *Materials Chemistry and Physics*, **97**, 481–487.
- 58 Ding, Y., Xu, L., Chen, C., Shen, X. and Suib, S.L. (2008) Syntheses of nanostructures of cobalt hydroxylalcite like compounds and Co_3O_4 via a microwave-assisted reflux method. *Journal of Physical Chemistry C*, **112**, 8177–8183.
- 59 Nyutu, E.K., Chen, C., Sithambaram, S., Crisostomo, V.M.B. and Suib, S.L. (2008) Systematic control of particle size in rapid open-vessel microwave synthesis of K-OMS-2 nanofibers. *Journal of Physical Chemistry C*, **112**, 6786–6793.
- 60 Yang, Z., Mao, D., Zhu, H. and Lu, G. (2009) Characterization of cerium-zirconium solid solutions prepared by the microwave-assisted approach. *Wuji Huaxue Xuebao*, **25**, 812–817.
- 61 Giri, J., Sriharsha, T., Asthana, S., Rao, T.K.G., Nigam, A.K. and Bahadur, D. (2005) Synthesis of capped nanosized $\text{Mn}_{1-x}\text{Zn}_x\text{Fe}_2\text{O}_4$ (0×0.8) by microwave refluxing for bio-medical applications. *Journal of Magnetism and Magnetic Materials*, **293**, 55–61.
- 62 Abrantes, M., Amarante, T.R., Antunes, M.M., Gago, S., Paz Filipe, A.A., Margioliaki, I., Rodrigues, A.E., Pillinger, M., Valente, A.A. and Goncalves, I.S. (2010) Synthesis, structure, and catalytic performance in cyclooctene epoxidation of a molybdenum oxide/bipyridine hybrid material: $\{[\text{MoO}_3(\text{bipy})][\text{MoO}_3(\text{H}_2\text{O})]\}_n$. *Inorganic Chemistry*, **49**, 6865–6873.
- 63 Moreno-Mañas, M. and Pleixats, R. (2003) Formation of carbon–carbon bonds under catalysis by transition-metal nanoparticles. *Accounts of Chemical Research*, **36**, 638–643.
- 64 Kamat, P.V. (2002) Photophysical, photochemical and photocatalytic aspects of metal nanoparticles. *Journal of Physical Chemistry B*, **106**, 7729–7744.
- 65 Kanel, S., Manning, B., Charlet, L. and Choi, H. (2005) Removal of arsenic(III) from groundwater by nanoscale zero-valent iron. *Environmental Science and Technology*, **39**, 1291–1298.
- 66 Cao, J., Elliott, D. and Zhang, W. (2005) Perchlorate reduction by nanoscale iron particles. *Journal of Nanoparticle Research*, **7**, 499–506.
- 67 Chen, S., Hsu, H. and Li, C. (2004) A new method to produce nanoscale iron for nitrate removal. *Journal of Nanoparticle Research*, **6**, 639–647.
- 68 Gillham, R.W. and O'Hannessin, S.F. (1994) Enhanced degradation of halogenated aliphatics by zero-valent iron. *Ground Water*, **36**, 958–967.
- 69 Lin, Y., Weng, C. and Chen, F. (2008) Effective removal of AB24 dye by nano/micro-size zero-valent iron. *Separation and Purification Technology*, **64**, 26–30.
- 70 Wang, C.B. and Zhang, W.X. (1997) Synthesizing nanoscale iron particles for rapid and complete dechlorination of TCE and PCBs. *Environmental Science and Technology*, **31**, 2154–2156.
- 71 Sun, Y., Mayers, B., Herricks, T. and Xia, Y. (2003) Polyol synthesis of uniform silver nanowires: a plausible growth mechanism and the supporting evidence. *Nano Letters*, **3**, 955–960.
- 72 Srikanth, H., Hajndl, R., Chirinos, C. and Sanders, J. (2001) Magnetic studies of polymer-coated Fe nanoparticles synthesized by microwave plasma polymerization. *Applied Physics Letters*, **79**, 3503–3505.
- 73 Valle-Orta, M., Diaz, D., Santiago-Jacinto, P., Vázquez-Olmos, A. and Reguera, E. (2008) Instantaneous synthesis of stable zerovalent metal

- nanoparticles under standard reaction conditions. *Journal of Physical Chemistry B*, **112**, 14427–14434.
- 74** Guo, L., Huang, Q., Li, X. and Yang, S. (2001) Iron nanoparticles: synthesis and applications in surface enhanced Raman scattering and electrocatalysis. *Physical Chemistry Chemical Physics*, **3**, 1661–1665.
- 75** Alqudami, A. and Annapoorni, S. (2007) Fluorescence from metallic silver and iron nanoparticles prepared by exploding wire technique. *Plasmonics*, **2**, 5–13.
- 76** Nadagouda, M.N., Hoag, G., Collins, J. and Varma, R.S. (2009) Green synthesis of Au nanostructures at room temperature using biodegradable plant surfactants. *Crystal Growth and Design*, **9**, 4979–4983.
- 77** Philip, D. (2010) Green synthesis of gold and silver nanoparticles using *Hibiscus rosa sinensis*. *Physica E*, **42**, 1417–1424.
- 78** Begum, N.A., Mondal, S., Basu, S., Laskar, R.A. and Mandal, D. (2009) Biogenic synthesis of Au and Ag nanoparticles using aqueous solutions of black tea leaf extracts. *Colloids and Surfaces B: Biointerfaces*, **71**, 113–118.
- 79** Ankamwar, B., Damle, C., Ahmad, A. and Sastry, M. (2005) Biosynthesis of gold and silver nanoparticles using *Emblica Officinalis* fruit extract, their phase transfer and transmetallation in an organic solution. *Journal for Nanoscience and Nanotechnology*, **5**, 1665–1671.
- 80** Huang, J., Li, Q., Sun, D., Lu, Y., Su, Y., Yang, X., Wang, H., Wang, Y., Shao, W., He, N., Hong, J. and Chen, C. (2007) Biosynthesis of silver and gold nanoparticles by novel sundried *Cinnamomum camphora* leaf. *Nanotechnology*, **18**, 105104–105115.
- 81** Nadagouda, M.N. and Varma, R.S. (2008) Green synthesis of silver and palladium nanoparticles at room temperature using coffee and tea extract. *Green Chemistry*, **10**, 859–862.
- 82** Chandran, S.P., Chaudhary, M., Pasricha, R., Ahmad, A. and Sastry, M. (2006) Synthesis of gold nanotriangles and silver nanoparticles using *Aloe vera* plant extract. *Biotechnology Progress*, **22**, 577–583.
- 83** Song, J.Y. and Kim, B.S. (2009) Rapid biological synthesis of silver nanoparticles using plant leaf extracts. *Bioprocess and Biosystems Engineering*, **32**, 79–84.
- 84** Lin, L., Wang, W., Huang, J., Li, Q., Sun, D., Yang, X., Wang, H., He, N. and Wang, Y. (2010) Nature factory of silver nanowires: plant-mediated synthesis using broth of *Cassia fistula* leaf. *Chemical Engineering Journal*, **162**, 852–858.
- 85** Jha, A.K., Prasad, K., Kumar, V. and Prasad, K. (2009) Biosynthesis of silver nanoparticles using *Eclipta* leaf. *Biotechnology Progress*, **25**, 1476–1479.
- 86** Shankar, S.S., Rai, A., Ahmad, A. and Sastry, M. (2005) Controlling the optical properties of lemongrass extract synthesized gold nanotriangles and potential application in infrared-absorbing optical coatings. *Chemistry of Materials*, **17**, 566–572.
- 87** Ankamwar, B., Chaudhary, M. and Sastry, M. (2005) Gold nanotriangles biologically synthesized using tamarind leaf extract and potential application in vapor sensing. *Synthesis and Reactivity in Inorganic and Metal-Organic Chemistry*, **35**, 19–26.
- 88** Engelbrekt, C., Sørensen, K.H., Zhang, J., Welinder, A.C., Jensen, P.S. and Ulstrup, J. (2009) Green synthesis of gold nanoparticles with starch–glucose and application in bioelectrochemistry. *Journal of Materials Chemistry*, **19**, 7839–7847.
- 89** Nadagouda, M.N. and Varma, R.S. (2006) Green and controlled synthesis of gold and platinum nanomaterials using vitamin B₂: density-assisted self-assembly of nanospheres, wires and rods. *Green Chemistry*, **8** 516–518.
- 90** Cao, J., Hu, X. and Jiang, D. (2009) Synthesis of gold nanoparticle using halloysites. *e-Journal of Surface Science and Nanotechnology*, **7**, 813–815.
- 91** Shahwan, T., Abu Sirriah, S., Nairat, M., Boyacı, E., Eroğlu, A.E., Scott, T.B. and Hallam, K.R. (2011) Green synthesis of iron nanoparticles and their application as a Fenton-like catalyst for the degradation of aqueous cationic and anionic dyes. *Chemical Engineering Journal*, **172**, 258–266.

- 92 Nadagouda, M.N., Castle, A.B., Murdock, R.C., Hussain, S.M. and Varma, R.S. (2010) *In vitro* biocompatibility of nanoscale zerovalent iron particles (NZVI) synthesized using tea polyphenols. *Green Chemistry*, **12**, 114–122.
- 93 Nadagouda, M.N. and Varma, R.S. (2008) Microwave-assisted shape-controlled bulk synthesis of Ag and Fe nanorods in poly(ethylene glycol) solutions. *Crystal Growth and Design*, **8**, 291–295.
- 94 Sathishkumar, M., Sneha, K., Kwak, I.S., Mao, J., Tripathy, S.J. and Yun, Y.-S. (2009) Phyto-crystallization of palladium through reduction process using *Cinnamomum zeylanicum* bark extract. *Journal of Hazardous materials*, **171**, 400–404.
- 95 Rodriguez, E., Parsons, J.G., Peralta-Videa, J.R., Cruz-Jimenez, G., Romero-Gonzalez, J., Sanchez-Salcido, B.E., Saupe, G.B., Duarte-Gardea, M. and Gardea-Torresdey, J.L. (2007) Potential of *Chilopsis linearis* for gold phytomining: using XAS to determine gold reduction and nanoparticle formation within plant tissues. *International Journal of Phytoremediation*, **9**, 133–147.
- 96 Haverkamp, R.G., Marshall, A.T. and Agterveld, D.V. (2007) Pick your carats: nanoparticles of gold–silver–copper alloy produced *in vivo*. *Journal of Nanoparticle Research*, **9**, 697–700.
- 97 He, S., Guo, Z., Zhang, Y., Zhang, S., Wang, J. and Gu, N. (2007) Biosynthesis of gold nanoparticles using the bacteria *Rhodopseudomonas capsulata*. *Materials Letters*, **61**, 3984–3987.
- 98 Bhainsa, K.C. and D’Souza, S.F. (2006) Extracellular biosynthesis of silver nanoparticles using the fungus *Aspergillus fumigatus*. *Colloids and Surfaces B: Biointerfaces*, **47**, 160–164.
- 99 Mukherjee, P., Roy, M., Mandal, B., Dey, G., Mukherjee, P., Ghatak, J. et al. (2008) Green synthesis of highly stabilized nanocrystalline silver particles by a non-pathogenic and agriculturally important fungus *T. asperellum*. *Nanotechnology*, **19**, 75103–75110.
- 100 Anastas, P. and Warner, J. (1998) *Green Chemistry: Theory and Practice*, Oxford University Press, New York, p. 160.
- 101 Dahl, J.A., Maddux, B.L.S. and Hutchison, J.E. (2007) Toward greener nanosynthesis. *Chemical Reviews*, **107**, 2228–2269.
- 102 Suib, S.L. (2008) Porous manganese oxide octahedral molecular sieves and octahedral layered materials. *Accounts of Chemical Research*, **41**, 479–487.
- 103 Sithambaram, S., Xu, L., Chen, C., Ding, Y., Kumar, R., Calvert, C. and Suib, S.L. (2009) Manganese octahedral molecular sieve catalysts for selective styrene oxide ring opening. *Catalysis Today*, **140**, 162–168.
- 104 Cao, H., Jiang, H., Yuan, G., Chen, Z., Qi, C. and Huang, H. (2010) Nano-Cu₂O-catalyzed formation of C–C and C–O bonds: one-pot domino process for regioselective synthesis of α -carbonyl furans from electron-deficient alkynes and 2-yn-1-ols. *Chemistry- A European Journal*, **16**, 10553–10559.
- 105 Sithambaram, S., Ding, Y., Li, W., Shen, X., Gaenzler, F. and Suib, S.L. (2008) Manganese octahedral molecular sieves catalyzed tandem process for synthesis of quinoxalines. *Green Chemistry*, **10**, 1029–1032.
- 106 Santos, V.P., Bastos, S.S.T., Pereira, M.F. R., Órfão, J.J.M. and Figueiredo, J.L. (2010) Stability of a cryptomelane catalyst in the oxidation of toluene. *Catalysis Today*, **154**, 308–311.
- 107 Kumar, R., Sithambaram, S. and Suib, S.L. (2009) Cyclohexane oxidation catalyzed by manganese oxide octahedral molecular sieves – effect of acidity of the catalyst. *Journal of Catalysis*, **262**, 304–313.
- 108 Sithambaram, S., Kumar, R., Son, Y. and Suib, S.L. (2008) Tandem catalysis: direct catalytic synthesis of imines from alcohols using manganese octahedral molecular sieves. *Journal of Catalysis*, **253**, 269–277.
- 109 Kumar, R., Garces, L.J., Son, Y., Suib, S.L. and Malz, R.E. (2005) Manganese oxide octahedral molecular sieve catalysts for synthesis of 2-aminodiphenylamine. *Journal of Catalysis*, **236**, 387–391.
- 110 Opembe, N.N., Son, Y., Sriskandakumar, T. and Suib, S.L. (2008) Kinetics and mechanism of 9H-fluorene oxidation catalyzed by manganese oxide octahedral molecular sieves. *ChemSusChem*, **1**, 182–185.

- 111** Jin, L., Reutenuer, J., Opembe, N., Lai, M., Martenak, D.J., Han, S. and Suib, S.L. (2009) Studies on dehydrogenation of ethane in the presence of CO₂ over octahedral molecular sieve (OMS-2) catalysts. *ChemCatChem*, **1**, 441–444.
- 112** Couttenye, R.A., De Vila, M.H. and Suib, S.L. (2005) Decomposition of methane with an autocatalytically reduced nickel catalyst. *Journal of Catalysis*, **233**, 317–326.
- 113** Luo, J., Zhang, Q., Garcia-Martinez, J. and Suib, S.L. (2008) Adsorptive and acidic properties, reversible lattice oxygen evolution, and catalytic mechanism of cryptomelane-type manganese oxides as oxidation catalysts. *Journal of the American Chemical Society*, **130**, 3198–3207.
- 114** Luo, J., Zhang, Q., Huang, A. and Suib, S.L. (2000) Total oxidation of volatile organic compounds with hydrophobic cryptomelane-type octahedral molecular sieves. *Microporous and Mesoporous Materials*, **35–36**, 209–217.
- 115** Sriskandakumar, T., Opembe, N., Chen, C., Morey, A., King'ondu, C. and Suib, S.L. (2009) Green decomposition of organic dyes using octahedral molecular sieve manganese oxide catalysts. *Journal of Physical Chemistry A*, **113**, 1523–1530.
- 116** Hu, B., Chen, C., Frueh, S.J., Jin, L., Joesten, R. and Suib, S.L. (2010) Removal of aqueous phenol by adsorption and oxidation with doped hydrophobic cryptomelane-type manganese oxide (K-OMS-2) nanofibers. *Journal of Physical Chemistry C*, **114**, 9835–9844.
- 117** Yuan, J., Liu, X., Akbulut, O., Hu, J., Suib, S.L., Kong, J. and Stellacci, F. (2008) Superwetting nanowire membranes for selective absorption. *Nature Nanotechnology*, **3**, 332–336.
- 118** Li, X., Hu, B., Suib, S., Lei, Y. and Li, B. (2010) Manganese dioxide as a new cathode catalyst in microbial fuel cells. *Journal of Power Sources*, **195**, 2586–2591.
- 119** Katikaneni, S.P., Patel, P. and Suib, S.L., US Patent Application (2006) 20060019130.
- 120** Bidault, F., Brett, D.J.L., Middleton, P.H., Abson, N. and Brandon, N.P. (2010) An improved cathode for alkaline fuel cells. *International Journal of Hydrogen Energy*, **35**, 1783–1788.
- 121** Liu, X., Sun, X., Huang, Y., Sheng, G., Zhou, K., Zeng, R.J., Dong, F., Wang, S., Xu, A., Tong, Z. and Yu, H. (2010) Nanostructured manganese oxide as a cathodic catalyst for enhanced oxygen reduction in a microbial fuel cell fed with a synthetic wastewater. *Water Research*, **44**, 5298–5305.
- 122** Sun, W., Hsu, A. and Chen, R. (2011) Carbon-supported tetragonal MnOOH catalysts for oxygen reduction reaction in alkaline media. *Journal of Power Sources*, **196**, 627–635.
- 123** Jin, L., Xu, L., Morein, C., Chen, C., Lai, M., Dharmarathna, S., Dobley, A. and Suib, S.L. (2010) Titanium containing γ-MnO₂ (TM) hollow spheres: one-step synthesis and catalytic activities in Li/air batteries and oxidative chemical reactions. *Advanced Functional Materials*, **20**, 3373–3382.
- 124** Liu, Q., Mao, D., Chang, C. and Huang, F. (2007) Phase conversion and morphology evolution during hydrothermal preparation of orthorhombic LiMnO₂ nanorods for lithium ion battery application. *Journal of Power Sources*, **173**, 538–544.
- 125** Hu, C., Liao, S., Chang, K., Yang, Y. and Lin, K. (2010) Electrochemical characterization of MnOOH–carbon nanocomposite cathodes for metal–air batteries: impacts of dispersion and interfacial contact. *Journal of Power Sources*, **195**, 7259–7263.
- 126** Crisostomo, V.M.B., Ngala, J.K., Alia, S., Dobley, A., Morein, C., Chen, C., Shen, X. and Suib, S.L. (2007) New synthetic route, characterization, and electrocatalytic activity of nanosized manganite. *Chemistry of Materials*, **19**, 1832–1839.
- 127** Iyer, A., Galindo, H., Sithambaram, S., King'ondu, C., Chen, C. and Suib, S.L. (2010) Nanoscale manganese oxideoctahedral molecular sieves (OMS-2) as efficient photocatalysts in 2-propanol oxidation. *Applied Catalysis A: General*, **375**, 295–302.
- 128** Genuino, H.C., Njagi, E.C., Benbow, E.M., Hoag, G.E., Collins, J.B. and Suib, S.L. (2011) Enhancement of the photodegradation of *N*-nitrosodimethylamine in water using amorphous and platinum manganese

- oxide catalysts. *Journal of Photochemistry and Photobiology A: Chemistry*, **217**, 284–292.
- 129** Zhang, L., He, D. and Jiang, P. (2009) MnO₂-doped anatase TiO₂ – an excellent photocatalyst for degradation of organic contaminants in aqueous solution. *Catalysis Communications*, **10**, 1414–1416.
- 130** Li, S., Ma, Z., Zhang, J., Wu, Y. and Gong, Y. (2008) A comparative study of photocatalytic degradation of phenol of TiO₂ and ZnO in the presence of manganese dioxides. *Catalysis Today*, **139**, 109–112.
- 131** Cai, J., Liu, J., Willis, W.S. and Suib, S.L. (2001) Framework doping of iron in tunnel structure cryptomelane. *Chemistry of Materials*, **13**, 2413–2422.
- 132** Fujishima, A. and Zhang, X. (2006) Titanium dioxide photocatalysis: present situation and future approaches. *Comptes Rendus Chimie*, **9**, 750–760.
- 133** Barthelmy, D. *Rutile Mineral Data* <http://webmineral.com/data/Rutile.shtml> (last accessed 14 December 2010).
- 134** Mills, B. *Rutile* <http://en.wikipedia.org/wiki/File:Rutile-unit-cell-3D-balls.png> (last accessed 14 December 2010).
- 135** Han, F., Kambala, V.S.R., Srinivasan, M., Rajarathnam, D. and Naidu, R. (2009) Tailored titanium dioxide photocatalysts for the degradation of organic dyes in wastewater treatment: a review. *Applied Catalysis A: General*, **359**, 25–40.
- 136** Akpan, U.G. and Hameed, B.H. (2009) Parameters affecting the photocatalytic degradation of dyes using TiO₂-based photocatalysts: a review. *Journal of Hazardous materials*, **170**, 520–529.
- 137** Karatasios, I., Katsiotis, M.S., Likodimos, V., Kontos, A.I., Papavassiliou, G., Falaras, P. and Kilikoglou, V. (2010) Photo-induced carbonation of lime–TiO₂ mortars. *Applied Catalysis B: Environmental*, **95**, 78–86.
- 138** Kesmez, O., Erdem Camurlu, H., Burunkaya, E. and Arpac, E. (2009) Sol-gel preparation and characterization of anti-reflective and self-cleaning SiO₂–TiO₂ double-layer nanometric films. *Solar Energy Materials and Solar Cells*, **93**, 1833–1839.
- 139** Prado, R., Beobide, G., Marcaide, A., Goikoetxea, J. and Aranzabe, A. (2010) Development of multifunctional sol-gel coatings: antireflection coatings with enhanced self-cleaning capacity. *Solar Energy Materials and Solar Cells*, **94**, 1081–1088.
- 140** Burunkaya, E., Kesmez, O., Kiraz, N., Camurlu, H.E., Asiltuerk, M. and Arpac, E. (2010) Sn⁴⁺ or Ce³⁺ doped TiO₂ photocatalytic nanometric films on antireflective nano-SiO₂ coated glass. *Materials Chemistry and Physics*, **120**, 272–276.
- 141** Kiwi, J. and Pulgarin, C. (2010) Innovative self-cleaning and bactericide textiles. *Catalysis Today*, **151**, 2–7.
- 142** Veronovski, N., Rudolf, A., Smole, M.S., Kreze, T. and Gersak, J. (2009) Self-cleaning and handle properties of TiO₂-modified textiles. *Fibers and Polymers*, **10**, 551–556.
- 143** Moafi, H.F., Shojaie, A.F. and Zanjanchi, M.A. (2010) The comparative study of photocatalytic self-cleaning properties of synthesized nanoscale titania and zirconia onto polyacrylonitrile fibers. *Journal of Applied Polymer Science*, **118**, 2062–2070.
- 144** Mihailović, D., Šaponjić, Z., Molina, R., Puač, N., Jovančić, P., Nedeljković, J. and Radetić, M. (2010) Improved properties of oxygen and argon RF plasma-activated polyester fabrics loaded with TiO₂ nanoparticles. *ACS Applied Materials & Interfaces*, **2**, 1700–1706.
- 145** Bedford, N.M. and Steckl, A.J. (2010) Photocatalytic self cleaning textile fibers by coaxial electrospinning. *ACS Applied Materials & Interfaces*, **2**, 2448–2455.
- 146** Yaghoubi, H., Taghavinia, N. and Alamdar, E.K. (2010) Self cleaning TiO₂ coating on polycarbonate: surface treatment, photocatalytic and nanomechanical properties. *Surface and Coatings Technology*, **204**, 1562–1568.
- 147** Lam, S.W., Soetanto, A. and Amal, R. (2009) Self-cleaning performance of polycarbonate surfaces coated with titania nanoparticles. *Journal of Nanoparticle Research*, **11**, 1971–1979.
- 148** Fujishima, A. and Zhang, X. (2006) Titanium dioxide photocatalysis: present situation and future approaches. *Comptes Rendus Chimie*, **9**, 750–760.

- 149** Kurn, B., Masciangioli, T., Zhang, W., Colvin, V. and Alivasatos, P. (eds). (2005) *Nanotechnology and the Environment: Applications and Implications*, Oxford University Press, Oxford.
- 150** Rodriguez J.A. and Fernandez-Garcia,M. (2007) *Synthesis, Properties, and Applications of Oxide Nanomaterials*, John Wiley & Sons, Inc., Hoboken, NJ.
- 151** Guczi, L. (2005) Bimetallic nanoparticles: featuring structure and reactivity. *Catalysis Today*, **101**, 53–64.
- 152** Tseng, Y.H., Lin, H.Y., Kuo, C.S., Li, Y.Y. and Huang, C.P. (2006) Thermostability of nano-TiO₂ and its photocatalytic activity. *Reaction Kinetics and Catalysis Letters*, **89**, 63–69.
- 153** Poyatos, J.M., Muñio, M.M., Almecija, M.C., Torres, J.C., Hontoria, E. and Osorio, F. (2010) Advanced oxidation processes for wastewater treatment: state of the art. *Water, Air, & Soil Pollution*, **205**, 187–204.
- 154** Liu, Z., He, Y., Li, F. and Liu, Y. (2006) Photocatalytic treatment of RDX wastewater with nano-sized titanium dioxide. *Environmental Science and Pollution Research*, **13**, 328–332.
- 155** Zhang, L., Yan, F., Wang, Y., Guo, X. and Zhang, P. (2006) Photocatalytic degradation of methamidophos by UV irradiation in the presence of nano-TiO₂. *Inorganic Materials*, **42**, 1379–1387.
- 156** Yang, Y., Ma, J., Qin, Q. and Zhai, X. (2007) Degradation of nitrobenzene by nano-TiO₂ catalyzed ozonation. *Journal of Molecular Catalysis A: Chemical*, **267**, 41–48.
- 157** Aarthi, T. and Madras, G. (2007) Photocatalytic degradation of rhodamine dyes with nano-TiO₂. *Industrial and Engineering Chemistry Research*, **46**, 7–14.
- 158** Kato, S., Hirano, Y., Iwata, M., Sano, T., Takeuchi, K. and Matsuzawa, S. (2005) Photocatalytic degradation of gaseous sulfur compounds by silver-deposited titanium dioxide. *Applied Catalysis B: Environmental*, **57**, 109–115.
- 159** Sobana, N., Muruganadham, M. and Swaminathan, M. (2006) Nano-Ag particles doped TiO₂ for efficient photodegradation of direct azo dyes. *Journal of Molecular Catalysis A: Chemical*, **258**, 124–132.
- 160** Lee, K., Lee, N.H., Shin, S.H., Lee, H.G. and Kim, S.J. (2006) Hydrothermal synthesis and photocatalytic characterizations of transition metals doped nano TiO₂ sols. *Materials Science and Engineering B*, **129**, 109–115.
- 161** Fan, C., Xue, P. and Sun, Y. (2006) Preparation of nano-TiO₂ doped with cerium and its photocatalytic activity. *Journal of Rare Earths*, **24**, 309–313.
- 162** Han, J.K., Choi, S.M. and Lee, G.H. (2007) Synthesis and photocatalytic activity of nanocrystalline TiO₂–SrO composite powders under visible lightirradiation. *Materials Letters*, **61**, 3798–3801.
- 163** Zhang, J.C., Li, Q. and Cao, W.L. (2005) Preparation of TiO₂–MoO₃ nano-composite photo-catalyst by supercritical fluid dry method. *Journal of Environmental Sciences*, **17** (China), 350–352.
- 164** Zhou, W., Liu, Q., Zhu, Z. and Zhang, J. (2010) Preparation and properties of vanadium-doped TiO₂ photocatalysts. *Journal of Physics D: Applied Physics*, **43**, 1–6.
- 165** Park, H., Neppolian, B., Jie, H.S., Ahn, J.-P., Park, J.-K., Anpo, M. and Lee, D.-K. (2007) Preparation of bimetal incorporated TiO₂ photocatalytic nano-powders by flame method and their photocatalytic reactivity for the degradation of diluted 2-propanol. *Current Applied Physics*, **7**, 118–123.
- 166** Yamashita, H., Nishida, Y., Yuan, S., Mori, K., Narisawa, M., Matsumura, Y., Ohmichi, T. and Katayama, I. (2007) Design of TiO₂–SiC photocatalyst using TiC–SiC nano-particles for degradation of 2-propanol diluted in water. *Catalysis Today*, **120**, 163–167.
- 167** Li, Y. and Kim, S.J. (2005) Synthesis and characterization of nano titania particles embedded in mesoporous silica with both high photocatalytic activity and adsorption capability. *Journal of Physical Chemistry B*, **109**, 12309–12315.
- 168** Wilhelm, P. and Stephan, D. (2007) Photodegradation of rhodamine B in aqueous solution via SiO₂@TiO₂ nanospheres. *Journal of Photochemistry and Photobiology A: Chemistry*, **185**, 19–25.
- 169** Lam, R.C.W., Leung, M.K.H., Leung, D.Y.C., Vrijmoed, L.L.P., Yam, W.C. and

- Ng, S.P. (2007) Visible-light-assisted photocatalytic degradation of gaseous formaldehyde by parallel-plate reactor coated with Cr ion-implanted TiO₂ thin film. *Solar Energy Materials and Solar Cells*, **91**, 54–61.
- 170 Venkatachalam, N., Palanichamy, M., Arabindoo, B. and Murugesan, V. (2007) Enhanced photocatalytic degradation of 4-chlorophenol by Zr⁴⁺ doped nano TiO₂. *Journal of Molecular Catalysis A: Chemical*, **266**, 158–165.
- 171 Park, H.S., Kim, D.H., Kim, S.J. and Lee, K.S. (2006) The photocatalytic activity of 2.5 wt% Cu-doped TiO₂ nano powders synthesized by mechanical alloying. *Journal of Alloys and Compounds*, **415**, 51–55.
- 172 Tiwari, V., Jiang, J., Sethi, V. and Biswas, P. (2008) One-step synthesis of noble metal titanium dioxide nanocomposites in a flame aerosol reactor. *Applied Catalysis A: General*, **345**, 241–246.
- 173 Hariharan, C. (2006) Photocatalytic degradation of organic contaminants in water by ZnO nanoparticles: revisited. *Applied Catalysis A: General*, **304**, 55–61.
- 174 Wang, H., Xie, C., Zhang, W., Cai, S., Yang, Z. and Gui, Y. (2007) Comparison of dye degradation efficiency using ZnO powders with various size scales. *Journal of Hazardous materials*, **141**, 645–652.
- 175 Comparelli, R., Fanizza, E., Curri, M.L., Cozzoli, P.D., Mascolo, G. and Agostiano, A. (2005) UV-induced photocatalytic degradation of azo dyes by organic-capped ZnO nanocrystals immobilized onto substrates. *Applied Catalysis B: Environmental*, **60**, 1–11.
- 176 Fouad, O.A., Ismail, A.A., Zaki, Z.I. and Mohamed, R.M. (2006) Zinc oxide thin films prepared by thermal evaporation deposition and its photocatalytic activity. *Applied Catalysis B: Environmental*, **62**, 144–149.
- 177 Xu, L., Hu, Y.-L., Pelligra, C., Chen, C.-H., Jin, L., Huang, H., Sithambaram, S., Aindow, M., Joesten, R. and Suib, S.L. (2009) ZnO with different morphologies synthesized by solvothermal methods forenhanced photocatalytic activity. *Chemistry of Materials*, **21**, 2875–2885.
- 178 Huang, W.J., Fang, G.C. and Wang, C.C. (2005) A nanometer-ZnO catalyst to enhance the ozonation of 2,4,6-trichlorophenol in water. *Colloids and Surfaces A: Physicochemical and Engineering Aspects*, **260**, 45–51.
- 179 Jang, Y.J., Simer, C. and Ohm, T. (2006) Comparison of zinc oxide nanoparticles and its nano-crystalline particles on the photocatalytic degradation of methylene blue. *Materials Research Bulletin*, **41**, 67–77.
- 180 Sobana, N. and Swaminathan, M. (2007) Combination effect of ZnO and activatedcarbon for solar assisted photocatalytic degradation of direct blue 53. *Solar Energy Materials and Solar Cells*, **91**, 727–734.
- 181 Sobana, N. and Swaminathan, M. (2007) The effect of operational parameters on the photocatalytic degradation of Acid Red 18 by ZnO. *Separation and Purification Technology*, **56**, 101–107.
- 182 Chen, C.C. (2007) Degradation pathways of ethyl violet by photocatalytic reaction with ZnO dispersions. *Journal of Molecular Catalysis A: Chemical*, **264**, 82–92.
- 183 Zhao, H. and Li, R.K.Y. (2006) A study on the photo-degradation of zinc oxide (ZnO) filled polypropylene nanocomposites. *Polymer*, **47**, 3207–3217.
- 184 Behnajady, M.A., Modirshahla, N., Daneshvar, N. and Rabbani, M. (2007) Photocatalytic degradation of C.I. Acid Red 27 by immobilized ZnO on glass plates in continuous-mode. *Journal of Hazardous materials*, **140**, 257–263.
- 185 Peng, F., Wang, H., Yu, H. and Chen, S. (2006) Preparation of aluminum foil-supported nano-sized ZnO thin films and its photocatalytic degradation to phenol under visible light irradiation. *Materials Research Bulletin*, **41**, 2123–2129.
- 186 Anandan, S., Vinu, A., Mori, T., Gokulakrishnan, N., Srinivasu, P., Murugesan, V. and Ariga, K. (2007) Photocatalytic degradation of 2,4,6-trichlorophenol using lanthanum doped ZnO in aqueous suspension. *Catalysis Communications*, **8**, 1377–1382.
- 187 Wu, W., Cai, Y.W., Chen, J.F., Shen, S.L., Martin, A. and Wen, L.X. (2006) Preparation and properties of composite particles made by nano zinc oxide coated with titanium dioxide. *Journal of Materials Science*, **41**, 5845–5850.

- 188** Paknikar, K.M., Nagpal, V., Pethkar, A.V. and Rajwade, J.M. (2005) Degradation of lindane from aqueous solutions using iron sulfide nanoparticles stabilized by biopolymers. *Science and Technology of Advanced Materials*, **6**, 370–374.
- 189** Phenrat, T., Saleh, N., Sirk, K., Tilton, R.D. and Lowry, G.V. (2007) Aggregation and sedimentation of aqueous nanoscale zerovalent iron dispersions. *Environmental Science and Technology*, **41**, 284–290.
- 190** Liu, Y., Majetich, S.A., Tilton, R.D., Sholl, D.S. and Lowry, G.V. (2005) TCE dechlorination rates, pathways, and efficiency of nanoscale iron particles with different properties. *Environmental Science and Technology*, **39**, 1338–1345.
- 191** Sung, H.J., Feitz, A.J., Sedlak, D.L. and Waite, T.D. (2005) Quantification of the oxidizing capacity of nanoparticulate zero-valent iron. *Environmental Science and Technology*, **39**, 1263–1268.
- 192** Kanel, S.R., Manning, B., Charlet, L. and Choi, H. (2005) Removal of arsenic(III) from groundwater by nanoscale zero-valent iron. *Environmental Science and Technology*, **39**, 1291–1298.
- 193** Mayo, J.T., Yavuz, C., Yean, S., Cong, L., Shipley, H., Yu, W., Falkner, J., Kan, A., Tomson, M. and Colvin, V.L. (2007) The effect of nanocrystalline magnetite size on arsenic removal. *Science and Technology of Advanced Materials*, **8**, 71–75.
- 194** Varanasi, P., Fullana, A. and Sidhu, S. (2007) Remediation of PCB contaminated soils using iron nano-particles. *Chemosphere*, **66**, 1031–1038.
- 195** Seidel, H., Gorsich, K., Amstatter, K. and Mattusch, J. (2005) Immobilization of arsenic in a tailings material by ferrous iron treatment. *Water Research*, **39**, 4073–4082.
- 196** Darwish, M.I.M., van Beek, V.M. and Bruining, J. (2006) Visualization experiments of iron precipitates: application for *in-situ* arsenic remediation. *Journal of Geochemical Exploration*, **88**, 19–23.
- 197** Joo, S.H. and Zhao, D. (2008) Destruction of lindane and atrazine using stabilized iron nanoparticles under aerobic and anaerobic conditions: effects of catalyst and stabilizer. *Chemosphere*, **70**, 418–425.
- 198** Liao, C.J., Chung, T.L., Chen, W.L. and Kuo, S.L. (2007) Treatment of pentachlorophenol-contaminated soil using nano-scale zero-valent iron with hydrogen peroxide. *Journal of Molecular Catalysis A: Chemical*, **265**, 189–194.
- 199** Kanel, S.R., Greeneche, J.M. and Choi, H. (2006) Arsenic(V) removal from groundwater using nano scale zero-valent iron as a colloidal reactive barrier material. *Environmental Science and Technology*, **40**, 2045–2050.
- 200** Tratnyek, P.G. and Johnson, R.L. (2006) Nanotechnologies for environmental cleanup. *Nano Today*, **1**, 44–48.
- 201** Hoag, G.E., Collins, J.B., Holcomb, J.L., Hoag, J.R., Nadagouda, M.N. and Varma, R.S. (2009) Degradation of bromothymol blue by ‘greener’ nano-scale zero-valent iron synthesized using tea polyphenols. *Journal of Materials Chemistry*, **19**, 8671–8677.
- 202** Zhong, L.S., Hu, J.S., Liang, H.P., Cao, A.M., Song, W.G. and Wan, L.J. (2006) Self-assembled 3D flowerlike iron oxide nanostructures and their application in water treatment. *Journal of Advanced Materials*, **18**, 2426–2431.
- 203** Ngomsik, A.F., Bee, A., Draye, M., Cote, G. and Cabuil, V. (2005) Magnetic nano- and microparticles for metal removal and environmental applications: a review. *Comptes Rendus Chimie*, **8**, 963–970.

9

Use of Extracted Anthocyanin Derivatives in Nanostructures for Solar Energy Conversion

Gabriele Giancane, Vito Sgobba, and Ludovico Valli

Electron transfer is fundamental and essential in basic vital processes such as those in the thylakoid membranes in the photosynthetic cells in green plants or mitochondrial membranes in living cells [1]. Consequently, the reproduction of these processes in the laboratory has prompted substantial research efforts. In this context, investigations on solar cells must also be considered. The typical arrangement of a photoelectrochemical cell (Figure 9.1) consists of photoelectrode–electrolyte–counter-electrode components. The photoelectrode is generally a semiconducting material which functions as a photoelectron generator upon illumination. The most studied sensitized photoelectrodes are based on titanium oxide, TiO_x (a cheap, readily available, environmentally friendly, and stable cornerstone in nanostructured electrodes) [2], but alternative materials such as ZnO [3], SnO_2 [4], Nb_2O_5 [5], FeTiO_3 [6], Ta_2O_5 [7], CeO_2 [8], SrTiO_3 [9], WO_3 [10], and NiO [11] have also been described.

The critical and predominant rationale in the utilization of the above components is a significant distinction between the photoelectrode and the electrolyte Fermi levels: this induces, upon irradiation, a certain potential difference and consequently a measurable current will be supplied by the apparatus. Regarding counter-electrodes, graphite and platinum catalysts can be mentioned.

The use of dye materials allows the enhancement of the photoelectrochemical cell performance, since upon illumination the dye is promoted to the electronic excited state; if the conduction band edge of the nanocrystalline semiconducting photoelectrode is located at energy lower than the excited electron state of the dye, electron injection to the semiconductor takes place very rapidly. A redox pair (usually iodide/triiodide ion pair) in the electrolyte reduces the oxidized dye, and photocurrent together with photovoltage evolves in the devices [12]. Various kinds of dyes have been used: polypyridine–ruthenium complexes [13], coumarin [14], merocyanine [15], perylene [16], phthalocyanines and porphyrins [17], rhodamine [18], and xanthene derivatives [19], to mention a few examples. Nevertheless, most of these materials exhibit an unsatisfactory behavior mainly as a consequence of weak ligation on the TiO_2 surface and the limited absorption wavelength range. For many of these dyes, the lack of functional groups capable of forming strong bonds with the

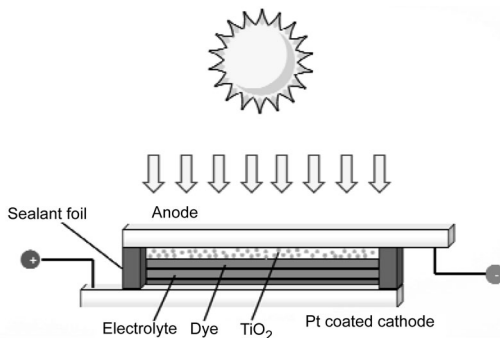


Figure 9.1 Representation of a TiO_2 -sensitized solar cell with a platinum counter-electrode.

photoelectrode and, in some instances, the remarkable steric hindrance induced by bulky or long-chain substituents prevent adequate interaction with TiO_2 . The absence of strong bonding between the dye and the photoelectrode therefore precludes electron transport from the excited dye moiety to the TiO_2 films.

Among natural/green dyes: anthocyanins [20], carotenoids [21], and chlorophylls [22] have been employed in the so-called dye-sensitized solar cells (DSSCs), based on solid–liquid junctions and where the photoanode (porous TiO_2) has to adsorb the dye [23]. They represented one of the first significant steps towards the construction of inexpensive solar cells with the aim of abating the cost/Wp ratio (where Wp is the watt peak measurements) and with fairly good efficiency. The simulation of natural photosynthesis is the motivation of the intimate organization of DSSCs [15]: the dye duplicates the radiation collector to supply excited electrons, the inorganic semiconductor substitutes CO_2 as the acceptor, and the role of oxygen and water is played by the triiodide ion/iodide ion pair. DSSCs were first reported and described by O'Regan and Grätzel in 1991 [24]. DSSCs suffer from low conversion efficiencies and the reason has been ascribed to the interface charge recombination between the porous photoanode and dye moieties. The intercalation of a dielectric film between the electrode and the dye is the usually recommended solution to this problem [25, 26].

The wide availability of colored bacteria, flowers, fruits, insects, and leaves permits the extraction of different pigments suitable for utilization in DSSCs. The characteristic interaction with radiation of flavonoids, a commonly encountered natural class of compounds, renders them very appealing biomaterials. The intense absorption in the UV–visible region prevents degradation induced by radiation in plants. The majority of these dyes belong to the class of anthocyanins, which are glycosylated products of 2-phenylbenzopyrylium cation and flavylium cation (Figure 9.2). Multifarious derivatives of this class of compounds exhibit different functionalization by various numbers of hydroxyl and methoxyl groups in different positions.

Anthocyanins exhibit a broad absorption band in the visible region due to HOMO–LUMO charge-transfer transitions (energy separation between 2.2 and 2.4 eV, equivalent to peaks in the region 560–520 nm) and give rise to blue, purple, and red pigmentation in the vegetable kingdom. These easily bioavailable, nonpolluting, fully biodegradable, inexpensive, natural, and nontoxic derivatives have

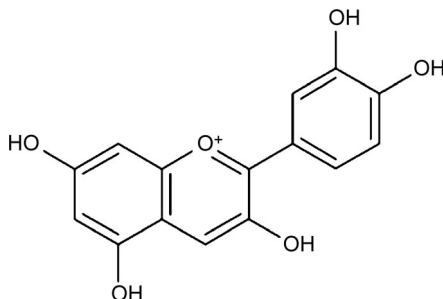


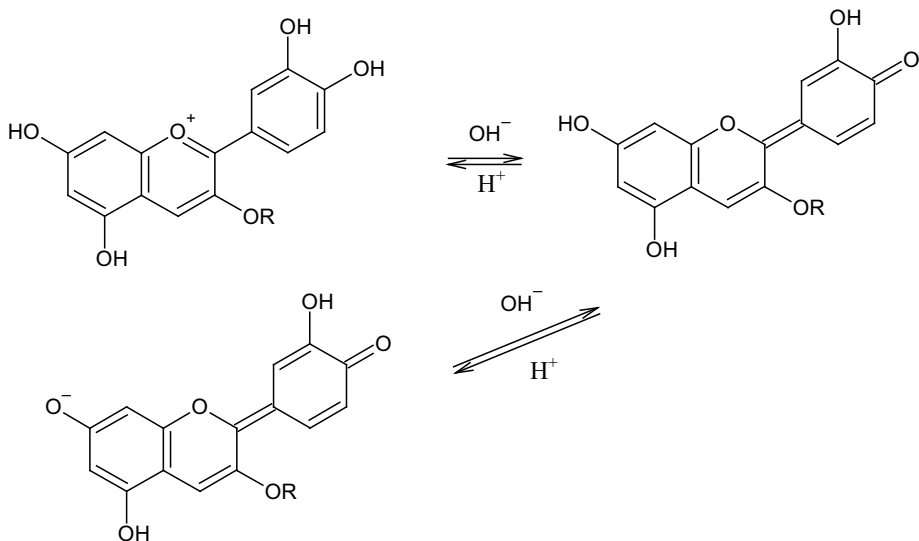
Figure 9.2 Chemical structure of unsubstituted flavylium cation.

successfully replaced inorganic materials, usually expensive and not permanently available, such as expensive and environmentally polluting ruthenium(II)-poly-pyridyl complexes (open-circuit voltage of 0.74 V and solar-to-electrical energy conversion of 11% have been monitored; these complexes show a strong charge-transfer absorption in the entire visible range, durable excited lifetimes, and effective metal-to-ligand charge transfer) [27]. There is nevertheless great confidence in being able to elaborating DSSCs with 20% efficiency, larger than the present 11%, in the next decade [28], accomplishing their main task of the sensitization of broad bandgap semiconductors for the conversion of visible radiation into current, due to their UV-visible light-harvesting ability [29]. Other important characteristics of anthocyanins are their ability to act as free radical scavengers and to chelate metal ions. Condensation of alcoholic hydrogen atoms with the OH groups on the surface of a TiO₂ electrode is usually claimed. This translates into a modification of the electronic energy levels and as a consequence in a red shift of the absorption peaks. This shift has usually been considered a demonstration of the interaction of the dye with the electrode surface. Finally, these materials are subject to structural and color changes depending on concentration, pH, temperature, and ligation to metal ions. For example, the absorption maximum of anthocyanins, or anthocyanidins (without a sugar moiety), can change as a function of the substituent: apigeninidin appears orange, cyanidin (the most often used in the DSSCs) is red-magenta, and europinidin is bluish red [30, 31].

As reported before, and as widely demonstrated in the literature, the hydroxyl groups ensure anchorage to TiO₂ nanoparticles, as in the case of the most popular ruthenium-based dyes [32, 33].

As can be deduced from the electronic transition in the visible spectra, the HOMO and LUMO of flavonoids can shift strongly on changing the substituents, pH and solvents. For acidic pH values, the molecule is positively charged, whereas for basic pH values the species is negatively charged (see Scheme 9.1).

Theoretical calculations demonstrated that the energy gap between HOMO and LUMO levels is not particularly affected by pH variations, but a systematic downshift is recorded with increasing pH. The energetic levels are not influenced by the substituent, which is usually a glucosidic unit, even though has been widely demonstrated that it increases dye stability [34].



Scheme 9.1 Structural transformation of a generic anthocyanin in aqueous solvent at different pH values.

A red shift of the absorption band in the visible spectrum is also recorded after the anthocyanin–metal ion interaction. In such a configuration, metallic ions compete with protons and the flavonoids adopt the quinonoidal form (Figure 9.3).

Absorption and fluorescence steady-state studies carried out on flavonoids coupled with different wide-gap semiconductors indicated that the interaction between the compounds induces a shift towards lower energy and a large tail in the red region of the visible spectrum [20]. Such behavior is recorded for TiO_2 , Al^{3+} , and ZrO_2 . The fluorescence steady state furnishes additional information about the electron transfer from the dye to the metallic element. Cherepy *et al.* [20] showed that the fluorescence quantum efficiency remains substantially unchanged for ZrO_2 and Al, and it is halved when TiO_2 is used as an electron acceptor layer. The dyad anthocyanin– TiO_2 was excited at 390 nm and the emission was monitored at 720 nm: stimulated emission can be fitted by means of a biexponential function with $\tau_1 = 0.52 \text{ ps}$ and

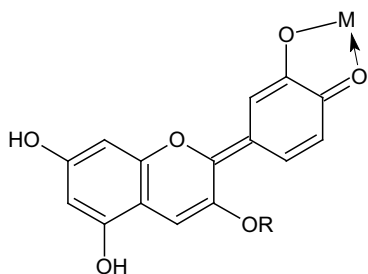


Figure 9.3 Interaction between the anthocyanin hydroxyl groups and the metal of the semiconductor layer.

$\tau_2 = 67$ ps; in contrast, cyanine absorbed on ZrO₂ or Al(III) ion emission can be fitted with a first-order exponential with $\tau = 3$ ps. Biexponential decay suggests the simultaneous existence of two different physical processes: direct recombination of the charge-separated state and an indirect pathway mediated by means of electron trapping. The stimulated emission recorded for dye-ZnO₂ [or Al(III)] can be interpreted as a rapid recombination of the electron promoted in the conduction band of the semiconductor after the dye excitation and the hole localized on the valence band of the dye, and this dynamic drastically reduces the device efficiency.

The semiconductor structure is crucial for both electron injection and charge transport after the exciton separation. Meng *et al.* [35] published a theoretical study focused on the electron injection mechanism in dyad anthocyanine-TiO₂ nanowires. The sugar substituent absorbs at 210 nm, far from the solar excitation, so the authors neglected its contribution. Before cyanine deprotonation, the HOMO level of the dye lies under the valence band of TiO₂ nanowires and the LUMO is lower than the titanium oxide conduction band energy level. Obviously, such a configuration is not propitious for an efficient charge injection; after the metal chelation, the LUMO shifts towards higher energy values but still slightly lower than the conduction band of TiO₂ (it corresponds to the above-mentioned blue shift in the visible range). Even though this energetic arrangement is not the best one (the cyanine HOMO level should be higher than the conduction band of the electron acceptor), Meng *et al.* calculated that this structure facilitates ultrafast electron injection from the excited flavonoid to the semiconductor nanowires: they showed that there is a high probability (about 90%) of observing the electron injection during the first 50 fs after the photon absorption. Finally, the electron motion on to the nanowires was studied and it was found that the most probable pathway followed by the electron injected is along the nanowire axis.

Calogero and Di Marco used the red antioxidant cyanidine-3-glucoside and a mixture of *cis* and *trans* isomers of delphinidin 3-[4-(*p*-coumaroyl)-L-rhamnosyl-(1-6)-glucopyranoside]-5-glucopyranoside (Figure 9.4), extracted from the red Sicilian

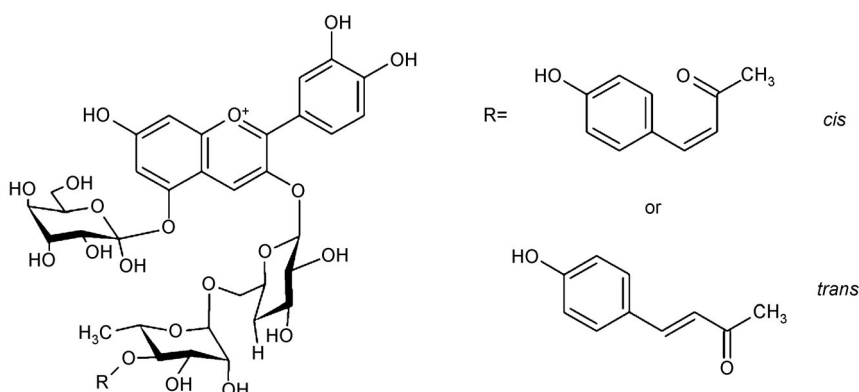


Figure 9.4 Structure of *cis* and *trans* isomers of delphinidin 3-[4-(*p*-coumaroyl)-L-rhamnosyl-(1-6)-glucopyranoside]-5-glucopyranoside.

orange (Moro variety) and eggplant (aubergine), respectively [36]. Both of these materials belong to the anthocyanin family; however, whereas the eggplant extract is stable for many months at room temperature in acidic solution, the red orange juice degrades after only 1 week even at 5 °C.

The filtered orange juice evidenced an absorption maximum at 515 nm, but upon adsorption on the photoanode [prepared by deposition of TiO₂ on fluorine-doped oxide (FTO) conducting glass] a bathochromic shift of about 20 nm was observed together with band broadening. The same behavior was shown by the eggplant extract. The interaction of anthocyanins with metal ions on the photoelectrode surface typically produces a red shift of the absorption band and in the case of TiO₂ photoanode their quinonoidal form establishes very stable complexes; a further contribution to this stability comes from the chelating effect, as illustrated in Figure 9.3.

The main result of Calogero and Di Marco's research is that the red Sicilian orange pigment showed, under simulated AM 1.5 light intensity (where AM is the air mass parameter that defines the path length crossed by light through the Earth's atmosphere), a solar energy conversion efficiency of 0.66%, which is the best ever observed for genuine fruit juice, without any chemical operation. Other measurements gave a short-circuit current density $J_{sc} = 3.84 \text{ mA cm}^{-2}$, an open-circuit voltage $V_{oc} = 0.340 \text{ V}$ and $FF = 0.50\%$ (where FF is the Fill Factor). Strawberry and blueberry juice showed worse characteristics, probably due to the presence of higher concentrations of cyanine in the orange juice; moreover, citric and hydroxycinnamic acid suppress dye association and diminish the recombination reaction through iodine solution [20]. In the case of eggplant peel extract, the three OH groups also promote the chelating effect with the titanium ion on the photoanode surface. This characteristic and steric constraints favor electron injection from the dye to the photoanode surface (the LUMO electron density is positioned on the hydroxyphenol portion of the dye). The values of photocurrent and conversion efficiency were 3.40 mA cm^{-2} and 0.48%, respectively.

Concerning the control of the stability of dyes under AM 1.5 solar light, the operating properties of orange juice dyes diminish after 3 h, whereas in the case of the eggplant extract this phenomenon was observed after 6 h. Under a voltage higher than 0.6 V (larger than the first oxidation potential of anthocyanin, about 0.5 V) [37], rapid deterioration was observed.

Chang *et al.* [38] used electrophoresis to prepare a photoanode layer with TiO₂ nanoparticles (average particle size ~25 nm) on ITO conductive glass; natural dyes adsorbed on the electrode surface after immersion of the photoelectrode for 1 day in their solutions. Chlorophyll extract from pomegranate leaf and anthocyanin extract from mulberry fruit and their 1 : 1 mixture were used as dye sensitizers; their performance was compared with that of N719 dye. The rationale for the use of the mixture is the increase in absorption in a large portion of the visible spectral range, thus improving the photo-electron conversion efficiency. Confirmation of this comes from Figure 9.5, where the $J-V$ characteristics of chlorophyll, anthocyanin, and their mixture are compared. Moreover, the photoelectric conversion efficiency for these three systems are 0.597, 0.548 and 0.722%, respectively. Finally, also the short-circuit current density is larger in the case of the mixed dye (2.8 mA cm^{-2}) than for the individual extracts.

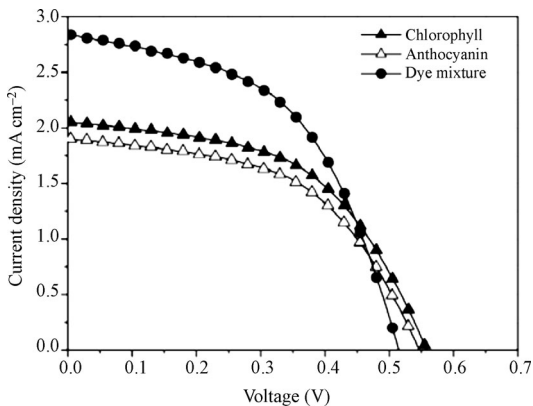


Figure 9.5 J – V characteristic of the devices using chlorophyll (full triangles), anthocyanin (open triangles), and their mixture (circles).

De Padova *et al.* [39] deposited colloidal solutions of TiO₂ nanoparticles on glass slides coated with ITO and then annealing up to 450 °C was performed. The porosity and surface roughness of the TiO₂ layers, confirmed also by scanning electron microscopy (SEM) images, are of paramount importance since the effectiveness of dye adsorption depends strongly on the high surface-to-volume ratio offered by titania nanodots. Annealing to 450 °C hardly influenced the particle size distribution (in the interval 60–250 nm) but allowed an electrical continuity among nanoparticles, thus affording ohmic contact.

The natural dye was extracted by immersion of fresh *Morus nigra* (black mulberry) in ethanol for several hours. The pure violet dye extract, a blend of β-carotene and *Morus nigra*, and a composite blend of chlorophyll A and B, carminic acid, *trans*-β-carotene, and *Morus nigra* extracts (hereafter called Mix) were deposited on TiO₂.

The adsorption spectra in the UV–visible range of the extracts exhibit different broad bands depending on the component of the mixtures; photocurrent measurements show larger bands in comparison with those derived from adsorbed dyes. In particular, in the case of Mix, a bathochromic shift of about 40 nm was observed; the proposed rationale is a band interruption between density states of TiO₂ and the HOMO–LUMO in the dye. Moreover, the photocurrent response derives predominantly from the superposition of those of *Morus nigra* and carminic acid.

Concerning the photovoltaic devices, when subjected to solar emission at AM 1.5, the short-circuit current (I_{sc}) signals were 480, 530, and 600 μA for *Morus nigra*, *Morus nigra* plus β-carotene and Mix, respectively. This means that the best performances were observed in the case of the blend of all organic derivatives used.

Fernando and Senadeera [40] used different natural pigments incorporating anthocyanins that were extracted from various tropical flowers. The extract was acidified to pH < 1, assuming a deeper coloration, and was used for the preparation of the photovoltaic apparatus. The generation at pH < 1 of the oxonium ion allows the wide conjugation of the π-electron density throughout the aglycone portion of the

anthocyanins, thus improving the light-harvesting capability. Higher values of pH induce the formation of the base and interrupt the electron delocalization. The TiO_2 electrodes (4–5 μm thick) were immersed for 12 h in the dye solutions. The radiation source was a standard solar irradiation of 100 mW cm^{-2} ($AM = 1.5$).

With the DSSCs containing *Hibiscus surattensis* extract, the best performances were probably obtained because of the large amount of dye adsorbed on TiO_2 ($1 \times 1 \text{ cm}^2$ active surface) in comparison with the other extracts from tropical flowers. Incident photon to current conversion efficiency (IPCE) values of 76% were calculated ($\lambda = 590 \text{ nm}$). J_{sc} was 5.45 mA cm^{-2} , $V_{oc} = 392 \text{ mV}$, $FF = 54\%$, and efficiency = 1.14%. Also, the stability of the photovoltaic devices was the best in the case of *Hibiscus surattensis*, even though it needs to be improved to achieve real long-term stability, especially as far as the sealing quality is concerned.

Hao *et al.* [41] used extracts from black rice, *Erythrina variegata* flower, and *Rosa xanthina*. Particularly promising are the results obtained with black rice extract. The unusual first observation is the significant blue shift of the peaks (from 598 to 566 nm) in the absorption spectrum of the black rice extract in comparison with the solution in ethanol; the rationale of this behavior is the polar alcohol solvent, association of the dye molecules in a face-to-face arrangement, and the probable behavior of TiO_2 as an electron-withdrawing group. The I – V characteristics under white light from a 100 W lamp in an ambient atmosphere gave the values $I_{sc} = 1.14 \text{ mA}$, $V_{oc} = 0.55 \text{ V}$, $FF = 0.52$, maximum power = $327 \mu\text{W}$, IPCE = 36.41% at 554 nm. In the case of the photoelectron spectra, a further blue shift to 554 nm was observed, probably because of the intensity and gap energy match of the incident light.

Black rice dye was deposited on a TiO_2 film electrode and dye-sensitized solar cells were used in order to check the effects of the calcination on TiO_2 [42] used in solar cell devices. Higher calcination temperatures resulted in a higher degree of crystallinity, and XRD measurements underlined that the samples treated at temperatures lower than 450°C showed an amorphous peak nature. Small-angle neutron scattering demonstrated that the average pore to pore distance increased with increase in calcination temperature, from 22 nm for TiO_2 treated at 400°C to 24 nm for samples heated at 450°C . The best performance was obtained for the DSSCs carried out with TiO_2 processed at 400°C : $J_{sc} \approx 1.287 \text{ mA cm}^{-2}$ and $V_{oc} \approx 550 \text{ mV}$. The efficiency was estimated to be 0.236%. A previous study [43] with TiO_2 sintered at 450°C reported the electrical characteristic of a DSSC with a blackberry extract as dye. In contrasting to the results in [40], the solar cell reached 1% efficiency.

Jin *et al.* [44] prepared a photoanode from TiO_2 powder, water, and nitric acid and, after mixing at 80°C for 8 h, the solution was dried at 100°C for 12 h. This preparation method gave a homogeneous surface of the TiO_2 film with nanoparticles with a diameter of about 25 nm; moreover, the utilization of nitric acid rendered the film adequately porous for thorough adsorption of the dye. In this case, maple leaves were used as the source of the anthocyanin; investigations under sunlight simulation (100 mW cm^{-2} , $AM = 1.5$) gave $V_{oc} = 0.65 \text{ V}$, $J_{sc} = 1 \text{ mA cm}^{-2}$, $FF = 0.60\%$, energy conversion efficiency = 0.4%.

Patrocinio *et al.* [45] exploited crude aqueous extracts of mulberry, blueberry, and jaboticaba (*Myrciaria cauliflora* Mart) fruit skin adsorbed on TiO_2 prepared by

the sol-gel method and immobilized on FTO substrates. The resulting DSSC had an active area of 0.5 cm^2 . Also in this case, adsorption of the sensitizer on the photo-electrode caused a bathochromic shift and loss of resolution of the peak in the absorption spectrum. Of the three dyes investigated, mulberry gave the best performance, which may be due not only to a better electron injection ability but also to the presence in the crude extracts of different compounds, as indicated by shoulders on the bands in the absorption spectra. The most significant values for mulberry extracts under the operating conditions of $AM = 1.5$ and 100 mW cm^{-2} were $J_{sc} = 6.1\text{ mA cm}^{-2}$, $V_{oc} = 0.49\text{ V}$, $P_{max} = 1.6\text{ mW cm}^{-2}$, and $FF = 0.52$, where P_{max} is the power point of the device. However, the most important finding is the stability of the I_{sc} and V_{oc} values of DSSCs with a 16 cm^2 active area over 14 weeks under the same simulated solar radiation and an operating period of 36 weeks. Such achievements are comparable to those with N3 (a ruthenium complex)-sensitized cells even though the latter shows higher photocurrents. It must be stressed that this behavior was obtained through optimization of the sealing method of the cells, thus avoiding contact of the dye with water and air, which lead to decomposition of the sensitizer.

Polo and Murakami Iha used anthocyanins extracted from jaboticaba (*Myrciaria cauliflora* Mart) and calafate (*Berberis buxifolia* Lam) as dyes for DSSCs. [46] The interaction between the dye molecules and TiO_2 was identified by comparing the visible absorption spectra of the bare dye in solution with those acquired after dye absorption on the semiconductor: a 15 nm red shift indicated the anchorage of the anthocyanin molecules on the TiO_2 nanoparticles. The inorganic semiconductor layer was deposited on ITO and the electrolyte employed was I^-/I_3^- dissolved in acetonitrile. The photovoltaic cell obtained with the jaboticaba extract gave an IPCE value of 0.2 with a short-circuit current (J_{sc}) of 7.2 mA cm^{-2} , a V_{oc} of 0.5 V and a fill factor of 54%.

Wongcharee *et al.* [47] performed a thorough analysis on DSSCs arranged using natural sensitizers extracted with water from flowers common in tropical regions and abundant in anthocyanins, such as roselle (*Hibiscus sabdariffa*) and blue pea (*Clitoria ternatea*). Adhesion of dyes on TiO_2 photoanodes was accomplished through immersion in an aqueous solution for 1 day. The absorption spectrum of roselle extract exhibited a peak centered at 520 nm (the main constituents are delphinidin and cyanidin) whereas that of blue pea showed peaks at 580 and 620 nm (with ternatin as the main component). A mixture of the two sensitizers (1 : 1 by volume) gave three peaks at the same wavelengths as the in the individual spectra, suggesting the absence of significant interactions among the dyes. The spectra of the photoanode after immersion in the dye solutions manifested different behavior: for the roselle extract, the usual red shift and loss of resolution were observed in comparison with the solution spectra. In contrast, with the blue pea extract no remarkable variations were displayed. This indicates the absence of a satisfactory interaction with the TiO_2 surface because of the significant steric hindrance brought about by the bulky functionalization. Consequently, the performances offered by the two kinds of sensitizers are differed considerably: $J_{sc} = 1.63\text{ mA cm}^{-2}$, $V_{oc} = 404\text{ mV}$, $FF = 0.57$, $\eta = 0.37\%$ for roselle and $J_{sc} = 0.37\text{ mA cm}^{-2}$, $V_{oc} = 372\text{ mV}$, $FF = 0.33$, $\eta = 0.05\%$ for blue pea (where η is solar cell's energy conversion). These values refer to the

sensitizers extracted with water at 100 °C and demonstrate a behavior of the DSSC sensitized by roselle equivalent to DSSCs containing different natural dyes. Considering the 1 : 1 mixture, the absorption spectrum on the TiO₂ electrode resembles that for roselle in solution; of course, this is a further indication of the preferential adsorption of roselle on the photoanode in comparison with blue pea. The performances of the DSSCs with the 1 : 1 mixture as sensitizer are intermediate between those of the two individual components.

The influence of the extraction temperature on the performance of DSSCs was also investigated with the optimum temperature being 50 °C: $J_{sc} = 2.06 \text{ mA cm}^{-2}$, $V_{oc} = 433 \text{ mV}$, $FF = 0.59$, $\eta = 0.52\%$ for roselle. Higher temperatures lead to thermal degradation of the dye, and lower temperatures imply inferior solubility.

When ethanol was used to extract the dye, the efficiency increased to 0.71%; the rationale is the higher solubility of the sensitizer in alcohol and minor association which favors a more homogeneous distribution of the anthocyanins on the TiO₂ surface. However, exposure to simulated sunlight ($AM = 1.5$, 100 mW cm^{-2}) caused a significant decrease in efficiency after 3 h, probably because alcohol favors the photocatalytic decomposition of anthocyanin.

Finally, the effect of pH was also explored: the natural value of pH of the roselle extract is 3.2; decreasing the pH to 1 led to $J_{sc} = 2.72 \text{ mA cm}^{-2}$, $V_{oc} = 408 \text{ mV}$, $FF = 0.63$, $\eta = 0.70\%$. The proposed reason is that the stable flavylium ion exists at pH values below 2, whereas at higher pH values the unstable quinonoidal form is predominant.

Garcia *et al.* [48] used extracts from chaste tree and mulberry fresh fruits and cabbage palm pulp. In all cases the binding of the anthocyanins to TiO₂ through hydroxyl and carbonyl groups caused a red shift of the absorption peak in comparison with solutions. The main parameters for DSSCs sensitized with chaste tree, mulberry, and cabbage palm fruits were $I_{sc} = 1.06$, 0.86 , 0.37 mA , $V_{oc} = 390$, 422 , 442 mV , $P_{max} = 198$, 154 , $99.3 \mu\text{W}$, $FF = 0.48$, 0.43 , 0.61 , respectively.

In another paper, Garcia *et al.* [49] reported the use of extracts of *Eugenia jambolana* Lam (Java plum), obtained by just squeezing the fresh fruits, as a natural sensitizer. The reported values of I_{sc} and V_{oc} were 2.3 mA and 711 mV , respectively.

In order to minimize the fast electron–hole recombination, Calzolari *et al.* [50] attached a donor–acceptor boronic acid spacer between the anthocyanins and a gold electrode, and the same molecule between the dye and a β-cyclodextrin which is able to bind I₃⁻ dissolved in the electrolyte near the chromophore. In that configuration, the device shows an increase in the quantum yield of the photocurrent from a negligible value to 1.75%. Such studies were not repeated on TiO₂ layers.

Usually, the I⁻/I₃⁻ redox couple is dissolved in organic solvents, because the negative effect of the interaction between water molecules and TiO₂ reduces the efficiency of the charge injection process. Moreover, the presence of water generates the highly corrosive HI, detrimental for the cell stability [51]. Dai and Rabani [52] reported an efficient DSSC realized using water as a solvent for the charge carriers and a mixture of anthocyanins extracted from pomegranate fruit. The reported results are remarkable both for the device stability (over 48 h no detectable change in photocurrent was recorded) and for the photocurrent quantum yield obtained. The device obtained using TiO₂ with a particle diameter of 5 nm and anthocyanin at pH

2.8 as dye in water as solvent showed a photocurrent quantum yield of 0.28, which increased to 0.74 at lower pH [53]. The photocurrent decreased when nanocrystallites of 18 nm diameter were used, showing an opposite behavior to ruthenium-based cells. The reported results suggest that smaller nanoparticles better select the components in the pigment mixture contributing to photocurrent generation.

Natural pigments, particularly cyanidin extracted from flowers, were employed in original photovoltaic solid-state solar cells [54] where liquid electrolyte was replaced with a solid charge transport material [55] in order to avoid the effect of the I^-/I_3^- couple on the degradation of the natural pigments. TiO_2 was deposited on a glass substrate (see [53] for the detailed procedure), then immersed for 10 min in the extracted juice. CuI solution in triethylamine hydrothiocyanate was spread on the TiO_2 coating in order to realize a p-type semiconductor, and a thin film of gold was applied on the top of CuI layer as a back contact. This device was initially employed in order to evaluate the pigment stability when irradiated with a wide range of frequencies under different experimental conditions. It was reported that the photocurrent stability is strongly dependent on the moisture, oxygen, and source of light. When the sample was placed in a thermostated chamber at 26 °C, under vacuum and using a UV cut-off filter, the device was stable for more than 15 h, and no relevant variation of the photocurrent was recorded. The cell stability was ensured by operating under not too restrictive conditions. In fact, Tennakone *et al.* [34] reported that a flux of dry argon did not affect cell efficiency. A rapid and notable worsening of the cell characteristics was induced by a moist air flux, keeping the other conditions unchanged, and such behavior was independent of the source employed, and the decay of the photocurrent was accompanied by a noticeable fading of the dye absorbed on TiO_2 . A water-saturated argon flux slightly affected the photocurrent values as a consequence of the effect of moisture on the electrical conductivity of the p-type CuI layer. When the sample was used in the presence of humidity, the photocurrent decay was very rapid and the absorption spectrum showed a rapid decrease in dye absorbance. When the UV filter was removed, the dye deposited on TiO_2 decomposed in the absence of oxygen and moist air. When oxygen was present, the degradation of the device performance in the presence of UV light was very rapid. The mechanism proposed by the authors is related to the tendency of O_2 to capture electrons transferred to the TiO_2 conduction band from the excited dye. The dye molecules accept holes and such cationic species react with the negatively charged O_2^- . Such a reaction induces degradation of dye molecules.

A mixture of chlorophyll and anthocyanins (particularly shisonin and malonylshisonin) was extracted from the shiso plant, very common in Japan, China, and southern Asia, and used as a dye in a TiO_2 |dye|CuI cell. The $I-V$ characteristic and photoaction spectrum of the cell carried out using the mixture of chlorophyll and anthocyanins under AM 1.5 illumination showed a very high efficiency (1.3%), an J_{sc} of $\sim 4.8\text{ mA cm}^{-2}$ and a V_{oc} of 534 mV. The photoaction spectrum showed two peaks corresponding to the absorption of shisonin pigment (600 nm) and chlorophyll (440 nm) and it remained stable under illumination for more than 5 h. When the chlorophyll was excluded from the dye composition, the cell showed lower efficiency (1.01%), and particularly J_{sc} decreased strongly. Similar results were obtained when a device using chlorophyll without shisonin was used. In this case, both J_{sc} and V_{oc} were lower and the

efficiency was $\sim 0.5\%$. A possible explanation for this behavior is the wider spectral range used for chromophore excitation and, probably, the simultaneous presence of two different species contributing to suppressing the concentration quenching phenomenon.

In another study [56], the gold contact was replaced with granular graphite and pomegranate extract was used as the dye coated on a TiO_2 film. Chelation of flavylium on TiO_2 was studied by recording the classical red shift of the absorption maximum in the visible absorption spectrum. The I - V characteristics showed a maximum photocurrent of 5 mA cm^{-2} and an open-circuit voltage (V_{oc}) of $\sim 300 \text{ mV}$. When the CuI was replaced with CuCNS, the higher conduction band (compared with CuI) led to a higher V_{oc} but a lower photocurrent (1.5 mA cm^{-2}) and decreased the performance of the device. The internal photon to current efficiency for the $\text{TiO}_2|\text{dye}|\text{CuI}$ cell was about 40%.

An improvement of the photoproperties of solid-state $\text{TiO}_2|\text{dye}|\text{CuI}$ cells was obtained by adding Mercurochrome to the TiO_2 surface before dipping the substrate in pomegranate juice. The absorption of Mercurochrome on TiO_2 induces dimerization of the Mercurochrome molecules. Visible spectra of Mercurochrome-coated TiO_2 , natural pomegranate juice, and natural pomegranate juice-coated TiO_2 and the diffuse reflectance spectrum of natural pomegranate juice-coated TiO_2 showed a 40 nm red shift as a consequence of the interaction between flavylium and the inorganic semiconductor; furthermore, the broadening of the spectrum with a shift of the absorption edge towards shorter frequency indicates an electrostatic coupling between pomegranate and Mercurochrome. Interestingly, Bach *et al.* [55] reported that the IPCE for the $\text{TiO}_2|\text{Mercurochrome}|\text{CuI}$ device reached 60% and for the $\text{TiO}_2|\text{pomegranate juice}|\text{CuI}$ device it was near 40%, and these results are comparable to those DSSCs realized with the same sensitizers [51]. The cell obtained by depositing pomegranate juice on Mercurochrome– TiO_2 showed a maximum IPCE of 58% at 510 nm and a quantum yield of 0.8. The $\text{TiO}_2|\text{pomegranate juice}|\text{Mercurochrome}|\text{CuI}$ cell showed an IPCE of 20% and a quantum yield of 0.4. Unfavorable LUMO levels of dye $\text{TiO}_2|\text{pomegranate juice}|\text{Mercurochrome}$ could be the reason for the low performances of the device. According to the proposed mechanism, the dimer of Mercurochrome is excited by a photon, then an electron can be transferred to the TiO_2 conduction band or part of its energy can be used to excite a pomegranate molecule, and finally the excited flavylium transfers the electron to the semiconductor. The V_{oc} measured for pomegranate juice deposited on Mercurochrome– TiO_2 was lower than that of the Mercurochrome– $\text{TiO}_2|\text{CuI}$ cell, probably as a consequence of the chelation of the pomegranate juice–Mercurochrome, which shifts the band towards the conduction band of TiO_2 .

A new approach to improve the performance of solar devices using natural pigments is to employ carbon nanotube (CNT)-based counter-electrodes. As previously reported, the excited dye transfers an electron to TiO_2 and so it acquires a positive charge. Then, the cationic molecule subtracts an electron from the counter-electrode which is transported by the electrolyte. This reaction is usually catalyzed by means of conductive and electrocatalytically active species for triiodide reduction of carbon coatings. CNTs have a high superficial area, which represents a very

interesting feature for electrochemical applications. Zhu *et al.* [57] reported the possibility of coupling such low-cost materials with anthocyanins in order to fabricate inexpensive and totally “green” photovoltaic systems. Anthocyanins extracted from blackberries were deposited on nanoporous TiO_2 , and a single-walled carbon nanotube (SWCNT) macrofilm was grown on FTO glass and used as a counter-electrode. A nanotube layer was obtained by means of the floating chemical vapor deposition technique [58]. The solar cell with the counter-electrode covered with purified SWCNTs showed a 1.46% efficiency, which is double that measured for an analogous cell with carbon black as counter-electrode [32, 33] and comparable to that of Pt-based cells [59]. The use of a film of unpurified nanotubes led to a worsening of the DSSC performance and the efficiency reached 0.57%. A recent study [60] related to the fabrication of nanotube-based counter-electrodes demonstrated the possibility of growing vertically aligned CNTs. A perpendicular orientation of such electrically anisotropic structures ensures a preferential pathway for the electron transport, reducing the series resistances and the recombination mechanisms. Red raspberry extract was deposited on a TiO_2 nanoparticle film 10 μm thick (diameter \sim 25 nm). The substrate was FTO glass. Counter-electrodes were obtained by growing vertical multi-walled carbon nanotubes (MWCNTs) and nitrogen-doped MWCNTs (N-MWCNTs) using microwave plasma chemical vapor deposition [60, 61].

The short-circuit current density and efficiency of the MWCNT DSSC with I^-/I_3^- as electrolyte were 4.98 mA cm^{-2} and 0.77%, respectively, both greater than the values reported for DSSCs using Pt electrodes or randomly deposited CNTs. Devices realized using nanotubes grown with an N_2 flux showed a lower efficiency than the undoped MWCNT DSSC, since both TiO_2 and N-MWCNT are n-type materials, which lowers the carrier concentration gradient. In the light of this, it would be interesting to check the device performance with a counter-electrode realized by depositing p-type CNTs.

Kashyout *et al.* [62] proposed the use of ZnO as the semiconductor electrode as its bandgap is comparable to that of TiO_2 . A ZnO layer was prepared by a colloid approach and in particular a dependence of grain size on centrifuge speed during preparation was observed (in the range 150 nm at 6000 rpm to 80 nm at 15 000 rpm). Annealing at 400 °C carried out on the ZnO layer on SnO_2 /glass gave crystalline wurtzite, and the bandgap became 3.18 eV. The anthocyanine dye was extracted with water (without the use of any other solvent) from blackberry seeds. Scanning electron micrographs revealed that the ZnO morphology was not substantially affected by the dye adsorption, suggesting an intimate adsorption on the electrode surface. The DSSC showed values of $V_{\text{oc}} = 0.55$ eV and $J_{\text{sc}} = 30 \mu\text{A cm}^{-2}$.

References

- 1** Smestad, G.P. and Gratzel, M. (1998) *Journal of Chemical Education*, **75**, 752–756.
- 2** Xia, J., Masaki, N., Jiang, K. and Yanagida, S. (2006) *Journal of Physical Chemistry B*, **110**, 25222–25228.

- 3 Mou, J., Zhang, W., Fan, J., Deng, H. and Chen, W. (2011) *Journal of Alloys and Compounds*, **509**, 961–965.
- 4 Chen, W., Qiu, Y., Zhong, Y., Wong, K.S. and Yang, S. (2010) *Journal of Physical Chemistry A*, **114**, 3127–3138.
- 5 Le Viet, A., Jose, R., Reddy, M.V., Chowdari, B.V.R. and Ramakrishna, S. (2010) *Journal of Physical Chemistry C*, **114**, 21795–21800.
- 6 Kozuka, H. and Kajimura, M. (2001) *J. Sol-Gel Sci. Technol.*, **22**, 125–132.
- 7 Wu, J.-M., Antonietti, M., Gross, S., Bauer, M. and Smarsly, B.M. (2008) *ChemPhysChem*, **9**, 748–757.
- 8 Li, W., Hao, Y., Wang, Y., Jiang, P., Yang, M., Cheng, H. and Cai, S. (1998) *Yingyong Huaxue*, **15**, 17–20.
- 9 Park, N.G. and Kim, K. (2008) *Physical Status Solidi A*, **205**, 1895–1904.
- 10 Zheng, H., Tachibana, Y. and Kalantar-zadeh, K. (2010) *Langmuir*, **26**, 19148–19152.
- 11 Odobel, F., Le Pleux, L., Pellegrin, Y. and Blart, E. (2010) *Accounts of Chemical Research*, **43**, 1063.
- 12 Fukui, A., Komiya, R., Yamanaka, R., Islam, A. and Han, L. (2006) *Solar Energy Materials and Solar Cells*, **90**, 649–658.
- 13 Polo, A.S., Itokazu, M.K. and Murakami Iha, N.Y. (2004) *Coordination Chemistry Reviews*, **248**, 1343–1361.
- 14 Koops, S.E., Barnes, P.R.F., O'Regan, B.C. and Durrant, J.R. (2010) *Journal of Physical Chemistry C*, **114**, 8054–8061.
- 15 Sayama, K., Hara, K., Mori, N., Satsuki, M., Suga, S., Tsukagoshi, S., Abe, Y., Sugihara, H. and Arakawa, H. (2000) *Chemical Communications*, 1173–1175.
- 16 Cappel, U.B., Karlsson, M.H., Pschirer, N.G., Eickemeyer, F., Schoneboom, J., Erk, P., Boschloo, G. and Hagfeldt, A. (2009) *Journal of Physical Chemistry C*, **113**, 14595–14597.
- 17 Martinez-Diaz, M.V., de la Torre, G. and Torres, T. (2010) *Chemical Communications*, 7090–7108.
- 18 Nasr, C., Liu, D., Hotchandani, S. and Kamat, P.V. (1996) *Journal of Physical Chemistry*, **100**, 11054–11060.
- 19 Hara, K., Horiguchi, T., Kinoshita, T., Sayama, K., Sugihara, H. and Arakawa, H. (2000) *Chemistry Letters*, 316–318.
- 20 Cherepy, N.J., Smestad, G.P., Graetzel, M. and Zhang, J.Z. (1997) *Journal of Physical Chemistry B*, **101**, 9342–9351.
- 21 Wang, X.F., Matsuda, A., Koyama, Y., Nagae, H., Sasaki, S.I., Tamiaki, H. and Wada, Y. (2006) *Chemical Physics Letters*, **423**, 470–475.
- 22 Kay, A. and Grätzel, M. (1993) *Journal of Physical Chemistry*, **97**, 6272–6276.
- 23 Grätzel, M. (2001) *Nature*, **414**, 338–344.
- 24 O'Regan, B. and Grätzel, M. (1991) *Nature*, **335**, 737–740.
- 25 Kay, A. and Grätzel, M. (2002) *Chemistry of Materials*, **14**, 2930–2935.
- 26 Palomares, E., Clifford, J.N., Haque, S.A., Lutz, T. and Durrant, J.R. (2003) *Journal of the American Chemical Society*, **125**, 475–482.
- 27 Gao, F., Wang, Y., Shi, D., Zhang, J., Wang, M., Jing, X., Humphrey-Baker, R., Wang, P., Zakeeruddin, S.M. and Grätzel, M. (2008) *Journal of the American Chemical Society*, **130**, 10720–10728.
- 28 Pagliaro, M., Palmisano, G. and Ciriminna, R. (2008) *Flexible Solar Cells*, Wiley-VCH Verlag GmbH, Weinheim.
- 29 Smestad, G.P. (1998) *Solar Energy Materials and Solar Cells*, **55**, 157–178.
- 30 Delgado-Vargas, F. and Paredes-López, O. (2003) *Natural Colorants for Food and Nutraceutical Uses*, CRC Press, Boca Raton, FL.
- 31 Hendry G.A.F. and Houghton J.D. (eds.) (1996) *Natural Food Colorants*, 2nd edn., Blackie Academic & Professional, Glasgow.
- 32 Kalyanasundaram, K. and Grätzel, M. (1998) *Coordination Chemistry Reviews*, **77**, 347–414.
- 33 Zakeeruddin, S.M., Nazeeruddin, M.K., Pechy, P., Rotzinger, F.P., Humphrey-Baker, R., Kalyanasundaram, K. and Graetzel, M. (1997) *Inorganic Chemistry*, **36**, 5937–5946.
- 34 Tennakone, K., Kumara, G.C., Kotegada, I.R. and Wijayantha, K. (1997) *Semiconductor Science and Technology*, **12**, 128–132.
- 35 Meng, S., Ren, J. and Kaxiras, E. (2008) *Nano Letters*, **8**, 3266–3272.
- 36 Calogero, G. and Di Marco, G. (2008) *Solar Energy Materials and Solar Cells*, **92**, 1341–1346.

- 37** De Lima, A.A., Sussuchi, E.M. and De Giovani, W.F. (2007) *Croatica Chemica Acta*, **80**, 29–34.
- 38** Chang, H. and Lo, Y.J. (2010) *Sol. Energy*, **84**, 1833–1837.
- 39** De Padova, P., Lucci, M., Olivieri, B., Quaresima, C., Priori, S., Francini, R., Grilli, A., Hricovini, K. and Davoli, I. (2009) *Superlattices and Microstructures*, **45**, 555–563.
- 40** Fernando, J.M.R.C. and Senadeera, G.K.R. (2008) *Current Science*, **95**, 663–666.
- 41** Hao, S., Wu, J., Huang, Y. and Lin, J. (2006) *Sol. Energy*, **80**, 209–214.
- 42** Yuliarto, B., Septina, W., Fuadi, K., Fanani, F., Muliani, L. and Nugraha, T. (2010) *Adv. Mater. Sci. Eng.*, **2010**, 1–6.
- 43** Olea, A., Ponce, G. and Sebastian, P.J. (1999) *Solar Energy Materials and Solar Cells*, **59**, 137–143.
- 44** Jin, E.M., Park, K.H., Jin, B., Yun, J.J. and Gu, H.B. (2010) *Physica Scripta*, **T139**, 014006.
- 45** Patrocínio, A.O.T., Mizoguchi, S.K., Paterno, L.G., Garcia, C.G. and Murakami Iha, N.Y. (2009) *Synthetic Metals*, **159**, 2342–2344.
- 46** Polo, A.S. and Murakami Iha, N.Y. (2006) *Solar Energy Materials and Solar Cells*, **90**, 1936–1944.
- 47** Wongcharree, K., Meeyoo, V. and Chavedej, S. (2007) *Solar Energy Materials and Solar Cells*, **91**, 566–571.
- 48** Garcia, C.G., Sarto, A.P. and Murakami Iha, N.Y. (2003) *Journal of Photochemistry and Photobiology A: Chemistry*, **160**, 87–91.
- 49** Garcia, C.G., Polo, A.S. and Murakami Iha, N.Y. (2003) *Annals of the Brazilian Academy of Sciences*, **75**, 163–165.
- 50** Calzolari, A., Varsano, D., Ruini, A., Catellani, A., Tel-Vered, R., Yildiz, H.B., Ovits, O. and Willner, I. (2009) *Journal of Physical Chemistry A*, **113**, 8801–8810.
- 51** Nazeeruddin, M.K., Kay, A., Rodicio, I., Humphry-Baker, R., Muller, E., Liska, P., Vlachopoulos, N. and Graetzel, M. (1993) *Journal of the American Chemical Society*, **115**, 638.
- 52** Dai, Q. and Rabani, J. (2002) *New Journal of Chemistry*, **26**, 421–426.
- 53** Dai, Q. and Rabani, J. (2001) *Chemical Communications*, 2142–2143.
- 54** Tennakone, K., Kumura, G.R.R.A., Kotegoda, I.R.M., Wijayantha, K.G.U. and Sirimanne, P.M. (1995) *Semiconductor Science and Technology*, **10**, 1689–1693.
- 55** Bach, U., Lupo, D., Comte, P., Moser, J.E., Weissortel, F., Salbeck, J., Spreitzer, H. and Graetzel, M. (1998) *Nature*, **395**, 583.
- 56** Sirimanne, P.M., Seneviranthna, M.K.I., Premalal, E.V.A., Pitigala, P.K.D.D.P., Sivakumar, V. and Tennakone, K. (2006) *Journal of Photochemistry and Photobiology A: Chemistry*, **177**, 324–327.
- 57** Zhu, H., Zeng, H., Subramanian, V., Masarapu, C., Hung, K.H. and Wei, B. (2008) *Nanotechnology*, **19**, 465204.
- 58** Zhu, H.W. and Wei, B.Q. (2007) *Chemical Communications*, 3042.
- 59** Wei, H.L., Yen, H.S., Lay, G.T. and Min, H.H. (2008) *Journal of Photochemistry and Photobiology A: Chemistry*, **307**, 313.
- 60** Sayer, R.A., Hodson, S.L. and Fisher, T.S. (2010) *Journal of Solar Energy Engineering*, **132**, 021007–021011.
- 61** Maschmann, M.R., Amana, P.B., Goyal, A., Iqbal, Z. and Fisher, T.S. (2006) *Carbon*, **44**, 2758.
- 62** Kashyout, A.B., Soliman, M., El Gamal, M. and Fathy, M. (2005) *Materials Chemistry and Physics*, **90**, 230–233.

10

Nanomaterials from Biobased Amphiphiles: the Functional Role of Unsaturations

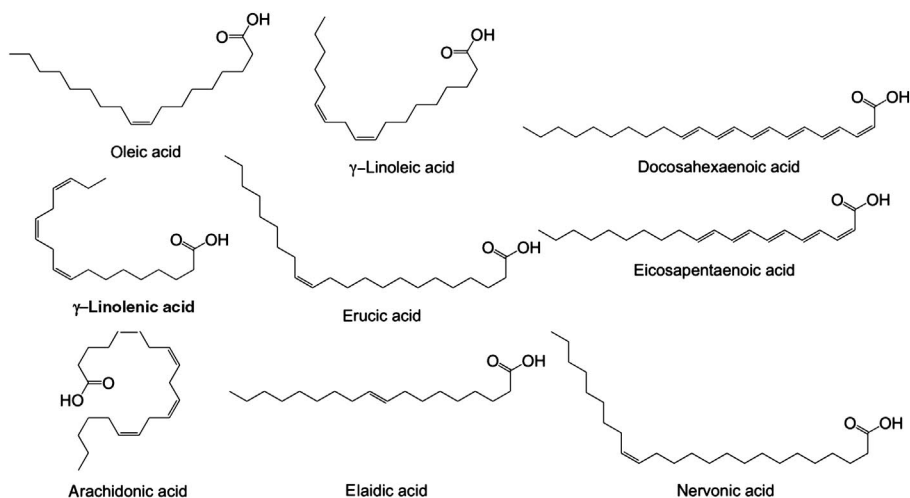
Vijai Shankar Balachandran, Swapnil Rohidas Jadhav, and George John

10.1 Introduction

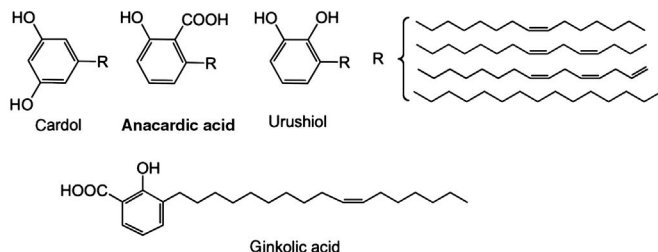
Unsaturated compounds are ubiquitous in Nature. They occupy a pivotal place in a range of hierarchically ordered and highly functional biological structures. Several naturally occurring fatty acids, such as oleic, linoleic, linolenic, and arachidonic acids, present as glycerol esters are unsaturated, and specifically possess *cis*-unsaturations. Polyunsaturated fatty acids that contain one or more double bonds are classified as essential fatty acids and are indispensable for several physiological phenomena such as dietary function and metabolism, energy centers, membrane integrity, and sustenance of active function [1–3]. Having high biological activity, they maintain the structure of cell membranes that participate in cholesterol exchange and also in the synthesis of prostaglandins and other substances. They are also involved in vital processes necessary for proper operation of the optic canal and affect the body's immunity status. Biological molecules such as phospholipids, *N*-acylethanolamides (NAEs), and fatty acids possess at least one side chain with unsaturations [4–7]. Phospholipids are known to be the integral building units of the cellular membrane whereas anandamides and other *N*-acylamino acids are the endogenous agonist of the cannabinoid receptors, recognized for their lipid signaling function in the nervous system [8, 9]. Unsaturated fatty acids linked in the 2-position of phospholipids, varying in type, number, position, and geometric configuration of unsaturated carbon–carbon bonds, are responsible for the broad variation in the biological properties of lipids (cf. Figure 10.1) [10].

Unsaturations of lipids play a key role in lipid homeostasis, where organisms adapt to temperature variations of the environment. Plants and animals maintain physiological functions by reversibly altering the composition and conformation of lipid molecules of the cell membrane. To achieve this, they extensively and elegantly use the unsaturations (double bonds) present in their side chains. This is the process by which cell membranes adjust their flexibility (fluidity) of the bilayer and adapt themselves to perturbations in temperature, pressure, and other variations in the natural environment [11–14]. They remain indispensable for the poikilothermism exhibited by fishes, invertebrates, and amphibians [15, 16]. Commercially,

FATTY ACIDS



PHENOLIC LIPIDS



BIOLOGICALLY ACTIVE MOLECULES

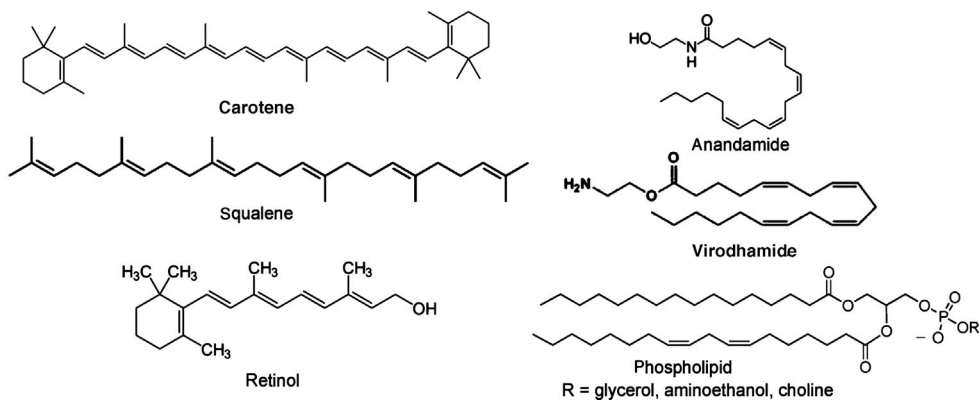


Figure 10.1 Selected examples of naturally available, biologically active unsaturated molecules and the molecular structures.

unsaturated oils are the main components of drying oils and paint formulations where an autoxidation process forms protective and esthetic coatings [17–20].

In view of the interesting and highly functional character of these molecules, the study of the double bonds in the structure of lipid and lipid-like self-assembling molecules has been attracting increased attention [21–23]. Several amphiphilic molecules with unsaturations in their side chains have been synthesized to develop biomimetic materials and have also shown unusual nonideal behavior in their self-assembled micellar state [24, 25]. In addition to offering functionality to embrace and drive these molecules towards utility in materials synthesis, such intriguing molecules are already abundant in Nature, perfect in design and yet remain to be produced in the laboratory. This provides a paradigm for green nanomaterials synthesis. Therefore, unsaturated molecular building blocks from plants are treasures that integrate green chemistry with self-assembly.

10.1.1

Plant/Crop-Based Resources for Practicing Sustainable Chemistry

In the search for methods and processes in sustainable chemistry, considerable importance is being given to raw materials that are renewable. Sustainable and environmentally responsible development is inevitable for the present century. Chemistry has always had a central role when it comes to ecological sustenance and it is indispensable for the economy–ecosphere material flows [26]. It is, however, imperative that current chemical practices should encompass developing the technological dimension of a sustainable civilization. Green or sustainable chemistry contributes to achieving the above goal in the following key aspects: (1) the renewable energy technologies are the axis of a sustainable high-technology civilization; (2) development of the economically feasible conversion of unconventional energy sources into chemical energy, for example for photocatalysis; and (3) increase in green manufacturing practices using the reagents developed or procured from plant/crop-based resources to reduce the carbon footprint [27, 28]. The paradigm shift to biobased feedstocks offers opportunities that are promising for the chemical processing industry. Several reviews addressing the diversity and wealth of renewable raw materials can provide the reader with a comprehensive idea of the efficient and innovative use of biobased products [29, 30]. Utilization of this interdisciplinary practice has started and will be the subject of discussion of this chapter. The concept of supramolecular chemistry is blended with green chemistry and is demonstrated with the help of the self-assembly tool.

Even though efforts have already been made to avoid using petroleum-based starting materials, the total replacement of petroleum-derived products by plant/crop-based chemicals and intermediates is not the governing factor for sustainable/green chemistry. However, it is the inexpensive, abundant availability, renewability and structural diversity of the plant/crop-based products that attract our attention. Nature provides bountiful opportunities for structurally diverse functional materials through its wide variety of raw resources that can rarely be met by fossil fuel-based technologies [31–35]. The building blocks such as sugars, fatty acids, and lipids

allow control of specific recognition events at the molecular level, by constructing nanoscale architectures with increasing structural and/or morphological complexity. This is a repetitive sentence, which occurred in the beginning of this paragraph. At present, oils and fats of vegetable and animal origin make up the major proportion of the current consumption of renewable raw materials utilized by industry.

10.1.2

Self-Assembly and Noncovalent Strategy for the Synthesis of Soft-Materials

Self-assembly is a process common throughout Nature and technology, seen in varied systems from the molecular to the planetary scale, connecting reductionism to complexity and emergence [36]. It is the autonomous organization of components into patterns or structures; the evolution of life is from the self-assembly of living cells which in turn involves organization of enzymes and membranes [37]. Self-assembly is thus one of the few practical strategies for making ensembles of nanostructures, this being a vital part of nanotechnology. Ever since its linguistic inception dating back to 1925, the popular adjective “supramolecular,” meaning “beyond the molecule,” seemed limitlessly elastic [38]. A grandeur view of supramolecular chemistry now has its niche [39] and has become the cynosure in diverse branches of applied and fundamental chemistry, materials chemistry, organic synthesis, and nanodevice fabrication for molecular electronics. The process of self-organization is directed by the molecular information encoded in the covalent framework of the components and is read out at the supramolecular level through specific interaction/recognition patterns. Programmed chemical systems are thus envisioned, which are of major interest for molecularly engineered utilities. Such systems when realized are termed “advanced functional supramolecular materials,” for example, supramolecular polymers [40] and liquid crystals and vesicles [41].

Molecules interact with other molecules through weak interactions ($0.1 \pm 5 \text{ kcal mol}^{-1}$), such as hydrogen bonding, or van der Waals forces, which are collectively known as noncovalent interactions. Such interactions play a key role in fundamental biological processes including protein folding and the expression and transfer of genetic information. This novel synthetic strategy, termed “non-covalent synthesis,” is considered energetically efficient in creating nanostructures on a par with the conventional covalent bonding of atoms. Table 10.1 gives a comparative view of the energetics involved in covalent and noncovalent strategies. Within a molecule, covalent bonds have energies in the range 170–450 kJ mol^{-1} , whereas interactions between molecules are typically much weaker [42]. In general, the enthalpy for intermolecular attractive forces ranges from 8–80 kJ mol^{-1} for a hydrogen bond to 8 kJ mol^{-1} for ionic interactions, and as low as 0.4–2 kJ mol^{-1} for van der Waals or CH–π interactions [43, 44].

When supramolecular chemistry emerged at the forefront of science, it embodied colloid chemistry as one of its facets. A semantic boundary exists between supramolecular chemistry and colloids, as the former involves design logistics *a priori* in addition to preselected synthetic strategies. The simplest kind of colloidal

Table 10.1 Energetics involved in various kinds of noncovalent interactions that play a role in self-assembly.

	Covalent	Non-covalent
Tecton	Atoms	Molecules, ions
Final ensemble	Molecule	Assembly
Molecular identity	1–1000 Da	1–100 kDa
Bond type	Covalent	Ionic, hydrophobic, hydrogen bond, metal–ligand coordination
Bond energy	35–135 kcal mol ⁻¹	2–20 kcal mol ⁻¹
Kinetic stability	High	Low
Thermodynamics	$\Delta H > T\Delta S$	$\Delta H \approx T\Delta S$
Solvent effect	Secondary	Primary
Directionality	Nondirectional	Cooperative

supramolecular assembly formed in three dimensions or more commonly the bulk phase self-assembly is the micelles of amphiphilic molecules. The micelles are in rapid exchange between the individual monomers and therefore are dynamic supramolecular self-assemblies. With increases in concentration, micelles transform into various phases such as lamellar, cubic, and hexagonal, and sometimes under specific conditions to form rod-like micelles. Kunitake and Okahata were the first to report that an ammonium salt with two long alkyl chains formed such liposome-like structures and triggered research into synthetic amphiphiles [45].

The systematic approach of generating amphiphilic building blocks begins with one of two strategies of modifications that are possible with renewable resource-based amphiphiles: either (i) the nonpolar hydrophobic part of the amphiphile can be obtained from biomass and synthetically attached to the polar headgroup, or (ii) the polar hydrophilic headgroups can be acquired from renewable feedstock and converted into amphiphiles by connecting an appropriate hydrophobic group. In this chapter, the focus is on the former, namely lipidic hydrophobic molecules from natural sources that are converted into amphiphiles by appending to polar headgroups such as sugars and amino acids. We specifically enumerate the synthetic capability of an interesting biobased molecule, cardanol, for creating exotic nanostructures such as fibers, helical ribbons, nanotubes, and thermo-reversible gels. The typical examples provide a new paradigm for biobased green nanomaterials with varied functional properties that will provide the reader with a flavor of such intriguing materials.

10.2

Cashew Nut Shell Liquid (CNSL)

10.2.1

Extraction of CNSL and Its Components

The processing of cashew nuts produces an enormous amount of cashew nut shells, which is a potential industrial waste that upon thermal treatment yields a dark-brown

liquid called cashew nut shell liquid (CNSL). Traditionally, the dark-colored nut from the cashew apple is removed manually, soaked in water and later roasted. During the roasting process, the leathery, soft shell becomes brittle and expels the dark CNSL liquid. CNSL is mainly composed of cardanol (60–65%), cardol (15–20%), polymeric material (10%), and traces of methylcardol [46].

Typically, CNSL is composed of number of phenolic lipids, of which the components such as anacardic acid, cardanol, and cardol are commercially important. Cardanol from CNSL is separated from other components by double vacuum distillation at 3–4 mmHg in which the fraction boiling at $220 \pm 15^\circ\text{C}$ is collected as a clear to pale yellow liquid. Cardanol is composed of four different *meta*-alkylated phenols differing in the degree of unsaturation in the side chain: 5% of 3-(pentadecyl)phenol, 50% of 3-(8*Z*-pentadecenyl)phenol, 16% of 3-(8*Z*,11*Z*-pentadecadienyl)phenol, and 29% of 3-(8*Z*,11*Z*,14-pentadecatrienyl)phenol (Figure 10.2). Cardanol, present in the CNSL, is considered to be one of the chief plant-derived renewable resources. It has been used extensively in varied materials such as resins, coatings, frictional materials, and surfactants (Figure 10.3) [47–49]. Cardanol, therefore, has evolved as a vital building block for the synthesis of polymers and fine chemicals and fabrication of materials [50, 51]. In the following part of this chapter, we demonstrate the unsaturations (double bonds) present in the alkyl chain of cardanol and their interesting facets for noncovalent supramolecular synthesis to form nanoscale assemblies, namely lipid nanotubes, gels, and so on. Also, we emphasize their key functional role, which could be conveniently used to tune such soft nanostructures.

10.2.2

Lipid Nanotubes and Helical Fibers from Cardanyl Glycolipids

Cardanol, being a phenolic derivative, possesses functional flexibility for further synthetic modification to generate amphiphiles. The typical structure with a benzene ring (of the phenol) allows π – π stacking and the long C₁₅-alkyl chain confers a lipidic nature that can associate through van der Waals interactions. Interestingly, the non-isoprenoic *cis*-double bonds also provide an opportunity to study systematically the influence of hydrophobic groups, such as the unsaturation of the hydrocarbon chain, on the self-assembly.

The cardanyl glycolipids behave as amphiphilic compounds and are able to self-assemble in water to form twisted fibers, helical coils, and high axial ratio nanotubes

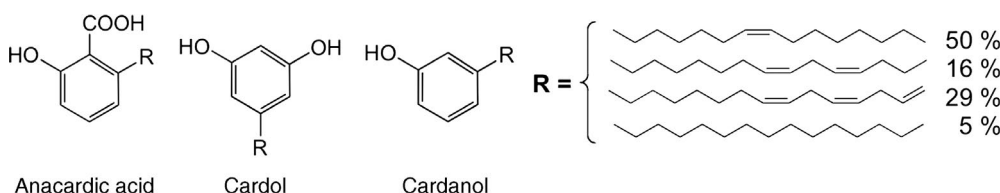


Figure 10.2 Major components of cashew nut shell liquid.

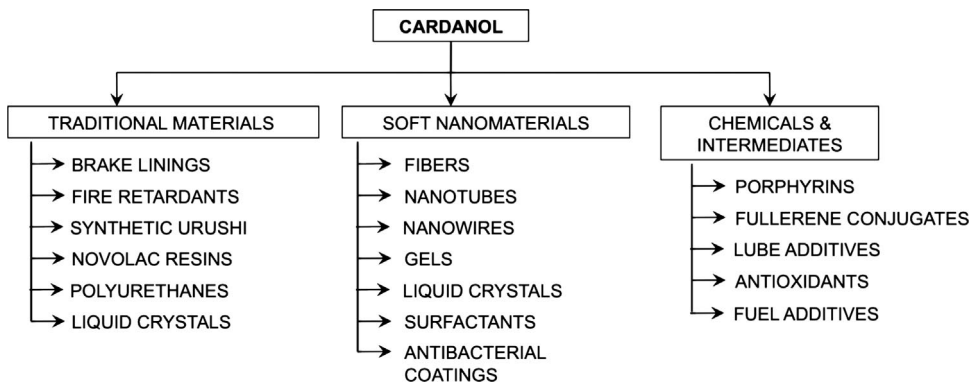


Figure 10.3 Cardanol as a potential material for various applications.

(HARNs) [52], as shown in Figure 10.4. The sugar moiety acts as a nonionic polar headgroup in addition to imparting chirality to the molecule. The glycolipid GLY-1, which is a mixture of four different components with varying numbers of double bonds, forms nanotubes, whereas the fully saturated analog GLY-2 forms twisted fibers. Energy-filtered transmission electron microscopy (EF-TEM) analysis of the nanostructures revealed that the thinnest fibers from GLY-1 are about 30–35 nm with typical helical twisting. Since self-assembly of an amphiphile is dependent on the

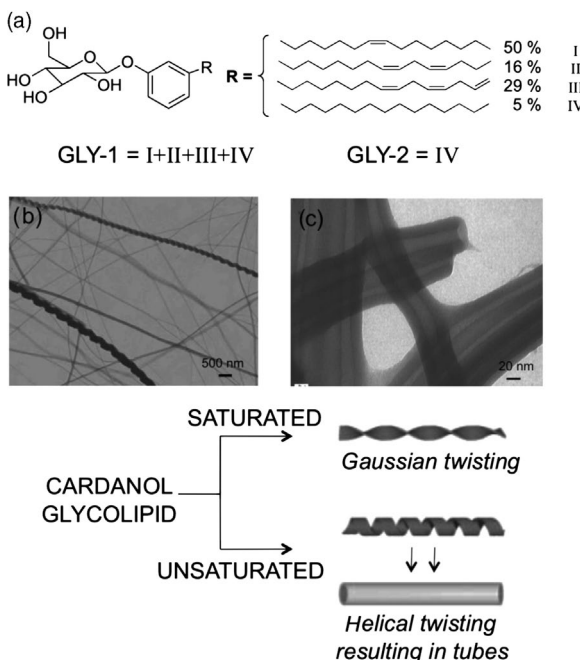


Figure 10.4 (a) Cardanyl glycoside and its constituents. Self-assembled nanostructures of cardanyl glycoside in water: (b) helical and twisted nanofibers and (c) high axial ratio nanotubes (HARNs).

packing of the molecules which in turn is governed by the packing parameter [53, 54], the presence of double bonds and their numbers control the morphology. Accordingly, X-ray analysis of the HARNs revealed a *d*-spacing of 3.9 nm, whereas the fibers from fully saturated side chain had 3.1 nm, reflecting the characteristic difference in the molecular packing.

The influence of the degree of unsaturation on the final morphology of self-assemblies was further dissected by fractionating GLY-1 into the individual components [55]. The study of binary mixtures of saturated and monoene derivatives of cardanyl glycolipids provided a rationale for the control of self-assembled helical structures (Figure 10.4). It was found that 90:10 and 80:20 (saturated:monoene) mixtures generated twisted ribbons in water and no significant effect on the twisted morphology was observed on doping with saturated GLY-2 up to 30–40%. On the other hand, an equimolar (50:50) composition gave a loosely coiled ribbon morphology, which structurally is in between the twisted and tight helical coil.

The HARNs act as well-defined one-dimensional capillaries with inner diameters of 10–100 nm, which could be exploited for templating nanomaterials to fabricate metal nanowires and inorganic nanotubes [56, 57]. Additionally they could be utilized as nanocontainers or channels to preserve and release biomolecules [58]. Water molecules in such an extremely confined space would show a higher level of extended hydrogen bonding. Interestingly, the local solvent polarity (ET_{30}) of the confined water in the nanochannel was estimated as 50 kcal mol⁻¹, which is 20% lower than that of bulk water as estimated from fluorescent probe techniques [59].

These nanotubes were very similar to carbon nanotubes in their dimensions and hence could be considered as an alternative. The bending rigidity *K* was found out to be 2.2×10^{-22} N m². The Young's modulus *E*, given by $E = K/I$, where $I = (d_o^4 - d_i^4)\pi/64$ (d_o and d_i being the outer and inner diameters of the tubule, respectively) was evaluated to be 720 MPa, which is comparable to that of the mechanical properties of biomembranes [60]. These tubules were able to be manipulated using a microinjection technique, thereby opening up the possibility of a nanoscale needle with one-dimensional nanospace for the separation of advanced macromolecules beyond the submicro total analysis system (sub- μ -TAS). Thus, the HARNs behave as well-defined one-dimensional capillaries which find potential applications in template synthesis: (i) nanomaterials to fabricate metal nanowires and inorganic nanotubes [57], (ii) containers for preservation/release of biomolecules, and (iii) nano-pipettes [61].

10.2.3

Self-Assembled Gels from Cardanyl Glycosides

Gels are soft nanomaterials that are formed as a result of a critical balance between precipitation and solubilization of gelator molecules in a given solvent [62, 63]. Gelator molecules are typically low molecular weight (≤ 1000 Da) amphiphilic compounds. A gel of a given solvent is formed when the gelator is allowed to relax from its molecularly dispersed state to the self-assembled state by spontaneous or energy-induced dissolution. Assisted by noncovalent forces, the gelator molecules

self-assemble to form a fibrous network, which entraps the solvent through capillary forces and resists the flow of the medium. The immobilized state is called a gel, which is typically thermo-reversible in nature. The recent demonstrations of molecular gels in applications such as scaffolds for regenerative medicines, electronic and photonic applications, and art conservation illustrate their potential utility [64–70].

The cardanyl glycosides showed self-assembling properties in nonaqueous media to form organogels in a number of organic solvents and also in water-alcohol mixtures (Figure 10.5) [71]. The organogels obtained from cardanyl glycolipid, as analyzed by scanning electron microscopy (SEM), had a three-dimensional network of inter-twisted fibers with a width of 20–30 nm and a pitch of 150–300 nm. The presence of unsaturations was critical in determining the strength of self-assembled gels. The fully saturated chains led to the formation of stronger gels and self-assembled nanofibers compared with the unsaturated analogs.

The presence of the C₁₅ saturated chain displayed an efficient gelling ability in a wide range of organic solvents, water, and protic solvent mixtures (1:1), whereas the unsaturated derivatives (mixture of four molecules) formed fibrous nanostructures as opposed to stronger gels. The diene and triene components of the cardanyl glycosides in their fully hydrated state formed fluid nanostructures at room temperature and could not self-assemble to form gels.

The monoene fraction of GLY-1 was able to gel most of the organic solvents tested such as toluene, cyclohexane, glycerol, and mixtures of solvents such as water-ethanol, water-tetrahydrofuran, and water-acetone. The average T_{gel} (gel melting temperature) for the monoene glycoside was 30 °C, which is ~43% lower than that of GLY-2 (70 °C). The difference in thermal stability has its origin in the extent of packing of alkyl chains in the bilayer assembly. The kinks of the unsaturation prevented efficient van der Waals association of the alkyl chain in the bilayer assembly. As a result, the saturated C₁₅ moiety showed a higher Bragg reflection, suggesting a highly crystalline assembly inside the bilayer. Interestingly, it was the *cis*-double bonds that were the deciding factor in promoting the formation of nanotubes.

The utility of double bonds in tuning the morphology of the nanostructures was inferred by the systematic study of binary mixtures by meticulously fractionating the components. The thermal behavior of the diene (II of GLY-1) and triene (III of GLY-1)

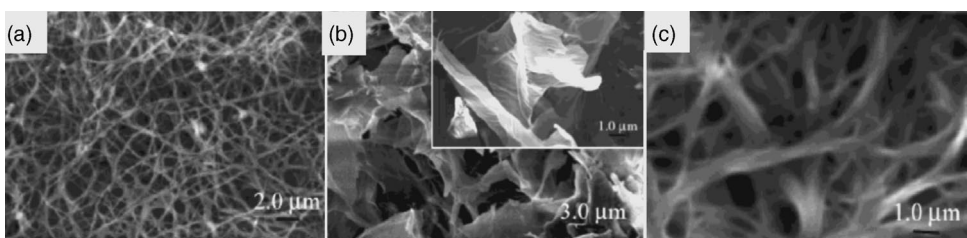


Figure 10.5 SEM images of self-assembled gel from cardanol glycolipids. (a) GLY-2 in cyclohexane; (b) EtOH–H₂O gel of the monoene derivative I; (c) EtOH–H₂O gel of GLY-2. Reprinted with permission from [71] © (2006) American Chemical Society.

in the fully hydrated form showed a gel to liquid crystalline phase at 17.0 and 25.0 °C, respectively, suggesting that their property resulted in more fluid structures at room temperature.

The series of saturated (GLY-2) and monoene derivatives (I of GLY-1) provided a rationale for the control of helicity in the self-assembled structures (Figure 10.4) [72]. For example, 90:10 and 80:20 (GLY-2:monoene) mixtures generated twisted ribbons in water and no significant effect on the twisted morphology was observed on doping with saturated component GLY-2 up to 30–40%. On the other hand, an equimolar (50:50) composition gave a loosely coiled ribbon morphology between the twisted and tight helical coil (Figure 10.6). These studies demonstrate that unsaturations could be used conveniently in designing and controlling the desired morphology of the nanostructures.

The study hinted that the presence of at least one double bond is required in the lipophilic side chain to form twisted nanostructures and impart supramolecular chirality. Studies on the formation of helical nanostructures are limited to the presence of chiral carbon centers and have been well established by Furhop *et al.* [73]. Various hydrophilic chiral moieties such as glucose, galactose, open-chain

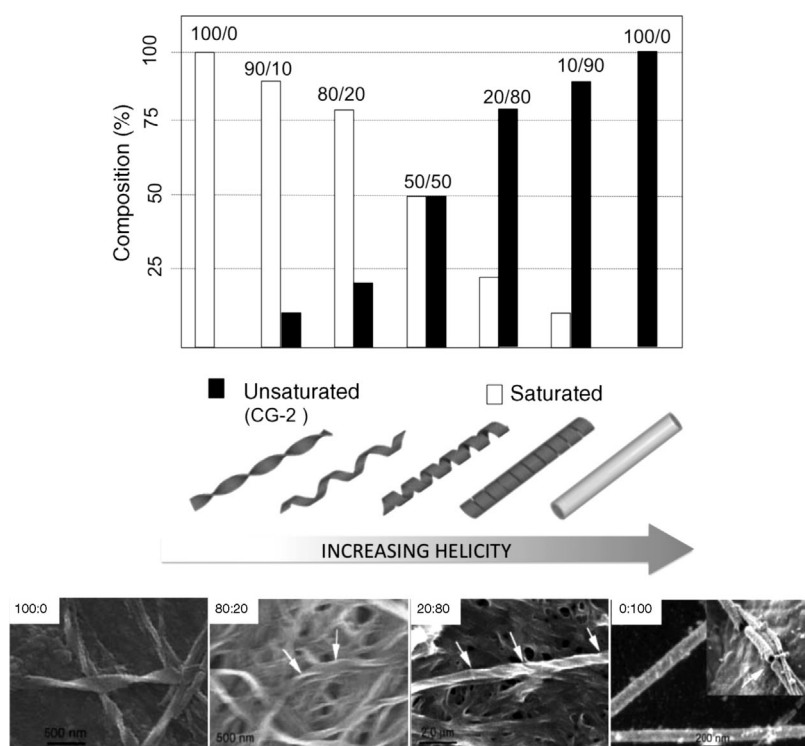


Figure 10.6 Binary self-assembly of cardanyl glycosides forming varied nanofibers of varied helicity upon proper mixing of monoene (GLY-1 I) with GLY-2. Reprinted with permission from [72] © (2002) Wiley-VCH Verlag GmbH.

sugars, and amino acids have been shown to influence the final morphologies. However, the influence of unsaturations on the formation of such helical structures is yet to be fully understood. It has been observed that the number and the position of double bond units had a huge effect on the formation of HARNs.

The hypothesis was tested with a series of glycosides AR-1 to AR-4 that differed in the number of double bonds in the lipophilic part. As expected, AR-1 without any double bonds formed typical nanofibers with diameters of 100–350 nm and lengths of several micrometers in 1:1 methanol–water mixture [74]. Twisted nanofibers of 50–200 nm were observed for AR-2 with one *cis*-unsaturation present at the C-9 position of the lipophilic part, whereas AR-3 with two such double bonds formed a helically coiled tube of inner diameter 150–200 nm (Figure 10.7). Interestingly, the AR-4 derivative with three *cis*-double bonds formed a smooth nanotube with inner diameter 70 nm. Chiroptical studies of the self-assemblies from AR-4, beyond the phase transition temperature of 70 °C, decreased the dichroism, indicative of the lipophilic packing in deciding the supramolecular chirality. The AR-2 derivatives showed a weak dichroism in comparison with AR-3 and AR-4, suggesting that the increase in the degree of double bonds affected the self-assembly with a disordered alkyl chain packing.

The role of *cis*-double bonds in directing helicity and nanotube formation was extended to other kinds of amphiphiles that promote noncovalent assembly to validate their vital role in forming high-curvature architectures. For example, diaminopyridine alkylamides with a sugar headgroup formed self-assembled helical fibers and nanotubes [75] that depended on the presence of a *cis*-double bond in the lipophilic part (Figure 10.8). The derivative DAP-1 with a *cis*-double bond at C-8 in the side chain formed helical nanofibers that progressively formed nanotubes with an inner diameter of 20 nm and a wall thickness of 20–30 nm. However, DAP-2, the fully saturated analog, formed fibrous assemblies of 80–150 nm. X-ray analysis of the nanotubes and helical fibers from DAP-1 showed a longer bilayer spacing on a par with DAP-2, indicating greater interdigitated packing of the alkyl chains in the latter. The kink in the self-assembled structures of DAP-1 appears to increase the fluidity of

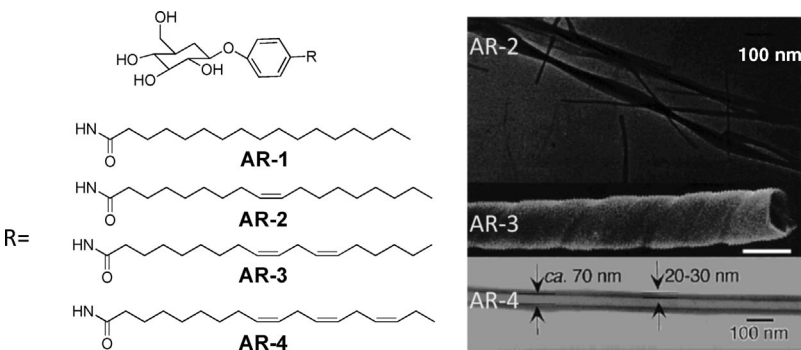


Figure 10.7 Effect of unsaturations in long-chain arylglycosides forming nanofibers and nanotubes. Reprinted with permission from [74] © (2004) American Chemical Society.

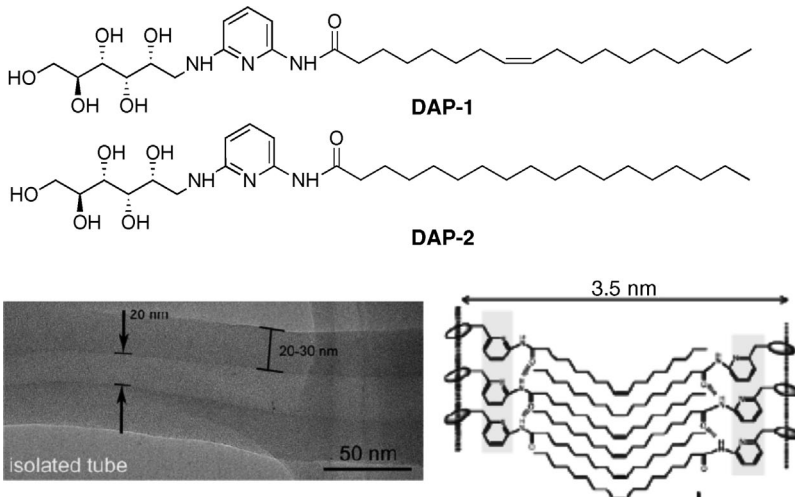


Figure 10.8 Nanotube formation upon introducing a *cis*-double bond in a diaminopyridine alkylamide and their corresponding alkyl chain packing in DAP-2. Reprinted with permission from [75] © (2004) American Chemical Society.

the assembly, allowing more facile formation of a nanotube. Furthermore, the C–H stretching peaks were shifted to 2854 cm^{-1} for DAP-2, consistent with a more crystalline structure for the nanofibers.

Kamiya *et al.* delved further into unraveling such an interesting tool and showed that the position of the double bonds with respect to the headgroups was also a directing factor for the formation of lipid nanotubes [76]. Thus, glucopyranosylamide lipids were synthesized with a progressive shift in the position of the double bonds from C-6 to C-13 (from the carbonyl carbon attached to the sugar headgroup). Among the series of glycolipids, the 11-*cis* derivative formed smooth nanotubes of diameter 200 nm with >98% yield. The position of the double bond significantly influenced the homogeneity of the outer diameters and also growth behavior of the self-assembled nanotubes (Figure 10.9).

Interestingly, the nanotubes from the 11-*cis* derivatives were smooth, indicating no helical markings on the outer surfaces. This is an exciting observation in view of the extensive observations relating the chirality of the diacetylenic phospholipid-derived lipid nanostructures to helical handedness and chirality [77]. Upon shifting the position of the double bond from C-11 to C-9, the size distribution of the outer and inner diameters of the nanotubes become less uniform compared with that obtained from the 11-*cis* derivative. Also, the position of the double bonds had no influence on the average outer diameters but significantly affected the distribution width. Table 10.2 gives the self-assembled morphologies of various unsaturated glycosyl lipids and their nanotube dimensions [76]. Thus, the above examples rationalize the exciting utility of unsaturations, particularly the *cis*-double bonds, in fabricating lipid nanotubes and other soft nano-assemblies.

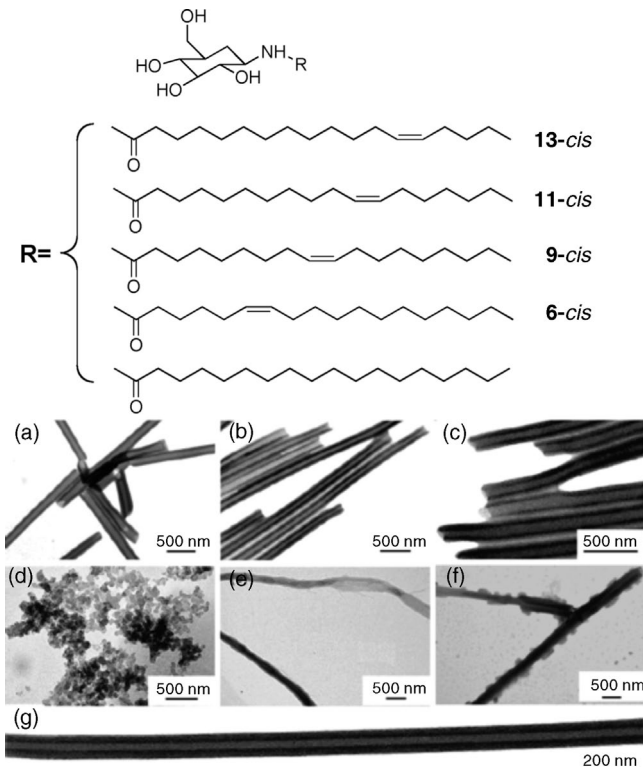


Figure 10.9 Unsaturated glycolipids with varying positions of the *cis*-double bond and the corresponding EF-TEM images of the self-assemblies; (a) 13-*cis*; (b) 11-*cis*; (c) 9-*cis*;

(d) 6-*cis*; (e) fibers from 6-*cis*; (f) deformed tube from saturated derivative; (g) smooth nanotube from 11-*cis*. Reprinted with permission from [76] © (2005) American Chemical Society.

10.2.4

Antibacterial Nanocomposite Films for Coatings

The use of vegetative resources in paint formulations and coatings has been a well-practiced technology since its inception dating back to the Egyptian civilization to protect surfaces from corrosion and degradation and also for decorative and esthetic purposes [78]. Common household oil paint uses vegetable oils such as linseed or soy bean oil as the medium in which various components are dispersed. When the oil medium dries, they cross-link themselves upon exposure to air by a chemical reaction called autoxidation [79]. Cardanol, by virtue of the double bonds present in their side chain and its inherent character of undergoing autoxidation to form polymeric films, is a potential medium for paint formulations [80, 81]. The greater the number of such unsaturations, the higher is the cross-linking ability. Therefore, aligning double bond-rich cardanol alkyl tails by tethering or polymerizing the phenolic moiety would enhance the cross-linking ability and also form self-assembled aligned

Table 10.2 Self-assemblies from the unsaturated glycolipids and their typical size and dimensions. Reprinted with permission from [76] © (2005) American Chemical Society^{a)}.

Glycolipid	Self-assembled morphology		Outer diameter D_{out}	Inner diameter D_{in}		Wall thickness ^{b)}	
	Major	Minor		A.v ^{c)} (nm)	S.d. ^{d)} (nm)	A.v ^{c)} (nm)	S.d. ^{d)} (nm)
1	Nanotube (~90%)	Amorphous aggregate (~10%)	214	55	76	26	60
2	Nanotube (>98%)	Was not observed	200	23	81	19	54
3	Nanotube (~90%)	Amorphous aggregate (~10%)	220	71	73	22	63
4	Amorphous aggregate (~80%)	Fiber (~20%)					
5	Amorphous aggregate (~70%)	Nanotube (~30%)					
6	Amorphous aggregate (>98%)						

a) Evaluated for 250 pieces of lipid nanotubes.

b) Thickness was also evaluated by measuring the distances of lipid nanotube walls. Therefore, the subtraction values of D_{in} from D_{out} are not always consistent with the values twice that of the wall thickness.

c) Average value.

d) Standard deviation.

structures. For example, aligned unsaturated side chains of poly(cardanyl acrylate) were able to form clear, scratch-free, transparent films when coated on surfaces and exposed to air.

The behavior was closely similar to that of conventional drying oils. Since the process is mediated through the formation of free radicals, concurrently it was also able to reduce any metal ions present in the medium to form the corresponding nanoparticles. The advantage is that the cross-linked medium itself acted as the protecting agent and therefore no external reducing agent/stabilizing agent is required for the formation of nanoparticles. The result is the creation of a free-standing, transparent film embedded with nanoparticles. This property was utilized for metal ions such as Au(III) and Ag(I) to form the corresponding gold and silver nanoparticle-embedded organic-inorganic nanocomposite films. As a control experiment, polymer with a saturated hydrocarbon chain, poly(pentadecylphenyl acrylate), failed to undergo oxidative drying due to the absence of essential unsaturation in the side chains that prevented nanoparticle formation in the matrix [82]. Similarly, small molecules with multipod structures with sufficient crowding of the unsaturations, such as hexakisbenzo derivatives of cardanol [83], were able to become cross-linked upon exposure to air and concurrently form gold and silver nanoparticle-embedded

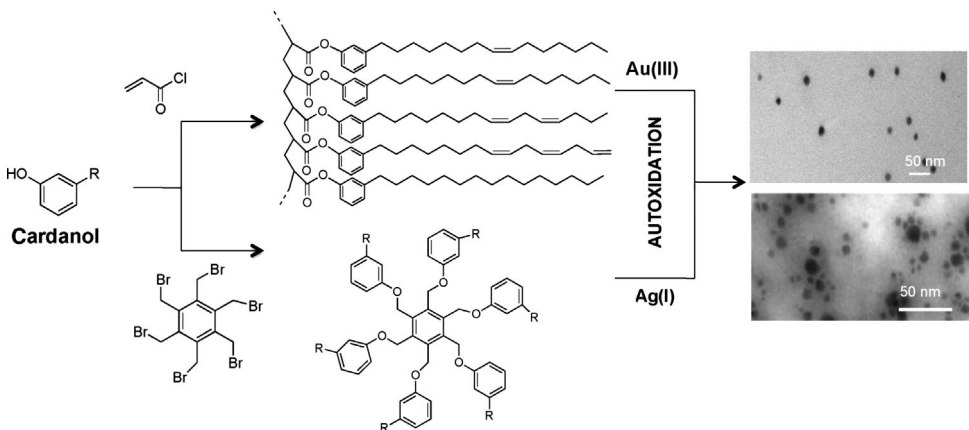


Figure 10.10 Antibacterial coatings and nanoparticle-embedded films obtained by cross-linking of double bonds by autoxidation.

polymeric films (Figure 10.10). The embedded Ag nanoparticles, because of their antibacterial activity, made the coatings effective in destroying the airborne Gram-positive human pathogen *Staphylococcus aureus* and Gram-negative *Escherichia coli* [84, 85].

10.2.5

Stimuli-Responsive Nature of Unsaturations

Cardanol has non-isoprenoic double bonds, very similar to the naturally occurring lipids and fatty acids such as oleic, linoleic, and linolenic acids. These double bonds are responsive to changes in temperature and hence can mimic homeoviscous alterations. Since cardanol has varying degrees of unsaturations in the form of *cis*-double bonds, one can envision an amphiphile, which shows thermo-responsive behavior, that could be utilized to reconfigure into functional architectures [86]. Cardanol has a structure very similar to that of linear alkylbenzenes (LABs), which are the most commonly used industrial and household surfactants. Therefore, surfactants could be conveniently synthesized from cardanol by appending appropriate headgroups to the phenolic moiety. However, it should be borne in mind that the reconfiguration of phases in response to temperature has to be at the cost of other noncovalent interactions prevalent in the molecule. A proper choice of headgroup with an appropriate linker would therefore be necessary in the molecular design. Recently a cardanol–taurine conjugate has shown such interesting thermal responsive behavior [87]. The molecule, *N*-cardanyltauramide, in which cardanol as the hydrophobic part is attached to an aminosulfonic acid through an amide linkage, behaved as a room temperature surfactant with a critical micellar concentration (CMC) of 1.2 mM (Figure 10.11). When the micellar solution is warmed, thermal fluctuations develop in the alkyl chains. The increased chain mobility leads to favorable conformations for a micelle to bilayer transformation and during

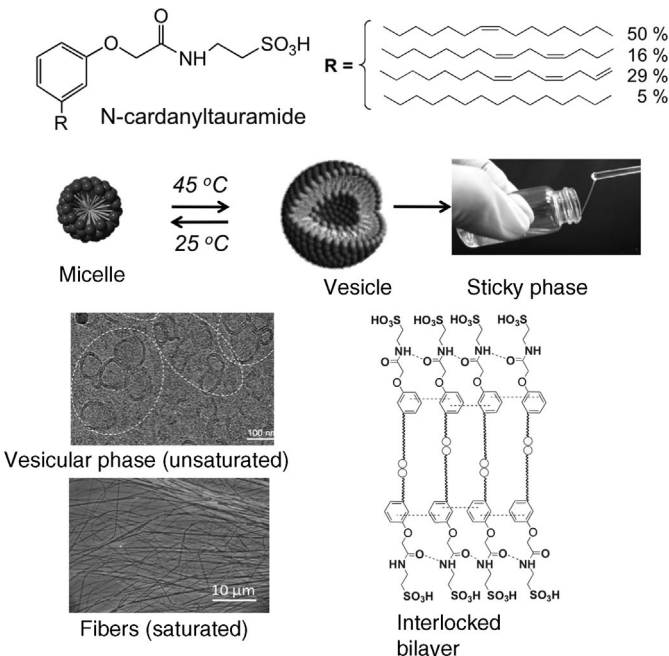


Figure 10.11 Adaptive response nature of *cis*-double bonds in *N*-cardanyltauramide that undergoes micelle–vesicle–micelle transition with respect to temperature.

reassemble the shorter kinked and longer extended alkyl chains interlock in the bilayer arrangement and eventually undergo curvature, forming individual vesicular structures. The stability of the assembly is complemented by the directional hydrogen bonding of the amide linkage, together with the π–π stacking of the aromatic ring. The vesicular phase was found to be stable in the temperature range 37–45 °C and reverted back to the micellar phase at room temperature.

10.3 Conclusion

Unsaturations in amphiphilic systems have the potential to exhibit a functional character in Nature, where the flora and fauna elegantly utilize such intriguing moieties for intricate biophysical phenomena such as cell membrane fluidity and integrity, dietary functions, and several other transmembrane processes. This has given colloid and material researchers a new paradigm to explore and employ in noncovalent syntheses of soft materials. Apart from such materials being abundant in Nature, they are obtained from plants and other bio based feedstocks, and provide opportunities for bio based synthesis and practice of green chemistry. The examples provided in this chapter in making hierarchical nanostructures such as nanofibers, gels, and nanotubes demonstrate the interesting role of double bonds in soft material

synthesis. However, they are not limited to the mentioned systems but extend to other similar unsaturated amphiphiles, thus acting as classical examples. The amalgamation of supramolecular and green chemistry would therefore open the avenue for new advances in the development of responsive and biomimetic soft materials.

References

- 1 Murphy D.J. (ed.) (2000) *Plant Lipids Biology, Utilization and Manipulation*, CRC Press, Boca Raton, FL.
- 2 Thompson Jr. G.A. (ed.) (2000) *The Regulation of Membrane Lipid Metabolism*, 2nd ed., CRC Press, Boca Raton, FL.
- 3 Subczynski, W.K. and Wisniewska, A. (2000) Physical properties of lipid bilayer membranes: relevance to membrane biological functions. *Acta Biochimica Polonica*, **47** (3), 613–625.
- 4 Sagnella, S.M., Conn, C.E., Krodkiewska, I., Moghaddam, M., Seddonand, J.M. and Drummond, C.J. (2010) Ordered nanostructured amphiphile self-assembly materials from endogenous nonionic unsaturated monoethanolamide lipids in water. *Langmuir*, **26** (5), 3084–3094.
- 5 Porter, A.C. and Felder, C.C. (2001) The endocannabinoid nervous system: unique opportunities for therapeutic intervention. *Pharmacology & Therapeutics*, **90** (1), 45–60.
- 6 Nakano, M., Karno, T., Sugita, A. and Handa, T. (2005) Detection of bilayer packing stress and its release in lamellar–cubic phase transition by time-resolved fluorescence anisotropy. *Journal of Physical Chemistry B*, **109** (10), 4754–4760.
- 7 Seddon, J.M., Squires, A.M., Conn, C.E., Ces, O., Heron, A.J., Mulet, X., Shearman, G.C. and Templer, R.H. (2006) Pressure-jump X-ray studies of liquid crystal transitions in lipids. *The Royal Society of London. Philosophical Transactions. Series A. Mathematical, Physical and Engineering Sciences*, **364** (1847), 2635–2655.
- 8 Sagnella, S.M., Conn, C.E., Krodkiewska, I., Mulet, X. and Drummond, C.J. (2011) Anandamide andanalogous endocannabinoids: a lipid self-assembly study. *Soft Matter*, **7**, 5319–5328.
- 9 Wells, D., Fong, C. and Drummond, C.J. (2006) Nonionic urea surfactants: formation of inverse hexagonal lyotropic liquid crystalline phases by introducing hydrocarbon chain unsaturation. *Journal of Physical Chemistry B*, **110** (25), 12660–12665.
- 10 Vysotsky, Y.B., Belyaeva, E.A., Fainerman, V.B., Vollhardt, D., Aksenenko, E.V. and Miller, R. (2009) Thermodynamics of the clusterization process of *cis* isomers of unsaturated fatty acids at the air/water interface. *Journal of Physical Chemistry B*, **113** (13), 4347–4359.
- 11 Mansilla, M.C., Cybulski, L.E., Albanesi, D. and de Mendoza, D. (2004) Control of membrane lipid fluidity by molecular thermosensors. *Journal of Bacteriology*, **186** (20), 6681–6688.
- 12 Zhang, Y.-M. and Rock, C.O. (2008) Membrane lipid homeostasis in bacteria. *Nature Reviews Microbiology*, **6**, 222–233.
- 13 Murata, N., Nishizawa, O.-I., Higashi, S., Hayashi, H., Tasaka, Y. and Nishida, I. (1992) Genetically engineered alteration in the chilling sensitivity of plants. *Nature*, **356**, 710–713.
- 14 Cossins, A.R. and Macdonald, A.R. (1989) The adaptation of biological membranes to temperature and pressure: fish from the deep and cold. *Journal of Bioenergetics and Biomembranes*, **21** (1), 115–135.
- 15 Willmer, P., Stone, G. and Johnston, I.A. (2000) *Environmental Physiology of Animals*, Blackwell Science, Oxford.
- 16 Sinensky, M. (1974) Homeoviscous adaptation – a homeostatic process that regulates the viscosity of membrane lipids in *Escherichia coli*. *Proceedings of the National Academy of Sciences of the*, **71** (2), 522–525.
- 17 van Gorkum, R. and Bouwman, E. (2005) The oxidative drying of alkyd paint catalysed by metal complexes. *Coordination Chemistry Reviews*, **249**, 1709–1728.

- 18 Bieleman, J.H. (2000) *Additives for Coatings*, Wiley-VCH Verlag GmbH, Weinheim.
- 19 Reich, L. and Stivala, S. (1969) *Autoxidation of Hydrocarbons and Polyolefins*, Marcel Dekker, New York.
- 20 Lewis, K. and Klibanov, A.M. (2005) Surpassing nature: rational design of sterile-surface materials. *Trends in Biotechnology*, **23**, 343–348.
- 21 Damas, C., Vannier, L., Naejus, R. and Couder, R. (1999) Influence of structural modifications near the polar head of sodium carboxylates on their aqueous solution behaviour. *Colloids and Surfaces A: Physicochemical and Engineering Aspects*, **152**, 183–187.
- 22 Larabee, C.E., Jr. and Sprague, E.D. (1986) Aggregation of sodium undecanoate and sodium 10-undecenoate in water at 37°C: vapor pressure osmometry. *Journal of Colloid and Interface Science*, **114** (1), 256–260.
- 23 Yokoyama, S. and Nakagaki, M. (1993) Effect of double bond on the surface properties of aqueous solutions of eicosapolyenoic acids. *Colloid and Polymer Science*, **271** (5), 512–518.
- 24 Sierra, M.B., Morini, M.A., Schulz, P.C., Junquera, E. and Aicart, E. (2007) Effect of double bonds in the formation of sodium dodecanoate and sodium 10-undecenoate mixed micelles in water. *Journal of Physical Chemistry B*, **111** (40), 11692–11699.
- 25 Sierra, M.B., Morini, M.A., Schulz, P.C. and Ferreira, M.L. (2005) Unusual volumetric and hydration behavior of the catanionic system sodium undecenoate:sodium decyltrimethylammonium bromide. *Colloid and Polymer Science*, **283** (9), 1016–1024.
- 26 Collins, T. (2001) Toward sustainable chemistry. *Science*, **291** (5501), 48–49.
- 27 Anastas, P.T. and Zimmerman, J.B. (2003) Design through the 12 principles of green engineering. *Environmental Science and Technology*, **37** (5), 94A–101A.
- 28 Anastas, P.T. and Warner, J. (1998) *Green Chemistry: Theory and Practice*, Oxford University Press, New York.
- 29 Herrera, S. (2004) Industrial biotechnology – a chance at redemption. *Nature Biotechnology*, **22** (6), 671–675.
- 30 Corma, A., Iborra, S. and Velty, A. (2007) Chemical routes for the transformation of biomass into chemicals. *Chemical Reviews*, **107** (6), 2411–2502.
- 31 Clark J.H. and Deswarte F. (eds.) (2008) *Introduction to Chemicals from Biomass*, John Wiley & Sons, Ltd., Chichester.
- 32 Vemula, P.K. and John, G. (2008) Crops: a green approach toward self-assembled soft materials. *Accounts of Chemical Research*, **41** (5), 769–782.
- 33 John, G. and Vemula, P.K. (2006) Design and development of soft nanomaterials from biobased amphiphiles. *Soft Matter*, **2**, 909–914.
- 34 John, G., Shankar, B.V., Jadhav, S.R. and Vemula, P.K. (2010) Biorefinery: a design tool for molecular gelators. *Langmuir*, **26** (23), 17843–17851.
- 35 Bierman, U., Friedt, W., Lang, S., Luhs, W., Machmuller, G., Metzger, J.O., Ruschmgen Klass, M., Schafer, H.J. and Schneider, M.P. (2000) New syntheses with oils and fats as renewable raw materials for the chemical industry. *Angewandte Chemie International Edition*, **39** (13), 2206–2224 and references therein.
- 36 Whitesides, G.M. and Grzybowski, B. (2002) Self-assembly at all scales. *Science*, **295** (5564), 2418–2421.
- 37 Dance, I. (2003) What is supramolecular? *New Journal of Chemistry*, **27**, 1–2.
- 38 Bergmann, M. (1925) AT Über den hochmolekularen Zustand von Kohlenhydraten und Proteinen und seine Synthese. *Z. Angew. Chem.*, **38** (50), 1141–1144.
- 39 Lehn, J.-M. (2002) Supramolecular chemistry and self-assembly special feature: toward complex matter: supramolecular chemistry and self-organization. *Proceedings of the National Academy of Sciences of the USA*, **99** (8), 4763–4768.
- 40 Brunsved, L., Folmer, B.J.B., Meijer, E.W. and Sijbesma, R.P. (2001) Supramolecular polymers. *Chemical Reviews*, **101** (12), 4071–4098.
- 41 Menger, F.M. (2002) Supramolecular chemistry and self-assembly. *Proceedings of the National Academy of Sciences of the USA*, **99** (8), 4818–4822.
- 42 Goshe, A.J., Steele, I.M., Ceccarelli, C., Rheingold, A.L. and Bosnich, B. (2002) Supramolecular chemistry and self-assembly special feature: supramolecular recognition: on the kinetic lability of thermodynamically stable host-guest association complexes. *Proceedings of the*

- National Academy of Sciences of the USA, **99** (8), 4823–4829.
- 43** Prins, L., Reinhoudt, D.N. and Timmerman, P. (2001) Noncovalent synthesis using hydrogen bonding. *Angewandte Chemie International Edition*, **40** (13), 2382–2426.
- 44** Meyer, E.A., Castellano, R.K. and Diederich, F. (2003) Interactions with aromatic rings in chemical and biological recognition. *Angewandte Chemie International Edition*, **42** (11), 1210–1250.
- 45** Kunitake, T. and Okahata, Y. (1977) Totally synthetic bilayer membrane. *Journal of the American Chemical Society*, **99** (11), 3860–3861.
- 46** Tyman, J.H.P. (2008) *Synthetic and Natural Phenols*, Elsevier, Amsterdam.
- 47** Pathak, S.K. and Rao, B.S. (2006) Structural effect of phenalkamines on adhesive viscoelastic and thermal properties of epoxy networks. *Journal of Applied Polymer Science*, **102** (5), 4741–4748.
- 48** Saminathan, M. and Pillai, C.K.S. (2000) Synthesis of novel liquid crystalline polymers with cross-linked network structures. *Polymer*, **41** (8), 3103–3108.
- 49** Alexander, H.T. (2008) “A nutty chemical.” *Chemical and Engineering News*, **86** (36), 26–27.
- 50** Mele, G. and Vasapollo, G. (2008) Fine chemicals and new hybrid materials from cardanol. *Mini-Reviews in Organic Chemistry*, **5**, 248–253.
- 51** Talbiersky, J., Polaczek, J., Ramamoorthy, R. and Shishlov, O. (2000) Phenols from cashew nut shell oil as a feedstock for making resins and chemicals. *OIL GAS European Magazine*, **35**, 33–40.
- 52** John, G., Masuda, M., Okada, Y., Yase, K. and Shimizu, T. (2001) Nanotube formation from renewable resources via coiled nanofibers. *Advanced Materials*, **2001**, **13**, 715–718.
- 53** Israelachvili, J.N. (1991) *Intermolecular and Surface Forces*, Academic Press, London.
- 54** Pashley, R.M. and Karaman, M.E. (2004) *Applied Colloid and Surface Chemistry*, John Wiley & Sons, Ltd., Chichester, p. 69.
- 55** John, G., Jung, J.-H., Minamikawa, H., Yoshida, K. and Shimizu, T. (2002) Morphological control of helical solid bilayers in high-axial-ratio nanostructures through binary self-assembly. *Chemistry-A European Journal*, **8** (23), 5494–5500.
- 56** Guo, X. and Matsui, H. (2005) Peptide-based nanotubes and their applications in bionanotechnology. *Advanced Materials*, **17** (17), 2037–2050.
- 57** Zhou, Y. and Shimizu, T. (2008) Lipid nanotubes: a unique template to create diverse one-dimensional nanostructures. *Chemistry of Materials*, **20** (3), 625–633.
- 58** Nogawa, K., Tagawa, Y., Nakajima, M., Arai, F., Shimizu, T., Kamiya, S. and Fukuda, T. (2007) Development of novel nanopipette with a lipid nanotube as nanochannel. *Journal of Robotics and Mechatronics*, **19** (5), 528–534.
- 59** Yui, H., Guo, Y., Koyama, K., Sawada, T., John, G., Yang, B., Masuda, M. and Shimizu, T. (2005) Local environment and property of water inside the hollow cylinder of a lipid nanotube. *Langmuir*, **21** (2), 721–727.
- 60** Fujima, T., Frusawa, H., Minamikawa, H., Ito, K. and Shimizu, T. (2006) Elastic precursor of the transformation from glycolipid nanotube to vesicle. *Journal of Physics: Condensed Matter*, **18**, 3089–3096.
- 61** Kameta, N., Minamikawa, H., Masuda, M., Mizuno, G. and Shimizu, T. (2008) Controllable biomolecule release from self-assembled organic nanotubes with asymmetric surfaces: pH and temperature dependence. *Soft Matter*, **4** (8), 1681–1688.
- 62** Weiss R.G. and Terech P. (eds.) (2006) *Molecular Gels: Materials with Self-Assembled Fibrillar Networks*, Springer, Dordrecht.
- 63** Fages F. (ed.) (2005) *Low Molecular Mass Gelators: Design, Self-Assembly Function, Topics in Current Chemistry*, Vol. 256 Springer, New York.
- 64** Xu, B. (2009) Gels as functional nanomaterials for biology and medicine. *Langmuir*, **25** (15), 8375–8377.
- 65** Ajayagosh, A. and Praveen, V.K. (2007) π-Organogels of self-assembled *p*-phenylenevinylanes: soft materials with distinct size, shape, and functions. *Accounts of Chemical Research*, **2007**, **40** (8), 644–656.
- 66** Estroff, L.A. and Hamilton, A.D. (2004) Water gelation by small organic molecules. *Chemical Reviews*, **4**, 1201–1218.
- 67** van Esch, J.H. and Feringa, B.L. (2000) New functional materials based on

- self-assembling organogels: from serendipity towards design. *Angewandte Chemie International Edition*, **39** (13), 2263–2266.
- 68** Hirst, A.R., Escuder, B. and Miravet, J.F. and Smith, D.K. (2008) High-tech applications of self-assembling supramolecular nanostructured gel-phase materials: from regenerative medicine to electronic devices. *Angewandte Chemie International Edition*, **47** (42), 8002–8018.
- 69** Zhao, F., Mab, M.-L. and Xu, B. (2009) Molecular hydrogels of therapeutic agents. *Chemical Society Reviews*, **38** (4), 883–891.
- 70** Garretti, E., Deia, L. and Weiss, R.G. (2005) Soft matter and art conservation. Rheoreversible gels and beyond. *Soft Matter*, **1**, 17–22.
- 71** John, G., Jung, J.-H., Masuda, M. and Shimizu, T. (2001) Self-assembly of a sugar-based gelator in water: its remarkable diversity in gelation ability and aggregate structure. *Langmuir*, **17** (23), 7229–7232.
- 72** John, G., Jung, J.-H., Masuda, M. and Shimizu, T. (2004) Unsaturation effect on gelation behavior of aryl glycolipids. *Langmuir*, **20** (6), 2060–2065.
- 73** Furhop, J.-H., Svenson, S., Boettcher, C., Roessler, E. and Vith, H.-M. (1990) Long-lived micellar *N*-alkylaldonamide fiber gels. Solid-state NMR and electron microscopic studies. *Journal of the American Chemical Society*, **112**, 4307–4312.
- 74** Jung, J.-H., John, G., Yoshida, K. and Shimizu, T. (2004) Self-assembling structures of long-chain phenyl glucoside influenced by the introduction of double bonds. *Journal of the American Chemical Society*, **124** (36), 10674–10675.
- 75** John, G., Mason, M., Ajayan, P.M. and Dordick, J.S. (2004) Lipid-based nanotubes as functional architectures with embedded fluorescence and recognition capabilities. *Journal of the American Chemical Society*, **2004**, **126** (46), 15012–15013.
- 76** Kamiya, S., Minamikawa, H., Jung, J.-H., Yang, B., Masuda, M. and Shimizu, T. (2005) Molecular structure of glucopyranosylamide lipid and nanotube morphology. *Langmuir*, **21** (2), 743–750.
- 77** Schnur, J.M. (1993) Lipid tubules: a paradigm for molecularly engineered structures. *Science*, **262** (5140), 1669–1676.
- 78** Talbert, R. (2007) *Paint Technology Handbook*, CRC Press, Boca Raton, FL.
- 79** Yin, H. and Porter, N.A. (2005) New insights regarding the autoxidation of polyunsaturated fatty acids. *Antioxidants & Redox Signaling*, **7**, 170–184.
- 80** John, G. and Pillai, C.K.S. (1992) Self-crosslinkable monomer from cardanol: crosslinked beads of poly(cardanyl acrylate) by suspension polymerization. *Makromolekulare Chemie Rapid Communications*, **13**, 255–259.
- 81** John, G. and Pillai, C.K.S. (1993) Synthesis and characterization of a self-crosslinkable polymer from cardanol: autoxidation of poly(cardanyl acrylate) to crosslinked film. *Journal of Polymer Science Part A: Polymer Chemistry*, **31**, 1069–1073.
- 82** Kumar, A., Vemula, P.K., Ajayan, P.M. and John, G. (2000) Silver-nanoparticle-embedded antimicrobial paints based on vegetable oil. *Nature Materials*, **7**, 236–241.
- 83** Jyothish, K., John, G., Vemula, P.K., Jadhav, S.R. and Francesconi, L.C. (2009) Self-standing, metal nanoparticle embedded transparent films from multi-armed cardanol conjugates through *in situ* synthesis. *Chemical Communications*, 5368–5370.
- 84** Morones, J.R. (2005) The bactericidal effect of silver nanoparticles. *Nanotechnology*, **16** (10), 2346–2353.
- 85** Martínez-Castañón, G.A., Niño-Martínez, N., Gutierrez, F.M., Mendoza, J.R.M. and Ruiz, F. (2008) Synthesis and antibacterial activity of silver nanoparticles with different sizes. *Journal of Nanoparticle Research*, **10** (8), 1343–1348.
- 86** Murray, S.M., O'Brien, R.A., Mattson, K.M., Ceccarelli, C., Sykora, R.E. and West, K.N. Jr. (2010) Fluid-mosaic model, homeoviscous adaptation, and ionic liquids: dramatic lowering of the melting point by side-chain unsaturation. *Angewandte Chemie International Edition*, **49** (15), 2755–2758.
- 87** Balachandran, V.S., Jadhav, S.R., Pradhan, P., Carlo, S.D. and John, G. (2010) Adhesive vesicles through adaptive response of a biobased surfactant. *Angewandte Chemie International Edition*, **49** (49), 9509–9512.